TECHNISCHE UNIVERSITÄT WIEN

DISSERTATION

Adsorption of Small Molecules and Metal Adatoms on Complex Oxide Surfaces: A Density Functional Theory Study

Ausgeführt zum Zwecke der Erlangung des akademischen Grades eines Doktors der technischen Wissenschaften unter der Leitung von

AO.UNIV.PROF. DR.TECHN. JOSEF REDINGER

und

PRIVATDOZ. DR.TECHN. FLORIAN MITTENDORFER

INSTITUT FÜR ANGEWANDTE PHYSIK E134

CENTER FOR COMPUTATIONAL MATERIALS SCIENCE

eingereicht an der Technischen Universität Wien
Fakultät für Physik

von

DIPL.-ING. WERNFRIED MAYR-SCHMÖLZER

e0125752
Rudolfsplatz 4/27
1010 Wien

Wien, am 6. September 2018

Acknowledgements

Abstract

Transition metal oxides are used for many chemical and physical applications. These include catalysis, sustainable energy generation in solid oxide fuel cells (SOFC), or sensory products. They exhibit a large variety of physical and chemical properties which can often be tuned by external parameters like strain, doping, or the application of electric or magnetic fields. In many cases, these oxides are used as support materials for catalysts or show an intrinsic catalytic ability. Therefore, a good understanding of their surface properties is crucial to improve their current applications or to find new ones.

The focus of this thesis is the study of the surface properties of certain transition metal oxides which are already used in SOFCs. Density functional theory (DFT) has shown its ability to provide a good description of both bulk and surface properties of many materials and is the main tool used to further the understanding of the studied materials. In this work, it was used as the workhorse method to provide an atomistic understanding of the surface properties of transition metal oxides. In all cases, the comparison with accompanying experiments conducted by various partnering groups highlights the viability of such an approach.

In the first part of this work, the adsorption of ultra-thin films of Zirconia (ZrO_2) on the (111) surfaces of metal substrates like pure Platinum and alloys of Platinum and Palladium containing Zirconium (Pt_3Zr, Pd_3Zr) was studied. Experiments show that a single layer of close to cubic ZrO_2 can be grown on both alloyed substrates, yielding very large super cells ($(\sqrt{19} \times \sqrt{19})R23.4°$ and $(\sqrt{217} \times \sqrt{217})R10.16°$ on Pt_3Zr and Pd_3Zr, respectively) with an oxide lattice constant of $3.5\,\text{Å}$, just slightly smaller than the experimental value for cubic bulk ZrO_2 of $3.61\,\text{Å}$. Due to the large lattice mismatch of about $9\,\%$ between oxide and metal substrates the metal-oxide interfaces were modelled in simulation unit cells of increasing complexity. The smallest model cell consists of a single surface unit cell of Pt_3Zr or Pd_3Zr with one $(\sqrt{3} \times \sqrt{3})R30°$ unit cell of the cubic ZrO_2 trilayer on top. Due to the $9\,\%$ lattice mismatch this leads either to large strain either in the oxide or the substrate when calculated at the oxide or substrate lattice constant. Nevertheless, the buckling of the oxide film of $43\,\text{pm}$ to $73\,\text{pm}$ yields good agreement with the experimental value of about $50\,\text{pm}$ and $100\,\text{pm}$ for the Pt_3Zr and Pd_3Zr substrate, respectively. To better describe the real unit cell, further simulations using larger $(\sqrt{19} \times \sqrt{19})R23.4°$ model cells with both pure Pt and Pt_3Zr substrates were done. It turned out that the lattice match which is governed by the lattice constant of the oxide film plays a decisive role in the stability of the oxide film. These findings are reflected in an increased buckling at larger lateral strain and large lateral distortions of the oxide film. A comparison between PBE and the van-der-Waals corrected optB86b functionals shows the importance of including these non-local contributions since already at just slight compression of the oxide film the strength of the metal-oxide bonds are underestimated with PBE.

A study of the thermodynamic stability of the oxide film by introduction of additional oxygen at the metal-oxide interface or oxygen vacancies revealed a high stability of a stoichiometric film at the usual experimental parameters.

Next, the previously described model cells were used to study the adsorption of various metal adatoms (Au, Ag, Pd, and Ni) and water molecules in comparison to adsorption on ZrO_2 bulk. On the cubic c(111) bulk surface the simulations yield weak adsorption for Ag, followed by Au and stronger adsorption for Pd and Ni. Both Ag and Au adsorb at Zr–O bridge sites while Pd and Ni prefer an O–O bridge site. The corrugated monoclinic m($\bar{1}$11) surface leads to slightly stronger binding to the surface with the same order of stability. On the ultra-thin oxide film the Au and Ni metal adatoms bind more strongly. Ag binds even stronger than Au but an extensive analysis of the adsorption energy landscape revealed a much flatter surface for Ag which leads to a much lower diffusion barrier compared to Au. Additionally, Ag, Au, and Ni show charging effects when adsorbed on the ultra-thin ZrO_2 films where an electron is transferred to the Au adatom and removed from both Ag and Ni. The electronic configuration of the adsorbed Pd adatom on the other hand is the same as for the free atom.

To study the surface properties of zirconia with respect to the adsorption of water H_2O molecules were placed in both intact molecular and dissociated configurations on bulk and ultra-thin film surfaces. The calculations performed with the van-der-Waals corrected optB86b functional show that water prefers dissociative adsorption on both ZrO_2 bulk and ultra-thin film surfaces. In all cases the water molecule prefers adsorption on top of a surface Zr atom. On the monoclinic m($\bar{1}$11) surface, the van-der-Waals corrected DFT yields adsorption energies of up to $-1.3\,\mathrm{eV}$, while on the ultra-thin oxide film this value is lower by about $0.3\,\mathrm{eV}$. Water molecules adsorbed in an intact molecular configuration are bound by about $0.25\,\mathrm{eV}$ weaker than in a dissociated configuration. The value of the adsorption energy is defined by the accessibility of the surface Zr, in particular the distance to surrounding O atoms, and whether under-coordinated O are present at the oxide surface. At increased water coverage the dissociated H_2O serve as nucleation sites where additional intact water molecules are bound by additional hydrogen bonds to the formed $(OH)_{ads}$.

The second part of this work focused on the bulk and surface properties of two ternary oxides, strontium and calcium ruthenate ($Sr_3Ru_2O_7$ and $Ca_3Ru_2O_7$, respectively). In particular, the adsorption of water and oxygen molecules was studied. Both ternary transition metal oxides are members of the Ruddelsden-Popper series series ($A_{n+1}B_nC_{3n+1}$) which consist of perovskite layers in $A_nB_nO_{3n}$ stoichiometry, separated by a rock-salt like interface layer in the (001) direction. In experiments, they can be cleaved very easily along this particular plane and form well-ordered surfaces with AO (A = Sr, Ca) termination. Even though $Sr_3Ru_2O_7$ and $Ca_3Ru_2O_7$ exhibit a similar stoichiometry, the size of the A-site cation leads to decisive differences in the bulk and surface structures. In $Sr_3Ru_2O_7$, the ruthenium atom at the B-site is located at the centre of octahedra formed by the surrounding oxygen atoms which are rotated along the (001) axis. The smaller ionic radius of the calcium atoms in $Ca_3Ru_2O_7$ leads to both rotation and tilting of these octahedra. In the former case, these cleaved surfaces show the same surface structure as

the related binary oxide, SrO(001), which is not the case for the cleaved $Ca_3Ru_2O_7(001)$ surface. The DFT calculations yield surface energies of $49 \, \text{meV/Å}^2$ and $61 \, \text{meV/Å}^2$ for the $Sr_3Ru_2O_7(001)$ and $Ca_3Ru_2O_7(001)$ surfaces, respectively. The predicted oxygen vacancy formation energy of $-4.73 \, \text{eV}$ and $-3.86 \, \text{eV}$, respectively, indicates high stability of the cleaved surfaces at usual experimental ultra-high vacuum conditions.

Water prefers dissociative adsorption on both perovskite surfaces. The adsorption energy predicted by the van-der-Waals corrected optB86b functional for low coverage is $-1.26 \, \text{eV}$ and $-1.64 \, \text{eV}$ for $Sr_3Ru_2O_7$ and $Ca_3Ru_2O_7$, respectively. The corresponding surfaces of binary bulk oxide surfaces SrO(001) and CaO(001) show much weaker adsorption at $-1.08 \, \text{eV}$ and $-0.82 \, \text{eV}$. The dissociated water molecule prefers adsorption at cation-cation bridge sites with the split-off hydrogen forming a surface hydroxyl with the apical oxygen of a nearby octahedron. The residual $(OH)_{ads}$ then forms a hydrogen bond to this surface hydroxyl. On the $Sr_3Ru_2O_7(001)$ the singular adsorbed water molecule shows a small activation energy of $169 \, \text{meV}$, enabling the residual $(OH)_{ads}$ to hop to the next Sr–Sr bridge site. On the $Ca_3Ru_2O_7(001)$, the lower symmetry of the surface prohibits a similar behaviour. At higher coverage the water molecules start to form specific superstructures. On $Sr_3Ru_2O_7(001)$ first dimers are formed, followed by line structures. At high coverages the dissociated water molecules form cages which then capture intact water molecules. The different surface symmetry of the $Ca_3Ru_2O_7(001)$ surface only leads to the formation of dimers and line structures of dissociated H_2O molecules. As an intermediate structure, water adsorption was also studied on Ca-doped $Sr_3Ru_2O_7$ surfaces at ¼ and ¹⁄₁₆ dopant concentration. Here the predicted adsorption energy is slightly reduced in the vicinity of the dopant.

Oxygen molecules adsorb in an undissociated configuration at cation bridge sites on both $Sr_3Ru_2O_7(001)$ and $Ca_3Ru_2O_7(001)$ with adsorption energies at low coverage of about $-1.4 \, \text{eV}$ calculated with the optB86b functional. On the Ca-doped $Sr_3Ru_2O_7(001)$ surface the binding to the surface is enhanced by $0.1 \, \text{eV}$. At high coverages, the adsorption energy is reduced to $-0.9 \, \text{eV}$ and $-1.2 \, \text{eV}$ for the strontium and calcium ruthenates, respectively. In all cases, the calculations predict adsorption as a charged superoxo molecule (O_2^-) with the additional charge originating from the metallic properties of the oxide substrate. The comparison with the experiment suggests much weaker binding of the adsorbate, highlighting inaccuracies with the representation of the structural and electronic properties at the DFT level. Here, the HOMO-LUMO gap of the charged O_2^- is underestimated for both standard PBE and optB86b functionals, resulting in an overestimation of the electron affinity of the adsorbate and hence an overestimated energy gain by charging. Using the HSE06 hybrid functional cures the problem of the HOMO-LUMO gap, but yields too low adsorption energies of $-0.58 \, \text{eV}$. Finally, the use of the many-electron RPA approach yields adsorption energies of $-1.0 \, \text{eV}$ and $-0.7 \, \text{eV}$ for $Sr_3Ru_2O_7$ and $Ca_3Ru_2O_7$ at ¼ and ½ ML coverage, respectively, in much better agreement with the experiment.

Zusammenfassung

Übergangsmetalloxide haben vielfältige chemische und physikalische Anwendungen, vor allem in der Katalyse, bei der Erzeugung von erneuerbarer Energie in Festoxid Brennstoffzellen (SOFC) oder in Gassensoren. Diese Oxide besitzen eine große Bandbreite an physikalischen und chemischen Eigenschaften, die durch eine Änderung externer Parameter verändert werden können. Dies kann durch eine externe mechanische Spannung, Dotierung oder durch das Aussetzen in elektrischen oder magnetischen Feldern bewerkstelligt werden. Oft zeigen Übergangsmetalloxide selbst katalytische Eigenschaften, oder sie werden als Substrat für andere Katalysatoren verwendet. Es ist daher sehr wichtig, die Eigenschaften ihrer Oberflächen gut zu verstehen um die bestehenden Anwendungen zu verbessern beziehungsweise neue zu entdecken.

Im Rahmen der vorliegenden Dissertation wurden die Oberflächeneigenschaften verschiedener Übergangsmetalloxide, die bereits in SOFC Verwendung finden, mit Hilfe der Dichtefunktionaltheorie (DFT) untersucht. Diese Methode wird schon seit Jahrzehnten sehr erfolgreich zur theoretischen Beschreibung der Eigenschaften von Kristallen und Oberflächen eingesetzt. Des Weiteren wurden die berechneten Eigenschaften durch Experimente, die von Kooperationspartnern durchgeführt wurden, verifiziert.

Der erste Teil dieser Dissertation beschäftigt sich mit der Grenzfläche zwischen einer ultradünnen Zirkonoxidschicht (ZrO_2) und eines Metallsubstrates, bestehend aus sowohl purem Platin (Pt) als auch Zirkon-haltigen Platin- und Palladiumlegierungen (Pt_3Zr, Pd_3Zr). Experimente haben gezeigt dass auf diesen Legierungen eine dünne Schicht von kubischem ZrO_2 aufgebracht werden kann. Auf Pt_3Zr ergibt sich eine $(\sqrt{19} \times \sqrt{19})R23.4°$ und auf Pd_3Zr eine $(\sqrt{217} \times \sqrt{217})R10.16°$ Einheitszelle. Die Gitterkonstante der dünnen Zirkonoxidschicht beträgt in beiden Fällen 3.5 Å, leicht verkürzt im Vergleich zur Gitterkonstante in kubischem ZrO_2 Kristall (3.61 Å). Da die Simulation der gemessenen Einheitszellen einen sehr großen Rechenaufwand benötigen, wurden zuerst kleinere Modelle die aus einer Einheitszelle der Legierung und einer $(\sqrt{3} \times \sqrt{3})R30°$ Einheitszelle des ultra-dünnen Films bestehen, untersucht. Da sich die Gitterkonstanten von Oxidschicht und Substrat um ca 9 % unterscheiden, wurden zwei Varianten dieser kleinen Modelle simuliert: für das erste Modell wurde der Oxidschicht um die 9 % lateral komprimiert, diese Kompression entspricht auch der Gleichgewichtsgitterkonstante einer einzelnen Lage frei stehendem ZrO_2. Im zweiten Modell wurde die gesamte Zelle auf die experimentelle Gitterkonstante der Oxidschicht expandiert. Die Simulationen zeigen, dass die Korrugation der Oberfläche von 43 pm to 73 pm gut mit der Gemessenen übereinstimmt. Die Verzerrungen des auf Pt_3Zr adsorbierten Oxids sind generell etwas geringer (50 pm) als auf Pd_3Zr (100 pm). In weiterer Folge wurde auch die große $(\sqrt{19} \times \sqrt{19})R23.4°$ Einheitszelle modelliert. Dies wurde zuerst mit einem puren Pt Substrat, später mit dem realen Pt_3Zr Substrat gemacht. Hier konnte gezeigt werden, dass die Gitterkonstante des Oxidfilms und dementsprechend ihre Übereinstimmung zwischen Oxid und Substrat die Stabilität der Oxidschicht stark beeinflusst, indem größere laterale Spannung die Korrugation der Oxidschicht vergrößert. Auch die Wahl des Funktionals in der DFT spielt eine große

Rolle. Mit dem optB86b Funktional, welches van-der-Waals Wechselwirkungen besser als PBE beschreibt, wird die Wechselwirkung zwischen Oxid und Substrat so weit verstärkt, sodass das Oxid auch bei größerer lateraler Kompression auf dem Substrat adsorbiert bleibt. Das PBE Funktional unterschätzt die Sauerstoff-Metall Bindungen, sodass selbst eine kleine Kompression die Oxidschicht vom Metallsubstrat löst. Um die thermodynamische Stabilität der Metall-Oxid Grenzfläche zu bestimmen, wurde die Bildungsenthalpie von Sauerstofffehlstellen in der Oxidschicht und von zusätzlichem Sauerstoff zwischen Metall und Oxid bestimmt. Die DFT Simulationen zeigten, dass beide bei den üblichen experimentellen Bedingungen sehr instabil sind.

Als nächstes wurden die eben vorgestellten Modelle für die Modellierung der Adsorption von Metallatomen (Au, Ag, Pd und Ni) und Wassermolekülen auf der Oxidoberfläche verwendet und mit den Oberflächen von purem ZrO_2 verglichen. Auf der kubischen c(111) ZrO_2 Oberfläche adsorbiert Ag am schwächsten, gefolgt von Au, Pd und Ni. Die beiden edlen Metalle Ag und Au bevorzugen die Adsorption auf einer Zr–O , Pd und Ni auf einer O–O Brückenposition. Auf der m($\bar{1}$11) Oberfläche des monoklinen ZrO_2, die eine starke Korrugation aufweist, ergeben die Simulationen im Allgemeinen eine stärkere Bindung der Metallatome an die Oberfläche bei gleicher Reihenfolge der Adsorptionsenergien. Auf der ultradünnen ZrO_2 Schicht ist die Wechselwirkung noch stärker, hier bindet Au am schwächsten, knapp gefolgt von Ag, während Pd und Ni sehr stark zum Oxid binden. Ag und Au unterscheiden sich zwar nur leicht in den Adsorptionsenergien, jedoch zeigt eine Analyse der Adsorptionsenergie an verschiedenen Positionen eine wesentlich flachere Verteilung was auf eine viel geringere Diffusionsbarriere für Ag als für Au hinweist. Bei Ag, Au und Ni zeigt sich bei Adsorption auf der dünnen ZrO_2 Schicht Ladungstransfer zwischen Metallatom und dem Metallsubstrat. Gold wird negativ, Silber und Nickel positiv geladen, während Palladium den ursprünglichen neutralen Ladungszustand beibehält.

Das Verhalten von adsorbierten Wassermolekülen auf der Oxidoberfläche wurde untersucht indem intakte und dissoziierte Wassermoleküle auf den zuvor erwähnten ZrO_2 Oberflächen aufgebracht wurden. Die DFT Simulationen zeigten, dass H_2O auf den Oberflächen sowohl von ZrO_2 Kristallen als auch von ultradünnen Schichten dissoziiert und über einem exponierten Zr atom adsorbiert. Auf der monoklinen m($\bar{1}$11) Oberfläche ergab sich eine Bindungsenergie von bis zu $-1.30\,\text{eV}$, auf der Oberfläche der dünnen Oxidschicht von nur ca $-1\,\text{eV}$. Intakte H_2O Moleküle zeigten generell eine um $0.25\,\text{eV}$ schwächere Bindung. Die Analyse der Adsorptionsenergie auf unterschiedlichen Plätzen zeigte, dass dieser Wert sehr stark von der lokalen Geometrie abhängt. Existiert ein unterkoordiniertes Sauerstoffatom in der Nähe des Adsorptionsortes, ist die Bindung wesentlich stärker und die Dissoziationsbarriere geringer. Einen ebenso großen Einfluss hat die Zugänglichgeit von Zirkonatomen an der Oberfläche: sind diese durch die Korrugation selbiger zu weit von der Oberfläche entfernt oder sind die umgebenden Sauerstoffatome der Oberfläche zu nahe, verringert dies die Aktivität dieses Ortes. Bei sehr hoher Bedeckung dienen die dissoziierten H_2O als Nukleationsorte für die Bildung einer Wasserschicht durch die Bildung von weiteren Wasserstoffbrückenbindungen zwischen den zusätzlichen intakten H_2O Molekülen zu den adsorbierten $(OH)_{\text{ads}}$.

Der zweite Teil der vorliegenden Dissertation beschäftigt sich mit den Eigenschaften von Strontium- ($Sr_3Ru_2O_7$) und Kalziumruthenat ($Ca_3Ru_2O_7$). Genaues Augenmerk wurde auf die chemische Aktivität bei Adsorption von Wasser und Sauerstoffmolekülen auf ihre (001) Oberflächen gelegt. Beide Ruthenate sind Teil der Ruddelsden-Popper Gruppe ($A_{n+1}B_nC_{3n+1}$). Diese beschreibt eine spezielle Klasse von Perovskiten, in denen die Perovskiteinheitszellen in Schichten von unterschiedlicher Dicke angeordnet und von einer Halit-artigen Grenzfläche in (001) Richtung separiert sind. Diese Kristalle können entlang dieser Grenzflächen sehr leicht gespalten werden und bilden sehr ebene Oberflächen mit AO (A = Sr, Ca) Terminierung. In beiden Kristallen befindet sich das Ruthenium Atom auf der B Position in einem Oktaeder, der von sechs Sauerstoffatomen gebildet wird. Obwohl $Sr_3Ru_2O_7$ und $Ca_3Ru_2O_7$ isostöchiometrisch sind, ergeben sich durch die Größe des Kations auf der A Position entscheidende Unterschiede in der Kristallstruktur. Bei $Sr_3Ru_2O_7$ sind die Oktaeder gegeneinander um die (001) Achse verdreht, während sie durch den kleineren Radius des Ca Atoms sowohl verdreht als auch zur (001) Achse gekippt sind. Während sich die (001) Oberfläche von $Sr_3Ru_2O_7$ abgesehen von der leicht größeren Gitterkonstante nicht vom verwandten binären Oxid SrO unterscheidet bewirkt die erwähnte Verkippung den entscheidenden Unterschied zur (001) Oberfläche von CaO. Die berechneten Oberflächenenergien der ternären oxide sind $49\,meV/Å^2$ für $Sr_3Ru_2O_7$(001) und $61\,meV/Å^2$ für $Ca_3Ru_2O_7$(001). Die resultierenden Oberflächen sind sehr stabil, wie die Aktivierungsenergie von Sauerstoffdefekten von $-4.73\,eV$ und $-3.86\,eV$ für die jeweiligen Materialien zeigt.

Auf beiden Perovskitoberflächen bevorzugen Wassermoleküle dissoziative Adsorption mit Bindungsenergien von $-1.26\,eV$ für $Sr_3Ru_2O_7$ und $-1.64\,eV$ für $Ca_3Ru_2O_7$ bei niedriger Bedeckung. Im Vergleich ist die Adsorptionsenergie auf den verwandten binären Oxidoberflächen wesentlich geringer, zwischen $-1.08\,eV$ für SrO(001) und $-0.82\,eV$ auf CaO(001). Das vom H_2O Molekül abgespaltene Wasserstoffatom bildet ein Oberflächenhydroxyl mit einem Sauerstoffatom der Spitze eines der Oktaeder, während sich der Molekülrest auf einer Brückenposition zwischen zwei Kationen befindet. Dieses $(OH)_{ads}$ bildet einen zusätzliche Wasserstoffbrückenbindung zu dem Oberflächenhydroxyl. Durch die hohe Symmetrie der $Sr_3Ru_2O_7$(001) Oberfläche kann der $(OH)_{ads}$ Molekülrest mit einer geringen Aktivierungsenergie von $169\,meV$ über einen Übergangszustand um das Oberflächenhydroxyl rotieren. Die Verkippung der Oktaeder bei $Ca_3Ru_2O_7$ verhindert dies, hier ist die Rotationssymmetrie aufgehoben. Bei höherer Bedeckung beginnen die adsorbierten H_2O Moleküle Überstrukturen zu bilden: bei $Sr_3Ru_2O_7$ bewirkt attraktive Wechselwirkung zwischen den H_2O die Bildung von Dimern, die bei höherer Bedeckung zu langen Reihen und Käfigen werden. Diese umschließen intakte H_2O Adsorbate. Auf der $Ca_3Ru_2O_7$(001) Oberfläche verhindert die geringere Oberflächensymmetie die Bildung dieser Käfige, hier sind Dimere und Linien bevorzugt. Um die Bedeutung der Oberflächensymmetrie herauszustreichen, wurde auch der Einfluss von Ca Dotierung auf der $Sr_3Ru_2O_7$(001) Oberfläche bei ¼ und ¹⁄₁₆ Ca-Konzentration untersucht. Die Simulationen zeigten, dass die Dotierung die Reaktivität dieser Orte etwas reduziert.

Sauerstoff adsorbiert als intaktes Molekül auf einer Position zwischen den Kationen der Oberfläche. Bei niedriger Bedeckung beträgt die Bindungsenergie, bestimmt mit dem

van-der-Waals korrigierten optB86b Funktional, zu beiden Perovskitoberflächen circa $-1.4\,\mathrm{eV}$. Dotierung der $Sr_3Ru_2O_7(001)$ Oberfläche verstärkt die Bindung um etwa $0.1\,\mathrm{eV}$. Die Bindungsenergie verringert sich bei hoher Bedeckung auf $-0.9\,\mathrm{eV}$ auf Kalzium- und $-1.2\,\mathrm{eV}$ auf Strontium Ruthenat. Auf beiden Materialien wird das Sauerstoffmolekül durch Transfer eines Elektrons vom metallischen Substrat geladen und adsorbiert als sogenanntes Superoxo (O_2^-). Verglichen mit experimentellen Daten für Adsorption auf $Ca_3Ru_2O_7$ scheint Standard-DFT die Bindungsenergie um bis zu $0.5\,\mathrm{eV}$ zu überschätzen, da auf DFT-Level wichtige Eigenschaften bei der Adsorption schlecht beschrieben wird. Im konkreten Fall ist die berechnete Bandlücke des geladenen O_2^- mit PBE und optB86b zu gering und daher die Elektronenaffinität zu groß, also die Kosten der Ladung des Moleküls zu klein. Das Hybridfunktional HSE06 verbessert die Beschreibung der Bandlücke, die Bindungsenergie von $-0.58\,\mathrm{eV}$ auf $Ca_3Ru_2O_7(001)$ ist jedoch noch zu gering. Die Verwendung der Vielelektronen-Methode RPA bringt eine weitere Verbesserung der Übereinstimmung mit experimentellen Werten und ergibt Bindungsenergien von $-1.0\,\mathrm{eV}$ auf $Sr_3Ru_2O_7$ und $-0.7\,\mathrm{eV}$ auf $Ca_3Ru_2O_7$ bei jeweils ¼ ML und ½ ML Bedeckung.

List of Publications

- J I J Choi, W Mayr-Schmölzer, et al. "The growth of ultra-thin zirconia films on $Pd_3Zr(0001)$". en. In: *J. Phys. Condens. Matter* 26.22 (June 2014), p. 225003. DOI: [10.1088/0953-8984/26/22/225003](10.1088/0953-8984/26/22/225003)

- Daniel Halwidl, Bernhard Stöger, Wernfried Mayr-Schmölzer, et al. "Adsorption of water at the SrO surface of ruthenates". In: *Nat. Mater.* 15.4 (Dec. 2015), pp. 450–455. DOI: 10.1038/nmat4512

- Hao Li, Joong-Il Jake Choi, Wernfried Mayr-Schmölzer, et al. "Growth of an Ultrathin Zirconia Film on Pt_3Zr Examined by High-Resolution X-ray Photoelectron Spectroscopy, Temperature-Programmed Desorption, Scanning Tunneling Microscopy, and Density Functional Theory". In: *J. Phys. Chem. C* (Jan. 2015), pp. 2462–2470. DOI: [10.1021/jp5100846](10.1021/jp5100846)

- Joong Il Jake Choi, Wernfried Mayr-Schmölzer, et al. "Metal Adatoms and Clusters on Ultrathin Zirconia Films". In: *J. Phys. Chem. C* 120.18 (May 2016), pp. 9920–9932. DOI: 10.1021/acs.jpcc.6b03061

- Daniel Halwidl, Wernfried Mayr-Schmölzer, et al. "Ordered hydroxyls on $Ca_3Ru_2O_7(001)$". In: *Nat. Commun.* 8.1 (Dec. 2017), p. 23. DOI: [10.1038/s41467-017-00066-w](10.1038/s41467-017-00066-w)

- Daniel Halwidl, Wernfried Mayr-Schmölzer, et al. "A Full Monolayer of Superoxide: Oxygen Activation on the Unmodified $Ca_3Ru_2O_7(001)$ Surface". In: *Journal of Materials Chemistry A* (2018). DOI: [10.1039/C8TA00265G](10.1039/C8TA00265G)

- Peter Lackner, Jan Hulva, Joong-Il Jake Choi, Eva Maria Köck, Wernfried Mayr-Schmölzer, et al. "Water adsorption at zirconia: from the $ZrO_2(111)/Pt_3Zr(0001)$ model system to powder samples". In: *Journal of Materials Chemistry A* (2018). DOI: [10.1039/C8TA04137G](10.1039/C8TA04137G)

- Wernfried Mayr-Schmölzer et al. "Adsorption of superoxo O_2^- species on the pure and Ca-doped $Sr_3Ru_2O_7(001)$ surface". In: *Surface Science, accepted* (2018)

- Wernfried Mayr-Schmölzer, Daniel Halwidl, et al. "Adsorption of CO on the $Ca_3Ru_2O_7(001)$ surface". In: *Surface Science, accepted* (2018)

Contents

1. Introduction

For a long time, oxides and their surfaces have garnered a lot of interest in the scientific community. This is driven by the large variety of physical and chemical properties of oxide materials, leading to many different scientific and technological applications. Transition metal oxides, in particular, span a wide range of electronic, magnetic, catalytic, and mechanical features. The surfaces of these oxides often exhibit catalytic properties themselves or can be used as support materials. In many cases, these properties can be tuned by slight structural or electronic modifications, for example by the introduction of a dopant.

One of the main issues of the future will be the supply of sustainable energy. For decades, research has been done on the topic of fuel cells which directly convert chemical into electric energy. Due to their high efficiency, fuel cells are very attractive to address the energy problem, but going from scientific experiments to commercial products has been challenging. At the moment, both the manufacturing process and commonly used materials are too expensive to replace existing technology. In contrast to fuel cells which rely on pure hydrogen as fuel - like polymeric-electrolyte-membrane fuel cells (PEMFCs), alkaline fuel cells (AFCs), or phosphoric-acid fuel cells (PAFCs) - in solid-oxide fuel cells (SOFCs) both hydrogen and CO are oxidised at the anode[10]. Additionally, the total system efficiency of an SOFC of $\approx 50\%$ is much higher due to their simpler thermal design. SOFC are often designed to operate at high temperatures of $850\,°C$ and above, therefore the materials selected for the electrodes and electrolyte need to retain their desired properties. In particular, for the electrolyte, Yttria-stabilised zirconia (YSZ) has been widely used due to its large electronic band gap and its ability to conduct oxygen ions at operating temperatures of $\approx 900\,°C$. This limits the choice of materials for the electrodes, giving rise to increased interest in other materials which could replace YSZ, allowing the operation of the SOFC at lower temperatures. Also, most of the materials used in conventional SOFCs are not fully understood at a fundamental level. The research into the properties of pure zirconia (ZrO_2), which might be able to replace YSZ as an electrolyte, is lacking a detailed insight into its surface properties. Pure zirconia has a large band gap and therefore impedes studies of its surface with common surface sensitive techniques like Scanning Tunnelling Microscopy (STM) which often require electronic conductivity. To overcome this problem, thin $ZrO_2(111)$ films are grown on a suitable conducting substrate. Additionally, the material selected for the cathode side of the SOFC is also important. At the cathode, oxygen is adsorbed and reduced to oxygen ions, which then travel through the electrolyte to react with hydrogen at the anode. Ternary oxides which crystallise in a so-called perovskite structure are heavily studied, for example calcium and strontium ruthenates ($Ca_3Ru_2O_7$ and $Sr_3Ru_2O_7$). Both are members of a special group of ordered perovskites, the Ruddelsden-Popper series, which

consists of slabs of standard perovskite building blocks of different thickness separated by a rock-salt-like layer.

Density functional theory (DFT) has for a long time been employed as a powerful tool to predict the properties of a large range of materials by modelling their complete electronic structure at the quantum level. In particular, DFT has proven itself to be a valuable tool to determine the chemical and physical properties of various transition metal oxides, in particular the binary zirconia (ZrO_2), and the ternary calcium and strontium ruthenates, $Ca_3Ru_2O_7$ and $Sr_3Ru_2O_7$. In the first part of this thesis, chapter 2, the theoretical background of DFT is described. This is followed by an in-depth study of the structure of ultra-thin zirconia films adsorbed on metal substrates in chapter 3 using structural models of different levels of complexity. These models are then used to study the adsorption of metal adatom adsorbates (Au, Ag, Pd, Ni) in section 4.1 and water molecules in section 4.2. In the second part, following a description of the bulk structures of calcium and strontium ruthenate in chapter 5, the adsorption properties of water and oxygen molecules on the surfaces of both ruthenates are explained in chapter 6 and chapter 7.

2. Computational Methods

One of the fundamental problems in theoretical physics and chemistry is the description of the structure and dynamics of many-electron systems. The electronic band structure of a solid and generally the structure of the electronic shell of atoms is one of the most important properties of these systems since this is directly related to the stability of atoms. Additionally, other important physical and chemical properties like electric and magnetic moments or the electronic conductivity are determined by the electronic structure. The structural properties directly related to the electronic structure of its components are bond lengths and bond angles in multi-atomic systems, as well as the symmetry of the arrangement of the atoms. Additionally, dynamical properties of materials like the electronic excitation spectrum are determined by the electronic structure. These are essential to describe optical properties and other scattering processes. In this chapter a description of the theoretical foundation of density functional theory will be given, accompanied by a short description of the methodological implementation in the Vienna Ab-initio Simulation Package (VASP), the software used for all DFT calculations. For a more involved description the book *Density Functional Theory* by Engel and Dreizler [11] is recommended.

A well established approach to study different systems is to introduce the fundamental Hamiltonian to solve the corresponding many-body Schrödinger equation. Since this is a very demanding task, some approximations are unavoidable due to limitations in computing power. For example, the description of the many-body wave function in the Hartree-Fock approximation and the representation of its single-particle parts in terms of a finite basis set greatly reduce the computational effort. Since all approximations are only technical in nature it is still truly an *ab-initio* approach since no adjustable physical parameters are added to the characterisation of the many-body wave function.

The *ab-initio* many-body Hamiltonian of a coupled electron-nucleus system can be written as

$$\hat{H} = \hat{T}_{\mathrm{n}} + \hat{V}_{\mathrm{n-n}} + \hat{H}_{\mathrm{e}}(+\hat{V}_{\mathrm{n-field}}) \tag{2.1}$$

$$\hat{H}_e = \hat{T}_{\mathrm{e}} + \hat{V}_{\mathrm{n-e}} + \hat{V}_{\mathrm{e-e}}(+\hat{V}_{\mathrm{e-field}}) \tag{2.2}$$

with $\hat{T}_n$ representing the kinetic energy of K nuclei of the system,

$$\hat{T}_n = \sum_{\alpha=1}^{K} \frac{(-\imath\hbar\nabla_{\mathbf{R}_\alpha})^2}{2M_\alpha}, \tag{2.3}$$

with $\mathbf{R}_\alpha$ indicating the cartesian coordinates of nucleus α, M_α its mass and $\nabla_{\mathbf{R}_\alpha} = \partial/\partial\mathbf{R}_\alpha$. The additional terms denote the repulsion of the nuclei $\hat{V}_{\mathrm{n-n}}$,

$$\hat{V}_{\mathrm{n-n}} = \sum_{\alpha,\beta=1;\alpha<\beta}^{K} \frac{Z_\alpha Z_\beta e^2}{|\mathbf{R}_\alpha - \mathbf{R}_\beta|}. \tag{2.4}$$

The electronic Hamiltonian $\hat{H}_e$ is decomposed into the kinetic energy of the N electrons,

$$\hat{T}_e = \sum_{i=1}^{N} \frac{(-\imath\hbar\nabla_i)^2}{2m}, \tag{2.5}$$

the interaction between nuclei and electrons,

$$\hat{V}_{\mathrm{n-e}} = -\sum_{\alpha=1}^{K}\sum_{i=1}^{N} \frac{Z_\alpha e^2}{|\mathbf{R}_\alpha - \mathbf{r}_i|}, \tag{2.6}$$

and finally the interaction between the electrons,

$$\hat{V}_{\mathrm{e-e}} = \sum_{i,j=1;i<j}^{N} \frac{e^2}{|\mathbf{r}_i - \mathbf{r}_j|}. \tag{2.7}$$

The charges are denoted $Z_\alpha e$, $e = |e|$, $\mathbf{r}_i$ are the positions of the electrons and $\nabla_i \equiv \nabla_{\mathbf{r}_i}$. Finally, both nuclei and electrons can interact with an external electromagnetic field,

$$\hat{V}_{\mathrm{n-field}} = \sum_{\alpha=1}^{K} \left[Z_\alpha e\Phi_{ext}(\mathbf{R}_\alpha t) + \imath\frac{Z_\alpha e\hbar}{M_\alpha c}\mathbf{A}_{ext}(\mathbf{R}_\alpha t)\cdot\nabla_{\mathbf{R}_\alpha} - \mathbf{I}_\alpha\cdot\mathbf{B}_{ext}(\mathbf{R}_\alpha t) \right] \tag{2.8}$$

$$\hat{V}_{\mathrm{e-field}} = \sum_{i=1}^{N} \left[-e\Phi_{ext}(i_it) - 2\imath\mu_B\mathbf{A}_{ext}(\mathbf{r}_it)\cdot\nabla_i + \mu_B\sigma_i\cdot\mathbf{B}_{ext}(\mathbf{r}_it) \right]. \tag{2.9}$$

Usually, the dynamical treatment only needs to be done for the electrons, as long as there is no influence of an electromagnetic field. The Hamiltonian can then be transformed into a centre-of-mass frame, separating the the translational motion of the nuclei and the motion of the electrons. In multi-atomic systems the coupled dynamics between electrons and nuclei can then be described with the Schrödinger equation

$$\hat{H}\Psi_a(\mathbf{R}_1,...,\mathbf{R}_K;\mathbf{r}_1\sigma_1,...,\mathbf{r}_N\sigma_N) = E_a\Psi_a(\mathbf{R}_1,...,\mathbf{R}_K;\mathbf{r}_1\sigma_1,...,\mathbf{r}_N\sigma_N) \tag{2.10}$$

with σ_i being the spin-orientation of electron i with respect to an arbitrary axis. To solve this equation a partial decoupling of the electrons from the translational motion of the nuclei can be achieved by the *Born-Oppenheimer approximation* [12]. This can be justified since the kinetic energy of the electrons is of four orders of magnitude smaller than that of the atomic nuclei. The total wave-function Ψ_a therefore factorises into a

nuclear and an electronic wave function Ψ_{ik}^n and Ψ_k^e, respectively. The resulting electronic wave function Ψ_k^e satisfies the Schrödinger equation

$$\hat{H}_e \Psi_k^e(\mathbf{R}_1, ..., \mathbf{R}_K; \mathbf{r}_1\sigma_1, ..., \mathbf{r}_N\sigma_N) = E_k(\mathbf{R}_1, ..., \mathbf{R}_K)\Psi_k^e(\mathbf{R}_1, ..., \mathbf{R}_K; \mathbf{r}_1\sigma_1, ..., \mathbf{r}_N\sigma_N). \tag{2.11}$$

A commonly used approach to obtain an approximate solution of this Schrödinger equation is the *Hartree-Fock* or *Self-Consistent-Field approximation*, where the ground state wave function $\Psi_{k=0}^e$ is assumed to be a Slater determinant, i.e. a determinant of single-particle states. This approach enables an efficient handling of the electron problem where the N single-particle states ϕ_i in the approximate ground state wave function $\Phi_{1...N}$ are determined by a variational approach. However, depending on the nature of the implementation, this approach still scales by a factor of M^4 since it still describes a fully interacting system, reducing this method to rather small systems. To overcome this scaling problem in the treatment of more complex systems, the fully interacting many-body problem can be mapped onto an effective single-particle problem by employing the methods introduced in the Density Functional Theory (DFT).

2.1. Density Functional Theory

The density functional theory is based on the Hohenberg-Kohn [13] (HK) theorem which represents the most basic theorem ensuring that a stationary many-particle system is fully characterised by the ground state density. This theorem states that there is a one-to-one correspondence between the external potential v_{ext} in the Hamiltonian, the non-degenerate ground state $|\Psi_0\rangle$ and an associated ground state density n_0 according to

$$v_{ext}(r) \iff |\Psi_0\rangle \iff n_0(r) = \langle\Psi_0|\hat{n}(r)|\Psi_0\rangle. \tag{2.12}$$

The ground state $|\Psi_0\rangle$ can therefore be written as a functional dependent on the density $|\Psi[n_0]\rangle$. Explicit knowledge of v_{ext} is not needed to determine the ground state $|\Psi_0\rangle$ from the density n_0, therefore the particular geometry of the system is determined by the structure of the density. Furthermore, from the existence of this functional $|\Psi[n]\rangle$ follows the that any ground state observable is a density functional,

$$O[n] := \langle\Psi[n]|\hat{O}|\Psi[n]\rangle, \tag{2.13}$$

for example the ground state energy

$$E[n] := \langle\Psi[n]|\hat{H}|\Psi[n]\rangle = F[n] + \int d^3r v_{ext}(r)n(r) \tag{2.14}$$

$$F[n] := \langle\Psi[n]|\hat{T} + \hat{W}|\Psi[n]\rangle \tag{2.15}$$

Finally, a minimum principle exists for $E[n]$, which means that for all densities $n_0'(r) \neq n_0(r)$ which are not ground state densities the corresponding total energy $E[n_0'] > E[n_0]$. The ground state total energy is therefore determined by the ground state density.

An exact form for this ground state energy functional $E[n]$ was later introduced by Kohn and Sham [14] in the so-called Kohn-Sham (KS) scheme. Here, the interacting many-particle system is mapped onto a suitable noninteracting system. Using the fact that the non-degenerate ground state is uniquely determined by the ground state density the energy functional can be written as

$$E[n(\mathbf{r})] = T[n(\mathbf{r})] + V_{ee}[n(\mathbf{r})] + V_{ext}[n(\mathbf{r})], \tag{2.16}$$

with

$$V_{ext}[n(\mathbf{r})] = \int d\mathbf{r} n(\mathbf{r}) V_{ext}(\mathbf{r}). \tag{2.17}$$

The functional $T[n(\mathbf{r})]$ corresponds to the kinetic energy of the electrons, $V_{ee}[n(\mathbf{r})]$ represents the Coulomb interaction between the N electrons of the system, while $V_{ext}[n(\mathbf{r})]$ represents the interaction between the electrons and the nuclei. Furthermore, eq. (2.16) can be rewritten in terms of the kinetic energy $T_s[n(\mathbf{r})]$ of a virtual system of non-interacting electrons which yields the same electron density as the original, fully interacting one:

$$T_s[n(\mathbf{r})] = -\frac{1}{2} \sum_{i=1}^{N} \int d\mathbf{r} \phi_i^*(\mathbf{r}) \nabla^2 \phi_i(\mathbf{r}) \tag{2.18}$$

$$n(\mathbf{r}) = \sum_{i=1}^{N} |\phi_i(\mathbf{r})|^2 \tag{2.19}$$

The term $E_{xc}[n(\mathbf{r})]$ introduced in the following represents the exchange-correlation energy which encompasses all many-body effects not contained in the other terms, i.e. both the deviation from the Hartree energy from $V_{ee}[n(\mathbf{r})]$ and of $T_s[n(\mathbf{r})]$ from the real kinetic energy $T[n(\mathbf{r})]$:

$$E_{xc}[n(\mathbf{r})] = (T[n(\mathbf{r})] - T_s[n(\mathbf{r})]) + (V_{ee}[n(\mathbf{r})] - U[n(\mathbf{r})]) \tag{2.20}$$

$$U[n(\mathbf{r})] = \frac{1}{2} \int d\mathbf{r} \int d\mathbf{r}' \frac{n(\mathbf{r})n(\mathbf{r}')}{|\mathbf{r} - \mathbf{r}'|}, \tag{2.21}$$

leading to

$$E[n(\mathbf{r})] = T_s[n(\mathbf{r})] + U[n(\mathbf{r})] + V_{ext}[n(\mathbf{r})] + E_{xc}[n(\mathbf{r})]. \tag{2.22}$$

Equation (2.22) can now be minimized with respect to the electron density $n(\mathbf{r})$ according to

$$0 = \frac{\delta T_s}{\delta \phi_i^*} + \frac{\delta}{\delta n(\mathbf{r})} \left\{ U[n(\mathbf{r})] + V_{ext}[n(\mathbf{r})] + E_{xc}[n(\mathbf{r})] \right\} \frac{\delta n(\mathbf{r})}{\delta \phi_i^*}. \tag{2.23}$$

Here, ϕ_i denote one-electron wave functions. This finally leads to the Kohn-Sham equations [14]

$$\left\{ -\frac{1}{2} \nabla_i^2 + V_{eff}(\mathbf{r}) \right\} \phi_i(\mathbf{r}) = \epsilon_i \phi_i(\mathbf{r}) \tag{2.24}$$

with $i = 1, \ldots, N$ and

$$V_{eff}(\mathbf{r}) = V_{ext}(\mathbf{r}) + \int \frac{n(\mathbf{r}')}{|\mathbf{r} - \mathbf{r}'|} d\mathbf{r}' + \frac{\delta E_{xc}(\mathbf{r})}{\delta n(\mathbf{r})}. \tag{2.25}$$

As eq. (2.24) shows the original problem of the N-particle many-electron wave-function has now been reduced to N coupled Schrödinger equations describing non-interacting particles. By using an iterative variational approach these equations can be solved by starting from an initial guess for the electron density $n_0(r)$.

In this general formalism the exact form of the exchange-correlation functional E_{xc} is unknown, but there are several approximations obtained from model systems which are able to describe real systems with surprisingly good accuracy.

2.2. Local Density Approximation (LDA)

The most basic approach to approximate the exchange correlation energy term is the local density approximation (LDA). Here the electron density is modelled upon a well-known many-body system of interacting particles, the homogeneous electron gas. Here the relevant value is the total energy density. To make sure that all long-range Coulomb interactions are zero a uniform background charge n_+ is introduced. The xc-density of the inhomogeneous system is then locally approximated by the xc-density $\epsilon_{xc}(n_{hom} = n(\mathbf{r}))$ of the homogeneous electron gas, resulting in the exchange-correlation energy functional

$$E_{xc}^{LDA}[n(\mathbf{r})] = \int d\mathbf{r} \epsilon_{xc}(n_{hom}(\mathbf{r})) n_{hom}(\mathbf{r}). \tag{2.26}$$

To determine $\epsilon_{xc}(n_{hom})$ advanced many-body techniques like quantum Monte-Carlo simulations [15] can be employed. The LDA is still consistent with the *ab-initio* concept of the DFT since E_{xc} is determined by the properties of the homogeneous electron gas. One deficiency of this method becomes apparent when studying various physical properties of crystals like lattice constants and bond lengths. Generally, the LDA yields an over-binding and therefore underestimates lattice constants.

2.3. Generalised Gradient Approximation (GGA)

To improve the results for physical parameters, the LDA exchange-correlation functional was improved upon in various ways. One important expansion of the LDA is the generalised gradient approximation (GGA) which is still based on the homogeneous electron gas, but takes the gradient of the electron density into account in addition to the density itself. This results in the functional

$$E_{xc}^{GGA}[n_\uparrow, n_\downarrow] = \int d\mathbf{r} \epsilon_{xc}(n_\uparrow, n_\downarrow, \nabla n_\uparrow, \nabla n_\downarrow) n(\mathbf{r}) \tag{2.27}$$

with $n = n_\uparrow + n_\downarrow$ and the electron spin densities $n_\uparrow(\mathbf{r})$ and $n_\downarrow(\mathbf{r})$.

In many cases, the GGA yields a much better description of crystal parameters compared to the LDA since an improved description of the exchange and correlation energies directly relates to an improvement of the ground state total energy. Due to its increased accuracy it has been established as the main workhorse for DFT calculations. Unfortunately, the GGA does not cure the general underestimation of the band gap in the LDA due to its lack of the so-called derivative discontinuities. Also, there exist multiple parameterisations of the GGA. The most widely used is the so-called PBE functional introduced by Perdew, Burke, and Ernzerhof [16] where all parameters are derived from fundamental constants. The PBE functional improves upon older semi-empirical GGA functionals like B88 [17] or PW91 [18].

2.4. DFT+U

One major problem of both L(S)DA[1] and GGA type functionals is their difficulty to describe highly localised states, often found in transition metal and rare-earth compounds. Compared to the s- and p-states, d- and f-states are often much more localised in these materials. One general deficiency of the LDA approach is the insufficient treatment of the self-interaction, meaning that the LDA exchange does not reduce to the exact Coulomb self-interaction integral in the limit of a single particle. Additionally, the LDA correlation does not vanish in this limit. In many-particle systems, this results in the prediction of a metallic ground state and itinerant d states in many transition metal oxides like FeO or CoO [19, 20] in contrast to experiments. Obviously, the description of the band structure is not adequate for these materials.

To overcome these problems the complete Hilbert space is split into a localised part for the d- and f-states where the Coulomb effects are treated in an orbital-dependent fashion, and a part for the s- and p-states where a description in the LDA (or GGA) is sufficiently accurate. This amounts to the addition of a strong screened inter-atomic interaction as an on-site replacement of the respective L(S)DA energy. In a simplified implementation introduced by Dudarev et al. [21], the resulting term is

$$E_{LSDA+U} = E_{LSDA} + \frac{(U-J)}{2} \sum_\sigma \left[\left(\sum_{m_1} n^\sigma_{m_1,m_2} - \sum_{m_1,m_2} \hat{n}^\sigma_{m_1,m_2} \hat{n}^\sigma_{m_2,m_1} \right) \right]. \quad (2.28)$$

The strength of the on-site Coulomb interaction is characterised by the Hubbard parameter U and the exchange parameter J. In this implementation only the difference $U - J$ is relevant. The last term E_U in eq. (2.28) represents the double counting correction which cancels the E_U part if the shell of bands emerging from the atomic shell is completely filled.

The DFT+U approach has successfully been used to describe the physics of Mott-Hubbard insulators like MnO, FeO, CoO, and NiO where metal $3d$ states strongly hybridise with oxygen $2p$ states. The additional computational cost to calculate the on-site Coulomb kernel is almost negligible. While well chosen values for U and J can yield very

---

[1]L(S)DA: spin-polarised LDA

good results for the band gap, it is also the major drawback of this approach. The parameters U and J are determined by comparison to values for the band gap determined by experiments, hybrid or constrained RPA [22, 23] calculations.

2.5. Hybrid Functionals

To increase the amount of the exchange part of the E_{xc} energy the original GGA functional is modified by adding a certain part of the exact Hartree-Fock exchange energy according to

$$E_{xc}^{hyb} = aE_x^{HF} + (1-a)E_x^{GGA} + E_c^{GGA} \tag{2.29}$$

with a mixing parameter a. Originally, this parameter was set to $a = 1/4$ in the so-called PBE0 [24] functional. While this parametrisation shows improvement of atomisation energies and band gaps [24] compared to the PBE functional, in metallic systems various problems arise. The derivative of the Hartree-Fock single band energies diverge logarithmically due to the long range of the unscreened Coulomb interaction and the non-local nature of the HF exchange potential. To solve this problem the concept of a screened hybrid functional was introduced where the Coulomb interaction is split into a short-range and a long-range part. Since the long-range exchange part of the resulting energy functional which is problematic for metallic systems is rather small the exchange energy was modified according to

$$E_x^{HSE} = \frac{1}{4}E_x^{exact,sr} + \frac{3}{4}E_x^{PBE,sr} + E_x^{PBE,lr}. \tag{2.30}$$

Adding the unmodified PBE correlation energy E_c^{PBE} yields

$$E_{xc}^{HSE} = \frac{1}{4}E_x^{HF,sr} + \frac{3}{4}E_x^{PBE,sr} + E_x^{PBE,lr} + E_c^{PBE} \tag{2.31}$$

which has been proposed by Heyd, Scuseria, and Ernzerhof [25–27]. Their so-called HSE06 [28] functional with an optimised screening parameter yields good results for crystal properties of semiconductors and insulators, mitigating some of the errors of the LDA and GGA functionals. The band gaps of various solids are also very well described compared to both PBE and other hybrid functionals.

2.6. Van-der-Waals Corrections

Another deficiency of the LDA and standard GGA functionals like PBE is the lack of a description of long range dispersion effects or van-der-Waals interactions. Therefore, to improve the description of weakly bonded systems, many approaches were introduced to extend the standard DFT to include these effects. In one approach proposed by Langreth and Lundqvist [29] called vdW-DF the exchange-correlation energy term is written as

$$E_{xc} = E_x^{GGA} + E_c^{LDA} + E_c^{nl} \tag{2.32}$$

with E_c^{nl} denoting the non-local correlation energy. In its simplest form it can be written as

$$E_c^{nl} = \frac{1}{2} \int d\mathbf{r} d\mathbf{r}' n(\mathbf{r}) \phi(\mathbf{r}, \mathbf{r}') n(\mathbf{r}') \tag{2.33}$$

where $\phi(\mathbf{r}, \mathbf{r}')$ is a given, general function depending on $\mathbf{r} - \mathbf{r}'$ and the densities n in the vicinity of $\mathbf{r}$ and $\mathbf{r}'$. The non-local kernel E_c^{nl} is then calculated from a model response function for electron densities. In this approach, the choice of the GGA used for the exchange part of E_{xc} plays an important role in the accuracy of the calculated total energies. Klimeš et al. [30] have shown that a modified B88 or B86 functional yield very good results for the S22 benchmark set of weakly bonded dimers. Both functionals are implemented in the VASP code as functionals optB88 and optB86b [31].

Another method to correct for van-der-Waals interaction was introduced by Grimme et al. [32] called DFT-D3. Here the dispersion correction is simply added to the Kohn-Sham DFT energy according to

$$E_{DFT-disp} = E_{KS-DFT} + E_{disp} \tag{2.34}$$

with

$$E_{disp} = -\frac{1}{2} \sum_{i=1}^{N_{at}} \sum_{j=1}^{N_{at}} \sideset{}{'}\sum_{\mathbf{L}} (f_{d,6}(r_{ij,L}) \frac{C_{ij}}{r_{ij,L}^6} + f_{d,8}(r_{ij,L}) \frac{C_{8ij}}{r_{ij,L}^8}). \tag{2.35}$$

The summation is done over all atoms N_{at} and all translations of the unit cell $L = (l_1, l_2, l_3)$. The prime $'$ indicates that $i \neq j$ for $L = 0$. C_{ij} denote geometry-dependent dispersion coefficients for the atom pair ij which are adjusted according to the coordination number of the atoms surrounding sites i and j by interpolation between their dispersion coefficients. The dampening function $f_{d,n}$ is defined as

$$f_{d,n} = \frac{s_n}{1 + 6(r_{ij}/(s_{R,n} R_{0ij}))^{-\alpha_n}} \tag{2.36}$$

with $R_{0ij} = \sqrt{\frac{C_{8ij}}{C_{6ij}}}$, and the parameters α_6, α_8, and $s_{R,8}$ which are fixed at 14., 16, and 1, respectively. The values of s_6, s_8, and $s_{R,6}$ depend on the choice of the exchange-correlation functional.

This approach combines a low additional computational cost with good accuracy compared to the S22 benchmark set [32]. Also, it can be combined with a large number of existing exchange-correlation functionals since the correction takes place after the full electronic optimisation. This also enables the augmentation of DFT+U or hybrid calculations with van-der-Waals corrections. Nevertheless, this lack of interaction with the electronic structure is also its major flaw, ultimately limiting accuracy compared to more advanced approaches like the Random Phase Approximation (RPA) or perturbatively corrected coupled cluster methods like CCSD(T).

2.7. Many-electron Methods

Density functional theory has long been established as a great tool to model ground state properties of a wide variety of materials. Since DFT is a ground state theory, its description of excited state properties is severely lacking. Except for the highest occupied eigenvalue which corresponds to the ionisation energy, the Kohn-Sham eigenvalues ϵ_i calculated in the LDA do not have an exact physical meaning. They are often interpreted as single-particle excitation energies, which in many cases is in good agreement to photoemission spectra in some *sp* systems. Nevertheless, in most cases the discrepancies can be large, especially in *d* and *f* systems. Methods expanding upon the basic LDA like gradient corrections (see section 2.3), the DFT+U (see section 2.4), or self-interaction corrections certainly yield improvements of the calculated ground state properties but do not improve the quasiparticle energies. To properly calculate the single-particle excitation energies the Green function [33, 34] theory can be employed. The quasiparticle energies E_i introduced in

$$\left[-\frac{1}{2}\nabla^2(\mathbf{r}) + V^H(\mathbf{r}) \right] \Psi_i(\mathbf{r}) + \int d^3\mathbf{r}\prime\Sigma(\mathbf{r}, \mathbf{r}\prime; E_i)\Psi_i(r\prime) = E_i\Psi_i(\mathbf{r}) \qquad (2.37)$$

define the energy spectrum of single particle excitations. The term Σ is called self-energy. It is non-local and depends on the energy and contains all effects of exchange and correlations. Since the calculation of the self-energy is very complex different approximations are made, for example the *GW* approximation which in essence extends the Hartree-Fock approximation by taking screening into account dynamically, solving the the most serious errors of the latter. In the following section a very short overview of the concept of the *GW* approximation will be given. A more detailed derivation can be found in the very informative review article by Aryasetiawan and Gunnarsson [35] and the related references.

2.7.1. *GW* Approximation

Hedin [36] was the first to show a rigorous way to calculate the self-energy by expansion of the dynamically screened Coulomb interaction. Also in the same work, the first full calculation of the self-energy of the electron gas in the *GW* framework was performed. Since the computational effort of the *GW* approximation is much larger compared to standard DFT, its application to real materials has only started in the mid 1980s.

To properly describe the electronic excitation spectrum of a solid, the theory has to take the electron-hole interaction into account. In experiment, the spectra are obtained from the measured kinetic energy in photoemission measurements. These photoemission and inverse photoemission processes can be described using one-particle Green functions

defined as

$$i G(x, x') = \langle N | T[\hat{\psi}(x) \hat{\psi}^\dagger(x')] | N \rangle \tag{2.38}$$

$$= \begin{cases} \langle N | \hat{\psi}(x) \hat{\psi}^\dagger(x') | N \rangle & \text{for } t > t' \text{ (electron)} \\ -\langle N | \hat{\psi}^\dagger(x') \hat{\psi}(x) | N \rangle & \text{for } t < t' \text{ (hole)} \end{cases} \tag{2.39}$$

with $|N\rangle$ the exact N-electron ground state, $\hat{\psi}(x)$ a field operator in the Heisenberg representation annihilating an electron at $x = (\mathbf{r}, t)$ and T the time-ordering operator. The so defined Green function G can now be interpreted as the probability amplitude that an electron added at x' will propagate to x at $t < t'$ and that an electron hole created at x will propagate to x' for $t' > t$. Therefore, it is possible to obtain the ground state energy, the expectation value of any single-particle operator in the ground state, and the one-electron excitation spectrum from the Green function. After some rather extensive transformations in the evaluation of the self-energy by introducing a time-varying field, one arrives at a set of coupled integral Dyson-like equations called Hedins [36] equations

$$\Sigma(1, 2) = i \int d(34) G(1, 3^+) W(1, 4) \Lambda(3, 2, 4) \tag{2.40}$$

$$G(1, 2) = G_0(1, 2) + \int d(34) G_0(1, 3) \Sigma(3, 4) G(4, 2) \tag{2.41}$$

$$\Lambda(1, 2, 3) = \delta(1 - 2)\delta(2 - 3) + \int d(4567) \frac{\delta \Sigma(1, 2)}{\delta G(4, 5)} G(4, 6) G(7, 5) \Lambda(6, 7, 3) \tag{2.42}$$

$$W(1, 2) = \nu(1, 2) + \int d(34) \nu(1, 3) P(3, 4) W(4, 2) \tag{2.43}$$

with the polarisation function

$$P(1, 2) = -i \int d3 d4 G(1, 3) \Lambda(3, 4, 2) G(4, 1^+). \tag{2.44}$$

The term W describes the screened Coulomb potential, Λ the vertex function, ν the bare Coulomb interaction and G_0 the Green function corresponding to $\Sigma = 0$. The notation $1 = (\mathbf{r}_1, t_1)$ is commonly used to describe a certain state. The equations eq. (2.40) are exact and replace the Schrödinger equation for the many-body problem. Since solving this system of equation is very demanding, in the GW approximation the vertex function is neglected and only the bare vertex $\Lambda(1, 2, 3) = \delta(1 - 2)\delta(2 - 3)$ is used. The screened interaction W is then constructed including only the Coulomb kernel in the so-called random phase approximation (RPA). Looking back to the Hartree-Fock approximation the GW approximation can be considered as a replacement of the bare Coulomb interaction ν by a screened interaction W. After a Fourier transformation of the equation for the self-energy:

$$\Sigma(\mathbf{r}, \mathbf{r}', \omega) = \frac{i}{2\pi} \int d\omega' G(\mathbf{r}, \mathbf{r}', \omega + \omega') W(\mathbf{r}, \mathbf{r}', \omega') \tag{2.45}$$

the correlation part of the non-interacting G_0 can be calculated by explicit evaluation of the imaginary part of the self-energy. Its real part can then be obtained by integration using the Kramers-Kronig relation. The first iteration G_0 of the Green function

$$G_0(\mathbf{r}, \mathbf{r}', \omega) = \sum_{n\mathbf{k}} \frac{\phi^{*(0)}(\mathbf{r})\phi^{(0)}(\mathbf{r}')}{\omega - E_{(0)_{n\mathbf{k}}}} \tag{2.46}$$

denotes the non-interacting Green function with $\psi_{n\mathbf{k}}^{(0)}(\mathbf{r})$ being a set of one-electron orbitals and $E_{n\mathbf{k}}^{(0)}$ the corresponding energies. Therefore, to evaluate the quasiparticle energies a first guess of the one-electron eigensystem needs to be provided which is usually done by an initial DFT calculation employing either a GGA or hybrid functional. Since the computational effort of the evaluation of the quasi-particle energies is very high compared to standard DFT usually single-shot G_0W_0 calculations are performed. Here all off-diagonal matrix elements of the self-energy are neglected and a Taylor expansion of the DFT energies $E_{n\mathbf{k}}^{(0)}$ is done. In practice, the single-shot G_0W_0 approach already yields good values for the quasi-particle energies [37] and related properties like the band gap [38] and the band structure [39]. Yet, as shown shown by Bruneval and Marques [40], the choice of initial quasi-particle energies does play a role in the accuracy of the following G_0W_0 calculation.

2.7.2. RPA Total Energies

Treatment of the non-local nature of long-range interaction effects like van-der-Waals interactions or London dispersion forces is lacking in the most common functionals used in DFT calculations. As discussed before in section 2.6, these many-body contributions can be added in an approximate manner, but in many cases the accuracy of these approximations is not sufficient. An exact description of the correlation functional is given by the adiabatic connection fluctuation-dissipation theorem (ACFDT) [41–43], which relates the exchange-correlation energy to the electronic response of a system with an electron density $n(\mathbf{r})$ when moving from the Kohn-Sham Hamiltonian to an exact many-body description. This approach provides both van-der-Waals dispersion forces and is at the same time reasonably accurate for overlapping electron densities. In practice, the exchange-correlation functional E_{xc} is calculated from the dynamic susceptibility of the system which can be obtained by a time-dependent density functional theory calculation or, in a simpler way, in the random phase approximation (RPA) where the exchange-correlation kernel is neglected. In this method the correlation energy is evaluated by integrating over the interaction strength λ of the system [44, 45].

To obtain the ACFDT RPA total energy $E[n]$ this term is split into a Hartree-Fock (HF) ($E_{EXX} = T_{KS}[\{\Psi_i\} + E_H[n] + E_x[n] + E_{ion-el}[n])$ and a correlation part $E_c[n]$ which are evaluated separately. The HF term includes the Hartree, Ewald and kinetic energy terms. The RPA total energy is therefore

$$E_{RPA} = E_{EXX} + E_c \tag{2.47}$$

with

$$E_c = \int_0^\infty \frac{d\omega}{2\pi} \text{Tr} \left\{ \ln \left[1 - \chi^0(\imath\omega)\nu \right] + \chi^0(\imath\omega)\nu \right\}. \tag{2.48}$$

The independent-particle response function $\chi^0_{\mathbf{G'G}}(\mathbf{q}, \imath\omega)$ is then calculated using one-electron wave functions and eigenvalues of a large number of virtual Kohn-Sham orbitals. For insulators and semiconductors with integer occupancies, the exact exchange term E_{EXX} is identical to the Hartree-Fock case. In metals on the other hand, a correction term has to be added to take partially occupied orbitals into account.

2.8. Vienna Ab-initio Simulation Package (VASP)

The previously described theoretical approaches are implemented in the software package VASP, short for Vienna *Ab-initio* Simulation Package. This software is mainly developed by the group of Georg Kresse [46, 47] at the University of Vienna. It implements the projector augmented wave (PAW) [48, 49] formalism with a plane wave basis set. This approach greatly improved basis set convergence and therefore computational cost compared to earlier ultra-soft pseudo-potential methods. To construct the PAW potentials the frozen core approach is used where the core electrons are kept frozen inside a the augmentation sphere which describes the collective system of the nuclei and core electrons. The one-electron wave-function is then derived from the pseudo orbitals with a linear transformation. All previously mentioned functionals and computational methods are implemented, allowing the calculation of a multitude of physical parameters. In the recent decade the code has been improved to include the simulation of excited state properties in the *GW* approximation [37, 39, 50, 51] and ACFDT RPA total energies [52–54]. A recently developed low-scaling algorithm [55, 56] for the calculation of RPA total energies where the independent-particle response function is evaluated using Green's functions $G(\imath\tau)$ on the imaginary time axis $\imath\tau$ allows the examination of much larger systems.

2.9. Equation of State

A formula which correlates the multiple state functions of a material under certain physical conditions is called an equation of state. One of the oldest introduced was the ideal gas law $pV = R(T_C + 273.15)$ which describes the correlation of temperature and pressure of an ideal liquid. To describe bulk properties, Hooke's law can predict the virtual work of all forces acting upon a medium at very small amounts of external strain. This only works in the infinitesimal limit and not for finite matter. To describe in isotropic elastic solid under hydrostatic pressure Murnaghan [57] derived the formula eq. (2.49) to calculate the stress in an elastic medium in dependence of external strain and its elastic energy density using only two elastic constants λ and μ.

$$p(V) = a(f(V) + 5f(V)^2), \quad f(V) = \frac{1}{2} \left\{ \left(\frac{V_0}{V} \right)^{\frac{2}{3}} - 1 \right\}, \quad a = 3\lambda + 2\mu. \tag{2.49}$$

This formula was expanded upon by Birch [58] for a cubic symmetric medium under hydrostatic compression of any amount, and a homogenous infinitesimal strain. This more involved formula eq. (2.50) describes the correlation of the pressure with the equilibrium volume V_0, the bulk modulus B_0, and the pressure derivative of the bulk modulus B_0'.

$$p(V) = \frac{3B_0}{2} \left[\left(\frac{V_0}{V} \right)^{\frac{7}{3}} - \left(\frac{V_0}{V} \right)^{\frac{5}{3}} \right] \left\{ 1 + \frac{3}{4} \left(B_0' - 4 \right) \left[\left(\frac{V_0}{V} \right)^{\frac{2}{3}} - 1 \right] \right\} \quad (2.50)$$

An integration of eq. (2.50) for the pressure according to the thermodynamic equation $p = -(\partial E / \partial V)_S$ gives an equation for the energy:

$$E(V) = E_0 + \frac{9V_0 B_0}{16} \left\{ \left[\left(\frac{V_0}{V} \right)^{\frac{2}{3}} - 1 \right]^3 B_0' + \left[\left(\frac{V_0}{V} \right)^{\frac{2}{3}} - 1 \right]^2 \left[6 - 4 \left(\frac{V_0}{V} \right)^{\frac{2}{3}} \right] \right\}. \quad (2.51)$$

This formula can be used to determine the equilibrium volume and therefore the lattice constants of a bulk structure by performing DFT total energy calculations at various volumina.

2.10. *Ab-initio* Thermodynamics

Often, DFT is described as a zero-pressure, zero-temperature technique since the total energy is the main value obtained from the calculation. While this energetic information is usually sufficient to compare e.g. different phases of the same material, properly accounting for all experimental conditions where usually other observables like the number of particles, pressure, and temperature are not constant is not directly possible. Gaining information on the order of stability of different stoichiometries would involve the comparison of another quantity which takes the atomic configuration into account. For example, to describe a system at constant pressure and temperature, the Gibbs free energy $G(T, p)$ is the appropriate thermodynamic potential that needs to be considered. If total energies calculated within the DFT framework are applied to the calculation of $G(T, p)$ in a suitable way, the stability of surfaces or interfaces at experimental temperatures or pressure ranges can be calculated. To do this in the context of an oxide-metal interface, the environment acts as a reservoir to take from or transfer to any amount of oxygen atoms. The appropriate Gibbs free energy $G(T, p, N_O)$ depends on the number of additional oxygen atoms N_O and takes the chemical potential and therefore oxygen partial pressure $p(O_2)$ into account. To calculate the stability of both additional oxygen atoms at the oxide-metal interface and of oxygen vacancies, the corresponding Gibbs free energy is comprised of that of the stoichiometric components of the model cell and that of the free O_2 molecule. This leads to the definition of the Gibbs free energy of formation according to

$$\Delta G(T, p) = g_{\text{Slab}}(T, p) + g_{O_2}^{\text{Gas}}(T, p). \quad (2.52)$$

The DFT total energies calculated for the components correspond to the Helmholtz free energy at $T = 0\,\text{K}$ neglecting zero-point vibrations and are therefore not exactly related to thermodynamic quantities. In the present study the latter are completely neglected since these contributions are usually small. Therefore, the Gibbs free energy of formation can be rewritten as

$$\Delta G(T, p) = E_{\text{Tot,Slab}}(T, p) + N \times E_{\text{Tot,O}_2}^{\text{Gas}}(T, p). \tag{2.53}$$

Usually, to compare the stability of surfaces with varying stoichiometry, a generalised surface energy is defined by referencing the Gibbs free energy to the surface area A, leading to

$$\frac{\Delta G(T, p)}{A} = \frac{1}{A} \left(E_{\text{Tot,Slab}}(T, p) + N \times E_{\text{Tot,O}_2}^{\text{Gas}}(T, p) \right). \tag{2.54}$$

A more detailed description of the formalism is given by Reuter and Scheffler [59] where a DFT study of the stability of the RuO_2 surface at varying oxygen partial pressure was discussed. In this work, this method was used in section 3.3.10 to study the stability of oxygen vacancies and of additional oxygen atoms at the ZrO_2-metal interface.

3. Ultra-thin Zirconia (ZrO$_2$) films adsorbed on a metal substrate

3.1. Introduction

Zirconia (ZrO$_2$) is a very versatile material with multiple use-cases in engineering, catalysis, sensory applications, and solid-oxide fuel cells (SOFC). Due to its high melting point (2983 K) and its high mechanical strength it is used for example as a thermal barrier in turbines [60], but also in dentistry [61]. It is also an excellent support material for catalysis [62] and can also itself function as a catalyst [63, 64]. ZrO$_2$ is a very good electric insulator due to its large band gap ($\geq$5 eV) [65, 66], but by doping the crystal with Yttrium and consequently creating Oxygen vacancies it can be made conducting for Oxygen ions [67–70]. This is the basis of the applications in solid-state electrochemistry in gas sensors [71, 72] and SOFCs [10, 73].

The pure, undoped ZrO$_2$ crystal crystallises in a monoclinic $P2_1/c$ phase and shows two phase transitions at elevated temperatures: at about 1440 K the crystal transforms into the tetragonal $P4_2/nmc$ phase [74] and at about 2650 K into the cubic $Fm\bar{3}m$ phase. There also exist high pressure phases: these transitions are observed at an ambient pressure of 8 GPa to 11 GPa to an orthorhombic $Pbca$ phase and at 21 GPa to 27 GPa to an orthorhombic $Pnma$ phase. The cubic phase can be stabilised at ambient temperature by Yttrium doping or by creating thin ZrO$_2$ films on a suitable support material.

Unfortunately, the large band gap makes it almost impossible to successfully apply methods like scanning tunnelling microscopy (STM) to bulk ZrO$_2$ surfaces. To overcome this problem thin ZrO$_2$(111) films are grown on a suitable conducting substrate. This can be achieved by oxidising Zr by vapour deposition in an O$_2$ atmosphere on a suitable single-crystal substrate, or by oxidisation of an alloy single crystal like Pt$_3$Zr or Pd$_3$Zr. The former approach has successfully been employed by Meinel et al. [75] who have grown epitaxial ZrO$_2$ films on the Pt(111) surface. More recently Lackner et al. [76] have used a sputter source for the growth of ZrO$_2$ films on a Rh(111) surface. This method makes it easier to control for the quality of the ZrO$_2$ film due to the high melting point of Zirconium. The latter method, oxidisation of an alloy, has successfully lead to the creation of ultra-thin zirconia films on the Pt$_3$Zr(0001) [3, 4, 77, 78] and Pd$_3$Zr(0001) [1] surface. On both substrates the oxide forms well-ordered films consisting of a single ZrO$_2$ trilayer. On the Pt$_3$Zr substrate, where after oxidation a pure platinum layer at the metal-oxide interface is observed, the ZrO$_2$ film shows a $(\sqrt{19} \times \sqrt{19})R23.4°$ superstructure with respect to this platinum surface layer. In contrast, the Pd$_3$Zr surface is bulk alloy terminated, and the ZrO$_2$ superstructure shows a $(\sqrt{217} \times \sqrt{217})R10.16°$

periodicity with respect to the alloy lattice. The lattice constant of the oxide film varies slightly, from $3.5\,\text{Å}$ on the Pt-terminated Pt_3Zr surface to $3.512\,\text{Å}$ on the $Pd_3Zr(0001)$ surface. On the Pt_3Zr and Pd_3Zr substrate the STM measurements suggest a buckling of the oxide surface of up to $50\,\text{pm}$ and $100\,\text{pm}$, respectively.

This chapter will cover the characterisation of the surface properties of ultra-thin ZrO_2 films, the zirconia-metal interface, and their adsorption properties based on computational models of different complexity using density functional theory. Later, the formation of ZrO_2 clusters on the Pt_3Zr substrate is discussed. The computational models build upon the diploma thesis [78] in which DFT studies of the ZrO_2 bulk phases and the zirconia-metal interface using a simple model were performed. Most of the DFT results presented here, which complement experimental measurements, have also been published in Choi, Mayr-Schmölzer, et al. [1], Li, Choi, Mayr-Schmölzer, et al. [3], Choi, Mayr-Schmölzer, et al. [4], and Antlanger, Mayr-Schmölzer, et al. [77].

The calculations were performed mainly using van-der-Waals corrected optB86b and optB88 functionals using methods introduced by Dion et al. [29], supplemented by standard PBE calculations. As was shown by Antlanger, Mayr-Schmölzer, et al. [77] and Mayr-Schmölzer [78] the treatment of the non-local interactions is essential to yield a proper description of the structure of adsorbed thin ZrO_2 films. Similar behaviour can be found for other thin films adsorbed on metal substrates like graphene on nickel [79]. In all cases, the computational parameters were converged with respect to the number of k-points to properly sample the Brillouin sphere. All structures were relaxed until the residual forces were $<0.01\,\text{eV/Å}$. The proper treatment of dispersion effects is important to properly describe the ZrO_2-metal interface, as the previous work has shown. To complement experiments, STM simulations were performed with the method introduced by Tersoff and Hamann [80], and XPS measurements were simulated by calculating the core level binding energies (see section 3.4).

3.2. ZrO_2-Metal Interface: $(\sqrt{3} \times \sqrt{3})R30°$ model

This chapter covers the so-called "small" model cells which were used to perform the DFT studies of the zirconia-metal interface. As mentioned before, the real $(\sqrt{217} \times \sqrt{217})R10.16°$ unit cell shown in fig. 3.2 would be computationally too demanding. Therefore, a simpler model was devised, called "$\sqrt{3}$" in the following, where a single $(\sqrt{3} \times \sqrt{3})R30°$ trilayer consisting of three $ZrO_2(111)$ formula units is adsorbed on the (0001) surface of a single unit cell of the Pt_3Zr and the Pd_3Zr alloy (see fig. 3.4). The ZrO_2 trilayers consist of slices of the (111) layers of cubic ZrO_2. The lattice mismatch between both alloys and the unsupported cubic ZrO_2 trilayer of about 9% in this $\sqrt{3}$ model is very large, but the main features of the interface, like interface energies and the buckling of the ZrO_2 film, can already be studied at low computational cost using these basic models. Additionally, the optimised lateral lattice constant of a single, unsupported $ZrO_2(111)$ layer contracts to $3.299\,\text{Å}$ (PBE [81], optB88[1]). Adding more layers

---

[1]This work.

increases the lattice constant of these oxide slabs, converging towards the bulk value. This behaviour has also been reported by Meinel et al. [81] and studied in more detail by [82]. Due to the lattice mismatch of the substrate and the oxide film, two extremal cases were considered: on the one hand a contraction of the $(\sqrt{3} \times \sqrt{3})R30°$ zirconia unit cell to fit to the substrate lattice, and on the other hand an expansion of the combined cell to fit to the experimentally measured ZrO_2 lattice constant of ≈ 3.5 Å. These models have been published by Choi, Mayr-Schmölzer, et al. [1], Antlanger, Mayr-Schmölzer, et al. [77], and Choi [83]. A sketch of the primitive unit cell of the ZrO_2 oxide film is shown in fig. 3.1.

As a measurement of the stability of the oxide-metal interface a generalised surface energy of the ZrO_2 film was calculated according to

$$E_{\text{surf}} = (E_{\text{substrate}+ZrO_2\text{film}} - E_{\text{substrate}} - E_{ZrO_2,\text{bulk}})/A_{\text{surface}} \tag{3.1}$$

with $E_{\text{substrate}+ZrO_2\text{film}}$ as the total energy of the complete system, $E_{\text{substrate}}$ the total energy of the substrate at the respective lattice constant, and $E_{ZrO_2,\text{bulk}}$ the total energy of the monoclinic ZrO_2 bulk, the experimental ground state structure of bulk ZrO_2. A_{surface} refers to the exposed surface area of the model.

(a) side view   (b) top view
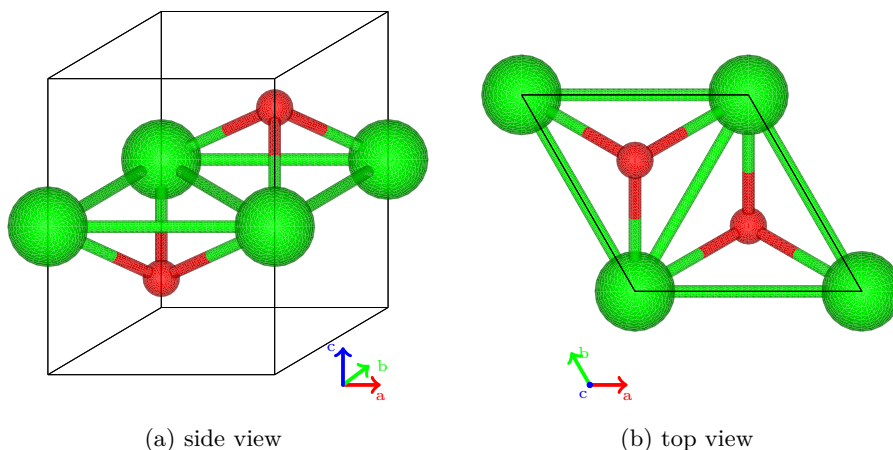
Figure 3.1.: Primitive unit cell of a single layer cubic ZrO_2. Zr atoms in green, O atoms in red.

3.2.1. Pt$_3$Zr and Pd$_3$Zr Substrate

Pd$_3$Zr Bulk Properties

Pt$_3$Zr and Pd$_3$Zr are so-called "Engel-Brewer" alloys, which show exceptionally strong bonding due to their half-filled d shells [84, 85]. Both crystallise in the hexagonal Ni$_3$Ti

(a) ZrO$_2$/Pd$_3$Zr   (b) ZrO$_2$/Pd$_3$Zr, one supercell   (c) ZrO$_2$/Pd$_3$Zr, FFT
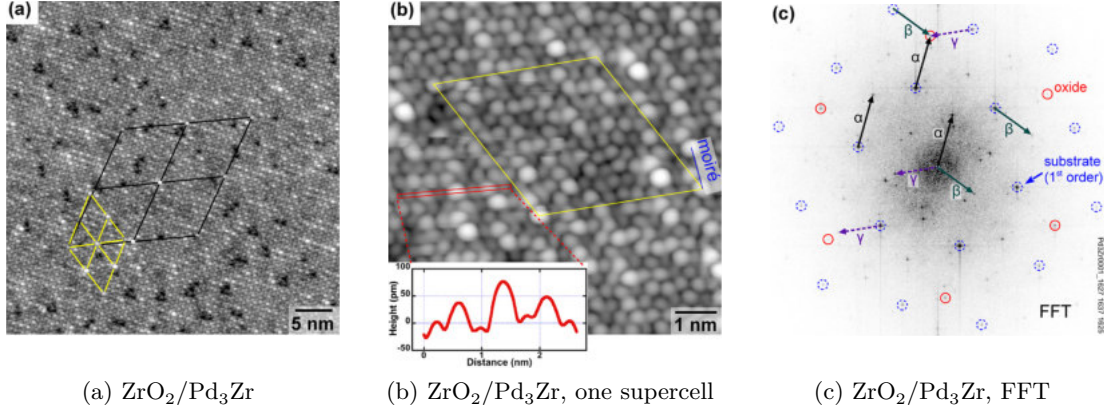
Figure 3.2.: (a) STM image ($V_{\text{sample}} = -43\,\text{mV}$, $I = 0.300\,\text{nA}$ of ultra-thin ZrO$_2$ on Pd$_3$Zr(0001), annealed to 870 °C. (b) High-resolution STM image of the same film. The $(\sqrt{217} \times \sqrt{217})R10.16°$ periodicity is indicated by black lines in (a), while an approximate $(\sqrt{43} \times \sqrt{43})R7.6°$ is shown in yellow. The inset shows a height profile. (c) Fourier transform of an STM image similar to (a). Red circles indicate the reciprocal oxide lattice, dashed blue circles the reciprocal Pd$_3$Zr alloy lattice. Experimental data courtesy of Choi, Mayr-Schmölzer, et al. [1].

(D0$_{24}$) structure and exhibit similar lattice parameters (see table 3.1). They have high melting points of 2523 K [86] and 2163 K [87] for Pt$_3$Zr and Pd$_3$Zr, respectively, higher than those of pure Pt, Pd, and Zr (2042 K, 1828 K, and 2128 K). The hexagonal crystal structure shows ABAC stacking where each Zr atom is surrounded only by Pt (Pd) atoms (see fig. 3.3). This closely packed structure, where the number of bonds between unequal atoms is maximised, prevents stacking faults and dislocations, leading to the very high mechanical stability.

The optimal lattice parameters of the Pt$_3$Zr crystal have previously been reported [78]. For the Pd$_3$Zr crystal an identical procedure was performed: the total energies of the alloy unit cell was calculated at different static unit cell volumes. For each step the internal coordinates of the ions and the shape of the unit cell were relaxed simultaneously and the resulting total energies were then fit to a Birch-Murnaghansection 2.9 equation of state. To ensure electronic convergence, the calculations were done using a $12 \times 12 \times 12$ Γ-centred $\vec{k}$-point grid which corresponds to 301 irreducible $\vec{k}$-points, and the energy cutoff was set to 400 eV. As shown in table 3.1 the deviation of the calculated lattice constants to the experimental values is $\leq 1.5\,\%$. While the PBE functional slightly underestimates the c/a ratio ($-0.7\,\%$ with respect to the experiment), the optB88 functional only deviates by $-0.2\,\%$. Still, both functionals yield slightly larger lattice parameters compared to the experiment. The calculated interlayer distance of the Pd$_3$Zr crystal at equilibrium lattice parameters are 2.338 Å and 2.328 Å for the PBE and the optB88

functional, respectively. To be consistent with the model cells described by Antlanger, Mayr-Schmölzer, et al. [77], the substrate at PBE equilibrium lattice constants was used to build the interface model cells, except where otherwise noted.
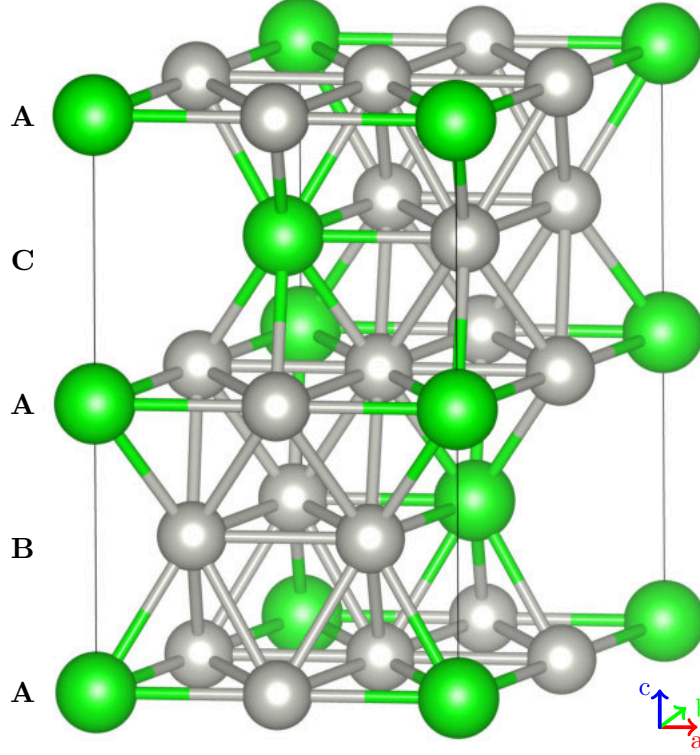
Figure 3.3.: Pt_3Zr/Pd_3Zr crystal structure. Zr atoms in green, Pt/Pd atoms in grey.

Surface Termination

In experiments, both Pt_3Zr and Pd_3Zr surfaces show steps with $c/4$ height, indicating that different translational domains exist on both surfaces. Since both bulk alloys show an ABAC stacking the surface can be terminated either by a type A or a type B/C layer. To determine the stability of the surface termination, the surface energy energy was calculated for two 5-layered slabs where the stoichiometric bulk layers were arranged in ABACA and CABAC stacking. Their lattice parameters in a and b direction were fixed to the PBE bulk values while the ions were allowed to relax in all directions. In c direction the lattice vector was increased to 30 Å, yielding a vacuum between upper and lower surface of the slab of >20 Å. For the slab calculations a $12\times12\times1$ Γ-centred $\vec{k}$-point

Table 3.1.: Pt_3Zr and Pd_3Zr lattice constants and equilibrium volumes. The Pt_3Zr values were taken from previously published work [78].

| | Pt_3Zr | | | Pd_3Zr | | |
	PBE [78]	optB88 [78]	Expt [88]	PBE	optB88	Expt [89]
a [Å]	5.729	5.742	5.624	5.699	5.693	5.612
c [Å]	9.364	9.380	9.213	9.310	9.349	9.235
V [Å^3]	266.300	267.800	252.400	261.900	262.400	251.900

mesh with 74 irreducible $\vec{k}$-points was used. The surface energies of the $Pd_3Zr(0001)$ and $Pt_3Zr(0001)$ were then calculated with both the PBE and the optB88 functional at the respective lattice constants. The PBE results for the $Pt_3Zr(0001)$ surface were identical to the previously reported values [78].

As can be seen in table 3.2, the calculated surface energies, referenced either to the number of atoms in the surface layer or the surface area, are lower for the A-termination for both alloys. The PBE functional yields lower surface energies than the van-der-Waals corrected optB88 functional because of its lack of a description of long range effects [90–93]. For both functionals, the $Pd_3Zr(0001)$ surface energies are lower than for the $Pt_3Zr(0001)$ surface.

For the $Pd_3Zr(0001)$ surface, the comparison using the PBE (optB88) functional yields a surface energy of 749 meV/atom (650 meV/atom) for the A-terminated surface, which is lower by 57 meV/atom (55 meV/atom) than for the B/C terminated surface. For the Pt_3Zr slabs, this energy difference is slightly higher at 66 meV/atom. Since the relative arrangement of the first two layers is the same for both the ABACA and the CABAC configuration the third monolayer plays a significant role in the stability of the surface, stabilising the A termination for both Pt_3Zr and Pd_3Zr (see table 3.2).

Compared to the bulk, the first two surface layers show slight changes in the interlayer distances. In the A-terminated Pd_3Zr slab, the surface layer relaxes inwards by -2.4%, while the second layer relaxes outwards by 0.3%. At the surface, the Zr atom is depressed into the surface by 8.1%, in contrast to the almost unchanged movement of the Pd atoms (-0.4%) with respect to the bulk interlayer distance. A similar pattern was found for the A-terminated Pt_3Zr surface, discussed by Antlanger, Mayr-Schmölzer, et al. [77]. Since the inwards relaxation of pure Zr is much less (-2.3% [94]), this large inwards relaxation of the surface Zr is a property of both Pt_3Zr and Pd_3Zr alloys. This unusual relaxation can be explained by the opposite direction of movement for the Zr atoms in the surface and the subsurface layers: since the Pd atoms in the second layer slightly buckle inwards, the surface Zr atom is displaced inwards. The Zr atom in the subsurface layer in contrast buckles towards the surface, hindering the inward movement of the surface Pd atoms.

To further compare the two substrate alloys the stability of the different surface terminations were also tested for a hypothetical Pd-terminated surface (see fig. 3.5). For

Pt$_3$Zr, the experiment has shown [77] that after oxidation of the surface a pure Pt-terminated surface remains. To create the equivalent configuration the Zr atoms at the surface of the slab were replaced by Pd atoms. Similar to the stoichiometric surface, the A-termination is more stable than the B/C-termination by 7 meV, a much lower energy difference. After relaxation of the surface layers, the interlayer distances are reduced to $d_{12} = 224$ pm and $d_{23} = 232$ pm compared to the bulk value of 233 pm, a larger contraction (-4.2%) than for the Pd$_3$Zr terminated surface. For the Pt/Pt$_3$Zr(0001) surface the surface layer only contracts by -0.4% [77]. Like with the Pt/Pt$_3$Zr(0001) surface the Pd-terminated surface shows almost no buckling (6 pm) as only the surface Pd atom positioned at a hollow site with respect to the subsurface layer buckles downwards.

Table 3.2.: Pt$_3$Zr and Pd$_3$Zr surface energies for ABACA and CABAC stacking order.

| | Pt$_3$Zr | | Pd$_3$Zr | |
	PBE [78]	optB88	PBE	optB88
ABACA [meV/atom]	732	830	650	749
CABAC [meV/atom]	797	900	705	805
ABACA [meV/Å^2]	103	117	92	105
CABAC [meV/Å^2]	112	127	99	113

3.2.2. The ZrO$_2$/Pd$_3$Zr Interface

Experiments done by Choi, Mayr-Schmölzer, et al. [1] have shown that the ZrO$_2$ film forms a hexagonal lattice on top of the (0001) surface of the stoichiometric Pd$_3$Zr alloy. Auger spectroscopy measurements indicate a 2:1 ratio between oxygen and zirconium atoms. Fourier analysis of STM measurements of the oxide lattice shows a $(\sqrt{217} \times \sqrt{217})R10.16°$ superstructure with respect to the Pd$_3$Zr lattice with a lattice constant of 3.512 Å.

ZrO$_2$/Pd$_3$Zr Interface: Compressed Oxide

To construct the previously mentioned $(\sqrt{3} \times \sqrt{3})R30°$ model cells the A-terminated 5-layer slabs introduced in section 3.2.1 were used as a substrate, on which a single trilayer of ZrO$_2$ was placed. To compensate for the lattice mismatch the oxide film was compressed by 9.8 % with respect to the cubic bulk value. In contrast to the ZrO$_2$/Pt/Pt$_3$Zr interface introduced above, the presence of Zr atoms in the surface/interface layer and hence the formation of Zr–O bonds to these interface Zr atoms suggests four different interface configurations to be considered: both a zirconium atom or a lower oxygen atom of the oxide film can be placed above either an interface zirconium or palladium atom. These four models illustrated in fig. 3.6, labelled O1Pd, O1Zr, ZrPd, and ZrZr, provide an efficient sampling of the large $(\sqrt{217} \times \sqrt{217})R10.16°$ unit cell. As an example, in
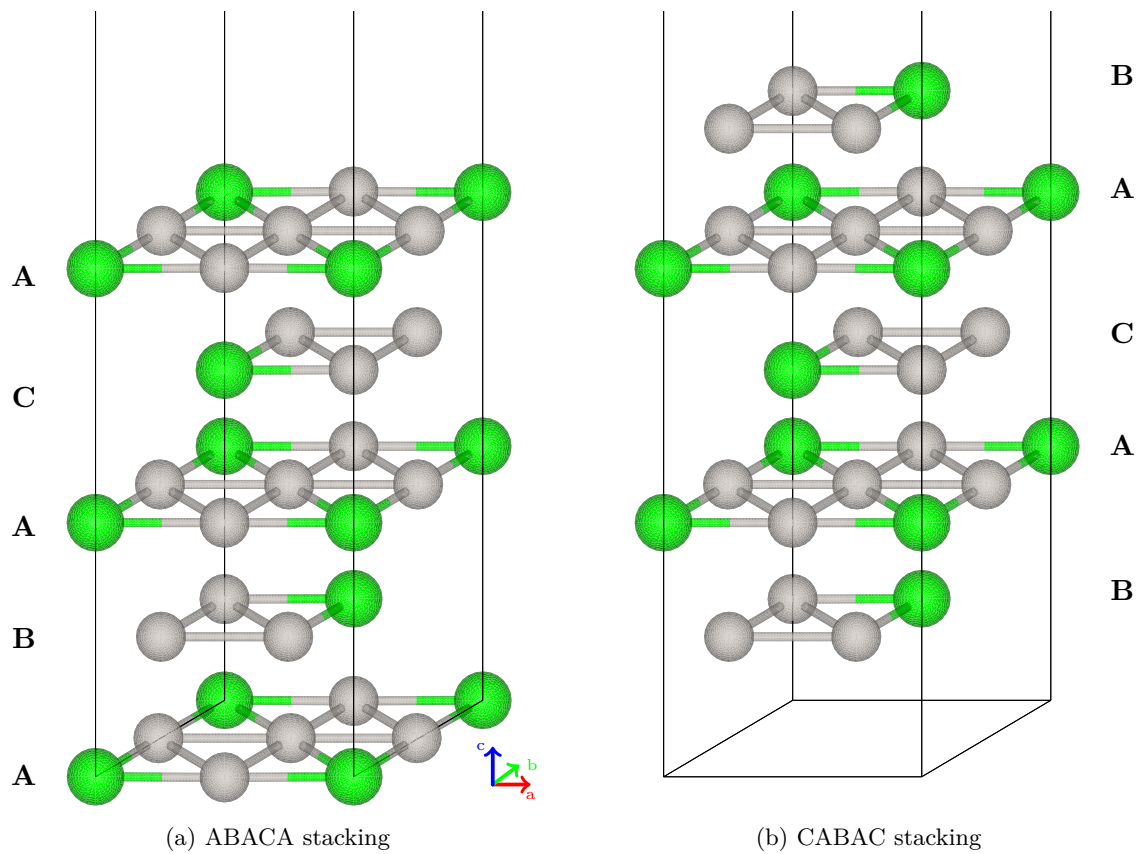
(a) ABACA stacking

(b) CABAC stacking

Figure 3.4.: 5-layered Pd$_3$Zr slab in (a) ABACA and (b) BACAB stacking order. Zr atoms in green, Pt/Pd atoms in grey.

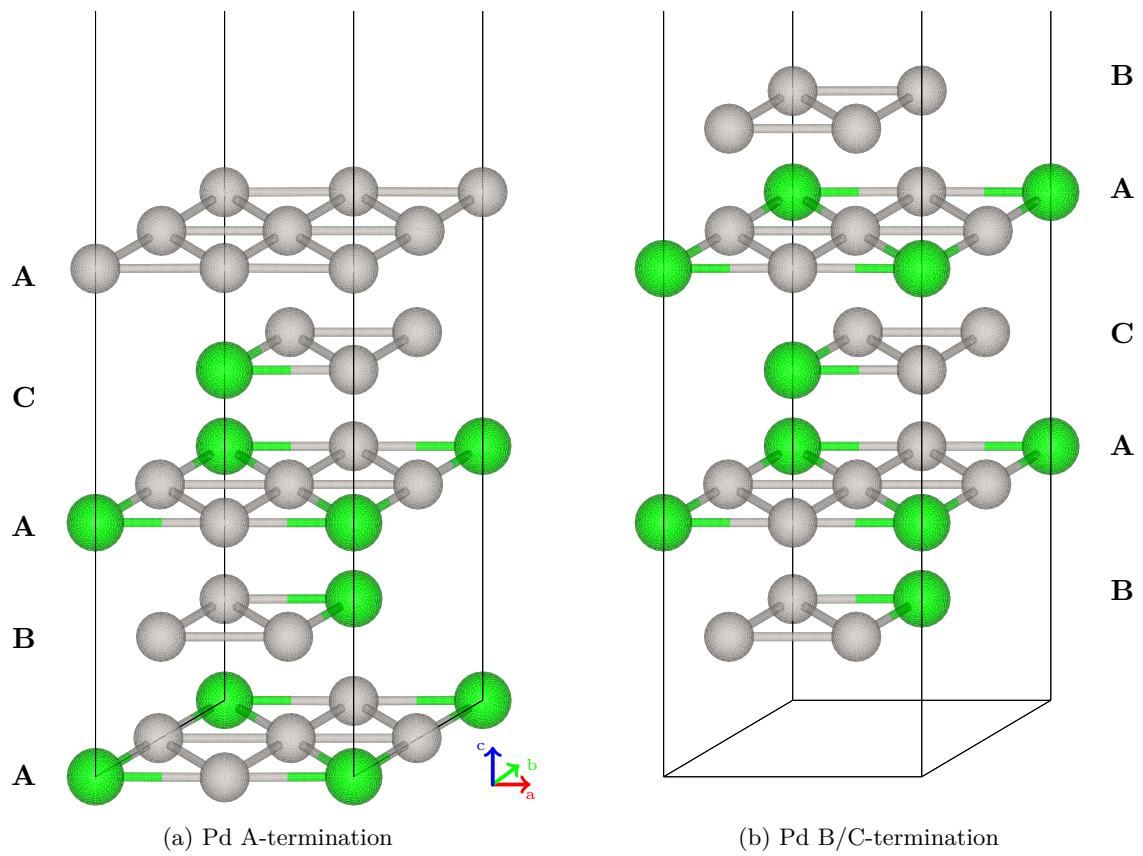(a) Pd A-termination

(b) Pd B/C-termination

Figure 3.5.: 5-layered Pd$_3$Zr slab with a pure Pd (a) A- and (b) B/C-termination. Zr atoms in green, Pd atoms in grey.

the "ZrZr" model a Zr atom of the oxide film is placed directly on top of a surface Zr atom, while for the "O1Zr" this is the case for a lower oxygen atom of the ZrO_2 trilayer. For the calculations, the atoms defining the model were fixed in x and y direction to suppress lateral movement of the oxide film. Without this restriction, only the O1Zr model shows lateral relaxation into a different configuration O1Zr' (see fig. 3.8a), which also exhibits the lowest surface energy of all models.

The relaxed ZrO_2/Pd_3Zr structure models show that even the PBE functional yields strong chemical bonding between oxide film and metallic substrate. The optB88 functional does not lead to significantly different bonding distances. This is in contrast to the $ZrO_2/Pt/Pt_3Zr$ model, where the lack of the van-der-Waals contributions in the PBE functional leads to very large, unrealistic, distances between adsorbate and alloy and very low surface energies. Now, an oxygen atom (O1) of the oxide film binds to a zirconium atom (Zr_S) in the uppermost surface layer at bonding lengths $d_{O_1-Zr_S}$ between 211 pm and 242 pm for the ZrZr and O1Zr models, respectively. Table 3.3 shows a compilation of bond lengths and surface energies calculated using the PBE and the optB88 functional.

Comparing the four fully relaxed models, calculated using the optB88 functional, an average interlayer distance between lower oxygen layer O1 and substrate Pd_3Zr layer of 214 pm is predicted. This average distance is defined as the mean height of the atoms assigned to each layer; due to the buckling individual bond lengths can differ. Except for the ZrZr configuration, the models show the that the presence of the surface Zr atom plays a significant role in the oxide-alloy bonding. The O1–Zr_S bonds lengths for those three models are between 209 pm and 224 pm, close to the Zr–O length in cubic ZrO_2 (223 pm at optB88 equilibrium lattice constant). For the ZrZr configuration, three O1 atoms are positioned around the surface Zr_S atom at distances of 238 pm. In this model the Zr_S atom is slightly pulled out of the surface by 27 pm towards the oxide film and the distances between the three O1 in the lower oxygen layer are reduced to 281 pm from 347 pm. The calculations predict significant buckling of the substrate for all model cells. While the top-most oxygen layer of the oxide is fairly flat in for all models, the zirconium layer exhibits buckling between 75 pm and 109 pm. The O1Pd model is a special case because due to the constraint keeping one lower oxygen atom fixed above one palladium atom the oxide is laterally more strongly distorted. Here two O1 atoms bind strongly to the Zr_S atom. The lowest amount of buckling is found in the ZrZr model where the lateral strain is the smallest and the Zr atom of the Pd_3Zr surface is surrounded by three oxygen atoms of the ZrO_2 film.

The same model cells, relaxed with the PBE functional, only show slight differences with respect to parameters like interlayer distances and buckling with differences of just a few pm. Though, the calculated surface energies are significantly lower, in the range of -90 meV compared to about -450 meV for the optB88 functional. Also, since the optB88 functional takes the polarisation into account, the Zr–Zr interaction between ZrO_2 film and Pd_3Zr substrate is decreased for the PBE results. This becomes apparent comparing the stability of the different models: for the PBE functional the model variants resulting in the lowest O1–Zr_S bond lengths are more stable than the ZrZr model. The

optB88 calculations, on the other hand, show an in increase of the stability of this model where the Zr–Zr distance is minimal.

The Tersoff-Hamann STM simulation (see fig. 3.7) of the fully relaxed O1Zr' structure show, at positive bias voltages, the two upwards buckled zirconium atoms as bright features. The remaining Zr of the unit cell occupies a dark spot. At negative bias the pattern is different, here both oxygen and zirconium states contribute to the bright features. This contrasts with the simulations done for the $ZrO_2/Pt/Pt_3Zr$ interface where the zirconium atoms were visible as bright features at both positive and negative bias voltages [78].

Table 3.3.: Surface energies and lattice parameters of one trilayer of $ZrO_2(111)$ on Pd_3Zr, calculated using the optB88 functional. Values in parentheses were calculated using the PBE functional.

Configuration	O1Pd		O1Zr		ZrPd		ZrZr		O1Zr'	
d_{O_2-Zr} [pm]	97	(100)	96	(95)	96	(95)	92	(91)	96	(96)
d_{Zr-O_1} [pm]	96	(93)	97	(95)	97	(95)	89	(88)	96	(95)
d_{O_1-S} [pm]	231	(238)	242	(246)	238	(242)	211	(212)	240	(244)
b_{O_2} [pm]	20	(41)	2	(4)	5	(7)	0	(0)	3	(5)
b_{Zr} [pm]	99	(105)	75	(68)	80	(77)	109	(107)	83	(77)
b_{O_1} [pm]	16	(21)	25	(28)	20	(24)	0	(0)	22	(26)
b_S [pm]	17	(21)	11	(14)	11	(14)	48	(46)	9	(13)
l_{Zr-Pd_S} [pm]	283	(283)	297	(303)	283	(288)	315	(313)	289	(295)
$l_{O_1-Zr_S}$ [pm]	231	(229)	221	(221)	225	(224)	233	(236)	222	(221)
E_{surf} [meV/Å^2]	48	(47)	40	(38)	43	(42)	43	(50)	37	(36)

(a) O1Pd (b) O1Zr (c) ZrPd (d) ZrZr (e) O1Zr'
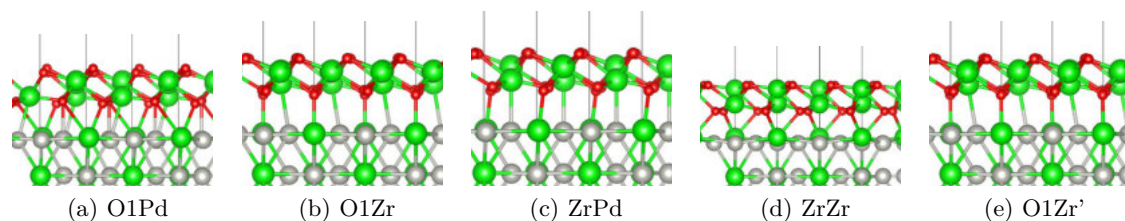
Figure 3.6.: Side view of the five ZrO_2/Pd_3Zr models, viewed along the axis normal to the *bc* plane. Zr, O, and Pd atoms in green, red, and grey.

ZrO_2/Pd_3Zr Interface: Expanded Pd_3Zr Substrate

Since the previously discussed model cells greatly underestimates the experimental oxide lattice constant the model cells were also studied in an alternative configuration. Here, the model cell was stretched so that the Zr–Zr distances of the oxide film were 3.5 Å,

(a) Bias: $+0.500\,\mathrm{V}$ (b) Bias: $-0.500\,\mathrm{V}$
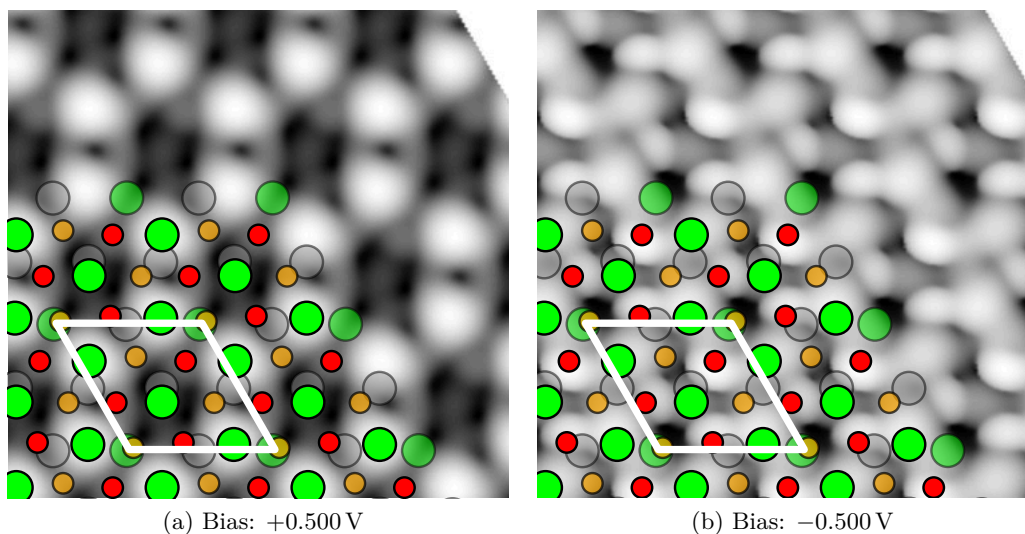
Figure 3.7.: STM simulation of the fully relaxed optB88 O1Zr' structure. Zr, upper and lower O, and Pd atoms in green, red and orange, and grey.

corresponding to a Pd_3Zr lattice constant of 6.062 Å. This puts the substrate under heavy strain, increasing the reactivity of the substrate, but the structural properties of the oxide film are described in a more realistic manner.

The structural properties of the relaxed model cells at this expanded lattice constant (see table 3.5) are similar to the compressed case. Generally, the interlayer distances are slightly lower, and due to the higher reactivity of the substrate, the oxide film sits closer to the substrate. In the calculations using the van-der-Waals corrected optB88 functional, the oxide film shows heavier lateral distortion but less buckling compared to the compressed case. All models—except for the ZrZr model—show reduced surface energies. For this model, the close distance between the eponymous surface and oxide Zr atoms reduces the total energy of this configuration by a large amount. Like in the case of the compressed substrate, the O1Zr' configuration, where no atoms are kept fixed, is the global ground state (see fig. 3.8b). Due to the larger lattice constant the oxide film is less buckled compared to the compressed model, yielding layer distances of 87 pm to 89 pm. The distance to the substrate is reduced to 226 pm for the van-der-Waals relaxed structure. Additionally, the optB88 calculations predict less buckling of the Zr layer than for the compressed model at 46 pm. One main difference to the compressed model is that for all configurations, except for the ZrZr model, one O–Zr bond at the surface is broken, leading to one under-coordinated oxygen atom per unit cell, see fig. 3.8b.

The PBE functional on the other hand yields a heavily distorted oxide film with buckling of the Zr layer of up to 137 pm. The strong binding between surface Zr and oxide O leads to downwards buckling of the one oxide Zr located close to the surface Zr. The two other oxide Zr of the unit cell interact much less with the substrate and

87 pm				85 pm
89 pm				82 pm
226 pm				209 pm

(a) 3.3 Å   (b) 3.5 Å

Figure 3.8.: 1 trilayer of ZrO_2 adsorbed on stoichiometric Pd_3Zr in the fully relaxed O1Zr' configuration. (a): compressed oxide film, (b): expanded Pd_3Zr substrate. Zr, 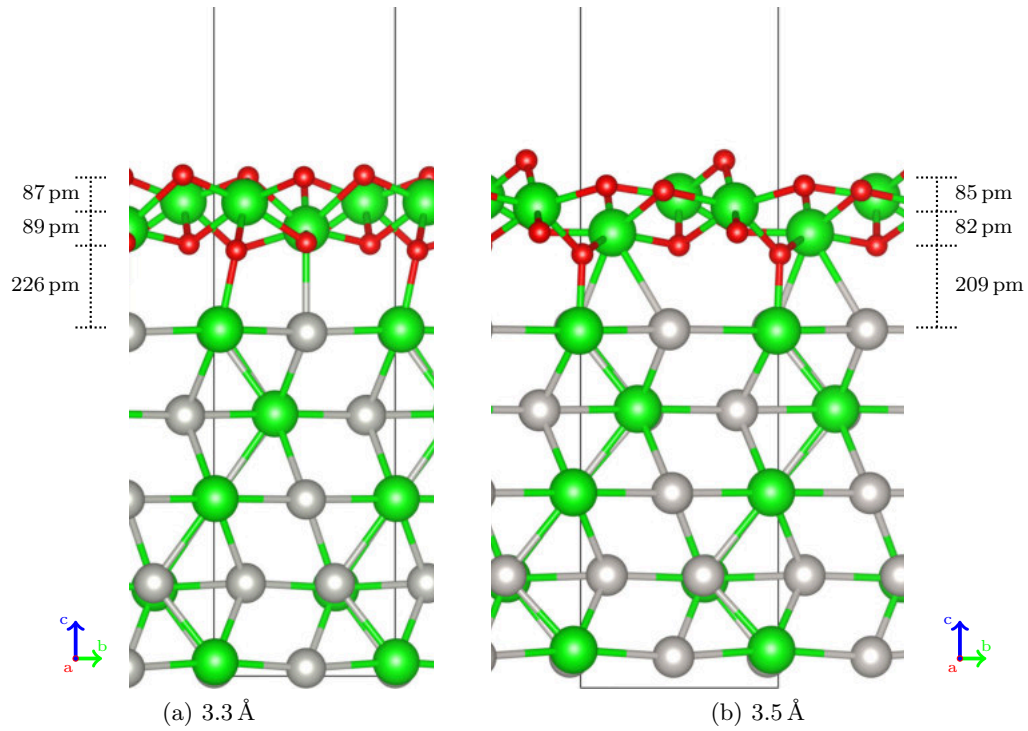O, and Pd atoms in green, red, and grey. In the expanded model one under-coordinated surface oxygen and the increased distortions of the ZrO_2 film is well visible.

29

buckle upwards. Finally, the oxide film is no trilayer anymore, since the downwards buckled Zr is displaced below the lower oxygen atoms, a structure that is not detected in the experiment [1]. This structural difference also becomes apparent in the density of states, illustrated in fig. 3.14, where the oxide film states of the heavily distorted PBE structure shift by about 0.5 eV to higher energies and hybridise much less with the substrate states.

For the fully expanded O1Zr' cell the STM simulations show one bright feature per surface unit cell. At positive bias voltage this spot is centred on the bridge between the upwards buckled Zr atoms of the oxide film, while for negative bias voltage the spot is formed by the superposition of Zr and upper oxygen states (see fig. 3.10). The comparison with the STM simulations of the compressed model shows that the height difference between upper oxygen and zirconium atoms plays a big role in their visibility in STM measurements.

Table 3.4.: Surface energies and lattice parameters of one trilayer of $ZrO_2(111)$ on Pd_3Zr, expanded to the experimental oxide lattice constant. Relaxed using the optB88 functional, values in parentheses were calculated using the PBE functional. STM measurements show buckling of the oxide film of up to 100 pm.

| Configuration	O1Pd		O1Zr		ZrPd		ZrZr		O1Zr'	
d_{O_2-Zr} [pm]	94	(93)	86	(95)	85	(89)	82	(80)	87	(96)
d_{Zr-O_1} [pm]	89	(68)	88	(72)	90	(85)	87	(86)	89	(70)
d_{O_1-S} [pm]	220	(267)	224	(265)	219	(239)	193	(194)	226	(264)
b_{O_2} [pm]	79	(136)	3	(127)	15	(84)	0	(0)	4	(128)
b_{Zr} [pm]	101	(137)	41	(137)	45	(101)	87	(77)	46	(137)
b_{O_1} [pm]	46	(140)	32	(136)	27	(72)	0	(0)	30	(134)
b_S [pm]	29	(15)	7	(10)	11	(3)	27	(24)	4	(13)
l_{Zr-Pd_S} [pm]	271	(285)	306	(294)	299	(297)	307	(307)	289	(293)
$l_{O_1-Zr_S}$ [pm]	224	(206)	210	(204)	209	(204)	238	(240)	212	(206)
E_{surf} [meV/Å^2]	47	(28)	47	(30)	48	(41)	70	(73)	46	(27)

(a) O1Pd   (b) O1Zr   (c) ZrPd   (d) ZrZr   (e) O1Zr'
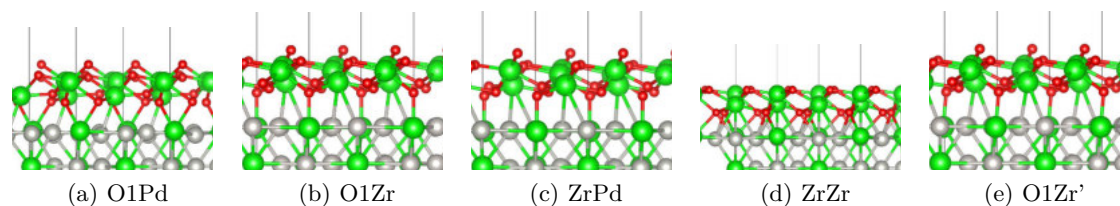
Figure 3.9.: Side view of the five ZrO_2/Pd_3Zr models expanded to 3.5 Å oxide lattice constant, viewed along the axis normal to the *bc* plane.

(a) Bias: $+0.5\,\mathrm{V}$ (b) Bias: $-0.5\,\mathrm{V}$
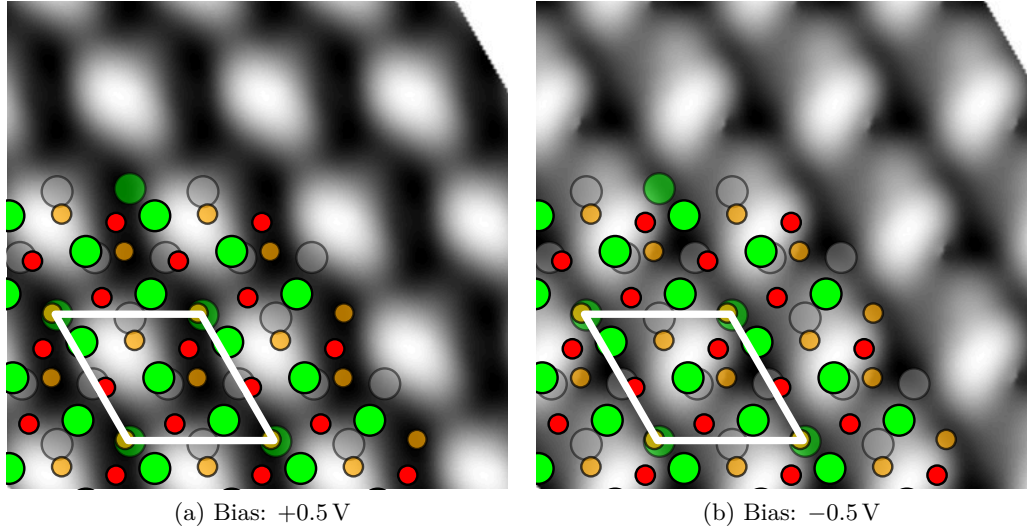
Figure 3.10.: STM simulation of the fully relaxed O1Zr' structure stretched to an oxide lattice constant of 3.5 Å. Zr atoms, upper O atoms, lower O, Pd, are denoted in green, red, orange, and grey, respectively.

Pd-terminated Model: $ZrO_2/Pd/Pd_3Zr$

All models discussed in the previous section are distinctly different from to the Pt-terminated $ZrO_2/Pt/Pt_3Zr$ model discussed by Antlanger, Mayr-Schmölzer, et al. [77]: there, the alloy is terminated by a pure platinum layer, and at the interface only O1–Pt bonds exist. These bonds are decisively weaker than the O1–Zr_S bond, leading to much higher surface energies. To quantify the influence of the chemical differences between Pt and Pd the oxide-alloy interface was also investigated using a hypothetical Pd-terminated Pd_3Zr substrate, both in the compressed and expanded configurations. In the former case, after relaxation, the geometries of the model cells are almost identical to the Pt_3Zr substrate case with differences in the interlayer distances below 3 pm. Only the O1–substrate interlayer distance is slightly shorter by 10 pm to 15 pm for $ZrO_2/Pd/Pd_3Zr$. The predicted surface energies are very similar with the optB88 functional predicting slightly stronger binding for the Pd-terminated Pd_3Zr substrate. Nevertheless, the influence of the Zr atom in the surface layer is much more important, since the surface energy decreases by $\approx 13\,\mathrm{meV/Å}^2$ for the stoichiometric substrate. The PBE functional, like for the $ZrO_2/Pt/Pt_3Zr$ interface, results in an almost flat ZrO_2 film at a large distance ($>300\,\mathrm{pm}$) which is very weakly bound to the substrate ($E_{\mathrm{surf}} \approx 49\,\mathrm{meV/Å}^2$). Similar to the $ZrO_2/Pt/Pt_3Zr$ case, the van-der-Waals corrected optB88 functional results in a $4\,\mathrm{meV/Å}^2$ more stable configuration when a Zr atom of the oxide is placed directly above a surface Pd ("ZrPd") than the "OPd" modification where a lower O of the oxide is located above the surface Pd.

Stretching the model cells laterally to the experimental oxide lattice constant increases the surface energy by about $20\,\mathrm{meV/\mathring{A}^2}$ for both functionals. For the $ZrO_2/Pt/Pt_3Zr$ case a similar increase is predicted for the optB88 functional, while the PBE functional yields an increase of $>27\,\mathrm{meV/\mathring{A}^2}$. The interlayer distance between oxide film and substrate is reduced to $210\,\mathrm{pm}$ (optB88) and $226\,\mathrm{pm}$ (PBE). Both oxygen layers buckle less compared to the stoichiometric substrate due to the weaker interaction with the Pd-terminated substrate. Additionally, the buckling of the zirconium layer is greatly reduced to $30\,\mathrm{pm}$ (optB88) and $32\,\mathrm{pm}$ (PBE).

The STM simulations of the compressed $ZrO_2/Pd/Pd_3Zr$ model (see fig. 3.11) show bright triangular spots, separated by slightly darker lines for positive bias voltages. The former are caused by the upwards buckled Zr atom, while the darker lines denote the downwards buckled Zr and upper oxygen atoms. At negative bias voltage, depicting occupied states, the upper oxygen atoms of the oxide film are visible as bright spots. For the stretched $ZrO_2/Pd/Pd_3Zr$ model (see fig. 3.12) a similar pattern exists, the upwards buckled Zr atoms again appear as triangular bright spots. At negative bias voltage both Zr and upper O atoms appear as bright spots. Since the height difference between Zr and O is slightly lower compared to the compressed structure the Zr atoms are slightly brighter.

Table 3.5.: Surface energies and lattice parameters of a single trilayer of $ZrO_2(111)$ on Pd-terminated Pd_3Zr, both at alloy and experimental oxide lattice constant. Relaxed using the optB88 functional, values in parentheses were calculated using the PBE functional.

	3.3 Å				3.5 Å			
Configuration	ZrPd		OPd		ZrPd		OPd	
d_{O_2-Zr} [pm]	95	(96)	94	(96)	86	(91)	85	(86)
d_{Zr-O_1} [pm]	93	(96)	93	(94)	83	(84)	82	(83)
d_{O_1-S} [pm]	237	(314)	230	(254)	209	(225)	209	(218)
b_{O_2} [pm]	1	(0)	0	(0)	12	(48)	0	(0)
b_{Zr} [pm]	61	(10)	64	(54)	35	(63)	30	(32)
b_{O_1} [pm]	3	(1)	0	(0)	9	(24)	0	(0)
b_S [pm]	4	(7)	2	(3)	9	(5)	3	(2)
E_{surf} [$\mathrm{meV/\mathring{A}^2}$]	50	(49)	54	(49)	71	(70)	76	(73)

Projected density of states

The density of states calculated for the most stable O1Zr' configuration at Pd_3Zr lattice constant shows that the band gap of the ZrO_2 is still about $3.5\,\mathrm{eV}$ (see fig. 3.13). In the vicinity of the Fermi level a few occupied mid-gap states of the oxide appear due to hybridisation with the metal substrate. Both functionals predict a conduction band

(a) Bias: $+0.5\,\mathrm{V}$　　　　　　　　(b) Bias: $-0.5\,\mathrm{V}$
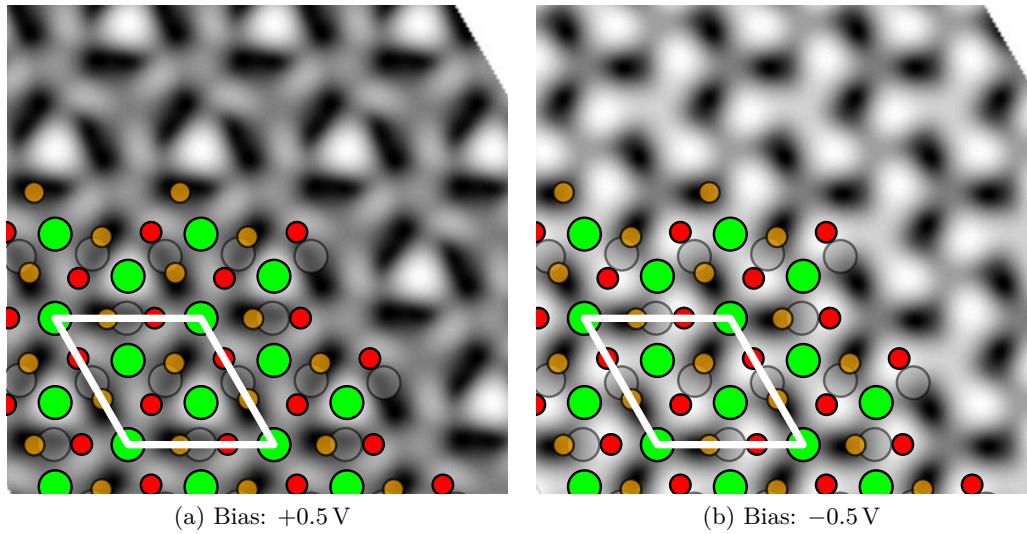
Figure 3.11.: STM simulation of the fully relaxed Pd-terminated ZrPd structure, calculated with the optB88 functional. Zr, upper O, lower O, and Pd atoms are denoted in green, red, orange, and grey, respectively.

(a) Bias: $+0.5\,\mathrm{V}$　　　　　　　　(b) Bias: $-0.5\,\mathrm{V}$
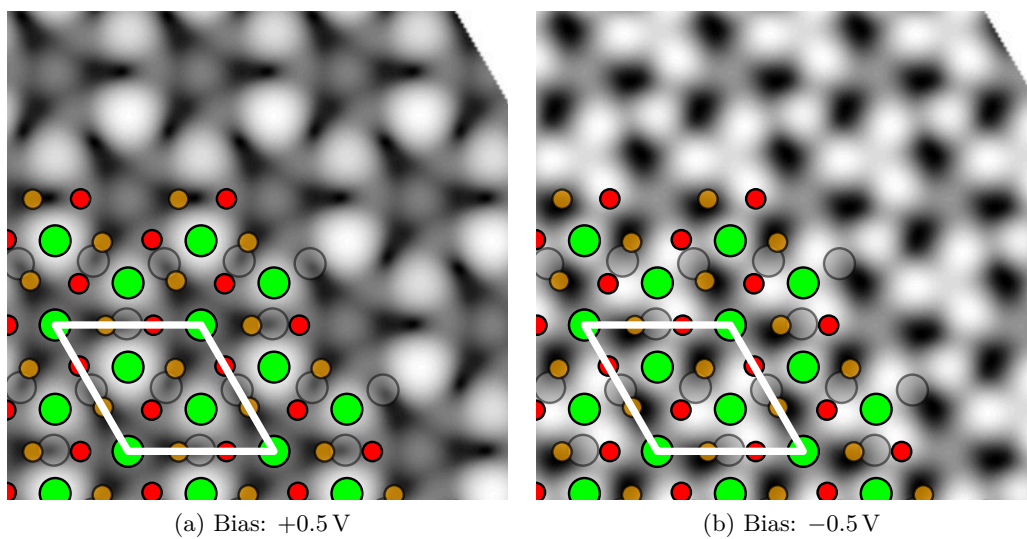
Figure 3.12.: STM simulation of the fully relaxed Pd-terminated ZrPd structure expanded to an oxide lattice constant of $3.5\,\text{Å}$, calculated with the optB88 functional. Zr, upper and lower O, and Pd atoms are denoted in green, red, orange, and grey, respectively.

minimum at $\approx 1.5\,\mathrm{eV}$. The DOS of the oxide film adsorbed in the expanded configuration (see fig. 3.14) shows a smaller mid-gap state right below the Fermi edge and the conduction band minimum is shifted to higher energies, especially for the PBE functional. Here the strong distortions of the oxide film discussed in section 3.2.2 lead a shift of $\approx 0.5\,\mathrm{eV}$ to higher energies and a narrowing of the conduction band for the oxide film states.

ZrO$_2$/Pd$_3$Zr, compressed, PBE

ZrO$_2$/Pd$_3$Zr, compressed, optB88
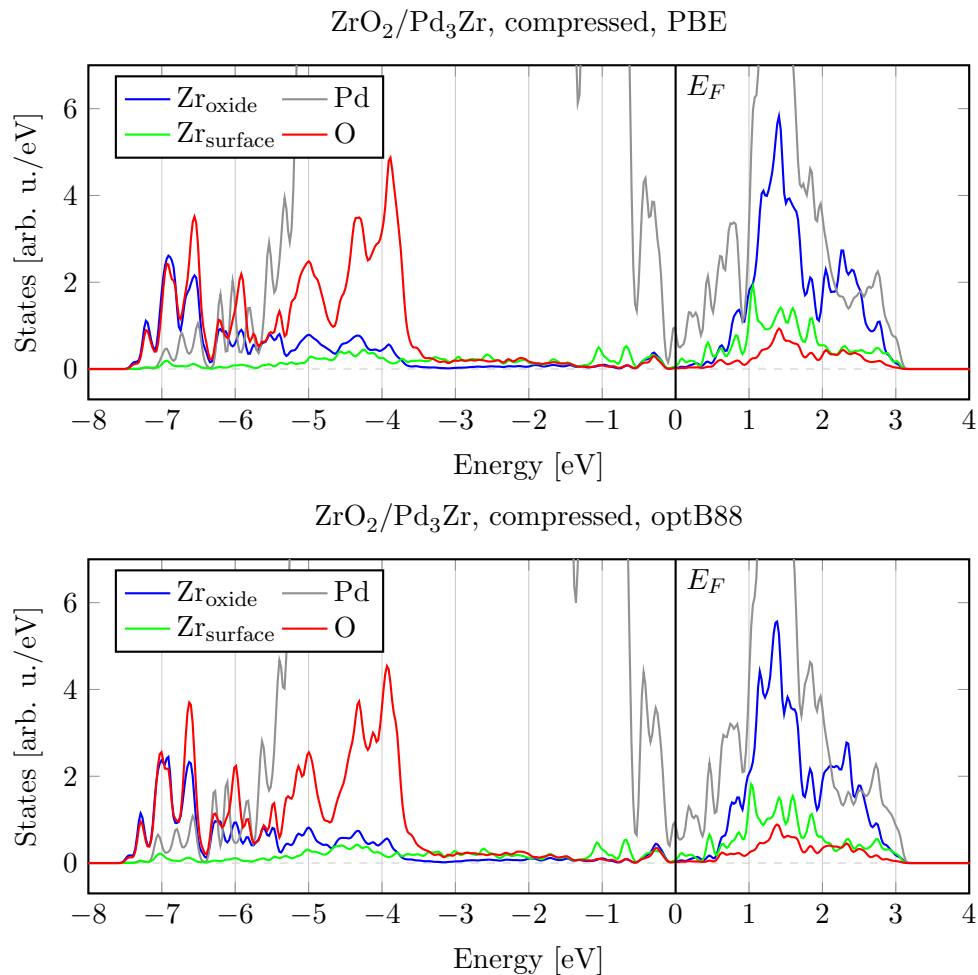
Figure 3.13.: Projected DOS of the fully relaxed O1Zr' model cell at Pd$_3$Zr bulk lattice constant. The Zr and O lines are projected on the oxide film sites, while Zr$_{sub}$ indicates the Zr states in the surface layer of the substrate.

3.2.3. The ZrO$_2$/Pt/Pt$_3$Zr Interface

The ZrO$_2$/Pt/Pt$_3$Zr Interface: Expanded Pt$_3$Zr Substrate

To complement the results published in Choi, Mayr-Schmölzer, et al. [1] and Antlanger, Mayr-Schmölzer, et al. [77], the ZrO$_2$/Pt/Pt$_3$Zr interface was also studied in an expanded
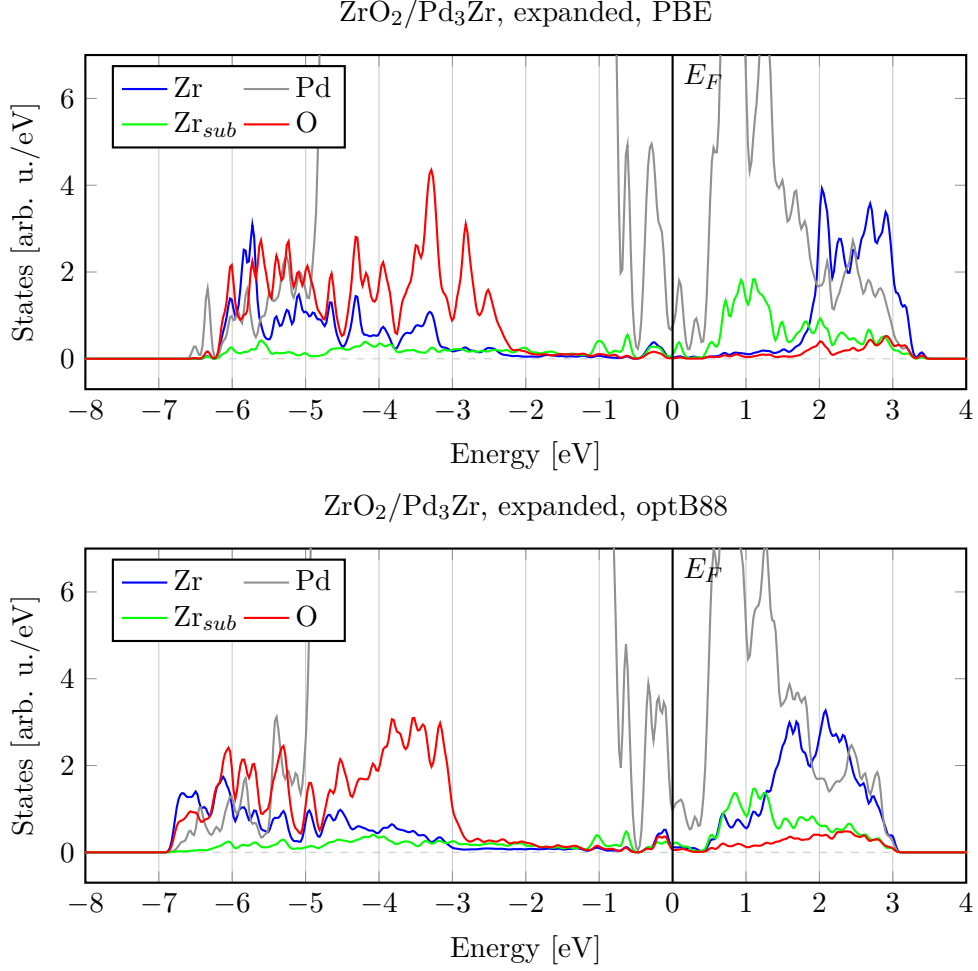
Figure 3.14.: Projected DOS of the fully relaxed expanded O1Zr' model cell at 3.5 Å oxide lattice constant. The Zr and O lines are projected on the oxide film sites, while Zr$_{\text{sub}}$ indicates the Zr states in the surface layer of the substrate.

configuration. Like for the corresponding ZrO$_2$/Pd$_3$Zr and ZrO$_2$/Pd/Pd$_3$Zr models, the model cells were stretched to a Pt$_3$Zr lattice constant of 6.060 Å, yielding an oxide lattice constant of 3.5 Å. Again two adsorption configurations were studied, one where a Zr atom was positioned on top of a substrate Pt atom named ZrPt, and another where a lower oxygen atom of the oxide was positioned above a Pt atom named OPt. To prevent lateral movement of the film these two atoms are kept fixed in x and y direction. These calculations were performed using the same setup as for the compressed ZrO$_2$/Pd$_3$Zr model, see section 3.2.2, both with the PBE and the van-der-Waals corrected optB88 functional.

The increased reactivity of the substrate due to the stretched lattice is apparent when looking at the fully relaxed PBE structure. As reported in Antlanger, Mayr-Schmölzer,

et al. [77], in the compressed case the oxide film only binds very weakly to the substrate. In contrast, for the expanded oxide film chemisorption is observed even with the PBE functional. For both the OPt and ZrPt models the oxide film is positioned much closer to the surface, 241 pm and 224 pm, respectively, compared to the compressed models. The optB88 functional further decreases the oxide-alloy distance to 227 pm and 212 pm. While for the compressed case only the ZrPt model showed buckling of the Zr layer of the oxide due to the Zr–Pt interaction, in this case the film undergoes buckling between 43 pm and 83 pm, regardless of the model or functional used. Another difference can also be observed for the oxygen layers: for the ZrPt model both upper and lower oxygen atoms are at the same height, the oxygen layers of the OPt model show buckling of up to 66 pm in the upper layer and 40 pm in the lower interface layer. These distortions are slightly larger for the PBE functional. The surface energies experience an increase of $\approx 29 \, \text{meV/Å}^2$ for the PBE and $\approx 22 \, \text{meV/Å}^2$ for the optB88 functional due to the stretching, quite similar to the Pd-terminated Pd_3Zr case.

Table 3.6.: Surface energies and lattice parameters of a single trilayer of $ZrO_2(111)$ on Pt-terminated Pt_3Zr, expanded to the experimental oxide lattice constant. The values for all structures were obtained using the optB88 functional, values in parentheses were calculated using the PBE functional. The values from the compressed case were recalculated from the models introduced by Antlanger, Mayr-Schmölzer, et al. [77].

| Configuration | 3.3 Å | | | | 3.5 Å | | | |
	ZrPt		OPt		ZrPt		OPt	
d_{O_2-Zr} [pm]	94	(95)	94	(95)	90	(92)	84	(86)
d_{Zr-O_1} [pm]	92	(95)	92	(95)	81	(82)	80	(82)
d_{O_1-S} [pm]	261	(338)	241	(331)	227	(241)	212	(224)
b_{O_2} [pm]	0	(0)	0	(0)	59	(66)	0	(0)
b_{Zr} [pm]	49	(5)	65	(10)	73	(83)	43	(48)
b_{O_1} [pm]	6	(1)	0	(0)	31	(40)	0	(0)
b_S [pm]	7	(8)	2	(7)	8	(12)	13	(10)
E_{surf} [meV/Å^2]	51	(47)	56	(47)	73	(74)	80	(76)

Multilayer ZrO$_2$ Films on Pt/Pt$_3$Zr

In the experiment, the preparation of the film might in some cases cause the ZrO_2 film not only to adsorb as a single trilayer, but also form clusters. Li, Choi, Mayr-Schmölzer, et al. [3] have shown that the formation of clusters can be suppressed by increasing the annealing temperature, but some clusters still remain. This was confirmed by XPS measurements where an additional ZrO_x species was observed. To mimic the properties of these clusters, the $ZrO_2/Pt/Pt_3Zr$ model was extended to multiple layered structures which were then used to calculated the Zr 3d and O 1s core level binding energies. As

will be shown in section 3.4.4, a 3-trilayer film already shows bulk-like properties.

The calculations were performed mainly using the van-der-Waals corrected optB88 functional to properly describe the metal-oxide interface. As the starting point for the unit cell the ZrPt model of the $ZrO_2/Pt/Pt_3Zr$ configuration was used. The two additional layers of ZrO_2 were then placed on top of the already adsorbed oxide layer, each laterally shifted to conform with the stacking order in the [111] direction of the cubic ZrO_2 crystal. Again, both a compressed and stretched variant of this model cell was created to address the limiting cases of a lattice constant determined either by the alloy or the oxide film.

In the so-called compressed case the fully relaxed oxide film shows the effect of the large strain due to its compression. The interlayer distances in the oxide film are quite large, 381 pm between the upper and the middle ZrO_2 layer and 353 pm between middle and lower ZrO_2 layer, compared to the bulk value of 3.6 pm [74]. The zirconium atoms in each layer show quite strong buckling: while the Zr atoms at the surface buckle only by 65 pm those at the alloy interface buckle by 94 pm. The oxygen atoms move laterally from their symmetry positions to accommodate for these distortions. At the surface and at the alloy interface the O do not buckle, but the oxygen between the oxide layers buckle by ≈27 pm.

For the expanded model these effects are less pronounced since the lattice constant of the substrate is now closer to that of the free-standing 3 trilayer ZrO_2 film. In this fully relaxed model the two outer ZrO_2 layers show almost no buckling, except for the lower oxygen of the middle ZrO_2 layer (34 pm). This is caused by the slight distortion of the zirconium atoms (61 pm buckling) in the lowest layer, which is caused by the oxide-alloy interface like like in the case of single layer adsorption. The oxygen atoms in the lowest layer only show lateral displacements to accommodate for the movement of the Zr atoms.

The calculated surface energies predict higher stability for the stretched model, which can be expected since the equilibrium lattice constant of a 3-trilayer slab is more in the range of 3.500 Å to 3.510 Å (PBE, optB88).

3.3. ZrO$_2$-Metal Interface: Large Model Cells

The small model cells discussed in section 3.2 have turned out to be good approximations of the metal-oxide interface, but they cannot be expected to capture all physical and chemical properties of the full experimental $(\sqrt{19} \times \sqrt{19})R23.4°$ and $(\sqrt{217} \times \sqrt{217})R10.16°$ unit cells. Due to the large contraction of the oxide film in the compressed $(\sqrt{3} \times \sqrt{3})R30°$ model the reactivity of the oxide surface might be too low, while for the expanded model the distortion of the metal substrate might heavily influence the metal-oxide interaction. To properly capture the interface properties, additional models were introduced to allow for a better matching fo the substrate and the oxide. Since the experimental unit cell of the ZrO_2/Pd_3Zr interface would be too large to perform DFT calculations, the main focus will be on the $ZrO_2/Pt/Pt_3Zr$ interface.

Not much theoretical research has been done before. Meinel et al. [81] have used a reduced model of the interface with a pure platinum substrate to study differently

Table 3.7.: Surface energies and lattice parameters of three trilayers of $ZrO_2(111)$ on Pt-terminated Pt_3Zr. Both structures were relaxed using the optB88 functional.

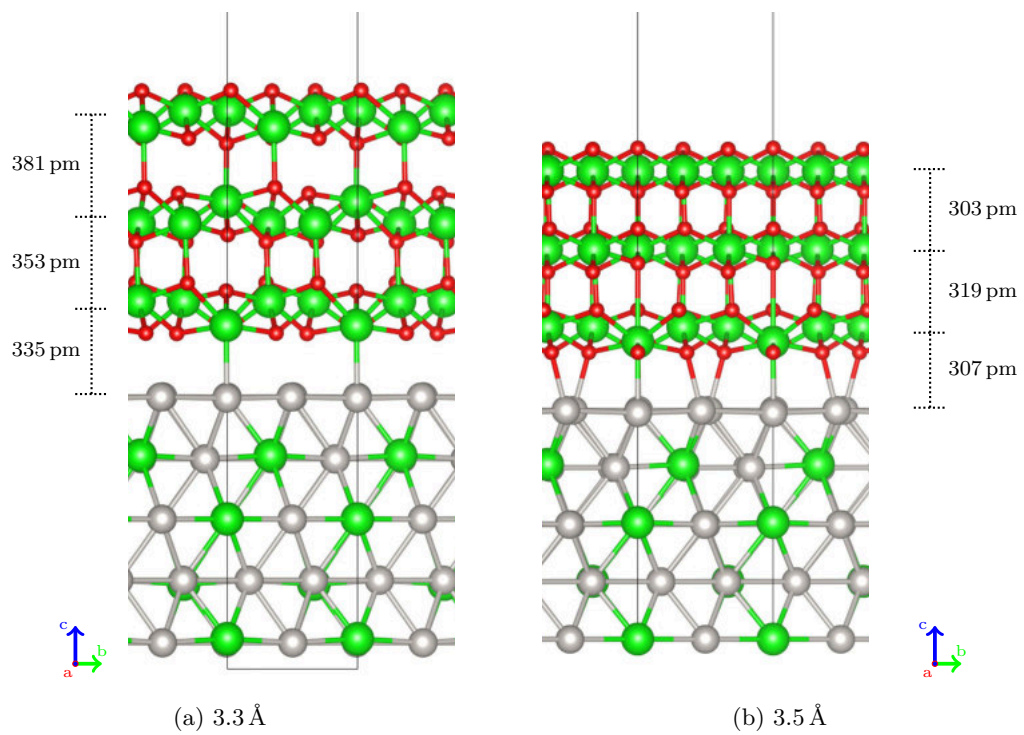| [pm]	3.3 Å	3.5 Å
$d_{O_6-Zr_3}$	95	86
$d_{Zr_3-O_5}$	92	79
$d_{O_5-O_4}$	197	144
$d_{O_4-Zr_2}$	92	80
$d_{Zr_2-O_3}$	89	76
$d_{O_3-O_2}$	176	159
$d_{O_2-Zr_1}$	89	84
$d_{Zr_1-O_1}$	90	80
d_{O_1-S}	245	227
b_{O_6}	2	5
b_{Zr_3}	65	0
b_{O_5}	20	0
b_{O_4}	27	0
b_{Zr_2}	85	0
b_{O_3}	27	34
b_{O_2}	32	0
b_{Zr_1}	94	61
b_{O_1}	7	0
b_S	5	10
$E_{\text{surf}}\ [\text{meV/Å}^2]$	86	62

(a) 3.3 Å   (b) 3.5 Å

Figure 3.15.: 3-trilayers of ZrO_2 adsorbed on Pt-terminated Pt_3Zr, relaxed with the optB88 functional.

sized models at various lattice mismatches. They have found good agreement with their experimental results for a $(\sqrt{19} \times \sqrt{19})R23.4°$ model cell and a tendency of the oxide film to contract upon adsorption on the metal substrate. A unrotated $(4 \times 4)/(5 \times 5)$ ZrO_2/Pt_3Zr model is reported to be slightly less stable. Nevertheless, all of their models show quite pronounced buckling of up to 112 pm, much higher than the values reported by Antlanger, Mayr-Schmölzer, et al. [77]. Much more recently, Ruiz Puigdollers and Pacchioni [95] have come to similar conclusions for the $(\sqrt{19} \times \sqrt{19})R23.4°$ model with a pure Pt substrate, but their $(4 \times 4)/(5 \times 5)$ ZrO_2/Pt_3Zr model shows almost no buckling of the oxide film. In both cases, the calculations were done with standard PBE functionals.

In this work, to expand on this previous research, the $\sqrt{19}$ model where a single trilayer of ZrO_2 is adsorbed on a pure platinum substrate was studied more closely. As has already been shown for the small $(\sqrt{3} \times \sqrt{3})R30°$ morels, accounting for van-der-Waals corrections is important to properly model the metal-oxide interface for weakly interacting systems. Additionally, the dependency of the interface properties on the oxide lattice constant was studied by modification of the $\sqrt{19}$ model cell. Improvements on the $\sqrt{19}$ model were done by replacing the pure Pt substrate with the real Pt-terminated Pt_3Zr substrate. Furthermore, using a lattice matching algorithm [96] implemented in the Virtual NanoLab software package by QuantumWise, a $(\sqrt{13} \times \sqrt{13})R13.8°$ model cell was created where the oxide film is compressed by just 1.7 % compared to the experimental lattice constant of 3.5 Å [77].

The simulations discussed in this chapter were mostly done with the van-der-Waals corrected optB86b functional, in some cases complemented by PBE calculations. Both the optB86b and optB88 functional give very good results with respect to physical properties of solids [31], the S22 benchmark [30] or adsorption energies [97, 98]. For the systems studied here, the optB88 functional shows very slow electronic convergence, therefore the optB86b functional was preferred.

3.3.1. $\sqrt{19}$ Model Cell: Platinum Substrate

This chapter will cover the smaller $(\sqrt{19} \times \sqrt{19})R23.4°$ model cell where a single trilayer of ZrO_2 is adsorbed on a platinum substrate. First, the stability of Pt is discussed, followed by a description of the metal-oxide interface at the calculated Pt lattice constant, followed by a description of the influence of the oxide lattice constant on the interface properties.

The Platinum Substrate

To build the $(\sqrt{19} \times \sqrt{19})R23.4°$ unit cell, as a first step the platinum bulk structure was optimised with respect to the lattice constant. The primitive unit cell of platinum is face-centred cubic with a lattice constant of 3.924 Å [99]. Since the Pt(111) surface is of interest here, for the calculations a hexagonal unit cell was set up where the Pt(111) plane is parallel to the xy-plane. This model cell, composed of four Pt atoms in ABAC stacking order, similar to the Pt_3Zr and Pd_3Zr alloys. The calculations were performed using a $12 \times 12 \times 12$ Γ-centred $\vec{k}$-point grid with an energy cutoff of 400 eV, using both the standard PBE and the van-der-Waals corrected optB86b functionals. The equilibrium

volumes predicted by both functionals are very close to the experimental value (table 3.8) with even the PBE result differing by just 0.5 % from the experiment. Since the optB86b functional yields a slightly better result with respect to the experimental value, these lattice parameters were used for all further calculations.

Table 3.8.: Calculated and experimental Pt bulk lattice parameters.

|	PBE	optB86	Experiment [99]
a [Å]	2.790	2.777	2.775

The $\sqrt{19}$ Model Cell

As the next step to build the $(\sqrt{19} \times \sqrt{19})R23.4°$ unit cell, the ZrO_2 trilayer unit cell was extended to include 12 ZrO_2 formula units, yielding a $2\sqrt{3} \times 2\sqrt{3}$ supercell. A five layered hexagonal platinum unit cell was multiplied in x and y direction and rotated to fit 19 surface platinum atoms below the ZrO_2 supercell, see fig. 3.16. The resulting unit cell consists of five layers of platinum in ABACA order which a single ZrO_2 trilayer on top at a lattice constant of 1211 pm. Two special configurations of this $\sqrt{19}$ cell were considered, similar to the case of the smaller unit cells (see section 3.2.3): in one configuration a lower oxygen atom of the oxide film is placed directly above a platinum atom (OPt), while the second configuration is shifted by ⅓ of the primitive ZrO_2 unit cell so that a zirconium atom is located above a platinum atom (ZrPt). Both starting configurations are shown in fig. 3.16, indicating the lateral placement of the oxide film.

Both the OPt and ZrPt were then relaxed either using the PBE or the optB86b functional. The convergence of the $\vec{k}$-point grid has shown that a single $\vec{k}$-point was sufficient to achieve electronic convergence of <10 meV/atom while keeping the computational effort at a reasonable level. Again, the energy cutoff for the plane waves was set to 400 eV. The lowest three platinum layers were kept fixed and only the top two Pt layers were allowed to relax. The ZrO_2 film was not restricted in any way.

After a full relaxation, all four final configurations show very large distortions of the ZrO_2 film. In all cases, the DFT calculations predict very a strong buckling of the oxide film. Additionally, the oxide film exhibits lateral distortions, causing a large variation of the Zr–Zr distances. As shown in fig. 3.17, this is apparent in the formation of "isles" of ZrO_2, which buckle away from the Pt surface and the Zr–Zr distances are contracted to 323 pm, separated by deep "valleys" where the lateral distortion is very strong and the Zr–Pt interaction is increased. The difference of the computed total energies of the OPt and ZrPt models is very small, regardless of the functional used. For the both functionals the ZrPt model is slightly favoured: while the energy difference for the PBE functional is 246 meV, the optB86b functional yields a very small energy difference of 13 meV. A more accurate calculation with a $3 \times 3 \times 1$ Γ-centred $\vec{k}$-point grid yielded almost identical energy differences. Considering that there are 131 atoms in the unit cell this means that per atom both models are essentially energetically degenerate.
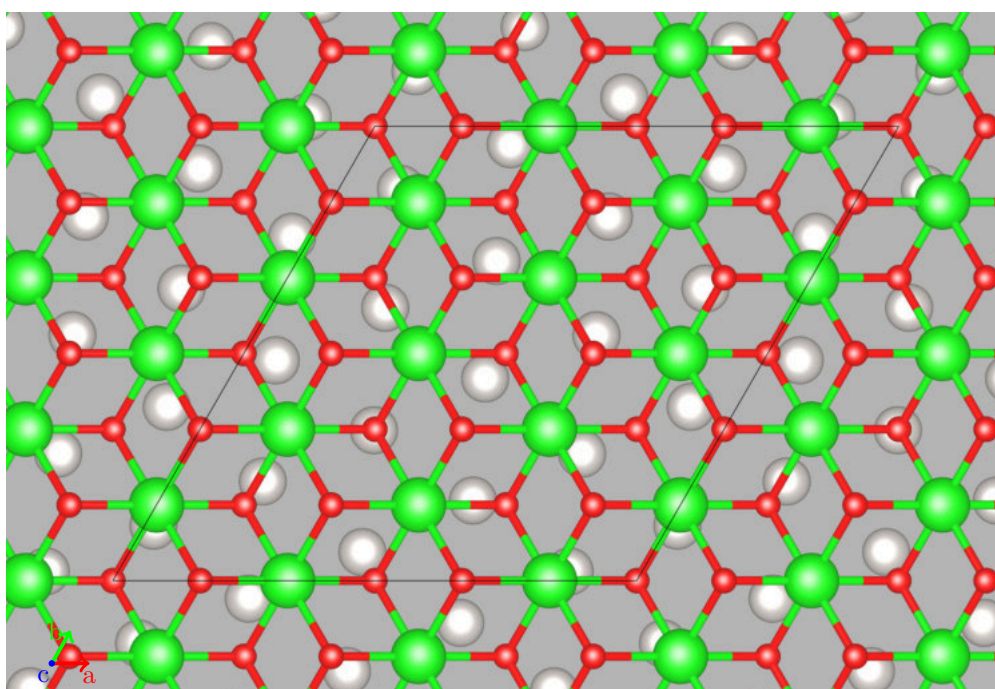
(a) OPt model
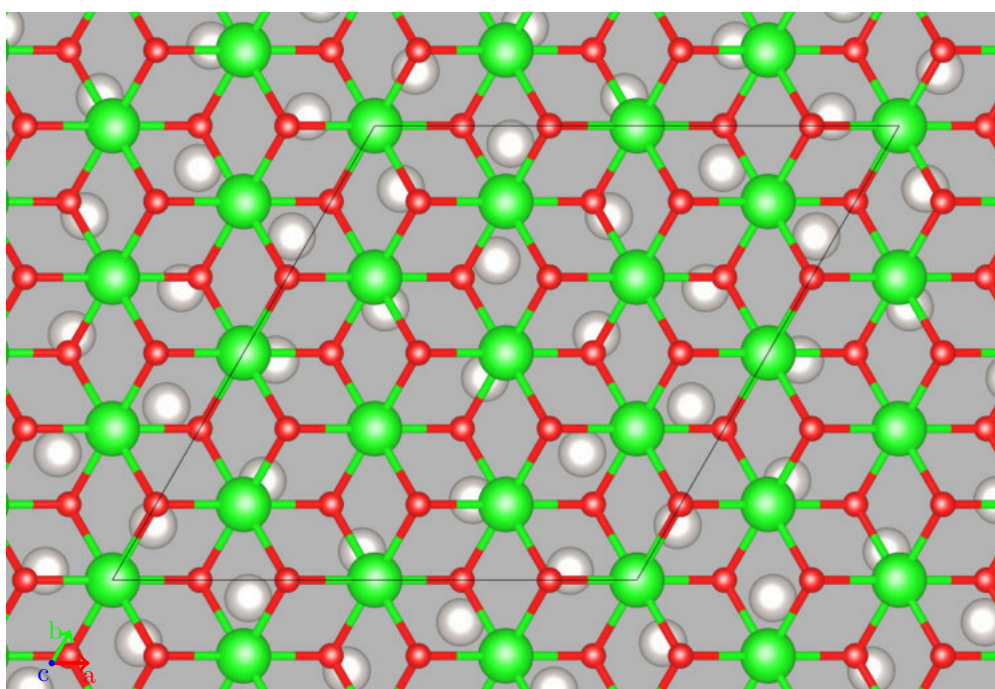
(b) ZrPt model

Figure 3.16.: OPt and ZrPt starting configurations. Only one Pt layer of the substrate is shown.

While the energetic difference is very small, there still exist structural differences between the fully relaxed structures. The PBE functional yields a film thickness of 247 pm for both models, while the optB86b functional leads to a thicker film 250 pm for the OPt model than for the ZrPt model (240 pm). The distance between oxide film and metallic substrate also depends on the functional. Taking the average height of the lower oxygen atoms and the Pt surface layer as references, the oxide-metal distance calculated with the PBE functional is 212 pm and 219 pm for the OPt and the ZrPt model, respectively. Both structures show nine Pt–O bonds at the metal-oxide interface with a maximum bond length of 241 pm. The optB86b functional yields ZrO_2–Pt interlayer distances of 209 pm and 210 pm for the OPt and the ZrPt structure, respectively. The closer distance of the ZrO_2 film to the substrate increased the number of Pt–O bonds to 10 with the same maximum bond length as before. One common feature of all relaxed structures is the large lateral distortion, reflected in the large variance of the Zr–Zr distances. The maximum nearest neighbour Zr–Zr distance found is 399 pm, while the minimum distance is as low as 314 pm for the OPt_{PBE} model. In these areas the aforementioned "isles" are formed, where the oxide-metal interaction is dominated by the covalent Pt–O bonds at the bottom of the ZrO_2 film. In these areas, the lower oxygen atoms do not experience large lateral displacement unless a bond to the substrate can be formed. These "isle" areas are then laterally contracted and show Zr–Zr distances between 322 pm and 366 pm. In the "valley" areas the ZrO_2 film is stretched heavily due to larger displacement of the lower oxygen atoms, causing the Zr atoms to buckle towards the surface. In all cases, one Zr–O bond of the oxide film at the interface is broken and a Pt–O bond is formed, see fig. 3.17. At the oxide surface, even more Zr–O bonds are broken due to the heavy distortions, creating three (OPt_{PBE}) or four under-coordinated oxygen atoms. Interestingly, despite these distortions, the average Zr–O bond length is nearly identical for all models (216 pm to 217 pm). Due to the formation of the Pt–O bonds the surface layer of the metal substrate shows buckling of 31 pm to 43 pm.

All these atomic displacements lead to heavy buckling of the ZrO_2 film. In the upper oxygen layer, buckling of up to 124 pm is predicted, while the zirconium layer buckles up to 117 pm. This is much larger than in the experiment, where height differences of up to 50 pm were observed [77]. The STM measurements also do not show the large lateral displacements apparent in the relaxed configurations, indicating that the DFT simulations underestimate the stability of the oxide film.

To compare the stability of these structures with the small $\sqrt{3}$ models, the generalised surface energy γ was calculated according to section 3.2 (see tables 3.11 and 3.12 for the comparison). The calculated value of $49 \, meV/\text{Å}^2$ to $51 \, meV/\text{Å}^2$ (PBE) and $44 \, meV/\text{Å}^2$ to $45 \, meV/\text{Å}^2$ (optB86b) is lower than for the expanded Pt-terminated $ZrO_2/Pt/Pt_3Zr$ model ($\approx 73 \, meV/\text{Å}^2$, see table 3.9), supporting the better description of the metal-oxide interface with the $\sqrt{19}$ model. Compared to the compressed model ($51 \, meV/\text{Å}^2$) the optB86b functional yields slightly lower surface energies, while the PBE values for the $\sqrt{19}$ model are slightly larger than for the $\sqrt{3}$ model ($47 \, meV/\text{Å}^2$).

Table 3.9.: Surface energies and lattice parameters of the fully relaxed $\sqrt{19}$ models. The number of Pt–O bonds is given per unit cell with a threshold of $2.4\,\text{Å}$.

Configuration	PBE		optB86b	
	ZrPt	OPt	ZrPt	OPt
$d_{O_2-O_1}$ [pm]	247	247	240	250
$d_{\varnothing ZrO_2-S}$ [pm]	297	289	288	289
d_{O_1-S} [pm]	219	212	209	209
b_{O_2} [pm]	119	100	109	124
b_{Zr} [pm]	113	109	107	117
b_{O_1} [pm]	98	123	92	102
b_S [pm]	31	43	31	34
Pt–O Bonds	9	9	10	10
Under-coordinated O	4	3	4	4
E_{surf} [meV/Å^2]	49	51	44	45

(a) OPt PBE

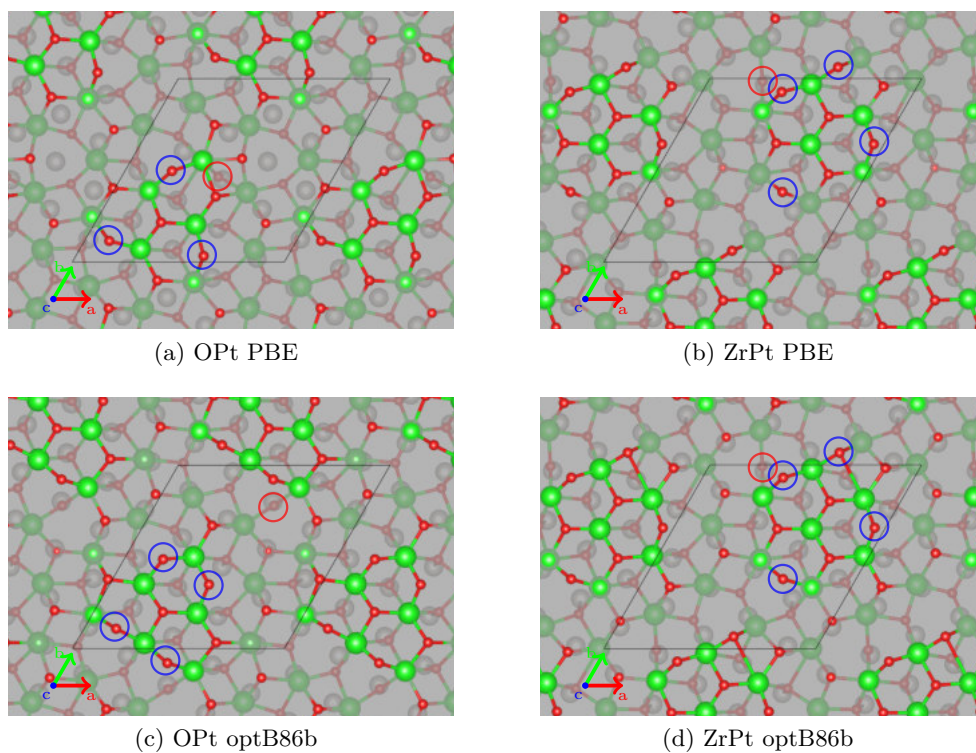
(b) ZrPt PBE

(c) OPt optB86b

(d) ZrPt optB86b

Figure 3.17.: OPt and ZrPt models relaxed with the (a), (b) PBE and (c), (d) optB86b functional. Under-coordinated oxygen atoms are indicated by blue (top layer) and red (bottom layer) circles.

3.3.2. Mismatch of Oxide Film and Substrate

One topic of interest when describing the metal-oxide surface is the dependence of the surface energy γ on the lattice constant of the substrate. Antlanger, Mayr-Schmölzer, et al. [77] have shown that the pure platinum layer on which the ZrO_2 oxide adsorbs forms dislocation lines of reconstructed Pt, and the Pt(111) surface is known to show reconstruction [100]. The $\sqrt{3}$ model has shown that the buckling of the ZrO_2 film is dependent on its lattice constant, as discussed by Antlanger, Mayr-Schmölzer, et al. [77] for the Pt_3Zr substrate and in section 3.2.2. Meinel et al. [81] have also shown that the equilibrium lattice constant of the unsupported ZrO_2 trilayer is $>9\,\%$ smaller than the cubic bulk lattice constant. This indicates that to compensate for the absence of a second ZrO_2 trilayer, a single adsorbed ZrO_2 trilayer needs to bind quite strongly to the substrate to expand to a lattice constant close to the bulk value. Therefore, the optimal matching of the lattice constant of both oxide film and substrate plays an important role in the resulting adsorption mode, since even small distortions lead to different buckling of the adsorbed film.

To study this behaviour, as a first step the lattice constant of the Pt substrate was varied between $2.632\,\text{Å}$ and $2.853\,\text{Å}$, corresponding to a compression of $5\,\%$ and an expansion of $3\,\%$ with respect to the bulk Pt lattice constant (see table 3.8). While the slab thickness for sure is too low, this result already gives an indication of the surface reconstruction of the Pt(111) surface. As fig. 3.18 shows, the calculated surface energy γ of this 5-layer slab has a minimum at $2.730\,\text{Å}$ and $2.717\,\text{Å}$ for the PBE and optB86b functionals, respectively. The unsaturated bonds at the surface cause lateral stress and therefore a contraction of the slab, which in a real system would lead to mesoscopic reconstruction of the Pt(111) surface layer.

Next, this was repeated with the whole $\sqrt{19}$ model cell. At each step, the structure was fully relaxed. As shown in fig. 3.19, the optB86b calculations result in one minimum of the surface energy γ at $1.0\,\%$ contraction, corresponding to a Pt lattice constant of $2.754\,\text{Å}$. The PBE calculations on the other hand show two minima, a global minimum at the (optB86b) Pt bulk lattice constant and a local minimum at a substrate lattice constant of $2.710\,\text{Å}$.

Here two effects add up: the saturation of the Pt(111) surface bonds by the ZrO_2 film, and the existence of unsaturated bonds at the ZrO_2 surface itself. As indicated in fig. 3.20, the lack of van-der-Waals corrections in the PBE functional weakens the binding between ZrO_2 film and Pt substrate, thereby leading to a disconnect of the ZrO_2 trilayer from the Pt substrate below the optB86b Pt lattice constant. Including van-der-Waals interactions in the optB86b functional on the other hand stabilises the interface. At lateral compression of the cell, both surface energy and interlayer distance decreases, but the buckling of the oxide film does not change up to a compression of $4\,\%$ (see fig. 3.20). Below this value the interaction between oxide and metal substrate is weakened to the point where the oxide film adsorbs only weakly at a larger distance of $282\,\text{pm}$ and the buckling almost vanishes, similar to the PBE results at less compression.

These results indicate that the adsorbed ZrO_2 trilayer is very sensitive to changes in its lattice constant. The interplay between reactivity of both substrate and oxide is the

key factor in the structure of the adsorbed oxide film, where very small changes in the lattice constant can cause large changes in its buckling. As shown in table 3.8, the DFT error with respect to the experimental lattice constant for the Pt bulk is 0.6 % and 0.1 % for the PBE and optB86b functionals, respectively. For the cubic ZrO_2 bulk the DFT overestimates the lattice constant by 1.0 % and 0.2 % for PBE and optB86b, respectively. The comparison between PBE and optB86b functional again shows that accounting for polarisation effects is essential to properly study this system. Nevertheless, neither functional is able to reproduce the experimental buckling of 50 pm at the measured lattice constant of 3.5 Å.
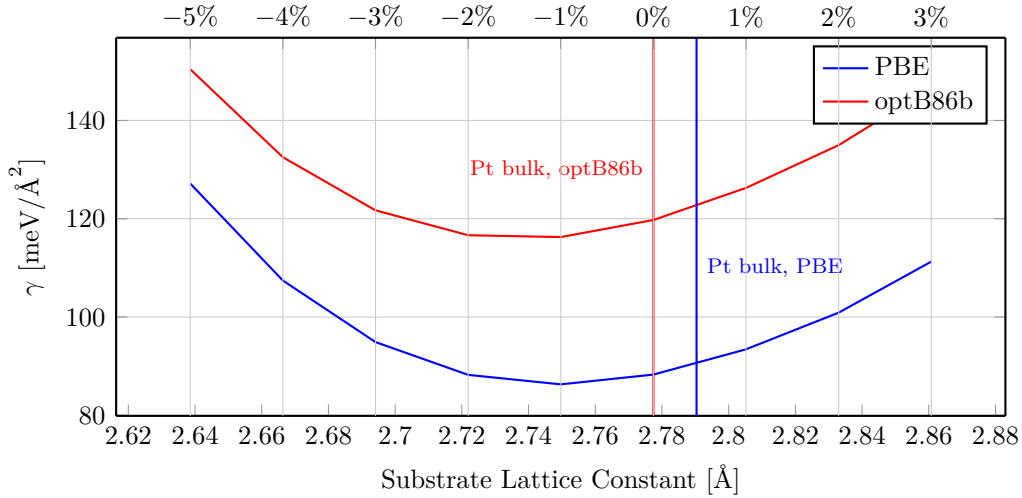

Figure 3.18.: Surface energy γ of the 5-layer Pt slab. PBE shows an energy minimum at 2.730 Å, optB86b at 2.717 Å. The vertical lines indicate the bulk equilibrium lattice constants from table 3.8.

3.3.3. $\sqrt{19}$ Model Cell: Compressed Platinum Substrate

To reconcile the calculations with the experiment one would need a slightly reduced oxide lattice constant. Indeed, there are hints that this might be actually the case by X-ray diffraction (XRD) measurements done in the research group of Andreas Stierle at DESY (Hamburg) [101]. A preliminary analysis of these measurements suggest an average lateral contraction of the Pt-like interface layer of 3.3 %. This would lead to a platinum substrate lattice constant of 2.679 Å. Reconstruction of the Pt(111) surface has already been discussed by Bott et al. [100]. To test the stability of this structure, the OPt model cell which was discussed in section 3.3.1 was compressed by the given amount, yielding a $\sqrt{19}$ unit cell with a lattice constant of 11.707 Å, called $\sqrt{19}_{comp}$ in the following discussion. The z coordinate was adjusted accordingly to keep the lower three layers of the Pt substrate, which were fixed like for the $\sqrt{19}$ model, at the bulk lattice
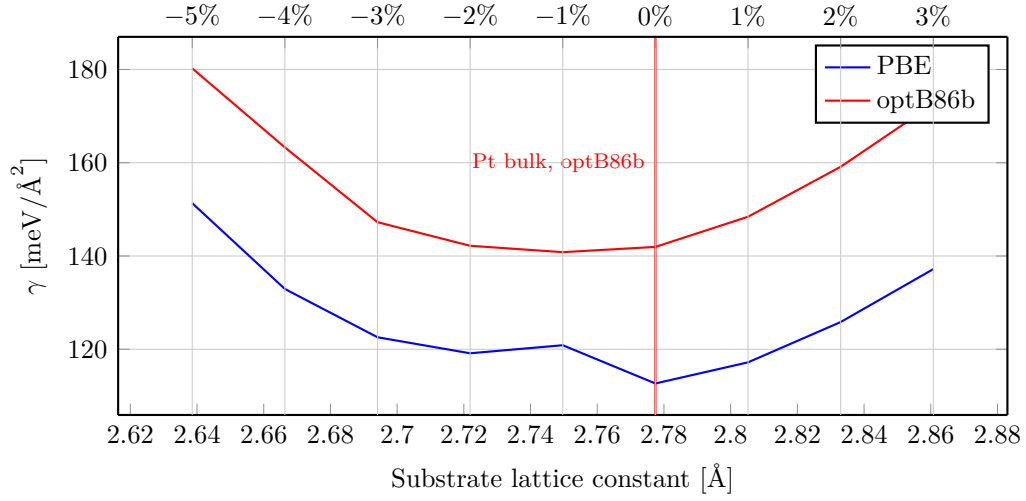
Figure 3.19.: Surface energy γ of the complete $\sqrt{19}$ model, referenced to the most favourable structure. Slight lateral compression of 1% already reduces the binding between ZrO_2 film and Pt substrate for the PBE functional, indicated by the kink in the PBE curve. Here the ZrO_2 film starts to lift off the substrate, see fig. 3.20.
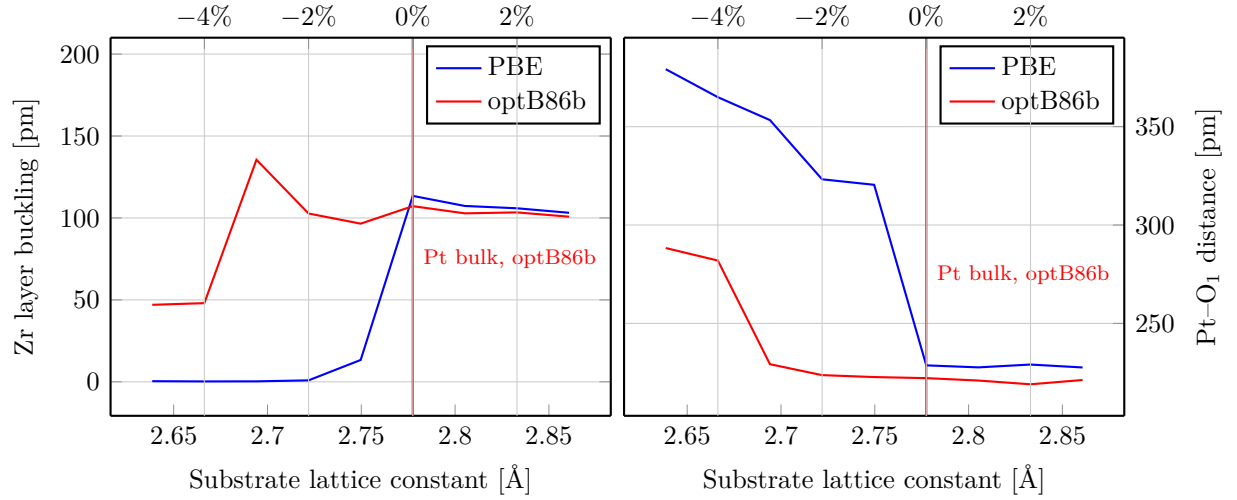

Figure 3.20.: Buckling and film-substrate interlayer distance at compression of the substrate.

constant. Again, all other ions in the model cell were fully relaxed until the residual forces were $<0.01\,\text{eV/Å}$. The computational settings were identical to calculations on the uncompressed model where a single $\vec{k}$-point at the Γ-point was used and the energy cutoff was set to $400\,\text{eV}$. The calculations were performed both with the PBE and the optB86b functional.

The relaxed structures shown in fig. 3.21 are decisively different from the relaxed structures discussed before. Generally, the buckling of the zirconium atoms in the ZrO_2 film is much reduced for the optB86b relaxation and vanishes completely for the PBE relaxed cell. In the former case the zirconium atoms buckle by $78\,\text{pm}$ and the upper and lower oxygen atoms by $56\,\text{pm}$ and $43\,\text{pm}$, respectively. For the PBE relaxed structure the buckling of both species of the ZrO_2 film is $\leq 1\,\text{pm}$. In the optB86b structure there exist two upwards buckled areas, consisting of three zirconium atoms each. Here, the interaction between these zirconium atoms and the platinum atoms of the substrate is the weakest since the Zr sit in hollow positions with respect to the Pt lattice. At the corner of the unit cell the oxide film buckles downwards, here the Zr are at top positions with respect to the Pt atoms and a lower oxygen atom is in a hollow position. Therefore, in one unit cell, half of the zirconium atoms buckle upwards and the other half downwards. The calculations predict an increase of the interlayer distances between substrate and ZrO_2 film to $2.360\,\text{Å}$ and $3.370\,\text{Å}$ for the optB86b and the PBE calculations, respectively. Additionally, the ZrO_2 film shows almost no lateral distortion and the surface layer does not show a single under-coordinated oxygen atom. Compared to the published oxide lattice constant, due to the compression of the model cell the oxide lattice constant is $335\,\text{pm}$ to $351\,\text{pm}$ for the optB86b functional, a result of the buckling of the zirconium layer. Since there are no distortions after relaxation with the PBE functional, the oxide lattice constant of $338\,\text{pm}$ is given by the unit vectors of the model cell. The surface energies of the compressed $\sqrt{19}$ model are $63\,\text{meV/Å}^2$ and $61\,\text{meV/Å}^2$ for the optB86b and the PBE functional, respectively. Compared to the values of the uncompressed $\sqrt{19}$ models (see tables 3.9 and 3.12) these structures are about $20\,\text{meV/Å}^2$ less favoured.

The general behaviour of the oxide film with respect to its buckling and distance to the substrate bears resemblance to the small $(\sqrt{3} \times \sqrt{3})R30°$ model cells discussed by Antlanger, Mayr-Schmölzer, et al. [77], where the compression of the single ZrO_2 trilayer compared to the cubic bulk lead to an underbinding of the PBE functional which lead to an unbuckled ZrO_2 film far from the surface. Only by including van-der-Waals corrections the structural parameters of the relaxed models were comparable to the experiment.

The STM simulations of the optB86b relaxed structure show a large bright feature in the occupied states (bias voltage: $+0.5\,\text{eV}$) which is positioned at the centre of a triangle formed by upwards buckled zirconium atoms. Thin grey lines in the larger dark areas between these triangles grey lines can be attributed to the downwards buckled zirconium atoms. The oxygen atoms do not contribute to the features. In the unoccupied states (bias voltage: $-0.5\,\text{eV}$) the STM simulations show more bright features which are caused mostly by the oxygen atoms in the upper layer of the oxide film. In the whole unit cell only one very dark area at the corner of the surface unit cell, exactly where the oxide

film strongly buckles downwards.

For the flat PBE relaxed structure the STM simulations show a perfectly regular grid of bright dots, positioned exactly on top of the upper oxygen atoms for both the occupied and unoccupied states.

Table 3.10.: Surface energies and lattice parameters of the fully relaxed $\sqrt{19}_{comp}$ models, compressed to a Pt lattice constant of 2.679 Å. The number of Pt–O bonds is given per unit cell with a threshold of 2.4 Å.

	PBE	optB86b
$d_{O_2-O_1}$ [pm]	184	209
$d_{\varnothing ZrO_2-S}$ [pm]	429	323
d_{O_1-S} [pm]	337	236
b_{O_2} [pm]	0	56
b_{Zr} [pm]	0	78
b_{O_1} [pm]	0	43
b_S [pm]	6	43
Pt–O Bonds	0	6
Under-coordinated O	0	0
E_{surf} [meV/Å^2]	61	63

3.3.4. Projected Density of States

The density of states of the $\sqrt{19}$ ground state models still show an oxide band gap of about $-3.5\,\mathrm{eV}$, similar to the value seen for the ZrO_2/Pd_3Zr and $ZrO_2/Pt/Pt_3Zr$ models. For both the standard (fig. 3.23) and compressed (fig. 3.24) $(\sqrt{19} \times \sqrt{19})R23.4°$ model cells some mid-gap states appear. In both cases, the valence band of the oxide film is dominated by the O $2p$ states, in addition to Zr d states. The DFT calculations predict a conduction band minimum at about $1.5\,\mathrm{eV}$. For the compressed $\sqrt{19}$ model, the Zr states are shifted slightly to lower energies and show stronger hybridisation with the O states.

3.3.5. Real $(\sqrt{19} \times \sqrt{19})R23.4°$ Model: Pt$_3$Zr Substrate

As mentioned before, the Pt supported oxide film model cells offer a decent description of the real metal-oxide interface. Nevertheless, neglecting the different stoichiometry and lattice parameters of the real substrate crystal may lead to wrong conclusions. Additionally, the single layer of platinum that is left after oxidation of the Pt$_3$Zr substrate might show different reconstruction than the bulk Pt(111) surface. Therefore, the $\sqrt{19}$ model cell was rebuilt using the same 5-layered Pt-terminated Pt$_3$Zr slab discussed for the small model cells in section 3.2.3. This yields a unit cell comprised of 524 atoms and a lattice parameter $a = 24.971\,\text{Å}$ where a $(4\sqrt{3} \times 4\sqrt{3})$ ZrO$_2$ unit cell is

(a) compressed OPt, PBE
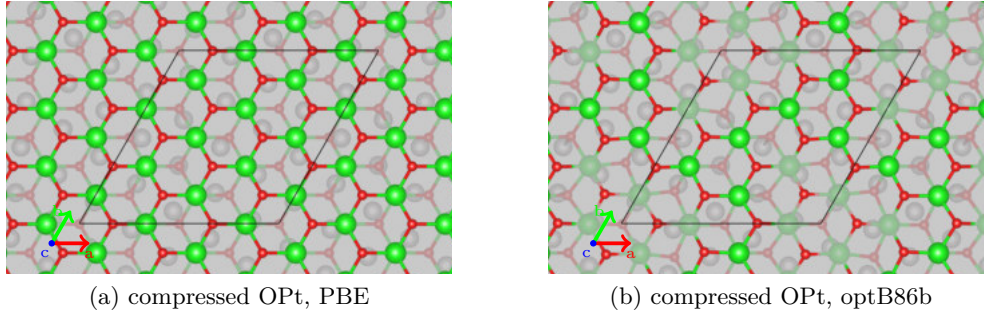   (b) compressed OPt, optB86b

Figure 3.21.: Top views of the (a) PBE and (b) optB86b relaxed compressed $\sqrt{19}$ model cells. The grey lattice plane is positioned at the middle of the oxide film, indicating the increased buckling of the film relaxed with the optB86b functional. A grey plane was added at the mean height of the ZrO_2 film to illustrate the buckling in the top view images.

adsorbed on a $(\sqrt{19} \times \sqrt{19})$ Pt_3Zr unit cell. In the initial model the oxide film was placed at a distance of $3.3\,Å$ to the Pt layer of the substrate slab. Furthermore, to simulate the reconstruction of the Pt layer of the substrate, two more variants of this model were constructed by compressing of the whole unit cell to both the previously calculated platinum bulk lattice constant and to the further reduced lattice constant used in section 3.3.3 for the compressed $\sqrt{19}$ model.

Finally, these model cells were fully relaxed using both the optB86b and the PBE functionals. Due to the large real space size of the models a single $\vec{k}$-point at the Γ point was used. The energy cutoff was set to $400\,eV$ and the relaxation was done until the residual forces were below $0.01\,eV/Å$.

After relaxation, all six structures were analysed with respect to the structural parameters of the oxide film. At the Pt_3Zr bulk lattice constant, shown in fig. 3.25, the oxide film shows very large distortions with Zr–Zr distances of up to $4\,Å$. The buckling of the Zr layer of the oxide film is $95\,pm$ for the optB86b relaxed structure and the lateral distortions are comparable to the $\sqrt{19}$ model with a pure Pt substrate. The upper and lower oxygen layers shows height differences of $123\,pm$ and $107\,pm$, respectively. The interlayer distance between the lower oxygen atoms and the Pt surface is $226\,pm$. The Pt surface buckles by $27\,pm$. Generally, the oxide film shows a similar "isle" and "valley" pattern due to the large variance in Zr–Zr distances from $305\,pm$ up to $400\,pm$ with a mean distance of $356\,pm$. The Zr atoms are buckled down towards the substrate in the valleys and upwards at the isle areas. In the latter case, this is caused by the lower oxygen atoms that are displaced laterally to occupy top-positions with respect to the Pt layer below. In the valleys the lateral displacements are larger since the oxygen atoms mostly occupy hollow-like sites, causing larger distortions in the Zr and upper oxygen layers in these areas. The PBE relaxation on the other hand results in an oxide film with large holes between areas of contracted oxide. While an isle-like structure of the oxide

(a) PBE, Bias: $+0.5\,\mathrm{eV}$

(b) PBE, Bias: $-0.5\,\mathrm{eV}$

(c) optB86b, Bias: $+0.5\,\mathrm{eV}$

(d) optB86b, Bias: $-0.5\,\mathrm{eV}$
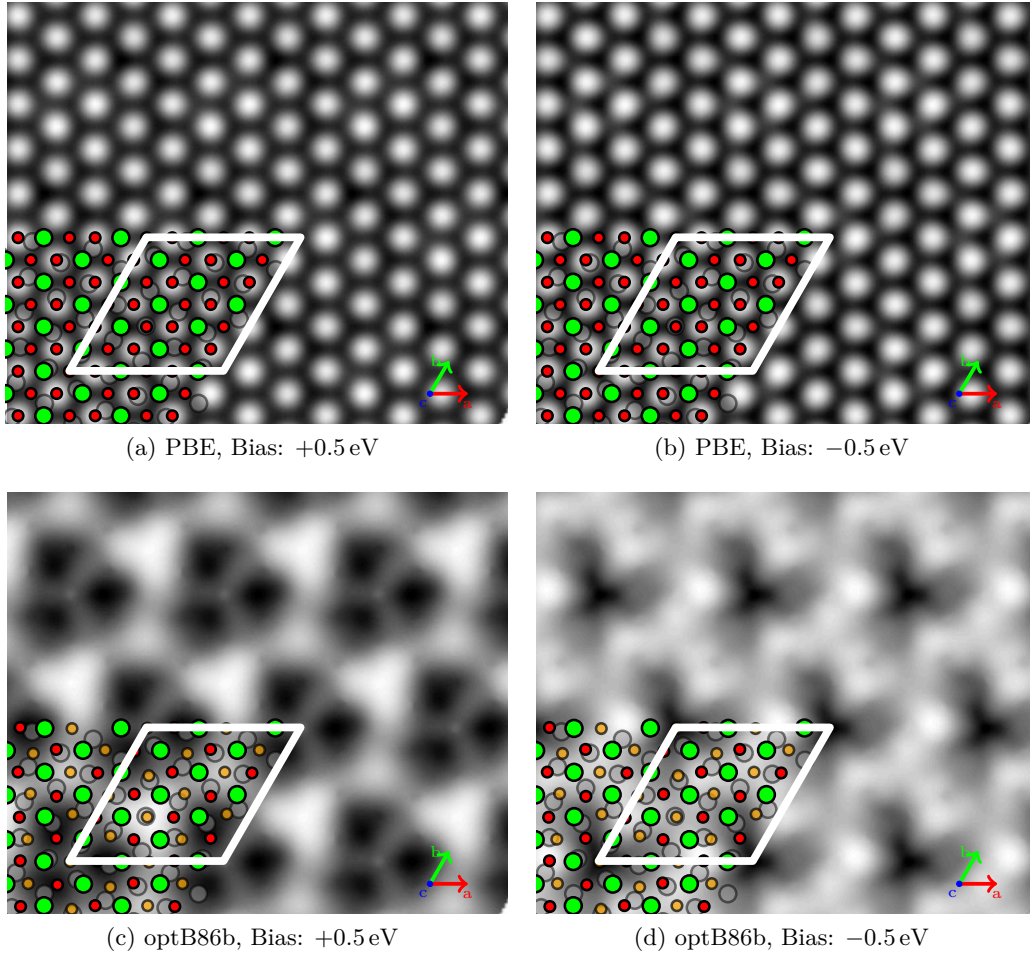
Figure 3.22.: STM of the fully relaxed $\sqrt{19}_{comp}$ structure, i.e. the $\sqrt{19}$ model compressed by $3.3\,\%$. The unit cell in white; Zr, O, and Pt atoms are green, red, and grey, respectively.
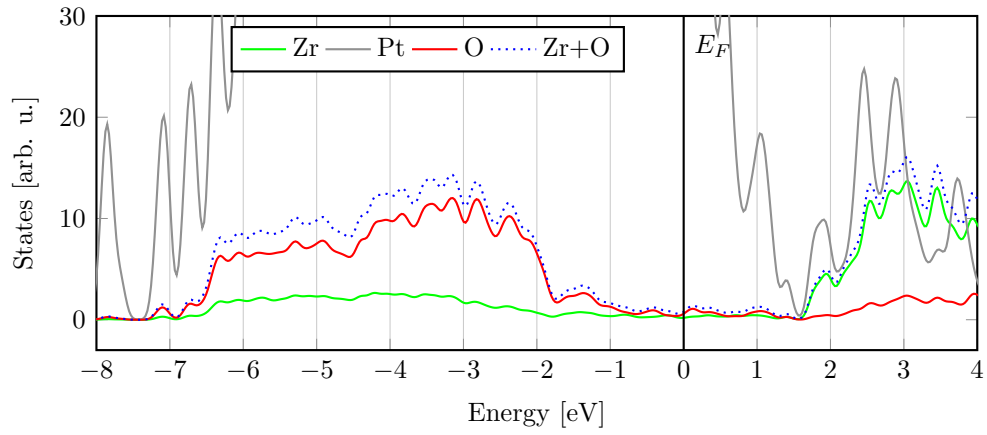
Figure 3.23.: Projected density of states of the fully relaxed $\sqrt{19}$ model cell.
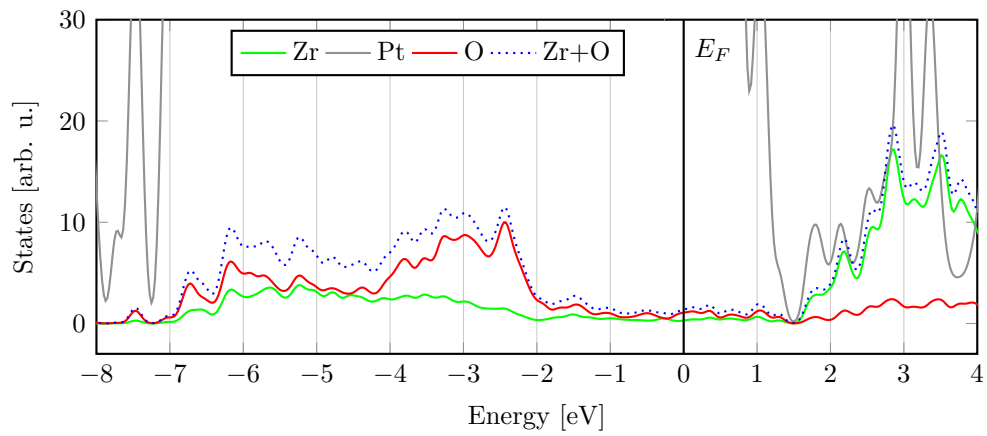

Figure 3.24.: Projected density of states of the fully relaxed $\sqrt{19}_{comp}$ model cell.

film can be observed in some areas, the distortions in the valleys are so large that the oxygen film is completely torn apart, as can be seen in figs. 3.25a and 3.25b. For both the optB86b and the PBE functional, the distortions lead to 20 and 23 under-coordinated oxygen atoms at the surface respectively with a maximal bond length of 241 pm.

Compression of the substrate to the optimal optB86b Pt lattice constant of 278 pm, shown in fig. 3.26, yields a $\sqrt{19}$ model cell with $a = 24.213$ Å. The relaxation of this structure with the optB86b functional leads to a structure very similar to the case of a pure Pt substrate. Again, the Zr layer oxide film shows buckling of 98 pm, but that of the oxygen atoms is reduced to 97 pm and 70 pm for the upper and lower oxygen layer. The Pt layer of the substrate buckles only by 24 pm. The metal-oxide interlayer distance is 232 pm, measured between the average height of the surface Pt and the lower oxygen atoms. Compared to the previously described case at the Pt$_3$Zr lattice constant, the variance of the Zr–Zr distances is smaller, starting at 323 pm. The mean Zr–Zr distance is 353 pm, but the maximum Zr–Zr distance is still 400 pm. Compared to the pure Pt substrate model cell, the same "isle" and "valley" can be found, caused by the aforementioned lateral distortions of the lower oxygen atoms. At the surface of the oxide film, again 12 under-coordinated oxygen atoms are found, the same number as for the pure Pt substrate.

The PBE relaxed structure at the same lattice constant yields an even more strongly buckled structure with height differences of up to 115 pm in the the Zr layer of the oxide. The top oxygen atoms buckle by 126 pm while those at the metal interface buckle by 95 pm. Similar to the case of a pure Pt substrate, the distance between the metal surface and the lower oxygen layer is 245 pm. Zr–Zr distances between 320 pm and 399 pm can be found in the oxide film with a mean value of 352 pm. At the surface of the oxide film there are 13 under-coordinated oxygen atoms.

The whole picture changes when compressing the unit cell to 23.414 Å, i.e. 2.685 Å per Pt(1×1) unit cell, the same value used for the $\sqrt{19}_{comp}$ model, reflecting a reconstructed Pt(111) surface. For these calculations, the lower four layers of the substrate had to be fixed, otherwise the compression would cause the Zr atoms to move out of the layered Pt$_3$Zr structure. The relaxed structures shown in fig. 3.27 yield an almost completely flat oxide film. Its Zr atoms show height differences of just 26 pm and both lower and upper oxygen layers only buckle by about 15 pm for the optB86b functional. Almost no lateral displacement of the Zr atoms is found, the Zr–Zr distances are between 337 pm and 340 pm. The distance of the lower oxygen layer and the Pt layer of the substrate is increased to 277 pm. For the PBE functional, the structure of the oxide film is almost the same as for the optB86b functional. Due to the lack of van-der-Waals interactions, the film shows similar behaviour to the small compressed $\sqrt{3}$ model with an interlayer distance of 340 pm. In both cases, there are no under-coordinated oxygen atoms at the surface of the oxide film.

The STM simulations of the various structures show that the emerging pattern is largely dependent on the buckling and distortions at the surface of the oxide film. The surface of the real $\sqrt{19}$ model at the Pt$_3$Zr lattice constant shows, as described before, large height differences, and this is reflected in the STM simulations shown in fig. 3.28.

For both the optB86b and PBE relaxed structures Zr and O surface atoms generate bright spots in the occupied state picture, depending on their local height differences (figs. 3.28a and 3.28c). At negative bias, depicting the unoccupied states (fig. 3.28b), the simulation mostly shows the surface oxygen. Those that are buckled upwards due to losing a bond to a nearby Zr are indicated by the brighter spots. The large lateral distortions yielded in the PBE calculation cause low contrast in the oxygen atoms since one area, where the oxide film is almost completely ripped apart, is shown as a large dark spot (fig. 3.28d).

At the optimal Pt lattice constant the oxide film is less distorted which is well reflected in the STM simulations. For the optB86b relaxed structure (figs. 3.29a and 3.29b) the bright spots are generated by surface oxygen. In the surface unit cell one triangular shape bounded by three bright spots can be identified: here the oxide film is laterally compressed and buckled upwards, forming the aforementioned isle. The bright spots and bright grey area in between are generated by 2-fold and 3-fold coordinated surface oxygen. Zr are only lightly visible where the oxide film is laterally expanded. The PBE structure (figs. 3.29c and 3.29d) shows an identical pattern.

Further compression of the $\sqrt{19}$ model cell to a Pt lattice constant of 2.685 Å (-3.3% with respect to pure Pt) yields a lightly buckled and completely smooth film for the optB86b and PBE relaxation, respectively. In the STM simulations, the lightly buckled oxide film (figs. 3.30a and 3.30b) shows U-shaped patterns at positive bias voltage, caused by an overlap of bright features caused by both Zr and O at the surface. At negative bias voltage the pattern is different, but larger bright areas are again caused by this overlap where the height difference between Zr and O is appropriate. The completely smooth oxide film on the other hand only shows the surface oxygen as well separated bright spots, shown in figs. 3.30c and 3.30d.

The comparison of the calculated surface energy of these models (see table 3.12) shows a preference for the last model that is compressed to an oxide lattice constant of 338 pm. For this model the influence of the substrate is small, especially for the PBE functional. For the optB86b model the film binds more strongly to the pure Pt substrate. At the experimental oxide lattice constant the calculations all functionals predict stronger binding to the pure Pt than to the Pt-terminated Pt_3Zr substrate.

3.3.6. $(\sqrt{13} \times \sqrt{13})R13.8°$ Model

To further study the dependence of the oxide lattice constant on the metal-oxide interface properties third supercell was used with a small lattice mismatch between optimal Pt_3Zr and the experimental ZrO_2 lattice. Using a lattice matching algorithm [96] a model cell consisting of a (6×6) ZrO_2 unit cell on top of a $\sqrt{13} \times \sqrt{13}$ Pt_3Zr unit cell was found. In this model the Pt_3Zr substrate is rotated by 13.9° with respect to the oxide lattice and the oxide unit cell is compressed by 1.7% to 3.443 Å with respect to the experimental value of 3.5 Å. The resulting unit cell used for the calculations consisted of a 5-layer Pt-terminated Pt_3Zr slab where the lower three layers were kept fixed in all directions. The lattice constant of the model cell was 20.656 Å and the cell was extended in z direction to include about 18 Å vacuum. Initially, the oxide film was placed at a distance of 1.8 Å

(a) $\sqrt{19}$/Pt$_3$Zr, PBE

(b) $\sqrt{19}$/Pt$_3$Zr, PBE

(c) $\sqrt{19}$/Pt$_3$Zr, optB86b

(d) $\sqrt{19}$/Pt$_3$Zr, optB86b
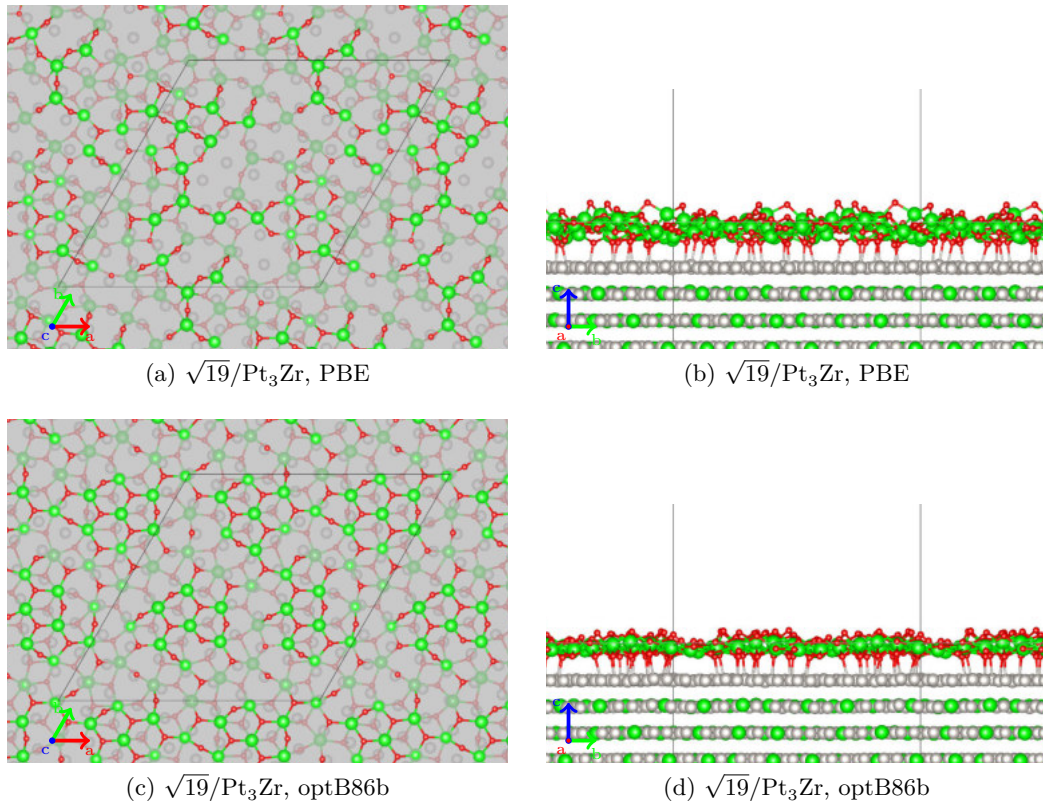
Figure 3.25.: Top and side view of the relaxed $\sqrt{19}$/Pt$_3$Zr model cell at the optimal Pt$_3$Zr lattice constant. Top row: relaxed with the PBE, bottom row: with the optB86b functional. A grey plane was added at the mean height of the ZrO$_2$ film to illustrate the buckling in the top view images.

(a) $\sqrt{19}$/Pt$_3$Zr, Pt lattice constant, PBE

(b) $\sqrt{19}$/Pt$_3$Zr, Pt lattice constant, PBE

(c) $\sqrt{19}$/Pt$_3$Zr, Pt lattice constant, optB86b

(d) $\sqrt{19}$/Pt$_3$Zr, Pt lattice constant, optB86b

Figure 3.26.: Top and side view of the relaxed $\sqrt{19}$/Pt$_3$Zr model cell compressed to the Pt lattice constant (2.777 Å Pt lattice constant). Top row: relaxed with the PBE, bottom row: with the optB86b functional. A grey plane was added at the mean height of the ZrO$_2$ film to illustrate the buckling in the top view images.

(a) $\sqrt{19}$/Pt$_3$Zr, compressed, PBE

(b) $\sqrt{19}$/Pt$_3$Zr, compressed, PBE

(c) $\sqrt{19}$/Pt$_3$Zr, compressed, optB86b

(d) $\sqrt{19}$/Pt$_3$Zr, compressed, optB86b

Figure 3.27.: Top and side view of the relaxed $\sqrt{19}$/Pt$_3$Zr model cell compressed to the lattice constant used for the $\sqrt{19}_{comp}$ model (2.685 Å Pt lattice constant). Top row: relaxed with the PBE, bottom row: with the optB86b functional. A grey plane was added at the mean height of the ZrO$_2$ film to illustrate the buckling in the top view images.

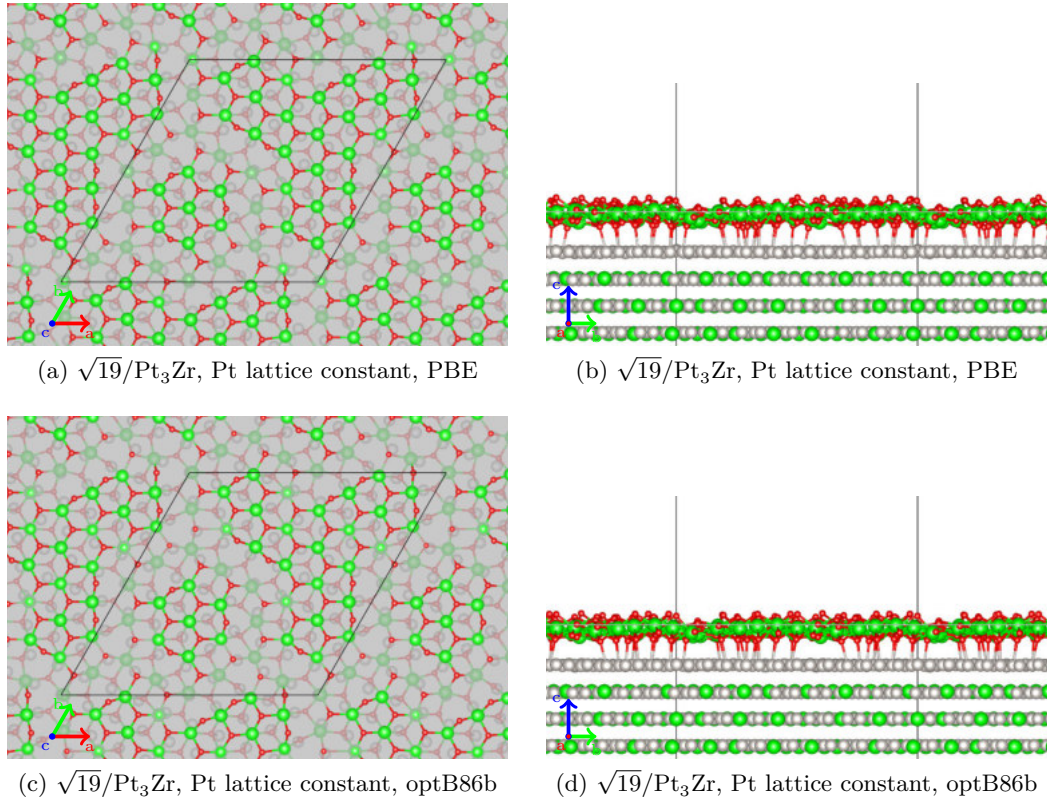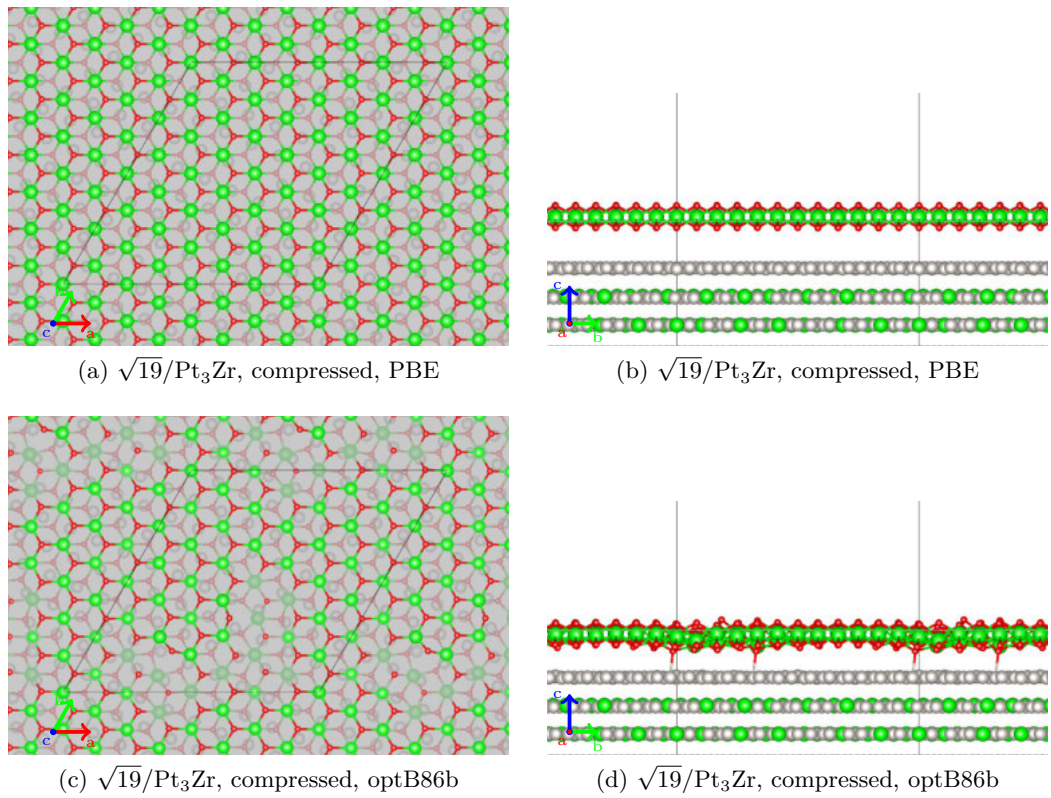(a) optB86b, Bias: $+0.5\,\mathrm{V}$

(b) optB86b, Bias: $-0.5\,\mathrm{V}$

(c) PBE, Bias: $+0.5\,\mathrm{V}$

(d) PBE, Bias: $-0.5\,\mathrm{V}$
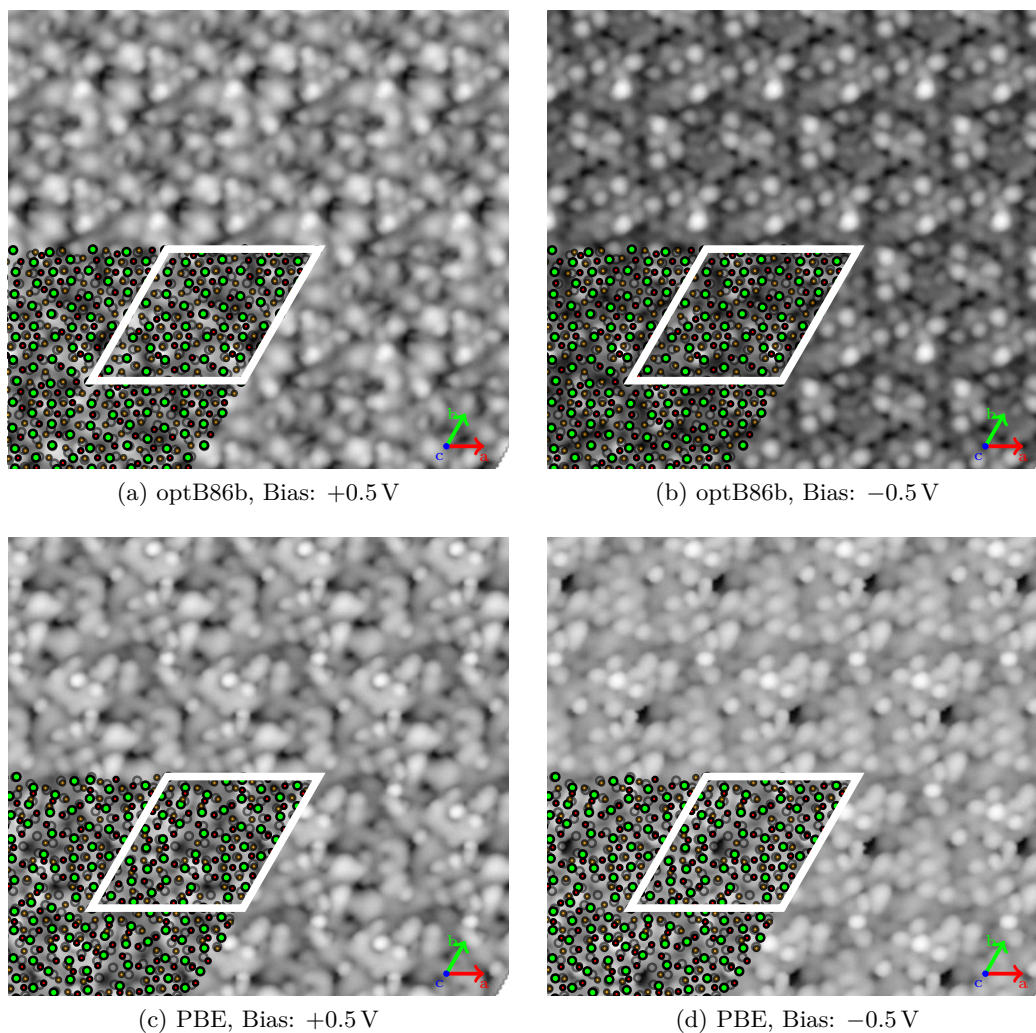
Figure 3.28.: STM Simulations of the $\sqrt{19}/\mathrm{Pt}/\mathrm{Pt_3Zr}$ model at $\pm 0.5\,\mathrm{V}$ bias voltage at the optimal $\mathrm{Pt_3Zr}$ lattice constant. Relaxations were performed with the ((a)-(b)) optB86b and ((c)-(d)) PBE functionals.

(a) optB86b, Bias: $+0.5\,\mathrm{V}$

(b) optB86b, Bias: $-0.5\,\mathrm{V}$

(c) PBE, Bias: $+0.5\,\mathrm{V}$

(d) PBE, Bias: $-0.5\,\mathrm{V}$
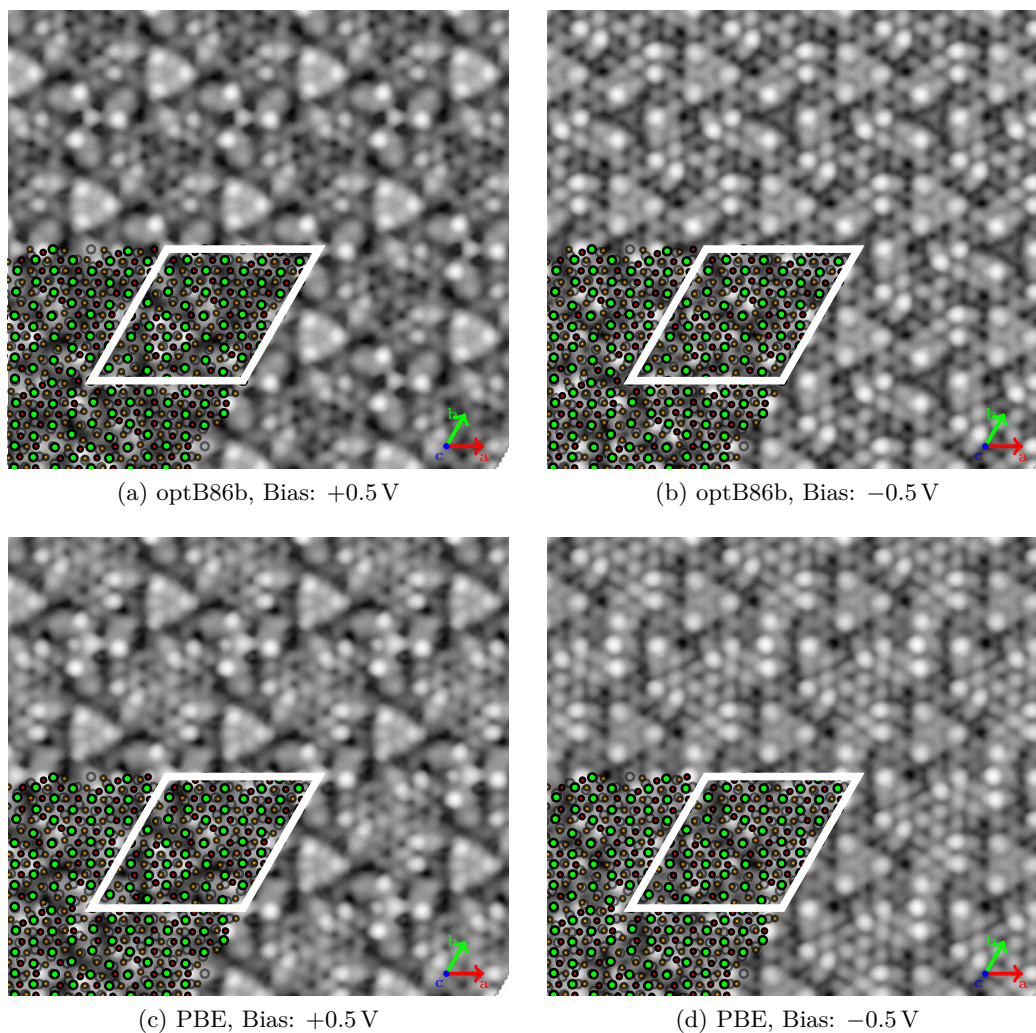
Figure 3.29.: STM Simulations of the $\sqrt{19}/\mathrm{Pt}/\mathrm{Pt_3Zr}$ model compressed to the optimal optB86b Pt lattice constant of $2.777\,\text{Å}$ at $\pm0.5\,\mathrm{V}$ bias voltage. Relaxations were performed with the ((a)-(b)) optB86b and ((c)-(d)) PBE functionals.

(a) optB86b, Bias: +0.5 V

(b) optB86b, Bias: −0.5 V

(c) PBE, Bias: +0.5 V

(d) PBE, Bias: −0.5 V
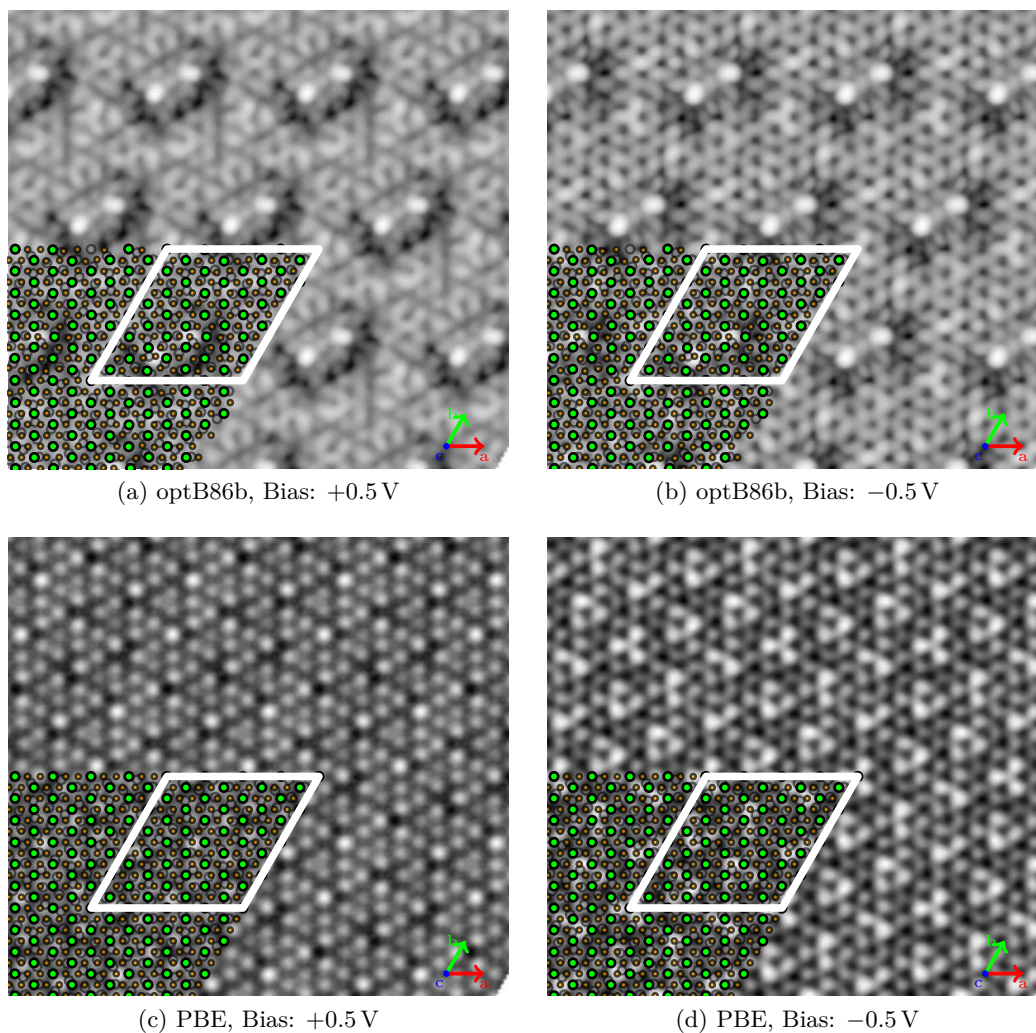
Figure 3.30.: STM Simulations of the $\sqrt{19}$/Pt/Pt$_3$Zr model compressed to a Pt lattice constant of 2.685 Å, reflecting a reconstructed Pt(111) surface, at ±0.5 V bias voltage. Relaxations were performed with the ((a)-(b)) optB86b and ((c)-(d)) PBE functionals.

to the Pt_3Zr substrate. The relaxations were first performed at the optimal Pt_3Zr lattice constant. Later, the $\sqrt{13}$ unit cell was slightly expanded to 21 Å to simulate an oxide lattice constant of 3.5 Å.

For both cases, the relaxation was performed with both the optB86b and the PBE functional. At the experimental lattice constant, shown in fig. 3.31, the oxide film again exhibits similar behaviour to the $\sqrt{19}$ model cells. The optB86b relaxed structure shows buckling of the Zr layer of 102 pm. Also, both upper and lower oxygen layer buckle more strongly compared to the $\sqrt{19}$ model at 109 pm and 79 pm respectively. The Zr–Zr distances of 320 pm to 400 pm are an indication of the heavy lateral distortions of the oxide film. Due to the different register of the lower oxygen atoms with respect to the Pt layer, the compressed areas of the film are not as localised as for the $\sqrt{19}$ model. In this $\sqrt{13}$ model the upwards buckled areas are much larger and only smaller areas where the Zr atom strongly buckles towards the substrate can be found. Nevertheless, the pattern causing the strong lateral displacements is similar as the oxygen atoms have to move more to bind to the Pt atoms below. In addition to that, the accompanying downwards movement of the Zr atoms increases their bonds to the Pt substrate. The interlayer distance between lower oxygen and Pt layer is 224 pm. At the surface of the oxide, the distortions cause eight under-coordinated oxygen atoms, one more per ZrO_2 formula unit compared to the $\sqrt{19}$ model. The relaxation with the PBE functional yields an even more distorted structure where the oxide film buckles by 160 pm. Both upper and lower oxygen buckle by 154 pm and 68 pm, respectively. The Zr–Zr distances are similar to the optB86b structure, ranging from 318 pm to 399 pm. The heavily distorted oxide film accumulates 15 under-coordinated oxygen atoms at the surface. This is due to a stronger lateral compression in one area of the oxide film, which leads to a triangular isle structure where the other parts of the unit cell show the large distortions. Compared to the optB86b structure, the oxide film is positioned slightly farther from the substrate at 232 pm.

Repeating the same calculations at the Pt_3Zr lattice constant leads to very smooth oxide films for both functionals. For the optB86b relaxed structure, the buckling of the Zr layer of the film is still 102 pm, but the oxygen layers are less buckled at 94 pm and 50 pm for the upper and lower layer, respectively. The Zr–Zr distances show a slightly smaller range from 324 pm to 391 pm, yielding an average distance of 348 pm. The distance between oxide and metal is slightly larger at 230 pm. Looking at the surface structure of the adsorbed oxide, the film exhibits large smooth areas, interrupted by individual sites where the film distorts. There, again lower oxygen atoms are displaced due to the formation of a Pt–O bond, causing their neighbouring Zr atoms to displace as well. This effect is even more reduced for the PBE relaxed structure. Here the oxide film is much smoother, buckling by only 67 pm. Also, both upper and lower oxygen layer are very smooth. The weaker binding to the Pt/Pt_3Zr substrate is also indicated by the larger distance of 250 pm between metal and oxide. Due to the low amount of distortion of the ZrO_2 film no under-coordinated oxygen atoms are at the surface.

The calculated surface energies are about $6\,meV/Å^2$ lower compared to the $(\sqrt{19} \times \sqrt{19})R23.4°$ model, indicating a preference of the interface to form this $(\sqrt{13}\times\sqrt{13})R13.8°$

interface (see table 3.12). This indicates that both DFT functionals overestimate the surface energy of the ZrO_2 film, as also seen for the compressed $(\sqrt{3} \times \sqrt{3})R30°$ model with its much lower surface energy (see table 3.11). Nevertheless, the large contraction of the ZrO_2 film contrasts with the measured oxide lattice constant.

STM simulations of the $(\sqrt{13} \times \sqrt{13})R13.8°$ models show the familiar dependence of the pattern on the height differences of surface Zr and O. For the slightly expanded model, the bright features are mostly generated by the oxygen atoms (figs. 3.33b to 3.33c), except for the optB86b relaxed structure at positive bias voltage (fig. 3.33a) where one spot at the centre of the surface unit cell is generated by a Zr atom. At the Pt_3Zr lattice constant the oxide film is less buckled and therefore the height differences at the surface are lower, yielding a quite regular pattern of bright spots generated by surface oxygen (fig. 3.34). A couple of very bright spots are again caused by upwards buckled surface O. The very flat structure resulting from the PBE relaxation shows just one site where the highest Zr atom contributes to a bright rotor shaped bright structure.

(a) $\sqrt{13}$, oxide at 3.5 Å, PBE

(b) $\sqrt{13}$, oxide at 3.5 Å, PBE

(c) $\sqrt{13}$, oxide at 3.5 Å, optB86b
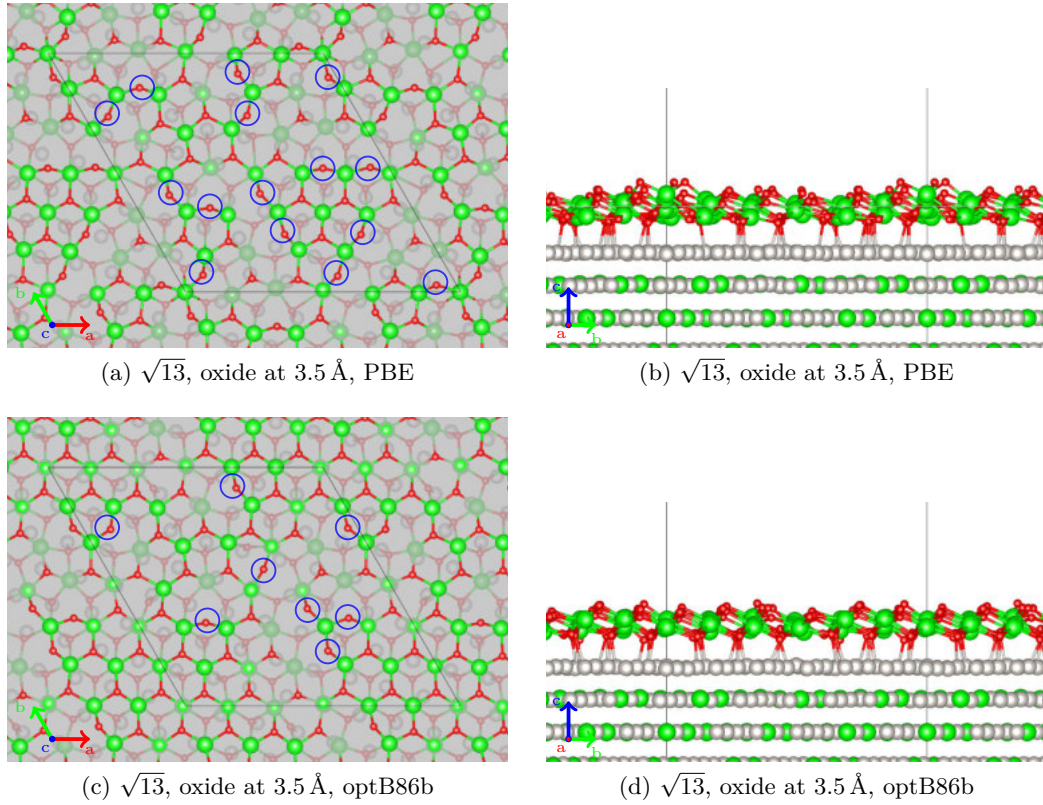
(d) $\sqrt{13}$, oxide at 3.5 Å, optB86b

Figure 3.31.: Top and side view of the relaxed $\sqrt{13}$ model cells, expanded to 3.5 Å oxide lattice constant. The relaxations were performed with the PBE (top row) and optB86b (bottom row) functionals. Under-coordinated oxygen atoms at the surface are indicated by blue circles.

(a) $\sqrt{13}$, PBE

(b) $\sqrt{13}$, PBE

(c) $\sqrt{13}$, optB86b

(d) $\sqrt{13}$, optB86b

Figure 3.32.: Top and side view of the relaxed $\sqrt{13}$ model cells, at the optimal Pt_3Zr lattice constant, equaling a compression of the oxide film to $3.47\,\text{Å}$. The relaxations were performed with the PBE (top row) and optB86b (bottom row) functionals. Under-coordinated oxygen atoms at the surface are indicated by blue circles.
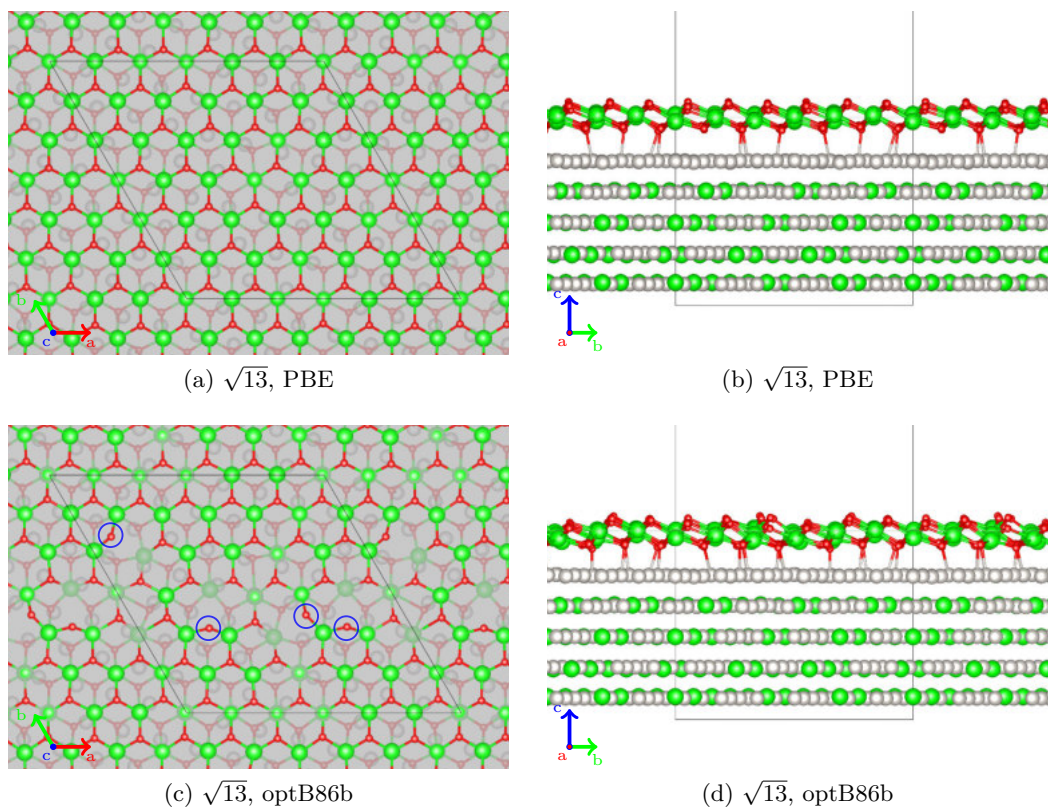
(a) optB86b, Bias: $+0.5\,\mathrm{V}$

(b) optB86b, Bias: $-0.5\,\mathrm{V}$

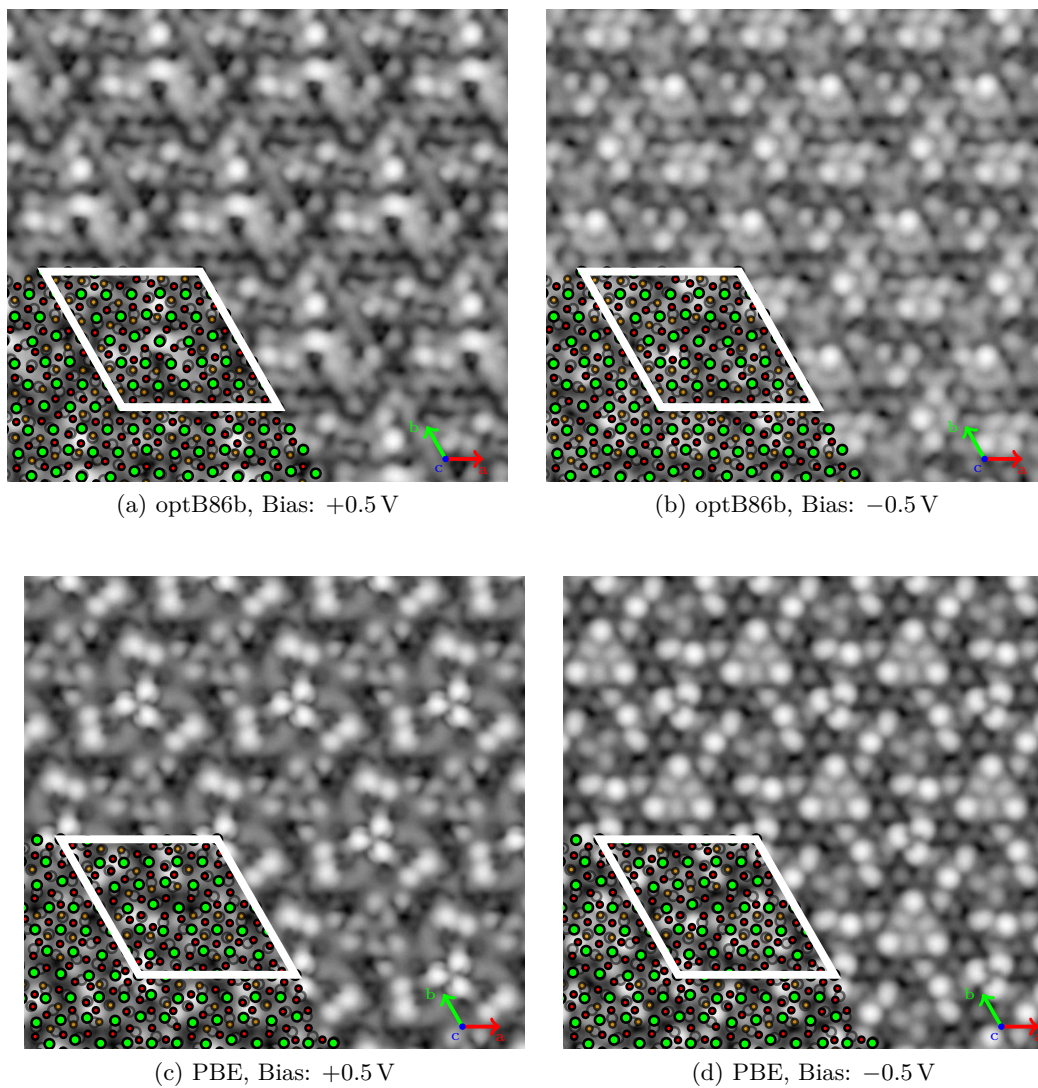(c) PBE, Bias: $+0.5\,\mathrm{V}$

(d) PBE, Bias: $-0.5\,\mathrm{V}$

Figure 3.33.: STM Simulations of the $(\sqrt{13} \times \sqrt{13})R13.8°$ model expanded to an oxide lattice constant of $3.5\,\text{Å}$ at $\pm0.5\,\mathrm{V}$ bias voltage. Calculations done with the ((a)-(b)) optB86b and ((c)-(d)) PBE functional, respectively.

(a) optB86b, Bias: $+0.5\,\mathrm{V}$

(b) optB86b, Bias: $-0.5\,\mathrm{V}$
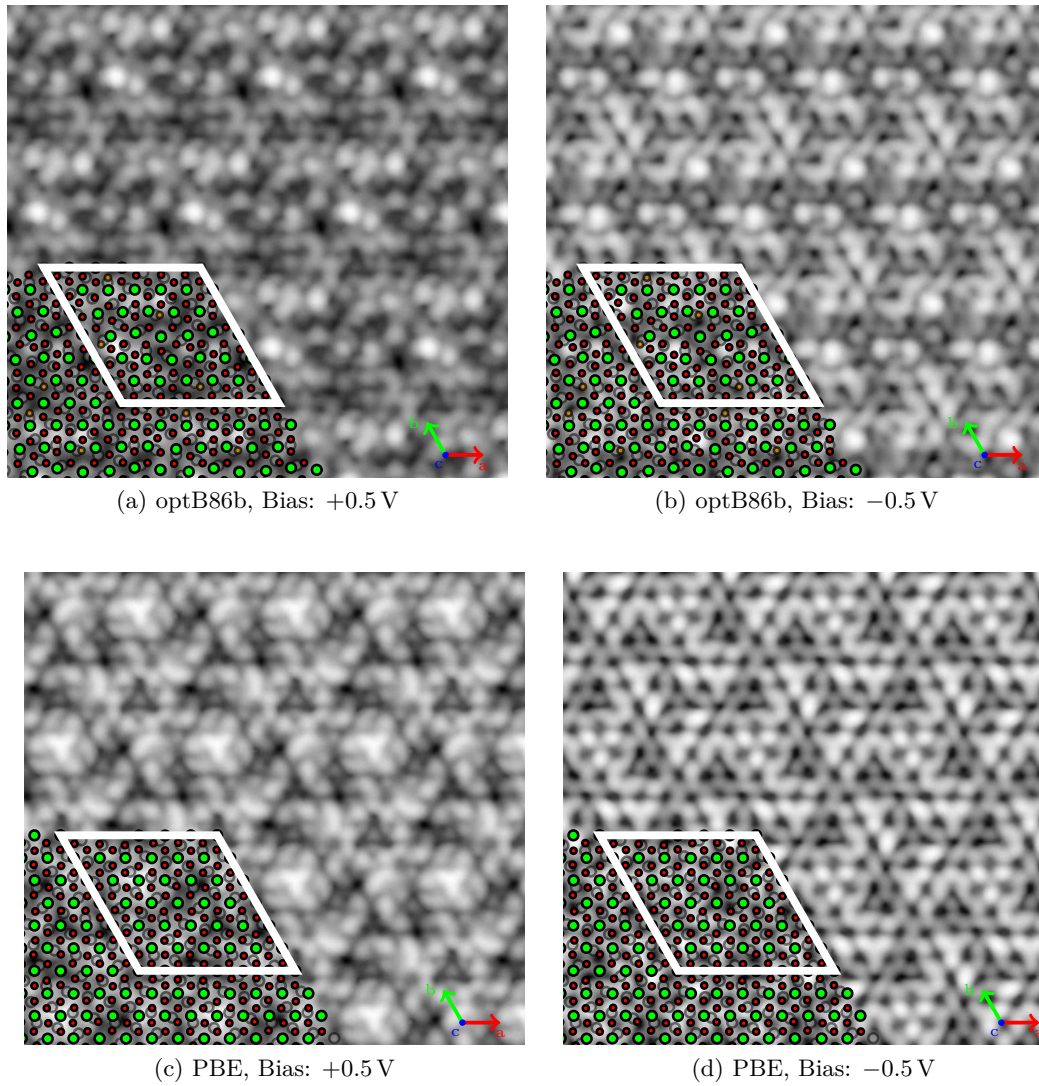
(c) PBE, Bias: $+0.5\,\mathrm{V}$

(d) PBE, Bias: $-0.5\,\mathrm{V}$

Figure 3.34.: STM Simulations of the $(\sqrt{13}\times\sqrt{13})R13.8°$ model at the Pt_3Zr lattice constant at $\pm0.5\,\mathrm{V}$ bias voltage. Calculations done with the (a)-(b) optB86b and ((c)-(d)) PBE functional, respectively.

Table 3.11.: Surface energies and lattice parameters (d: distances, b: buckling) of a single adsorbed ZrO_2 trilayer film adsorbed on stoichiometric Pd_3Zr, Pd-terminated Pd_3Zr, and Pt-terminated Pt_3Zr in the $(\sqrt{3} \times \sqrt{3})R30°$ configurations discussed in sections 3.2.2 and 3.2.3.

Configuration	ZrO2/Pd3Zr O1Zr'		ZrO2/Pd/Pd3Zr ZrPd				ZrO2/Pt/Pt3Zr ZrPt			
Functional	PBE	optB88	PBE	optB88	PBE	optB88	PBE	optB88	PBE	optB88
ZrO2 lat. const. [pm]	329		329		350		331		350	
Substrate lat. const. [pm]	570		570		606		573		606	
$d_{O_2-O_1}$ [pm]	191	192	192	188	175	169	190	186	174	171
$d_{\varnothing ZrO_2-S}$ [pm]	339	336	410	330	309	292	433	353	323	308
d_{O_1-S} [pm]	244	240	314	237	225	209	338	261	241	227
b_{O_2} [pm]	5	3	0	1	48	12	0	0	66	59
b_{Zr} [pm]	77	83	10	61	63	35	5	49	83	73
b_{O_1} [pm]	26	22	1	3	24	9	1	6	40	31
b_S [pm]	13	9	7	4	5	9	8	7	12	8
E_{surf} [meV/Å²]	36	37	49	50	70	71	47	51	74	73

Table 3.12.: Surface energies and lattice parameters (d: distances, b: buckling) of a single adsorbed ZrO$_2$ trilayer film adsorbed on pure Pt and Pt-terminated Pt$_3$Zr in the $(\sqrt{19}\times\sqrt{19})R23.4°$ and $(\sqrt{13}\times\sqrt{13})R13.8°$ configurations discussed in sections 3.3.1, 3.3.3, 3.3.5 and 3.3.6. The number of Pt–O bonds is given per unit cell with a threshold of 2.4 Å.

| Configuration Functional	Pt substrate $(\sqrt{19}\times\sqrt{19})R23.4°$				Pt$_3$Zr substrate $(\sqrt{19}\times\sqrt{19})R23.4°$						Pt$_3$Zr substrate $(\sqrt{13}\times\sqrt{13})R13.8°$			
	PBE	optB86b	PBE	optB86b	PBE	optB86b	PBE	optB86b	PBE	optB86b	PBE	optB86b	PBE	optB86b
ZrO$_2$ lat. const. [pm]	350		338		360		349		338		350		347	
Substrate lat. const. [pm]	278		268		573		555		537		582		573	
$d_{O_2-O_1}$ [pm]	247	240	184	209	369	360	265	248	187	197	284	256	219	246
$d_{\varnothing ZrO_2-s}$ [pm]	297	288	429	323	350	299	327	313	432	367	315	305	336	315
d_{O_1-s} [pm]	219	209	337	236	266	226	245	232	340	277	232	224	250	230
b_{O_2} [pm]	119	109	0	56	219	123	126	99	4	15	154	109	66	94
b_{Zr} [pm]	113	107	0	78	221	95	115	98	5	26	160	102	67	102
b_{O_1} [pm]	98	92	0	43	144	107	95	70	4	14	68	79	44	50
b_S [pm]	31	31	6	43	32	27	21	24	10	13	15	24	16	19
Pt–O Bonds per cell	9	10	0	6	32	32	21	19	0	0	21	21	8	16
Under-coordinated O	4	4	0	0	23	20	13	12	0	0	15	8	0	4
E_{surf} [meV/Å^2]	49	44	61	63	79	79	77	76	60	70	70	74	71	69

3.3.7. Simulated Annealing: $\sqrt{19}$ Model

In the following chapter, the adsorption of various adsorbates on the $\sqrt{19}$ model will be discussed in detail, see sections 4.1 and 4.2. During these simulations it was noticed that the addition of an adsorbate strongly modifies the oxide film, in some cases leading to an even more stable structure. Therefore, simulated annealing simulations were performed to verify the structural ground state. This simulation was performed with VASP by doing a canonic molecular dynamics (MD) calculation with a simple Verlet algorithm. The temperature is supplied by a Nosé-Hoover thermostat [102, 103]. The cooling ramp is defined by the choice of the initial and final temperature, and the total number of steps. Finally, a selection of structures from local energy minima can then be relaxed further using a standard relaxation algorithm to find the global equilibrium structure. For these calculations only the optB86b functional was used. The other computational setting were identical to the standard relaxations discussed before.

As a first step, a simulated annealing run, starting from an initial temperature of 800 K and a ramp down to 0 K with 1000 iterations, was done on the $\sqrt{19}$ model cell. As can be seen in fig. 3.35a, the total energy of the system increases sharply as the structure absorbs the temperature supplied by the thermostat. The temperature of the system peaks at 1366 K after 120 steps, but the system cools down quickly until the first local energy minimum is reached after 277 steps. After 617 steps the first local energy minimum is reached, but here the temperature is still at about 230 K. The global minimum is reached after 1000 steps where the energy supplied by the external thermostat is completely removed. The structures at these two minima and the global minimum structure from the last step were then further relaxed using the standard conjugate gradient algorithm.

As can be seen in table 3.13, three of the structures suggested by the simulated annealing approach lead to identical structures. The structure taken from step number 277 shows just a slight increase, about 1 meV per atom. Compared to the standard ZrPt model, the energy gain is one order of magnitude larger. While this would amount to an energy difference of just 10 meV per atom, the total energy difference of the whole $\sqrt{19}$ system plays a big role when calculating adsorption energies.

To confirm that the global ground state structure was found with the short simulated annealing run the same calculation was performed a second time with 4000 steps, illustrated in fig. 3.35b. Of this run, the structures of the last three energy minima (step #2940, #3491 and #4000) were chosen, but no further improvement could be found.

The structural properties of the final ground state structure (see fig. 3.36) are similar to the earlier mentioned OPt$_{optB86b}$ structure relaxed using the optB86b functional. The ZrO$_2$ film exhibits the same "isle" and "valley" structure and similar Zr–Zr distances between 323 pm and 399 pm. The optB86b functional predicts a film thickness of 250 pm and an average distance of the lower oxygen atoms to the metal substrate of 212 pm, slightly larger than for the OPt$_{optB86b}$ and ZrPt$_{optB86b}$ structures. The buckling of this ground state structure amounts to 116 pm for the Zr atoms and 125 pm of the upper oxygen atoms. Again, due to the shorter metal-oxide distance 10 O–Pt bonds are formed, inducing slight buckling of the upper Pt layer of 32 pm. The lower oxygen atoms buckle
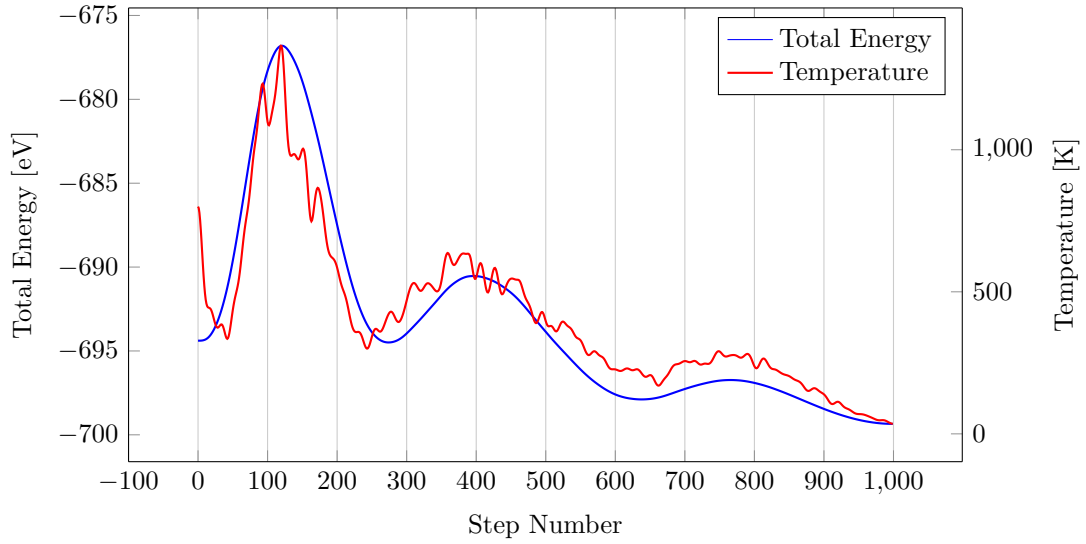
(a) 1000 Steps
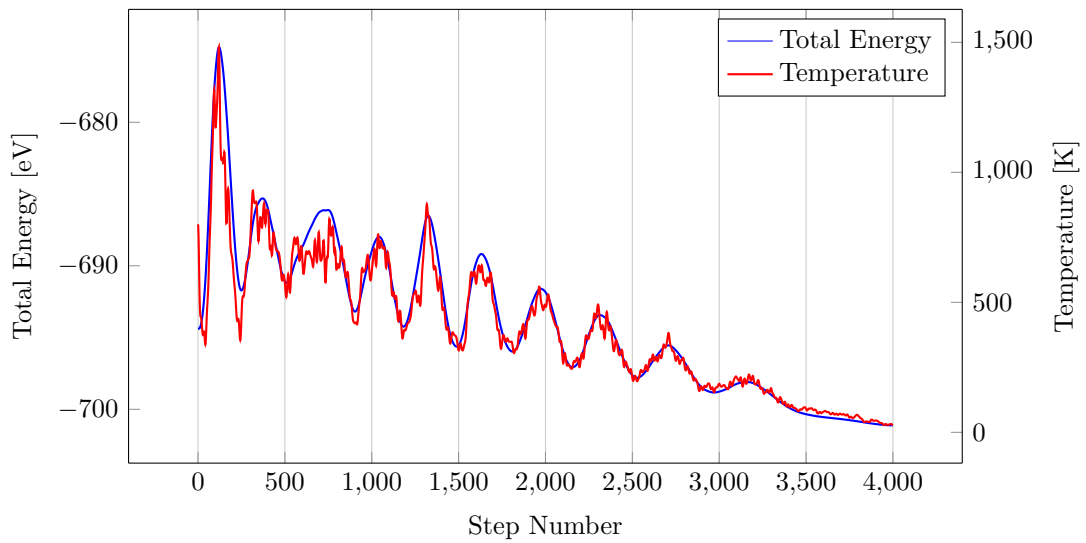
(b) 4000 Steps

Figure 3.35.: Progression of total energy and temperature during the simulated annealing run of the $\sqrt{19}$ model.

Table 3.13.: Total energy differences in meV of $\sqrt{19}$ structures extracted from the simulated annealing runs.

Step number, run #1	Energy difference [meV]
ZrPt	1295
277	120
617	1
1000	0
Step number, run #2	
2940	166
3491	165
4000	166

by 96 pm. Finally, the calculations predict four under-coordinated oxygen atoms at the surface and one at the metal-oxide interface.

The STM simulation of the bare oxide surface shows large differences in their brightness due to the strong buckling. In the occupied states the brightest spot indicates one of the 2-fold coordinated oxygen atoms, while another neighbouring bright spot indicates a second 2-fold coordinated oxygen. Both are displaced normal to the surface, causing the high brightness. At the "valley" sites can be identified by the large dark areas in between the brighter "isle" areas. In the "valley" two darker grey spots can be identified with zirconium atoms buckling towards the Pt(111) surface. The brighter "isle" areas show a hexagonal structure with only small differences in brightness.

3.3.8. Simulated Annealing: Compressed $\sqrt{19}_{comp}$ Model

For the compressed $\sqrt{19}$ model described in section 3.3.3 simulated annealing calculations were also done according to the procedure described here. The initial temperature was again set to 800 K with a ramp of 3000 steps to $T = 0$ K. The computational parameters were identical to the previous calculations on the $\sqrt{19}$ model. As shown in fig. 3.38, compared to the $\sqrt{19}$ model at Pt lattice constant the energy introduced into the system dissipates more quickly after the first high temperature peak after 130 steps. To find the global minimum, the structures at steps #2431, #2685, and #3000 were further relaxed using the standard VASP algorithms. These calculations yield structures which are 1.348 eV, 1.233 eV, and 1.348 eV more favourable than the slightly buckled structure found in section 3.3.3.

The fully relaxed compressed $\sqrt{19}_{comp}$ structure after simulated annealing shows a heavily distorted zirconia film with very large buckling of both the Zr and the O layers. The buckling of the Zr layer is increased to 137 pm while the upper oxygen atoms buckle by 130 pm. The Zr–Zr distances show great variance, ranging from 320 pm to 387 pm where the film is heavily distorted. Zr–O bond lengths in the oxide film range from
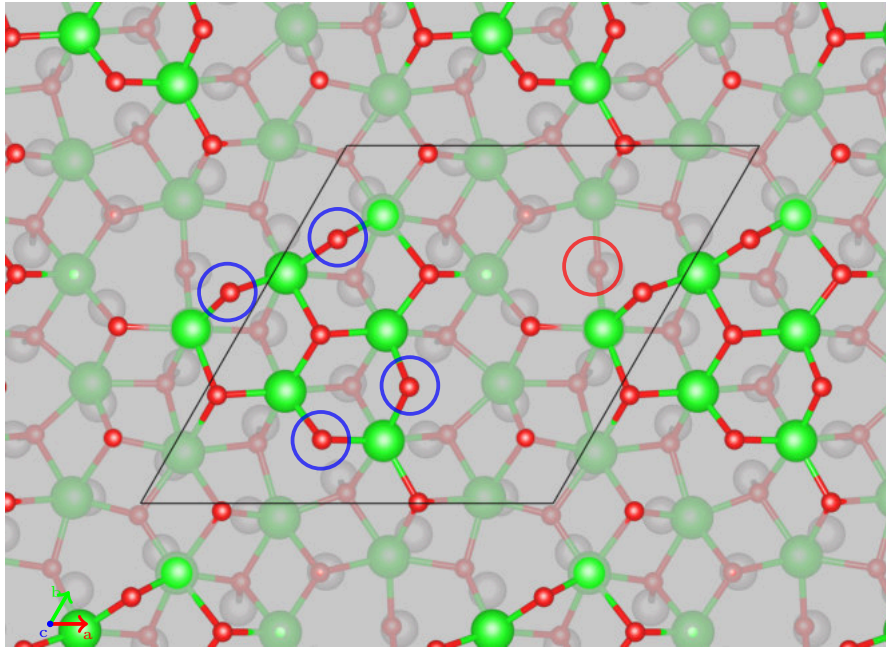
Figure 3.36.: Fully relaxed $\sqrt{19}$ model cell after simulated annealing. 2-fold coordinated top oxygen atoms indicated by blue, under-coordinated bottom oxygen by red circles.

(a) Bias: $+0.5\,\mathrm{eV}$
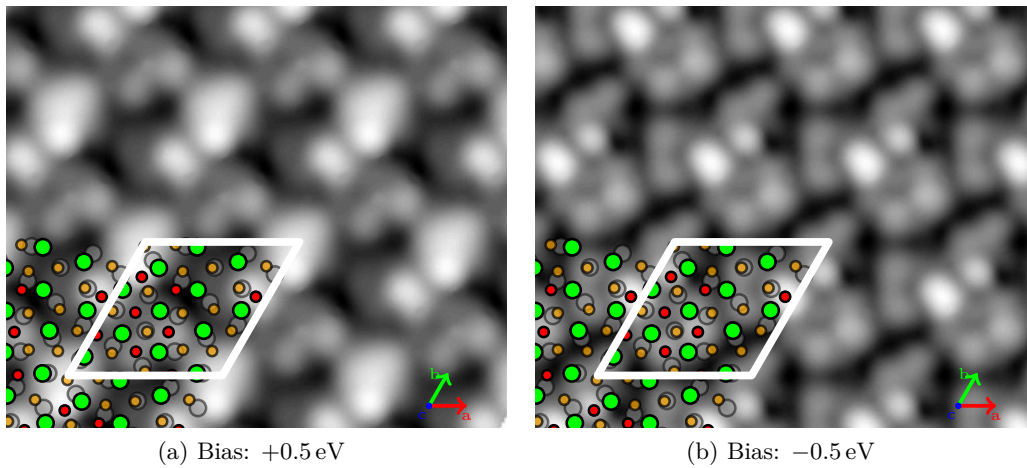
(b) Bias: $-0.5\,\mathrm{eV}$

Figure 3.37.: STM of the fully relaxed ground state $\sqrt{19}$ structure. The unit cell in white; Zr, O, Pt atoms green, red, and grey, respectively.

Table 3.14.: Total energy differences in meV of the fully relaxed $\sqrt{19}$ structures selected from the simulated annealing run.

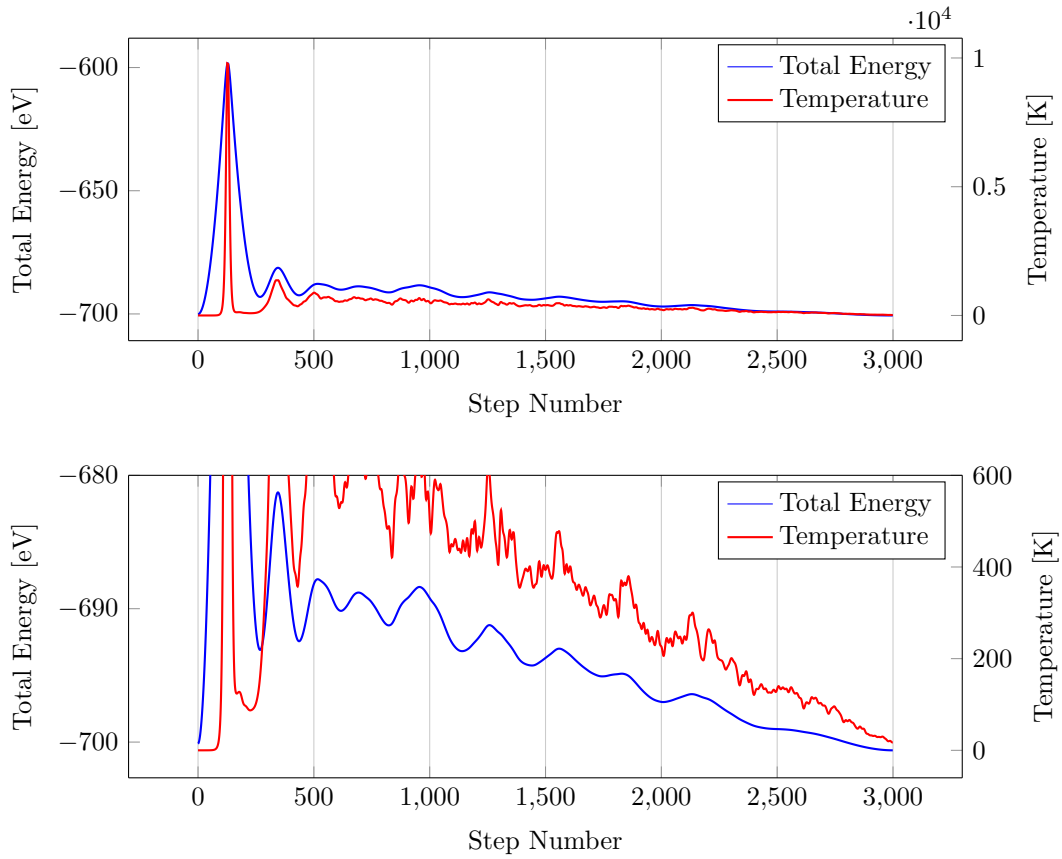| Step number	Energy difference [meV]
OPt$_{compressed}$	1348
2431	0
2685	115
3000	0

Figure 3.38.: Temperature and total energy curves of the simulated annealing calculation of the compressed $\sqrt{19}$ model. The bottom graph shows a magnification of the top graph.

197 pm to 251 pm. While the distance between the oxide film and the Pt substrate is slightly larger than for the fully relaxed $\sqrt{19}$ model (229 pm vs 223 pm) and the rumpling of the lower oxygen atoms is decreased (66 pm vs 96 pm), the surface layer of the Pt substrate experiences strong buckling of 53 pm (uncompressed: 32 pm). Of course, the compression of the lattice constant does play a big role in these distortions of the platinum layer, since due to the lateral strain they can only move out towards the oxide film. Compared to the slightly buckled compressed $\sqrt{19}$ model, the calculations predict the formation of nine Pt–O bonds at the oxide-metal interface and three under-coordinated oxygen atoms at the surface of the ZrO_2 film.

Figure 3.39 shows a top view of the relaxed compressed $\sqrt{19}_{comp}$ structure. In comparison to the standard $\sqrt{19}$ model the film does show some resemblance to the "isle" and "valley" structure, but the areas where the distortions are the strongest are smaller and again located mostly where the Zr–Pt interaction is stronger, i.e. where the Zr atoms are positioned on top of Pt atoms.

The STM simulations show flower-like bright features at both positive and negative bias voltages, located where the oxide film is buckled upwards. The bright spots which comprise these features are located at the upper oxygen atoms. The slight differences in brightness are induced by the height differences of the oxygen atoms. Separating these larger features are dark valleys, which are exactly located where the oxide film buckles downwards.
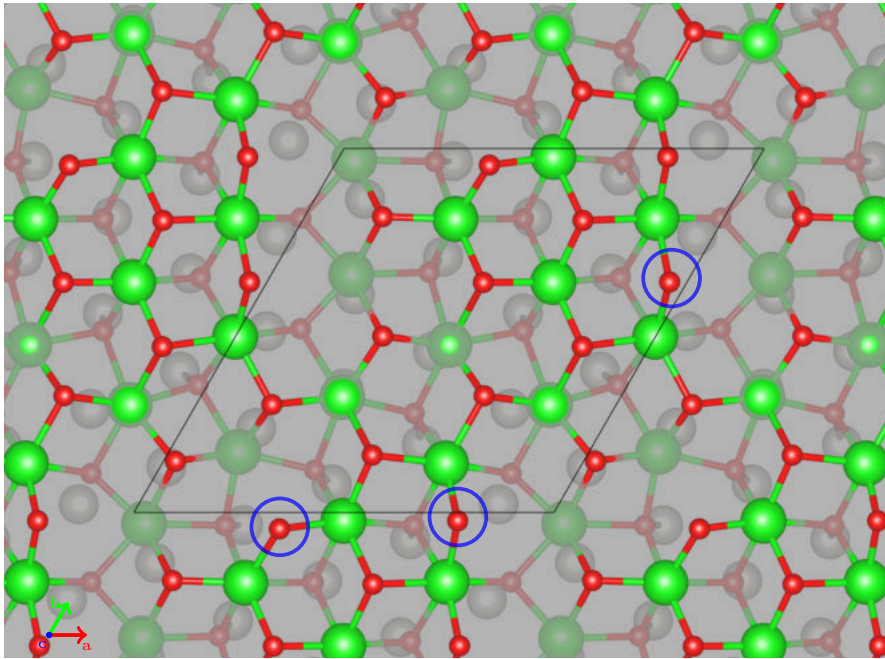

Figure 3.39.: Fully relaxed compressed $\sqrt{19}_{comp}$ model cell after simulated annealing. 2-fold coordinated top oxygen atoms indicated by blue circles.

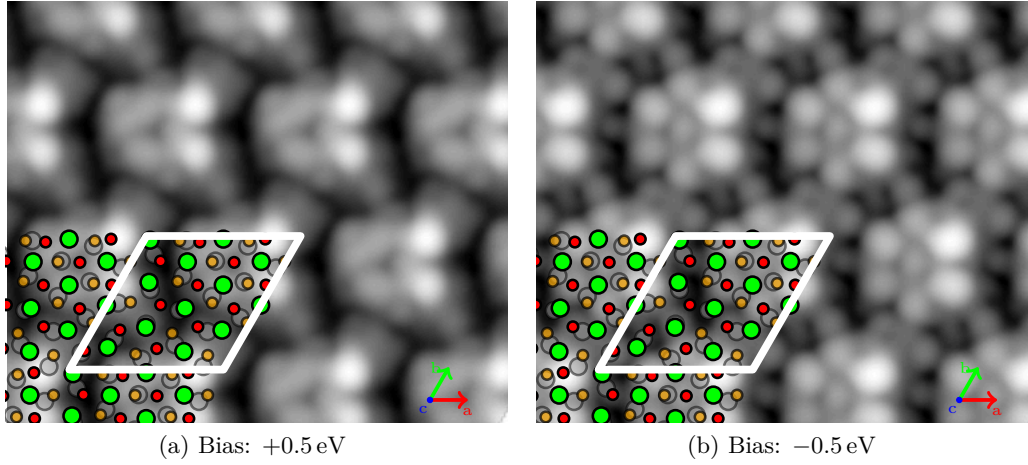(a) Bias: $+0.5\,\mathrm{eV}$ (b) Bias: $-0.5\,\mathrm{eV}$

Figure 3.40.: STM of the fully relaxed ground state compressed $\sqrt{19}_{comp}$ structure. The unit cell in white; Zr, upper O, lower O, Pt atoms green, red, orange, and grey, respectively.

3.3.9. Oxygen Defects in the ZrO$_2$ Film

Defects can have a large effect on the surface properties of metal oxides. In many cases they are the reactive sites of the material. Oxygen vacancies in particular can modify the behaviour strongly. For example, excess electrons can be trapped in a vacancy site for MgO, or they can form a rather mobile polaron in rutile TiO$_2$. On TiO$_2$ oxygen vacancies have also been found to be the reactive sites [104, 105]. Since the adsorption behaviour on ZrO$_2$ surfaces is a large topic in this work, the formation energies, calculated according to

$$V_O = E_{\mathrm{Slab}} - E_{\mathrm{Slab+Vacancy}} - E_{\mathrm{O}_2}/2 \qquad (3.2)$$

of these vacancies have been studied using the previously discussed models. The slab total energy E_{Slab} refers to the total energy of the $\sqrt{3}$ and $\sqrt{19}$ structure, respectively, and E_{O_2} to that of the free insulated O$_2$ molecule. The oxygen vacancy was created by removing the respective atom from the structure. The total energy was calculated by relaxing the resulting structure until the residual forces were $<0.01\,\mathrm{eV/\AA}$. All calculations were performed starting from the optB86b relaxed structures with the same functional. The other computational setting were chosen identically to the previous calculations on the pristine structures.

$\sqrt{3}$ Model Cells

The oxygen vacancy formation energies were calculated for both the compressed and expanded $\sqrt{3}$ described in section 3.2.3. For the compressed $\sqrt{3}$ model, the calculations predict a V$_O$ of abour $4.4\,\mathrm{eV}$ for both a vacancy created at the vacuum and the metal

74

interface side of the oxide film. Expanding the model cell to the experimental oxide lattice constant of 3.5 Å reduces the vacancy formation energy to about 2.1 eV, see table 3.15.

For the compressed model shown in figs. 3.41b and 3.42a, the buckling of the oxide film unchanged after creating an oxygen vacancy at the metal interface layer (V_{O1}, V_{O2}, V_{O3}). Also, the interlayer distance between metal and oxide does not change. Nevertheless, the lack of an oxygen atom at the interface induces a Zr atom to move closer to the substrate. When creating a vacancy at the vacuum interface (V_{O4}, V_{O5}, V_{O6}) the buckling of the Zr layer is decreased to 60 pm compared to 95 pm of the original structure. The film moves slightly farther from the metal substrate, from 211 pm to 225 pm. The rumpling of the top platinum layer of the substrate is also slightly reduced, from 44 pm to 23 pm. In all cases, the lower coordination of the Zr atoms leads to stronger bonding to the substrate, yielding an oxide film where two Zr atoms are buckled downwards and one upwards. Additionally, when creating an oxygen vacancy at the vacuum interface one of the three lower oxygen is pushed through the Zr layer, forming a 3-fold coordinated bond to the surrounding Zr atoms. Therefore, no under-coordinated oxygen can be found at the vacuum layer.

Expanding the whole unit cell to fit the experimental oxide lattice constant (see figs. 3.42c and 3.42d) reduces the stability of the oxide film, as indicated by the large reduction of the vacancy formation energy. The film thickness is reduced from 222 pm to 128 pm for a metal interface vacancy and to 131 pm for a vacuum interface vacancy. In all cases, the buckling of the Zr layer is reduced to 5 pm to 7 pm. In case of a vacancy at the metal interface, the distance to the substrate is reduced from 227 pm to 219 pm. Here, just like for the compressed model, one of the lower oxygen atoms moves to the vacuum interface layer. Still, the oxide film is heavily distorted, as depicted in fig. 3.42d.

Table 3.15.: Oxygen vacancy formation energy in eV for both the compressed and expanded $\sqrt{3}$ models.

#O	compressed	expanded
1	4.410	2.142
2	4.409	2.142
3	4.411	2.143
4	4.403	2.036
5	4.403	2.036
6	4.405	2.036

$\sqrt{19}$ Model Cells

For the larger, more realistic $\sqrt{19}$ model cells, the same procedure was performed. To calculate the vacancy formation energies at the various sites the oxygen atom was simply
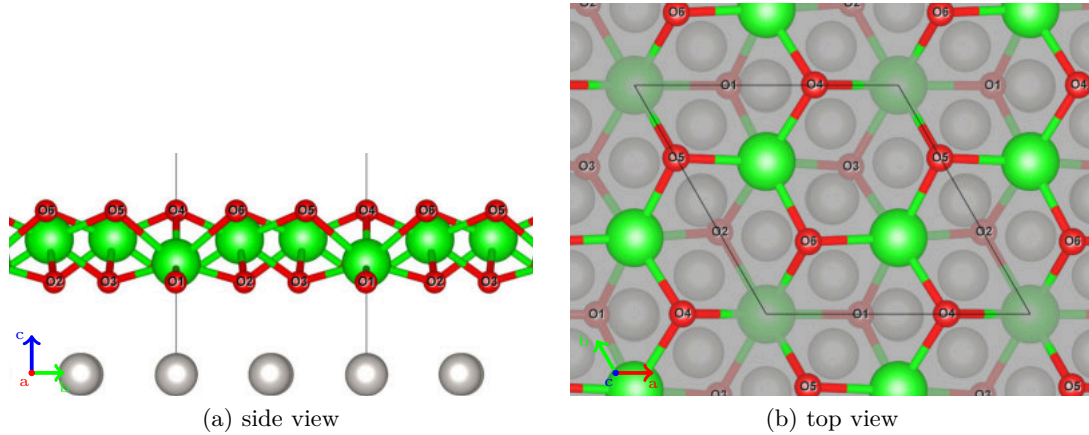
(a) side view   (b) top view

Figure 3.41.: Top and side view of the compressed $\sqrt{3}$ model. The numbers indicate the oxygen site where the vacancy is created.

deleted from the structure filed the resulting cells were relaxed using the same computational settings as for the unmodified structure. The heavy distortion of the oxide film leads to a greater variety of the oxygen vacancy formation energies, as can be seen in table 3.16. Generally, for the standard $\sqrt{19}$ model, the V_O ranges from 2.337 eV to 4.618 eV, depending on the local coordination of the oxygen at the defect site. For the compressed $\sqrt{19}_{comp}$ case, the formation energy is reduced to 2.263 eV to 3.304 eV. In the former case, the energy needed to create the vacancy is lowest for 3-fold coordinated oxygen sites where the Zr–O bonds are stretched (O2, O4, O9): here, at least one Zr–O bond is 2.2 Å long. Also, 2-fold coordinated sites (O23, O18) are more easily vacated. In all cases, vacancy induces further distortions of the oxide film. Depending on the chosen site, the film thickness changed from 245 pm to about 219 pm to 250 pm, while the buckling of the Zr layer is modified by about ±6 pm. The layer distance between oxide and metal substrate is mostly unchanged, but the buckling of the Pt layer is increased from 29 pm to 30 pm to 57 pm. The fact remains that in each unit cell, four 2-fold coordinated oxygen atoms exist at the surface even after creating a vacancy at one of their sites.

In the case of the compressed $\sqrt{19}_{comp}$ model, the introduction of an oxygen vacancy causes even larger distortions compared to the unmodified structure than for the standard $\sqrt{19}$ case. This compounds the discovery of the simulated annealing calculations which have shown great instability of the just slightly distorted $\sqrt{19}_{comp}$ model cell. The film thickness is increased from 209 pm to up to 319 pm, as is the buckling of the Zr layer from 78 pm to up to 170 pm. Additionally, both the oxygen layers at the metal and the vacuum interface experience much larger distortions. In some cases (e.g. O6, O15) the oxide film moves laterally by ⅓ of the primitive oxide unit cell to accommodate for the induced strain. The increased buckling also causes the formation of one to three 2-fold coordinated oxygen atoms at the oxide surface.

(a) compressed $\sqrt{3}$, side view

(b) compressed $\sqrt{3}$, top view

(c) expanded $\sqrt{3}$, side view
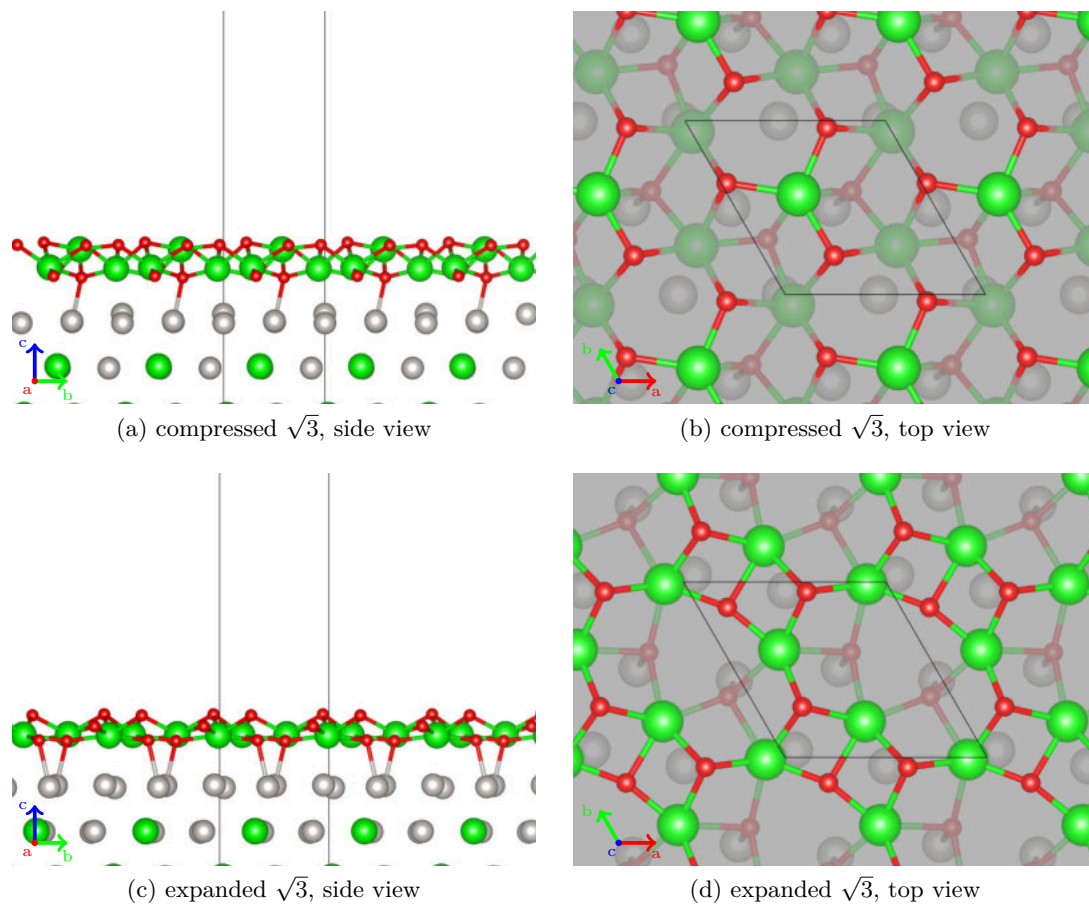

(d) expanded $\sqrt{3}$, top view

Figure 3.42.: Top row: fully relaxed compressed $\sqrt{3}$ structure after removal of oxygen #1. The top view shows that two Zr are now buckled downward and no under-coordinated O at the surface exist. Bottom row: fully relaxed expanded $\sqrt{3}$ structure with V_{O1}. The top view shows the heavy distortion of the oxide film.

To summarise, the low oxygen vacancy formation energy of about $2.3\,\text{eV}$ calculated for both $(\sqrt{19} \times \sqrt{19})R23.4°$ models indicates a certain probability to create a vacancy at the oxide surface during annealing. Calculating the oxygen chemical potential at typical annealing temperatures of $\approx 800\,\text{K}$ using the formulae discussed by Reuter and Scheffler [59] and thermochemical data from Chase [106] yields $-1.565\,\text{eV}$. The vacancy formation energy is much lower compared to the bulk where DFT predicts values of about $7.2\,\text{eV}$ for the $\text{m}(\bar{1}11)$ and $7.0\,\text{eV}$ for the $\text{c}(111)$ surfaces (see appendix B.2).

Table 3.16.: Oxygen vacancy formation energy in eV for both the standard ($\sqrt{19}$) and compressed ($\sqrt{19}_{comp}$) $(\sqrt{19} \times \sqrt{19})R23.4°$ models.

#O	$\sqrt{19}$	$\sqrt{19}_{comp}$
1	2.993	2.263
2	2.337	2.952
3	3.160	2.887
4	2.859	3.016
5	2.905	2.717
6	2.998	2.443
7	2.998	2.799
8	3.813	2.801
9	2.660	2.500
10	3.205	2.554
11	3.283	2.327
12	2.889	2.329
13	3.174	2.840
14	3.639	2.828
15	3.160	2.503
16	4.148	2.908
17	3.235	2.887
18	2.890	3.304
19	4.125	2.487
20	3.285	2.886
21	2.968	3.261
22	4.618	2.672
23	2.795	2.599
24	3.822	2.855

3.3.10. Thermodynamic Stability of off-stoichiometric Films

Since these ultra-thin ZrO_2 films are grown by oxidation of an alloy with zirconium content, the thermodynamic stability of the metal-oxide interface is dependent on the

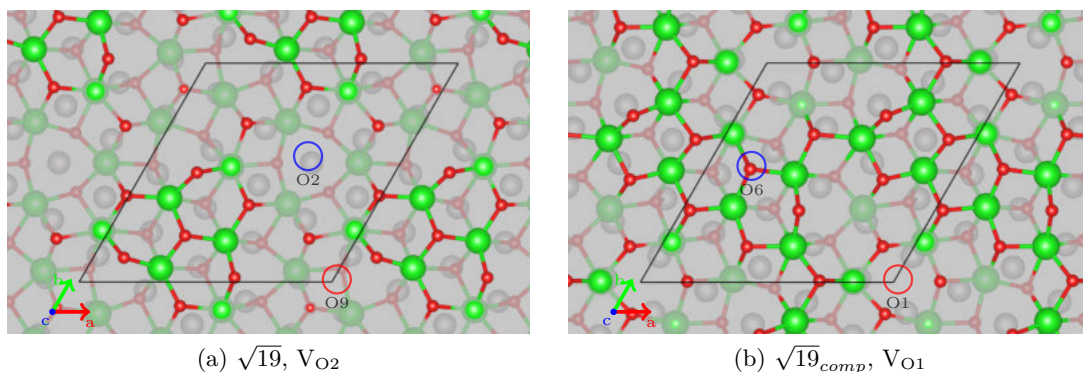(a) $\sqrt{19}$, V_{O2} (b) $\sqrt{19}_{comp}$, V_{O1}

Figure 3.43.: Structures indicating the most stable oxygen vacancy sites of the $\sqrt{19}$ model. A vacancy created at the metal interface is indicated by a red, at the vacuum layer by a blue circle.

chemical potential of the oxygen environment. The idealised $\sqrt{19}$ model cells do not take varying oxygen content into account since the number of atoms is always fixed, which is usually not the case under experimental conditions. There the oxygen chemical potential varies with the oxygen partial pressure $p(O_2)$. To estimate the stability of non-stoichiometric structures with both additional oxygen at the metal-oxide interface and missing oxygen at the surface, the Gibbs free energy was calculated as described in section 2.10.

The following calculations were only done on the standard $\sqrt{19}$ model cell described in section 3.3.1, again with the identical computational settings used for the unmodified structure. In a first step, one additional oxygen atom was placed below Zr_{10} and Zr_{12}, as depicted in fig. 3.44. The former Zr site is one component of the "isle" configuration, and in contrast to the other Zr which comprise the "isle" one of the lower oxygen atoms it forms a bond to does not bind to the Pt substrate, leaving enough room below for an oxygen atom. The Zr_{12} on the other hand is buckled downwards and the bonds to the surrounding lower oxygen are stretched, since the lower oxygen move towards Pt atoms to bind to. It is located in a "valley" site and is only 5-fold coordinated due to the lateral distortion of the oxide film.

After relaxation of the "$O_{Zr_{10}}$" structure the Zr_{10} loses one bond to a lower oxygen atom, but gains one to the additional oxygen below. The formerly bound lower oxygen atom moves closer to a Pt. The Pt–O bond length of the additional oxygen is $1.940\,\text{Å}$, slightly shorter than the $\approx 2.1\,\text{Å}$ of the other Pt–O bonds. The oxide film undergoes some displacements, but the resulting structure is not too different to the stoichiometric oxide. The buckling of the Zr layer is slightly enlarged to $130\,\text{pm}$, as is the buckling of the oxide layers ($97\,\text{pm}$).

The relaxed "$O_{Zr_{12}}$" structure is more distorted than the "$O_{Zr_{10}}$" variant. The additional oxygen at the metal-oxide interface is pushed downwards into a hollow position
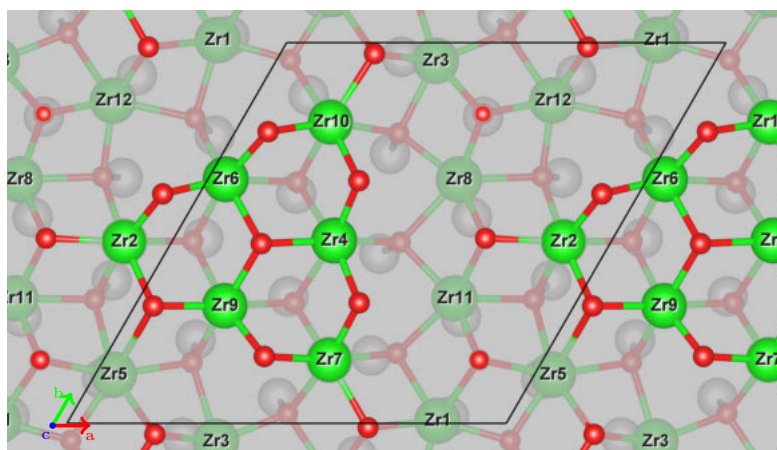
(a) $\sqrt{19}$ model cell

Figure 3.44.: Top view of the $\sqrt{19}$ model. The additional oxygen was introduced below Zr_{10} and Zr_{12}.

with respect to the Pt lattice, forcing the Zr_{12} to buckle upwards and forms three Pt–O bonds. The buckling of the Zr layer is increased to just 116 pm, less than for the "$O_{Zr_{10}}$" configuration. At the top oxygen layer, the under-coordinated oxygen atoms tend to stick up even more, accommodating for the additional stress. The Zr lattice on the other hand does not change, the average Zr–Zr distance is almost identical to the un-modified model. Calculating the difference of the Gibbs free energy, the "$O_{Zr_{10}}$" and "$O_{Zr_{12}}$" structures gain 1.228 eV and 1.481 eV, respectively.

In a second iteration, two additional oxygen atoms were added at the interface at the two sites selected before. Per oxygen atom, the $\Delta\mu_O$ of -1.240 eV is slightly less than for the two configurations described before. The two additional oxygen atoms are both pushed towards the Pt substrate, forming three Pt–O bonds. Due to the displacement of the Zr above the oxide film again undergoes distortions. Since the Zr_{12} buckles upwards the oxide film "isle" structure is now connected to the one in the next unit cell. In this area the heavy lateral expansion which forms the valley is revoked and the Zr–O distances more resemble the isle sites.

Figure 3.45 shows a phase diagram where the calculated Gibbs free energy are plotted for the structures described above. In this diagram, the area of stability is indicated by a hull curve below the individual straight lines. The thick black line indicates the stoichiometric case, while the lines at increasing steepness indicate variants where one ("+1 O at Zr_{10}", "+1 O at Zr_{12}"), two ("+2 O"), and three ("+3 O") additional oxygen atoms are present at the metal-oxide interface. Finally, the two dashed lines represent structures with an oxygen vacancy. The oxygen chemical potential is referenced to the partial oxygen pressure at temperatures of 800 K and 1070 K, representing typical annealing temperatures used in the experiment by Antlanger, Mayr-Schmölzer, et al. [77].

The red dashed line indicating the oxygen vacancy with a formation energy of $V_O = 2.337\,\text{eV}$ indicates a stability of this configuration at very lowly pressurised environments, below $10^{-8}\,\text{mbar}$ at an annealing temperature of $1070\,\text{K}$. The comparison with the second dashed line which represents an oxygen vacancy at another site with $V_O = 2.660\,\text{eV}$ shows that the former site will first be vacated by the oxygen atom. The DFT calculations predict the first intersection of a solid line indicating additional oxygen at the interface at an oxygen chemical potential of $\Delta\mu_O \approx -1.5\,\text{eV}$. The model cell with two additional oxygen at the interface is stable at an oxygen chemical potential larger than $\approx -0.75\,\text{eV}$. Since the typical pressure during annealing is about $10^{-7}\,\text{mbar}$ [77], the calculations indicate that annealing temperatures above $800\,\text{K}$ are sufficiently high to remove all additional oxygen from the metal-oxide interface.

Table 3.17.: Calculated oxygen chemical potential of additional oxygen at the metal-oxide interface of the $\sqrt{19}$ model cell.

Site	$\Delta\mu_O$ per O [eV]
Zr_{10}	1.228
Zr_{12}	1.481
Zr_{10}, Zr_{12}	2.237
Zr_{10}, Zr_{12}, Zr_1	1.867

3.4. Oxide-Metal Interfaces: Core Level Shifts

X-ray Photoelectron Spectroscopy (XPS) measurements are an excellent surface sensitive tool to determine the chemical and electronic state of a material. To supplement experimental data, the core level binding energies of the Zr $3d$ and O $1s$ states were calculated in both the initial and the final state approximation for the ground state structures discussed in the previous chapters. The initial state calculations only involve a recalculation of the Kohn-Sham eigenenergies, while in the latter case a core electron is excited and transferred into the valence band. In this case additional errors can be introduced due to the interaction of excited atoms in neighbouring supercells. To minimise this effect the unit cells were doubled in x and y direction for the smaller $\sqrt{3}$ slab unit cells and in all directions for the bulk cells. The calculations were performed with the van-der-Waals corrected optB86b functional, which greatly improves electronic convergence for these systems compared to the optB88 functional and yields almost identical physical properties. These results were then referenced to metallic hcp bulk Zr and cubic ZrO_2 for the Zr $3d$ and O $1s$ states, respectively. It should be noted that no absolute values for the core level binding energies can be calculated, but relative energy shifts with respect to a reference structure are usually well reproduced, especially in the case of metals.
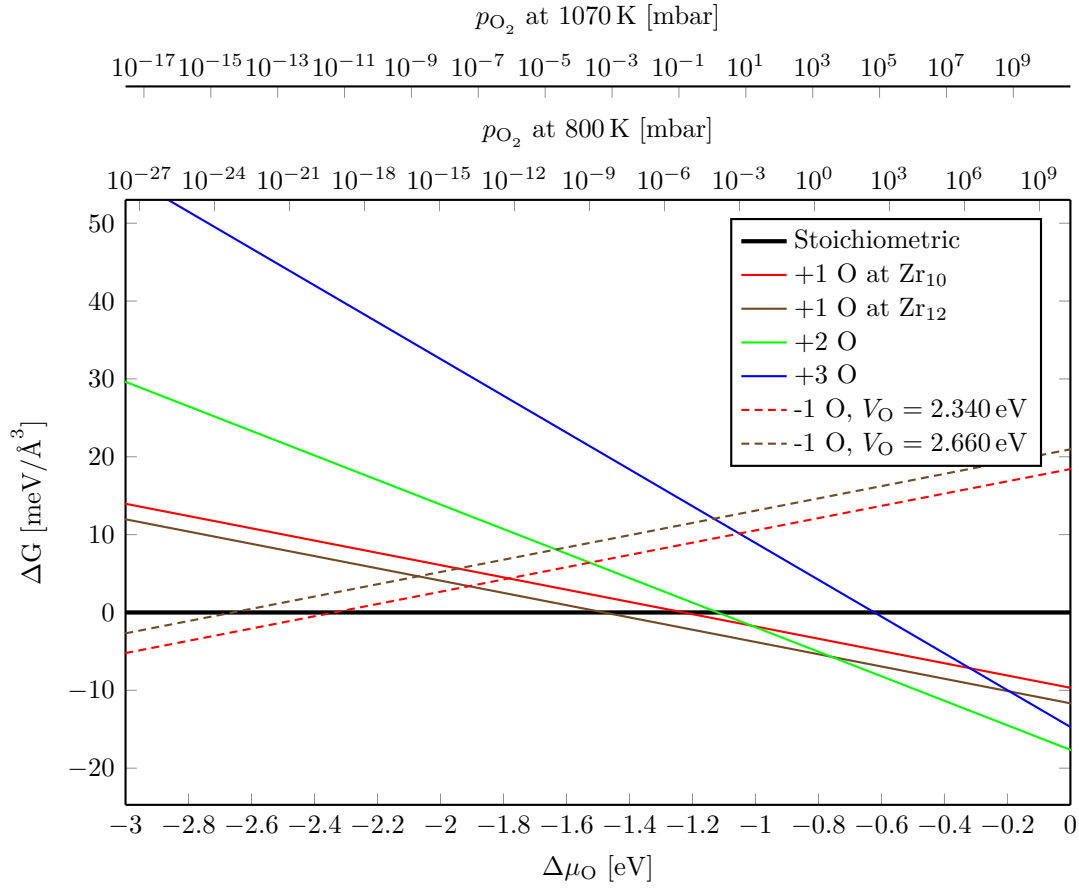
Figure 3.45.: Phase diagram of additional oxygen at the oxide-metal interface (solid lines) and oxygen vacancies at different sites (dashed lines). The calculations predict stability of the stoichiometric $\sqrt{19}$ model structure at an oxygen chemical potential between $-2.25\,\text{eV}$ and $-1.5\,\text{eV}$. This corresponds to oxygen partial pressure ranges of $10^{-15}\,\text{mbar}$ to $10^{-5}\,\text{mbar}$ and $10^{-7}\,\text{mbar}$ to $1\,\text{mbar}$ at temperatures of $800\,\text{K}$ and $1070\,\text{K}$, respectively.

(a) clean alloy and ZrO$_2$ film

(b) ZrO$_2$ film after annealing
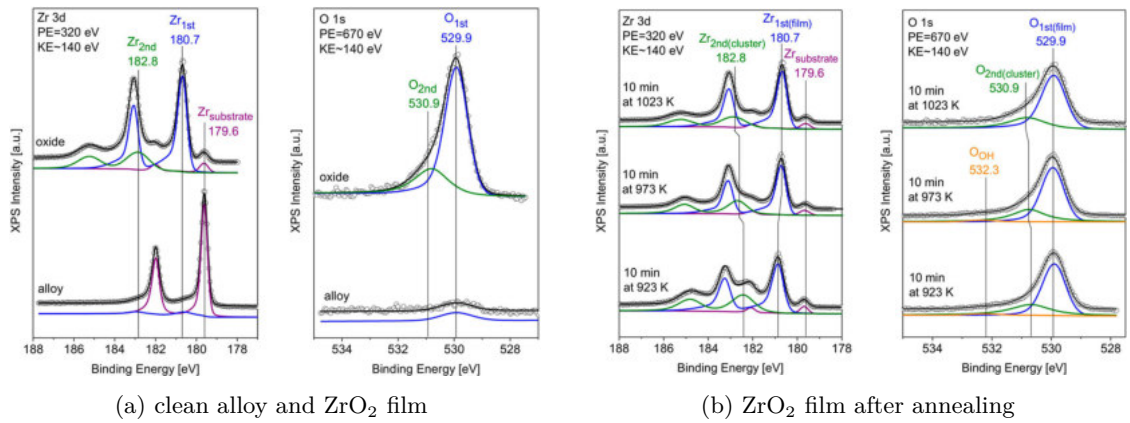
Figure 3.46.: (a) Zr 3d and O 1s XP spectra of the clean Pt$_3$Zr alloy and ultra-thin ZrO$_2$ film annealed at 1023 K. (b) Zr 3d and O 1s XP spectra of the oxide film formed at 673 K, postannealed to 923 K, 973 K, and 1023 K. The Zr 3d peaks show a $d_{3/2}$ and a $d_{5/2}$ peak due to spin-orbit splitting. Zr$_{1st}$ indicates the ultra-thin ZrO$_2$ oxide, while the Zr$_{2nd}$ peak is attributed to ZrO$_2$ clusters. All spectra were recorded at 300 K with a kinetic energy of $\approx$140 eV at beam line I511 at the MAX II synchrotron in Lund. Experimental data courtesy of Li, Choi, Mayr-Schmölzer, et al. [3].

3.4.1. Bulk Systems

The reference values to which the core binding energies can be compared to were calculated for metallic hcp bulk Zr and bulk ZrO_2. In the latter case, both the monoclinic and cubic phase were studied to enable the identification of different ZrO_2 phases. The Zr $3d$ states were also calculated for bulk Pd_3Zr and Pt_3Zr.

Pd_3Zr and Pt_3Zr Bulk

For the Pt_3Zr and Pd_3Zr bulk the calculation was performed at the optB86b optimised lattice constant. The unit cell was doubled in all directions to minimise the influence of the excited site due to the periodic boundary conditions, yielding a unit cell comprised of 128 atoms. Due to the size of the unit cell a $3 \times 3 \times 3$ Γ-centred $\vec{k}$-point grid (10 irreducible $\vec{k}$-points) was sufficient to ensure electronic convergence. The energy cutoff was set to $400\,eV$, like for all other calculations mentioned in this chapter. For both Pd_3Zr and Pt_3Zr the Zr $3d$ core state in the A-type layer exhibits the largest binding energy, the Zr $3d$ states in the B/C-type layer shift slightly ($\approx -0.2\,eV$ with respect to the A-type layer, see table 3.18) towards lower binding energies. The averaged shift of $0.92\,eV$ in the initial state approximation compares very well with the shift of $0.9\,eV$ reported between the $Zr_{substrate}$ peak in fig. 3.46a and the reported value of $178.7\,eV$ for the Zr $3d_{5/2}$ line of bulk Zr [107]. The calculations in the final state approximation gives a shift of $1.35\,eV$.

Table 3.18.: Core level shifts in eV of the Zr $3d$ electrons in bulk Pd_3Zr and Pt_3Zr, referenced to the metallic hcp Zr bulk. Columns labeled IS and FS denote initial state and final state core level shifts, respectively. A positive sign indicates a shift to higher binding energy.

Structure	Pd_3Zr		Pt_3Zr	
[eV]	IS	FS	IS	FS
A-type	1.22	1.44	1.01	1.43
B/C-type	1.02	1.27	0.82	1.26

Monoclinic and Cubic ZrO_2 Bulk

The Zr $3d$ and O $1s$ core level energies were investigated for both monoclinic and cubic ZrO_2. To calculate these values, both bulk unit cells cell were expanded in all directions, resulting in a 96 atom supercell. A $3 \times 3 \times 3$ Γ-centred $\vec{k}$-point grid (14 irreducible $\vec{k}$-points) ensured electronic convergence. Again the optB86b functional and the respective optimised lattice parameters were used here. Comparing the two bulk phases, the initial state core level calculations show a shift of $0.64\,eV$ to higher binding Zr $3d$ binding energies for the cubic phase, while that shift is negligible for the final state calculations.

For the oxygen states, the calculations show a split of about 0.4 eV of the O $1s$ states in monoclinic ZrO_2 due to the monoclinic symmetry where half of the oxygen atoms are 3-fold coordinated and the other half is 4-fold coordinated. The O $1s$ states of the cubic bulk lie between the two different levels shown for monoclinic ZrO_2. This has to do with the Zr–O bond lengths in these compounds: in monoclinic ZrO_2 two of the four Zr–O bonds are quite short (2.18 Å), but these short bonds do not exist in cubic ZrO_2. As can be seen in table 3.19, the comparison with the calculated Zr $3d$ states in metallic systems like bulk Zr and bulk Pt_3Zr highlights a big issue with the simulations: De González and García [107] report the Zr $3d_{5/2}$ line of bulk Zr at 178.7 eV and of bulk ZrO_2 at 182.9 eV, reflecting a chemical shift of 4.2 eV to higher binding energies after oxidation of Zr, which is not reproduced in the calculations. The different screening of the Zr $3d$ electron in metals and insulators leads to a severe underestimation of the calculated chemical shift, predicting way too low binding energies for both insulating ZrO_2 phases. The initial state calculations exacerbate this problem, yielding lower binding energies for the Zr $3d$ states in the oxide than in the metal. This will also play a role in the prediction of thicker ZrO_2 films and clusters, discussed in section 3.4.4.

Table 3.19.: Core level shifts in eV of the Zr $3d$ and O $1s$ states. The energy differences are referenced to the bulk Zr hcp value for the Zr $3d$ and the cubic ZrO_2 value for the O $1s$ states. Columns labeled IS and FS denote initial state and final state core level shifts, respectively. A positive sign indicates a shift to higher binding energy.

[eV]	IS	FS
Zr_{c-ZrO_2}	−0.45	2.81
Zr_{m-ZrO_2}	−1.09	2.77
$Zr_{Pt_3Zr_{(A)}}$	1.01	1.43
$Zr_{Pt_3Zr_{(B)}}$	0.82	1.26
$Zr_{Pd_3Zr_{(A)}}$	1.22	1.44
$Zr_{Pd_3Zr_{(B)}}$	1.02	1.27
O_{3fold}	−0.39	−0.19
O_{4fold}	0.04	0.23

3.4.2. Pt_3Zr Slabs

For the Pt-terminated pristine slab the Zr $3d$ core levels were calculated and compared to the Pt_3Zr bulk values. To converge the unit cell with respect to the number of layers, a 9-layer (i.e. 3-trilayer) slab, terminated with a pure Pt layer was used. In this relaxed structure the three middle layers are basically bulk-like, and this is also reflected in the Zr $3d$ core levels, which shift by 0.18 eV (0.16 eV) in the initial (final) state approximation with respect to the central (A-type) layer. The next A-type layers on the other hand

shift by $0.13\,\mathrm{eV}$ ($0.14\,\mathrm{eV}$) to lower binding energies with respect to the central layer, and the following B/C-type layers below the surface Pt layer shift by $0.08\,\mathrm{eV}$ for both methods to higher binding energies.

The stoichiometric 9-layered $\mathrm{Pt_3Zr}$ slab shows a similar pattern: the core level shift between middle A-type layer and the surrounding B/C-type layers is $0.12\,\mathrm{eV}$ for both initial and final state calculations, and the next A-type layers give the same value as the central A-type layer. Close to the $\mathrm{Pt_3Zr}$ terminated surface, the core level binding energies of the surface A-type and subsurface B/C-type layers are switched, probably due to the surface relaxations. While the core level binding energies of the first subsurface layer (B/C-type) only show a minuscule shift with respect to the central layer the surface, A-type, layer shifts by $0.24\,\mathrm{eV}$ in the initial state approximation. In the final state approximation the surface Zr $3d$ state has the same energy as the central layer, showing that the initial state calculations fail to capture surface effects.

(a) Pt-terminated $\mathrm{Pt_3Zr}$ (b) stoichiometric $\mathrm{Pt_3Zr}$
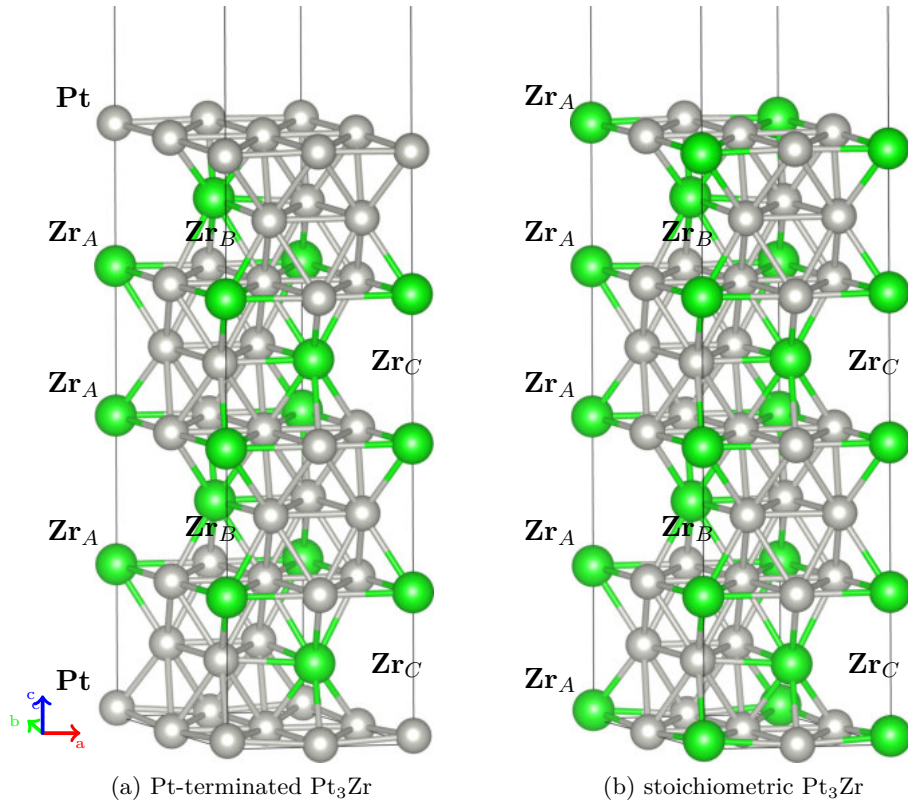
Figure 3.47.: Pt-terminated and stoichiometric $\mathrm{Pt_3Zr}$ slabs used to calculated Zr $3d$ core levels.

3.4.3. ZrO$_2$/Pd$_3$Zr Interface

The changed chemical environment of the zirconium atoms can easily be determined by the differences in core level binding energies. For the O1Zr' model cell where the oxide film is compressed, the slab Zr $3d$ binding energies only differ by 0.1 eV to 0.3 eV at the slab surface, indicating a surface core level shift. The Zr $3d$ states of the oxide film shift by 1.95 eV to 2.02 eV (2.49 eV to 2.60 eV) to higher binding energies with respect to the hcp metal Zr, calculated in the initial (final) state approximation. In the case of the expanded model (oxide lattice constant at 3.5 Å), the Zr $3d$ oxide film core level shifts are slightly smaller (larger) at 1.62 eV to 1.87 eV (2.19 eV to 2.50 eV) for the initial (final) state calculations. Interestingly, the core level shift of the surface Zr that forms a bond to one O1 of the oxide film is just slightly increased compared to the surface Zr $3d$ state at the pristine surface. The O $1s$ states, referenced to the cubic ZrO$_2$ bulk, show a small variance of their binding energies of $\approx$0.2 eV ($\approx$0.25 eV) in the initial (final) state for both the compressed and the expanded oxide case. As mentioned in the previous section, the initial state calculations yield too low binding energies for the c-ZrO$_2$ bulk reference and therefore a huge shift artificial shift to higher binding energies for the ultra-thin ZrO$_2$ film. Only the final state approximation yields the correct reference with a shift of -0.42 eV and -0.89 eV for the O $1s$ states with respect to the cubic ZrO$_2$ bulk value for the compressed and expanded model, respectively.

3.4.4. ZrO$_2$/Pt/Pt$_3$Zr Interface

For the ZrO$_2$/Pt/Pt$_3$Zr interface the Zr $3d$ and O $1s$ core level energies were calculated for both the compressed and expanded model cells introduced in section 3.2.3. Only the so-called ZrPt configuration, where a Zr atom of the oxide is placed directly above a surface Pt atom, was selected. Additionally, to determine whether clusters of ZrO$_2$ exist on the Pt-terminated surface, core level shifts calculated for the multilayer structures mentioned in section 3.2.3 were used, again in the ZrPt configuration. For the final state calculations, to determine whether the size of the unit cell was already large enough to maximise shielding from the excited site, a series of test calculations were done with the standard compressed ZrPt model unit cell, and two modified cells which were doubled and tripled in x and y. Comparison of the Zr $3d$ binding energies showed an error of about 20 meV, way below the line width of a standard XPS lab source. The calculations were performed on the model cells relaxed with the van-der-Waals functional, and the same functional was used for the core level calculations. As was shown before for the alloy bulk, the choice of functional does not significantly influence the calculated energy differences. To rule out electronic convergence problems a very fine $12 \times 12 \times 1$ Γ-centred $\vec{k}$-point grid (74 irreducible $\vec{k}$-points) was used for all calculations. For the Zr $3d$ core levels the hexagonal bulk zircon value and for the O $1s$ states the cubic ZrO$_2$ bulk values were used as references, respectively.

The calculations are summarised in table 3.21 and show that the Zr $3d$ states of the Pt$_3$Zr slab are shifted by 0.38 eV to 0.49 eV and 0.85 eV to 1.02 eV with respect to the pure hcp metal Zr level in the initial state and final state approximation, respectively

Table 3.20.: Core level shifts in eV of the Zr $3d$ and O $1s$ binding energies for the $ZrO_2/Pd_3Zr \sqrt{3}$ model. Energy differences are referenced to hexagonal bulk Zr for the Zr $3d$ states and to the c-ZrO_2 for the O $1s$ states. Columns labeled IS and FS denote initial state and final state core level shifts, respectively. A positive sign indicates a shift to higher binding energy.

Lattice	compressed		expanded	
[eV]	IS	FS	IS	FS
$Zr_{Oxide,1}$	2.02	2.49	1.87	2.44
$Zr_{Oxide,2}$	1.96	2.54	1.62	2.19
$Zr_{Oxide,3}$	1.95	2.60	1.75	2.50
$Zr_{Substrate,Surface}$	1.02	1.23	1.48	1.59
$Zr_{Substrate,2}$	0.78	1.11	1.06	1.27
$Zr_{Substrate,3}$	0.76	1.04	1.05	1.24
$Zr_{Substrate,4}$	0.78	1.10	1.03	1.28
$Zr_{Substrate,5}$	1.07	1.15	1.35	1.32
$O_{Interface,1}$	3.07	−0.57	2.72	−1.11
$O_{Interface,2}$	2.93	−0.63	3.29	−0.47
$O_{Interface,3}$	3.43	−0.11	2.75	−0.90
$O_{Surface,1}$	2.94	−0.38	2.56	−0.92
$O_{Surface,2}$	2.95	−0.39	2.56	−0.88
$O_{Surface,3}$	2.87	−0.46	2.54	−1.04

($Zr_{substrate,2}$ and $Zr_{substrate,3}$). In the first subsurface layer of the slab, after adsorption of a single ZrO_2 trilayer, this initial (final) state shift is somewhat reduced to $0.55\,eV$ ($0.97\,eV$). Expanding the Pt_3Zr substrate by $5.5\,\%$ to fit the oxide to its experimental lattice constant causes a shift of the Zr $3d$ states of the slab of $0.59\,eV$ to $0.64\,eV$ and $1.01\,eV$ to $1.10\,eV$ for the initial and final state calculations, respectively. The Zr $3d$ states of the compressed single layer ultra-thin film experience a shift to higher binding energies of $1.15\,eV$ to $1.26\,eV$ and $2.26\,eV$ to $2.47\,eV$ in the initial state and final state approximation, respectively, referenced to metal hcp Zr. Depending on whether the Zr atom is buckled towards the substrate or not, the respective shift of the Zr $3d$ state is higher (lower) in the in the initial (final) state approximation. For the stretched model cell with only one oxide trilayer, only the initial state calculations show significant differences to the compressed model as the calculated shift is increased to $1.31\,eV$ to $1.52\,eV$. The final state calculations predict shifts of $2.15\,eV$ to $2.44\,eV$.

Finally, the Zr $3d$ states of the multilayer structure at experimental lattice constant show a similar shift in the initial state calculations as for the compressed model, while it is further increased in the final state calculations for the second and third ZrO_2 trilayer. Noticeably, the interface layer of the oxide film with the Pt_3Zr substrate shows almost identical results to the single layer values. Comparing these results with the bulk ZrO_2 indicates that thicker ZrO_2 films show bulk-like Zr $3d$ core levels starting at three layers. Still, the calculated shift is underestimated in the final state approximation, which might be rooted in a still too low number of ZrO_2 trilayers structure to properly model a ZrO_2 cluster. As mentioned in section 3.4.1, the chemical shift between hexagonal Zr and both phases of bulk ZrO_2 is not described correctly in the initial state approximation.

The calculation of the O $1s$ states in the initial state approximation indicates the same difficulties with this implementation. Like the Zr $3d$ core levels, the O $1s$ states of cubic ZrO_2 bulk are predicted at much lower binding energies than those of the adsorbed ZrO_2 trilayer. Since these initial state results do not conform with the experimental results published by Li, Choi, Mayr-Schmölzer, et al. [3], the oxygen O $1s$ core levels were mainly evaluated in the final state approximation.

With this method, the O $1s$ core states for the expanded film shift by about $0.5\,eV$ to higher binding energies with respect to the compressed film. Compared to the cubic bulk ZrO_2 values, the O $1s$ states of the compressed and expanded film shift by about $1.3\,eV$ and $1.7\,eV$ to higher binding energies, respectively. The lower shift for the compressed film is caused by the shorter Zr–O bonds. For the thick 3-layer film, the O $1s$ states at the metal-oxide interface are similar to the single expanded trilayer, but in the middle of the film the the O $1s$ chemical shift is reduced to about $0.9\,eV$, indicating a change towards bulk-like O $1s$ levels. At the vacuum interface, the O $1s$ shift of $1.27\,eV$ is similar to that of the compressed ZrO_2 film.

Compared to the experimental results by Li, Choi, Mayr-Schmölzer, et al. [3] shown in fig. 3.46, the final state approximation is well able to capture the main features of the Zr $3d$ XPS measurements, even though the absolute values of the calculated core level shifts of the ZrO_2 bulk are underestimated. In the currently implemented final state approach the excited electron is not removed from the system, as the charge balance has

to be maintained, but it is simply transferred into the conduction band at or above the Fermi level. This results in a localisation of this excited electron at the atom with the core hole in bulk ZrO_2 and in the middle layers of the thick ZrO_2 film, while in Pt_3Zr bulk it is delocalised in the metal substrate. The strong localisation leads to additional screening and therefore a smaller core level shift. The thicker 3-layer ZrO_2 film is also not able to properly capture the cluster peak discussed ("Zr_{2nd}" in section 3.4) since the calculated core levels for the Zr $3d$ states only show a very small increase of the shift with respect to metallic hcp Zr. For oxygen this does not pose a problem since the excited electron is always localised around the core hole, leading to a static offset of the core level energies. Therefore, the final state calculations of the O $1s$ states are better able to capture the measured shift of $1.2\,eV$ towards higher binding energies for the ZrO_2 clusters which appear after further annealing of the ZrO_2 film, even though the absolute value of the shift is still underestimated.

(a) $ZrO_2/Pt/Pt_3Zr$, 1l
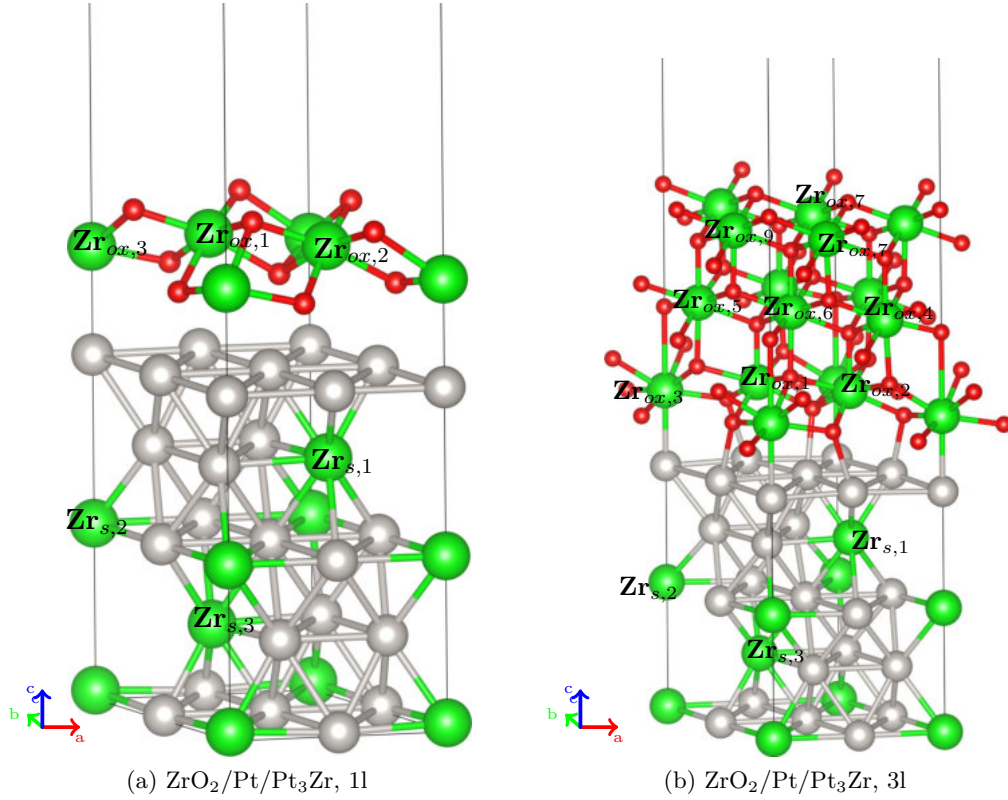
(b) $ZrO_2/Pt/Pt_3Zr$, 3l

Figure 3.48.: Model structures used for the calculation of the Zr $3d$ and O $1s$ core level binding energies of the oxide film in the $ZrO_2/Pt/Pt_3Zr$ 1-layer and 3-layer models, indicating the labels used in table 3.21.

Table 3.21.: Core level shifts in eV of the Zr $3d$ and O $1s$ binding energies for the $\sqrt{3}$ ZrO$_2$/Pt/Pt$_3$Zr models, referenced to hexagonal bulk Zr for Zr $3d$ and to the cubic ZrO$_2$ O $1s$ level, respectively. For the Zr $3d$ shifts of the middle and the top ZrO$_2$ trilayer only averaged values are given due to their small spread. Columns labeled IS and FS denote initial state and final state core level shifts, respectively. A positive sign indicates a shift to higher binding energy.

Model	compressed, 1l		expanded, 1l		expanded, 3l	
[eV]	IS	FS	IS	FS	IS	FS
Zr$_{\text{Surface},\varnothing}$					1.20	2.78
Zr$_{\text{Middle},\varnothing}$					1.20	2.64
Zr$_{\text{Interface,1}}$	1.15	2.47	1.50	2.44	1.20	2.40
Zr$_{\text{Interface,2}}$	1.17	2.46	1.52	2.37	1.24	2.43
Zr$_{\text{Interface,3}}$	1.26	2.26	1.31	2.15	1.25	2.14
Zr$_{\text{Pt}_3\text{Zrsubstrate,1}}$	0.55	1.02	0.59	1.01	0.55	0.99
Zr$_{\text{Pt}_3\text{Zrsubstrate,2}}$	0.38	0.85	0.64	1.02	0.64	1.03
Zr$_{\text{Pt}_3\text{Zrsubstrate,3}}$	0.49	0.97	0.64	1.10	0.63	1.10
Zr$_{\text{Substrate,Experiment}}$			1.0			
Zr$_{\text{ZrO}_2\ \text{Film,Experiment}}$			2.1			
Zr$_{\text{ZrO}_2\ \text{Cluster,Experiment}}$			4.2			
O$_{\text{Surface}}$	2.01	-1.26	1.68	-1.87	1.44	-1.27
O$_{\text{Layer3,bottom}}$					1.68	-1.23
O$_{\text{Layer2,top}}$					1.89	-0.89
O$_{\text{Layer2,bottom}}$					2.20	-0.93
O$_{\text{Layer1,top}}$					1.78	-1.51
O$_{\text{Interface}}$	2.26	-1.36	2.30	-1.63	2.21	-1.59
O$_{\text{Experiment}}$			-1.2			

3.4.5. Large $\sqrt{19}$ ZrO$_2$/Pt Models

Both Zr $3d$ and O $1s$ core levels were also calculated for the $\sqrt{19}$ ground state structure described in section 3.3.7. Due to the large distortions of the oxide film both core levels show a large spread, $0.891\,\text{eV}$ $(0.573\,\text{eV})$ for the Zr $3d$ states and $1.465\,\text{eV}$ $(1.028\,\text{eV})$ for the O $1s$ states, calculated in the initial (final) state approximation. Taking the average Zr $3d$ binding energies, the oxide film shows a shift of $1.94\,\text{eV}$ to higher binding energies, referenced to hexagonal bulk zircon, which is in very good agreement with the measured value of $2.1\,\text{eV}$ presented by Li, Choi, Mayr-Schmölzer, et al. [3]. The large spread of the O $1s$ states is especially caused by the under-coordinated oxygen atoms in the surface layer of the oxygen film, which show the smallest binding energies. All other O $1s$ states exhibit a shift to larger binding energies of $0.31\,\text{eV}$ to $1.47\,\text{eV}$ and $0.25\,\text{eV}$ to $1.03\,\text{eV}$ for the initial and final state calculations, respectively, referenced to the smallest binding energy found in the oxide film. The other surface atoms generally show a smaller spread in the initial (final) states of $0.98\,\text{eV}$ $(0.77\,\text{eV})$. In the initial state approximation, the oxygen atoms at the interface generally exhibit a larger O $1s$ binding energy than those at the oxide film surface. As is shown in fig. 3.49, the Zr atoms that are buckled towards the platinum substrate show the smallest Zr $3d$ binding energies, while the others exhibit a shift to larger binding energies. In the same plot, the O $1s$ states are given in the final state approximation referenced to the cubic ZrO$_2$ bulk, like in the sections before. Compared to the smaller $(\sqrt{3} \times \sqrt{3})R30°$ model discussed in section 3.4.4 the final state calculations predict smaller shifts for the Zr $3d$ states with respect to metallic hcp Zr bulk but better agreement with the experiment. The O $1s$ shifts with respect to cubic ZrO$_2$ on the other hand are larger.

For the compressed $\sqrt{19}_{comp}$ structure, the calculated spread in the core level binding energies is smaller, $0.77\,\text{eV}$ $(0.57\,\text{eV})$ for the Zr $3d$ and $1.45\,\text{eV}$ $(0.88\,\text{eV})$ for the O $1s$ states, respectively. Again, referenced to metallic hcp Zr, the average core level shift of the Zr $3d$ states of the oxide film is $1.91\,\text{eV}$. In the O $1s$ states the under-coordinated surface oxygen atoms again exhibit the smallest binding energies, compared to the aforementioned model the shift with respect to the lowest binding energy is slightly smaller at $1.25\,\text{eV}$ to $1.45\,\text{eV}$ and $0.66\,\text{eV}$ to $0.88\,\text{eV}$ for the initial and final state calculations, respectively.

3.5. Summary

The DFT studies have shown that the interesting properties of the zirconia-metal interface can be explained by the use of different model cells. Since the experimentally found $(\sqrt{19} \times \sqrt{19})R23.4°$ (ZrO$_2$/Pt/Pt$_3$Zr) and $(\sqrt{217} \times \sqrt{217})R10.16°$ (ZrO$_2$/Pd$_3$Zr) unit cells are too large to be computationally feasible, model cells of different sizes were devised: a $(\sqrt{3} \times \sqrt{3})R30°$ model cell, covering both the real substrate and oxide film lattice constants, and for ZrO$_2$ adsorbed on Pt-terminated Pt$_3$Zr a platinum supported $(\sqrt{19} \times \sqrt{19})R23.4°$ model cell. The physical properties of the adsorbed oxide film are mostly well described and comparable to the experiment. Nevertheless, each of these
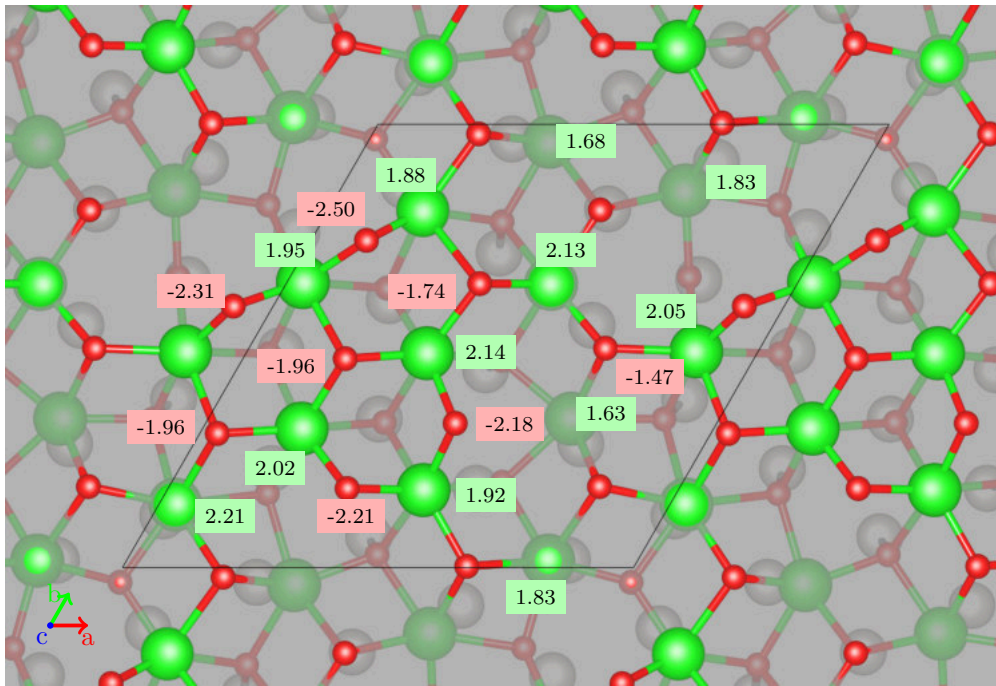
(a) $\sqrt{19}$
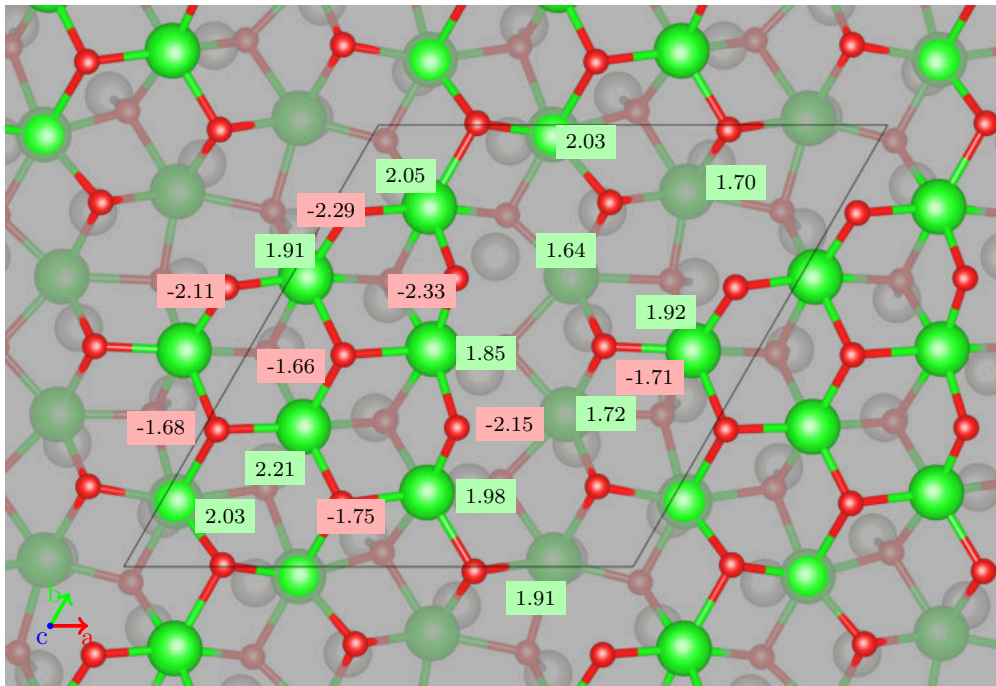
(b) $\sqrt{19}_{comp}$

Figure 3.49.: Zr $3d$ and O $1s$ core level shifts in eV of the $\sqrt{19}$ and $\sqrt{19}_{comp}$ ZrO$_2$/Pt models. Again, Zr $3d$ shifts are referenced to the hcp Zr bulk, while O $1s$ shifts are referenced to the cubic ZrO$_2$ bulk. Positive sign therefore indicates a shift to higher binding energies, and vice versa for negative sign.

models suffer from certain inconsistencies: while the small $(\sqrt{3} \times \sqrt{3})R30°$ model cells yield comparable buckling with respect to the experiment, the description of the interface suffers from the large lateral strain of either the oxide film or the Pt_3Zr/Pd_3Zr substrate due to the large lattice mismatch. In the more realistic $(\sqrt{19} \times \sqrt{19})R23.4°$ model cell, the distortions of the oxide film are much larger than what is measured, and the "isle" and "valley" structure is not seen in the experiments. Slight lateral compression of the unit cell did lead to a much less buckled structure, but at a too small oxide lattice constant. The lattice parameters and calculated surface energies of all studied structures are summarised in tables 3.11 and 3.12.

Building more complex large model cells which include the correct Pt-terminated Pt_3Zr do not necessarily cure these problems. The experimental $(\sqrt{19} \times \sqrt{19})R23.4°$ unit cell with the correct substrate shows even larger distortions compared to the pure Pt substrate model. Also, using a $(\sqrt{13} \times \sqrt{13})R13.8°$ model cell which results in a slightly smaller oxide lattice constant without causing lateral stress of the Pt_3Zr substrate, only slightly reduces the buckling. This confirms that the nature of the substrate, be it pure Pt or Pt-terminated Pt_3Zr, plays a very minor role. Consequently, there are two connected parameters that play the decisive role in how strong the distortions of the oxide film are: the choice of the functional and the lateral stress of the oxide film. Varying the lattice constant of the model cells for both the pure Pt and the Pt/Pt_3Zr substrate on the one hand shows that for all model cells, the inclusion of van-der-Waals corrections changes the stability of the ZrO_2-metal interface. As soon as the oxide film is compressed to a lattice constant lower than $3.49 \, \text{Å}$ the adsorption energy is greatly lowered when calculated with the PBE functional and the ZrO_2 film moves to a much larger distance, while with the van-der-Waals corrected optB86b functional the interface is stable up to much smaller oxide lattice constants of $3.39 \, \text{Å}$. Consequently, the amount of distortion of the adsorbed oxide film is determined by the subtle balance between the stability of the oxide film itself and the strength of the interaction with the metal substrate.

One possible explanation for this discrepancy might be an overestimation of the Pt–O bonds in DFT. Calorimetry measurements have estimated the standard enthalpy of formation of α-PtO_2 to be $-80 \, \text{kJ/mol}$ or $-0.83 \, \text{eV}$ [108], while DFT yields about $-147 \, \text{kJ/mol}$ or $-1.5 \, \text{eV}$ for both the PBE and the optB86b functional. For monoclinic zirconia on the other hand, the PBE heat of formation of $-10.4 \, \text{eV}$ compares well with the standard enthalpy of formation of $1042.6 \, \text{kJ/mol}$ or $-10.81 \, \text{eV}$ [109]. This suggests an overestimation of the stability of PtO_2 and therefore overestimation of the Pt–O bonds. For the $\sqrt{19}$ ground state structure, the lower oxygen atoms are displaced laterally to maximise the number of possible Pt–O bonds, inducing additional lateral strain into the oxide film. The second contribution is the interaction of the Zr ions with the Pt substrate which cause the downwards buckling of those Zr located above a surface Pt atom. Additionally, the stability of ZrO_2 bulk phases depends greatly on the functional: by distorting tetragonal multilayer ZrO_2 slabs, a so-called meta-monoclinic phase was found (Planer [82]), which is even more stable than the tetragonal phase on the PBE level.

Despite these shortcomings, the small $(\sqrt{3} \times \sqrt{3})R30°$ model of the ZrO_2/Pd_3Zr interface was used successfully to identify the character of features seen in STM measurements, where the bright spots could be assigned to zirconium atoms. These findings were, together with experimental results, published by Choi, Mayr-Schmölzer, et al. [1]. On the Pt_3Zr substrate, it could be shown that thicker layers of ZrO_2 are also stable, preferably on the expanded $(\sqrt{3} \times \sqrt{3})R30°$ model. By calculating the core level shifts of these thicker films the formation of ZrO_2 clusters was confirmed. These results were published by Li, Choi, Mayr-Schmölzer, et al. [3] in another combined experimental and theoretical paper.

In the following chapter, the viability of these models to study adsorption of metal adatoms and water molecules will be discussed.

4. Adsorption Studies on ZrO$_2$ Surfaces

4.1. Metal Adatom Adsorption on Zirconia Surfaces

In various catalytic processes, small particles of transition metal atoms play a decisive role in increasing their efficiency. Zirconia has shown itself to be catalytically active, but is also often used as a support material for these metal clusters. For example, gold clusters can be used as catalyst for CO oxidation on TiO$_2$ or ZrO$_2$ [110, 111] or the water gas shift reaction [112]. Platinum clusters supported on ZrO$_2$ can be used to reform CO$_2$/CH$_4$ to syngas [113]. In many cases increasing the accessibility of the metal atoms forming the cluster further boosts efficiency, therefore smaller clusters are preferred.

In this section a comprehensive DFT study of the adsorption of transition metal adatoms, namely Au, Ag, Pd, and Ni on both the monoclinic and cubic ZrO$_2$ surfaces and on ultra-thin ZrO$_2$ films is presented. This selection of adsorbates covers both reactive and noble elements. The theoretical research was done in parallel to experimental studies, published by Choi, Mayr-Schmölzer, et al. [4]. There, STM studies were performed to determine the cluster size of Au, Ag, Pd, and Ni particles adsorbed on ultra-thin ZrO$_2$ films grown on a metal substrate. These measurements showed decreasing cluster size in the sequence Ni < Pd ≈ Au < Ag, hinting towards increasing metal-oxide interaction Ni > Pd ≈ Au > Ag. Ag clusters are so weakly bound that they can be moved by the STM tip.

To perform the DFT studies, single atoms were placed at selected high symmetry sites on the most favourable surfaces of both monoclinic and cubic ZrO$_2$ and on the $\sqrt{19}$ model cell introduced in section 3.3.1. In the cubic case, the high symmetry of the surface allows for a thorough study of different adsorption configurations. The monoclinic surface is more distorted, giving rise to a much larger number of possible sites, but only those have been included in the study which mimic the most favoured sites on the cubic surface. For the adsorption studies on the ultra-thin film, a scan of the adsorption energy landscape was performed by placing the metal adatoms on a regular grid and interpolating between those sites. All calculations were performed using the optB86b functional to properly account for van-der-Waals polarisation effects.

4.1.1. ZrO$_2$ Bulk Surfaces

The bulk ground state of zirconia is a monoclinic structure (C_{2h}^5, $P2_1/c$, space-group 14) with four formula units in the unit cell [114]. This monoclinic unit cell can be considered as a heavily distorted cubic CaF$_2$ structure where each Zr is 7-fold coordinated. Four of the oxygen are 4-fold, the other four are 3-fold coordinated. To properly treat the

adsorption configurations on its most stable surface, as a first step the volume of the cell had to be optimised for the optB86b functional. These calculations were performed using a $6 \times 6 \times 6$ Γ-centred $\vec{k}$-point grid and the energy cutoff was increased to $540\,\mathrm{eV}$. The equilibrium lattice constants shown in table 4.1 agree well with the experiment.

Furthermore, the cubic bulk ZrO_2 phase was also studied to bridge the gap between pure ZrO_2 surfaces and the ZrO_2 monolayer films. The cubic ZrO_2 crystal was optimised with the optB86b functional and a $8 \times 8 \times 8$ Γ-centred $\vec{k}$-point grid at the same energy cutoff as for the monoclinic phase, yielding again lattice parameters in good agreement with the experiment (table 4.1).

According to earlier work by Christensen and Carter [115] and confirmed in appendix B the most stable surface determined by the PBE functional of monoclinic ZrO_2 is the $(\bar{1}11)$ and of cubic ZrO_2 the (111) orientation. The m$(\bar{1}11)$ can be viewed as a distorted cubic $ZrO_2(111)$ surface, where the zirconium atoms are both buckled and laterally displaced, see fig. 4.1. Additionally, one 2-fold coordinated oxygen atom per surface unit cell is present, while all other surface oxygen are 3-fold coordinated. In analogy to c(111), the m-$ZrO_2(\bar{1}11)$ structure can be though of a a stack of distorted ZrO_2 trilayers, just like c-$ZrO_2(111)$. Due to the O–Zr–O like arrangement these trilayers are again charge neutral. The m$(\bar{1}11)$ surface unit cell gives rise to a multitude of different adsorption sites as the four zirconium atoms show different degrees of accessibility. Also, the under-coordinated (2-fold) oxygen atom might play a role in the reactivity of these sites. The c(111) unit cell on the other hand is only terminated by 3-fold coordinated oxygen atoms. Here, due to the high symmetry of the surface, there are only four possible adsorption sites: a top and a hollow position with respect to the top oxygen atoms, a Zr–O bridge and an O–O bridge position, as indicated in fig. 4.1c.

For all further calculations, the thickness of the m$(\bar{1}11)$ slab was kept at four ZrO_2 trilayers. During the relaxation the bottom two layers were frozen. The $\vec{k}$-point grid was reduced to a $5 \times 5 \times 1$ Γ-centred grid consisting of 13 irreducible $\vec{k}$-points. For the cubic c(111) surface mainly a six trilayer thick slab and a $(2\sqrt{3} \times 2\sqrt{3})$ surface unit cell was used for the calculations. To ensure electronic convergence, a Γ-centred $10 \times 10 \times 1$ $\vec{k}$-point grid, yielding 52 irreducible $\vec{k}$-points was used.

4.1.2. Metal Adatom Adsorption on Bulk ZrO_2

To find the most favoured adsorption site on cubic ZrO_2, the four transition metal adatoms (Au, Ag, Pd, Ni) were placed at the high symmetry positions mentioned before. Then, the unit cell was relaxed without any restrictions. In all cases, the adatoms could be stabilised at these high symmetry positions. In contrast, for the monoclinic surface the adsorbates were first placed on top of different Zr atoms and relaxed only vertically. In a second step, in-plane relaxations were enabled as well. To calculate the adsorption energies, defined as the total energy difference between the combined structure and the separate parts, the total energy of the free atom was calculated at the same energy cutoff, but only with a single $\vec{k}$-point, the Γ point. The sign of the adsorption energy was chosen such that a more negative number means stronger adsorption. The electronic properties of the adsorbed adatoms are then discussed in section 4.1.4.
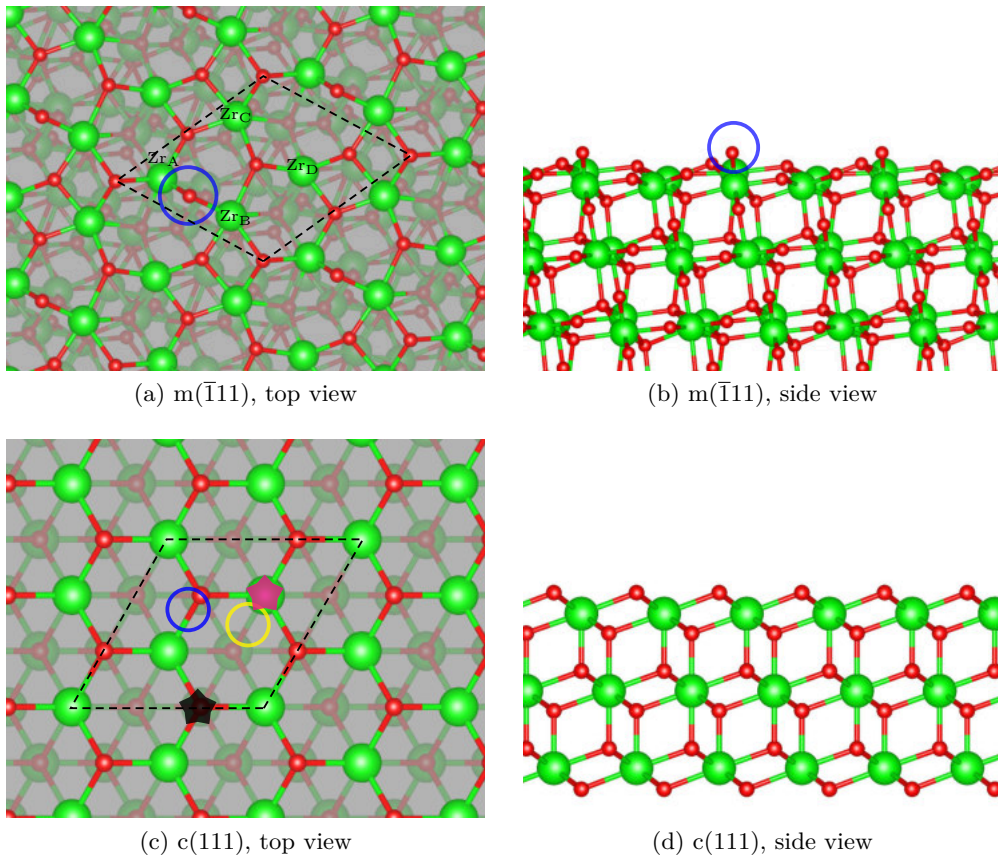
97

(a) m($\bar{1}$11), top view

(b) m($\bar{1}$11), side view

(c) c(111), top view

(d) c(111), side view

Figure 4.1.: Top and side view of the (a), (b) m-ZrO_2($\bar{1}$11) and (c), (d) c-ZrO_2(111) surface. Zr atoms in green, O in red. The surface unit cell is indicated by the dashed line, the under-coordinated oxygen at the surface by blue circles. The dedicated adsorption sites in the c(111) unit cell are indicated by coloured circles (yellow: O–O bridge, blue: O–Zr bridge) and stars (black: top, magenta: hollow).

Table 4.1.: Calculated and experimental lattice parameters of monoclinic and cubic ZrO$_2$.

	optB86	Exp. [74]
	monoclinic	
a [Å]	5.166	5.151
b [Å]	5.215	5.212
c [Å]	5.355	5.317
γ [deg]	99.670	99.230
V [Å^3]	142.200	140.900
	cubic	
a [Å]	5.096	5.086
V [Å^3]	132.370	131.560

After full relaxation of the c(111) model, the similarities and differences between the two groups of metal adatoms become apparent. For palladium and nickel, which are both group 10 elements, the preferred adsorption sites are very similar. The DFT simulations predict the most favoured adsorption site at an O–O bridge site for both Pd and Ni but with a 543 meV higher adsorption energy for nickel (see table 4.2). The atomic distances of the nickel adsorbate to the surface atoms are 1.959 Å for a O–Ni and 2.372 Å for a Zr–Ni bond, respectively, and are shorter than for palladium (2.254 Å for O–Pd and 2.521 Å for Zr–Pd). This trend can be expected since the ionic radius of nickel (1.49 Å) is smaller than for palladium (1.69 Å). Both Pd and Ni adatoms cause a displacement of 46 pm of the oxygen atoms they bind to. The Zr atom close by is hardly affected by the adsorbates. On the other hand, the two group 11 elements Au and Ag, prefer adsorption at a O–Zr bridge. The calculated adsorption energy of the silver adatom is 608 meV less than for gold, even though the atomic distances are not much different (see table 4.3). A similar trend as also found by Grau-Crespo et al. [116] who calculated adsorption energies of -0.419 eV and -0.178 eV for Au and Ag respectively. The values reported in this work are higher due to the addition of van-der-Waals contributions. Gold forms a bond to the nearest oxygen atom with a length of 2.261 Å and an Au–Zr bond of 2.948 Å. The larger ionic radius of the silver atom leads to bond lengths of 2.494 Å and 3.001 Å for Ag–O and Ag–Zr, respectively. In both cases the oxygen atom where the bond to the adsorbate is formed is displaced by 82 pm and 70 pm for gold and silver, respectively. The closest Zr also moves slightly by 23 pm and 21 pm.

On the more complex m($\bar{1}$11) ZrO$_2$ surface the energy landscape is much steeper than for the c(111) case and metal adatoms do not remain at metastable sites. Yet the most preferred adsorption sites are of similar character as on to the c(111) surface. Both palladium and nickel adsorb strongly at O–O bridge sites by forming a bond with the 2-fold coordinated protruding oxygen atom and another 3-fold coordinated oxygen. The

adsorption energies are $-2.276\,\text{eV}$ and $-2.708\,\text{eV}$, respectively. Interestingly, the second oxygen atom participating in the bond is different for Pd and Ni, as illustrated in figs. 4.2g and 4.2h. Due to the distortions at the surface the O–O bridge sites in question differ in the respective distances of the oxygen atoms, and the smaller nickel atom, which has shorter and stronger bonds to the surface oxygen atoms, prefers to adsorb at a position where the separation is smaller. Nevertheless, the energy difference between these two sites, calculated by simply switching the nickel and palladium atoms, is just $20\,\text{meV}$ for the nickel and $6\,\text{meV}$ for the palladium case. The distances to the surrounding atoms participating in the bonds are again similar to the c(111) case. For palladium, the length of the O–Pd bonds is $2.249\,\text{Å}$ and $2.306\,\text{Å}$, the latter sightly elongated. The distance to the nearest Zr atom is $2.607\,\text{Å}$, slightly more than on c(111). The equilibrium position of the nickel adsorbate shows shorter Ni–O bonds at $1.825\,\text{Å}$ and $1.876\,\text{Å}$, and the the nearest Zr atom is closer as well ($2.344\,\text{Å}$).

Both Au and Ag adsorb more weakly with adsorption energies of $-1.222\,\text{eV}$ and $-0.816\,\text{eV}$, respectively. They again bind at O–Zr bridge sites, similar to c(111). Interestingly, the Au atom does not bind to the 2-fold coordinated oxygen atom like an Ag adatom. Placing the gold adatom at the most preferred site of the silver adatom incurs an energy penalty of $105\,\text{meV}$, while the reversed placement is $53\,\text{meV}$ less favoured. Compared to adsorption on the c(111) surface, the bond lengths are longer for both Au and Ag. The Au–O and Au–Zr distances are increased to $2.261\,\text{Å}$ and $2.948\,\text{Å}$, while the Ag–O and Ag–Zr bond lengths are $2.494\,\text{Å}$ and $3.001\,\text{Å}$.

Table 4.2.: Adsorption energy in eV of (Au, Ag, Pd, Ni) on the c(111) and m($\bar{1}$11) ZrO_2 surfaces, referenced to the free atom. The initial placement of the metal adatoms on the monoclinic surface is given by the respective Zr atom above which the adatom was placed.

	Au	Ag	Pd	Ni
		c(111)		
Hollow	-0.877	-0.543	-1.708	-1.359
O–O bridge	-0.945	-0.565	-2.225	-2.762
O–Zr bridge	-1.255	-0.646	-2.188	-2.614
Top	-0.753	-0.438	-2.037	-2.004
		m($\bar{1}$11)		
Zr_A	-1.117	-0.765	-1.744	-2.708
Zr_B	-1.019	-0.603	-1.799	-2.197
Zr_C	-0.916	-0.816	-2.276	-2.041
Zr_D	-1.222	-0.676	-2.079	-2.409

Table 4.3.: Atomic distances in Å at the ground state adsorption configurations on the c(111) and m($\bar{1}$11) ZrO$_2$ surfaces. The respective adsorbate is indicated by the letter X.

	Au	Ag	Pd	Ni
	c(111)			
O–X	2.180	2.275	2.254	1.959
Zr–X	2.793	2.956	2.521	2.372
	m($\bar{1}$11)			
O$_I$–X	2.261	2.494	2.249	1.825
O$_{II}$–X			2.306	1.876
Zr–X	2.948	3.001	2.607	2.344

(a) c(111): Au   (b) c(111): Ag   (c) c(111): Pd   (d) c(111): Ni

(e) m($\bar{1}$11): Au   (f) m($\bar{1}$11): Ag   (g) m($\bar{1}$11): Pd   (h) m($\bar{1}$11): Ni
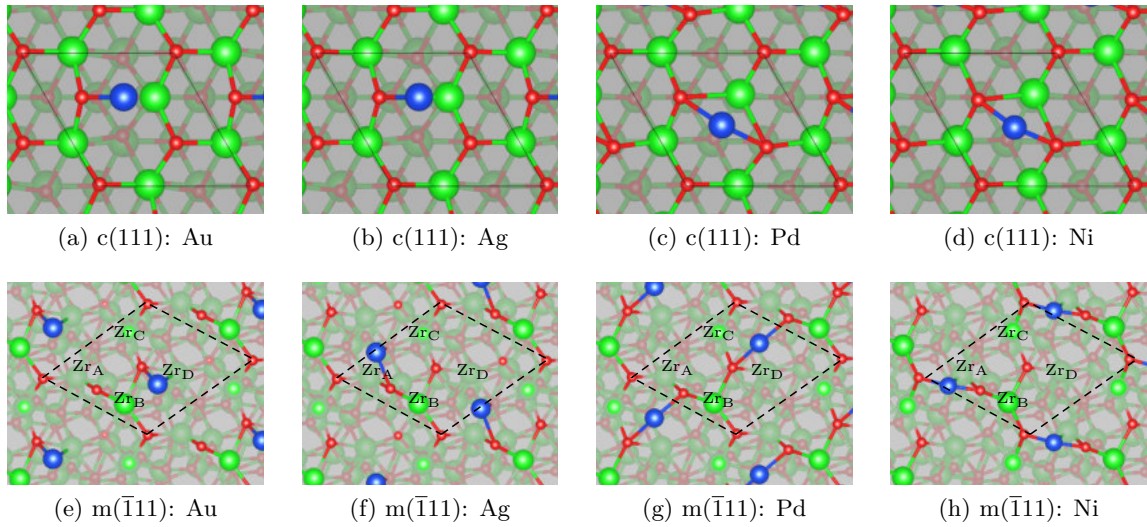
Figure 4.2.: Top view of the most preferred adsorption sites of (a), (e) gold, (b), (f) silver, (c), (g) palladium, and (d), (h) nickel. Zr and O are coloured green and red, respectively. The adsorbate is coloured.

4.1.3. Metal Adatom Adsorption on Ultra-thin ZrO$_2$ Films

To model the adsorption of metal adatoms on ultra-thin ZrO$_2$ films the adsorbates were also placed on the $(\sqrt{19} \times \sqrt{19})R23.4°$ model cell discussed in section 3.3.1. There the ZrO$_2$ film shows a larger surface corrugation than the monoclinic m($\bar{1}$11) surface and four 2-fold coordinated oxygen atoms protruding from the ZrO$_2$ film. To properly scan the resulting large number of possible adsorption sites one of the metal adatoms was first placed on top of each of the 12 Zr atoms. First, the adsorbate was allowed to relax only vertically, and after reaching this constrained energy minimum the adatoms were allowed to fully relax. Since this still low number of configurations showed a large variance of the adsorption energies, the adatoms were also placed on a regular 6×6 grid (36 initial adsorption sites), which for the Au and Ag case was further supplemented by a second 6×6 grid which was shifted by $1/12$ of the unit cell length in x and y direction, resulting in 72 initial adsorption sites. Again, the adsorbate was first only allowed to relax in the vertical direction.

The calculations were performed using the same settings as for the pristine $\sqrt{19}$ model: due to the size of the unit cell a single $\vec{k}$-point at the Γ point and an energy cutoff of 400 eV was used. All calculations were done with the optB86b functional. During the relaxation, the lower three platinum layers of the substrate were fixed in all directions.

After full relaxation of both the ZrO$_2$ film and the adsorbates, the analysis of the adsorption energies showed an increase for all four transition metal adatoms. The largest increase was found for silver and nickel, whose binding energy increased by 671 meV. The increase for the gold adatom was 316 meV, and for palladium only slightly stronger binding (167 meV) was found. This can be explained by analysis of the particular adsorption sites, depicted in fig. 4.4: Ni and Ag both gain an additional oxygen neighbour compared to the m($\bar{1}$11) surface, but the metal-oxygen bond lengths do not change by a large amount. For silver, this results in an adsorption site in the "valley" structure of the oxide film, which allows the Ag to form two bonds to neighbouring 2-fold coordinated oxygen atoms. The nickel adsorbate on the other hand adsorbs at the edge of the "isle", forming bond to two under-coordinated surface oxygen atoms and a third bond to a 3-fold coordinated O, breaking one Zr–O bond in the process. The Ni adatom also displaces the Zr atom beneath it by about 0.8 Å. Compared to adsorption on the monoclinic bulk surface, the palladium adatom has the same number of oxygen neighbours, but on the ultra-thin film the bond lengths are slightly reduced to 2.177 Å and 2.088 Å. Additionally, the gold adatom again behaves differently as it adsorbs on top of downwards buckled oxygen atom of the oxide film. The bond length to this oxygen atom is larger than on m($\bar{1}$11), but an additional strong Zr–Au bond is formed with a bond length of 2.836 Å.

According to the experiment presented by Choi, Mayr-Schmölzer, et al. [4], gold adatoms show a much larger island density than silver, which would indicate stronger interaction of Au with the ZrO$_2$ thin film. Considering that the DFT predicts similar adsorption energies of Au and Ag adatoms on the oxide film this is a striking discrepancy. Therefore, the barriers for the diffusion of the adatoms were evaluated by calculating the adsorption energies at a large number of sites to map the potential energy surface

of the $\sqrt{19}$ unit cell. Interpolation of the calculated adsorption energies showed, as depicted in fig. 4.5, that for gold the potential is rather flat, corresponding not only to the "isle" features on the pristine $\sqrt{19}$ model cell, but also to most of the "valley" sites. In one surface unit cell only one site shows exceptionally strong adsorption. The energy difference between this site and the surrounding plateau is up to $0.9\,\mathrm{eV}$. For the silver adsorbate on the other hand, fig. 4.5b shows large areas of strongly bound sites, separated by rather small ridges. In one direction only small barriers of about $0.45\,\mathrm{eV}$ are found. This suggests that at elevated temperatures, the silver adatom have much higher mobility on the ZrO_2 thin film, while the gold adatom adsorbs strongly at certain sites and its diffusion barrier is much higher.

Table 4.4.: Adsorption energy in eV of (Au, Ag, Pd, Ni) on the ultra-thin ZrO_2 film, referenced to the total energy of the free atom.

	Au	Ag	Pd	Ni
$\sqrt{19}$	−1.487	−1.538	−2.443	−3.379

Table 4.5.: Atomic distances in Å at the ground state adsorption configurations. The adsorbate is indicated by the letter X.

	Au	Ag	Pd	Ni
O_I–X	2.748	2.269	2.088	1.866
O_{II}–X		2.358	2.177	1.904
Zr–X	2.836	2.843	2.580	2.622

4.1.4. Charge Transfer

To gain a better understanding of the adsorption mechanism it is instructive to analyse the projected density of states (PDOS) of the interacting atoms. Additionally, studying the Bader charges [117–123] of the adsorbates gives an indication of their ionic state. This is done by comparing the predicted Bader charge of the adsorbed atom to that of a free neutral atom. As a general trend, the PDOS for the different adatoms are very similar for the two ZrO_2 bulk surfaces, while on the ultra-thin film only the PDOS for a palladium adatom is similar to the bulk surface, while the PDOS for Ni, Ag, and Au differs. For the adsorption on bulk ZrO_2, shown in figs. 4.6a to 4.6h, two cases can be distinguished: the d states of Au and Ag are at low energies of about $-3.5\,\mathrm{eV}$ to $-1.8\,\mathrm{eV}$ (Au) or $-4\,\mathrm{eV}$ to $-2.5\,\mathrm{eV}$ (Ag). These d states overlap with the valence band of the ZrO_2, and some hybridisation of the O $2p$ and metal d states at about $-2\,\mathrm{eV}$ (Au) and $-3\,\mathrm{eV}$ (Ag) is visible. Pd and Ni on the other hand show a weak but broad
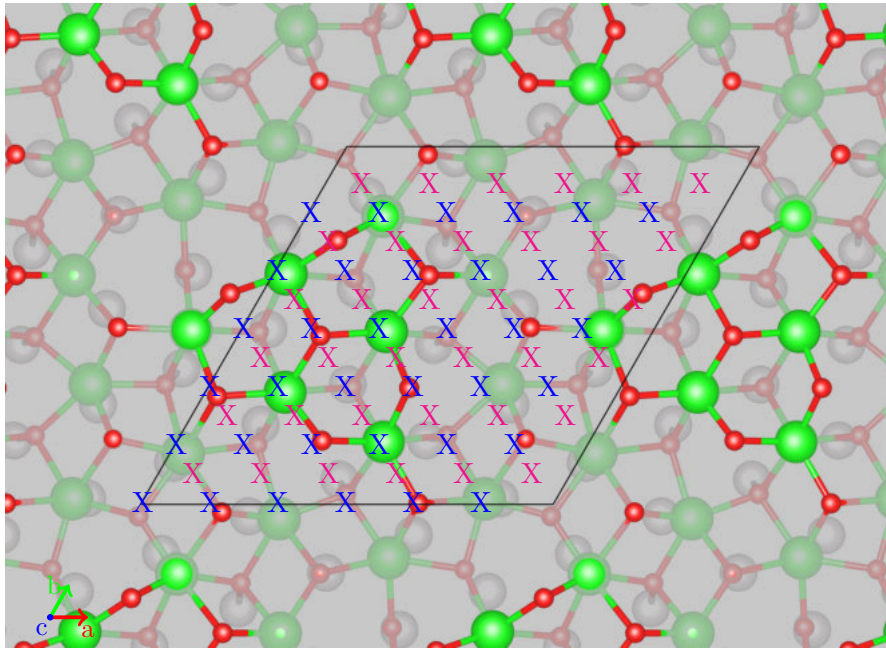
Figure 4.3.: Fully relaxed $\sqrt{19}$ model cell. Initial adsorption on the 6×6 sites are marked with a blue X. For Au and Ag an additional grid, shifted by $1/12$ of the unit cell length was added. Zr, O, and Pt are coloured green, red, and grey.

(a) $\sqrt{19}$: Au   (b) $\sqrt{19}$: Ag   (c) $\sqrt{19}$: Pd   (d) $\sqrt{19}$: Ni

(e) $\sqrt{19}$: Au   (f) $\sqrt{19}$: Ag   (g) $\sqrt{19}$: Pd   (h) $\sqrt{19}$: Ni
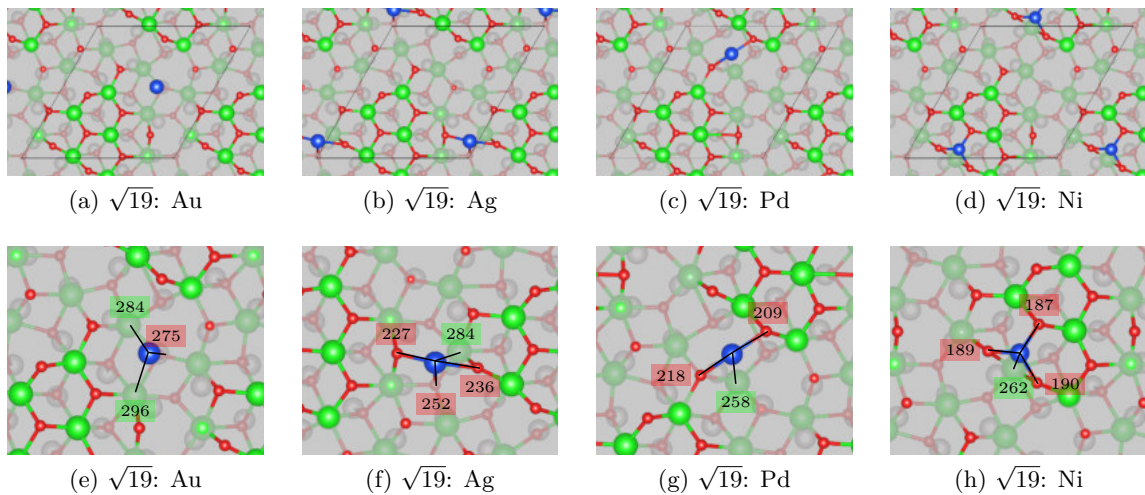
Figure 4.4.: (a)-(d): fully relaxed equilibrium structures of one metal adatom adsorbed on the $\sqrt{19}$ model cell. (e)-(h): magnification around the most favoured adsorption site. Zr, O, and Pt are coloured green, red, and grey. The adsorbate is coloured blue in all cases.

104

(a) Au   (b) Ag
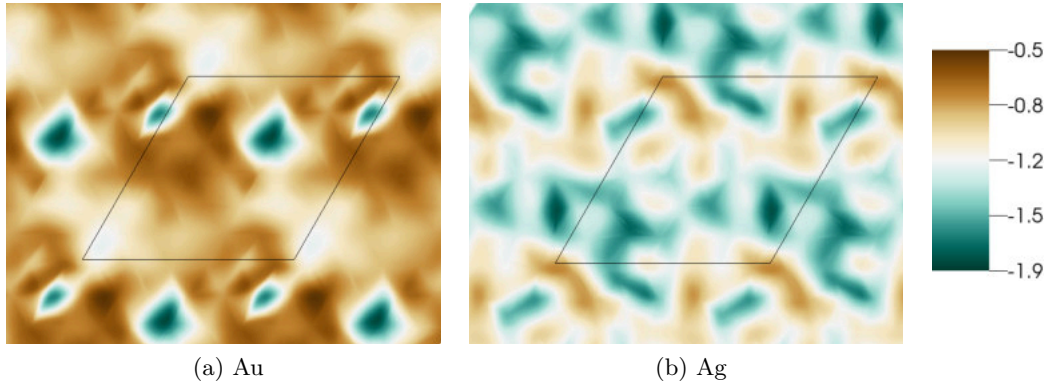
Figure 4.5.: Potential energy landscape of (a) Au and (b) Ag adsorbed on the $\sqrt{19}$ model cell.

contribution of d states and a free-atom-like, crystal field split d-manifold in the oxide gap. Additionally, Au and Ag show spin polarisation, where the singly occupied $5s$ ($6s$) state at the Fermi level induces a small magnetic moment. This is not the case for Pd and Ni which show no spin polarisation. Compared to the free atoms, the electronic configuration of Au, Ag and Pd is similar to the free atoms, $d^{10}s^1$ for Au and Ag, and d^{10} for Pd. Ni adatoms behave differently: the free Ni atom has a d^8s^2 configuration, which after adsorption changes to a d^{10} configuration, similar to Pd, indicating that an internal s-d transfer occurs upon adsorption. The higher adsorption energy of Ni compared to Pd is reflected in the increased interaction of the Ni d states with both Zr and O states of the oxide. Additionally, the Bader analysis shows that the Ni atom transfers a small amount of charge to the substrate. The interaction of the Ag adsorbate with O is clearly visible in the broadening of the Ag $4d$ states. Due to the filled $4d$ shell of the Ag atom the energy gain is not large. The situation for Au $5d$ states is similar, but its d band is broader. Additionally, its $6s$ states interact more strongly with the O $2p$ states than Ag, contributing to its higher adsorption energy. The calculated Bader charges confirm the free-atom-like PDOS of the Ag adatom, while Au gains some charge from the neighbouring Zr atom.

On the ultra-thin ZrO_2 film, the PDOS shown in figs. 4.6i to 4.6l reveal a stronger interaction with the valence band states of the oxide and a general broadening of the d states for Ag, Pd, and Ni. For Ni, which is now spin-split, additional Zr and O states are pulled into the band gap, again proving the enhanced interaction. A magnetic moment is induced due to the partial filling of the minority d states. The analysis of the Bader charges shows that the adatoms except for Pd are now charged. In the case of Ag, the spin-split $5s$ state is completely emptied, and the Bader charge indicates an Ag^+ ion. For Au on the other hand, the situation is reversed: its $6s$ states are now filled, and the Bader charged indicates an Au^- ion. Additionally, the Au d band is narrowed, decreasing the interaction with the O p states. The formation of a negatively charged

Au$^-$ can be explained by this particular adsorption site, since here the Au–O bonds are long and weak in contrast to the Au–Zr bond. Nevertheless, at other adsorption sites the gold adatom can also adsorb as a positively charged Au$^+$: at the second most favoured adsorption site the Au shows a similar local configuration as the most favoured Ag site, located in a O–O bridge site. There, the Au shows a Bader charge of +0.31, suggesting a Au$^+$ ion. Other, less favoured, adsorption sites indicate both Au$^+$ and Au$^-$ adsorption.

Similar behaviour of differently charged Au adatoms adsorbed on an oxide surface has been found for Au on CeO$_2$(111). There, gold adsorbs as a negatively charged Au$^-$ if a Ce^{3+} supplies an electron. On the stoichiometric surface gold adsorbs either as a neutral or positive Au [124, 125]. Since ZrO$_2$ is not a reducible oxide, in contrast to CeO$_2$, the charge transfer can only originate from or go to the metallic substrate.

(a) c(111): Au   (b) c(111): Ag   (c) c(111): Pd   (d) c(111): Ni

(e) m($\bar{1}$11): Au   (f) m($\bar{1}$11): Ag   (g) m($\bar{1}$11): Pd   (h) m($\bar{1}$11): Ni

(i) $\sqrt{19}$: Au   (j) $\sqrt{19}$: Ag   (k) $\sqrt{19}$: Pd   (l) $\sqrt{19}$: Ni
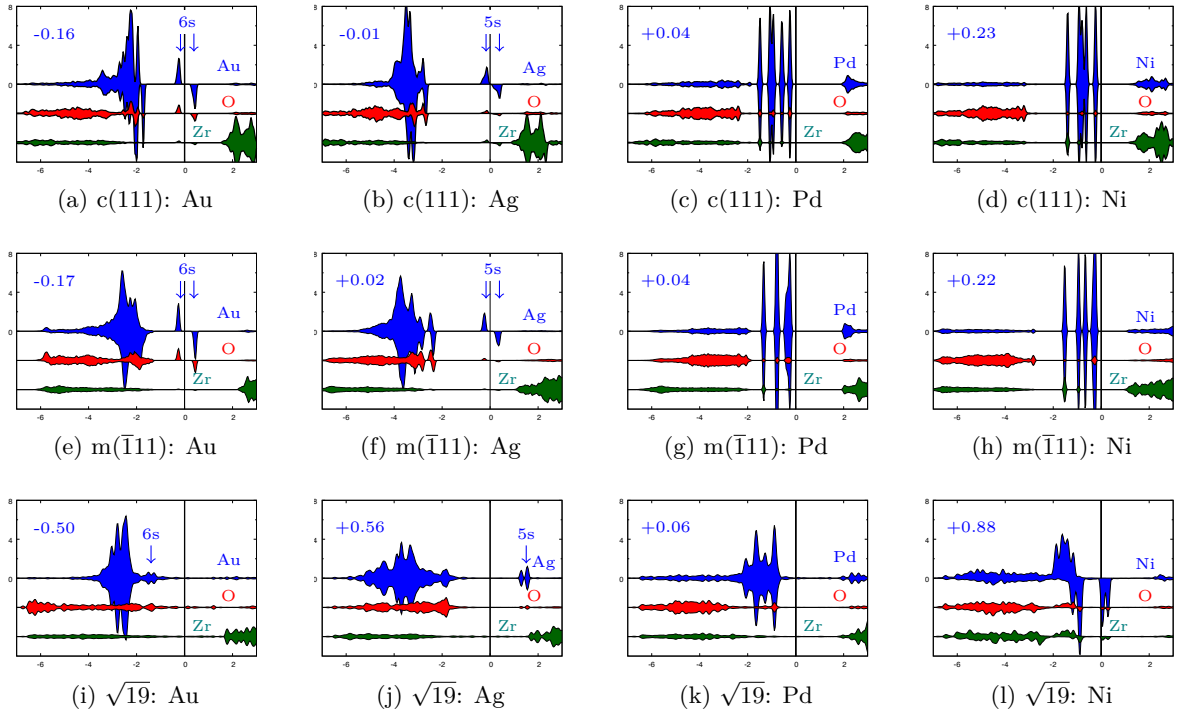
Figure 4.6.: Projected DOS of the metal adsorbate (blue) and the Zr (green) and O (red) atoms participating in the bond to the adsorbate. Top row: metal adatom adsorption on cubic ZrO$_2$; middle row: adsorption on the m($\bar{1}$11) ZrO$_2$ surface; bottom row: adsorption on the ultra-thin ZrO$_2$ film. The number in the top left corner of each plot indicates the Bader charge, referenced to the insulated free atom.

4.1.5. Summary

The DFT studies of transition metal adatom adsorption show that on the two different ZrO_2 bulk surfaces, c(111) and m($\bar{1}$11), the adsorption mechanism is almost identical. The adsorption energies rise with increasing reactivity of the adsorbate, starting with Ag and followed by Au, Pd, and Ni. On the cubic c(111) surface, both Au and Ag adsorb at O–Zr bridge sites, while Pd and Ni adsorb at O–O bridge sites. While the distortions of the more open monoclinic surface gives rise to more adsorption sites, the general trend of the c(111) continues. Three metal adsorbates, Ag, Pd, and Ni, bind more strongly to the oxide than on the c(111) surface but the local adsorption configurations are similar. The 2-fold coordinated oxygen at the monoclinic surface plays a decisive role in this increase of the adsorption energies since it facilitates the creation of a bond to the adsorbate. Au is a special case since it prefers to adsorb at a Zr–O bridge with a 3-fold coordinated oxygen, and it adsorbs slightly weaker on the more corrugated m($\bar{1}$11) surface. The analysis of the projected density of states and the Bader charges shows that except for Ni, all metal adsorbates adsorb in a charge neutral free-atom-like state. In the case of Ni, a s-d transfer takes place, quenching the magnetic moment of the free Ni atom. Since none of the metals studied here are electropositive enough to reduce the Zr ions of ZrO_2 they remain essentially neutral.

On the ultra-thin ZrO_2 film, the larger corrugation of the surface provides a much larger variety of adsorption sites. Ag and Ni show a large increase of the adsorption energies ($\approx 1\,\mathrm{eV}$), while Au and Pd only bind moderately stronger ($\approx 0.5\,\mathrm{eV}$). Hence, the Au atom is now the most weakly bound, followed by Ag, Pd, and Ni. At the most favoured adsorption sites, Ag and Ni form additional bonds to a surface oxygen atom, while Au and Pd are similarly coordinated compared to the monoclinic surface. In addition to that, as has been shown in section 3.3.4, the oxide film is not completely insulating anymore, enabling charge transfer either from or to the platinum substrate. While Pd adatoms stay neutral, Ag adsorbs as a positively charged Au^+ ion. Au has been found to adsorb both as Au^+ and Au^- ion, depending on the adsorption site. Performing a scan of the adsorption energy landscape shows that for Au the diffusion barrier at the favoured adsorption site is $0.9\,\mathrm{eV}$. This is not the case for Ag, where at least in one direction the calculated diffusion barriers were only about $0.45\,\mathrm{eV}$. Additionally, Au is found as a positively charged ion at these less favoured sites, meaning that on movement it would have to transfer two electrons through the ZrO_2 film. Considering that an adsorbed neutral Au_0 is only weakly bound this explains the higher cluster density for Au seen in the experiments. Generally, the simulations show very good agreement with the experiment and the results were successfully published by Choi, Mayr-Schmölzer, et al. [4].

4.2. Water Adsorption on Zirconia Surfaces

As ZrO_2 plays a big role in various technological applications like catalysis, it is essential to understand the properties of the water-oxide interface on a fundamental level. Many

studies have been done on other oxide surfaces: on most defect-free oxides water adsorbs only weakly [126, 127], desorbing below room temperature [128, 129]. For example on the rutile $TiO_2(110)$ [105, 130] surface, which shows a large number of oxygen defects, H_2O adsorbs dissociatively, filling the vacancy with the OH group while the split off hydrogen forms a surface hydroxyl. However, weak interaction with water on oxide surfaces should not be considered a general rule since e.g. α-$Cr_2O_3(001)$ [131] and α-$Fe_2O_3(012)$ [132] are shown to be reactive even without surface defects. The review article by Henderson [127] indicates that the cost of forming a bond of a surface cation to the O_{H_2O} is the decisive factor facilitating water dissociation.

For ZrO_2 not much published data are available. Ushakov and Navrotsky [133] have done calorimetry measurements of water adsorbed on the monoclinic surfaces of ZrO_2 and HfO_2 and found adsorption enthalpies of $-1.140\,eV$ to $-1.762\,eV$ and $-1.347\,eV$ to $-1.969\,eV$, respectively. More recent temperature-programmed desorption (TPD) experiments on polycrystalline ZrO_2 powder samples on the other hand have shown an inconclusive picture, as H_2O seems to be largely inert [134]. Orlando et al. [135] report much lower desorption energies of H_2O of $0.6\,eV$ in TPD. Up to now, research was done only on polycrystalline samples, but no data has yet been published concerning water adsorption on well-defined crystalline ZrO_2 surfaces. Therefore, DFT studies of the adsorption of water molecules were performed using the ZrO_2 surface models discussed in the previous chapters. As has also been shown for adsorption of metal adsorbates, the model cells presented in this work can aid in the characterisation of adsorption behaviour by modelling a more or less well defined ultra-thin zirconia film which is adsorbed on a metal substrate. To compare the adsorption properties on thin films, the studies were also performed on the most stable bulk surfaces of cubic and monoclinic ZrO_2. The theoretical studies were done in conjunction with scanning tunnelling microscopy (STM), temperature-programmed desorption (TPD), and Fourier Transform Infrared Spectroscopy (FT-IR) experiments and can be found in a very recent paper by Lackner, Hulva, Choi, Köck, Mayr-Schmölzer, et al. [7].

To properly capture the adsorption properties of molecules it is essential to properly account for polarisation effects. Therefore, the van-der-Waals corrected optB86b functional was used for all calculations discussed in this chapter. Similar to the definition used for the adsorption of metal adsorbates, the adsorption energies were calculated according to

$$E_{Ads} = E_{Slab+H_2O} - E_{Slab} - E_{H_2O} \qquad (4.1)$$

where E_{Slab} is the total energy of the fully relaxed pristine surface structure and E_{H_2O} the total energy of molecular H_2O in the gas phase. The sign was chosen so that a smaller, more negative number means stronger adsorption.

4.2.1. Adsorption on Bulk ZrO_2 Surfaces

The DFT adsorption studies of water adsorption on ZrO_2 bulk surfaces were done in analogy to the metal adsorption studies discussed in section 4.1.2. The interaction of water molecules was investigated on the most favourable cubic and monoclinic ZrO_2
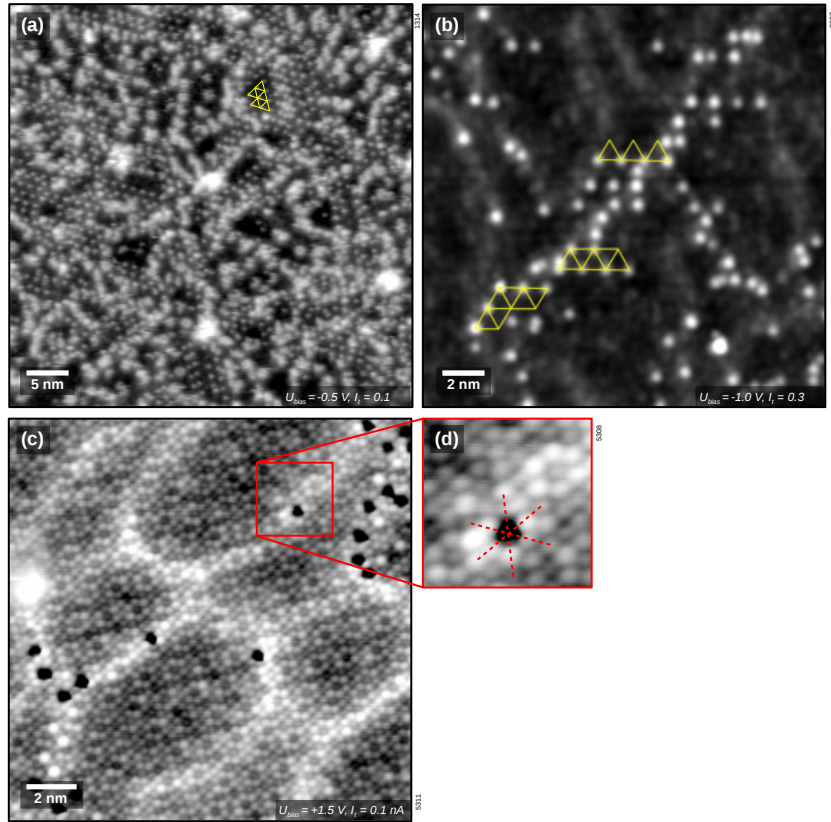
Figure 4.7.: STM of small coverages of H_2O adsorbed on the ultra-thin ZrO_2 film. Top left: $0.12(4)\,ML$ H_2O dosed at $100\,K$, measured at $78\,K$. Yellow dashes indicate the $\sqrt{19}$ unit structure which H_2O molecules are arranged in. Top right: after dosing $15\,L$ of H_2O at room temperature, water species prefers adsorption above subsurface dislocation lines (grey areas). Bottom left: after dosing of $30\,L$ of H_2O and storage in UHV for 8 hours. Due to a special STM tip the contrast of the OH is inverted. Bottom right: the magnified part shows that the H_2O are located on top of the bright surface lattice, i.e. the Zr atoms. Experimental data courtesy of Lackner, Hulva, Choi, Köck, Mayr-Schmölzer, et al. [7].

bulk surfaces, the c(111) and the m($\bar{1}$11) orientation, both of which are discussed in the chapter regarding metal adadom adsorption, see section 4.1.1. In the case of the c(111) surface, the calculations were done both at the bulk equilibrium lattice constant of 3.603 Å and at 3.5 Å which corresponds to the lattice constant of the ultra-thin ZrO_2 films adsorbed on Pt_3Zr. To model the cubic bulk surface, slabs consisting of three ZrO_2 c-(111) trilayers were constructed from the bulk unit cell. The surface unit cell was rotated by 30° and enlarged, yielding a $(\sqrt{3} \times \sqrt{3})R30°$ surface unit cell, to model a coverage of ⅓ if one H_2O molecule is placed on the surface. The resulting distance between adsorbed H_2O molecules due to the periodic boundary conditions is around 5 Å.

Cubic ZrO$_2$

To study the interaction of a water molecule with the c(111) surface a single H_2O was placed in both a molecular and dissociated configuration on the surface of the slab. For both initial configurations the oxygen atom of the H_2O molecule was positioned above a surface Zr. In the case of molecular adsorption, the H_2O was rotated so that the hydrogen atoms each point towards a surface oxygen atom, as it is expected that the adsorbed molecule forms hydrogen bonds. For dissociative adsorption, the $(OH)_{ads}$ was again placed above a Zr atom while the split off hydrogen was moved closer to one of the neighbouring oxygen atoms. Two values of the lattice constants, namely the DFT bulk value of 3.610 Å and the experimental value for the ultra-thin film (3.5 Å) were considered to evaluate the dependence of the reactivity of the surface on the lattice constant.

The calculations on the cubic ZrO_2 slabs were done using a $6 \times 6 \times 1$ Γ-centred $\vec{k}$-point grid at an energy cutoff of 600 eV and using the optB86b functional.

For both lattice constants, the DFT calculations predict a preference for dissociative adsorption. At both lattice constants the H_2O molecule binds strongly to the substrate at adsorption energies of -1.436 eV and -0.965 eV for the bulk and reduced lattice constant, respectively. Nevertheless, the H_2O does not dissociate spontaneously and adsorbs as a molecule with adsorption energies of -0.975 eV and -0.790 eV, respectively. As shown in table 4.6, this large increase of the adsorption energy at the bulk lattice constant of 3.610 Å indicates much higher reactivity of the ZrO_2 cubic bulk surface.

Considering dissociative adsorption, the $(OH)_{ads}$ is located 2.025 Å above the Zr atom at the ZrO_2 bulk lattice constant, at the compressed lattice this distance is reduced to 2.018 Å, see figs. 4.8c and 4.8d. The dissociated $(OH)_{ads}$ is not positioned right above the Zr atom, but shifted slightly towards the surface hydroxyl due to a hydrogen bond connecting the two separated segments of the H_2O molecule. The O–H length of the $(OH)_{ads}$ is 0.969 Å in both cases, but the bond length of the surface hydroxyl is slightly longer at 0.999 Å. The $(OH)_{ads}$ is tilted by 41.5° with respect to the vertical axis at bulk lattice constant and by 45.5° at 3.5 Å. The tilting of the surface hydroxyl is different depending on the lattice constant: 49.6° at 3.6 Å and 36.7° at 3.5 Å. The surface oxygen atom the split off hydrogen binds to shifts away from the adsorption site, by 61 pm and 45 pm at 3.6 Å and 3.5 Å ZrO_2 lattice constant, respectively. The Zr below the $(OH)_{ads}$ is displaced by 18 pm and 17 pm in the other direction, respectively.

For molecular adsorption the water molecule adsorbs almost exactly above a surface Zr atom, see figs. 4.8a and 4.8b. The hydrogen atoms form hydrogen bonds with surface oxygen atoms which causes the H_2O to adsorb in an almost flat configuration. The tilting angle of the H_2O is just 0.6° at 3.6 Å and 5° at 3.5 Å lattice constant. In the former case, the angle formed by the two O–H bonds of the water molecule is 111°, in the latter case 109°, an increase of the bending angle from 104.7° of the free molecule calculated with the optB86b functional. The O–H bonds of the H_2O are also slightly elongated to 0.999 Å for both models. The distance of the adsorbed H_2O to the Zr atom is 2.282 Å and 2.312 Å for the bulk and film lattice constants, respectively.

(a) top view, molecular H_2O

(b) side view, molecular H_2O

(c) top view, dissociated H_2O

(d) side view, dissociated H_2O
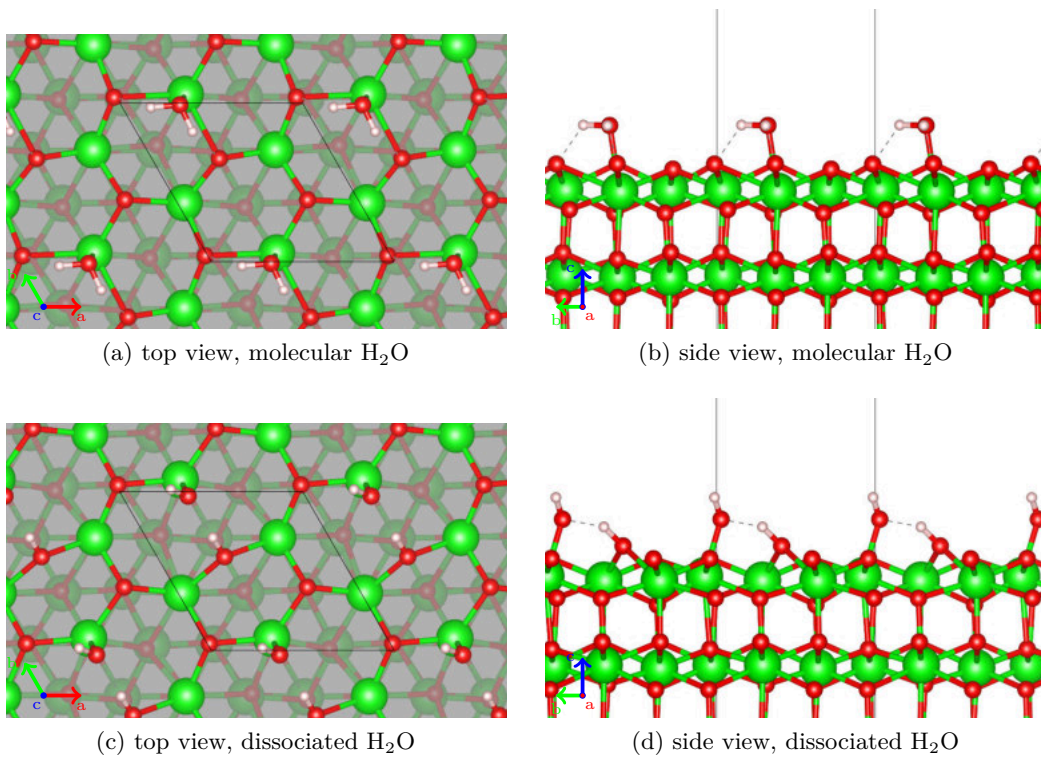
Figure 4.8.: One H_2O molecule adsorbed on the c(111) bulk ZrO_2 surface. Top row: molecular adsorption, bottom row: dissociative adsorption. Zr, O, H are coloured green, red, and white. The hydrogen bonds formed between (a), (b): hydrogen of the adsorbed H_2O and surface oxygen, (c), (d): $(OH)_{ads}$ and surface hydroxyl are indicated by the dashed line.

Monoclinic ZrO₂: ¼ ML coverage

As has been noted in section 4.1.2, the distortions of the surface compared to the cubic case gives rise to a large number of possible adsorption sites. Considering that water

prefers adsorption on top of Zr atoms, as seen for the c(111) surface, four main sites can be identified in the smaller surface unit cell. To find the most favoured adsorption site, a water molecule was placed on top of these four Zr atoms in a molecular configuration. Each site differs in the height of the Zr atom and the distance to the surrounding O atoms, and therefore their accessibility to the adsorbate. The sites are labeled P1, P2, P3, and P4. One Zr atom (P4) is buckled downwards and its accessibility is greatly reduced by a lateral contraction of the oxygen atoms in the top layers above it.

During the relaxation, only three of the four initial adsorption sites remain stable, as shown in fig. 4.10. The molecule adsorbed at site P4 where the Zr is much less accessible is not stable, it is laterally displaced into the P3 position. The strongest bond to the substate is found for the P3 position ($E_{Ads} = -1.098$ eV), followed by P1 and P2 with adsorption energies of $E_{Ads} = -0.910$ eV and $E_{Ads} = -0.872$ eV (see table 4.6). In all cases, the oxygen atom of the water molecule forms a bond to the surface Zr with a bond length of 2.396 Å. For position P2, this is slightly enlarged to 2.370 Å. This adsorption site is also exceptional in that the water molecule does not form a hydrogen bond to the 2-fold coordinated oxygen atom at the m($\bar{1}$11) surface, apparently since the 2-fold coordinated surface O is too far away and all other surface oxygen are located too far in the bulk. For P1 and P3, the adsorbed water molecule is rotated until one of its O–H bonds points towards this 2-fold coordinated surface oxygen. Since P1 is located at the Zr directly next to this special surface oxygen, it is slightly pushed away, and the resulting $H–O_{2-fold}$ bond length is 1.830 Å. The P3 adsorption site is farther away; here the H_2O molecule tilts and moves to a final hydrogen bond length of 1.759 Å. In all cases, the water molecules are just slightly tilted with respect to the m($\bar{1}$11) surface plane. The adsorbed H_2O causes a slight modification of the surface, pulling out the Zr atom it adsorbs above by about 12 pm.

The case of dissociative adsorption was studied by manually moving one hydrogen atom of the water molecule next to surface oxygen atoms, starting from the relaxed positions found for molecular adsorption. The hydrogen atom prefers to bind to the 2-fold coordinated oxygen atom, forming a surface hydroxyl, while the $(OH)_{ads}$ is located on top of a Zr atom. Generally, the separated H_2O parts adsorb more strongly than the intact water molecule ($E_{Ads} = -1.241$ eV to -1.327 eV), as noted in table 4.6. The distance between $(OH)_{ads}$ and the substrate Zr is 2.008 Å for sites P1 and P3, and 2.085 Å for site P2. The distance between $(OH)_{ads}$ and the hydroxyl is much larger than for dissociative adsorption on the c(111) surface at 2.530 Å, 2.780 Å, and 2.265 Å for sites P1, P2, and P3.

The transition barrier between molecular and dissociative adsorption was calculated with the improved dimer method[1]. The DFT calculation predicts a dissociation barrier of 94 meV and 217 meV for sites P1 and P2, respectively.

---

[1]VASP setting: IBRION = 44

Table 4.6.: Adsorption energies in eV of a single water molecule on the c(111) and m($\bar{1}$11) ZrO_2 bulk surfaces.

E_{Ads} [eV]	molecular	dissociated
c(111), 3.5 Å	−0.902	−0.965
c(111), 3.6 Å	−0.975	−1.436
m($\bar{1}$11), P1	−0.910	−1.274
m($\bar{1}$11), P2	−0.872	−1.327
m($\bar{1}$11), P3	−1.098	−1.241

(a) P1, molecular   (b) P2, molecular   (c) P3, molecular

(d) P1, molecular   (e) P2, molecular   (f) P3, molecular
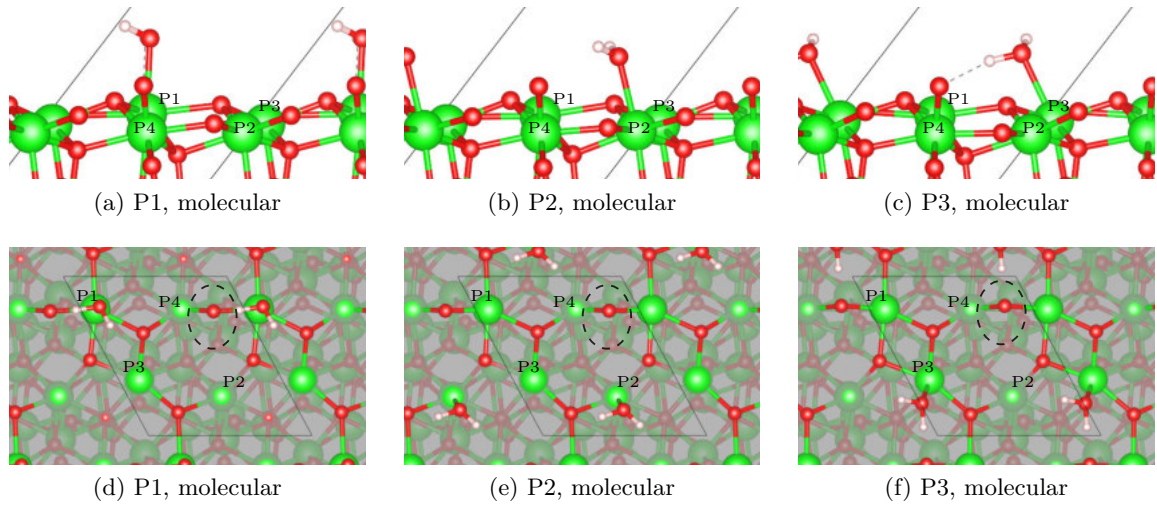
Figure 4.9.: One H_2O molecule adsorbed on the m($\bar{1}$11) bulk ZrO_2 surface as an intact molecule (¼ ML coverage). Zr, O, H are coloured green, red, and white, the 2-fold coordinated surface oxygen is indicated by a dashed circle. The additional hydrogen bond formed between H_2O and surface O is indicated by the dashed line.

(a) P1, dissociated   (b) P2, dissociated   (c) P3, dissociated

(d) P1, dissociated   (e) P2, dissociated   (f) P3, dissociated
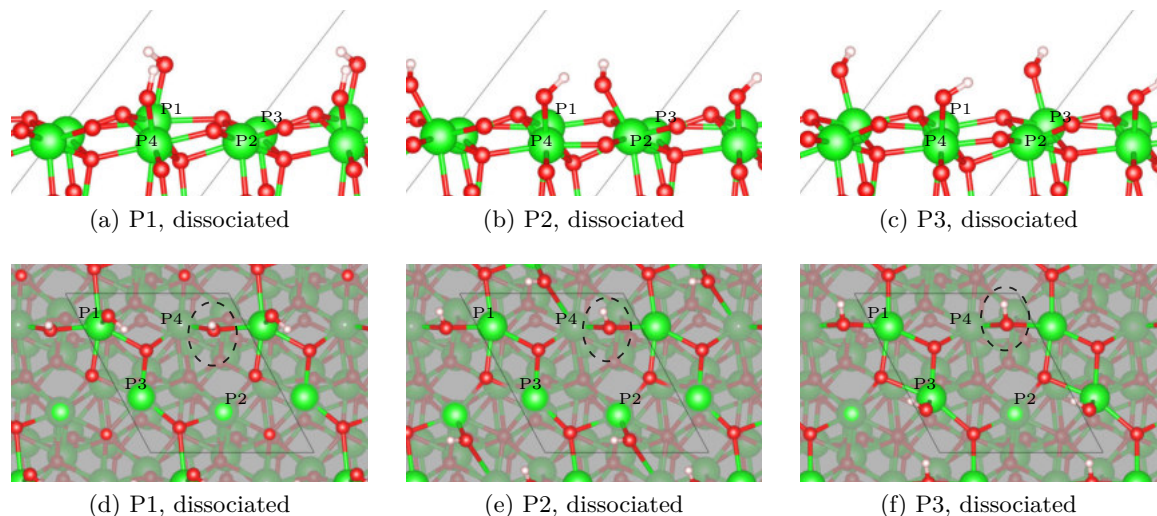
Figure 4.10.: One H_2O molecule adsorbed on the m($\bar{1}11$) bulk ZrO_2 surface as a disso-
ciated molecule (¼ ML coverage). Zr, O, H are coloured green, red, and
white, the surface hydroxyl formed with the 2-fold coordinated surface oxy-
gen is indicated by a dashed circle. The distances between $(OH)_{ads}$ and
surface hydroxyl are too large to form an additional hydrogen bond.

Monoclinic ZrO$_2$: 1 ML coverage

A full monolayer (ML) of H_2O adsorbed on the monoclinic bulk surface, defined as the
placement of four water molecules on the m($\bar{1}11$) surface unit cell, was also simulated.
The configuration of the adsorbed H_2O molecules were generated using the relaxed posi-
tions from the previous models at ¼ ML coverage. The relaxed structure (see fig. 4.11a)
shows that all four H_2O adsorb as intact molecules. Three are located above surface
Zr atoms with Zr–O distances between 2.367 Å and 2.417 Å and are only slightly tilted
with respect to the surface plane. The fourth water molecule is rotated so that its hy-
drogen atoms are pointed towards the surface and forms hydrogen bonds to the 2-fold
coordinated and one 3-fold coordinated oxygen atom of the surface. Except for one case
(2.515 Å), the O_{H_2O}–O_{H_2O} distances of the adsorbed molecules are quite large at 2.937 Å
to 4.299 Å, arising from the average distance of the adsorption sites of about 3.481 Å and
the fact that some H_2O are not located directly above a Zr. The adsorption energy per
H_2O of this configuration is -0.961 eV, identical to the averaged value of -0.960 eV
calculated for the three previously described sites at ¼ ML coverage (see table 4.6).

To test whether this configuration really is the ground state solution, simulated anneal-
ing was performed on the fully relaxed structure. Similar to the calculations performed
in section 3.3.7, the initial temperature was set to 800 K and a linear cooling ramp of
1000 steps was selected. To reduce the computational effort a $3 \times 3 \times 1$ $\vec{k}$-point grid
was used and the energy cutoff was set to 400 eV. The resulting structure was then

relaxed further using the original settings described before. The fully relaxed structure, displayed in fig. 4.11b, shows that now one water molecule is dissociated with the split off hydrogen atom forming a surface hydroxyl at the 2-fold coordinated oxygen site. The residual $(OH)_{ads}$ is located in the vicinity of the surface hydroxyl, but no hydrogen bond is formed between the separated parts. Two other water molecules are again adsorbed in a flat configuration above the two remaining Zr sites that are available, so that the previously described P1, P2, and P3 sites are all occupied. Finally, the fourth adsorbed H_2O starts to form a new water layer as it does not bind to any surface atom at all, but forms hydrogen bonds to the surface hydroxyl, the separated $(OH)_{ads}$, and another intact water molecule. It is rotated to that one of its H–O bonds is almost normal to the $m(\bar{1}11)$ surface plane. Since one H_2O is now dissociated, the adsorption energy per H_2O of $-1.193\,eV$ indicates stronger average bonding to the substrate.

To determine the binding energy of the H_2O furthest from the $m(\bar{1}11)$ surface the structure was relaxed without this molecule. The positions of the remaining water molecules do not significantly change. The calculations predict an adsorption energy of $-1.278\,eV$ per H_2O. The comparison with the full monolayer configuration yields a binding energy of this fourth water molecule of $-0.939\,eV$, very high considering that it is only bound to the water layer via two long hydrogen bonds ($1.567\,Å$ and $1.749\,Å$). The split off $(OH)_{ads}$ is rotated towards it but the $H-O_{H_2O}$ distance is much larger ($2.162\,Å$).

Since the high value of the binding energy of the fourth water molecule was surprising, it was also calculated using the PBE, HSE06 and RPA methods (see appendix B.3) and compared to published values. The optB86b functional shows a general overestimation of the hydrogen bond strength, while all other methods predict a value of around $0.75\,eV$ (see table C.1). Piskorz et al. [136] and Korhonen et al. [137] both report similar binding energies compared to the PBE values obtained in this work using the PW91 and PBE functionals, respectively. The over-binding of the optB86b functional is also indicated by the high formation energy of bulk water (see appendix C) compared to other functionals.

Hydroxylated $m(\bar{1}11)$ Surface

As noted before, the 2-fold coordinated oxygen atom present at the $m(\bar{1}11)$ ZrO_2 bulk surface facilitates the dissociation of adsorbed water molecules. At higher coverages the adsorption energy of additional water molecules is reduced since this site is already occupied. To test this reduction at low coverage one more hydrogen atom was added to the unit cell used to calculated molecular adsorption at ¼ ML coverage to form a surface hydroxyl at the 2-fold coordinated surface oxygen. As the reference structure of the substrate to calculate the adsorption energies the hydroxylated ZrO_2 slab was fully relaxed. Again, the lack of accessibility of one Zr site result in three distinct adsorption sites, shown in fig. 4.12. Comparing the calculated adsorption energies (see table 4.7) with the un-hydroxylated case discussed in section 4.2.1 shows that the two adsorption sites P1 and P3 result in a reduction of the binding energy of $114\,meV$ and $149\,meV$, respectively. For the third site P2 this reduction of the predicted adsorption energy was only $10\,meV$. The reason lies in the distance between surface hydroxyl and adsorbed H_2O molecule. As can be seen in figs. 4.12a and 4.12c both adsorption sites P1 and P3 are
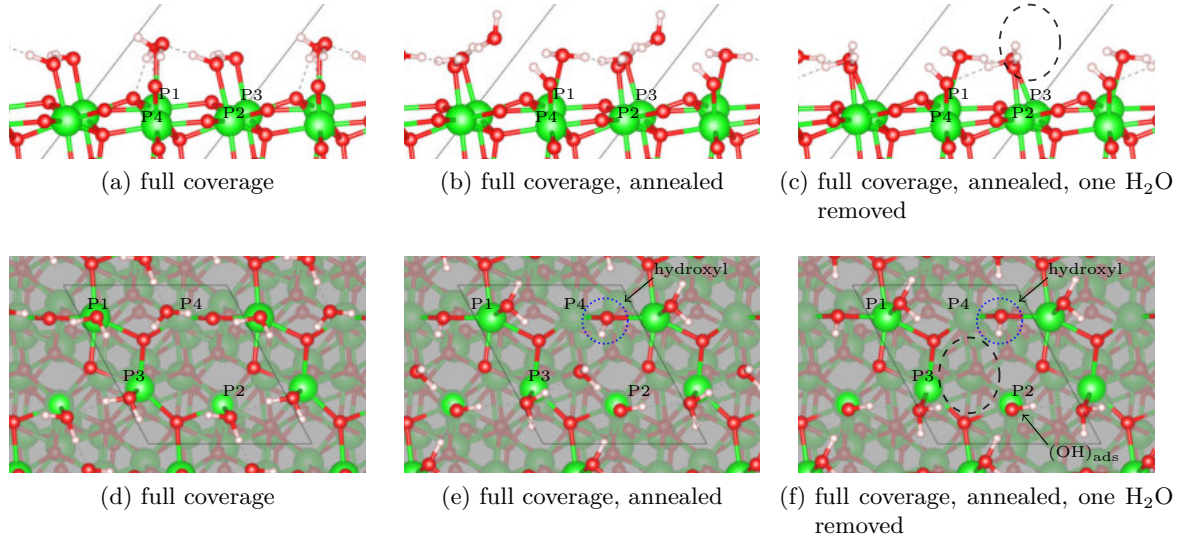
Figure 4.11.: Full coverage (1 ML) of water adsorbed on the m($\bar{1}$11) surface model. (a), (d): molecular adsorption; (b), (e): after simulated annealing, one H_2O is dissociated; (c), (f): after simulated annealing, one H_2O removed (dashed circle).

located very close to the surface hydroxyl (O_{H_2O}–$O_{Surface}$ distance of 2.854 Å and 2.887 Å for P1 and P3, respectively), while site P2 is located much farther away (3.771 Å). The strongest binding of the adsorbed H_2O is predicted for site P3, mainly because there an additional hydrogen bond is formed from the adsorbed H_2O to the surface oxygen of the surface hydroxyl. That hydroxyl is rotated away from the adsorption site. As mentioned before, site P2 shows almost the same adsorption energy compared to the un-hydroxylated surface. The weakest binding of the adsorbed water molecule is found at site P1. Here no hydrogen bond is formed to the surface and the water molecule is rotated perpendicular to the surface with its oxygen atom closest to the Zr atom.

At full coverage, defined as the adsorption of four H_2O molecules per surface unit cell, all H_2O stay intact. Three water molecules are located at the three adsorption sites above Zr atoms in fairly flat configurations (see fig. 4.13). The fourth H_2O adsorbs in an upright position in the vicinity of the fourth surface Zr which is buckled downwards and forms a hydrogen bond to the surface hydroxyl close by. Another hydrogen bond is formed to the H_2O molecules adsorbed at sites P2 and P3. The predicted mean adsorption energy per H_2O calculated with the optB86b functional is -0.931 eV. Here the reduction of the binding energy is 256 meV per H_2O compared to the clean m($\bar{1}$11) surface.

Similar to adsorption on the pristine surface, discussed in the previous section, the overestimation of the H–O binding energy of the optB86b functional yields inflated

adsorption energies, especially at full coverage (see section 4.2.1 and appendix B.3).

Table 4.7.: Adsorption energy in eV per water molecule on the hydroxylated m($\bar{1}$11) ZrO$_2$ bulk surface. The calculations were performed with the optB86b functional.

E$_{\text{Ads}}$ [eV]	molecular
m($\bar{1}$11), +1 H, P1	−0.771
m($\bar{1}$11), +1 H, P2	−0.833
m($\bar{1}$11), +1 H, P3	−0.923
m($\bar{1}$11), +1 H, full coverage	−0.931

(a) P1, hydroxylated, molecular (b) P2, hydroxylated, molecular (c) P3, hydroxylated, molecular

(d) P1, hydroxylated, molecular (e) P2, hydroxylated, molecular (f) P3, hydroxylated, molecular
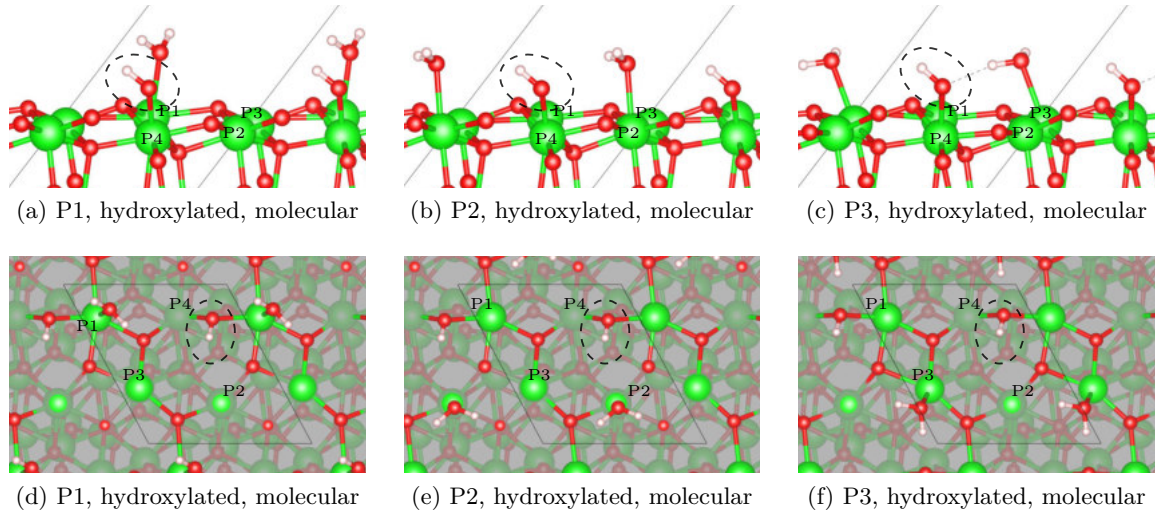
Figure 4.12.: Side and top views of one H$_2$O adsorbed on the hydroxylated m($\bar{1}$11) surface (¼ ML coverage). In all cases the 2-fold coordinated surface oxygen is passivated and the water adsorbs as an intact molecule. Only at site P3 the shorter distance to the surface hydoxyl enables formation of an additional hydrogen bond. Site P4 is again not accessible enough to enable water adsorption. The surface hydroxyl is indicated by a dashed circle.

4.2.2. Adsorption on Ultra-thin ZrO$_2$ Films: $\sqrt{3}$ Model

To study the adsorption properties of water molecules on the ultra-thin oxide film different computational models were chosen. As a first step, the ZrO$_2$/Pt/Pt$_3$Zr models introduced in section 3.2.3 were used. These structures have demonstrated quite well their ability to describe the experimental structure, recovering the measured buckled

(a) full coverage, hydroxylated, side view   (b) full coverage, hydroxylated, top view
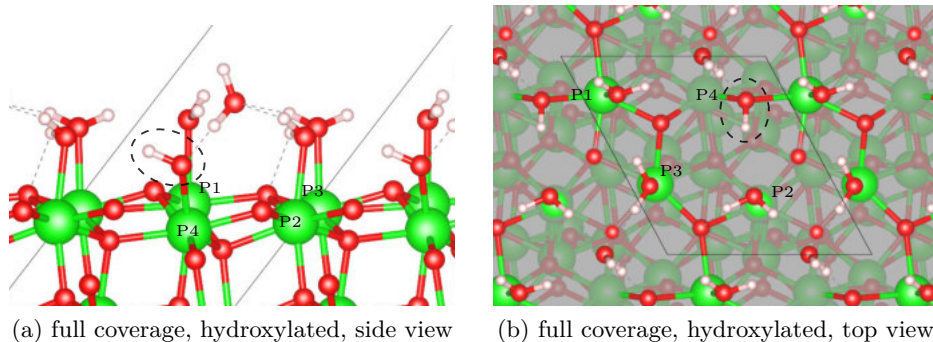
Figure 4.13.: Side and top views of four H_2O adsorbed on the hydroxylated m($\bar{1}$11) surface (1 ML coverage). The 2-fold coordinated surface oxygen is passivated and all water molecules adsorb as intact molecules. At sites P1-P3 the H_2O are located directly above the respective surface Zr while at site P4 the distance to the Zr is much larger and the H_2O forms a hydrogen bond with the surface hydroxyl. The surface hydroxyl is indicated by a dashed circle.

nature of the oxide film. Therefore, it is instructive to study the adsorption behaviour of H_2O molecules on both the compressed and the expanded $\sqrt{3}$ model cells. For the expanded model the oxide lattice constant is identical to the slightly compressed bulk c(111) model introduced in section 4.2.1.

The surface structure of the oxide film in both $\sqrt{3}$ model cells is fairly similar to the cubic c(111) case discussed before, except for the additional buckling due to the oxide-metal interface. The buckling of the oxide film decreases the symmetry of the surface compared to the cubic surface unit cell, yielding three different adsorption sites. This arises from the downwards displacement of one Zr atom, while the other two move upwards for the compressed $\sqrt{3}$ model. In the expanded case all three Zr atoms at the surface are found at different heights. As described before (section 3.2.3), both models consist of a single ZrO_2 trilayer adsorbed on a Pt-terminated Pt_3Zr substrate.

⅓ ML Coverage

As a first step, molecular adsorption at different adsorption sites was studied for ⅓ ML coverage with one H_2O adsorbed at the oxide surface of the $\sqrt{3}$ model cell. To scan the adsorption sites, the intact water molecule was placed on top of a surface Zr atom in a similar arrangement as for the cubic c(111) surface. In this initial configuration the water molecule is positioned at a distance of 2.100 Å from the Zr atom with its H atoms at the same height as its O atom. The hydrogen bonds were pointed towards surface oxygen atoms, just like on the c(111) surface. The same process was repeated for the other two adsorption sites and for both the compressed and the expanded model.

Finally, all structures were relaxed with the optB86b functional. To achieve electronic convergence, a $6 \times 6 \times 1$ Γ-centred $\vec{k}$-point grid and an energy cutoff of $400\,\text{eV}$ were chosen.

The full relaxation of the structures reveals that the H_2O in all cases adsorbs as an intact molecule. From the comparison of the calculated adsorption energies it is evident that one of the adsorption sites is more favourable than the two others for both compressed and expanded $\sqrt{3}$ model, see fig. 4.14. This site (P1) has one of the upwards buckled Zr atoms below which is located in a hollow position with respect to the Pt layer of the substrate. The second most favourable adsorption site P2 has a similar local environment, the only difference to P1 is that in the first sublayer of the substrate a Zr atom is located below the oxides Zr. The least favoured site (P3) is located above a Zr of the oxide which buckles downwards due to its stronger interaction with the Pt substrate and thus is less accessible. For the compressed $\sqrt{3}$ model, the energy penalty of adsorption site P2 and P3 compared to P1 are $58\,\text{meV}$ and $371\,\text{meV}$, respectively. At the expanded lattice constant, the same sites incur adsorption energy differences of $102\,\text{meV}$ and $557\,\text{meV}$.

At the most favourable site the distances between the oxygen of the H_2O molecule and the Zr atom below are $2.349\,\text{Å}$ and $2.288\,\text{Å}$ for the compressed and expanded model, respectively. The H_2O is just slightly tilted from the oxide surface, by $1.9°$ and $2.0°$ for the two respective models. The molecule is slightly less bent, $107°$ and $109°$ compared to $105°$ for the free molecule. In all cases the H–O bond lengths are $0.988\,\text{Å}$. As can be seen in figs. 4.14c and 4.14d, the adsorbate slightly modifies the oxide: the Zr it binds to is pulled upwards slightly while another Zr in a Pt hollow site is pushed downwards. At site P3 this effect weakens the Zr–Pt bond between oxide film metal substrate and makes this site less favoured than the other two. The buckling of the Zr layer is slightly increased from $65\,\text{pm}$ to $81\,\text{pm}$ in the compressed model and from $43\,\text{pm}$ to $53\,\text{pm}$ in the expanded model.

In all cases, the adsorbed H_2O monomer shows a bright feature in STM simulations at both positive and negative bias voltages (see fig. 4.15). The exact shape of this feature depends on the rotation of the molecule and the lattice constant of the oxide: for the compressed $\sqrt{3}$ model (figs. 4.15a to 4.15d), the water adsorbate shows a bright, moon shaped feature mainly caused by the oxygen. In the occupied states, the H atoms of the molecularly adsorbed H_2O contribute to the bent shape of the feature, while in the unoccupied states the upwards buckled Zr atom also contributes. This pattern is not that pronounced for dissociative adsorption since here the hydrogen atom of the $(OH)_{ads}$ sticks out. For the expanded $\sqrt{3}$ model (figs. 4.15e to 4.15h) the bright spot which indicates the water molecule shows much higher contrast compared to the oxide surface. Here the molecularly adsorbed water exhibits an almost completely round bright spot at both positive and negative bias voltages. For the dissociated configuration the $(OH)_{ads}$ causes the round bright spot while the surface hydroxyl is only slightly visible in between.

(a) P1, top view

(b) P3, top view

(c) P1, side view
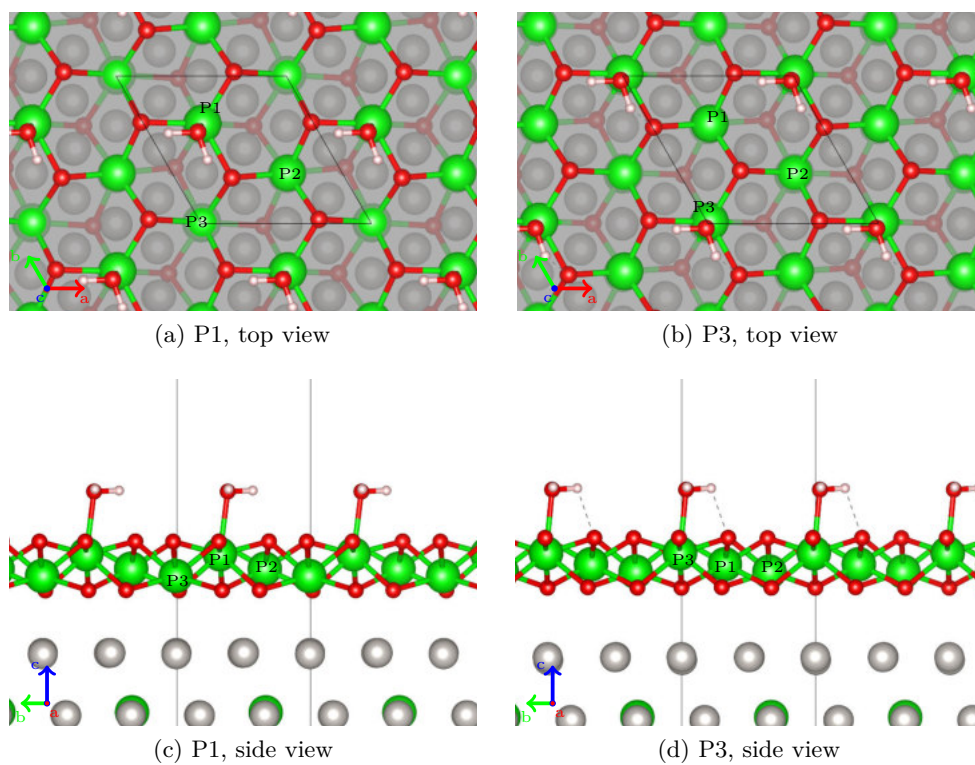
(d) P3, side view

Figure 4.14.: One H$_2$O molecule adsorbed on the ultra-thin $\sqrt{3}$ model cell. Top row: molecular adsorption, top view; bottom row: side view. Zr, O, H are coloured green, red, and white. the hydrogen bond is indicated by the dashed line.

(a) mol., Bias: $+0.5\,\mathrm{V}$ (b) mol., Bias: $-0.5\,\mathrm{V}$ (c) dis., Bias: $+0.5\,\mathrm{V}$ (d) dis., Bias: $-0.5\,\mathrm{V}$

(e) mol., Bias: $+0.5\,\mathrm{V}$ (f) mol., Bias: $-0.5\,\mathrm{V}$ (g) dis., Bias: $+0.5\,\mathrm{V}$ (h) dis. , Bias: $-0.5\,\mathrm{V}$
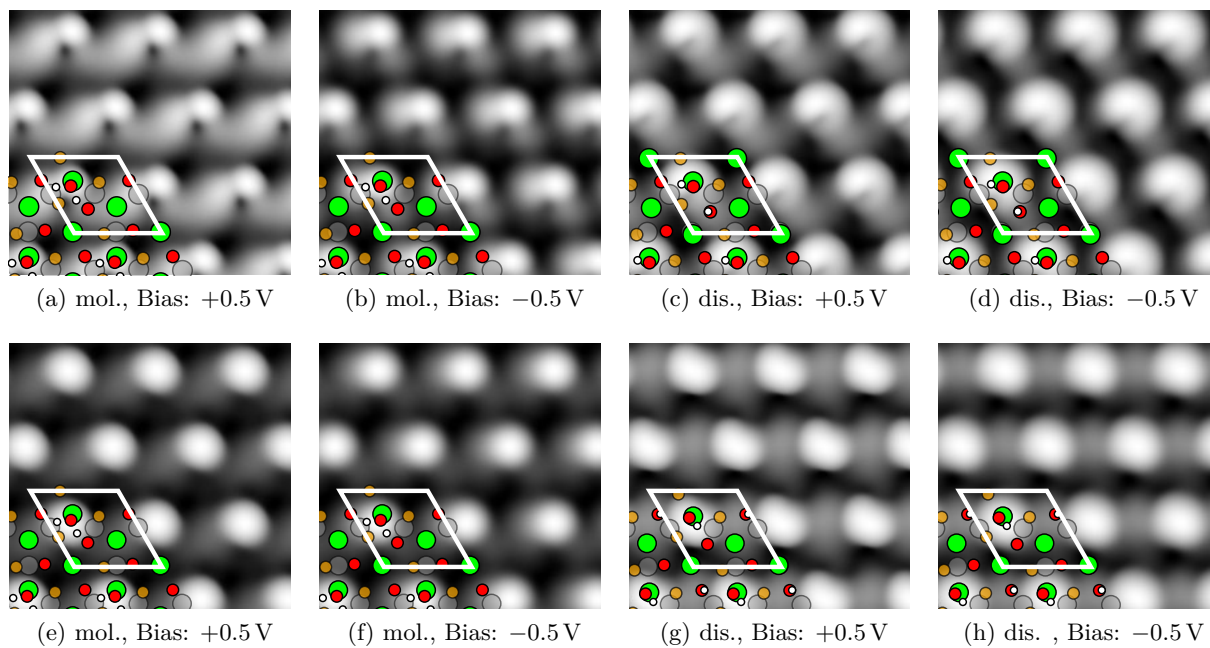
Figure 4.15.: STM Simulations of one H_2O adsorbed on the $\sqrt{3}$ model cell at $\pm 0.5\,\mathrm{V}$ bias voltage. Top row: compressed model, bottom row: expanded model. The H_2O is indicated by the bright feature like in the experiment (see fig. 4.7).

Higher Coverage

To study higher coverages of water an additional water molecule was added to the system raising the coverage to ⅔ ML. Taking all three possible adsorption sites of the $\sqrt{3}$ model into account there are three possible combinations of sites: P1+P2, P1+P3, and P2+P3, in the same naming convention used before.

For the compressed $\sqrt{3}$ model, depicted in fig. 4.16, the addition of the second H_2O leads to much different adsorption configurations: in the most favourable structure (P1+P3) the H_2O adsorb molecularly with an averaged adsorption energy of $-0.892\,\text{eV}$. While one H_2O molecule adsorbs on top of a Zr atom as in the case of ⅓ ML coverage, the second H_2O is rotated so that one O–H bond points downwards to a surface O atom. It is also displaced to a site above this oxygen atom. The distance to the first H_2O is $1.755\,\text{Å}$, whose hydrogen "legs" rotated upwards and form a hydrogen bond to the second water molecule. Therefore, the two water molecules form a 2D structure which is bound to the oxide only by one Zr–O and one O–H bond. For the second most favoured arrangement, P2+P3, the configuration is almost identical. The slight energy difference to the previous model comes from the different Zr atom that the H_2O is bound to. In both cases, the rotates molecule was initially placed above the downwards buckled Zr. in the least favoured structure with an averaged adsorption energy of $-0.774\,\text{eV}$ both H_2O adsorb on top of Zr atoms which are initially buckled upwards. This compounds the fact that a downward buckling of the Zr atom greatly reduces its accessibility.

As shown in fig. 4.17 the expanded model shows similar behaviour. As for the adsorption of a single molecule, the H_2O molecules bind more strongly to the oxide film compared to the compressed model, indicating an increased reactivity of the oxide film at the expanded lattice constant. The two configurations where the second H_2O molecule was initially placed above the downwards buckled Zr this H_2O also rotates and forms mentioned 2D structure. Here, the hydrogen bond between the two water molecules is slightly shorter at $1.544\,\text{Å}$. However, the P1+P2 configuration yields a completely different result. Here, the water adsorbs in a mixed molecular and dissociated configuration. The H_2O positioned at site P2 dissociates, its $(OH)_{ads}$ component binds to the Zr atom at a distance of $2.128\,\text{Å}$. The split off hydrogen atom forms a surface hydroxyl with a surface O close by and forms a hydrogen bond to the $(OH)_{ads}$ ($1.793\,\text{Å}$). Compared to ⅓˜,ML coverage, the intact molecule is rotated upwards and also forms a hydrogen bond with the $(OH)_{ads}$ ($1.646\,\text{Å}$).

At full coverage of the $\sqrt{3}$ surface the trend continues. The compressed model shows the formation of a water film where two H_2O molecules are bound to the Zr atoms and the third just by a hydrogen bond to a surface oxygen atom. The average adsorption energy is slightly lower at $-0.804\,\text{eV}$, indicating repulsive interaction of the water molecules. At the experimental lattice constant the higher reactivity of the oxide film again causes spontaneous dissociation of one H_2O molecule, resting in an arrangement similar to the P1+P2 configuration. The second water molecule is bound to a Zr atom of the oxide, while the third H_2O rotates upwards and forms hydrogen bonds to a surface oxygen atom and the surrounding H_2O and $(OH)_{ads}$ remnant. Again the mean adsorption energy is lowered due to the repulsive interaction between the water molecules.

(a) 2 H$_2$O, P1+P2

(b) 2 H$_2$O, P1+P3

(c) 2 H$_2$O, P2+P3

(d) 3 H$_2$O, P1+P2+P3
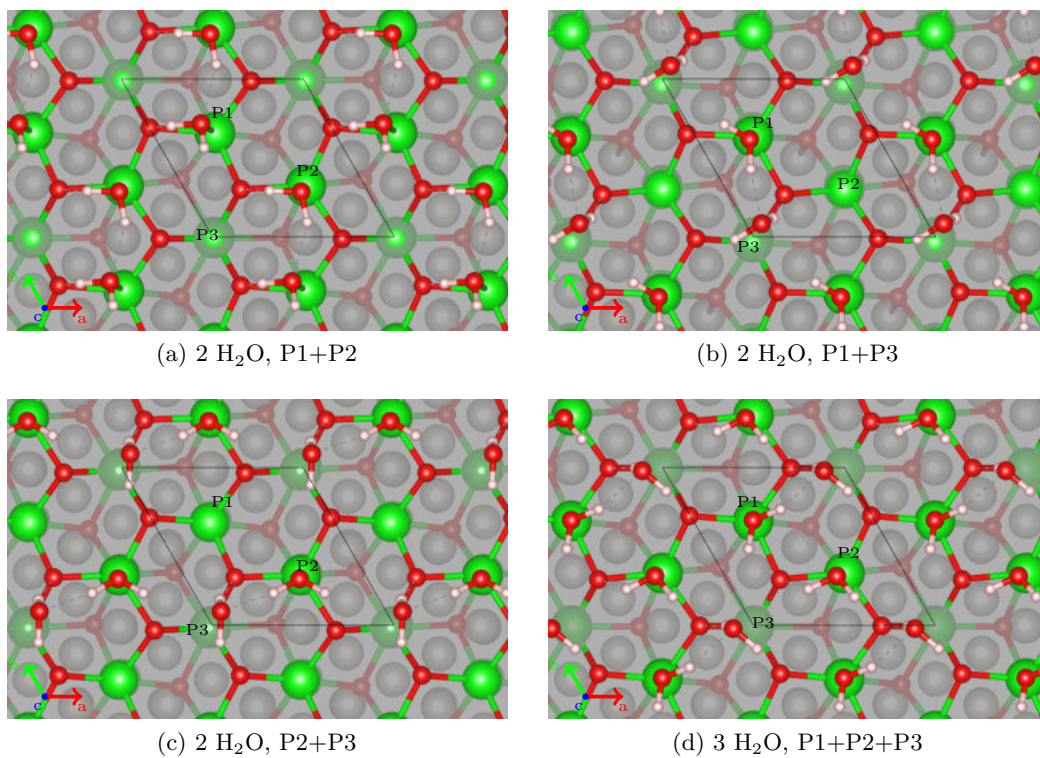
Figure 4.16.: Two ((a)-(c)) and three ((d)) H$_2$O molecules adsorbed on the compressed ultra-thin $\sqrt{3}$ model cell. Zr, O, H are coloured green, red, and white.

(a) 2 H$_2$O, P1+P2

(b) 2 H$_2$O, P1+P3

(c) 2 H$_2$O, P2+P3

(d) 3 H$_2$O, P1+P2+P3
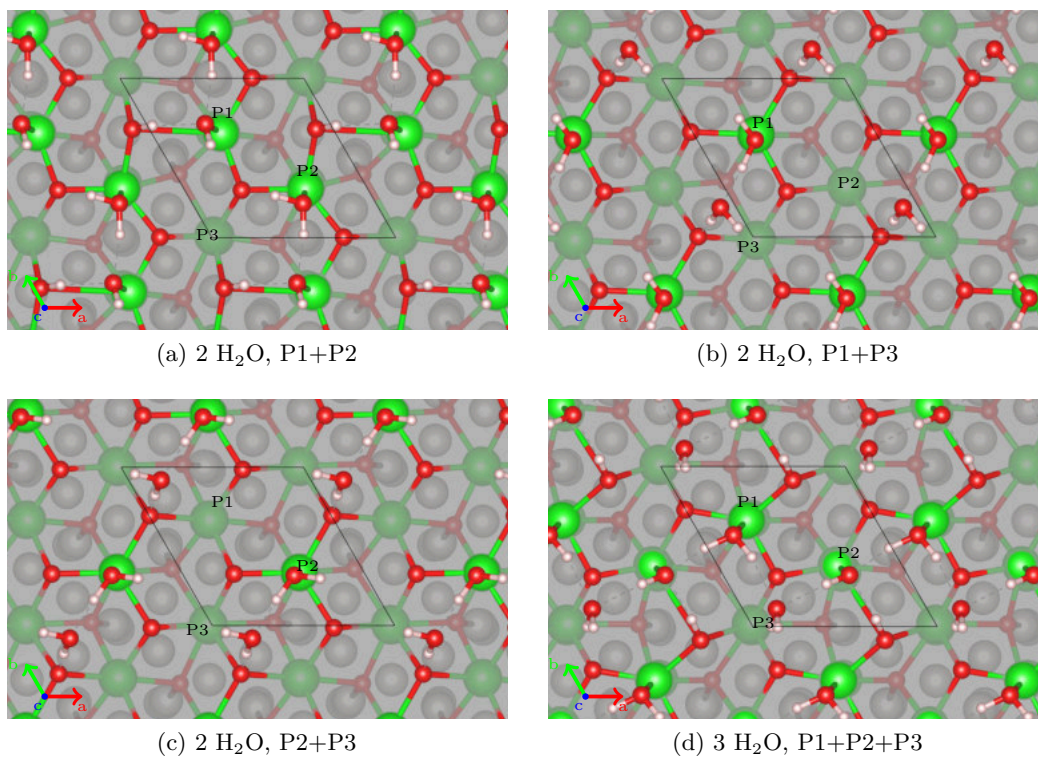
Figure 4.17.: Two ((a)-(c)) and three ((d)) H$_2$O molecules adsorbed on the expanded ultra-thin $\sqrt{3}$ model cell. At full coverage ((d)) the molecule adsorbed at P2 dissociates spontaneously. Zr, O, H are coloured green, red, and white.

Dissociative Adsorption

The previous studies of molecular adsorption of H_2O molecules have shown that at the expanded lattice constant, the H_2O molecule might dissociate spontaneously. To further test the stability of this dissociative state, H_2O was also placed in different dissociated configurations on the oxide surface. The starting point was the most favourable adsorption configuration found for molecular adsorption, P1 for both lattice constants. Then, one hydrogen atom was moved towards a surface oxygen atom, manually creating a surface hydroxyl. Since there are three individual surface oxygen atoms in the surface unit cell this process yielded three different initial models. The dissociation barrier was calculated using the improved dimer method[2].

The calculated adsorption energies, listed in table 4.8, show that the compressed oxide film (see figs. 4.18a and 4.18c) is completely passive as all dissociative adsorption configurations are >0.1 eV less favoured than molecular adsorption. Additionally, the molecules are further thermodynamically stabilised by a small barrier of 0.258 eV. The DFT calculations predict the opposite for the expanded oxide film (see figs. 4.18b and 4.18d), here all studied dissociative structures show >0.4 eV stronger bonding than molecular adsorption. As shown in table 4.8, the position of the surface hydroxyl with respect to the residual $(OH)_{ads}$ does not significantly influence the adsorption energies, since due to the limited size of the $\sqrt{3}$ model cell all possible surface oxygen are close to the adsorption site of the $(OH)_{ads}$. For the expanded model, the simulations predict a dissociation barrier of 0.582 eV.

4.2.3. Ultra-thin ZrO$_2$ film: $\sqrt{19}$ model

The H_2O adsorption studies on the $\sqrt{3}$ model cell has shown to be quite useful, but the model still suffers from the large lattice mismatch compared to the experimentally measured oxide film. Therefore, the studies were also performed on the more realistic $\sqrt{19}$ model cell. While this model yields too large buckling and lateral distortions, the model offers a large number of possible adsorption sites with different local geometries. The valley sites offer laterally stretched areas where both oxygen and zirconium atoms are accessible, reproducing parts of the experimental film which are located at displacement lines [77]. Additionally, though the slightly compressed $\sqrt{19}_{comp}$ model underestimates the experimental lattice constant, the buckling of the oxide film is much less pronounced, matching the experimental findings in the areas in between the ridge lines of the substrate quite well (see section 3.3.3).

To model the adsorption geometries of water molecules the H_2O was placed in an intact molecular configuration on a 6×6 grid of adsorption sites on both $\sqrt{19}$ and $\sqrt{19}_{comp}$ model cells, similar to the metal adsorption studies discussed in section 4.1.3. Figure 4.19 shows a sketch of the initial adsorption pattern on the $\sqrt{19}$ model cell. Additionally, for the $\sqrt{19}$ model, a few individual sites were studied more closely where the water molecule was positioned manually. A select number of high coverage configurations were also studied.

---

[2]VASP setting: IBRION = 44

(a) 1 dissoc. H_2O, compressed $\sqrt{3}$ (b) 1 dissoc. H_2O, expanded $\sqrt{3}$

(c) 1 dissoc. H_2O, compressed $\sqrt{3}$ (d) 1 dissoc. H_2O, expanded $\sqrt{3}$
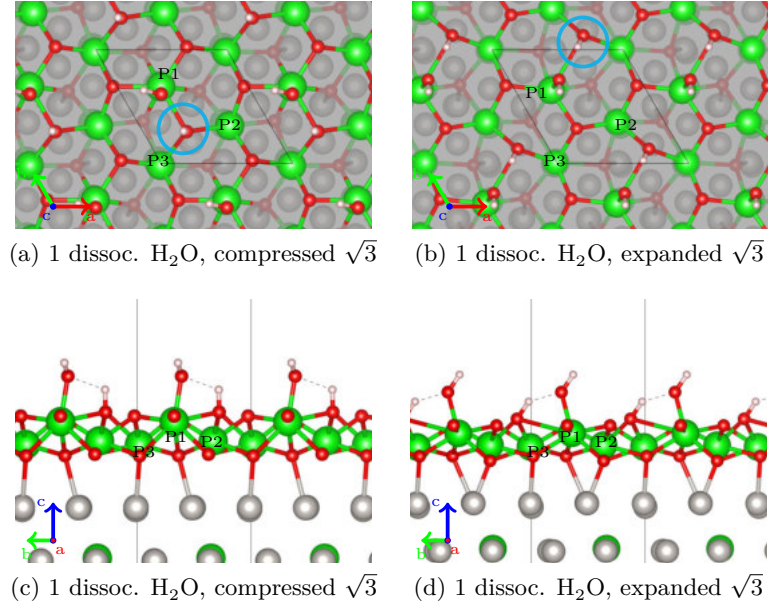
Figure 4.18.: One dissociated H_2O molecule adsorbed on the ultra-thin $\sqrt{3}$ model cell. Zr, O, H are coloured green, red, and white. The surface hydroxyl is indicated by a blue circle.

Table 4.8.: Adsorption energy in eV per H_2O of water molecules adsorbed on the compressed and expanded $\sqrt{3}$ models.

E_{Ads} [eV]	compressed, 3.3 Å	expanded, 3.5 Å
	1 H_2O	
P1	-0.883	-1.113
P2	-0.825	-1.011
P3	-0.512	-0.556
$P1_{dissoc}$, O_1	-0.797	-1.536
$P1_{dissoc}$, O_2	-0.784	-1.512
$P1_{dissoc}$, O_3	-0.798	-1.535
$P1_{dissoc}$, Transition	-0.641	-0.535
	2 H_2O	
P1+P2	-0.774	-1.220
P1+P3	-0.892	-0.984
P2+P3	-0.864	-0.924
	3 H_2O	
P1+P2+P3	-0.804	-1.062
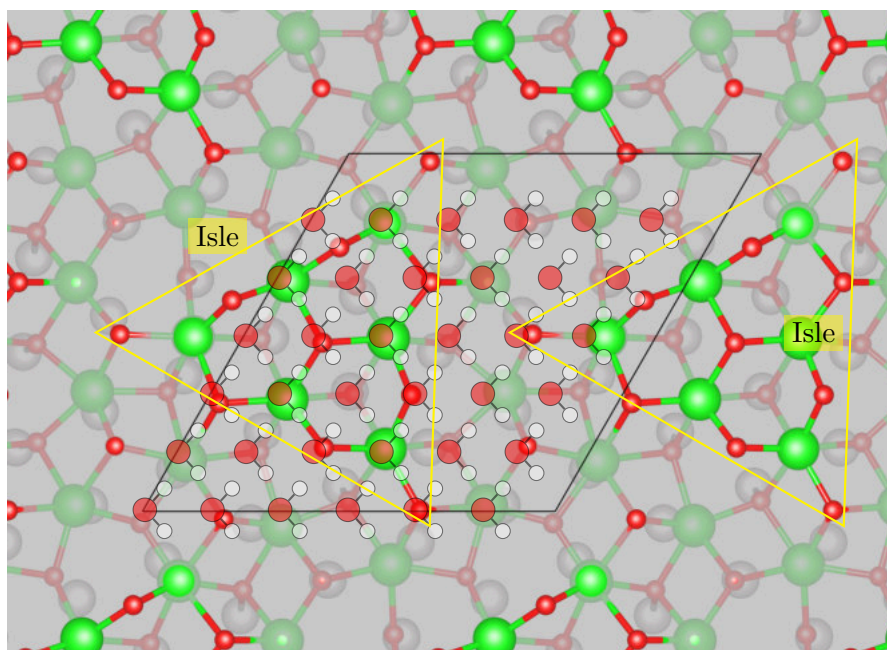
Figure 4.19.: Fully relaxed $\sqrt{19}$ model cell. Initial adsorption for the water molecules on the 6×6 sites are indicated by the sketched water molecules. The upwards buckled isle areas are indicated by the yellow triangles. Zr, O, and Pt are coloured green, red, and grey.

H$_2$O Monomer - Molecular Adsorption

On the $\sqrt{19}$ model cell at the Pt bulk lattice constant, after full relaxation of the 36 initial configurations only 8 distinct adsorption sites remain. At all adsorption sites the water molecule adsorbs in a molecular configuration. The analysis of the adsorption energies shows that the local configuration of the oxide film has a large influence on the strength of the water-oxide bond and that generally, three groups can be identified. The strongest binding energy of the H$_2$O to the surface, -0.986 eV to -0.709 eV, is found for adsorption at the "valley" sites where the oxide film shows the largest lateral distortion. Two factors play a role here: due to the stretching of the oxide film its zirconia atoms are more accessible since the height difference to the surrounding oxygen atoms is small and the Zr–O bonds are long. Additionally, the "valley" sites are surrounded by 2-fold coordinated oxygen atoms to which the adsorbed water molecules form hydrogen bonds to. The second group of adsorption sites is located at the edge of the "isle" area of the oxide film. There, the water molecule binds less strongly, showing adsorption energies of -0.629 eV to -0.527 eV. At these sites the H$_2$O molecule still forms the hydrogen bond to a close by 2-fold coordinated surface oxygen atom, but the molecule is located on top of a zirconium atom at the compressed isle area of the oxide. Finally, the water molecule can also adsorb on top of the isle area without forming a hydrogen bond to a 2-fold coordinated oxygen atom. At these sites the adsorption energy is just -0.497 eV to -0.394 eV. In the following paragraphs, for the sake of brevity a detailed description of a couple of selected adsorption sites will be given. For an overview of the different sites see fig. 4.21a and table 4.9.

At the most stable adsorption site on the $\sqrt{19}$ model, indicated in red in fig. 4.20, the water molecule adsorbs molecularly on top of a Zr atom in a valley site where the oxide film is heavily stretched with an adsorption energy of -0.986 eV. The H$_2$O molecule is rotated so that one hydrogen atom is pointed towards a under-coordinated surface oxygen atom nearby. The other hydrogen atom is tilted by 30.6° with respect to the oxide surface. The distance of the first hydrogen to the 2-fold coordinated surface oxygen atom is 1.430 Å while the O$_{H_2O}$ is located 2.229 Å above a surface Zr. The second hydrogen is rotated towards another 3-fold coordinated surface oxygen but the distance of 2.441 Å is too far to form a hydrogen bonds. During the scan of the adsorption energy landscape, two more adsorption sites with almost identical properties were found, indicated in light blue in fig. 4.20. The adsorption energies at these sites are almost identical to the most stable site at -0.955 eV and -0.973 eV, as are the atomic distances between adsorbate and neighbouring oxygen atoms. In all those cases, the adsorption of the H$_2$O modifies the ZrO$_2$ film: the Zr atom it binds to is slightly pulled upwards and the buckling of the Zr layer is increased to 107 pm.

At other valley sites the adsorbed water molecule adsorbs more weakly, in the range of -0.812 eV to -0.709 eV, coloured magenta in fig. 4.20. At the first site where the adsorption energy is -0.812 eV the local environment of the adsorbed H$_2$O is almost identical to sites with stronger adsorption (red and light blue in fig. 4.20), but the H–O distance to the nearby 2-fold surface oxygen is larger at 1.500 Å. For the other two sites which show adsorption energies of -0.723 eV and -0.709 eV the H$_2$O is positioned

slightly farther above the surface Zr at a distance of 2.251 Å and 2.257 Å, respectively.

Water molecules adsorbed at the edge of the isle area are adsorbed much more weakly in the range of $-0.629\,\text{eV}$ to $-0.547\,\text{eV}$. In fig. 4.20 they are coloured dark green. At the most favourable site the water molecule is positioned 2.34 Å above a Zr atom which is buckled upwards and part of the isle area. Again, one hydrogen atom is rotated towards a 2-fold coordinated surface oxygen atom, but here the distance is decisively larger at 1.91 Å. The other H–O bond of the water molecule is rotated by 31.1° from the surface plane. The reduction of the adsorption energy is caused by the lack of the additional hydrogen bond, since configuration with the H_2O adsorbed at the same Zr site but rotated upwards so that its H–O bonds are tilted by 13.9° and 41.0° from the surface gives the same adsorption energy.

The last group of adsorption sites show an even larger reduction in the adsorption energy to -0.497, to -0.394, coloured yellow in fig. 4.20. These sites are also located on top of the isle area but the water molecule is fully rotated towards the middle of the triangular isle, in contrast to the "isle edge" sites. Additionally, there is no 2-fold coordinated surface oxygen close by. At the most favourable site of this type, designated D_1, the water molecule adsorbs 2.36 Å above surface Zr which is buckled upwards and part of the "isle" area. The H_2O is adsorbed almost flat, the angles of the H–O bonds to the surface plane are just 7° and 17.3°. While the adsorbate is rotated to that its H–O bonds point in the direction of 3-fold coordinated surface oxygen close by the H–O_{surf} distances are quite large at 2.11 Å and 2.31 Å with the closer O_{surf} being located at the centre of the upwards buckled ZrO_2 isle.

Generally, the adsorbate can cause a modification of the ZrO_2 film. The H_2O molecule tends to pull out the Zr atom it binds to by up to 43 pm. Additionally, depending on whether the water forms a hydrogen bond with a surface oxygen, the positions of the under-coordinated surface oxygen inside the unit cell can change, but the total number is always four. This indicates a very high softness and flexibility of the oxide film.

Water molecules adsorbed on the compressed $\sqrt{19}_{comp}$ model also show a large spread of adsorption energies. Compared to the $\sqrt{19}$ model, these values range from $-0.849\,\text{eV}$ to $-0.162\,\text{eV}$, indicating slightly weaker binding to the compressed oxide film. Again, the sites where the H_2O binds more strongly to the adsorbate are found in the valley areas of the ZrO_2 film, which also exist in the $\sqrt{19}$ model but the lateral distortions within the film are lower (see section 3.3.3). Upon scanning the grid of adsorption sites the water molecules did not adsorb at valley sites, but moved towards the upwards buckled isle sites, testament to the decreased accessibility of these sites. Hence, an additional H_2O molecule was manually placed at two the two most promising valley sites, where finally the most reactive sites were found.

At the most favoured adsorption site ($E_{Ads} = -0.849\,\text{eV}$) the local adsorption configuration is almost identical to the case of the $\sqrt{19}$ model: the H_2O molecule is rotated so that one hydrogen points towards a 2-fold coordinated surface oxygen with an H–O_{sub} distance of 1.55 Å. The other H–O bond is rotated towards another surface oxygen with a distance of 2.31 Å. At this adsorption site the adsorbate is located 3.54 Å above the oxide film Zr. All other adsorption sites have an adsorption energy which is almost 80 meV
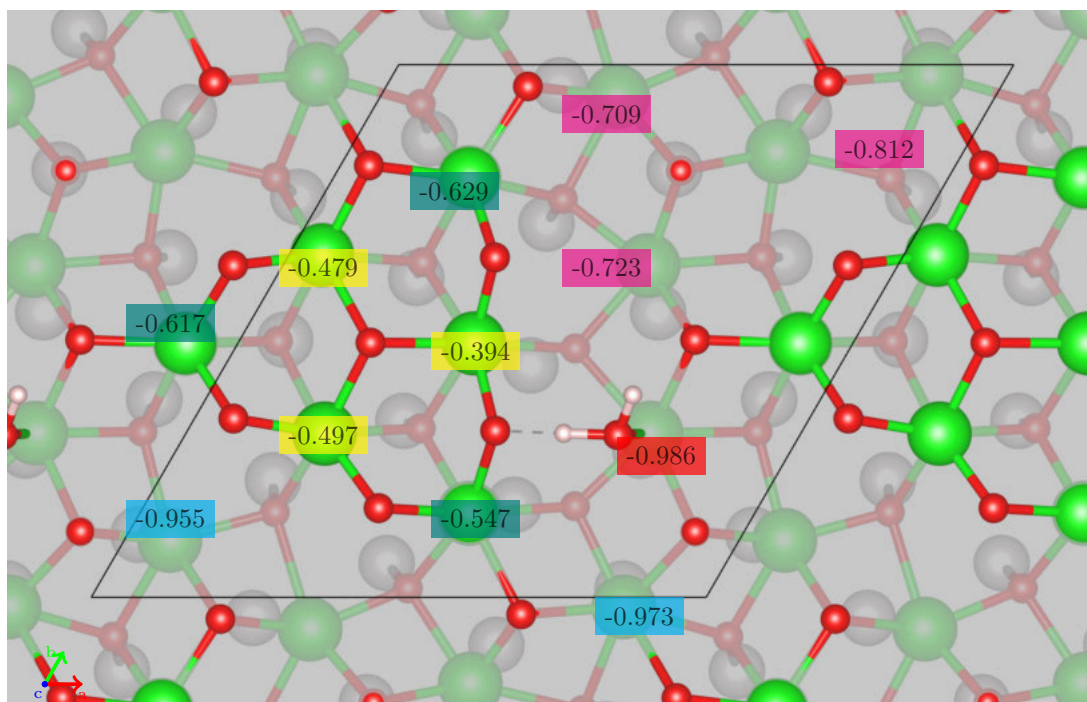
(a) H$_2$O monomer on $\sqrt{19}$

Figure 4.20.: Adsorption energies of a single H$_2$O molecule adsorbed on the $\sqrt{19}$ model cell. The H$_2$O at the most favoured site with an E$_{Ads}$ = -0.986 eV is shown next to the red label.

lower. Two different sites which have similar adsorption energies of about $-0.75\,$eV are found, one in the second valley site and another at the edge of an isle. Just like with the $\sqrt{19}$ model, depending on the local environment of the adsorption site the adsorption energy can be as low as $-0.162\,$eV.

The modification of the oxide film due to the H_2O adsorbate is more apparent in the compressed $\sqrt{19}_{comp}$ model: while initially no under-coordinated oxygen atoms were apparent, after adsorption there are three with one forming a hydrogen bond to the water molecule.

In all cases, the STM simulation of the adsorbed H_2O monomer shows the adsorbate as a bright spot in both the occupied and unoccupied states. Figures 4.22a and 4.22b shows the most stable adsorption site as an example: the bright spot appears centred on the adsorbed water molecule, slightly elongated into the direction of the tilted H–O bond. The second H–O bond hardly contributes to the bright spot. In the surrounding area, the surface oxygen are indicated by darker grey spots, grouped in a hexagonal flower-like structure indicating the upwards buckled ZrO_2 isle. Even darker grey spots indicate surface oxygen in the downwards buckled valley areas.

H_2O Monomer - Dissociative Adsorption

Dissociative adsorption was studied on both the $\sqrt{19}$ and $\sqrt{19}_{comp}$ model. To build the initial configurations, for both cases a few final structures with molecularly adsorbed water were selected and the water molecule was manually dissociated by moving one of its hydrogen atoms closer to a surface oxygen. On the $\sqrt{19}$ model, at the most favoured adsorption site for molecular adsorption, the dissociated H_2O is bound more strongly ($E_{Ads} = -1.045\,$eV) than the molecular H_2O by $61\,$meV. The hydrogen atom that forms the hydrogen bond to the 2-fold coordinated surface oxygen now forms a surface hydroxyl with a bond length of $1.02\,$Å. The distance to the remaining oxyl is $1.59\,$Å. A dissociation barrier of $67\,$meV was calculated with the improved dimer method[3]. It should be noted that the preference for the dissociative adsorption is much lower on other sites: another valley site with a molecular adsorption energy of $-0.746\,$eV has a much lower difference to dissociative adsorption energy of $-0.768\,$eV. Here the dissociation barrier is $30\,$meV. For the compressed $\sqrt{19}_{comp}$ model the most stable dissociated configuration has a calculated adsorption energy of $-0.930\,$eV, prolonging the pattern of reduction of the adsorption energy for a smaller lattice constant.

In the STM simulations of the dissociated water monomer shown in figs. 4.22c and 4.22d the pattern is almost identical to the molecularly adsorbed case as in both occupied and unoccupied states the $(OH)_{ads}$ is indicated by a bright feature. Since the bright feature indicating the adsorbed water molecule is mainly generated by the upwards rotated H–O bond the displacement of the second hydrogen which forms the surface hydroxyl does not change the bright spot significantly enough.

---

[3]VASP setting: IBRION=44

(a) H$_2$O monomer on $\sqrt{19}$

(b) H$_2$O monomer on $\sqrt{19}_{comp}$

(c) dissociated H$_2$O monomer on $\sqrt{19}$

(d) dissociated H$_2$O monomer on $\sqrt{19}_{comp}$
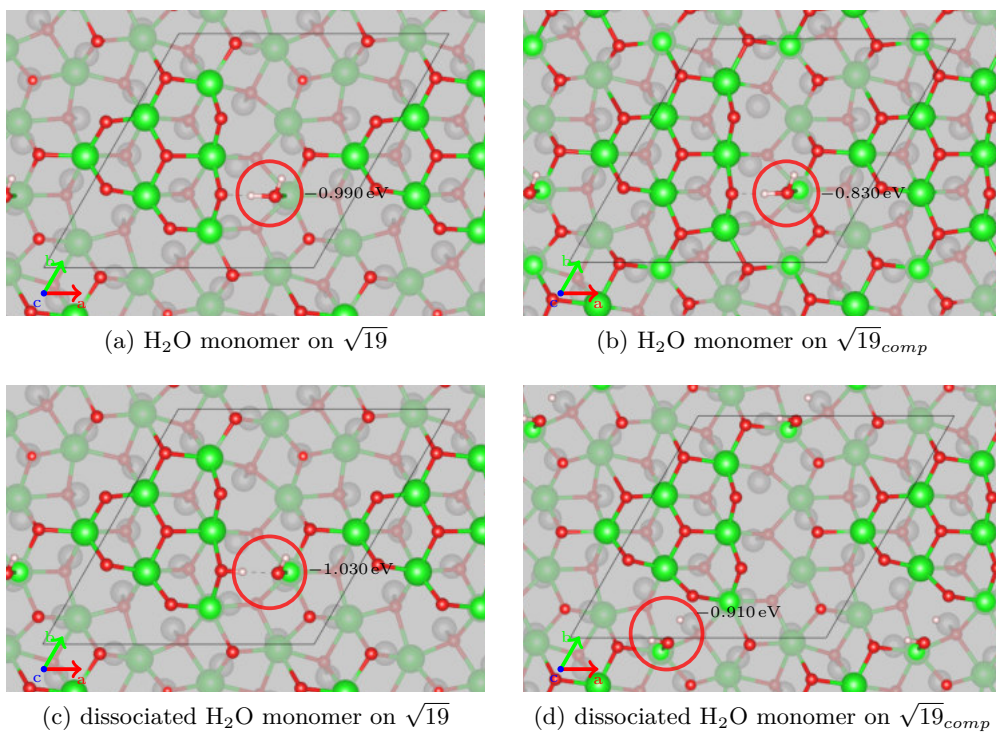
Figure 4.21.: Most favoured adsorption sites of a molecular and dissociated H$_2$O monomer on the $\sqrt{19}$ ((a), (c)) and $\sqrt{19}_{comp}$ ((b), (d)) model. Less favoured adsorption sites are labeled by coloured circles. The oxide structure in (a) and (b) is almost identical, except for there being less under-coordinated oxygen for the $\sqrt{19}_{comp}$ model.

(a) molecular, Bias: $+0.5\,\mathrm{V}$

(b) molecular, Bias: $-0.5\,\mathrm{V}$

(c) dissociated, Bias: $+0.5\,\mathrm{V}$

(d) dissociated, Bias: $-0.5\,\mathrm{V}$
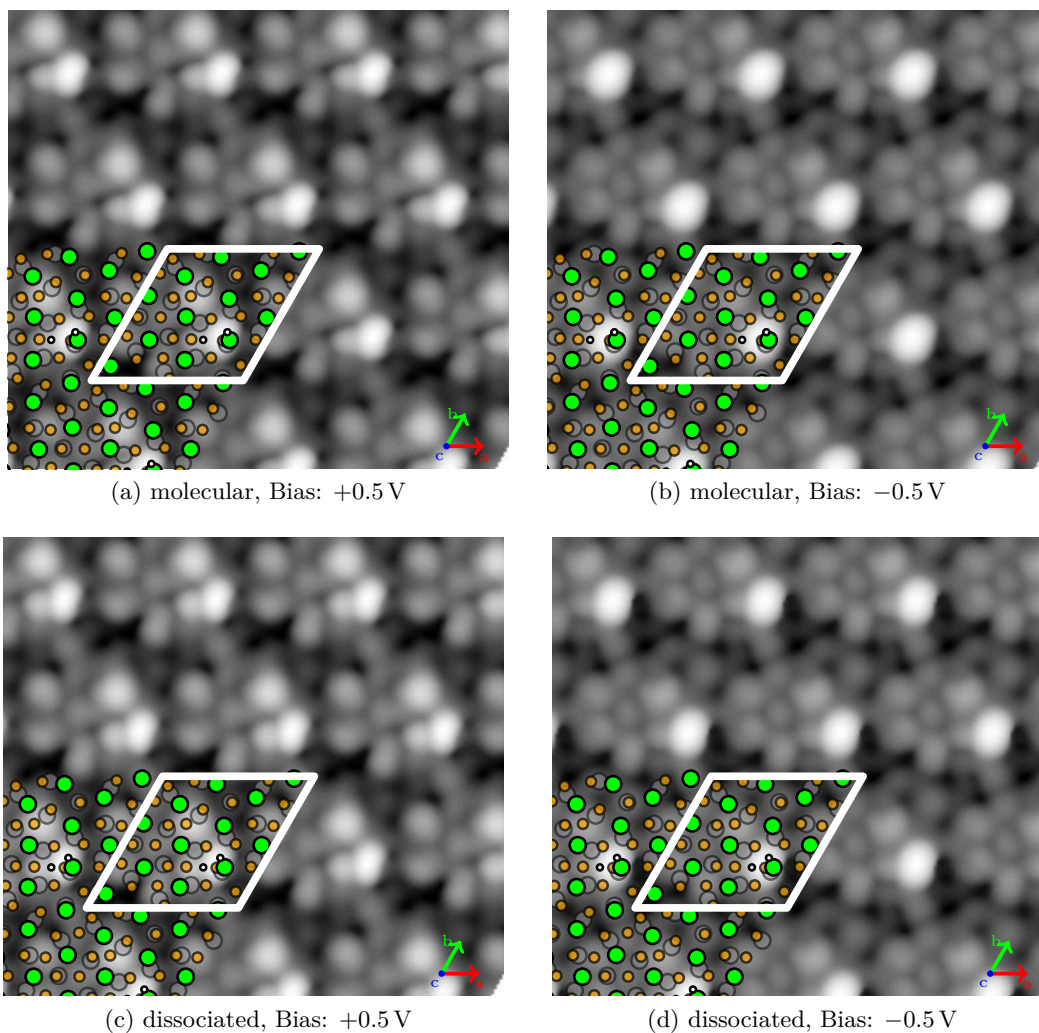
Figure 4.22.: STM Simulations of one H_2O adsorbed on the $\sqrt{19}$ model cell at $\pm0.5\,\mathrm{V}$ bias voltage. Top row: molecular, bottom row: dissociated adsorption. In both cases the bright spot indicating the adsorbed H_2O molecule is caused by the upwards rotated O–H part of the H_2O.

High Water Coverage

Higher coverages of water were tested by placing additional water molecules on the surface. The sites for these added molecules were chosen according to the previously found sites for the H_2O monomer calculations. On the $\sqrt{19}$ model, a single water molecule added at sites A_{2-4} to the most stable A_1 site yields an average adsorption energy between $-0.953\,\text{eV}$ to $-0.669\,\text{eV}$. Two H_2O molecules are therefore $0.04\,\text{eV}$ to $0.10\,\text{eV}$ more strongly bound compared to the average adsorption energy of the monomer at the respective sites. This difference is largest for a configuration where the two H_2O are adsorbed at neighbouring sites, indicating attractive interaction between the water molecules. In the next step a higher coverage of water was studied. To determine the maximum amount of water molecules that can be placed on the $\sqrt{19}$ model, initially all eight distinct adsorption sites found during the monomer scan were occupied. In all cases the H_2O adsorbs as an intact water molecule. Relaxation of this structure leads to an adsorption configuration where all water molecules are grouped on top of the isle area. Except for two H_2O which are rotated vertically and adsorb above a 2-fold coordinated surface oxygen, the other six H_2O are located above upwards buckled Zr atoms. The mean adsorption energy per water molecule for this structure is $-0.622\,\text{eV}$, almost exactly the same as for the water monomers adsorbed at isle edge sites. Some of the H_2O are rotated towards each other and start to form 2-D structures. To determine the maximum water coverage, a succession of up to eight additional water molecules were added to the water superstructure. At a coverage of 12 H_2O one would expect that all Zr sites to be occupied, but the additional water molecules placed at valley sites rather start to form a water over-layer by formation of hydrogen bonds to H_2O adsorbed at isle Zr sites, see table 4.9. Five H_2O are positioned above buckled up Zr sites, but the remaining seven water molecules are connected to surface oxygen atoms by hydrogen bonds, forming a bridge over the oxide valley. The mean adsorption energy of this structure is $-0.680\,\text{eV}$, close to the predicted binding energy for hexagonal 1H bulk ice $(-0.740\,\text{eV})$. Adding more H_2O leads to the formation of an ice-like structure, still connected to the oxide surface via some molecules. The mean adsorption energy does not significantly change and shows just slight variance in the range of $30\,\text{meV}$. The surface area of the $\sqrt{19}$ model cell allows up to 15 H_2O to form a single water over-layer, and with each additional H_2O a second water layer starts to form.

On the compressed $\sqrt{19}_{comp}$ model, only three select structures including the full coverage structure, defined as one H_2O molecule per Zr site, were studied. Again, in all cases only molecular adsorption of the H_2O was found. After adsorption of 5 H_2O on top of isle sites four are located above isle Zr sites, while the remaining water molecule is connected to the oxide by a hydrogen bond in a valley site. The adsorption energy per H_2O of this structure is $-0.704\,\text{eV}$, slightly more than for the water monomer. The calculation with 8 H_2O adsorbed on the oxide surface leads to each of the six surface Zr which comprise the oxide isle being covered by an H_2O molecule, while the remaining two are connected to this patch of water by hydrogen bonds. Additionally, these two H_2O molecules bind to surface oxygen in valley sites. At full coverage again all six isle sites are covered and the additional H_2O form an ice like structure similar to the $\sqrt{19}$

(a) 5 H_2O on $\sqrt{19}$

(b) 8 H_2O on $\sqrt{19}$

(c) 12 H_2O on $\sqrt{19}$

(d) 14 H_2O on $\sqrt{19}$

(e) 15 H_2O on $\sqrt{19}$

(f) 16 H_2O on $\sqrt{19}$
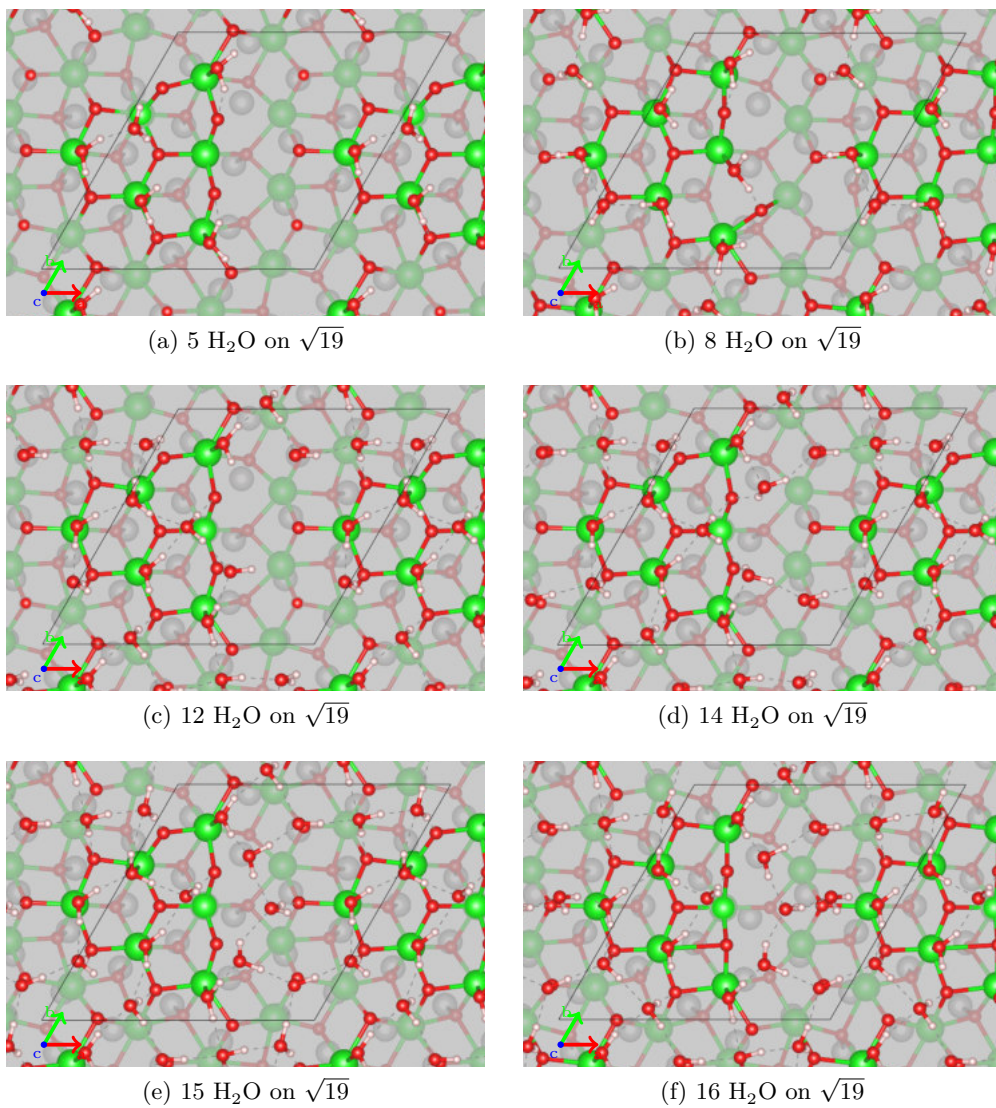
Figure 4.23.: Fully relaxed H_2O over-layer on the $\sqrt{19}$ model. At full coverage ((c)) no water is adsorbed at Zr valley sites. H_2O adsorbed at oxide valley sites form bridges connecting the H_2O bound on top of the oxide isles ((d)-(f)).

model.

(a) 5 H_2O on $\sqrt{19}_{comp}$ (b) 8 H_2O on $\sqrt{19}_{comp}$ (c) 12 H_2O on $\sqrt{19}_{comp}$
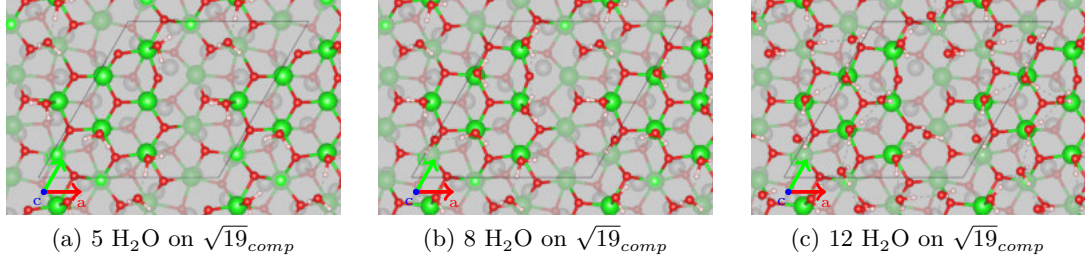
Figure 4.24.: Different water coverages calculated for $\sqrt{19}_{comp}$ model. Up to 8 H_2O, the molecules coalesce at the upwards buckled isle sites. Further increase to 12 H_2O leads to some H_2O being located at the valley sites, starting to form the ice layer.

Table 4.9.: Adsorption energy in eV per H_2O of water molecules adsorbed above the individual Zr sites on the $\sqrt{19}$ and $\sqrt{19}_{comp}$ models.

E_{Ads} [eV]	$\sqrt{19}$	$\sqrt{19}_{comp}$
Zr_1	-0.986	-0.459
Zr_2	-0.617	-0.257
Zr_3	-0.714	-0.931
Zr_4	-0.394	-0.808
Zr_5	-0.525	-0.335
Zr_6	-0.479	-0.162
Zr_7	-0.547	-0.389
Zr_8	-0.723	-0.635
Zr_9	-0.497	-0.379
Zr_{10}	-0.629	-0.773
Zr_{11}	-0.973	-0.849
Zr_{12}	-0.812	-0.492

4.2.4. Core Level Shifts

H_2O Adsorbed on Bulk ZrO_2

The O $1s$ core level binding energies of adsorbed water were calculated for both molecular and dissociative adsorption on the cubic and monoclinic ZrO_2 surfaces. The calculations were performed in both the initial and final state approximation using the same computational parameters as for the relaxations. Unfortunately, the initial state calculations

yield rather inaccurate results, showing a smaller O 1s binding energy for the adsorbed water than for the O 1s states in the oxide film, which is disproven by XPS experiments presented by [7]. The final state calculations do give reasonable results, therefore only these results will be discussed here.

In both cases, the surface area was quadrupled to minimise the crosstalk of the excited core-holes due to the periodic boundary conditions, as described in section 3.4. Generally, referenced to the average binding energy of the O 1s states of the oxide film in the $\sqrt{19}$ model, the water adsorbate shows a shift towards larger binding energies. This shift is much larger for a molecular H_2O (4.5 eV to 4.9 eV) than for a dissociated H_2O (2.3 eV to 2.8 eV). Water molecules adsorbed on the m($\bar{1}$11) surface show a smaller shift compared to those on the c(111).

H_2O Adsorbed on $(\sqrt{3} \times \sqrt{3})R30°$

For water molecules adsorbed on the ZrO_2 film of the $(\sqrt{3} \times \sqrt{3})R30°$ models described in section 4.2.2 the trend described for the bulk surfaces recurs. For the compressed oxide film, the adsorbed water at ⅓ ML coverage shows a shift of 4.7 eV towards larger binding energies, indicative of molecular adsorption (see table 4.10). On the expanded small model at the same coverage, the O 1s states are shifted by 4.5 eV. At full coverage, the O 1s shifts show a larger spread due to different bonding. For the compressed model, the O 1s states of the three H_2O shift by 3.8 eV, 4.6 eV, and 4.5 eV. The first H_2O which shows the smallest shift is rotated and binds to a surface oxygen by a hydrogen bond, while the other two H_2O are located above Zr atoms, like at low coverage. For the expanded model, the three H_2O shift by 4.2 eV, 3.5 eV, and 1.5 eV. Again, the largest shift is calculated for the O 1s states of a H_2O adsorbed above a surface Zr. The second H_2O is placed above a surface O and forms a hydrogen bond, while the last H_2O molecule dissociates.

H_2O Adsorbed on $(\sqrt{19} \times \sqrt{19})R23.4°$

The core level binding energies of the O 1s states of the adsorbed water on the $\sqrt{19}$ and $\sqrt{19}_{comp}$ models were calculated in both initial and final state approximation. Generally, both approaches reproduce the experimental trend quite well. Nevertheless, similar to the core level shift calculations discussed in section 3.4, the initial state approximation yields too low O 1s binding energies for the insulating systems like bulk ZrO_2 and the hexagonal ice reference (see table 4.10). For this reason only the final state results are discussed here.

The final state core level binding energies of the O 1s states of the adsorbed water were calculated for both the $\sqrt{19}$ and $\sqrt{19}_{comp}$ models. For the dissociated monomer, the initial state calculation shows a shift of 0.33 eV towards smaller binding energies, while the final state calculation (correctly) yields a shift of 1.09 eV towards larger binding energies, referenced to the average binding energy of the O 1s states in the oxide film. The molecular water monomer adsorbed at the most favourable adsorption site shows a more pronounced shift of 0.72 eV and 2.65 eV of the O 1s states towards higher binding

energies, calculated in the initial and final state approximations respectively. These values are virtually identical for both the $\sqrt{19}$ and the $\sqrt{19}_{comp}$ model. The final state core level shift depends slightly on the adsorption site as at other strongly bound sites a shift of 2.7 eV to 2.8 eV is predicted. Increasing the water coverage yields even larger shifts towards larger binding energies by 3.90 eV, 3.69 eV, and 3.34 eV for a water layer consisting of 5 H_2O, 8 H_2O, and 12 H_2O, and averaged over the O $1s$ binding energies. As can be seen in table 4.10, the spread of the binding energies is quite large, owing strongly to the particular adsorption geometry and bonding of the individual molecules. For example, the structure with the first 5 H_2O adsorbed on the $\sqrt{19}$ model, shows O $1s$ shifts of 3.67 eV, 3.24 eV, 4.16 eV, 4.10 eV, and 4.32 eV. The latter three H_2O are adsorbed on top of surface Zr and form a hydrogen bond to a nearby surface oxygen. The first H_2O with a shift of 3.67 eV is also adsorbed at a Zr site, but only forms a hydrogen bond to another neighbouring H_2O. This last H_2O adsorbs above a surface O to which it forms another hydrogen bond to. At full coverage the mean O $1s$ binding energy is smaller due to the larger number of hydrogen bonded H_2O that are formed in the water over-layer. These predicted shifts support the argument of the formation of ice since the O $1s$ states of hexagonal (1H) bulk ice show a shift of 4.78 eV towards larger binding energies.

4.2.5. Summary

The DFT calculations show that water molecules prefer dissociative adoption on both ZrO_2 bulk and thin film surfaces, except for the compressed $\sqrt{3}$ model. In all cases, the oxygen atom of the adsorbed molecule binds towards the surface zirconium atom and its hydrogen atoms rotate towards surface oxygen atoms. Generally, the H_2O molecule binds quite strongly to the oxide surface: the calculated adsorption energies including van-der-Waals corrections are in the area of -1.44 eV to -1 eV for the bulk oxide surfaces. For molecular adsorption the DFT calculations predict values of -0.9 eV to -1.1 eV, close to the experimental values reported by Ushakov and Navrotsky [133]. On the m($\bar{1}$11) surface a dissociation barrier of at least 94 meV is predicted.

On the smooth c(111) surface, the H_2O binds more strongly for an expanded lattice constant of the model cell, indicating an increase of the reactivity of the surface. On the monoclinic m($\bar{1}$11) surface the buckling reduces the accessibility of one surface Zr, resulting in just three possible adsorption sites on the (1×1) surface unit cell. Additionally, an under-coordinated oxygen atom decreases the dissociation barrier. At these sites a dissociated H_2O is more stable compared to molecular adsorption with the split off proton forming a surface hydroxyl with the under-coordinated oxygen. The remaining $(OH)_{ads}$ is still connected to this surface hydroxyl by a hydrogen bond. At higher coverage simulated annealing calculations show that this under-coordinated surface oxygen can be seen as a nucleation site for the formation of an ice film: one water molecule close to this site dissociates, while the remaining H_2O stay intact. The adsorption mechanism changes: while at low coverage the interaction with the surface is only driven by Zr–O and hydrogen bonds to the under-coordinated site, at higher coverage the water molecules also form hydrogen bonds to neighbouring H_2O molecules. The presence of

Table 4.10.: Core level shifts in eV of the O $1s$ states of water adsorbed on ZrO_2 surfaces, referenced to the mean O $1s$ binding energy of the clean ultra-thin ZrO_2 film in the $\sqrt{19}$ model cell, discussed in section 3.4.5. The sign was chosen in analogy to the binding energy of an electron measured by XPS where a positive number indicates higher binding energy.

	Initial State	Final State
	Bulk ZrO_2	
c(111), 1 molecular H_2O	−0.55	4.94
c(111), 1 dissociated H_2O	−2.18	2.78
m($\bar{1}$11), 1 molecular H_2O	0.52	4.47
m($\bar{1}$11), 1 dissociated H_2O	−1.08	2.31
	$(\sqrt{3} \times \sqrt{3})R30°$	
$\sqrt{3}$, compressed, 1 H_2O	2.14	4.66
$\sqrt{3}$, compressed, 3 $H2O_{\#1}$	1.41	3.82
$\sqrt{3}$, compressed, 3 $H2O_{\#2}$	2.15	4.55
$\sqrt{3}$, compressed, 3 $H2O_{\#3}$	2.13	4.50
$\sqrt{3}$, expanded, 1 H_2O	2.17	4.49
$\sqrt{3}$, expanded, 3 $H2O_{\#1}$	1.63	4.18
$\sqrt{3}$, expanded, 3 $H2O_{\#2}$	0.09	1.52
$\sqrt{3}$, expanded, 3 $H2O_{\#3}$	1.32	3.52
	$(\sqrt{19} \times \sqrt{19})R23.4°$	
$\sqrt{19}$, molecular H_2O monomer	0.72	2.65
$\sqrt{19}$, dissociated H_2O monomer	−0.33	1.09
$\sqrt{19}_{comp}$, molecular H_2O monomer	1.81	2.79
$\sqrt{19}_{comp}$, dissociated H_2O monomer	−0.34	1.08
$\sqrt{19}$, 5 molecular H_2O, $H_2O_{\#1}$	1.34	3.67
$\sqrt{19}$, 5 molecular H_2O, $H_2O_{\#2}$	0.64	3.24
$\sqrt{19}$, 5 molecular H_2O, $H_2O_{\#3}$	1.72	4.16
$\sqrt{19}$, 5 molecular H_2O, $H_2O_{\#4}$	1.69	4.10
$\sqrt{19}$, 5 molecular H_2O, $H_2O_{\#5}$	1.87	4.32
$\sqrt{19}$, 5 H_2O, $\varnothing$	1.45	3.90
$\sqrt{19}$, 8 H_2O, $\varnothing$	1.37	3.69
$\sqrt{19}$, full coverage, $\varnothing$	0.85	3.34
1H bulk ice	−1.94	4.78

additional hydrogen atoms also leads to the formation of surface hydroxyl groups which then block the dissociation of the adsorbed water molecule and reduce the adsorption energy of an intact H_2O molecule by up to $149\,meV$ at ¼ ML coverage. At full coverage the adsorption energy is reduced by $230\,meV$ per adsorbed H_2O. The corrugation of the oxide surface also has an influence on the orientation of the adsorbed molecule. On smooth surfaces (c(111), isle areas of the $\sqrt{19}$ and $\sqrt{19}_{comp}$ models) the molecule is positioned in a flat configuration. Where the oxide surface is more corrugated (m($\bar{1}$11), valley sites of the $\sqrt{19}$ and $\sqrt{19}_{comp}$ models) often one O–H bond of the adsorbate is rotated perpendicular to the surface.

On the ultra-thin film the water molecule is adsorbed in a similar configuration to the cubic c(111) surface where the H_2O molecule stays molecular at adsorption energies of about $-0.9\,eV$ and $-1.1\,eV$ for the compressed and expanded $\sqrt{3}$ models, respectively. The molecule binds more strongly in a dissociated configuration ($E_{Ads} = -0.8\,eV$ and $E_{Ads} = -1.5\,eV$), but spontaneous dissociation is only observed in one single case at increased water coverage. For this rather simple $\sqrt{3}$ model, the reduction of the lattice constant of the compressed $\sqrt{3}$ model causes a significant reduction of the reactivity of the ZrO_2 film, indicated in the higher stability of the molecular configuration. At full coverage the mean adsorption energy is reduced to about $-0.8\,eV$ and $-1.06\,eV$ for the compressed and expanded $\sqrt{3}$ models, respectively. Here, the some water molecules start to change orientation and form additional hydrogen bonds within the ice over-layer which starts to form.

The large distortions of the more realistic $\sqrt{19}$ model gives rise to a much larger number of different adsorption sites and a large spread of adsorption energies ranging from $-0.98\,eV$ to $-0.5\,eV$. As indicated by the simpler $\sqrt{3}$ model, the "local lattice constant", i.e. the local lateral distortion of the oxide film, heavily influences the strength of the bond between adsorbate and surface. The H_2O binds more strongly at heavily stretched sites with a larger "local lattice constant" where the surface Zr is much more accessible. Isle areas of the $\sqrt{19}$ model, where the oxide film is more contracted, show a reduction of the reactivity and the H_2O binds less strongly. At the border between these two general areas, i.e. at the edges of the isle areas, under-coordinated oxygen atoms slightly increase the binding energy again.

At the most favoured site, which is located in a strongly distorted area of the oxide film, the calculated adsorption energy is $-0.98\,eV$. The dissociation barrier at this site is quite low due to a 2-fold coordinated oxygen close by, indicating that in experiments both molecular and dissociated H_2O molecules can be expected. Unfortunately, the STM simulations show that distinguishing between molecular and dissociated adsorption is not possible with this technique.

At high coverage the DFT calculations predict the formation of an ice layer since the water molecules start to cluster at the isle areas close to the under-coordinated surface oxygen, analogous to the m($\bar{1}$11) case. Additional H_2O molecules are then connected by additional hydrogen bonds. At a coverage above 8 H_2O on the $\sqrt{19}$ model the H_2O molecules start to bridge the valley areas of the model cell. The mean adsorption energy of $-0.68\,eV$ at the coverage of 12 H_2O per unit cell can be well reconciled with the large

TPD peak at $180\,\mathrm{K}$ reported by Lackner, Hulva, Choi, Köck, Mayr-Schmölzer, et al. [7] and the predicted binding energy of hexagonal 1H bulk ice of $-0.74\,\mathrm{eV}$ (see appendix C).

Generally, the monoclinic ZrO_2 surface already shows some prominent features also found in the thin films. The surface is corrugated and under-coordinated surface oxygen atoms are present. These serve as nucleation sites for dissociation by lowering the transition barrier. The binding energy of an adsorbed water molecule is driven by the distance to such an under-coordinated site and the accessibility of the surface Zr atoms. The presence of the former leads to the formation of an additional hydrogen bond to the surface while downwards bucking of the latter or, in the case of the ultra-thin films, reduction of the lattice constant due to lateral compression reduces the local reactivity of the oxide surface. Nevertheless, on the ultra-thin films the water molecules bind much weaker compared to the bulk surfaces. On both bulk and thin film surfaces increasing the water coverage leads to the formation of an ice-like structure.

In principle, the van-der-Waals corrected optB86b functional yields adsorption energies in fairly good agreement with the experiment, with a slight overestimation compared to both the experiment and benchmark RPA calculations (see appendices B.3 and C). This especially becomes apparent at high coverages of water. Still, optB86b offers a good compromise resulting in reasonable predictions for both the description of the metal-oxide and the oxide-water interfaces. The combined experimental and theoretical results have recently been published by Lackner, Hulva, Choi, Köck, Mayr-Schmölzer, et al. [7].

5. Perovskites

5.1. Introduction

Understanding Transition Metal Oxides (TMOs) plays a big role in condensed matter physics research. For example, the group of materials called perovskites can exhibit a large variety of electronic and magnetic properties such as Mott insulating states, superconductivity, multiferroic behaviour or itinerant magnetism. These properties are driven by the spin, orbital and charge degrees of freedom in the open d-shell of the transition metal atom. Additionally, these properties can often be tuned by external influences, for example by magnetic fields, different dopants or external pressure.

In mineralogy the name "Perovskite" was initially assigned to $CaTiO_3$, but now it lends it name to a class of materials with similar crystal structure. The general chemical formula of a perovskite structure is ABX_3. The variables 'A' and 'B' in this generalised formula denote two cations of different sizes, whereas 'X' denotes an anion bonding to both cations. In many cases ternary oxides show this structure leading to a general ABO_3 stoichiometry. The idealised unit cell of such a compound is of cubic symmetry (space group $Pm\bar{3}m$) with the 'A' cations placed at the cube corner positions and the 'B' cations in the centre while the oxygen atoms are situated at face centred positions. Figure 5.1 shows the unit cell of an ideal perovskite with the A cations in 12-fold cub-octahedral coordination and the B cations surrounded by an octahedron of oxygen atoms (6-fold coordination). Usually A is represented by a transition metal atom (e.g. Ca, Sr, La, …) and B by an alkaline of rare earth metal (e.g. Mn, Ti, Ru, …).

Often, in real materials the cubic symmetry is broken. For example, $BaTiO_3$ exhibits ferroelectricity, and the required existence of an electric dipole can only be explained by a displacement of the Ti^{2+} ions at the centre of the TiO_6 octahedra from the centre position [138]. In other materials these distortions can also be caused by rotation or tilting of the BO_6 octahedra or by changes in the B–O bond lengths due to Jahn-Teller distortions [139].

In this chapter, the bulk and surface properties of strontium and calcium ruthenates, will be discussed.

5.2. The Ruddelsden-Popper Series $A_{n-2}A'_2B_nX_{3n+1}$

The Ruddelsden-Popper series describes a group of perovskites with a special ordering. They form layered structures consisting of slabs with the ideal ABO_3 stoichiometry separated by a rock-salt-like layer (see fig. 5.2). The generalised formula for these structures is $A_{n-2}A'_2B_nX_{3n+1}$ with A and B denoting the cations as described above, A' referring
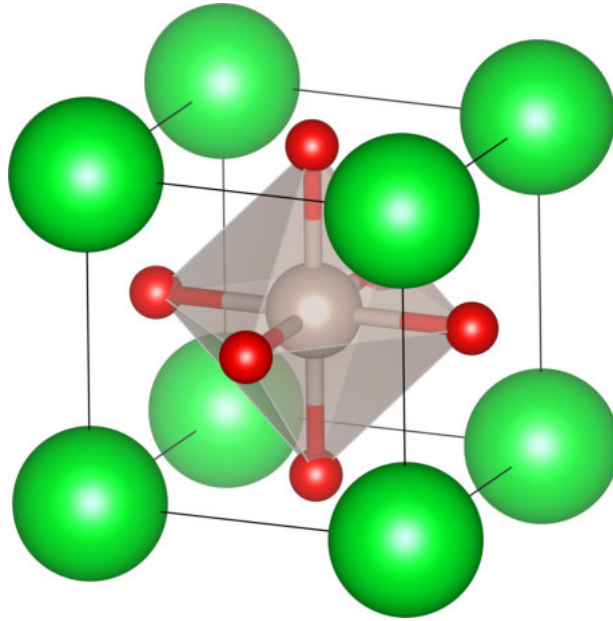
Figure 5.1.: Unit cell of the generalised perovskite building block ABO_3. A and B cations in green and grey, oxygen ions in red.

to the A-type cation at the perovskite boundary and X to the anion. The number n designates the number of perovskite layers between the rock-salt interface layers. The first structures with the parameter $n = 1$ that were described in this fashion were Sr_2TiO_4, Ca_2MnO_4, and $SrLaAlO_4$. Ruddlesden and Popper [140] used X-ray diffraction measurements to characterise the crystal structure of these compounds, eventually lending their names to this group of structures. Interestingly, materials with the same atomic composition but different parameter n can show different physical and chemical properties, for example higher correlation due to lower dimensionality. The materials studied in this work are good examples thereof. Strontium ruthenate, $Sr_{n+1}Ru_nO_{3n+1}$, can be a spin-triplet superconductor ($n = 1$, Sr_2RuO_4) [141–143] or can show an itinerant magnetic state with a field-tuned nematic phase ($n = 2$, $Sr_3Ru_2O_7$) [144–147]. At $n = \infty$ ($SrRuO_3$) an itinerant ferromagnetic phase can be found [148, 149]. Calcium ruthenates also show great variety, an example would be Ca_2RuO_4 with $n = 2$ which is an antiferromagnetic insulator below $100\,K$ [150, 151], while $Ca_3Ru_2O_7$ with $n = 3$ shows a first-order metal-to-nonmetal transition at $T_{MI} = 48\,K$ and antiferromagnetic order below the Neél temperature $T_N = 56\,K$ [145, 147, 152].

In this work only $Sr_{n+1}Ru_nO_{3n+1}$ with $n = \{1, 2\}$ and $Ca_3Ru_2O_7$ are discussed.

n=∞   n=1   n=2   n=3
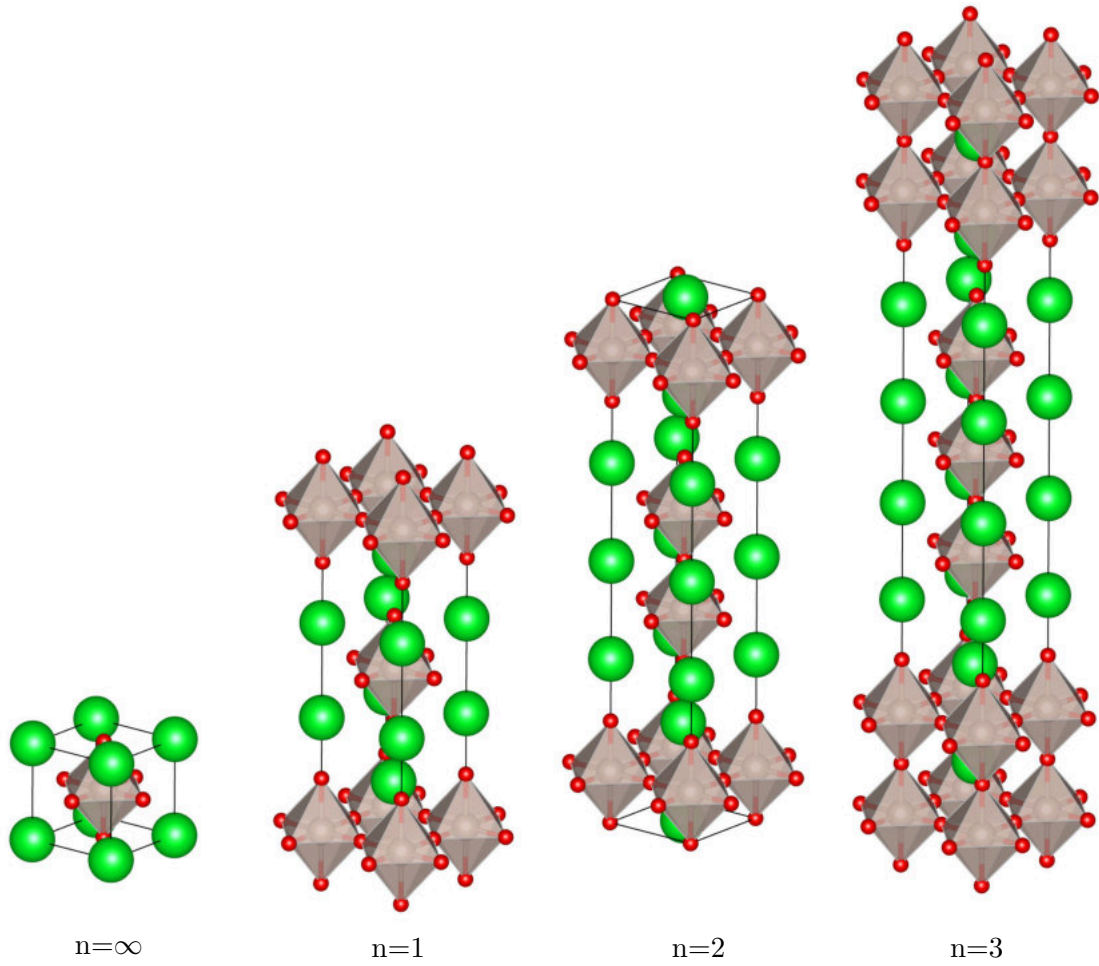
Figure 5.2.: Idealised depiction of the Ruddelsden-Popper series $A_{n-2}A'_2B_nX_{3n+1}$, start-
ing from the standard perovskite building block ($n = \infty$). The $n \geq 1$
Ruddelsden-Popper structures consist of n perovskite layers separated by a
rock-salt-like interface.

5.3. Strontium and Calcium Ruthenates: Bulk Structures

5.3.1. Sr_2RuO_4

Sr_2RuO_4 is a layered Ruddelsden-Popper type perovskite with parameter $n = 1$. According to X-ray diffraction ([153]) and powder neutron diffraction studies ([154–156]) it crystallises in the K_2NiF_4 structure (space group I4/mmm). As can be seen in fig. 5.3 the $SrRuO_3$ perovskite blocks are stacked in ABA order in the crystallographic c-direction, separated by a rock-salt like interface layer. The RuO_6 octahedra are not rotated or tilted against each other, but Neumeier et al. [157] have shown that they are slightly elongated by $0.12\,\text{Å}$ in the c direction perpendicular to the rock-salt plane.

The energy cutoff for the calculations was set to $400\,\text{eV}$, the default energy cutoff value for the standard oxygen potential. The $\vec{k}$-point convergence was reached with a $11\times11\times5$ Γ-centered Monkhorst-Pack grid. The unit cell was then constructed according to the crystallographic characterisation by Neumeier et al. [157] and optimised using both the standard PBE and the optB86b functional. As can be seen in table 5.1 the lattice parameters predicted by the optB86b functional agree much better with the experimental values, deviating from those by below $0.1\,\%$. The PBE functional on the other hand gives lattice parameters which are slightly larger, deviating from the experimental values by $0.83\,\%$ for both a and c direction.

The Ru–O bond lengths are very well reproduced by the optB86b functional: in the RuO plane almost no deviation from the experimental values were found, while the Ru–O bond lengths perpendicular to the rocksalt layer were $0.144\,\text{Å}$ larger compared to the measured value of $0.121\,\text{Å}$. With the PBE functional the octahedra are slightly less distorted as the bond length difference is $0.139\,\text{Å}$, but the RuO plane bond lengths are slightly larger (see table 5.1).

The optB86b functional was used for all further calculations due to its inclusion of long-range polarisation effects. Also, the deviation of the bulk lattice parameters from the experimental results is lower compared to the PBE functional.

The density of states (DOS) as seen in fig. 5.4 shows, as expected, a metallic ground state for Sr_2RuO_4. At the Fermi level the DOS is dominated by the hybridisation of the oxygen p-states and the ruthenium d-states. The strontium p-states are not visible in the region close to the Fermi level, they show a large peak around $15\,\text{eV}$ below E_{Fermi}. The layered structure of the crystal is also apparent in the orbital projected DOS of the oxygen atoms, shown in fig. 5.4b. The oxygen p-states at the rock-salt interface are more localised compared to those in the RuO_2 layer, especially in the p_z orbital. The $p_x p_y$-states in the RuO_2 layer are very broad, testament to the strong hybridisation with the ruthenium d states.

5.3.2. $Sr_3Ru_2O_7$

Adding a second layer to the perovskite building blocks of Sr_2RuO_4 in the Ruddelsden-Popper series leads to the two-layered $Sr_3Ru_2O_7$ strontium ruthenate ($n = 2$). Müller-Buschbaum and Wilkens [158] were first able to characterise the bulk properties by

Table 5.1.: Calculated Sr_2RuO_4 bulk parameters compared to experimental values. O_1 are 4-fold coordinated, while O_2 are 2-fold coordinated.

	PBE	optB86	Exp. [158]	Exp. [157], T = 13 K
Volume $[\text{Å}^3]$	194.547	189.893	190.330	189.810
$a = b$ [Å]	3.894	3.863	3.871	3.862
c [Å]	12.828	12.725	12.702	12.723
Ru–O1 (4x) [Å]	1.947	1.932	n/a	1.931
Ru–O2 (2x) [Å]	2.086	2.075	n/a	2.052
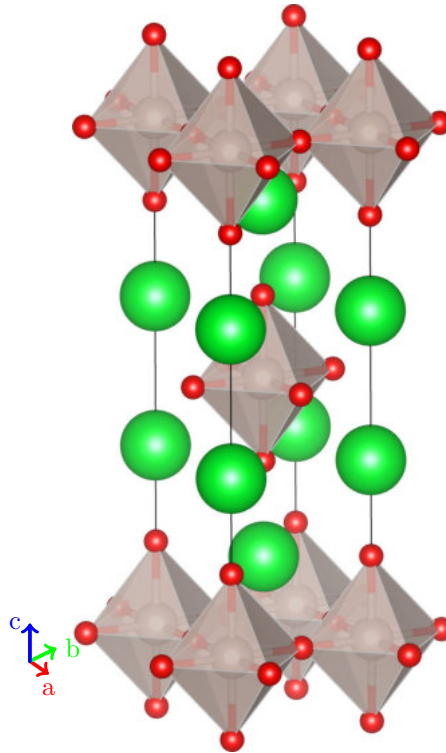
Figure 5.3.: Sr_2RuO_4 structure built from standard perovskite building blocks, separated by a rock-salt-like interface layer. Strontium, Ruthenium, and Oxygen atoms are labeled green, grey, and red, respectively.
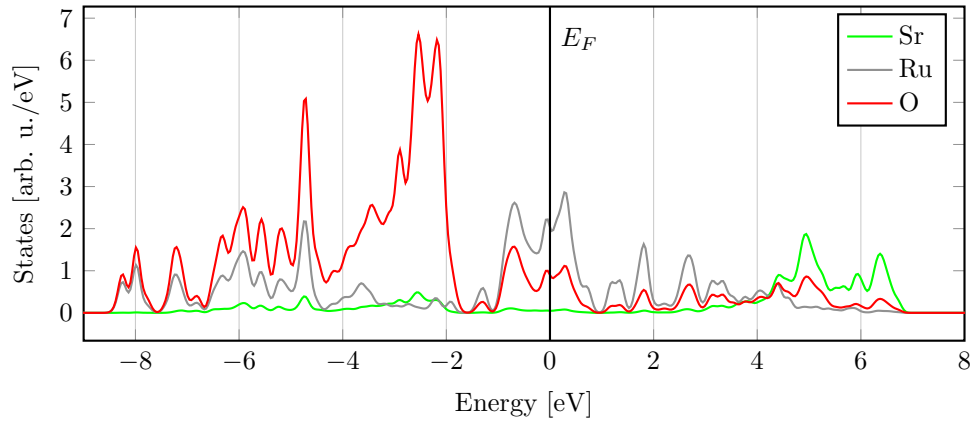
(a) Sr$_2$RuO$_4$ optB86b DOS
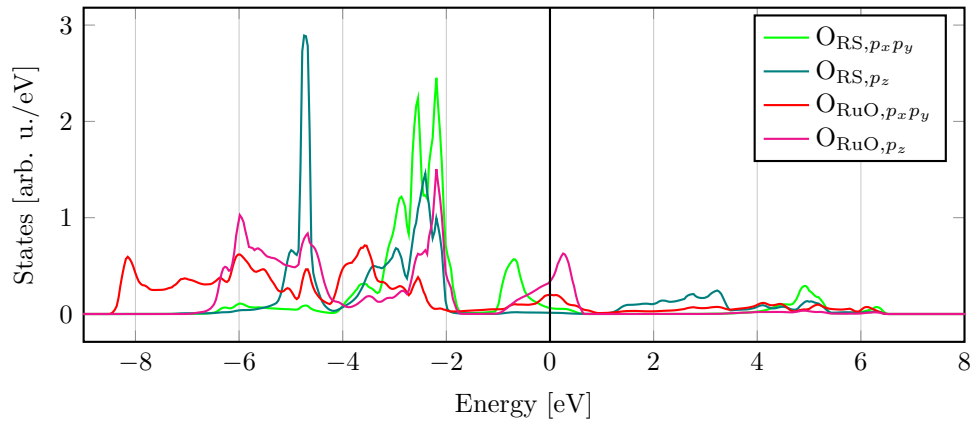
(b) Sr$_2$RuO$_4$ optB86b DOS, oxygen p-states

Figure 5.4.: Sr$_2$RuO$_4$ DOS calculated with the optB86b functional. (a): projected DOS of Sr, Ru, and O. (b): orbital projected DOS of the oxygen atoms.

X-ray diffraction. They concluded that $Sr_3Ru_2O_7$ was isostructural to $Sr_3Ti_2O_7$ and therefore assigned the structure to the tetragonal I4/mmm space group. More recent neutron powder diffraction studies by Huang et al. [159] and X-ray diffraction measurements by Ikeda et al. [145] at both ambient temperature and low temperatures, however, have shown that the RuO_6 octahedra rotate, leading to a considerable distortion of the Ru–O–Ru bonds in the RuO_2 planes from the ideal 180° to about 165°, see fig. 5.5. In each double layer two octahedra stacked along the vertical axis are rotated against each other while the rotations of octahedra in the next double layer are not correlated. While this rotation gives rise to an orthorhombic *Bbcb* unit cell (see [160]), it is standard practice to use the tetragonal (1×1) unit cell. The primitive $Sr_3Ru_2O_7$ unit cell is then referred to as a $c(2 \times 2)$ structure.

Measurements of the magnetic susceptibility on flux-grown $Sr_{1-x}Ca_xRuO$ compounds by Cao et al. [161] has shown $Sr_3Ru_2O_7$ to be a "bad" metal (i.e. resistivity tends to rise with increasing temperature) with ferromagnetic behaviour below $T_c = 104\,\mathrm{K}$. For the $Sr_3Ru_2O_7$ crystal grown by a floating-zone technique [145] the magnetic susceptibility shows Curie-Weiss behaviour above $200\,\mathrm{K}$ and a maximum at $16\,\mathrm{K}$. This susceptibility is nearly isotropic for all crystal axes below this temperature, and no long range magnetic order could be found. Therefore, $Sr_3Ru_2O_7$ was regarded to be paramagnetic. This discrepancy was resolved by measuring the pressure dependency of the magnetic susceptibility in the latter sample, showing ferromagnetic ordering at a pressure of around $1\,\mathrm{GPa}$.

The DFT calculations were done in a similar way as in section 5.3.1. For the optimisation of the $Sr_3Ru_2O_7$ bulk unit cell the same energy cutoff as for Sr_2RuO_4 was used, while a $6 \times 6 \times 6$ Monkhorst-Pack $\vec{k}$-point grid was found to be sufficient. The orthorhombic $c(2 \times 2)$ unit cell was optimised using both the PBE and the optB86b functional leading to good agreement with the experimental values published by Ikeda et al. [145]. As is shown in table 5.2, the lattice parameters calculated with the PBE functional deviate by $1.0\,\%$ and $0.8\,\%$ for the a and the c axis, respectively, while the van-der-Waals corrected optB86b functional yields deviations below $0.3\,\%$. The Ru–O bond lengths and octahedral distortions are well reproduced by both the PBE and the optB86b functional, showing slight stretching along the c direction. Compared to the case of Sr_2RuO_4 where the octahedra are stretched by $7.0\,\%$, this distortion is lower at $2.2\,\%$ for $Sr_3Ru_2O_7$. It is also slightly asymmetric due to the fact that each octahedron only borders to one rock-salt layer, as can be seen in fig. 5.5 and table 5.2. Both functionals yield larger rotations of the RuO octahedra than reported by Ikeda et al. [145] and Shaked et al. [160] which can be attributed to the larger in-plane Ru–O bond lengths.

The $Sr_3Ru_2O_7$ density of states (see fig. 5.7) of the ground state (see fig. 5.6) calculations predict a ferromagnetic solution. While the PBE functional predicts a half-metallic state the optB86b functional shows also a small occupation of the majority band at the Fermi level. For the PBE functional the direct gap in the spin-up channel is $0.599\,\mathrm{eV}$. This is in agreement with recent DFT studies by Rivero et al. [162] who found similar behaviour comparing the PBE and the PBEsol functional. They attribute this to the

difference in the exchange enhancement factors F_x for PBE and PBEsol which is used to scale the gradient dependence of the exchange energy of the local density approximation. An analogue conclusion can be drawn from the differences between PBE and optB86b functional.

In both cases the density of states close to the Fermi level is dominated by the hybridisation of the ruthenium d-states and the oxygen p-states, similar to the Sr_2RuO_4 case. However, the spin splitting is well visible as the spin-down states are shifted to higher energies due to the charge transfer from the spin-down to the spin-up states. The orbital-projected DOS of the oxygen p-states (see fig. 5.8) shows the difference in the binding configurations of the different oxygen sites. In addition to the two different sites found in the Sr_2RuO_4 case (oxygen in the RuO and the rock-salt plane) there is now a third oxygen site in a SrO plane, see fig. 5.5a. Each of the sites shows a difference in the DOS with respect to the $p_x p_y$ and p_z states: the p_z states of the oxygen atoms at the rock-salt layer and the SrO layer are shifted to lower energies compared to their $p_x p_y$ states, while the p_z states of the oxygen atoms in the RuO plane are shifted upwards compared to their respective $p_x p_y$ states. In the ferromagnetic solution the magnetic moments of the Ru ions carry a projected magnetic moment of 1.35 µB and 1.27 µB per ion for the PBE and the optB86b functional, respectively, in very good agreement to the experimental value of 1.34 µB [161].

Calculations using the hybrid HSE06 functional also yield a half-metallic ground state with a band gap in the spin-up channel of 1.768 eV (see fig. 5.7a) and a projected magnetic moment of 1.43 µB.

Table 5.2.: $Sr_3Ru_2O_7$ bulk parameters. The values for the a axis are given in the traditional tetrahedral denotation.

	PBE	optB86	Exp. [145]	Exp. [160]
Volume [Å^3]	322.429	315.020	313.267	311.895
$a = b$ [Å]	3.929	3.899	3.887	3.890
c [Å]	20.883	20.722	20.732	20.725
Ru–O1 [Å]	2.025	2.012	n/a	2.012
Ru–O2 [Å]	2.032	2.025	n/a	2.039
Ru–O3 [Å]	1.991	1.974	n/a	1.958
Octahedral rotation [°]	9.3	9.0	7	6.8

5.3.3. Ca$_3$Ru$_2$O$_7$

The crystal structure of $Ca_3Ru_2O_7$ is closely related to that of $Sr_3Ru_2O_7$. It is also a $n = 2$ perovskite of the Ruddelsden-Popper series and one would expect the structural, electronic, and magnetic properties to be similar, but there are significant differences.

(a) $Sr_3Ru_2O_7$, side view

(b) $Sr_3Ru_2O_7$, top view
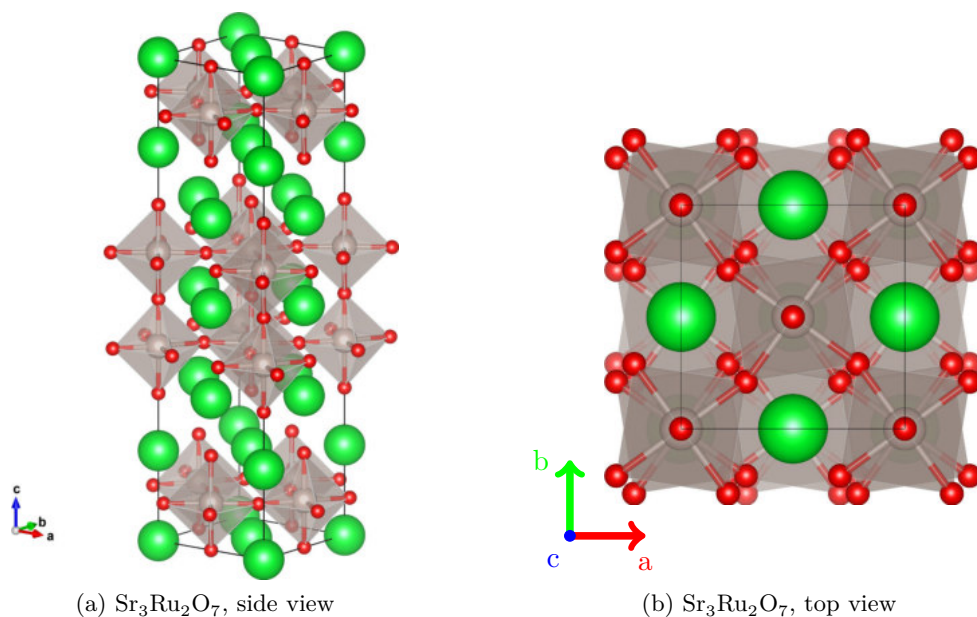
Figure 5.5.: Orthothombic $Bbcb$ c(2×2) $Sr_3Ru_2O_7$ crystal structure. Sr atoms are green, Ru atoms grey, O atoms red. The top view of the unit cell (fig. 5.5b) shows the rotation of the RuO_6 octahedra.

$Ca_3Ru_2O_7$ exhibits a more distorted structure due to the smaller ionic radius of Ca^{2+} compared to Sr^{2+}. The crystal structure of $Ca_3Ru_2O_7$ is of orthorhombic symmetry of the $Bb2_1m$ space group (No. 36). In contrast to $Sr_3Ru_2O_7$ the lattice shows slight distortion along the b axis and the RuO_6 octahedra are not only rotated but also tilted with respect to the c axis [152, 163] (see fig. 5.9). Cao et al. [163] have shown a first-order transition between a metallic to a non-metallic ground state at a transition temperature $T_M = 48$ K. Additionally, antiferromagnetic (AFM) ordering has been found below the Néel temperature $T_N = 56$ K.

To find the correct DFT equilibrium structure a similar approach to the Sr_2RuO_4 and $Sr_3Ru_2O_7$ cases was taken. The computational settings used for the $Sr_3Ru_2O_7$ structure proved to be a good starting point to converge the energies properly: the energy cutoff was set to the same 400 eV while a more finely grained $11 \times 11 \times 3$ Monkhorst-Pack $\vec{k}$-point grid was used for the calculations. As shown in table 5.3 the good agreement of the lattice parameters with the experiment seen for both strontium ruthenates continues here: compared to the neutron diffraction measurements by Yoshida et al. [152] at 8 K the optB86b functional shows very good agreement of the lattice parameters with deviations below 0.5 %. For the PBE functional the lattice parameters are just 0.9 % larger. The angles determining the aforementioned octahedral rotation and tilting are slightly smaller, attributable to the slightly larger lattice constants. In contrast to Sr_2RuO_4 and $Sr_3Ru_2O_7$, the experiment shows that the octahedra are not elongated, but even slightly
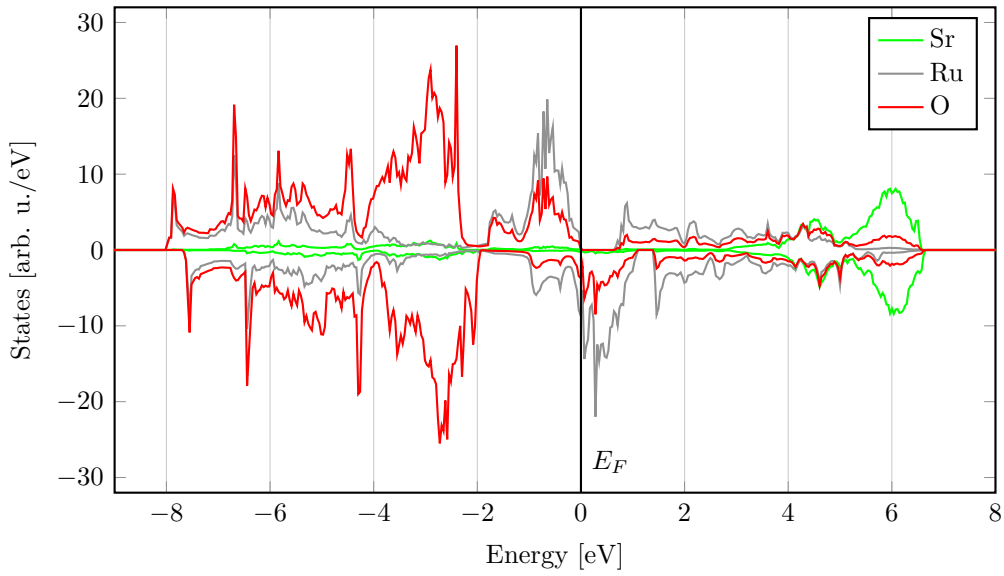
(a) PBE DOS
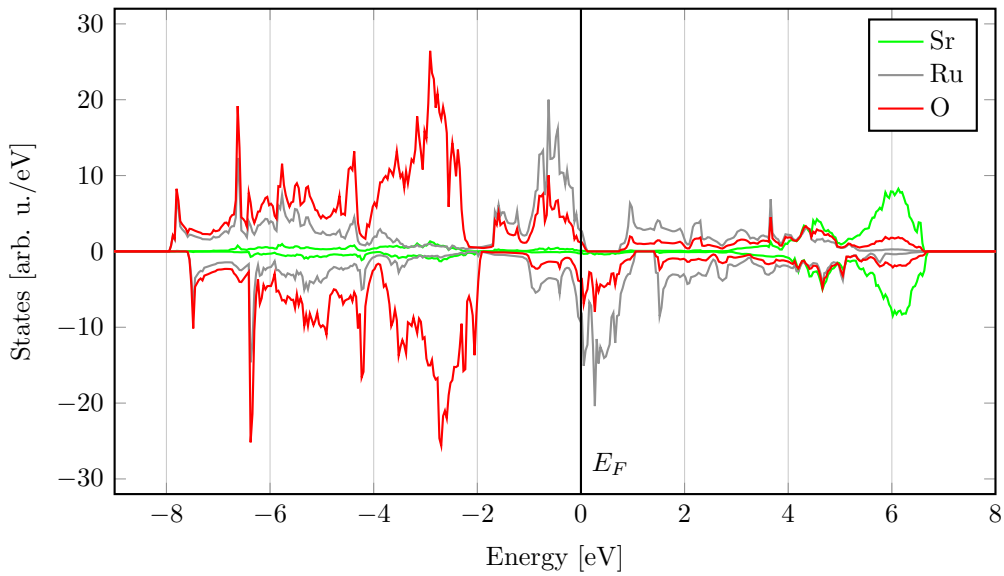
(b) optB86b DOS

Figure 5.6.: $Sr_3Ru_2O_7$ density of states, calculated using the PBE (fig. 5.6a) and optB86b (fig. 5.6b) functionals. The PBE functional yields the half-metallic ground state with a band gap in the spin up channel of 0.599 eV. The optB86b functional yields a "bad" metallic ground state where occupied electronic states spill over into the gap.
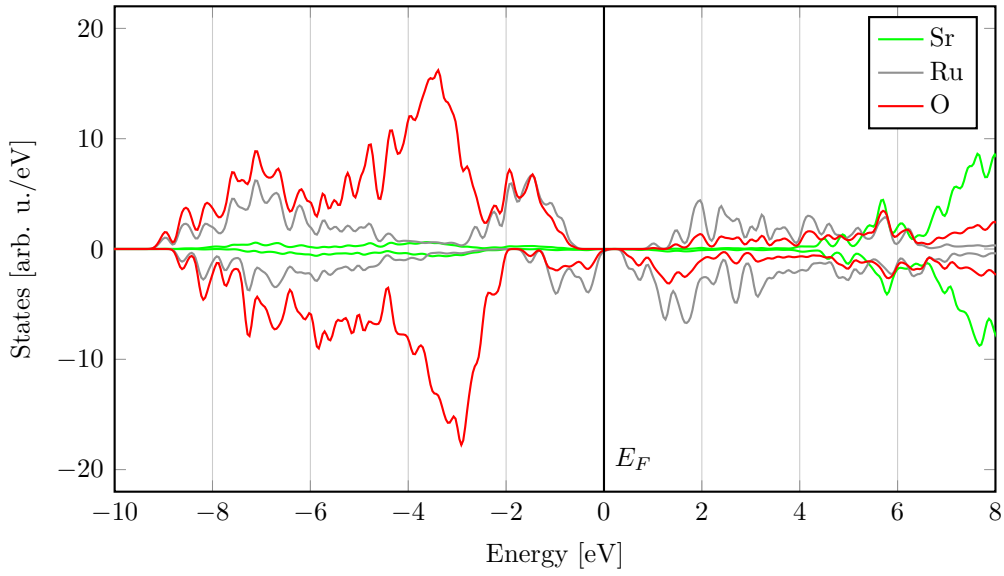
(a) HSE06 DOS

Figure 5.7.: $Sr_3Ru_2O_7$ density of states, calculated using the HSE06 functional, yielding the same half-metallic ground state as the PBE functional. The band gap in the spin up channel is enlarged to $1.768\,\text{eV}$.
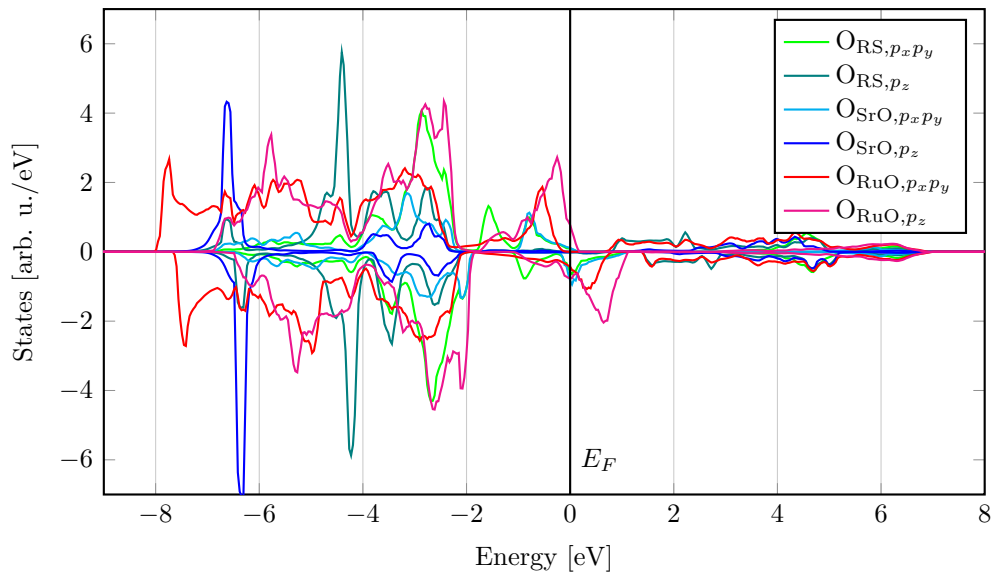
(a) optB86b oxygen p-states

Figure 5.8.: Orbital projected $Sr_3Ru_2O_7$ density of states calculated with the optB86b functional. Only the oxygen p-states of one layer are shown.

compressed along the c axis by 0.6 %. This is also well reproduced by both functionals where the contraction of the octahedra amounts to 0.7 % and 0.8 % for the PBE and the optB86b functional, respectively.

Both the PBE and the optB86b functional result in a metallic ground state. Since the magnetic ground state is antiferromagnetic (AFM), no spin splitting is visible in the total density of states. As this configuration is not the experimentally found, low temperature insulating ground state additional calculations using the PBE+U approach (see section 2.4) with an $U - J = 4.5$ eV added to the Ru ions and the HSE06 hybrid functional were done. With 48 atoms the size of the unit cell is rather large for hybrid calculations due to the computational cost involved (see section 2.5). Nevertheless, they serve as useful benchmarks for the PBE+U approach. In both approaches the opening of a band gap of 0.892 eV and 1.079 eV for PBE+U and HSE06 respectively can be observed, larger than the observed experimental gap of about 0.1 eV [164, 165]. As expected, the band gap calculated using the PBE+U method is increases with the value $U - J$: at a value of 5 eV the gap size is 1.286 eV. A lower value of $U - J = 4$ eV yields a half-metallic phase with a gap of 0.691 eV in the majority channel and a metallic minority channel. The failure of standard LSDA approaches to yield the insulating ground state has also been shown in earlier calculations by Singh and Auluck [166], while Liu [167] has shown that the DFT+U approach can reliably reproduce the insulating ground state.

For all functionals, the density of states at the Fermi level is dominated by the hybridisation of the ruthenium d-states and the oxygen p-states, similar to the strontium ruthenates. The PBE and optB86b DOS only show slight differences, which can be expected due to the different parameterisations of the gradient correction. For the insulating phase, the broad feature in the DOS at the Fermi level is split and the ruthenium d-states accompanied by the hybridised oxygen states are shifted down- and upwards, opening the band gap. The HSE06 functional results in a broader DOS structure compared to the GGA functionals, but the general structure is well reproduced.

Table 5.3.: $Ca_3Ru_2O_7$ bulk parameters.

	PBE	optB86	Experiment [152]
Volume [Å^3]	595.841	582.603	580.050
a [Å]	5.416	5.365	5.368
b [Å]	5.585	5.562	5.536
c [Å]	19.697	19.525	19.521
Ru–O1–Ca [°]	153.659	154.006	154.666
Ru–O2–Ru [°]	152.166	152.033	153.117
Ru–O3–Ru [°]	149.037	148.824	150.004
Ru–O4–Ru [°]	149.673	149.889	150.603
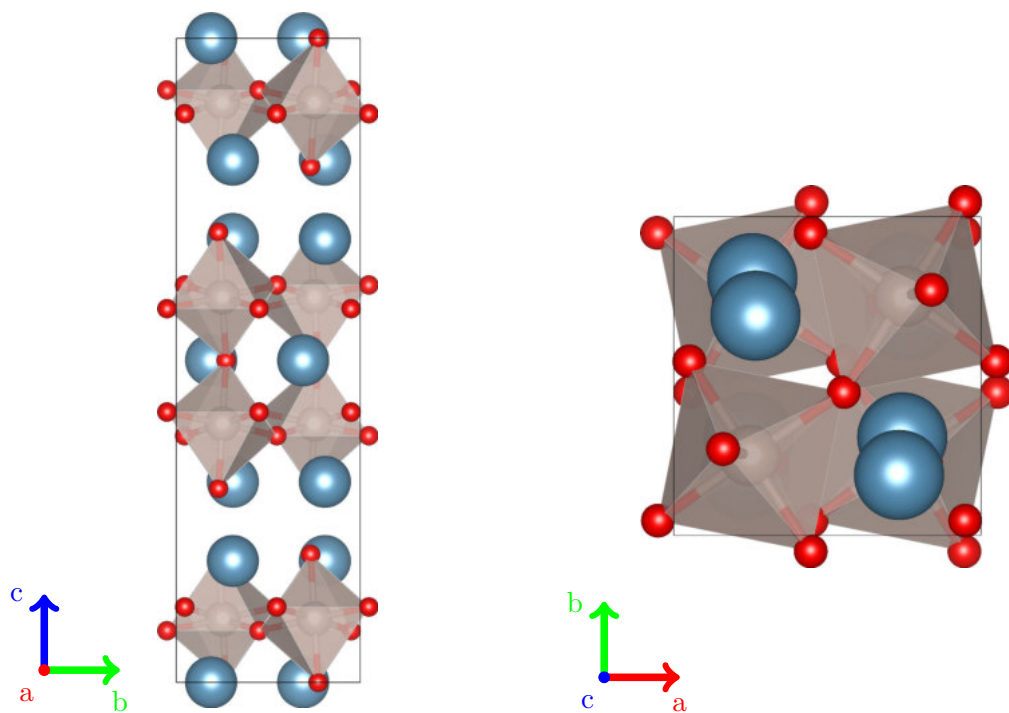
Figure 5.9.: Orthothombic $Bb2_1m$ (1×1) $Ca_3Ru_2O_7$ crystal structure. Ca atoms are blue, Ru atoms grey, O atoms red. The top view of the unit cell (fig. 5.9b) shows the rotation and tilting of the RuO_6 octahedra.
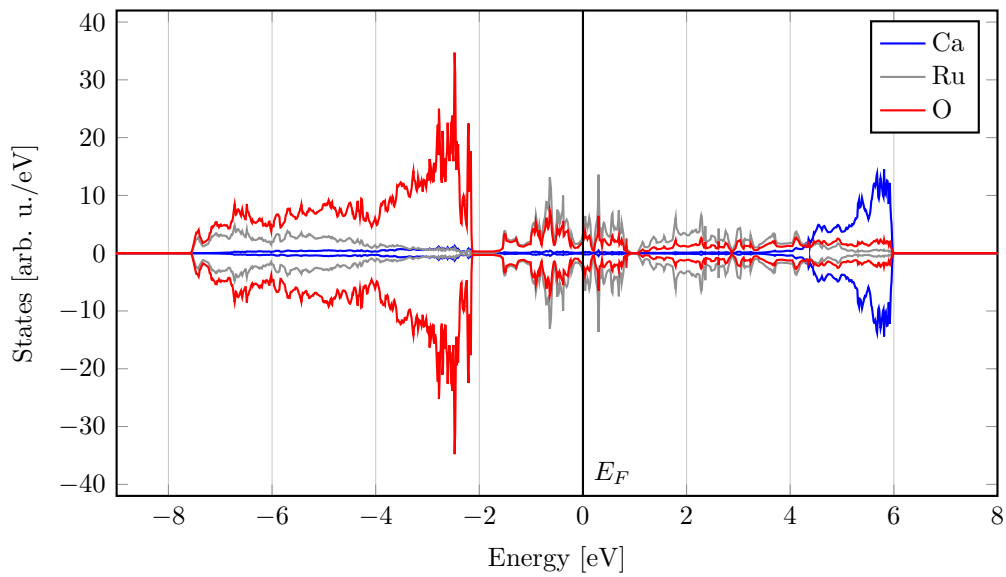
(a) Ca$_3$Ru$_2$O$_7$ PBE DOS
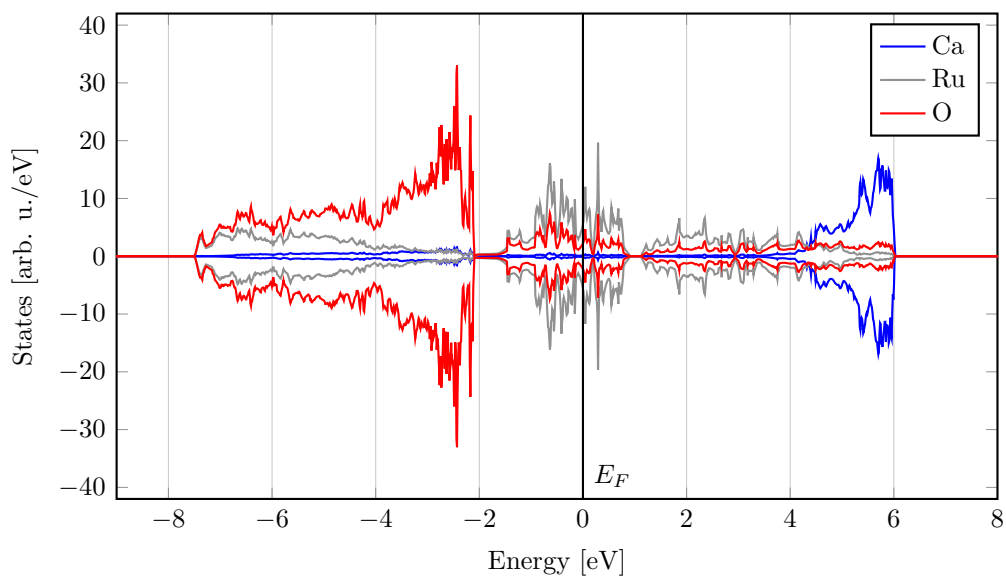
(b) Ca$_3$Ru$_2$O$_7$ optB86b DOS

Figure 5.10.: Ca$_3$Ru$_2$O$_7$ DOS, calculated with the PBE and optB86b functionals. Both yield the metallic ground state.
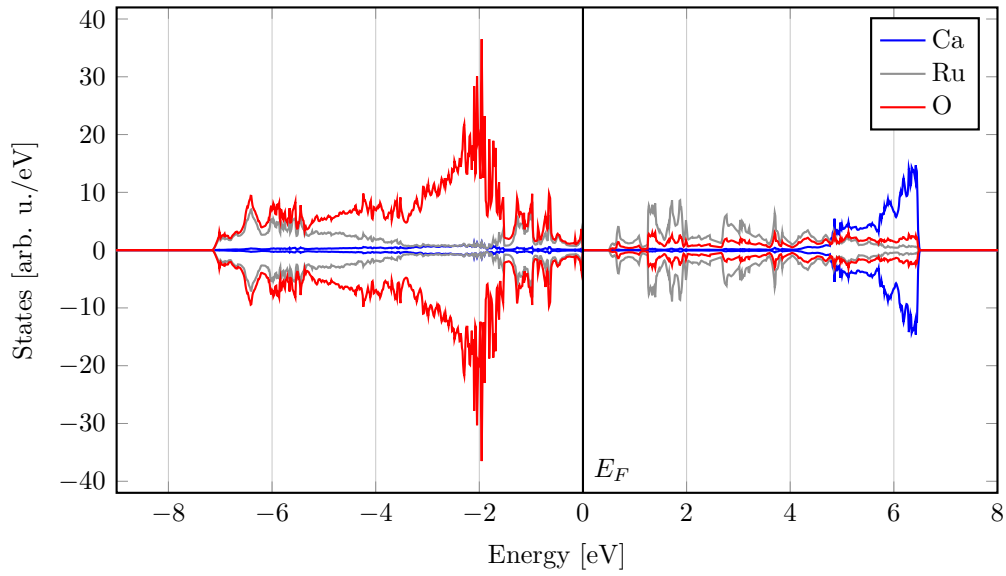
(a) $Ca_3Ru_2O_7$ PBE+U DOS, $U - J = 4.5\,\mathrm{eV}$
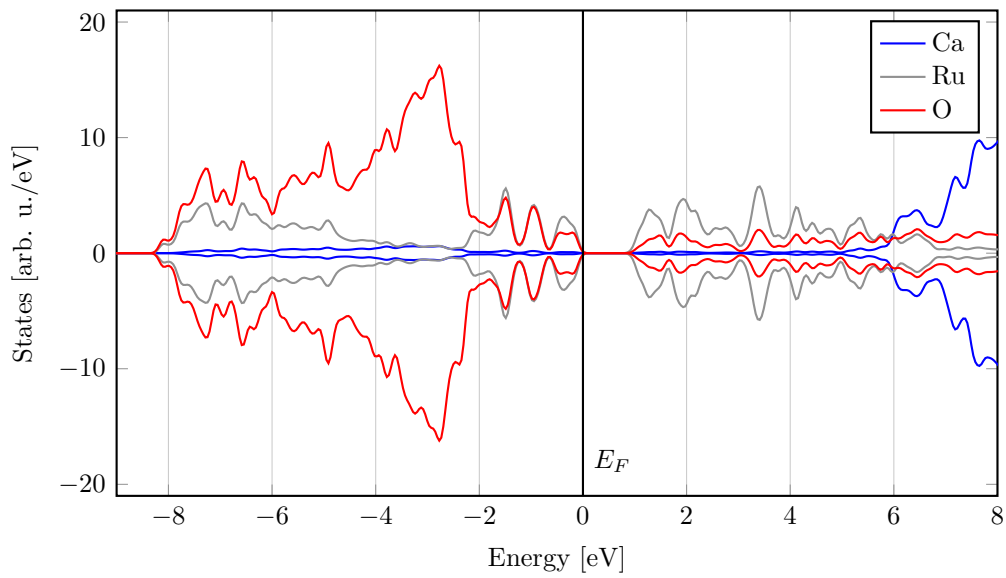
(b) $Ca_3Ru_2O_7$ HSE DOS

Figure 5.11.: $Ca_3Ru_2O_7$ DOS, calculated with the PBE+U ($U - J = 4.5\,\mathrm{eV}$) and HSE06 approaches. Both yield an insulating electronic ground state with band gaps of $0.892\,\mathrm{eV}$ and $1.079\,\mathrm{eV}$ respectively.

Magnetic Order in the Ca$_3$Ru$_2$O$_7$ Bulk

To calculate accurate adsorption energies, it is very important for the total energy of the reference structure to be well converged. As has been shown, the choice of the functional influences stability of the metallic or insulating ground state. This can also influence magnetic order in a crystal, so a small set of magnetic configurations were checked using the PBE, the PBE+U ($U-J = 4$ eV), and the HSE functional. Due to the computational cost involved no non-colinear solutions were considered. To reduce the computational effort, the $\vec{k}$-point grid was reduced to a $6 \times 6 \times 4$ Γ-centred mesh for the PBE and PBE+U calculations and a $4 \times 4 \times 2$ Γ-centred mesh for the hybrid calculations. First, a ferromagnetic (FM) and the experimentally found antiferromagnetic (AFM) ground state were calculated. In the FM state all spins were aligned in the same direction (see fig. 5.29a) while for the AFM state all spins within a Ca$_3$Ru$_2$O$_7$ double layer couple ferromagnetically and the spins in the next layer were flipped (see fig. 5.29b). In addition to that, three more different antiferromagnetic configurations AFM-1, AFM-2 and AFM-4 were considered where a different number of spins couples antiferromagnetically within a Ca$_3$Ru$_2$O$_7$ double layer (see figs. 5.29c to 5.29e).

As shown in table 5.4, the PBE functional yields the correct antiferromagnetic ground state, even though the energy difference of 10 meV is rather small, considering the 4 spins that are flipped. The PBE+U and the hybrid HSE06 functionals on the other hand incorrectly yields an insulating ground state with antiferromagnetic coupling of the spins in the Ca$_3$Ru$_2$O$_7$ double layer (AFM-4). Additionally, for the PBE+U calculation the FM state is more stable than the AFM state, indicating that the PBE+U approach prefers a magnetic structure with ferromagnetic coupling of the Ru spins at the rock-salt interface.

Table 5.4.: Total energy difference with respect to the magnetic ground state in meV. The PBE and the HSE functional lead to the correct AFM ground state, PBE+U yields the (incorrect) AFM-4 ground state. Figure 5.12 shows illustrations of these magnetic configurations.

	PBE	PBE+U	HSE
FM	10	206	119
AFM	0	301	96
AFM, 1 flipped	177	66	69
AFM, 2 flipped	269	140	73
AFM, 4 flipped	351	0	0

(a) FM   (b) AFM   (c) AFM-1   (d) AFM-2   (e) AFM-4
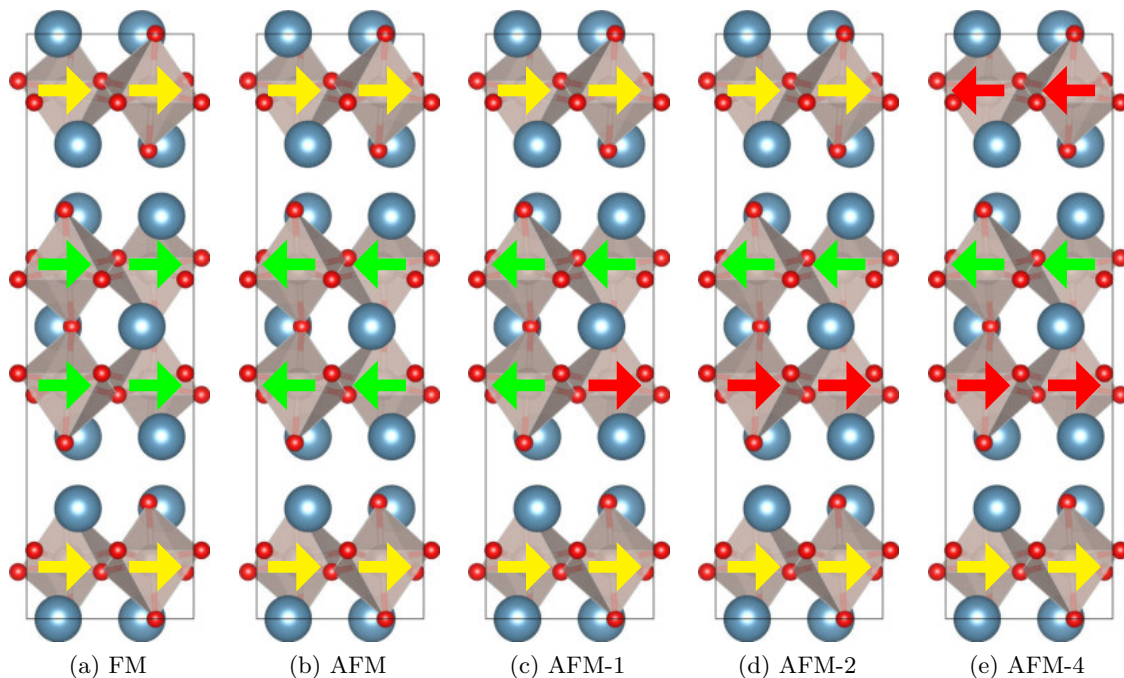
Figure 5.12.: Side view of the $Ca_3Ru_2O_7$ unit cell showing the various magnetic configurations. The green (red) arrows denote a positive (negative) magnetic moment at the given Ru site. A yellow arrow indicates the additionally flipped spin for the AFM-1, AFM-2 and AFM-4 configurations.

5.4. Strontium and Calcium Ruthenates: (001) Cutting Planes

While the previous chapter addressed the bulk structure and properties, in this chapter the surface properties of Sr_2RuO_4, $Sr_3Ru_2O_7$, $Ca_3Ru_2O_7$, and finally Ca-doped $Sr_3Ru_2O_7$ will be discussed. These layered perovskites often show different behaviour compared to their simpler binary oxides with similar surface terminations. For example, the SrO layers for $SrRuO_3$ and $Sr_3Ru_2O_7$ yield the same surface termination as the (001) surface of a binary SrO bulk crystal, but at a much larger lattice constant compared to the 5.159 Å of the latter. Another advantage is the ability to cleave them very easily in an experimental setup, leading to very flat surfaces without a significant amount of defects [2, 5, 168], ensuring well reproducible experimental conditions. This is also advantageous from the theoretical perspective as the theoretical model systems are expected to resemble the experimentally studied systems closely.

Since the main interest of this study was the (001) surface, only the cutting planes in this crystallographic direction were studied. Figures 5.13 to 5.15 indicate the studied cutting planes: cutting along the blue plane yields a rock-salt AO termination, along the magenta one an AO surface, and along the orange plane a BO_2 surface layer. Generally,

158

the blue plane only cuts though one A–O bond while both the magenta and the orange plane cut through a B–O bond. Considering that the calculation of the density of states of the three perovskites described in this work show almost no hybridisation of the oxygen atoms with the strontium and calcium (A-type) atoms, respectively, and strong hybridisation of the oxygen p-states and the ruthenium d-states, cutting through the Sr–O and the Ca–O planes should cost much less energy than breaking the Ru–O bond.

The cleaving energy in the (001) plane of the layered structures was determined by a series of total energy calculations where the bulk structure was pulled apart stepwise to create a slab structure. The surface energy is then the total energy difference between slab and bulk structures divided by the surface area. This set of calculations was done for both the PBE and the optB86b functional at the optB86b-optimised lattice constants for all three considered ruthenates Sr_2RuO_4, $Sr_3Ru_2O_7$, and $Ca_3Ru_2O_7$ (see figs. 5.16 to 5.18).

For the Sr_2RuO_4 crystal only two high-symmetry cutting planes in the (001) direction are possible: one at the rock-salt interface separating the perovskite layers and one cutting directly through the $SrRuO_3$ building blocks (see fig. 5.13). The low cost needed to break Sr–O bonds is well reflected in the calculations of the cleaving energy, see fig. 5.16. For both the PBE and the optB86b functional the cleaving energy is lowest for the SrO rock-salt structure between $SrRuO_3$ layers. The increase of the surface energy for the optB86b functional stems from the incorporation of dispersion effects.
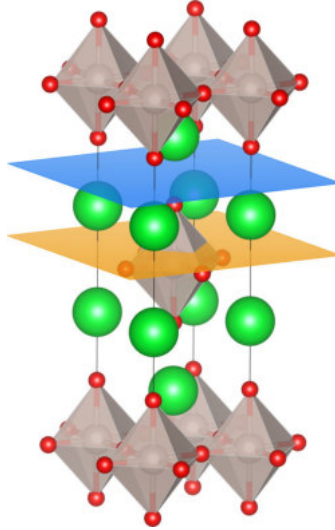
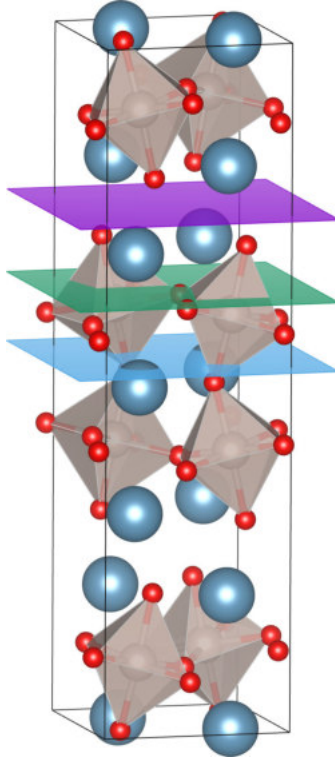

Figure 5.13.: Cleaving planes in the $n = 1$ Sr_2RuO_4 Ruddelsden-Popper series perovskite. The coloured planes indicate the cutting planes leading to different surface terminations. Blue: rock-salt interface, AO surface termination; orange: cutting through the $SrRuO_3$ perovskite block, leading to a RuO_2 surface termination.

The addition of another layer of $SrRuO_3$ in the $Sr_3Ru_2O_7$ structure gives rise to a third

cutting plane splitting the double layer apart, resulting in a SrO surface termination just like with the rock-salt interface (see fig. 5.14). Nevertheless, due to the Ru–O bond that would need to be broken, this cutting plane is less favoured compared to the rock-salt cutting plane, as can be seen in fig. 5.17. Still, the least favoured cutting plane is the one going through a $SrRuO_3$ building block, leading to the RuO_2 terminated surface. Again, both the PBE and the optB86b functional agree on the energetic order of the cutting planes, predicting the lowest cleaving energy at the rock-salt SrO plane.
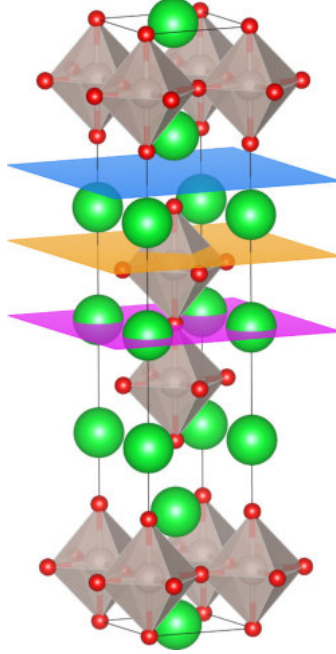
Figure 5.14.: Cleaving planes in the $n = 2$ $Sr_3Ru_2O_7$ Ruddelsden-Popper series perovskite. The coloured planes indicate the cutting planes leading to different surface terminations. Blue: rock-salt interface, SrO surface termination; magenta: SrO surface termination; orange: RuO_2 surface termination.

For the $Ca_3Ru_2O_7$ structure (see fig. 5.15) the calculations predict a similar behaviour as for the $Sr_3Ru_2O_7$ structure, again with lowest surface energy at the rock-salt terminated CaO surface. Additionally, the larger distortion of the octahedra results in larger differences in the surface energies compared to the $Sr_3Ru_2O_7$ structure: the difference between the cleaving energy in the rock-salt and the SrO or CaO plane is only $7\,meV/Å^3$ or $27\,meV/Å^3$ for $Sr_3Ru_2O_7$ at a distance of $10\,Å$ while for $Ca_3Ru_2O_7$ it is $38\,meV/Å^3$ or $45\,meV/Å^3$ for the PBE and the optB86b functional, respectively (see fig. 5.18). As can be seen in table 5.5, the $Sr_3Ru_2O_7$ crystal shows the lowest surface energy at the rock-salt terminated cutting plane. The surface energy at this cutting plane is higher for both the Sr_2RuO_4 and the $Ca_3Ru_2O_7$ crystal by $15.6\,\%$ ($26\,\%$) for the PBE (optB86b) functional for the former, respectively, and $12.5\,\%$ ($19.0\,\%$) for the latter.

Figure 5.15.: Cleaving planes in a $n = 2$ $Ca_3Ru_2O_7$ Ruddelsden-Popper series perovskite. The coloured planes indicate the cutting planes leading to different surface terminations. Magenta: rock-salt interface, CaO surface termination; blue: CaO surface termination; green: RuO_2 surface termination.

Table 5.5.: Surface energies of Sr_2RuO_4, $Sr_3Ru_2O_7$, and $Ca_3Ru_2O_7$ at the rock-salt terminated surface calculated with the PBE and the optB86b functionals at a slab distance of 10 Å.

$[meV/Å^2]$	PBE	optB86
Sr_2RuO_4	39	56
$Sr_3Ru_2O_7$	33	49
$Ca_3Ru_2O_7$	45	61
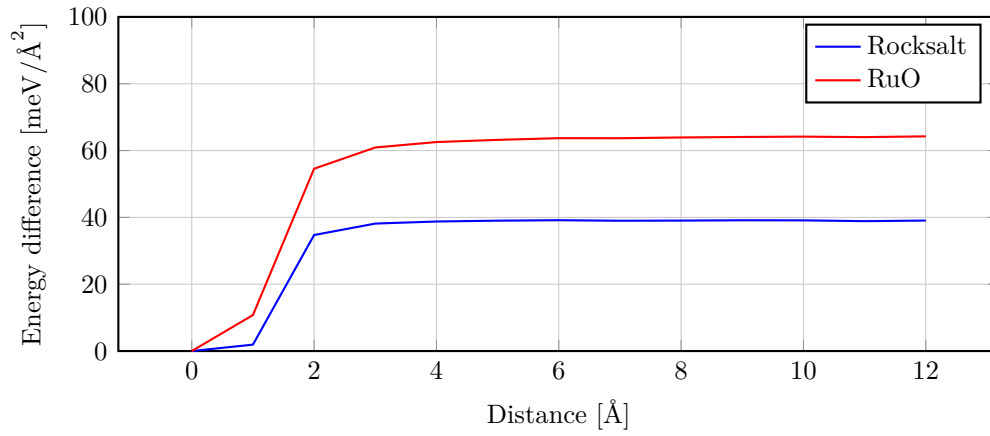
(a) Sr_2RuO_4 cleaving energy, PBE
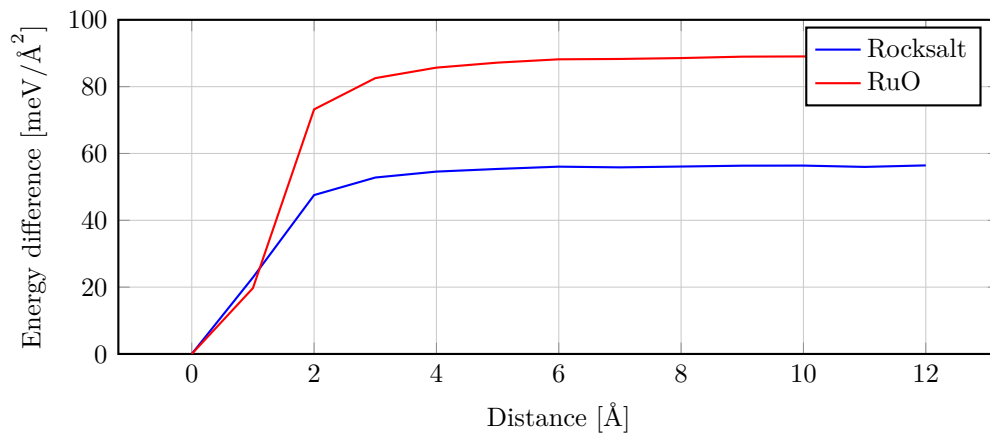
(b) Sr_2RuO_4 cleaving energy, optB86b

Figure 5.16.: Sr_2RuO_4 cleaving energies, calculated using both the PBE and optB86b functionals. The energy difference shows asymptotic behaviour at a layer distance of about $3\,\text{Å}$ for the PBE functional. Since the optB86b functional takes long-range interactions into account the some interaction can be detected at larger distances. The rock-salt cleaving plane is the most favoured for all functionals.
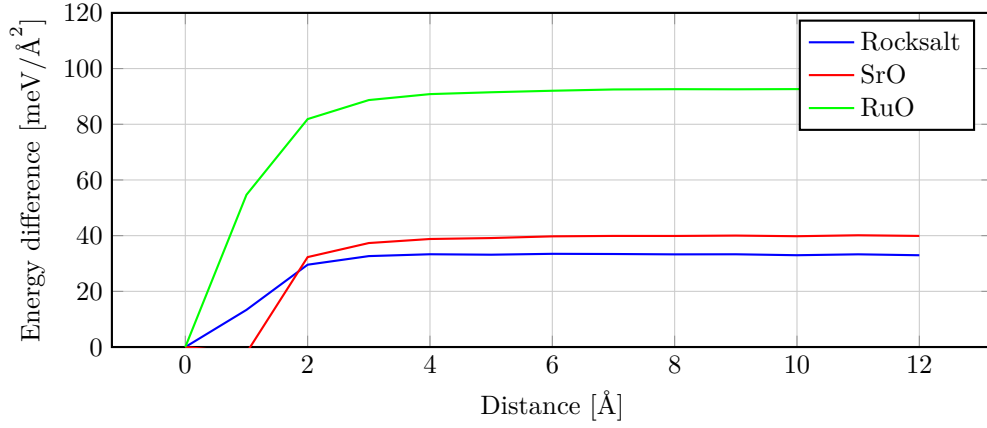
(a) Sr$_3$Ru$_2$O$_7$ cleaving energy, PBE
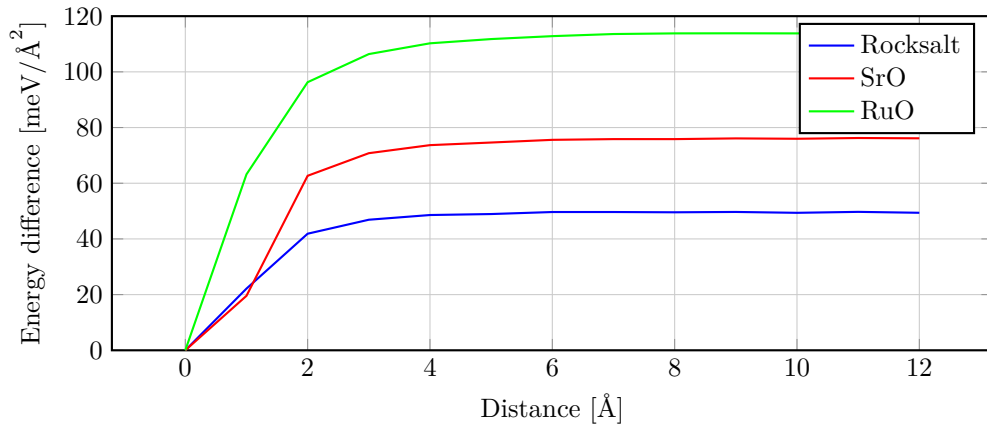
(b) Sr$_3$Ru$_2$O$_7$ cleaving energy, optB86b

Figure 5.17.: Sr$_3$Ru$_2$O$_7$ cleaving energies, calculated using both the PBE and optB86b functionals. The optB86b functional generally yields larger cleaving energies, and the difference between SrO or RuO$_2$ cutting plane is larger than for the PBE functional. The rock-salt cleaving plane is the most favoured for all functionals.
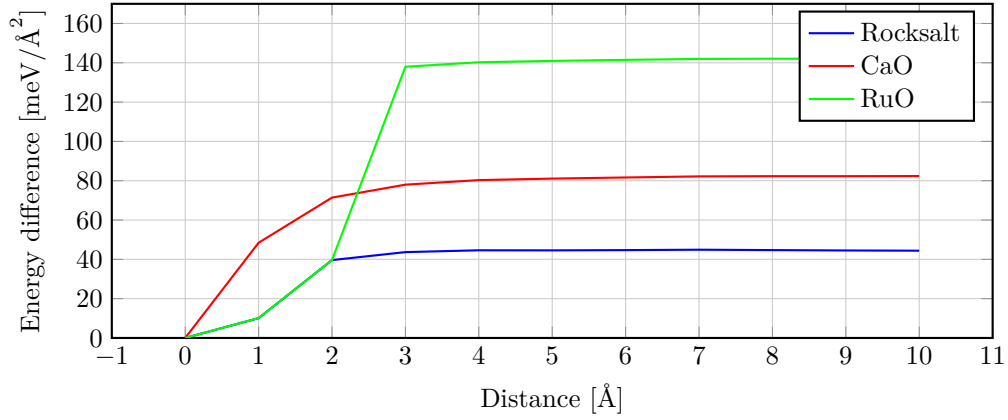
(a) $Ca_3Ru_2O_7$ cleaving energy, PBE
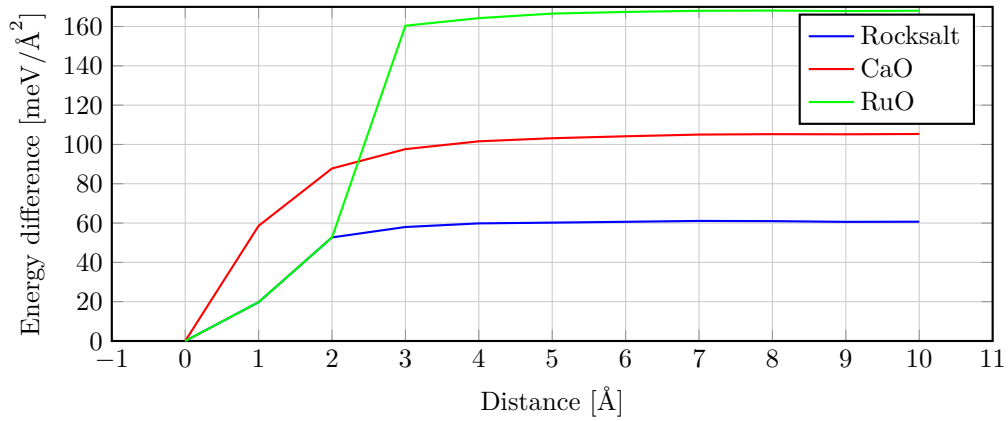
(b) $Ca_3Ru_2O_7$ cleaving energy, optB86b

Figure 5.18.: $Ca_3Ru_2O_7$ cleaving energies, calculated using both the PBE and optB86b functionals. The rock-salt cleaving plane is the most favoured for all functionals.

5.5. Strontium and Calcium Ruthenates: (001) Surface Structure

In this section the surface structure of the previously introduced perovskites is discussed. Many experiments have shown that these layered perovskites (e.g. Sr_2RuO_4: [169–173], $Sr_3Ru_2O_7$: [174–176]) can be cleaved easily in the (001) plane, resulting in flat well-defined surfaces which can be studied very accurately using surface sensitive methods such as atomic resolved STM, XPS, LEED, or AFM. Therefore, these slab geometries are good models to study their physical and chemical properties using DFT. The process to build these model cells (called "slabs" to differentiate from bulk cells) is fairly simple: one multiplies the bulk unit cell in the direction normal to the chosen cutting plane (which in the case of the (001) plane is normal to the crystallographic c axis) to get the desired slab thickness and elongates the c lattice vector while keeping the ions at their absolute positions. This creates a layered periodic unit cell at the bulk lattice constant in the ab plane where the slabs are separated by vacuum. The vacuum should be large enough so that surface effects of the "bottom" of the next slab do not influence the investigated surface. Usually, a vacuum gap of ≈ 15 Å is considered to be sufficient. Another important parameter, the slab thickness, also needs to be converged so that the influence of the bottom surface of the slab is not felt at the top through the crystal. This can be done by comparing the structural differences at different crystallographic layers to the bulk density of states to determine at which number of layers the middle of the slab is "bulk-like", or in a simpler way by comparing atomic and interlayer distances. By varying the number of surface unit cells it is possible to study for example different coverages of adsorbates or dopant concentrations. Generally, the optB86b functional was used as the workhorse for all model cells, except where otherwise noted. In some cases the optB86b results were compared to other functionals like PBE or Grimme-D3 (see section 2.6).

5.5.1. Sr_2RuO_4

As mentioned in section 5.3.1, the RuO_6 octahedra are neither rotated nor tilted in the Sr_2RuO_4 bulk, but as LEED *I(V)* [177] measurements and a combined STM and DFT study [172] has shown, the exposed surface reconstructs by rotation of the octahedra. This reported rotation of 9(3)° (DFT: 6.5°) gives rise to a c(2 × 2) surface unit cell. Additionally, a ferromagnetic ground state is reported, in contrast to the nonmagnetic state in the Sr_2RuO_4 bulk.

To properly model the Sr_2RuO_4 slab model, cells of different numbers of layers were created. The in-plane lattice constants of the c(2 × 2) surface unit cell are derived from the respective bulk values calculated for the PBE and optB86b functional (PBE: 5.507 Å, optB86b: 5.463 Å) while the c lattice constant was adjusted so that the vacuum separating the slabs amounted to >15 Å. The convergence with regard to the number of layers was evaluated by comparing the properties of a model cell consisting of two $SrRuO_3$ layers to one with four $SrRuO_3$ layers. For the calculations the $\vec{k}$-point grid was

set to a Γ-centred $6 \times 6 \times 1$ Monkhorst-Pack grid while the same energy cutoff used in the bulk calculations (400 eV) was selected.

The rotations of the octahedra was first studied using the 2-layer model cell. Three different starting configurations were considered: the unrotated, bulk-like configuration, one where the octahedra were rotated manually by 18.0° ("2 Layers" in table 5.6) and one where only the octahedra in one layer were rotated by the same amount and the other layer was fixed at the unrotated bulk parameters ("2 Layers†" in table 5.6) to mimic bulk behaviour. The latter configuration most closely represents a real Sr_2RuO_4 surface. Relaxation of the bulk-like model cell showed no change in the rotation of the octahedra as the ions remain in the high symmetry positions. Starting from the rotated configurations resulted in a rotation of the surface octahedra of 11.7° (9.3°) for the PBE (optB86b) functional for the first model and 10.7° (8.6°) for the PBE (optB86b) functional for the model where the second layer was fixed in a unrotated configuration. The calculated rotation angles bear close resemblance to the results reported by Matzdorf [172]. Nevertheless a comparison of the total energies showed a degeneracy of the rotated and the unrotated phase as the total energy difference per formula unit is below 1 meV.

A similar result was achieved for a larger, 4-layered model cell. Here the lower two layers were fixed at the bulk positions while the first upper layers were rotated by 18.0° and relaxed. Relaxing the cell with both the PBE and the optB86b functional yields a rotation of only the octahedra in the top $SrRuO_3$ layer of 10.5° and 6.0°, respectively. Like for the two-layer Sr_2RuO_4 slab the total energy differences between rotated and unrotated configuration again were <1 meV and the nonmagnetic ground state was preferred.

For the adsorption calculations, a two-layered slab was found to be thick enough to properly simulate adsorption geometries and energies as increasing the thickness lead to a change of the surface energy per area of <0.01 eV/Å^2

The Tersoff-Hamann STM simulations of the (001) surface of Sr_2RuO_4 (see fig. 5.21) show a two-fold symmetric pattern where the strontium atoms are visible as bright spots and the oxygen atoms as dark spots. This pattern holds for different bias voltages ranging from 0.2 eV to 0.8 eV for both the occupied and the unoccupied states.

5.5.2. $Sr_3Ru_2O_7$

The (001) surface structure of the $Sr_3Ru_2O_7$ crystal is very similar to the Sr_2RuO_4 case. Since the symmetry in the *ab* plane is already broken in the bulk due to the rotation of the octahedra, the c(2×2) surface unit cell arises naturally from the bulk unit cell. The $Sr_3Ru_2O_7$ surface slabs were modelled according to previous work [168, 179] where a single bilayer of $Sr_3Ru_2O_7$ was used to study the surface structure and to calculate adsorption energies of CO molecules. Here, these results could be confirmed independently. For the calculations a $6 \times 6 \times 1$ Γ-centered $\vec{k}$-point grid (20 irreducible $\vec{k}$-points) and an energy cutoff of 400 eV was used to perform the calculations, similar to the Sr_2RuO_4 case. In the $Sr_3Ru_2O_7$ slab the rotation of the octahedra is conserved but the angle is slightly larger at 10.5° (10.9°) compared to 9.4° (9.0°) in the bulk

Table 5.6.: Rotation angle of the octahedra in a two-layer ($\sqrt{2} \times \sqrt{2}$) Sr_2RuO_4 slab. In the "2 Layers†" model both layers were allowed to relax, leading to a rotation of the octahedra in both layers. For the two other models the lower layers were fixed at the bulk parameters. Only the top layer of the "4 Layers" model shows rotations of the octahedra.

	PBE	optB86b
Bulk	0	0
2 Layers	11.7	9.3
2 Layers†	10.7	8.6
4 Layers	10.5	6.0

(a) top view (b) side view (c) top view, rotated
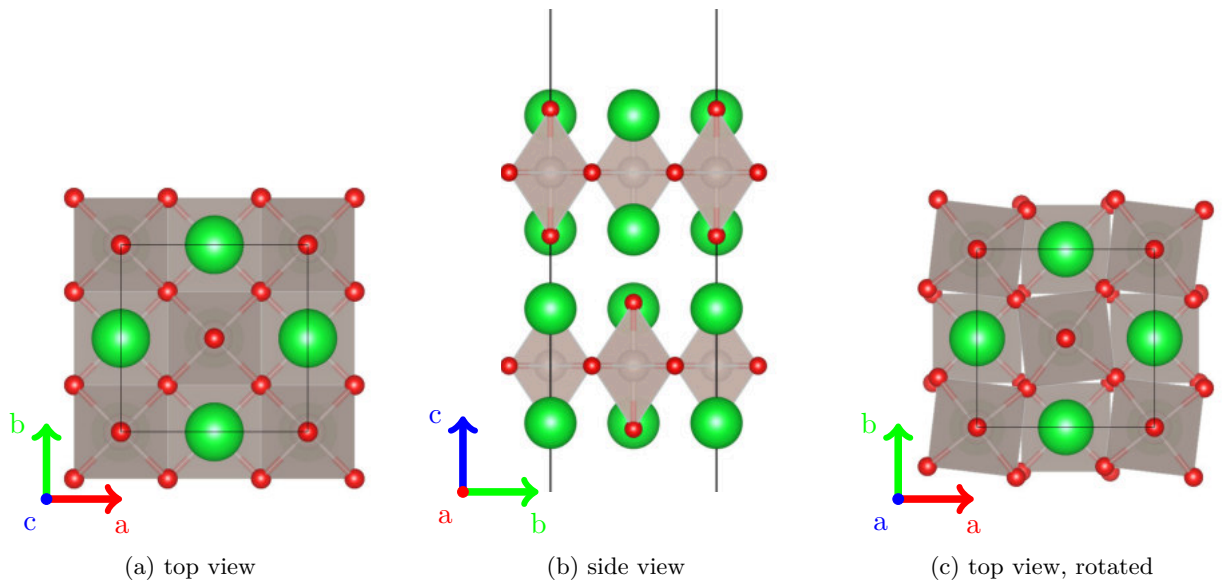
Figure 5.19.: 2-layer Sr_2RuO_4 model. (b) and (a) show the unrotated 2-layer structure, (c) the rotated one.

(a) top view   (b) side view   (c) top view, rotated
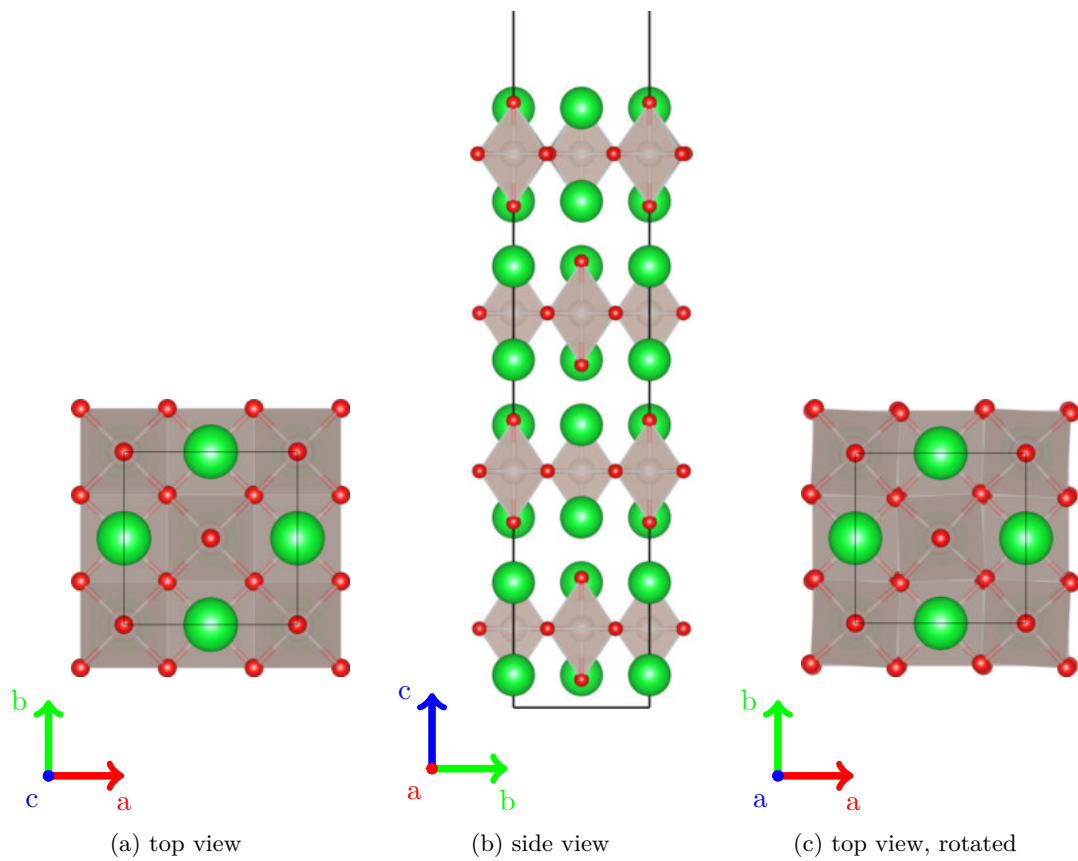
Figure 5.20.: 4-layer Sr_2RuO_4 model. (b) and (a) show the unrotated 2-layer structure, (c) the rotated one.

(a) PBE, Bias: $+0.5\,\text{V}$

(b) PBE, Bias: $-0.5\,\text{V}$

(c) optB86b, Bias: $+0.5\,\text{V}$

(d) optB86b, Bias: $-0.5\,\text{V}$

(e) experiment
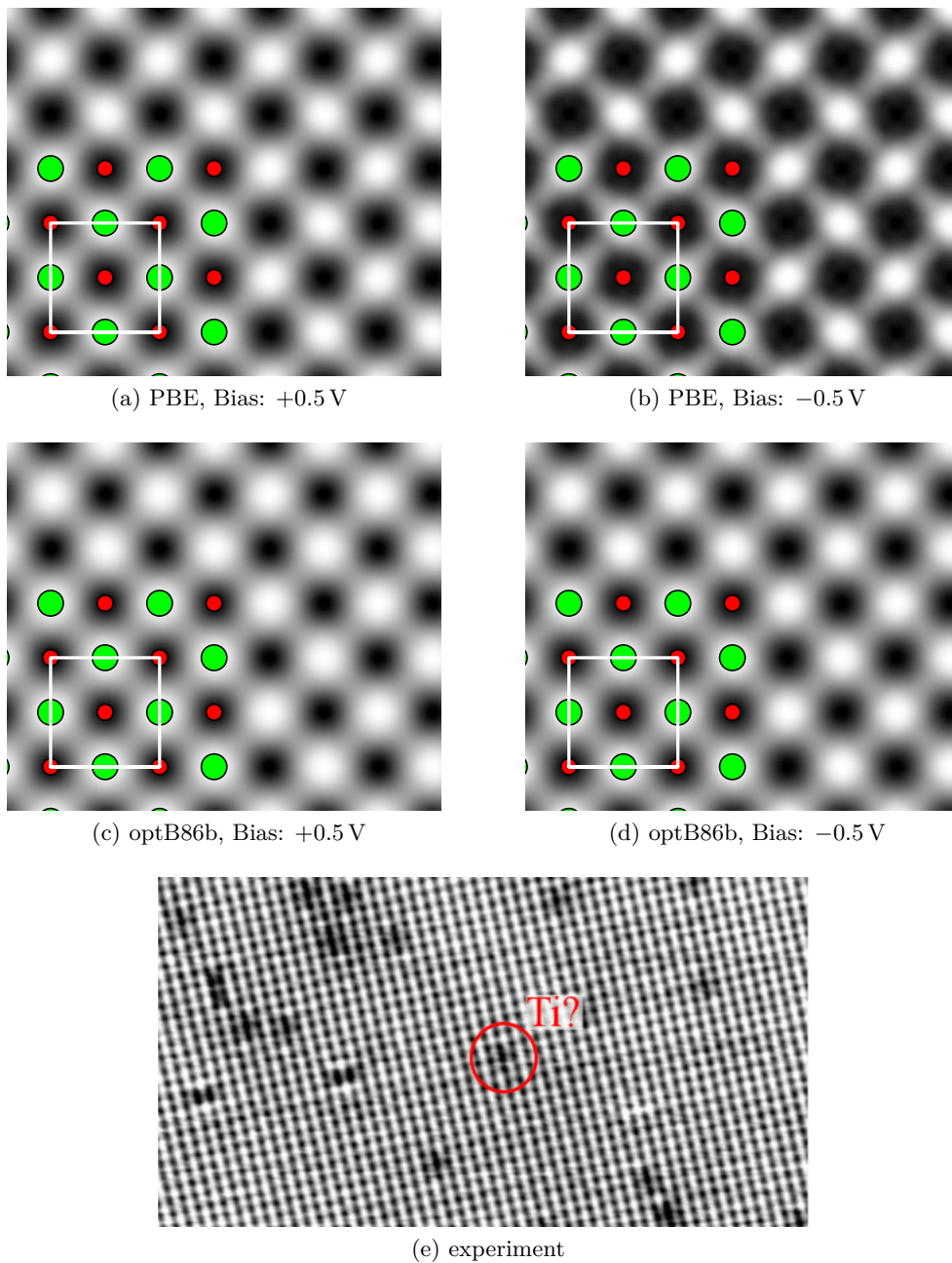
Figure 5.21.: 2-layer Sr_2RuO_4 model, STM simulation. Surface Sr atoms in green, O atoms in red. Bias voltage: $\pm 0.5\,\text{V}$. Isosurface at charge density of 10^{-7}. The Sr atoms are clearly visible as bright features in both the occupied and the unoccupied states. Both the PBE and the optB86b functional yield identical patterns. (e) STM image, measured at $U_s = 0.1\,\text{V}$, $I_t = 0.15\,\text{nA}$ by Stöger [178]. The dark features indicate (probably) Ti impurities.

for the PBE (optB86b) functional at the respective lattice constants. A slab model without rotated octahedra was found to be 161 meV (PBE, optB86b: 144 meV) per formula unit less favourable than the rotated structure. Figure 5.23 shows Tersoff-Hamann STM simulations of a single bilayer of $Sr_3Ru_2O_7$. The simulations indicate a regular structure of bright and dark patches with the strontium atoms occupying the bright spots. This pattern is preserved at both positive and negative bias and from 0.2 V to 0.800 V bias voltage. Compared to the STM simulations for Sr_2RuO_4 the images are virtually indistinguishable.

| (a) side view | (b) top view |
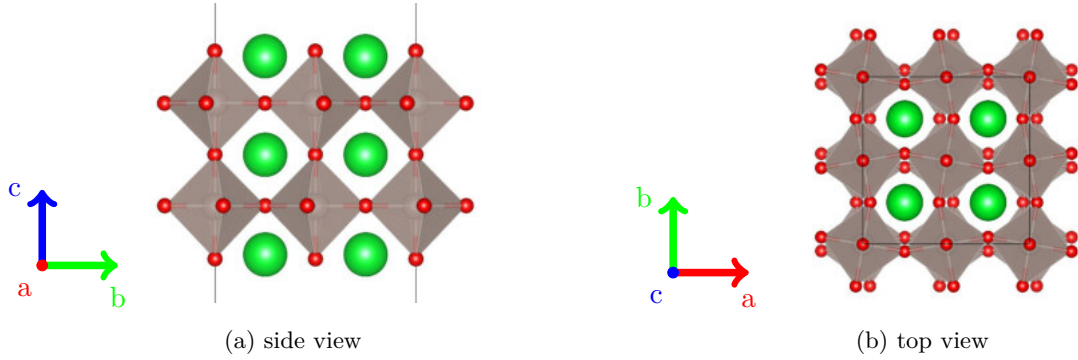
Figure 5.22.: 1-bilayer $Sr_3Ru_2O_7$ model cell. (a): side view: the octahedra are rotated against each other in one $SrRuO_3$ layer and alternately in the second layer. (b): top view: the box indicates the $c(2 \times 2)$ surface unit cell.

5.5.3. Ca-doped $Sr_3Ru_2O_7$

Substitution of strontium atoms by various dopants can alter the crystal structure and as a result thereof the physical and chemical properties of the surface. For example, varying the calcium content can transform the magnetic state of $Sr_3Ru_2O_7$ from an itinerant meta-magnetic state to an antiferromagnetic state [180–182]. Additionally, dopant and defect sites are often more reactive with respect to adsorption or dissociation [183]. Since calcium is often found as an impurity in $Sr_3Ru_2O_7$ samples [178] the influence of this dopant was investigated.

The surface of a doped $Sr_3Ru_2O_7$ crystal was simulated by replacing one strontium atom of the surface of the $Sr_3Ru_2O_7$ bilayer slab by a calcium dopant. In the smallest $c(2 \times 2)$ unit cell this corresponds to a dopant concentration at the surface of 25 % as one of four Sr atoms is replaced (model **A**). As this concentration is much higher than what is found in generally pure crystals the $Sr_3Ru_2O_7$ slab unit cell was doubled in x and y direction. In this new $c(4 \times 4)$ unit cell again one Sr atom was replaced by a Ca atom, yielding a dopant concentration of 6.25 % (model **B**). The computational parameters were the same as for the undoped slab for model **A**, for model **B** a $3 \times 3 \times 1$ Γ-centred Monkhorst-Pack $\vec{k}$-point grid (5 irreducible $\vec{k}$-points) was used.
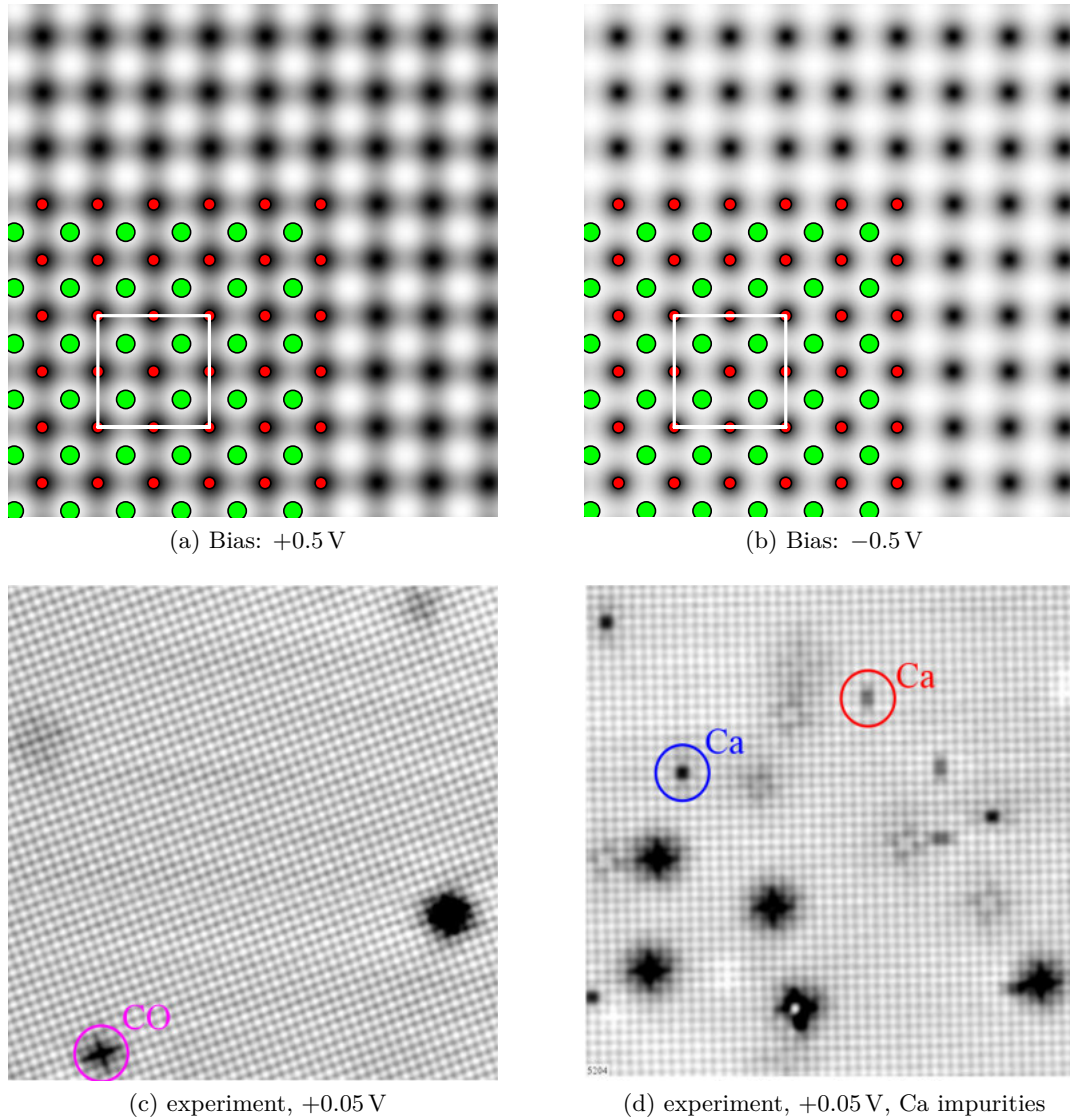
170

(a) Bias: $+0.5\,\text{V}$

(b) Bias: $-0.5\,\text{V}$

(c) experiment, $+0.05\,\text{V}$

(d) experiment, $+0.05\,\text{V}$, Ca impurities

Figure 5.23.: (a)-(b): One $Sr_3Ru_2O_7$ bilayer, STM simulation. Surface Sr atoms in green, O atoms in red. Bias voltage: $\pm 0.5\,\text{V}$. Isosurface at charge density of 10^{-7}. The Sr atoms are clearly visible as bright features in both the occupied and the unoccupied states while the O atoms occupy the dark spots in between. The rotation of the octahedra is not visible. (c)-(d): STM taken at $+0.05\,\text{V}$ bias voltage at $T = 78\,\text{K}$ and $I_t = 0.15\,\text{nA}$ courtesy of Stöger [178]. Dark spots indicated various defect, like adsorbed CO ((c)) and Ca impurities ((d)) at surface and subsurface, indicated by blue and red circles, respectively.

171

The relaxed structure of model **A** (see figs. 5.24a and 5.24b) shows the Ca atom occupying the site of the Sr atom it replaced. The Ca atom is moved slightly out of the high symmetry position (15 pm) otherwise occupied by the Sr atom and is depressed slightly by 17 pm due to its smaller ionic radius (Ca: 114 pm, Sr: 132 pm).

In the case of lower dopant concentration (model **B**) the in-plane displacement of the Ca atom was not observed. Nevertheless, the dopant moves 17 pm into the $Sr_3Ru_2O_7$ surface.

STM simulations of model **A** show the Ca atoms as dark feature in the Sr grid, but due to the high dopant concentration not all Sr atoms are visible at the same brightness. Additionally, due to the shift of the Ca atom out of the Sr position, the symmetry is broken. In the occupied states the bright spots that would indicate the Sr atoms in the undoped case are shifted into the intermediate region of a Sr–Sr or a Sr–Ca bridge. The picture is much clearer for **B**, again the calcium atom is visible as a dark feature but the $Sr_3Ru_2O_7$ surface symmetry is restored. Here the Sr atoms are clearly visible as bright spots while the O atoms occupy the dark areas in between for both positive and negative bias voltages. At positive bias the Ca atoms are indicated by large dark spots in the Sr grid while at negative bias they are shown as large grey spots.

5.5.4. $Ca_3Ru_2O_7$

As described in section 5.4, $Ca_3Ru_2O_7$ has the lowest cleaving energy in the (001) plane at the rocksalt interface, similar to both strontium ruthenates $Sr_3Ru_2O_7$ and Sr_2RuO_4. Similar to both other compounds the octahedra are rotated but also tilted, and therefore the (001) surface unit cell has the same symmetry as the bulk unit cell. To model the surface a slab consisting of a single bilayer of $Ca_3Ru_2O_7$ was chosen as the surface energy difference per area compared to thicker slabs is less than 1 meV (single bilayer: 61 meV/$Å^2$, double bilayer: 60 meV $Å^2$). To perform the calculations the same settings as for the $Sr_3Ru_2O_7$ slab was chosen: a $6 \times 6 \times 1$ Γ-centered $\vec{k}$-point grid yielding 16 irreducible $\vec{k}$-points and an energy cutoff of 400 eV. All calculations were done with the optB86b functional on the optB86b optimised bulk lattice constants, except where explicitly mentioned.

The bilayer is contracted slightly in the direction perpendicular to the surface plane: the Ca atoms move 10 pm into the bulk, the oxygen atoms 2 pm. This leads to a slight contraction by 0.2 % of the octahedra. The octahedra show slightly larger rotation of 15.7° compared to the bulk (13.0°) while the tilting is slightly smaller: 13.8° versus 15.6°. At the surface the rotation and tilting of the octahedra is changed slightly compared to the bulk: the tilting is slightly increased from 12.9° to 13.1° and the volume increases from 10.642 $Å^3$ to 10.690 $Å^3$. Figure 5.27 shows a closeup of a single unit cell: the apical oxygen atoms move towards the midpoint between two neighbouring Ca atoms.

In the STM simulations shown in fig. 5.28 the pattern differs from the strontium ruthenates: bright and dark lines are visible along the b direction of the unit cell between the Ca rows. The bright lines appear where the octahedra in the subsurface layer tilt away from the median of the Ca rows while the dark lines are shown were the octahedra
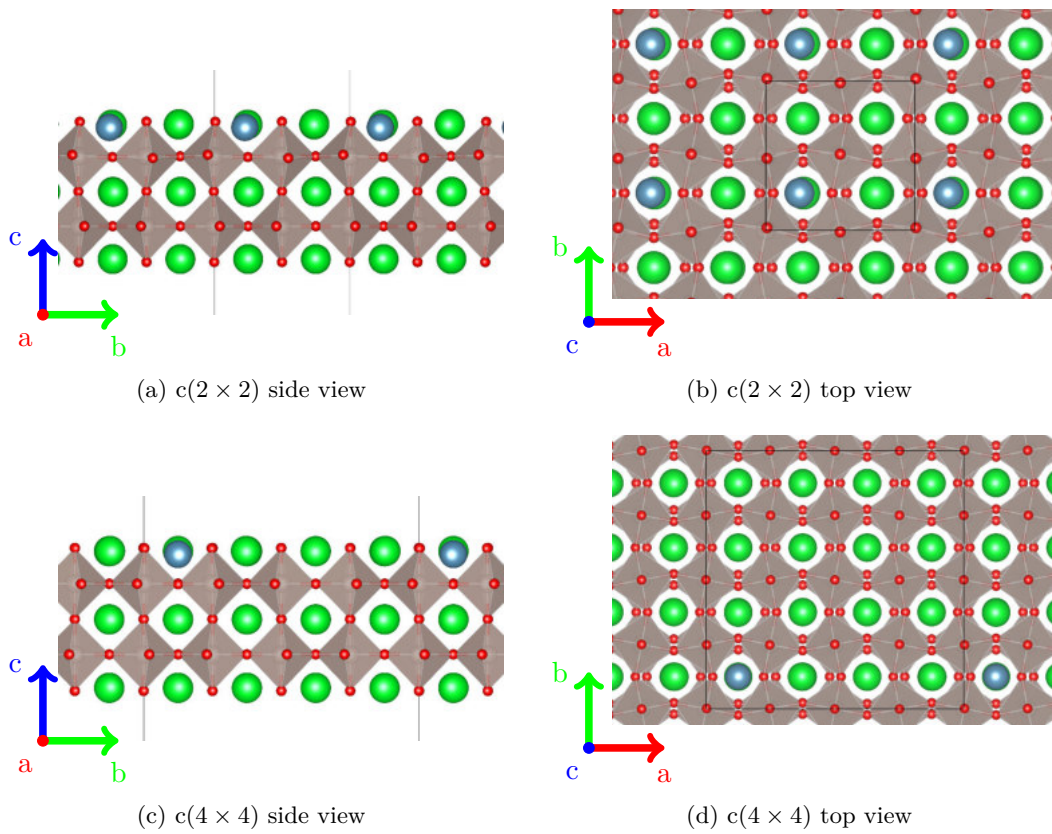
(a) c(2×2) side view

(b) c(2×2) top view

(c) c(4×4) side view

(d) c(4×4) top view

Figure 5.24.: 1-bilayer Ca-doped $Sr_3Ru_2O_7$ model cell. (a) and (b) show the c(2×2) unit cell at a Ca dopant concentration of 25 %; (c) and (d) with 6.25 % Ca content in the surface layer.
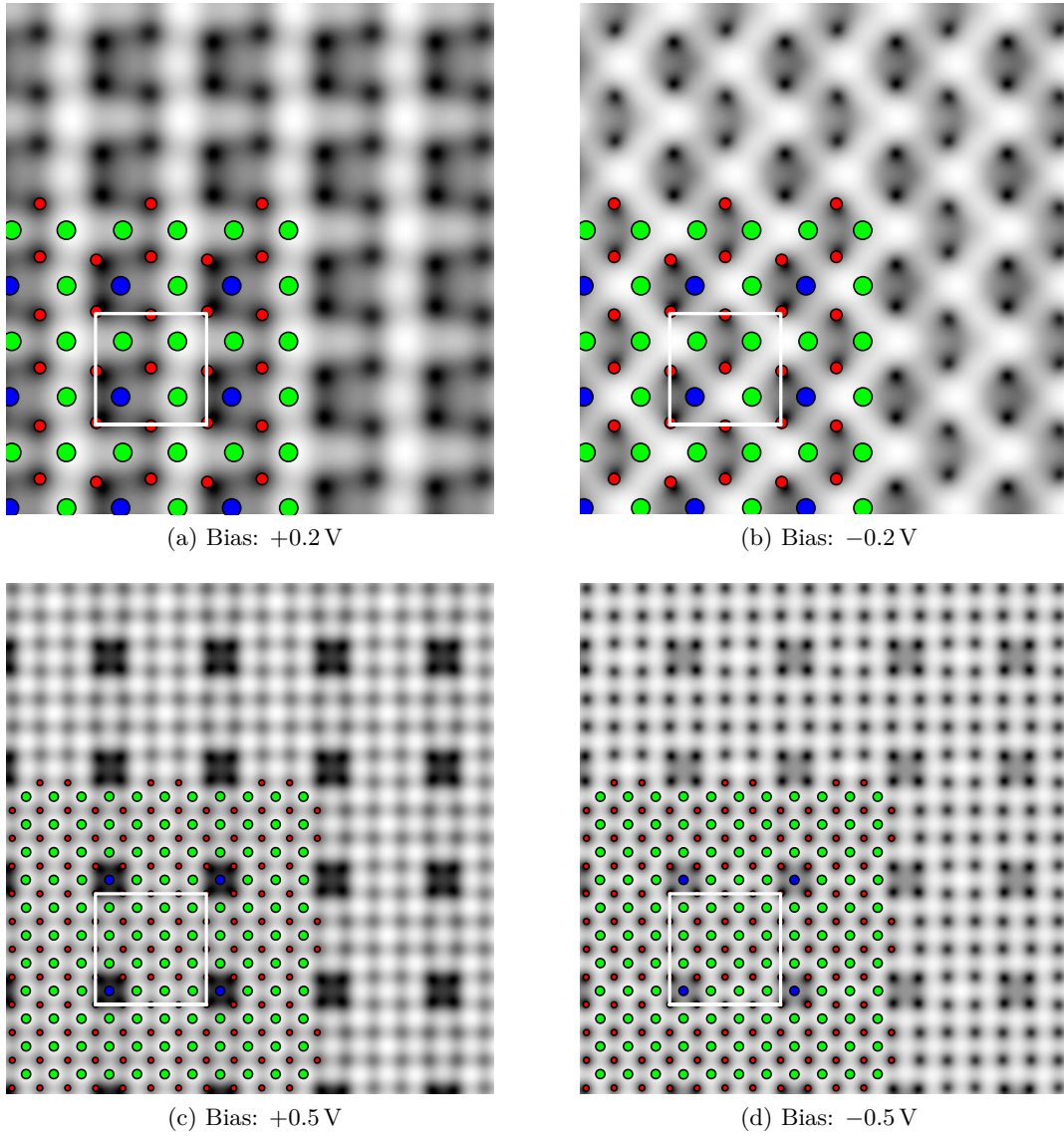
(a) Bias: $+0.2\,\text{V}$

(b) Bias: $-0.2\,\text{V}$

(c) Bias: $+0.5\,\text{V}$

(d) Bias: $-0.5\,\text{V}$

Figure 5.25.: One $Sr_3Ru_2O_7$ bilayer, one Sr per unit cell replaced by a Ca atom, STM simulation. Surface Sr atoms in green, O atoms in red, Ca atoms in blue. Bias voltage: $\pm 0.5\,\text{V}$. Isosurface at a charge density of 10^{-5}. For highly doped model **A** individual atoms are only visible at low positive bias voltages. In the occupied state picture ((b)) the bright spots are shifted into the area between the Sr and Ca atoms. Oxygen atoms always show as dark spots. The different symmetry compared to the pure $Sr_3Ru_2O_7$ surface can be attributed to the movement of the Ca atom from the high symmetry position. For model **B** the STM simulation is identical to the pure $Sr_3Ru_2O_7$ case in the undoped areas. The Ca atom can be easily distinguished as it shows up as a large dark spot at positive bias voltage ((c)) while at negative bias voltage it is visible as a grey spot ((d)), well in line with the STM done by Stöger [178] shown in fig. 5.23d.

tilt towards the median. The direction of these lines are given by the orthorhombic distortion of the unit cell in the *b* direction. The simulated images correspond well to the experimental image shown in fig. 5.28e.

(a) side view   (b) top view
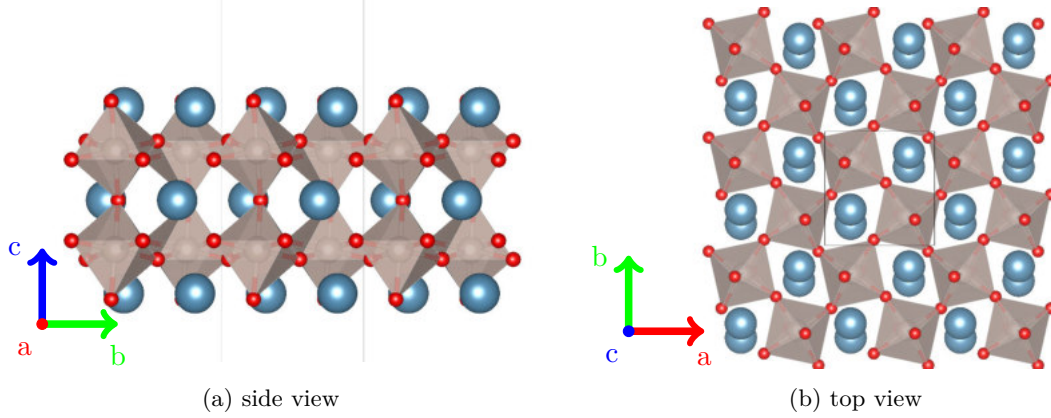
Figure 5.26.: 1-bilayer $Ca_3Ru_2O_7$ model. In contrast to $Sr_3Ru_2O_7$, the octahedra are not only rotated against each other but also tilted, leading to the symmetry breaking of the surface.

Magnetic Order in the $Ca_3Ru_2O_7$ slab

Similar to the bulk case in section 5.3.3, the magnetic order of the $Ca_3Ru_2O_7$ slab was investigated. As it is possible to consider both the metallic and the insulating state of $Ca_3Ru_2O_7$ by using a different computational approach, it is important to capture the correct magnetic ground state for both cases. This was done by comparison of the energy differences yielded by the PBE, PBE+U ($U - J = 4\,eV$), and the HSE06 functional. The $Ca_3Ru_2O_7$ slab configuration used for the calculations consists of two double layers of $Ca_3Ru_2O_7$ and one surface unit cell. Considering that in the bulk crystal the coupling between the double layers is antiferromagnetic, four additional magnetic configurations were chosen: one where *one* magnetic moment is flipped at either the rock-salt interface or at the surface (RS1 and VAC1), and one where *two* moments are flipped with respect to the bulk case (RS2 and VAC2). This was only done within one double layer, the magnetic moments in the "lower" double layer were all fixed in one direction. The energy differences calculated by the PBE functional show that in the metallic case the bulk magnetic structure (antiferromagnetic coupling between the double layers and ferromagnetic coupling within those) is preserved. Indeed, flipping a single magnetic moment at the rock-salt interface would take $223\,meV$, while the same process at the surface is much cheaper ($36\,meV$). The least preferred configurations compared to the bulk magnetic order are both the RS2 and VAC2 configurations ($\approx 245\,meV$).

Interestingly, for both the PBE+U and the hybrid calculations the magnetic ground
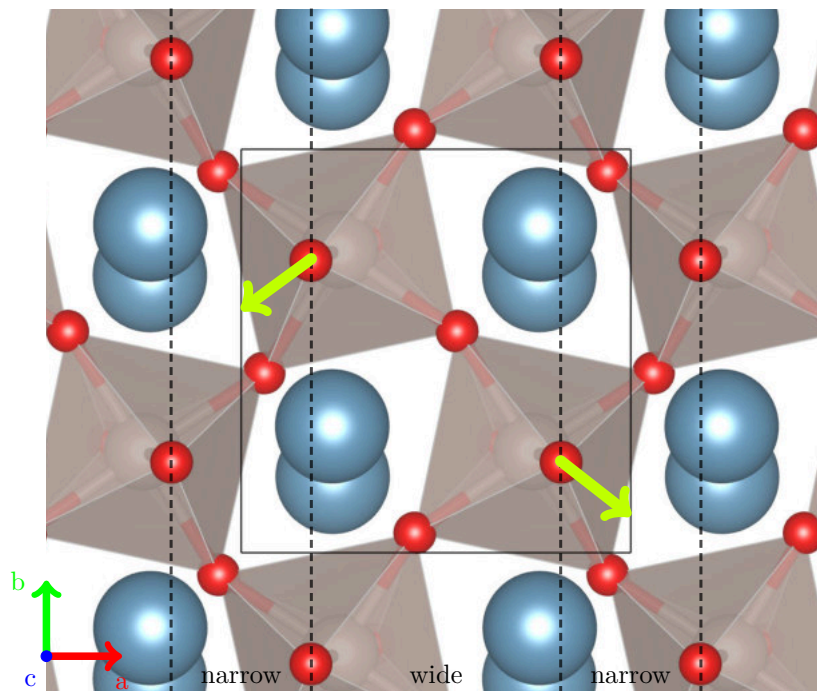
Figure 5.27.: Closeup of the $Ca_3Ru_2O_7$ surface unit cell. The bright arrows indicate the displacement of the apical oxygen atoms of the tilted surface octahedra, giving rise to the line structure in b direction seen in STM. The wide and narrow channels are indicated by dotted lines.
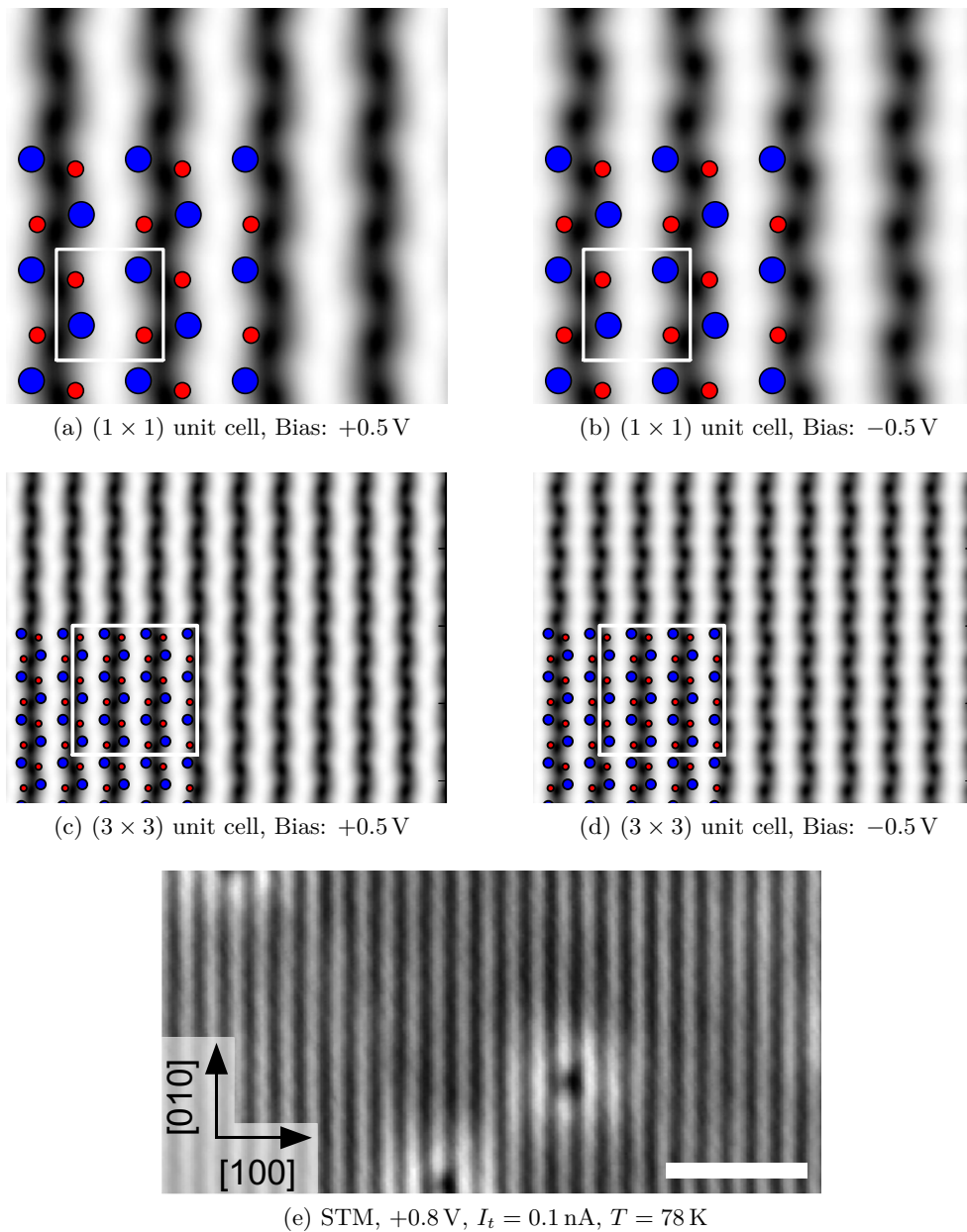
(a) $(1 \times$

(b) $(1 \times$

(c) (3×3) unit cell, Bias: $+0.5\,\mathrm{V}$

(d) (3×3) unit cell, Bias: -0.5

[010]
[100]

(e) STM, $+0.8\,\mathrm{V}$, $I_t = 0.1\,\mathrm{nA}$, $T = 78\,\mathrm{K}$

Figure 5.28.: One $Ca_3Ru_2O_7$ bilayer, STM simulation. Top row: (1×1) model cell, middle row: (3×3) model cell. Bottom: STM at $+0.8\,\mathrm{V}$, $I_t = 0.1\,\mathrm{nA}$, $T = 78\,\mathrm{K}$ published by Halwidl, Mayr-Schmölzer, et al. [5]. The white scale bar corresponds to $3\,\mathrm{nm}$. Surface Ca atoms in blue, O atoms in red. Bias voltage: $\pm0.5\,\mathrm{V}$. Isosurface at a charge density of 10^{-5}. For both positive and negative bias voltage bright and dark lines between the rows of Ca atoms are visible. The bright lines exist where the octahedra are tilted from each other, and the dark lines where the octahedra are tilted towards each other. The wiggles in the lines are due to the fact that the octahedra tilt towards the Ca–Ca bridge.

state of the slab is different: for both approaches a flipped magnetic moment at the surface is preferred to all other configurations. The RS1 configuration, where one magnetic moment at the rock-salt layer couples antiferromagnetically, is slightly less favoured ($\Delta E = 11$ meV for PBE+U, $\Delta E = 46$ meV for HSE06). The RS2 and VAC2 structures are, like in the PBE case, almost degenerated. Similar to the bulk case, the least favoured magnetic structure for the PBE+U approach is the bulk configuration (compare table 5.4) while the hybrid functional yields an energy difference very close to the RS2 and VAC2 configurations.

Table 5.7.: Total energy differences with respect to the magnetic ground state in meV. The PBE+U calculations were done with a value for $U - J = 4$ eV.

$(1 \times 1 \times 1)$ slab	PBE	PBE+U	HSE06
Bulk	0	170	232
RS1	223	11	49
VAC1	36	0	0
RS2	246	117	234
VAC2	245	116	237

A further set of calculations was done to determine the arrangement of the flipped spins at the vacuum layer for the insulating model. For this a double-layer $(1 \times 1 \times 1)$ unit cell was doubled in a direction. In the resulting $(2 \times 1 \times 1)$ unit cell three different arrangements of the magnetic were studied. For the first model the magnetic moment of only one Ru at the top layer was coupled antiferromagnetically to the moment in the layer, while for the other two arrangements the two flipped spins were either positioned next to each other (NN) or in the next (1×1) unit cell which is identical to the "VAC1" configuration. The comparison of the energy differences in table 5.8 shows that this "VAC1" configuration is indeed the magnetic ground state. Following the trend shown for the $(1 \times 1 \times 1)$ unit cell two having antiferromagnetic order in the double layer is less favoured in the insulating state, especially in the case of them being arranged next to each other ("2flip" NN configuration).

5.6. Surface Defects

Surface defects, such as vacancies, often alter the chemical properties of metal oxide surfaces and these sites are often more reactive than the surrounding material. In particular, oxygen vacancies have been investigated extensively on binary metal oxides. One example is TiO_2, where in the anatase phase electrons can be trapped only near oxygen vacancies, or where in the rutile phase polarons at the Ti sites are formed [104]. So far much less is known about oxygen vacancies on ternary oxides such as perovskites. Recently, some extensive work has been published regarding the surface structure of both $Sr_3Ru_2O_7(001)$ and $Ca_3Ru_2O_7(001)$ surfaces by Stöger et al. [168] and Halwidl,

Table 5.8.: Total energy differences per $(1 \times 1 \times 1)$ unit cell with respect to the magnetic ground state in meV. The PBE+U calculations were done with a value for $U - J = 4\,\text{eV}$.

$(2 \times 1 \times 1)$ slab	PBE+U
1flip	35
2flip NN	52
2flip VAC1	0
Bulk-like	173
FM	175

Vacuum

(a) Bulk   (b) RS1   (c) VAC1   (d) RS2   (e) VAC2
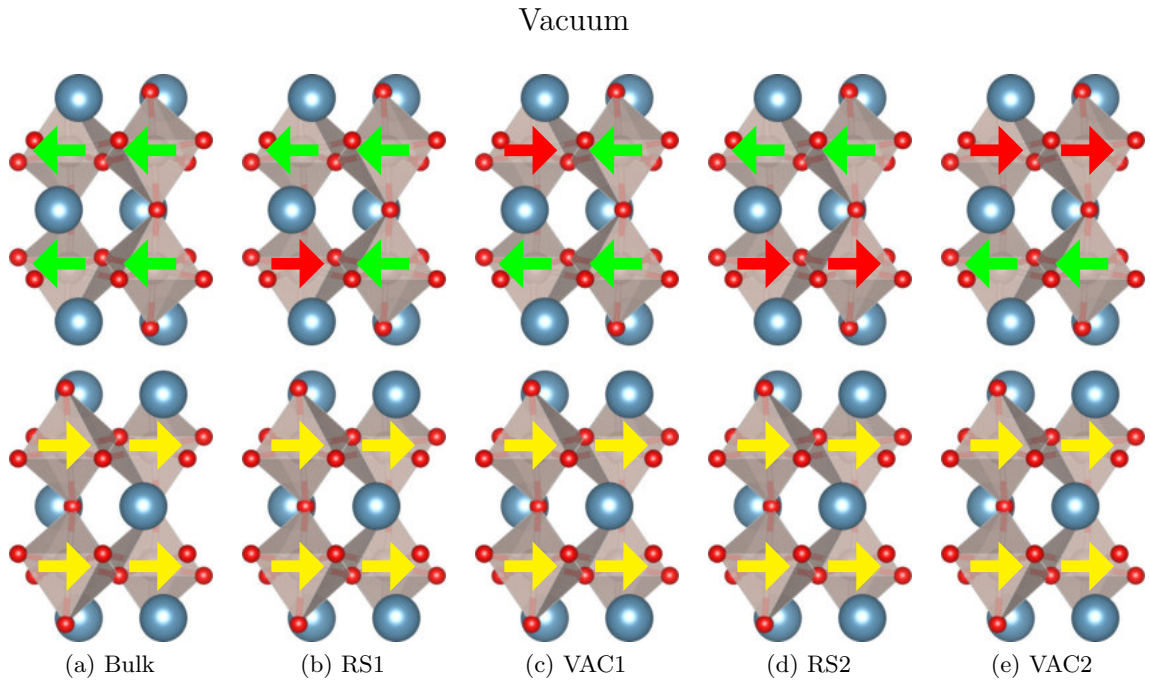
Figure 5.29.: Side view of the $Ca_3Ru_2O_7$ slab unit cell showing the various magnetic configurations. The green (yellow) arrows denote a positive (negative) magnetic moment at the given Ru site. A red arrow indicates the additionally flipped spins.

Mayr-Schmölzer, et al. [5] respectively (see fig. 5.30).

The vacancies were created using the slab model cells introduced in sections 5.5.2 and 5.5.4. In each case a large enough unit cell was created by multiplying the slab in a and b direction and removing an oxygen, strontium or calcium atom, respectively, from the surface layer. In the case of the $Sr_3Ru_2O_7$ the $c(2 \times 2)$ unit cell was doubled, yielding a $c(4 \times 4)$ unit cell, and for $Ca_3Ru_2O_7$ the unit cell the multiplication factor was 4. The energy necessary to create the surface vacancy of species X ($V_{X,surf}$) was calculated according to

$$V_{X,surf} = E_{Slab} - E_{Slab+Vacancy} - E_{Ref} \qquad (5.1)$$

with $E_{Slab+Vacancy}$ referencing the total energy of the relaxed slab including the vacancy and E_{Slab} the total energy of the pure stoichiometric slab. The total energy reference of the removed atom E_{Ref} was calculated from the binding energy of an oxygen molecule in the gas phase and the metallic bulk phases. The energy cutoff was set to the same value as for all previous calculations (400 eV).

(a) $Sr_3Ru_2O_7$, Bias: +0.1 V   (b) $Ca_3Ru_2O_7$, Bias: ±0.8 V
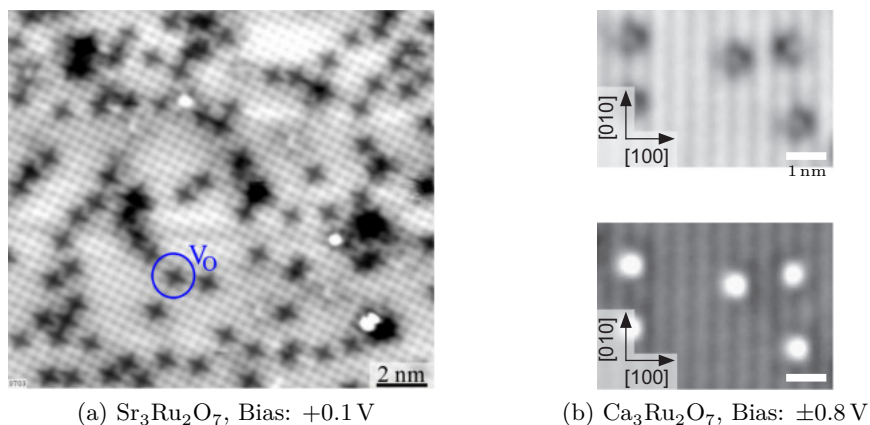
Figure 5.30.: (a) STM image of the $Sr_3Ru_2O_7(001)$ surface after bombardment with 1000 eV electrons at 105 K. Oxygen vacancies V_O appear as small, dark crosses. Image taken with $I_t = 0.15$ nA, $T = 78$ K, $U_s = +0.1$ V by Stöger, Hieckel, Mittendorfer, Wang, Schmid, Parkinson, Fobes, Peng, Ortmann, Limbeck, Mao, Redinger, and Diebold [168, 178]. (b) STM images of the $Ca_3Ru_2O_7(001)$ surface after the same procedure. Oxygen vacancies appear as small bright dots on the dark substrate line extending into the bright substrate line in the empty states, while in the filled states only a bright blob on the dark substrate line appears. Image taken with $I_t = 0.1$ nA, $T = 78$ K, $U_s = +0.8$ V (top right), $U_s = -0.8$ V (bottom right) by Halwidl, Mayr-Schmölzer, et al. [5].

5.6.1. $Sr_3Ru_2O_7(001)$

The stability of vacancies was simulated by using two different models. In the first case, the $c(4 \times 4)$ model introduced earlier, consisting of a single double layer of $SrRuO_3$, was employed to calculate the energies needed to create both surface oxygen and strontium vacancies. These results were tested against a second, thicker model with two double layers. This also allowed the consideration of subsurface defects. In this case a (4×4) unit cell was used to reduce computational effort, yielding a unit cell composed of the same number of atoms as in the former case. Due to the large size of the unit cell, a smaller $3 \times 3 \times 1$ Γ-centred Monkhorst-Pack $\vec{k}$-point grid was used.

For both models the introduction of a surface strontium vacancy yields an energy $V_{Sr,surf} = -4.726\,eV$, similar to the value given by Stöger et al. [168]. The surrounding Sr atoms relax slightly towards the vacancy ($\approx 0.211\,Å$) and the RuO_6 octahedra tilt slightly away from the vacancy (3.2°). Creating a subsurface Sr vacancy is more expensive at $-5.457\,eV$ for the SrO layer at the centre of the double layer. Here almost no structural change can be observed. Oxygen vacancies are easier to create, in the surface layer the cost to remove an O atom is $-4.155\,eV$. In this case the neighbouring strontium atoms move $\approx 0.275\,Å$ away from the oxygen vacancy. Due to this displacement the RuO_6 octahedra are slightly distorted and tilt by about 3° in response to the strontium atoms.

The Tersoff-Hamann STM simulations (see figs. 5.32a and 5.32b) show the oxygen vacancy as a very bright spot both at positive and negative bias voltages, embedded in the usual structure given by the pristine surface. Strontium vacancies on the other hand are indicated by dark spots in the unoccupied states, situated directly on the Sr grid. For the occupied states the pattern shown in the STM simulation is different, here they are indicated by grey spots on the brighter strontium grid. The four neighbouring strontium atoms are slightly brighter than the next nearest neighbours.

5.6.2. $Ca_3Ru_2O_7(001)$

As described before, a large (4×4) slab unit cell was used to calculate the vacancy formation energies $V_{Ca,surf}$ and $V_{O,surf}$. Due to the large size of the unit cell a $3 \times 3 \times 1$ Γ-centred $\vec{k}$-point grid was used. Compared to the $Sr_3Ru_2O_7$ case the vacancy formation energy is slightly lower at $-3.862\,eV$ for an oxygen vacancy, while the surface calcium atoms are more strongly bound ($V_{Ca,surf} = -5.245\,eV$). The presence of the oxygen vacancy results only in a minor distortion of the surface. The calcium atoms surrounding the vacancy site are displaced depending on the tilting of the next octahedron: for example, Ca_1 to the left of the vacancy is displaced by $0.302\,Å$ while Ca_2 right above the vacancy is displaced by only $0.080\,Å$. These displacements also influence the tilting of the octahedra in the neighbouring rows but the influence on the next nearest Ca atoms is negligible. In the case of a calcium vacancy the situation is quite similar, here the surrounding oxygen atoms move towards the next neighbour. The most displaced O atoms are O2 ($0.368\,Å$) and O3 ($0.436\,Å$) which causes the octahedra situated beneath it to tilt away from the vacancy.

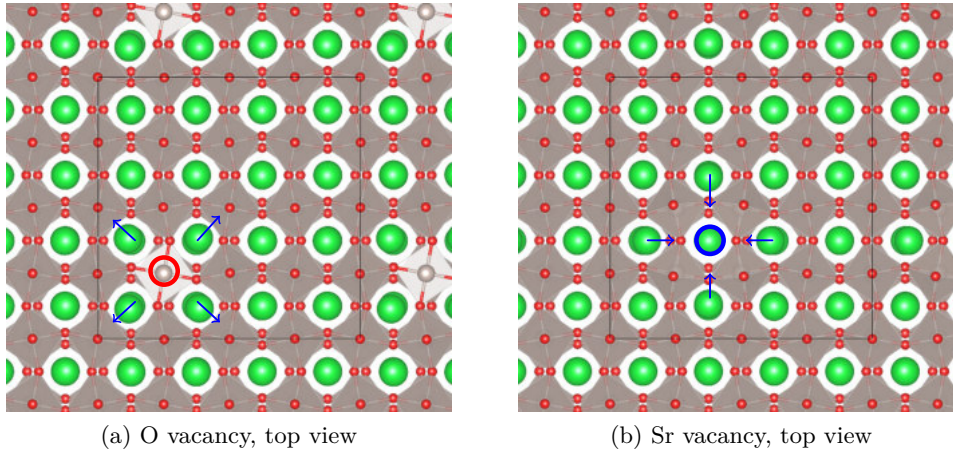The STM simulations show the oxygen vacancies as bright spots, a similar behaviour

(a) O vacancy, top view   (b) Sr vacancy, top view

Figure 5.31.: 1-bilayer c(4×4) $Sr_3Ru_2O_7$ model cell. (a) shows a top view of an oxygen vacancy indicated by the red circle, (b) a top view of a strontium vacancy indicated by a blue circle. Blue arrows indicate the displacement of the surrounding Sr atoms.

to the $Sr_3Ru_2O_7$ surface. The bright feature, smaller compared to the $Sr_3Ru_2O_7$ case, is positioned between the familiar bright lines of the pristine surface at the exact position of the vacancy. A calcium vacancy shows a dark spot at the position of the vacancy. In addition to that, the electronic states of the neighbouring atoms are influenced such that an additional dark spot in the unoccupied states appears in the next unit cell. In the occupied states an additional bright spot on the neighbouring bright line and a larger dark area surrounding the vacancy is visible. This pattern is most likely caused by the aforementioned distortion of the surface.

5.7. Summary

The DFT calculations show that the main properties of the three ternary perovskites Sr_2RuO_4, $Sr_3Ru_2O_7$, and $Ca_3Ru_2O_7$ are well described. All three consist of standard perovskite building blocks, which form layered structures separated by a rock-salt like interface in the SrO and CaO layers, respectively. While Sr_2RuO_4 consists of single layers, both $Sr_3Ru_2O_7$ and $Ca_3Ru_2O_7$ exhibit a double-layer structure. All three perovskites are structurally closely related, but some decisive differences exist which greatly influence the physical and chemical properties of both bulk and surfaces. In the single-layered Sr_2RuO_4 bulk, the RuO_6 octahedra are only slightly elongated in the c direction. The double-layered $Sr_3Ru_2O_7$ structure on the other hand exhibits rotations of the RuO_6 octahedra around the crystallographic c axis. For $Ca_3Ru_2O_7$ the smaller ionic radius of the Ca atoms leads to a orthorhombic distortion of the lattice. Additionally, the RuO_6 octahedra are both rotated and tilted with respect to the c axis.

(a) Bias: $+0.5\,\mathrm{V}$ (b) Bias: $-0.5\,\mathrm{V}$

(c) Bias: $+0.5\,\mathrm{V}$ (d) Bias: $-0.5\,\mathrm{V}$
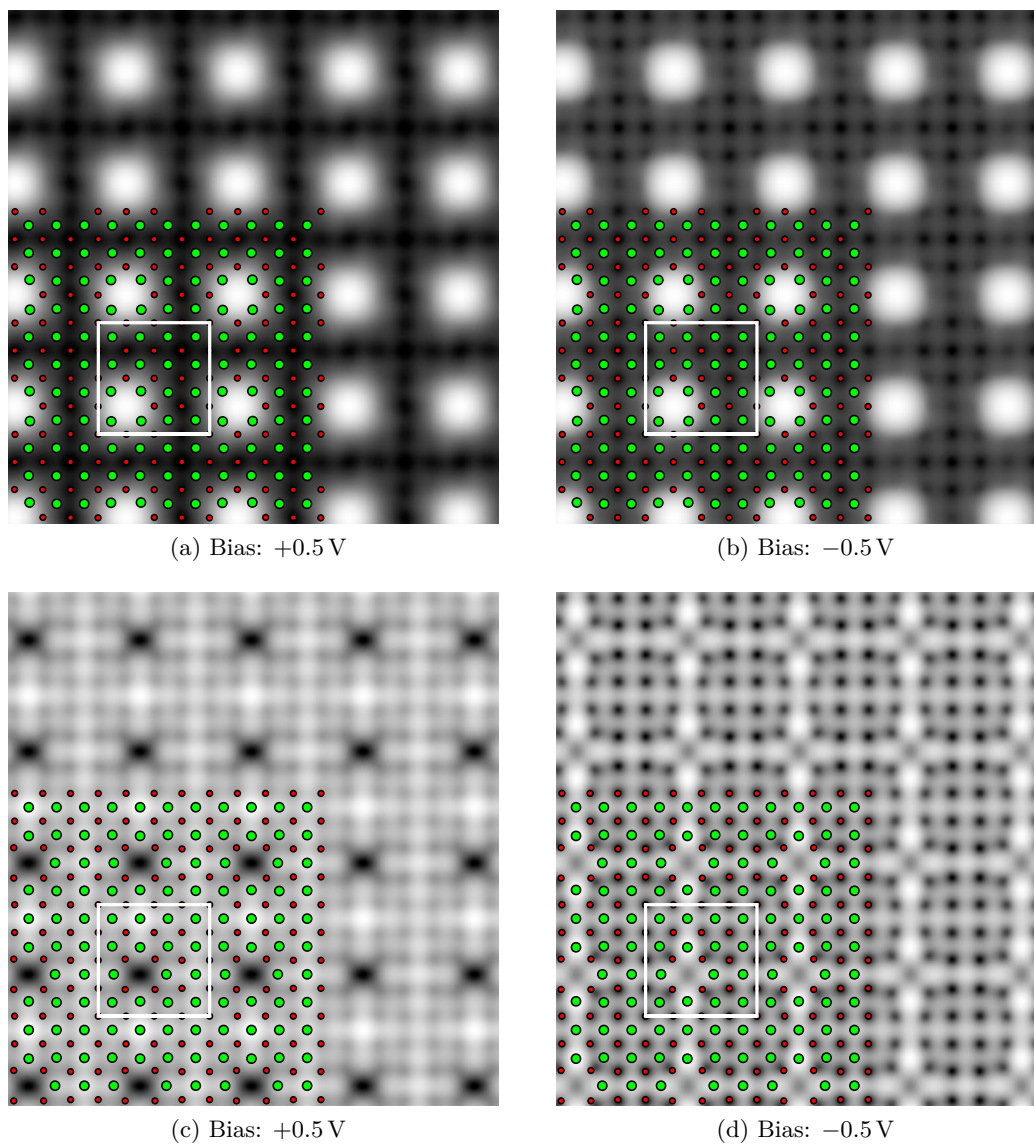
Figure 5.32.: STM Simulation of oxygen ((a), (b)) and strontium ((c), (d)) vacancies. An oxygen vacancy show a large bright spot in both the occupied and the unoccupied states. A strontium vacancy yields a dark spot in the occupied states, interrupting the bright grid of Sr atoms. At negative bias voltage the contrast between vacancy and dark oxygen spots is less pronounced, while neighbouring, displaced strontium spots are brighter than the rest.

(a) O vacancy, top view   (b) Ca vacancy, top view
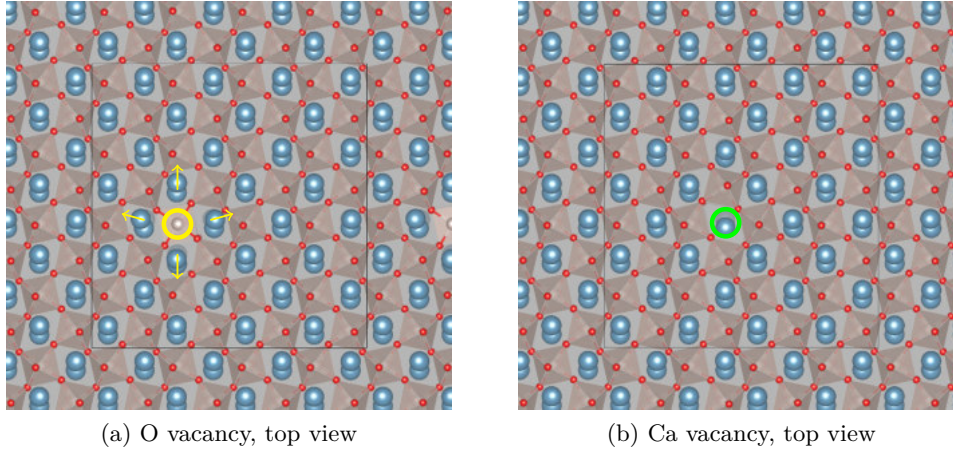
Figure 5.33.: 1-bilayer $Ca_3Ru_2O_7$ model cell. (a) shows a top view of an oxygen vacancy indicated by the yellow circle, (b) a top view of a calcium vacancy indicated by a green circle. Yellow arrows indicate the displacement of Ca atoms in case of the oxygen vacancy.

Comparing the predicted lattice parameters (see tables 5.1 to 5.3), the PBE functional yields a slight overestimation, while the van-der-Waals corrected optB86b functional results in very good agreement with experiment. Both approaches, which are still within the standard DFT regime, predict the correct metallic phase for the two strontium ruthenates. In the case of $Ca_3Ru_2O_7$, where a first-order transition to a non-metallic ground state below $T_M = 48\,K$ has been observed, standard DFT also yields a metallic ground state. Employing more advanced techniques like DFT+U or the HSE06 hybrid functional solves this deficiency, resulting in the correct insulating phase. This electronic transition also influences the magnetic structure of the $Ca_3Ru_2O_7$ bulk. In the metallic phase, DFT predicts an antiferromagnetic ground state where the spins within one double-layer are oriented in the same direction. A ferromagnetic state is energetically very close: according to DFT it would only cost $10\,meV$ to flip all four spins in the second double-layer. Within one double-layer the magnetic coupling is one order of magnitude stronger as flipping a single spin incurs an energy penalty of $177\,meV$ (see table 5.4). The situation is different in the insulating phase: both the PBE+U and HSE06 functionals predict antiferromagnetic coupling within the double-layer, as illustrated in fig. 5.29e and ferromagnetic coupling a the rock-salt like interface.

Due to the layered structure of these perovskites they can be cleaved very easily in (001) direction, resulting in large flat surfaces. By calculating the cleaving energies of different cleaving planes it could be determined that for all three perovskites the rock-salt layer shows the lowest surface energy. The values predicted by the optB86b functional are quite similar for all three crystals ($56\,meV/\text{Å}^2$, $49\,meV/\text{Å}^2$, and $61\,meV/\text{Å}^2$ for Sr_2RuO_4, $Sr_3Ru_2O_7$, and $Ca_3Ru_2O_7$, respectively).

(a) Bias: $+0.5\,\text{V}$

(b) Bias: $-0.5\,\text{V}$

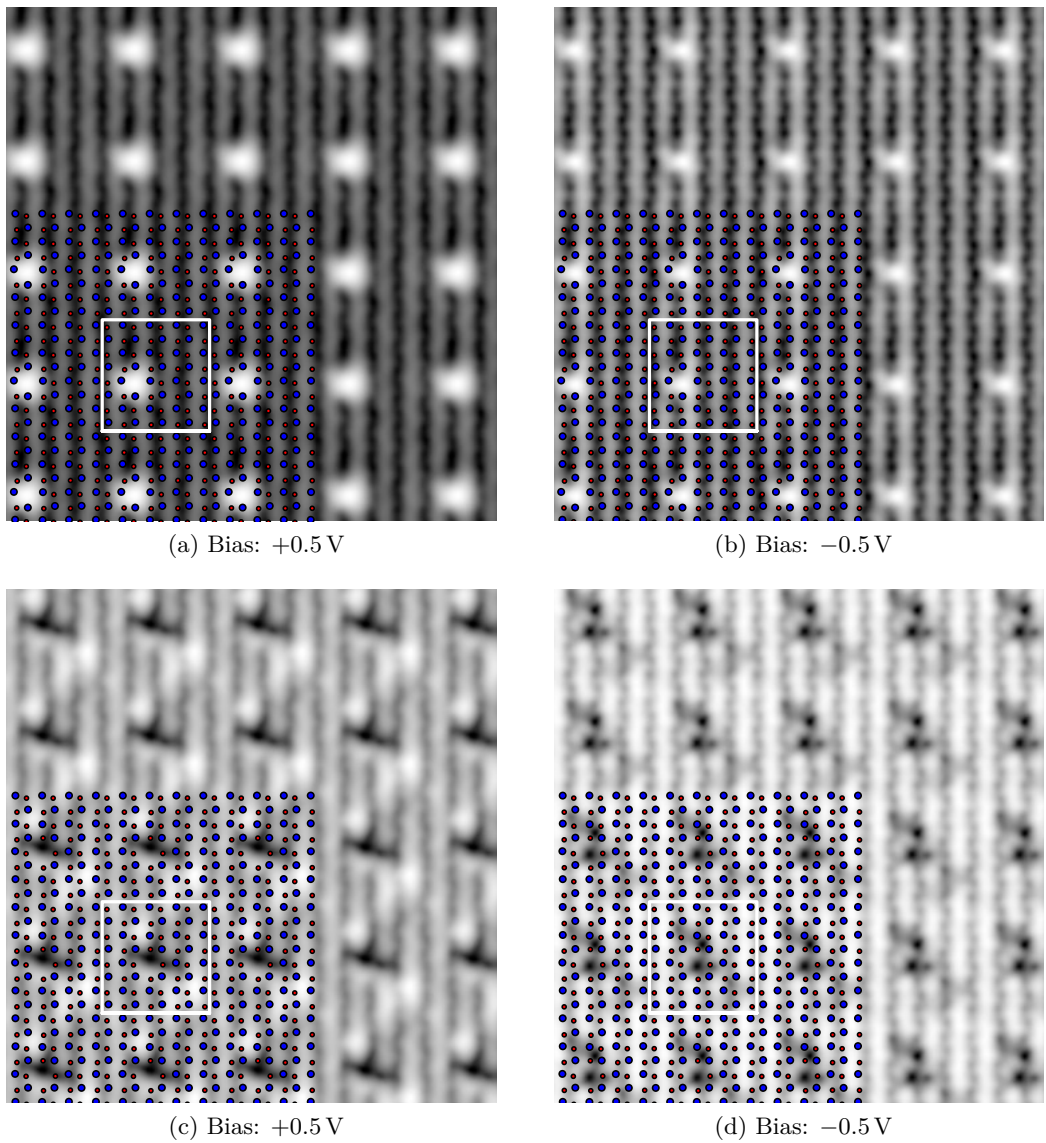(c) Bias: $+0.5\,\text{V}$

(d) Bias: $-0.5\,\text{V}$

Figure 5.34.: STM Simulation of oxygen ((a), (b)) and strontium ((c), (d)) vacancies. An oxygen vacancy show a large bright spot in both the occupied and the unoccupied states. The calcium vacancy is indicated by a large dark spot in the occupied states. In the unoccupied states a double feature is shown, indicating that the vacancy has a big influence on the electronic states of the neighbouring atoms.

185

Understanding the surface and subsurface structure of the aforementioned perovskites is of great interest to determine their physical and chemical properties with respect to adsorption of various materials. The cleaved SrO terminated Sr_2RuO_4 and $Sr_3Ru_2O_7$ (001) surfaces are very closely related to the binary SrO(001) surface but at a much larger lattice constant. For Sr_2RuO_4, the DFT calculations confirm the experimentally shown rotation of the RuO_6 octahedra, which gives rise to a c(2 × 2) surface unit cell similar to $Sr_3Ru_2O_7$. The STM simulations in both cases show a regular grid of bright and dark spots, with the surface Sr atoms occupying the bright and the O atoms the dark spots. The rotations of the RuO_6 octahedra in the subsurface are not apparent in these simulations. In addition to the pure surface, a Ca-doped $Sr_3Ru_2O_7$ surface was also studied at 25 % and 6.25 % dopant concentration. In both cases, the Ca dopant is slightly depressed into the surface due to its smaller ionic radius. Otherwise, the surface lattice is unchanged. The STM simulations show the Ca dopant as dark features in the bright Sr grid.

The CaO terminated $Ca_3Ru_2O_7$(001) surface on the other hand shows very large differences compared to the (001) surface of its related binary oxide. Due to the tilting of the RuO_6 octahedra the apical oxygen atoms are shifted from the central position in the Ca lattice in contrast to the CaO(001) surface. This, in conjunction with the orthorhombic distortion of the lattice, leads to a channel structure in b direction where in alternating rows the octahedra are tilted towards and away from the median. This channel structure becomes apparent in STM as bright and dark lines in b direction. The metal-insulating transition also influences the magnetic structure at the surface. In the metallic phase the bulk magnetic order persists. While flipping a single spin per surface unit cell at the vacuum interface only incurs a small energy penalty of 36 meV this is almost one order of magnitude larger at the rock-salt interface. After the transition to the insulating phase antiferromagnetic order at the surface is preferred. Indeed, studying the magnetic order in a larger (2 × 1) unit cell reveals that in the insulating phase a checkerboard pattern is preferred.

As surface defects play large role in surface chemistry the strontium, calcium, and oxygen vacancy formation energies were calculated for $Sr_3Ru_2O_7$(001) and $Ca_3Ru_2O_7$(001). For the former, introducing a strontium vacancy in the surface layer incurs an energy penalty of -4.730 eV, while the cost to remove an oxygen atom from the surface is -4.160 eV. On the latter surface, these values are slightly lower at -3.860 eV for the oxygen vacancy but higher for the calcium vacancy (-5.250 eV).

The results presented here agree very well with the experiment, and in the case of $Sr_3Ru_2O_7$ with older theoretical studies discussed by Stöger et al. [168]. For the $Ca_3Ru_2O_7$(001) surface, the DFT results were published in an academic paper by Halwidl, Mayr-Schmölzer, et al. [5] covering the adsorption of water molecules. In the following chapters, the $Sr_3Ru_2O_7$(001) and $Ca_3Ru_2O_7$(001) perovskite surfaces discussed here form the basis of comprehensive adsorption studies of water and oxygen molecules.

6. Adsorption of H$_2$O on Ruthenate (001) Surfaces

This chapter will focus on the structure and energetics of H$_2$O adsorbed on the ruthenate (001) surfaces introduced in the previous chapter.

The (001) surfaces of binary alkaline oxides show a wide variety of H$_2$O adsorption configurations, ranging from molecular to dissociative adsorption in different symmetries. For example, a combined experimental and theoretical study of high coverages of water on the (001) surface of MgO by Włodarczyk et al. [184] revealed partially dissociated H$_2$O adsorbing in two different stable superstructures, a low temperature c(4×2) symmetry and a p(3×2) structure at elevated temperatures. On CaO, which has a slightly larger lattice constant than MgO, again mixed molecular and dissociative adsorption even at low coverages was observed. A thorough theoretical study of water monomer adsorption on a multitude of materials by Hu et al. [185] has shown that certain trends can be derived for alkaline oxide surfaces. First, the lattice constant of the substrate plays a decisive role in the strength of the adsorption and the substrates ability to dissociate the water monomer. An increase of the lattice constant leads to enhanced hydrogen bonding with the surface due to the ability of the H$_2$O monomer to move closer to the substrate. Additionally, the flexibility of the substrate can influence the adsorption behaviour. Generally speaking, for the alkaline metal oxides CaO and SrO dissociative adsorption is preferred with one split off hydrogen ion binding to a surface oxygen atom (O$_S$H$_{Ads}$) and the remaining hydroxyl (OH)$_{ads}$ adsorbing at the bridge position with respect to the surface metal atoms. On MgO on the other hand, water adsorbs as an intact molecule. In some cases interesting dynamic behaviour of dissociated H$_2$O has been found. Grönbeck and Panas [186] have used *ab-initio* molecular dynamics calculations on BaO to predict rotation of the lightly bound ((OH)$_{ads}$) around a surface hydroxyl, to which it forms a hydrogen bond.

The following sections will expand upon the research done on binary metal oxide surfaces by showing that the adsorption behaviour on ternary transition metal oxides like Sr$_3$Ru$_2$O$_7$ and Ca$_3$Ru$_2$O$_7$ depends strongly on both surface and subsurface structure of the substrate.

6.1. Strontium Ruthenates

In this chapter the adsorption of varying coverages of water on the strontium ruthenates Sr$_2$RuO$_4$ and Sr$_3$Ru$_2$O$_7$ surfaces introduced in the previous chapter will be discussed. As Hu et al. [185] have shown, water monomers adsorb dissociatively on the binary SrO.

Recent data published by Halwidl, Stöger, Mayr-Schmölzer, et al. [2] shows that at low coverage the (001) surfaces of the ternary strontium oxides Sr_2RuO_4 and $Sr_3Ru_2O_7$ behave similarly, as water molecules prefer dissociative adsorption. Increasing the number of adsorbates leads to the formation of dissociated H_2O dimers and chains (see fig. 6.1). At high coverage a mixed adsorption is predicted, as the dissociated H_2O adsorbates form cages which contain molecular H_2O. Additionally, a low reaction barrier is predicted for the hopping of the H_2O monomer which allows the $(OH)_{ads}$ to move around a surface hydroxyl, similar to the behaviour predicted by Grönbeck and Panas [186] on BaO.

Due to the similarities of the Sr_2RuO_4 and the $Sr_3Ru_2O_7$ surface the main focus of this section will be on the $Sr_3Ru_2O_7$ substrate, except where explicitly mentioned. For all calculations the optB86b functional and the optB86b optimised lattice parameters were used. The energy cutoff was set to 400 eV. The calculations on the $Sr_3Ru_2O_7(001)$ surfaces were mainly performed on two model cells: the small c(2 × 2) structure introduced in section 5.5.2 with four Sr–Sr bridges in the surface unit cell and the large c(4 × 4) model with a four times larger surface area. This allows the simulation of different coverages of H_2O, ranging from full to ¹/₁₆ ML coverage. The $\vec{k}$-point grid used for these models were similar to the pure slabs: a Γ-centred 6 × 6 × 1 $\vec{k}$-point grid for the small c(2 × 2) model and a Γ-centred 3 × 3 × 1 $\vec{k}$-point grid for the large model. All structures were relaxed until the residual forces were below 0.01 eV/Å.

(a) H_2O on $Sr_3Ru_2O_7(001)$, Bias: +0.05 V

(b) H_2O chains on $Sr_3Ru_2O_7(001)$, Bias: +0.5 V
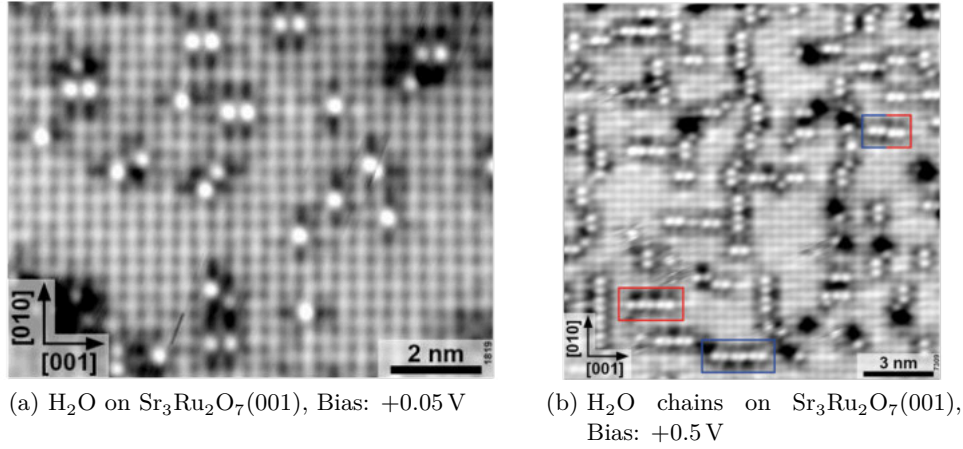
Figure 6.1.: STM images of water adsorbed on $Sr_3Ru_2O_7(001)$. (a) Image of 0.05 L of water, dosed at 115 K. H_2O monomer appear as bright dots. (a) After annealing at room temperature for 1 h the H_2O form chains. The dimers within the chains which are shifted upwards and downwards from the Sr–Sr bridges are indicated by the red and blue rectangles, respectively. The experimental parameters were $I_t = 0.15$ nA, $T = 78$ K, courtesy of Halwidl, Stöger, Mayr-Schmölzer, et al. [2].

6.1.1. H₂O Monomer

The H$_2$O molecule was placed in two different configurations on the Sr$_3$Ru$_2$O$_7$ surface. To reduce the configuration space the results by Hu et al. [185] were used as starting configurations. For the case of molecular adsorption the water molecule was placed so that its oxygen atom was positioned in the middle of a Sr–Sr bridge and the hydrogen atoms were pointing towards the apical oxygen atoms of the nearest RuO$_6$ octahedra, as shown in fig. 6.2. This position is identical to the "Type II" configuration introduced by Hu et al. [185]. For the dissociated configuration a similar approach was taken, here the split off hydrogen atom was placed at a distance of about 1 Å from the apical oxygen atom of one octahedron while the remaining hydroxyl was positioned on a Sr–Sr bridge, similar to the "Type III" configuration in the same paper (see fig. 6.3). On the small c(2 × 2) model cell which consists of two surface unit cells of the primitive lattice, this leads to a coverage of ¼ as one of four Sr–Sr bridges is occupied. To study lower coverages this unit cell was doubled, leading to a c(4 × 4) model cell with a coverage of ¹⁄₁₆. The adsorption energy E$_{Ads}$ was calculated according to

$$E_{\mathrm{Ads}} = E_{\mathrm{Slab+H_2O}} - E_{\mathrm{Slab}} - E_{\mathrm{H_2O}} \tag{6.1}$$

with E_{Slab} being the total energy of the clean slab and $E_{\mathrm{H_2O}}$ the total energy of molecular H$_2$O in the gas phase.

Relaxation of the structures revealed that dissociative adsorption is preferred by 241 meV and 185 meV for the small and large model cell respectively. Figures 6.2 and 6.3 show the final positions of the molecularly and dissociatively adsorbed H$_2$O molecule. Comparing the adsorption energies at the two coverages shows slight attractive interaction at a distance of 7.798 Å of dissociated H$_2$O molecules: 12 meV for dissociative and 44 meV for molecular adsorption. Compared to the binary alkaline oxide SrO (see appendix A), the adsorption energy is just ≈50 meV higher for the dissociated molecule, even though the Sr–Sr distance is 9 % larger in the ternary oxide. Generally, the influence of the adsorbate on the structure of the surface is rather small. In the case of dissociative adsorption the apical oxygen of the octahedron, where the split off hydrogen atom forms a bond, moves slightly away from the Sr–Sr bridge where the (OH)$_{ads}$ is located. This causes slight tilting of only that octahedron (≈12°). A molecularly adsorbed H$_2$O influences the surface even less as the hydrogen bond between the molecule and the apical oxygen only causes slight tilting (4°). As can be seen in table 6.2, the atomic distances are very similar at both coverages. An H$_2$O molecule in the gas phase has an O–H bond length of 0.974 Å and a bending angle of 104.7° calculated with the optB86b functional. The bond length of the adsorbed dissociated hydroxyl is very similar, while the O–H bond of the surface hydroxyl is slightly elongated. This stretching is also observed for molecular adsorption. Additionally, the bending angle is larger at ≈112°.

STM simulations (see fig. 6.4) of the dissociatively adsorbed water molecule show a bright spot at the position of the adsorbed hydroxyl which is slightly elongated into the direction of the surface hydroxyl at low bias voltages both for the occupied and the unoccupied states. Due to the position of the adsorbate which does not lie exactly on

the strontium grid, these spots are slightly shifted. In the case of molecular adsorption the H_2O molecule is again visible as a bright spot elongated along the direction of the molecule. Here the spot is positioned in the middle between strontium rows. Therefore dissociated and molecular water can be distinguished in experimental STM measurements (see fig. 6.1a).

Due to the symmetry of the $Sr_3Ru_2O_7(001)$ surface, a similar hopping mechanism of adsorbed hydroxyls can be expected predicted by Grönbeck and Panas [186] for H_2O on BaO. To calculate the energetic barrier that the $(OH)_{ads}$ needs to overcome the improved dimer method[1] introduced by Henkelman and Jónsson [187] was used to obtain the total energy of the transition state. These calculations predict that the adsorbed hydroxyl shows a transition state between two rotationally equivalent adsorption sites. For the low coverage case ($1/16$ ML) an energy barrier of 156 meV was obtained, at higher coverage ($1/4$ ML) a slightly higher energy barrier of 169 meV was predicted. In both cases the adsorbed hydroxyl is positioned close to a Sr atom at a distance of 2.388 Å, see fig. 6.5. The surface hydroxyl is slightly displaced as the hydrogen bond rotates with the position of the $(OH)_{ads}$. This prediction has been confirmed experimentally by imaging a single adsorbate multiple times at various temperatures and published by Halwidl, Stöger, Mayr-Schmölzer, et al. [2]. A simple model for one-dimensional diffusion [188] was used to evaluate the energy barrier: a fit to the Arrhenius equation of the average time between two hops gives an attempt frequency of $10^{11.0\pm0.7}s^{-1}$ and an activation energy $E_{act} = 187(10)$ meV, in good agreement with the predicted transition barrier.

On the Sr_2RuO_4 substrate the adsorption configuration is almost identical to the $Sr_3Ru_2O_7$ case. On the same $c(4 \times 4)$ unit cell the adsorption energies for dissociated and molecular water are slightly lower (-1.256 eV and -1.067 eV respectively) than on the $Sr_3Ru_2O_7$ substrate at the same coverage.

Table 6.1.: Adsorption energies in eV of a H_2O monomer on both the small and large model cell.

E_{Ads} [eV]	molecular	dissociated
Coverage	$Sr_3Ru_2O_7$	
$1/4$ ML	-1.031	-1.272
$1/16$ ML	-1.075	-1.260
	Sr_2RuO_4	
$1/16$ ML	-1.067	-1.256

6.1.2. H₂O Dimer

The two model cells introduced in the previous section have shown that increasing the water coverage leads to attractive interaction at a distance of 3.739 Å between the H_2O

---

[1]VASP setting: IBRION = 44

Table 6.2.: Atomic distances in Å of one H_2O monomer adsorbed on both the small and large $Sr_3Ru_2O_7$ model cells. H_2O molecule in the gas phase: O–H bond length: 0.974 Å, ∠(H–O–H): 104.7°.

| | c(2 × 2) | | c(4 × 4) | |
	molecular	dissociated	molecular	dissociated
(OH_{ads})	1.041	0.972	1.045	0.972
O_sH	1.585	1.032	1.562	1.030
H_{surf}–O_{ads}		1.526		1.531
γ_{H_2O}	112°		112°	
O_{ads}–Sr_1	2.678	2.575	2.682	2.595
O_{ads}–Sr_2	2.752	2.592	2.783	2.595

(a) top view   (b) side view
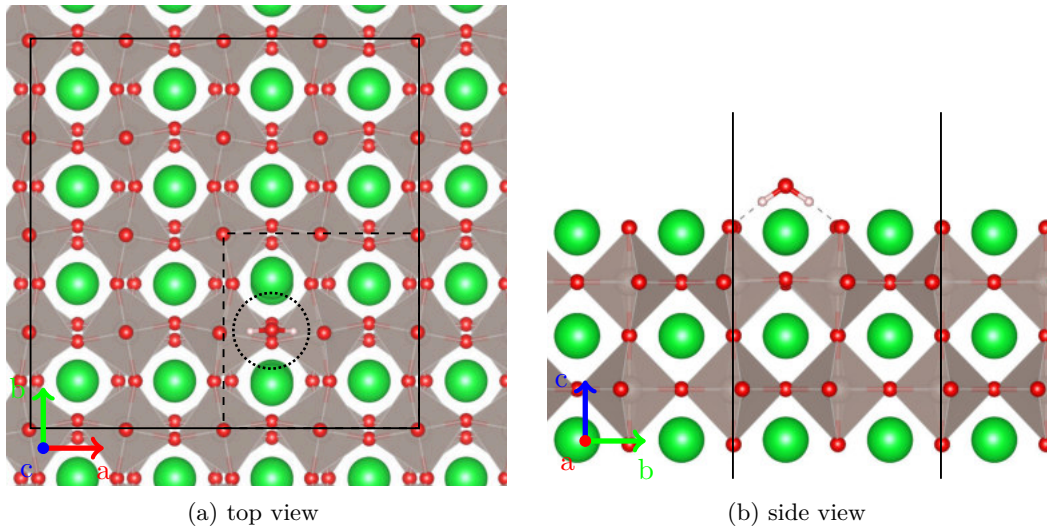
Figure 6.2.: Molecular adsorption of one H_2O on the $Sr_3Ru_2O_7(001)$ surface. Dashed line: c(2 × 2), solid line: c(4 × 4) surface unit cell.

(a) top view   (b) side view
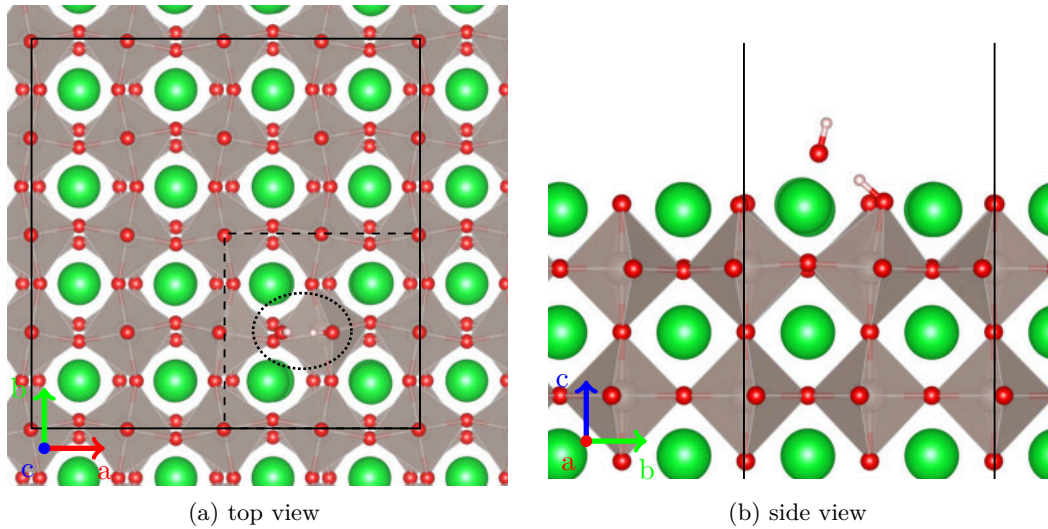
Figure 6.3.: Dissociated adsorption of one H_2O on the $Sr_3Ru_2O_7(001)$ surface. Dashed line: $c(2 \times 2)$, solid line: $c(4 \times 4)$ surface unit cell.

molecules, but even in the small model cell the monomer adsorbates were still separated by one unit cell. To investigate the behaviour of dissociated water at nearest neighbour sites, the coverage of H_2O was increased on the large model cell. If one only considers the surface layer, only two high-symmetry structures have to be considered: one where the surface hydroxyls are positioned at the same side formed by the $(OH)_{ads}$ (parallel) and one where the O_sH are situated at opposite sides (zig-zag). Considering also the symmetry of the subsurface layer, two different parallel dimer configurations can be distinguished. In the first configuration "wide" the H_2O are positioned at sites where the octahedra are rotated away from each other (fig. 6.6a) while in the second configuration "narrow" the octahedra are rotated towards each other (fig. 6.6b). The rotation away (towards) of the octahedra increases (decreases) the distance between oxygen atoms along the strontium rows to $4.539\,\text{Å}$ ($3.259\,\text{Å}$), resulting in a wide and a narrow structure.

Both the wide and narrow configuration show a higher adsorption energy per H_2O molecule than for the dissociated monomer (see table 6.3), indicating attractive interaction between the two adsorbates. Comparing the wide and narrow structure reveals that the narrow structure is preferred by $31\,\text{meV}$. The reason for this energy difference can be explained by the flexibility of the surface. In the wide configuration the surface Sr atom located between the two adsorbates shows just slight displacement ($14\,\text{pm}$) as its freedom of movement is constrained by the "narrow" configuration normal to the direction of the dimer and the $(OH)_{ads}$ of the dimer itself (see fig. 6.6a). On the other hand, in the narrow configuration (fig. 6.6b) the strontium atom is less constrained in the direction normal to the dimer, leading to a more stable configuration with a displacement of $31\,\text{pm}$. The atomic distances of the dissociated parts of the H_2O molecule are identical to the adsorbed monomer. The distance between the $(OH)_{ads}$ is $4.041\,\text{Å}$

192

(a) Bias: $+0.5\,\mathrm{V}$

(b) Bias: $-0.5\,\mathrm{V}$
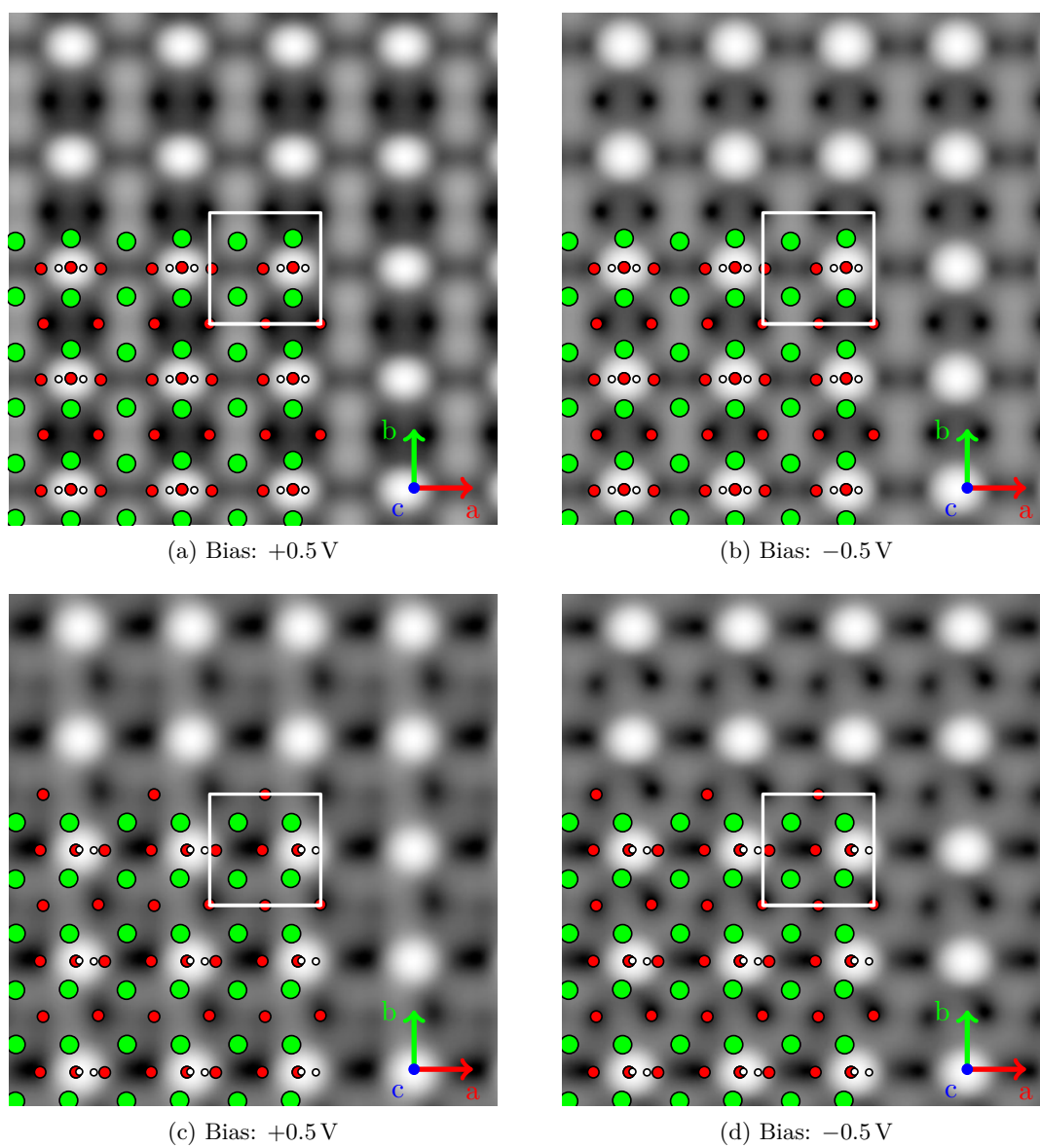
(c) Bias: $+0.5\,\mathrm{V}$

(d) Bias: $-0.5\,\mathrm{V}$

Figure 6.4.: STM Simulation of the H_2O monomer adsorption on the $c(2\times2)$ model cell. (a) and (b): molecular, (c) and (d): dissociative adsorption. In both cases the H_2O is indicated by a bright spot, in the former case positioned directly on top of the Sr rows, in the latter slightly shifted as the $(OH)_{ads}$ is tilted towards the surface hydroxyl.
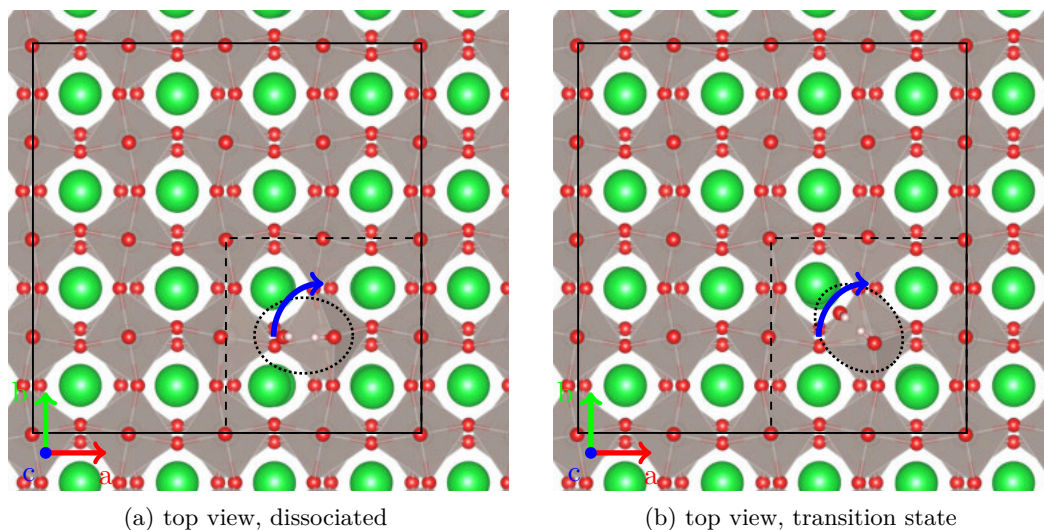
(a) top view, dissociated   (b) top view, transition state

Figure 6.5.: Transition state of the dissociated monomer. (a) dissociated ground state, (b) transition state.

for both the "wide" and the "narrow" case, slightly more than the Sr–Sr distance of $3.900\,\text{Å}$. Both H_2O are positioned slightly off the middle point between the vertical Sr rows, indicated by the asymmetric O_{ads}–Sr_{left} and O_{ads}–Sr_{right} distances respectively.

The STM simulations for both dimers show a similar structure to the H_2O monomer with the $(OH)_{ads}$ visible as bright, slightly elongated spots (see fig. 6.7). Although there are subtle differences in the luminosity of the surrounding substrate, it is not possible to distinguish between the wide and narrow configurations indicated in fig. 6.1b since the bright spot is generated by the adsorbed hydroxyls whose adsorption properties are close to identical for the two dimer configurations.

Table 6.3.: Adsorption energies in eV per H_2O molecule of the H_2O dimer structures on the large model cell ($^1\!/_{16}\,$ML coverage) in "parallel" configuration.

	"wide"	"narrow"
E_{Ads} [eV]	-1.338	-1.369

6.1.3. Higher H_2O Coverage Structures

Using the small model cell, further investigations were done considering different high coverage adsorption configurations. By increasing the coverage to $^1\!/_2$ H_2O molecules per unit cell, the arrangement of two adsorbed H_2O molecules on the model cell was

194

Table 6.4.: Atomic distances in Å of the H_2O dimer. The labels "left" and "right" of the strontium atoms are given with respect of the adsorbate position.

[Å]	"wide"		"narrow"	
	H_2O_{left}	H_2O_{right}	H_2O_{left}	H_2O_{right}
(OH_{ads})	0.972	0.972	0.972	0.972
O_sH	1.025	1.025	1.025	1.025
H_{surf}–O_{ads}	1.558	1.558	1.565	1.565
O_{ads}–Sr_{left}	2.543	2.591	2.540	2.578
O_{ads}–Sr_{right}	2.591	2.543	2.575	2.542
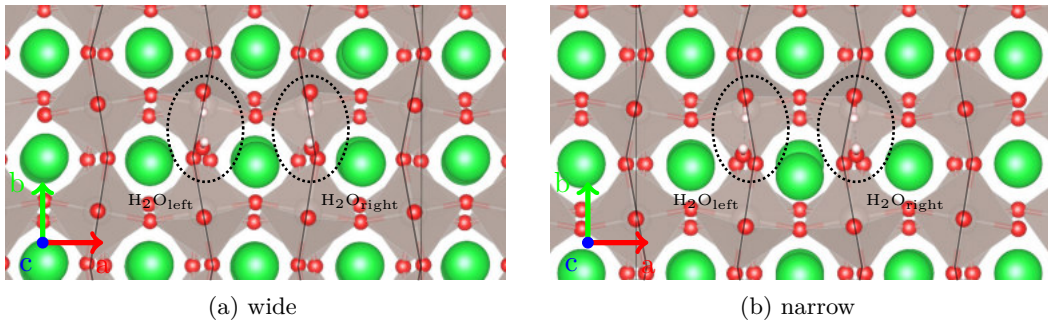
(a) wide

(b) narrow

Figure 6.6.: Two dissociated H_2O adsorbed next to each other, forming a dimer. (a): "wide" dimer, the octahedra in the subsurface are rotated away from the $(OH)_{ads}$. (b): "narrow" dimer, the octahedra in the subsurface are rotated towards the $(OH)_{ads}$.

(a) wide, Bias: +0.5 V

(b) wide, Bias: −0.5 V

(c) narrow, Bias: +0.5 V

(d) narrow, Bias: −0.5 V
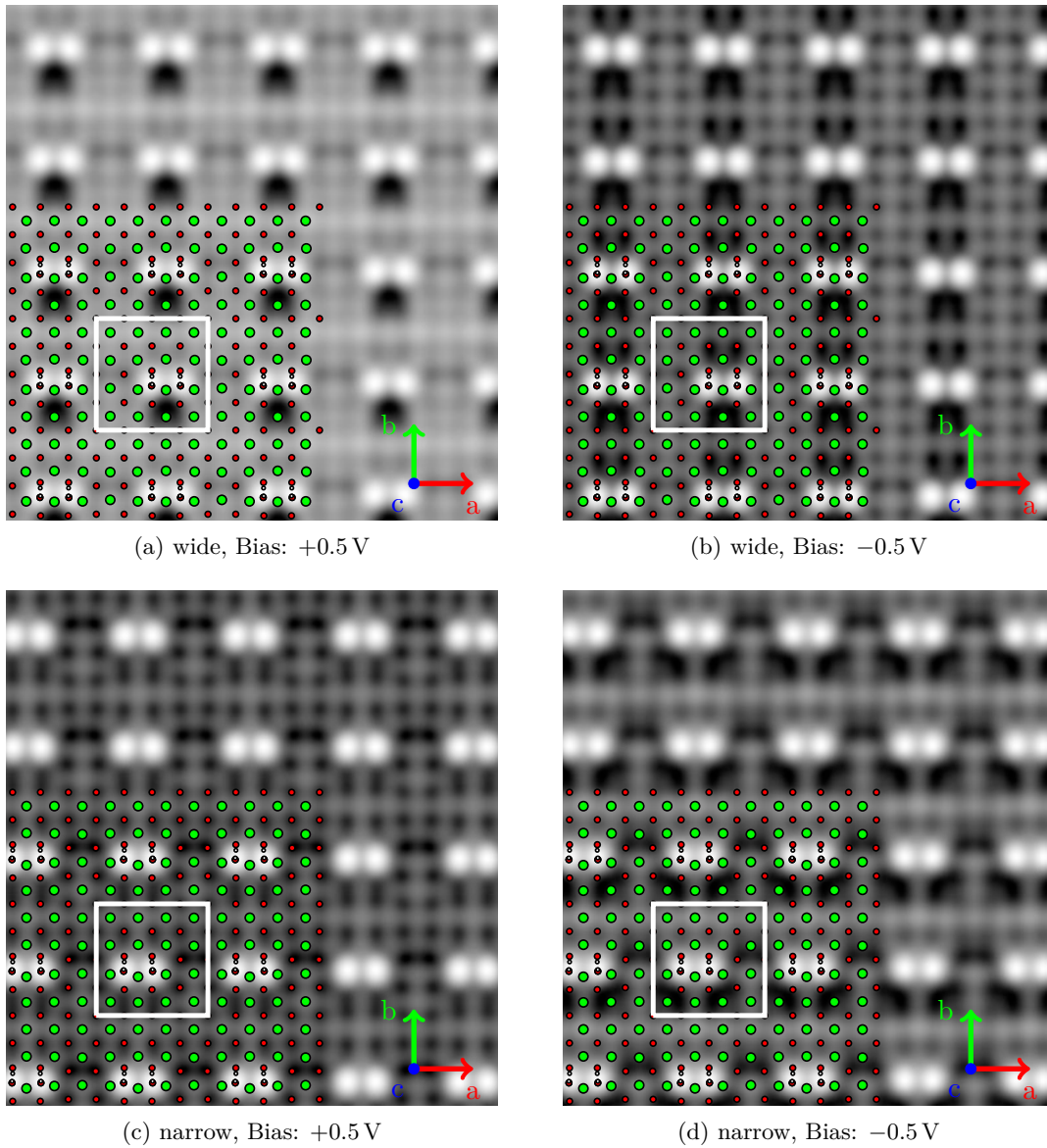
Figure 6.7.: STM Simulations of a H_2O dimer at a "wide" (top) and "narrow" (bottom) site at ±0.5 V bias voltage. Both far and wide dimer configurations exhibit bright spots caused by the adsorbed hydroxyls. Since the subsurface is not visible in STM it is impossible to distinguish between wide and far dimers.

tested. For example, two water molecules adsorbed at neighbouring sites would represent an infinite chain due to the periodic boundary conditions. Other arrangements that were tested included an "L"-shaped configuration, meaning that one $(OH)_{ads}$ and its accompanying surface hydroxyl is positioned at a 90° angle with respect to the other and two zig-zag configurations, modifications of the chain structure, where the adsorbates are placed on a grid diagonal with respect to the unit cell, either both in the same orientation (symmetric) or in an alternating order (antisymmetric). As can be seen in fig. 6.8, for the "L"-shaped configuration there are two possible configurations where the rotated adsorbate can be shifted by half a unit cell. Table 6.5 shows that both "L"-shaped structures are much less favoured than either a monomer, dimer, or a continuous line, indicating repulsive interaction between the $(OH)_{ads}$. Compared to both wide and narrow dimer structures it is also notable that the continuous line is less favoured by 63 meV and 93 meV. Both "zig-zag" structures are also less favoured than the "chain" structure (115 meV and 144 meV). All these tests point towards the propensity of the adsorbate to form well ordered structures, which is confirmed by experiments by Halwidl, Stöger, Mayr-Schmölzer, et al. [2] and Stöger [178].

Table 6.5.: Adsorption energies in eV per H_2O molecule of different H_2O structures at ½ ML coverage. The exact structures are shown in fig. 6.8.

Structure	E_{Ads} [eV]
"L wide"	−1.150
"L near"	−1.198
Chain	−1.277
Zig-zag, asymmetric	−1.133
Zig-zag, symmetric	−1.163

6.1.4. Full Coverage

To simulate one monolayer of adsorbed water on the $Sr_3Ru_2O_7$ surface four dissociated H_2O molecules were placed on the small model surface in a configuration similar to the relaxed monomer (see fig. 6.9a). Letting this structure relax leads to a recombination of the adsorbed $(OH)_{ads}$ with the separated proton. The final state of the calculation reveals rows of dissociatively adsorbed H_2O molecules alternating with rows of molecular, more weakly bound water molecules, indicated by the average adsorption energy of −1.084 eV per H_2O. The latter adsorbates still form a hydrogen bond towards the apical oxygen atom at bond lengths similar to the molecular monomer (1.510 Å to 1.623 Å) and move slightly away from the closer $(OH)_{ads}$ row. In the STM simulation bright double rows are visible which consist of the superposed spots of the adsorbates.
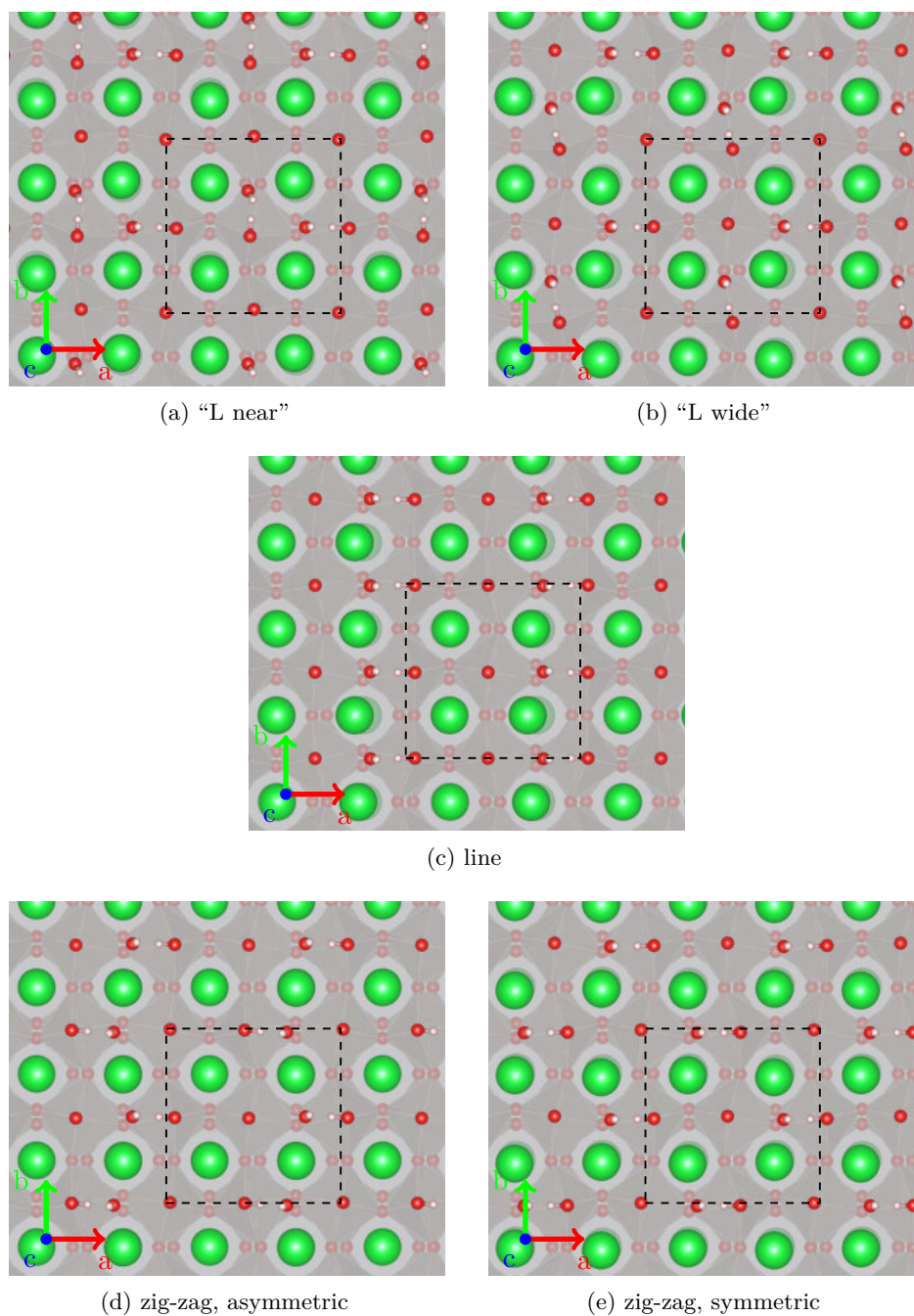
197

(a) "L near"

(b) "L wide"

(c) line

(d) zig-zag, asymmetric

(e) zig-zag, symmetric

Figure 6.8.: Relaxed positions of various high coverage configurations. (a): "L far''-type, one $(OH)_{ads}$ is right next to another adsorbed H_2O; (b): "L wide''-type, the adsorbed H_2O are further apart; (c): line structure; (d): asymmetric zig-zag arrangement, $(OH)_{ads}$ are positioned in a line, but the surface hydroxyls are placed alternately to the right and to the left of the $(OH)_{ads}$; (e): symmetric zig-zag arrangement.

(a) initial configuration

(b) relaxed structure
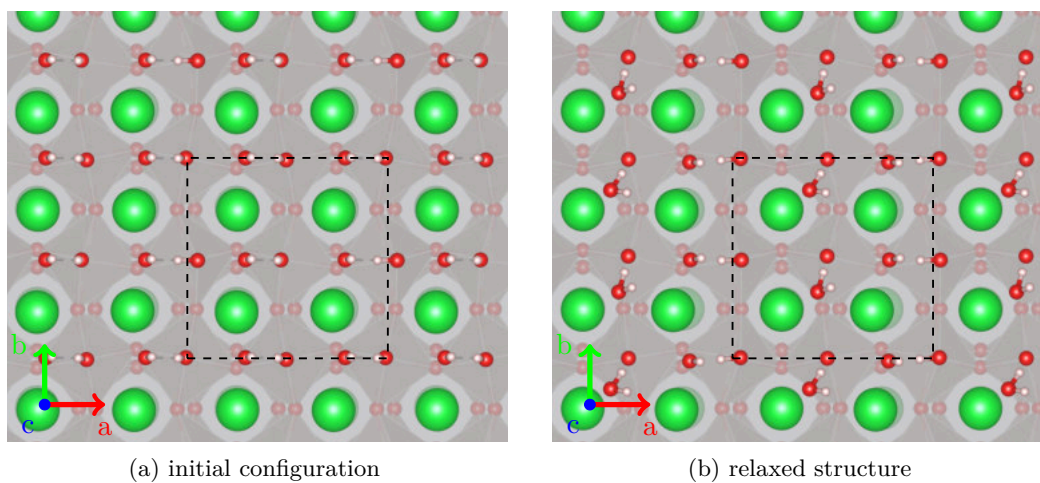
Figure 6.9.: Full coverage of H_2O on the $Sr_3Ru_2O_7(001)$ $c(2 \times 2)$ model cell. After relaxation, ever other dissociated H_2O molecule recombines and adsorbs molecularly.

(a) Bias: $+0.5\,V$

(b) Bias: $-0.5\,V$
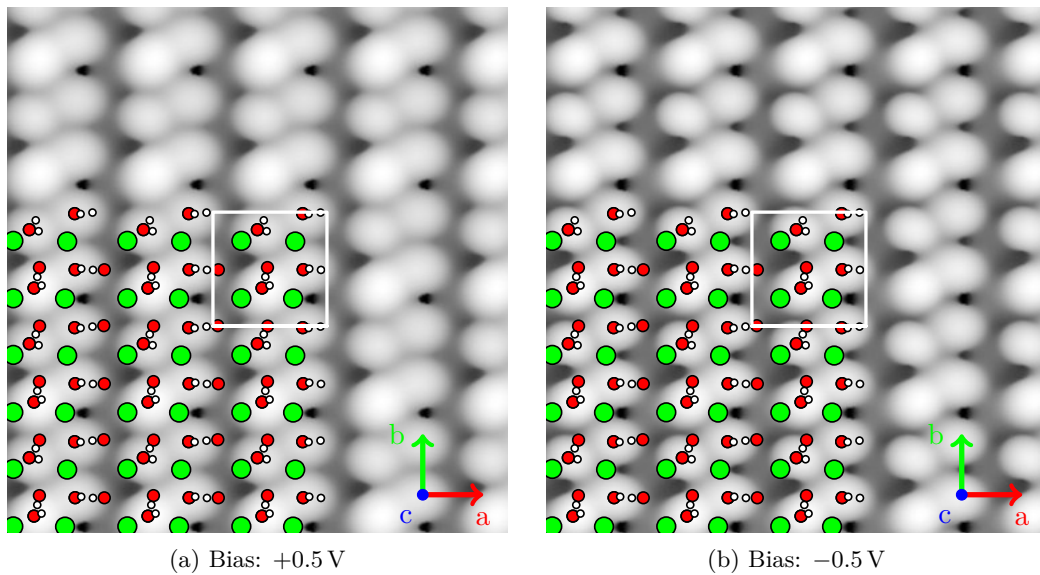
Figure 6.10.: STM Simulation of the final structure of fully covered $Sr_3Ru_2O_7$.

6.1.5. Complex H$_2$O Structures

The results regarding the high coverage structures in section 6.1.3 have already shown the disposition of the adsorbate to form line structures. Using the large c(4×4) model a few more special adsorption configurations were investigated. Experiments done by Halwidl, Stöger, Mayr-Schmölzer, et al. [2] have shown that at high coverage the dissociated adsorbate first forms lines (see fig. 6.1b) and later square cage-like structures, trapping molecular water inside.

Trimers and Lines

As could be seen from the calculations on the small model, the adsorbate shows a tendency to form continuous lines of dissociated H$_2$O molecules. Using the large model cell, the precursor configurations to this continuous lines were studied by adding a third water molecule to the dimer configuration, see fig. 6.11. The subsurface symmetry of the substrate does not influence the trimer structure which emerges from the addition of one more dissociated H$_2$O equally oriented on either side of a dimer as its components cover both a "wide" and a "narrow" site.

The third water molecule can also be rotated by 180°, either to a "wide" or a "narrow" dimer (see figs. 6.11b and 6.11c). Similar to the diagonal structures studied in section 6.1.3 both these configurations are less stable than the trimer by 56 meV to 22 meV, as can be seen in table 6.6. Compared to the monomer, the averaged adsorption energy is reduced by 117 meV, 147 meV, and 47 meV for the trimer, wide, and narrow configuration respectively, indicating repulsive interaction at the addition of the third H$_2$O molecule.

Table 6.6.: Average adsorption energies in eV per H$_2$O molecule of the H$_2$O trimer structures on the large model cell (³⁄₁₆ ML coverage) in "parallel" configuration.

Structure	E$_{\text{Ads}}$ [eV]
Trimer	-1.223
Wide + 1 rotated	-1.167
Narrow + 1 rotated	-1.201

Cages

The cage structure was simulated by building a rhombic structure consisting of 6 dissociated H$_2$O molecules. The edges of these rhombi can either be formed by a "wide" or a "narrow" dimer, see fig. 6.12, with one more H$_2$O closing off the rhombic cage. Due to the periodic boundary this results in a structure consisting of three dimers, two "wide" or "narrow" forming the cage and one "narrow" or "wide" closing off the cage. As could
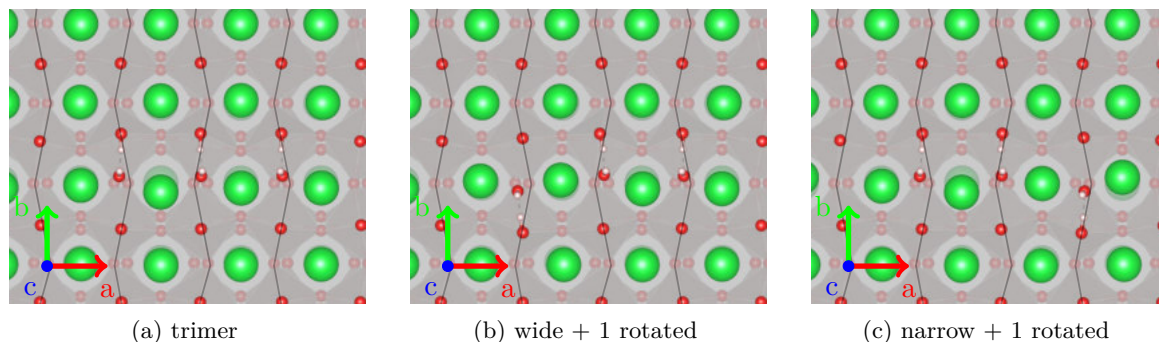
|(a) trimer|(b) wide + 1 rotated|(c) narrow + 1 rotated|

Figure 6.11.: 3 dissociated H_2O adsorbed on the $c(4 \times 4)$ $Sr_3Ru_2O_7(001)$ surface. (a): Trimer configuration; (b): one H_2O is rotated by 180°, forming one wide dimer plus the rotated H_2O; (c): similar to (b), but one narrow dimer remains.

be seen for the single dimer, the "narrow" configuration is preferred (see table 6.7), but the energy difference between the two configurations is reduced to just 12 meV.

Then one and two additional molecular H_2O were placed into the cage, as indicated by the suffix to the labels given in table 6.7. The DFT calculations predict that the additional single H_2O molecule in the cage dissociates as well, adsorbing in a 90° rotated configuration. The adsorption energy per H_2O is slightly reduced slightly by 11 meV to 16 meV, similar to the "L''-shaped configuration at higher coverage, described in section 6.1.3. Only after adding a second water molecule into the cage molecular H_2O could be stabilised: one H_2O in a "wide" cage and two H_2O in a "narrow" cage. In both cases one of these molecular H_2O adsorb close to a surface strontium atom, and are connected to the apical oxygen atom of a neighbouring RuO_6 octahedron by a hydrogen bond. In the narrow case the second molecular H_2O is predicted to adsorb between two surface Sr atoms, see fig. 6.14b. This H_2O does not form a hydrogen bond with the surface but with another adsorbed hydroxyl close by.

The STM simulations (see fig. 6.18) predict that the adsorbates exhibit bright spots in both the occupied and unoccupied states. Since the brightness of these spots of the dissociated and molecular adsorbate is similar one can not distinguish between these two in STM measurements. Nevertheless, since the adsorbed hydroxyls of the adsorbate are always predicted to adsorb at Sr–Sr bridge sites, molecular H_2O adsorbates can be identified by the off-grid placement of their spots.

Table 6.7.: Adsorption energy in eV per H_2O of complex adsorption structures forming a cage.

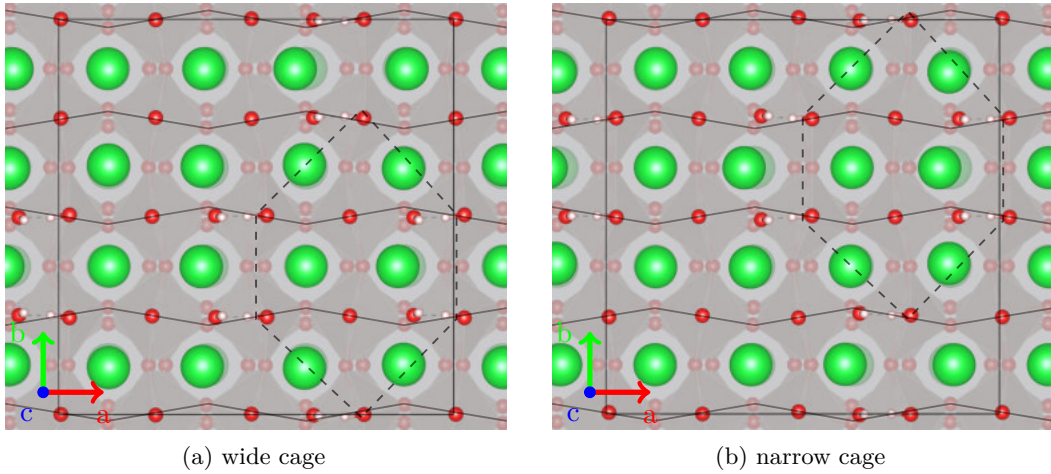| Structure	E_{Ads} [eV]
Wide cage	-1.151
Narrow cage	-1.163
Wide cage + 1 H_2O	-1.135
Narrow cage + 1 H_2O	-1.152
Wide cage + 2 H_2O	-1.098
Narrow cage + 2 H_2O	-1.083

(a) wide cage

(b) narrow cage

Figure 6.12.: 6 H_2O adsorbed on $Sr_3Ru_2O_7$ in cage structures. Edges of the cage are formed by two (a) "long" and (b): "short" dimers. The dashed line indicates the cage, solid lines the rotations of the octahedra.

(a) wide cage + 1H$_2$O   (b) narrow cage + 1H$_2$O
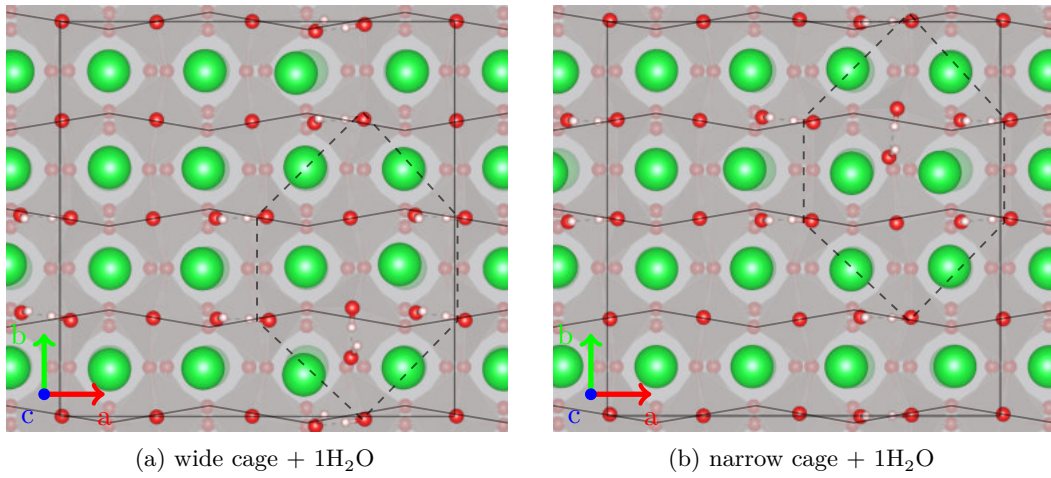
Figure 6.13.: 6 H$_2$O adsorbed on Sr$_3$Ru$_2$O$_7$ in cage structures. Edges of the cage (dashed line) are formed by two (a) "long" and (b) "short" dimers. The additional H$_2$O in the cage adsorbs dissociatively in both cases.

(a) wide cage + 2H$_2$O   (b) narrow cage + 2H$_2$O
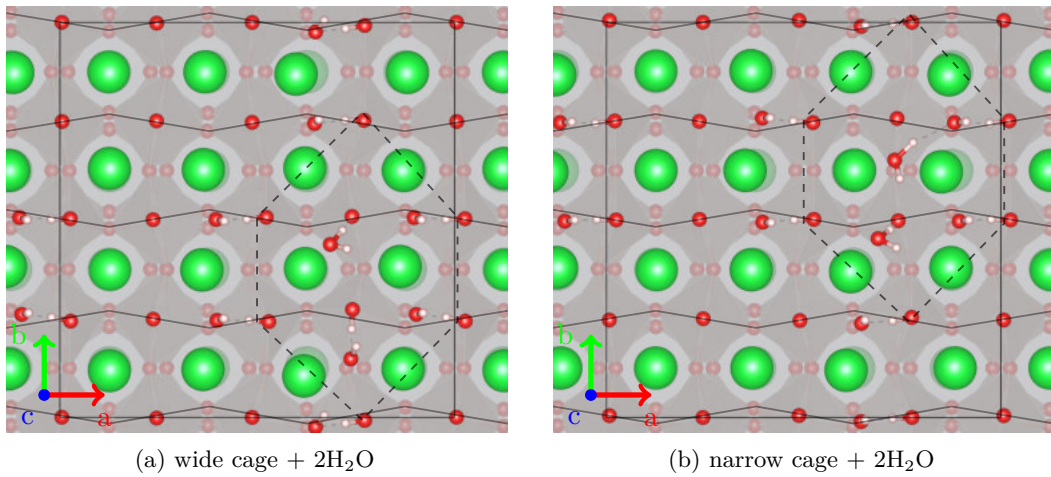
Figure 6.14.: 6 H$_2$O adsorbed on Sr$_3$Ru$_2$O$_7$ in cage structures. Edges of the cage (dashed line) are formed by two (a) "long" and (b) "short" dimers. Of the two additional H$_2$O in the cage one (a) or two (b) adsorb as intact molecules.

(a) Bias: $+0.5\,\text{V}$

(b) Bias: $-0.5\,\text{V}$
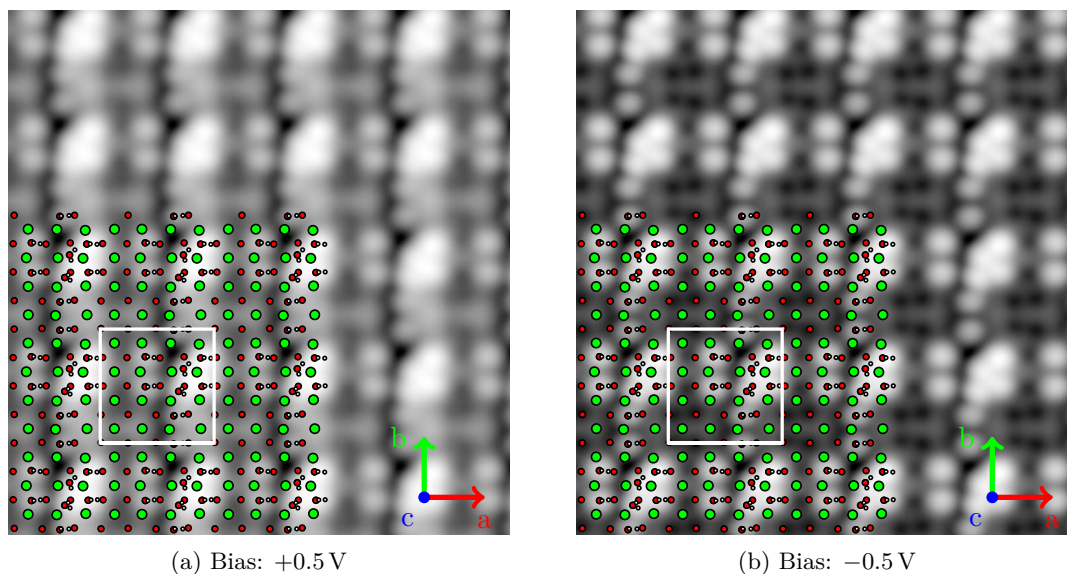
Figure 6.15.: STM Simulation of 2 molecular H_2O inside a "narrow" cage structure as shown in fig. 6.14b. The additional molecularly adsorbed H_2O are indicated by similar bright spots in both occupied and unoccupied states.

6.2. Calcium Doped Strontium Ruthenate

6.2.1. ¼ Dopant Concentration

To study the influence of a calcium dopant on the adsorption behaviour of water molecules as a first step the highly doped model cell introduced in section 5.5.3 was covered by different amounts of H_2O molecules, similar to the process for the undoped $Sr_3Ru_2O_7$ surface. The introduction of the dopant gives rise to two additional adsorption sites where a H_2O adsorbate can adsorb at a Ca–Sr bridge instead of a Sr–Sr bridge position, as depicted in fig. 6.16. Taking the predicted adsorption sites for the undoped case described in the previous section as cues, the adsorbate was positioned at a Ca–Sr or a Sr–Sr bridge.

The calculated adsorption energies (see table 6.8) show that the introduction of the calcium dopant increases the reactivity of the surface. Dissociative adsorption is still preferred, even though due to the implanted Ca atom the adsorption energy difference compared to molecular adsorption is much smaller than for the pure $Sr_3Ru_2O_7$ surface. Still, the highest activity is predicted at the Sr–Sr site. It should be noted that the calcium dopant is more flexible compared to the Sr atoms due to its smaller ionic radius (Ca: 114 pm, Sr: 132 pm [189]). The Ca dopant is displaced by 32 pm, 17 pm, 51 pm for the dissociated adsorption on the Ca–Sr, the Sr–Sr bridge, and for molecular adsorption at the Ca–Sr bridge, respectively. No displacement of the Ca dopant is predicted for the

case of molecular adsorption at the Sr–Sr bridge. The addition of more water molecules to this small model cell reduces the adsorption energy just slightly as the increased reactivity and the repulsive interaction of the adsorbed H_2O almost cancel each other out.

Table 6.8.: Adsorption energies in eV of H_2O on the Ca-doped $c(2 \times 2)$ slab. The adsorbate position is given by the atom species of the bridge the H_2O adsorbs at. A lowercase letter "d" indicates dissociative, a lowercase "m" molecular adsorption.

Adsorption site		E_{Ads} [eV]
1 H_2O		
Ca–Sr	d	−1.382
Ca–Sr	m	−1.325
Sr–Sr	d	−1.419
Sr–Sr	m	−1.044
2 H_2O		
Ca–Sr	d	−1.385
Sr–Sr	d	−1.448
3 H_2O		
Ca–Sr, Sr–Sr	d	−1.329

6.2.2. ¹⁄₁₆ Dopant Concentration

A more realistic model of the Ca-doped $Sr_3Ru_2O_7$ surface was also introduced in section 5.5.3 where only one surface strontium atom of the $c(4 \times 4)$ cell was replaced by a calcium dopant, yielding a dopant concentration of 6.25 %. Similar to the highly doped case this introduces an additional distinguished adsorption site next to the Ca dopant for the monomer and a second set of "wide" and "narrow" dimer sites.

The H_2O monomer shows higher adsorption energy at the calcium dopant site at −1.377 eV. Similar to the highly doped surface, dissociated adsorption is still preferred, the difference to a molecularly adsorbed H_2O is very low compared to the pure $Sr_3Ru_2O_7$ sites (25 meV). A comparison of the adsorption energies at the strontium sites of the doped model cell to the undoped surface produces similar values. This is in contrast to the highly doped model, showing that this large model cell is able to describe both pure and a Ca-doped sites.

The atomic distances of the dissociated monomer are almost identical to the adsorption on pure $Sr_3Ru_2O_7$. The distance of the $(OH)_{ads}$ to the Ca dopant is 2.330 Å and to the nearest Sr atom 2.732 Å, indicating higher attraction of the dopant compared to the Sr atoms. A molecularly adsorbed water monomer is rotated towards the dopant. The distance between O_{ads} to the Ca atom is 2.358 Å, again much lower than the distance
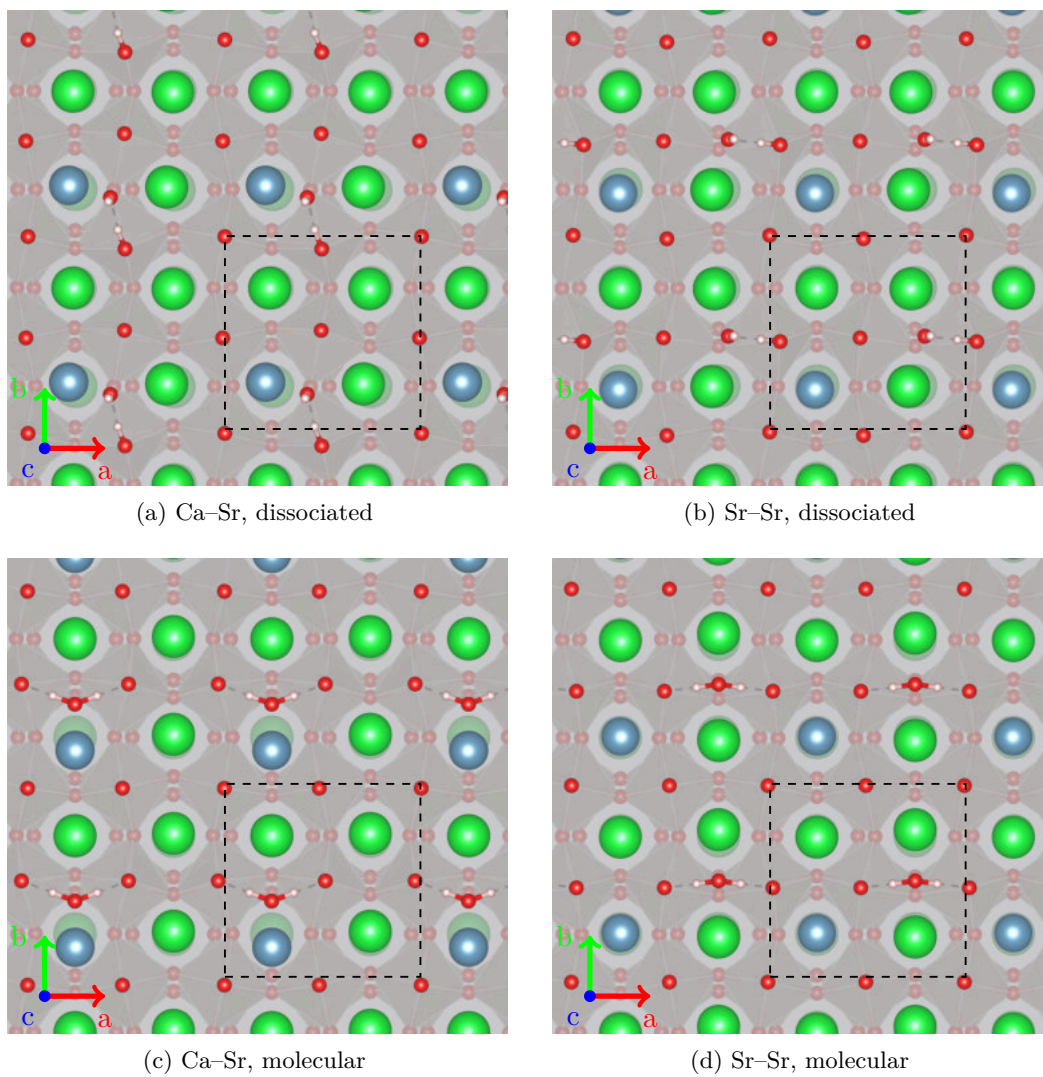
(a) Ca–Sr, dissociated

(b) Sr–Sr, dissociated

(c) Ca–Sr, molecular

(d) Sr–Sr, molecular

Figure 6.16.: Adsorption positions for 1 H_2O on the doped c(2×2) model cell. (a), (b): dissociated adsorption; (c), (d): molecular adsorption.

to the next Sr atom (3.044 Å). This is also shown in the STM simulation (see fig. 6.17) where the bright spot indicating the adsorbate is shifted with respect to the pure surface structure.

The addition of the Ca dopant influences the formation of dimers, mostly due to the stronger adsorption at the dopant site. For the case where the dimer is located directly above the dopant the "narrow" site is again preferred, and the energy difference to the "wide" configuration is higher (83 meV) compared to the undoped $Sr_3Ru_2O_7(001)$ surface. This increase can be attributed to the higher mobility of the dopant: in the "narrow" configuration the Ca atom is displaced by 55 pm while in the "wide" configuration this displacement amounts to 36 pm. The second set of "wide" and "narrow" sites consist of an H_2O dimer with one H_2O molecule at a Sr–Sr bridge and one at the Ca–Sr bridge. Here the energy difference between the "wide" and "narrow" configurations is much lower (6 meV) than for both the pure $Sr_3Ru_2O_7$ case and where the dimer is positioned above the Ca dopant, again attributable to the higher mobility of the Ca atom.

As shown in fig. 6.17, the STM simulations show hardly any difference to the pure $Sr_3Ru_2O_7$ case, except for the "narrow" Ca–Sr configuration where the $(OH)_{ads}$ next to the Ca dopant is slightly depressed compared to the other $(OH)_{ads}$ due to the displacement of the dopant into the surface.

Table 6.9.: Adsorption energies in eV of H_2O on the Ca-doped c(4 × 4) slab. The adsorbate position is given by the atom species of the bridge the H_2O adsorbs at. A lowercase letter "d" indicates dissociative, a lowercase "m" indicates molecular adsorption.

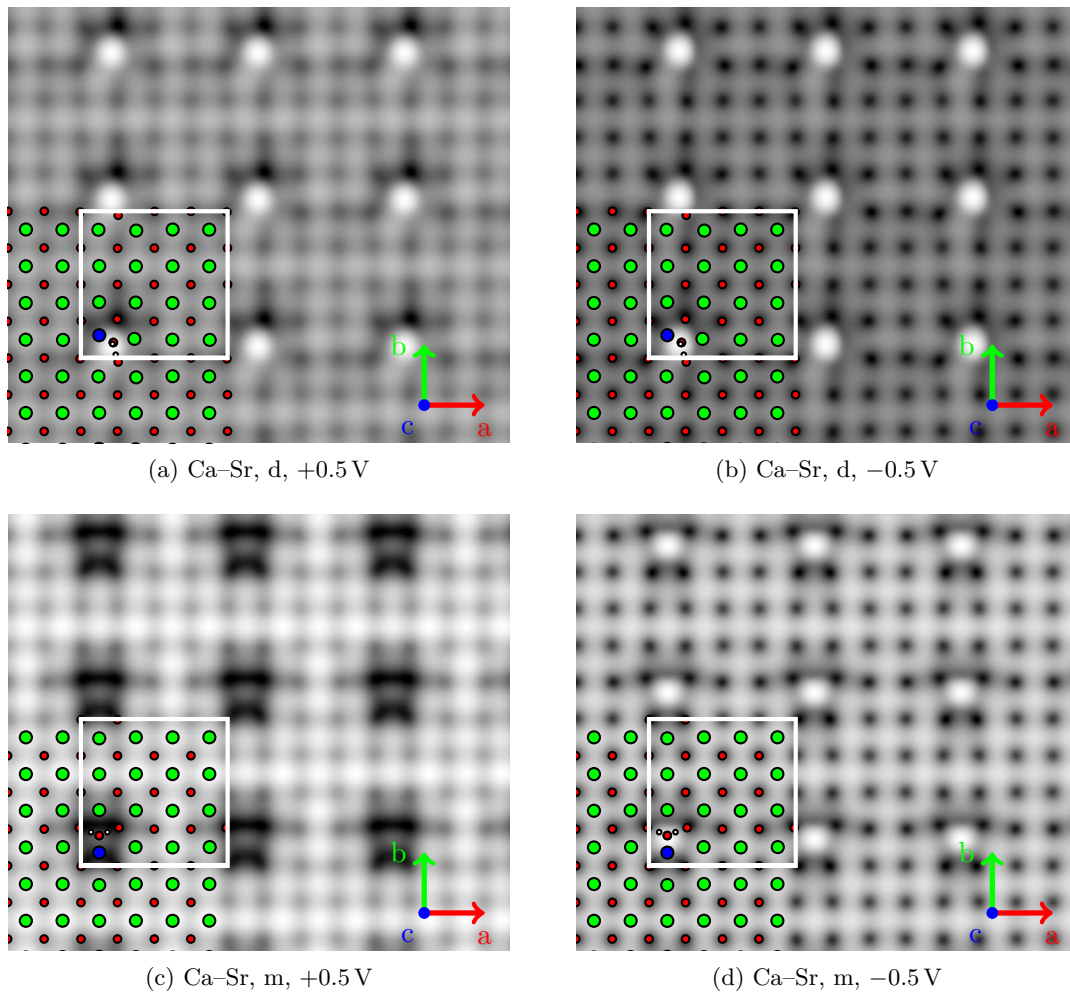| Adsorption site		E_{Ads} [eV]
Monomer		
Ca–Sr	d	−1.377
Ca–Sr	m	−1.352
Sr–Sr	d	−1.264
Sr–Sr	m	−1.098
Dimer		
Wide, Ca–Ca	d	−1.287
Narrow, Ca–Ca	d	−1.370
Wide, Ca–Sr	d	−1.339
Narrow, Ca–Sr	d	−1.345

(a) Ca–Sr, d, +0.5 V

(b) Ca–Sr, d, −0.5 V

(c) Ca–Sr, m, +0.5 V

(d) Ca–Sr, m, −0.5 V

Figure 6.17.: STM simulations 1 H_2O adsorbed on the Ca-doped $Sr_3Ru_2O_7(001)$ c(4×4) model cell. Top: dissociative, bottom: molecular adsorption. The dissociated H_2O is indicated by a bright feature in both occupied and unoccupied states, the molecular H_2O is hidden in the dark feature created by the Ca dopant in the unoccupied states.
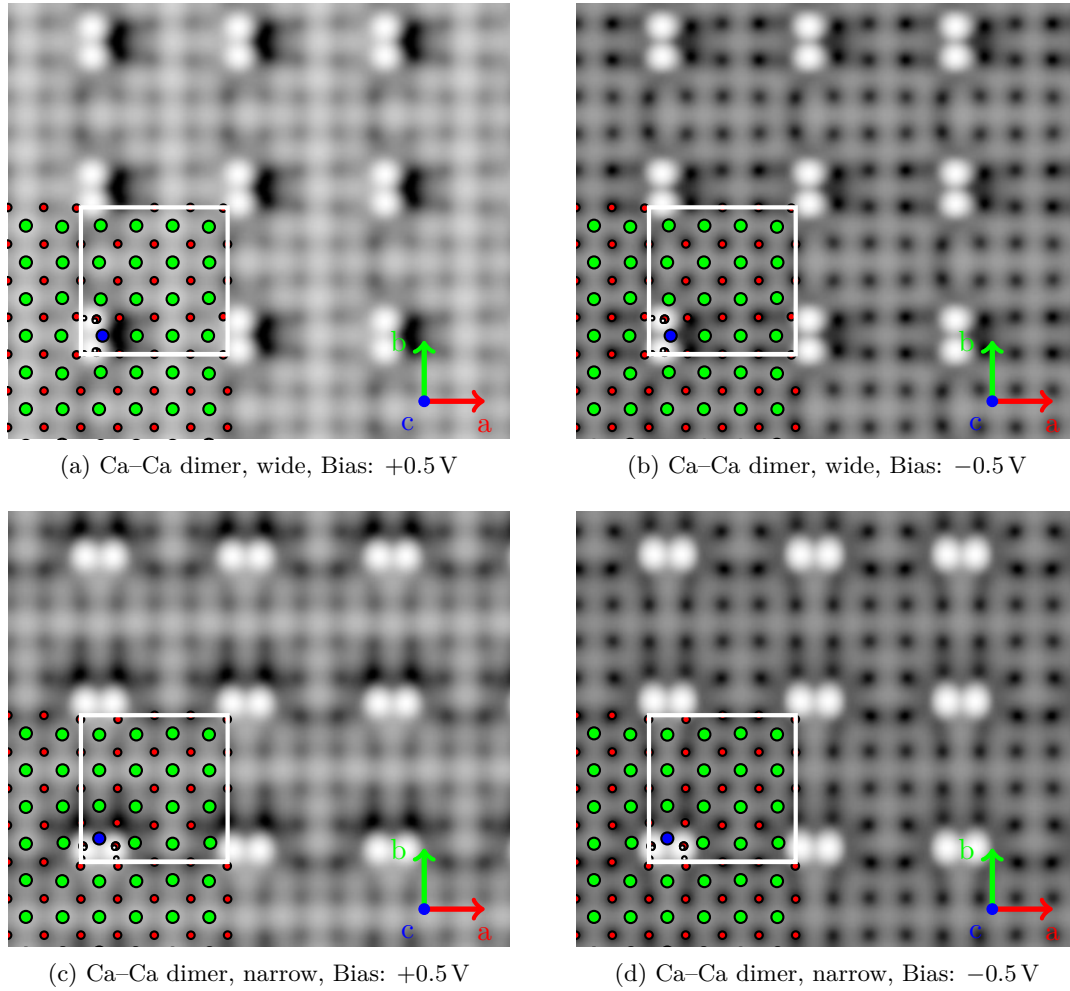
(a) Ca–Ca dimer, wide, Bias: $+0.5\,\text{V}$

(b) Ca–Ca dimer, wide, Bias: $-0.5\,\text{V}$

(c) Ca–Ca dimer, narrow, Bias: $+0.5\,\text{V}$

(d) Ca–Ca dimer, narrow, Bias: $-0.5\,\text{V}$

Figure 6.18.: STM Simulation of 2 H_2O adsorbed on the $Sr_3Ru_2O_7(001)$ c(4×4) model cell in a dimer formation across the Ca dopant, i.e. both H_2O are adsorbed at Ca–Sr sites.

209

6.3. Core Level Shifts

In surface science XPS measurements are a handy tool to determine the chemical state of the studied materials as it probes the binding energy of core electrons. As described in section 3.4 it is possible to calculate this binding energy in both an initial state (IS) and in the final state (FS) approximation [190, 191], and this has been done for various model structures to help identify the fingerprint of the adsorbate species in the XPS spectra. In the calculations presented here absolute values of calculated core electron binding energies do not have a physical meaning, but differences in binding energies (core level shifts) usually turn out to be quite accurate. In this section the focus is on the oxygen $1s$ binding energies as they can be used to determine the molecular or dissociative character of the H_2O adsorbate and to distinguish between the oxygen atoms at the various sites in the substrate. All calculations were performed using the optB86b functional and the respective optimised structures and the corresponding computational settings mentioned before. In some cases the unit cells were multiplied along the shorter crystallographic axes to properly screen the electronic core hole in the final state approximation.

Bulk Sr_2RuO_4 and $Sr_3Ru_2O_7$

The core binding energies were first calculated for all oxygen atoms at the unique symmetry sites for both the Sr_2RuO_4 and $Sr_3Ru_2O_7$ bulk. To properly screen the electron hole site in the final state approximation the unit cells were doubled and tripled in a and b direction for $Sr_3Ru_2O_7$ and Sr_2RuO_4 respectively. In the former case the O $1s$ binding energy of an apical oxygen atom ($O_{rocksalt}$) is higher than for the ones in the RuO_2 plane (O_{RuO_2}), an indication of their different chemical environment. In the initial state approximation the chemical shift between the two sites amounts to $1.34\,eV$ and in the final state approximation to $0.89\,eV$. Here the initial state calculation gives very good agreement with XAS measurements by Malvestuto et al. [192] who found a shift of $\approx 1.3\,eV$ between the apical and the planar O $1s$ levels.

In the $Sr_3Ru_2O_7$ bulk there are three characteristic oxygen sites, a second apical oxygen atom (O_{SrO}) in the SrO layer in addition to the apical ($O_{rocksalt}$) and planar (O_{RuO_2}) oxygen found in Sr_2RuO_4. All three sites show distinctive O $1s$ binding energies: the highest and lowest binding energy is found for the O $1s$ states in the RuO_2 plane and for those in the $O_{rocksalt}$ in the rock-salt plane, respectively, while the O $1s$ levels of O_{SrO} located in the SrO layer lie in between.

Considering the O $1s$ states of the $O_{rocksalt}$ at the rock-salt interface as the baseline, the O_{SrO} O $1s$ states are shifted by $0.42\,eV$ and $0.04\,eV$ in the initial and final state calculations, respectively. The O_{RuO_2} O $1s$ states show a larger shift of $0.63\,eV$ and $0.43\,eV$ with respect to the $O_{rocksalt}$ states. This reflects the different binding configuration at these sites. The splitting of the O $1s$ states in three distinct levels agrees with the experiment, since Malvestuto et al. [192] also identified three distinct peaks in the XAS spectra. They identify the most strongly bound oxygen with the planar O_{RuO_2} and show shifts of $\approx 0.8\,eV$ and $\approx 1.2\,eV$ for the O_{SrO} and the O_{RuO_2} site, respectively. The DFT calculations predict the same ordering in the both initial and final state calculations, but

in both cases the size of the shift is underestimated, especially in the latter case. In the final state calculations the experimental core level shift of 0.4 eV between the O_{SrO} and O_{RuO_2} sites is well reproduced, while the $O_{rocksalt}$ binds too strongly in the calculations.

Table 6.10.: Core level shifts in eV of the O $1s$ states of Sr_2RuO_4 and $Sr_3Ru_2O_7$ bulk and slab structures in the initial and final state approximation with respect to the O $1s$ state of the apical oxygen located at the rock-salt layer. The differences are given with respect to the lowest level in the appropriate bulk structure. Positive numbers indicate shifts to higher binding energies.

Core level shifts [eV]	Initial State	Final State
Sr_2RuO_4 bulk		
$O_{rocksalt}$	0	0
O_{RuO_2}	1.34	0.89
Sr_2RuO_4 slab		
$O_{surface}$	−0.10	−0.17
$O_{rocksalt}$	−0.05	−0.02
O_{RuO_2}	1.32	1.07
$Sr_3Ru_2O_7$ bulk		
$O_{rocksalt}$	0	0
O_{SrO}	0.42	0.04
O_{RuO_2}	0.61	0.44
$Sr_3Ru_2O_7$ slab, 1 double layer		
$O_{surface}$	0.01	−0.09
O_{SrO}	0.48	0.01
O_{RuO_2}	0.63	0.43
$Sr_3Ru_2O_7$ slab, 2 double layer		
$O_{surface}$	0.01	−0.19
$O_{rocksalt}$	0	0
O_{SrO}	0.47	0.07
O_{RuO_2}	0.62	0.44

6.3.1. Sr_2RuO_4 and $Sr_3Ru_2O_7$ slabs

The core electron binding energies at surfaces also show distinct shifts with respect to the equivalent sites in the bulk. To calculate the core level shifts for the slab structures a three layered Sr_2RuO_4 slab and a $Sr_3Ru_2O_7$ structure consisting of two double-layers were built. Both structures were also doubled in a and b direction to minimise the influence of the electron hole in the next periodic unit cell.

The O $1s$ binding energies for the Sr_2RuO_4 slab were calculated using a 3-layer c(2×2) slab doubled in x and y direction. The most weakly bound site is found at $O_{rocksalt}$ sites

at the rock-salt interface, like in bulk Sr_2RuO_4, which are slightly shifted by 0.05 eV and 0.02 eV (IS and FS) to lower binding energies with respect to the bulk. For the planar O_{RuO_2} site in the RuO_2 plane the calculations yield a large shift of 1.32 eV and 1.07 eV for the initial and final state approximation, respectively, in good agreement with the bulk values shown in table 6.10. At the surface of the slab, both approaches predict a slight shift to lower O $1s$ binding energies of 0.10 eV and 0.17 eV for initial and final state approximation.

The O $1s$ core level binding energies for the $Sr_3Ru_2O_7$ slab was calculated using a slab consisting of two double layers to include one rock-salt interface. Here four sites with distinct O $1s$ binding energies can be identified. The additional site arises from additional apical oxygen sites located in the SrO plane. Like in the bulk the lowest O $1s$ binding energy can be found at the $O_{rocksalt}$ sites in the SrO terminated layer at the rock-salt interface. The calculations show no shift with respect to the $O_{rocksalt}$ sites in the $Sr_3Ru_2O_7$ bulk. In the initial state approximation the O_{SrO} shift by 0.48 eV to higher binding energies, while in the final state calculations these sites are almost indistinguishable to the rock-salt site, see table 6.10. The planar O_{RuO_2} site in the RuO_2 plane on the other hand show a shift of 0.62 eV and 0.44 eV in the initial and final state approximation, respectively. At the surface of the slab the initial state calculation yields a negligible shift in the O $1s$ binding energies, while the final state calculation predicts a shift of 0.19 eV to lower binding energies. Finally, the O $1s$ core level positions were confirmed for a single double layer slab of $Sr_3Ru_2O_7$, see table 6.10.

6.3.2. Adsorbed H_2O

The O $1s$ binding energies of the adsorbed water molecules were calculated and used to identify the adsorbate peaks in XPS spectra provided by Halwidl, Stöger, Mayr-Schmölzer, et al. [2]. Since these measurements were done on a Sr_2RuO_4 substrate the lowest binding energy calculated for the Sr_2RuO_4 bulk crystal, the $O_{rocksalt}$ level, was chosen as a reference. The comparison with the $Sr_3Ru_2O_7$ bulk show a shift of 0.38 eV (IS) and 0.28 eV (FS) of the O $1s$ levels at the rock-salt interface sites. As can be seen in fig. 6.19 the XPS spectrum shows the distinct double peak (BE: SrO plane: 528.4 eV, RuO plane: 529.4 eV) structure of the bulk Sr_2RuO_4 crystal. After the adsorption of water at first a small shoulder is visible at a binding energy of 530.40 eV and at almost full coverage a second peak at 532.8 eV appears. Since these measurements were taken at various coverages and from what was known from the STM measurements, the first shoulder was identified as belonging to the dissociated adsorbates while the second peak appearing at high coverage was assigned to molecular water.

Since the XPS data was acquired on the Sr_2RuO_4 substrate the peak at the lowest binding energy at the $O_{rocksalt}$ site was used as the reference energy. All energy differences given in the next paragraph are referenced to this level and indicate shifts towards higher binding energies.

At low coverage, the calculations of the O $1s$ level of the adsorbate showed a core level shift of 0.64 eV (IS) and 2.31 eV (FS) for the dissociated monomer and 1.28 eV (IS) and 2.95 eV (FS) for the molecular monomer. The O $1s$ level of the apical $O_{surface}$ which

forms the surface hydroxyl is shifted by 0.98 eV and 1.81 eV for the initial and final state approximation, respectively, also contributing to the shoulder in the spectrum. Since the initial state approximation fails to properly account for the large shift of the O $1s$ states of the adsorbate with respect to the bulk O $1s$ states, only the core level shifts calculated in the final state approximation will be given for the other structures. The shifts for the initial state calculations can be found in table 7.3. Increasing the water coverage shows hardly any change in the binding energies of the adsorbate. Both the "wide" and "narrow" dimers are shifted by 2.29 eV and 2.30 eV respectively, while the shifts for the trimer and line structure are 2.26 eV and 2.25 eV. The calculated shifts in the "cage" structures introduced in section 6.1.5 vary slightly between 2.25 eV to 2.35 eV. Adding more H_2O molecules into these cages shows just slight differences in the case the additional molecule dissociates (shifts of 2.05 eV to 2.17 eV) while the O $1s$ level of the molecular adsorbate shifts by 3.99 eV to 4.88 eV. For the fully covered model cell (see section 6.1.4) the dissociated H_2O shift by 2.28 eV and the molecular H_2O by 4.28 eV. The calculated shifts confirm the assignment of the high coverage peak to molecular water and the shoulder peak to dissociated water.

Comparing the values for the O $1s$ shifts calculated in using both methods it is obvious that the initial state approximation can provide a qualitative description, but according to Köhler and Kresse [191] it generally underestimates core level shifts by a large amount.

Table 6.11.: Core level shifts in eV of the O $1s$ core levels of water molecules adsorbed on the $Sr_3Ru_2O_7(001)$ surface. The binding energies are referenced to the O $1s$ binding energy at the rock-salt interface of the Sr_2RuO_4 and $Sr_3Ru_2O_7$ bulk crystal, respectively.

| Core level shifts [eV]	$Sr_3Ru_2O_7$		Sr_2RuO_4	
	Initial State	Final State	Initial State	Final State
Monomer, dissociated	0.22	2.03	0.64	2.31
Monomer, molecular	0.60	2.67	1.28	2.95
Dimer, "wide"	0.16	2.01	0.53	2.29
Dimer, "narrow"	0.14	2.02	0.52	2.30
Trimer	0.05	1.98	0.43	2.26
Line	0.01	1.97	0.38	2.25
Box, "narrow"	0.15	2.07	0.53	2.35
Box, "wide"	0.10	2.03	0.48	2.31
Box, "narrow", +1 H_2O	−0.18	1.89	0.20	2.17
Box, "wide", +1 H_2O	−0.23	1.79	0.15	2.06
Box, "narrow", +2 H_2O, #1	2.04	4.60	2.42	4.88
Box, "narrow", +2 H_2O, #2	1.40	3.71	1.78	3.99
Box, "wide", +2 H_2O, #1	−0.24	1.77	0.14	2.05
Box, "wide", +2 H_2O, #2	1.37	3.79	1.74	4.07
Full coverage, dissociated H_2O	0.02	2.00	0.40	2.28
Full coverage, molecular H_2O	1.51	4.00	1.89	4.28
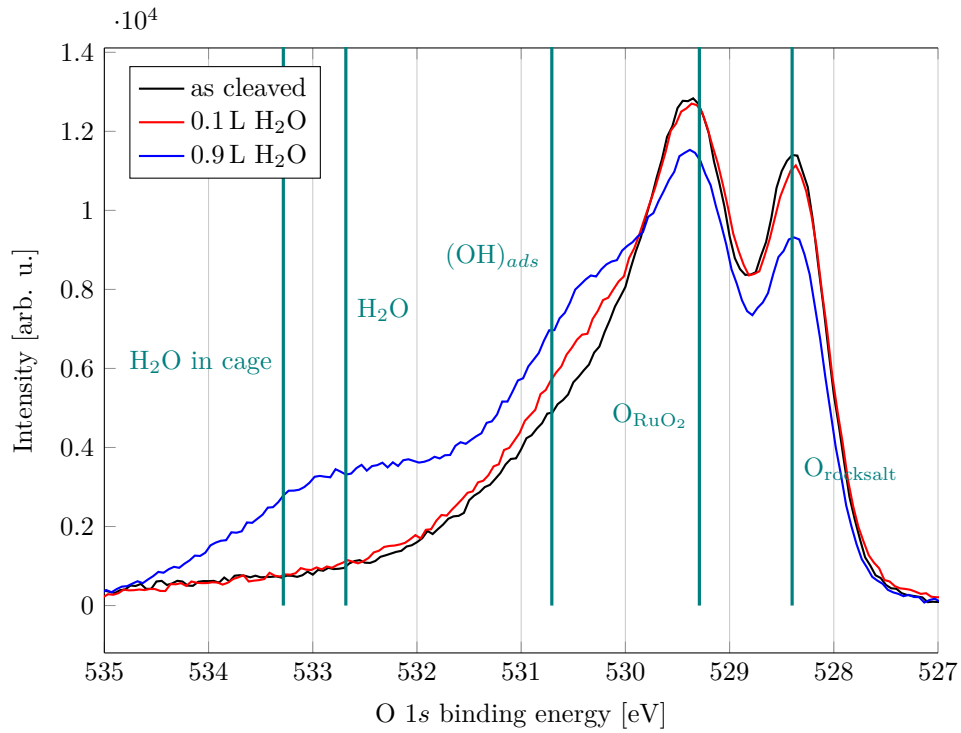
Figure 6.19.: XPS spectra of H_2O adsorbed on the Sr_2RuO_4 (001) surface at 0.1 and 0.9 Langmuir, measured at 140 K, as published by Halwidl, Stöger, Mayr-Schmölzer, et al. [2]. The double peak at 528.4 eV and 529.4 eV indicate the O 1s states in the SrO and RuO_2 plane respectively. At 530.4 eV and 532.8 eV the peaks corresponding to hydroxyls and molecular water are visible. The vertical bars represent the calculated core level binding energies referenced to the experimental SrO peak.

6.4. Calcium Ruthenate

This section will focus on the adsorption of water molecules on the $Ca_3Ru_2O_7$ surface. Following the studies on $Sr_3Ru_2O_7$ and Ca-doped $Sr_3Ru_2O_7$ surfaces the main differences originating from the different surface symmetry, in particular the influence of the additional tilting of the RuO_6 octahedra not present in the strontium ruthenate, will be discussed. The $Ca_3Ru_2O_7$ substrate follows the trend seen for the binary oxides (SrO, CaO, see appendix A.2) in that it shows dissociative adsorption of water molecules. The split off hydrogen again forms a surface hydroxyl while the remaining $(OH)_{ads}$ adsorbs at a bridge position between two metal atoms. Experiments published by Halwidl, Mayr-Schmölzer, et al. [5] have shown that increasing the H_2O coverage leads to several ordered structures, first with a (2×1), then a $c(2 \times 6)$, followed by a (1×3), and finally a (1×1) periodicity (see fig. 6.20). Due to the size of the $c(2 \times 6)$ unit cell only the other periodicities were studied.

For all calculations the optB86b functional and the correspondingly optimised unit cells introduced in section 5.5.4 were used. In addition, where computationally feasible the adsorption energies were assessed with RPA benchmark calculations. To model low coverages of the adsorbate, the primitive unit cell was simply multiplied in a and/or b direction. The computational parameters were similar to the previously mentioned calculations on the $Sr_3Ru_2O_7$ structures with an energy cutoff of 400 eV. For the (1×1) slab unit cell a $6 \times 6 \times 1$ Γ-centred $\vec{k}$-point grid was used. This choice facilitated the comparison of the adsorption energy calculated in various supercells, as the $\vec{k}$-mesh is easily divisible, leading to e.g. a $3 \times 6 \times 1$ grid for the (2×1) structure.

6.4.1. H$_2$O Monomer

In contrast to the strontium ruthenate (001) and the binary CaO(001) surfaces the surface symmetry is different for $Ca_3Ru_2O_7(001)$ (see section 5.5.4). Due to the tilting of the RuO_6 octahedra in $Ca_3Ru_2O_7$ the apical oxygen atoms are not situated in the middle of the rectangle formed by the surrounding calcium atoms. As can be seen in fig. 6.21 the tilting of the RuO_6 octahedron introduces 4 distinct adsorption sites. To limit confusion with the chemical formula of molecular oxygen, these sites are labeled Bx–Oy with respect to the (1×1) unit cell where the two apical oxygen atoms (O1, O2) and 4 Ca–Ca bridges (B1, B2, B3, B4), which due to symmetry considerations can be reduced to the 4 distinct sites (B1–O1 is equal to B2–O2). The main difference between these sites is the distance of the apical oxygen atom to the Ca–Ca bridge: for example, the B1–O1 site denotes the one with the largest distance as the RuO_6 octahedron is tilted away from the Ca–Ca bridge, while B3–O1 indicates the site with the closest oxygen-bridge distance. Using this naming convention, the B1–O1 site is equivalent to the B2–O2 site.

To determine the energetically favoured adsorption configuration of the H_2O monomer on the $Ca_3Ru_2O_7(001)$ surface, the molecule was placed in the surface in both a configuration similar to the dissociated and the molecular coordination found for the $Sr_3Ru_2O_7$ case. Both a (1×1) and a (3×3) (½ and ¹⁄₁₈ ML coverage, respectively) surface unit

(a) H₂O monomer   (b) (2 × 1) overlayer   (c) (1 × 3) overlayer
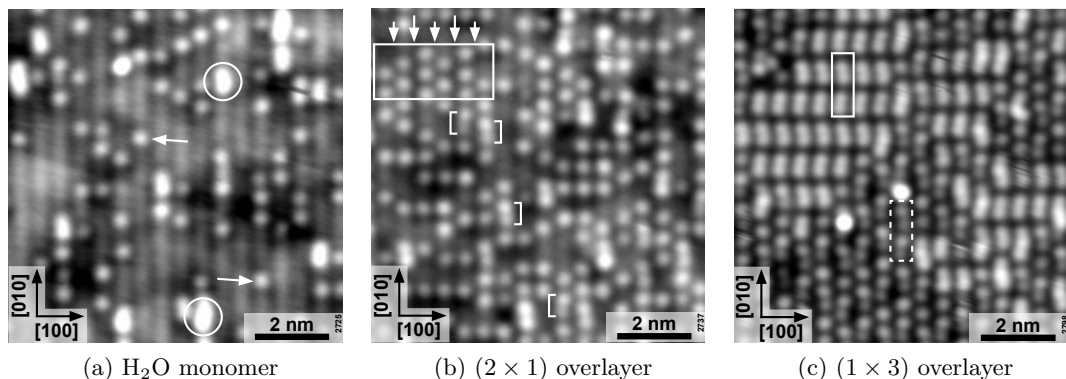
Figure 6.20.: STM images of water adsorbed on $Ca_3Ru_2O_7(001)$. (a) Image of 0.3 L of water, dosed at 105 K. $(OH)_{ads}$ of the adsorbed H_2O monomer appear as bright dots, indicated by bright arrows. (b) After annealing at room temperature for 1 h the (2 × 1) overlays is formed. (c) The (1 × 3) structure forms after exposure of the $c(2 × 6)$ overlayer to 0.15 L at 100 K. H_2O dimer are shown as the large bright double features. The experimental parameters were $I_t = 0.1$ nA, $T = 78$ K, and $U_s = -0.8$ V, courtesy of Halwidl, Mayr-Schmölzer, et al. [5].

cell were considered.

On the (3 × 3) model cell at all four adsorption sites the H_2O molecule dissociates spontaneously. A comparison of the adsorption energies of the H_2O monomer shows that the B1–O1 site is the most preferred adsorption site with an adsorption energy of −1.642 eV. The tilt angle of the octahedron increases from 12.9° to 16.3° compared to the pristine surface. The B2–O1 site is less stable by 199 meV due to the repulsive interaction with the apical O2 opposite of the Ca–Ca bridge. A dissociated H_2O could not successfully be stabilised at site B4–O1 as the $(OH)_{ads}$ was pushed to position B1–O1. The apical O2 at this site is tilted directly towards the Ca–Ca bridge causing the transition barrier to site B1 to vanish. The hydrogen bond connecting the $(OH)_{ads}$ to the surface hydroxyl is quite strong, moving the surface hydroxyl to another site would cost 0.733 eV. At the optimum adsorption configuration B1–O1 the distance of the components of the $(OH)_{ads}$ is 0.973 Å, slightly shorter than for the surface hydroxyl (1.033 Å). This hydroxyl is tilted towards the $(OH)_{ads}$, allowing the formation of a hydrogen bond with a H–$(OH)_{ads}$ distance of 1.539 Å. Due to this additional hydrogen bond the $(OH)_{ads}$ is positioned slightly off-center on the Ca–Ca bridge.

Using the small (1 × 1) unit cell, the coverage is now ½ ML with respect to the primitive surface unit cell. Nevertheless, similar behaviour could be observed. The B1–O1 adsorption site is again the most preferred one with an adsorption energy of −1.580 eV. The reduction compared to the low coverage case is the result of repulsive interaction between the water monomers, similar to the $Sr_3Ru_2O_7$ case. Additionally, in

217

this model cell the B2–O1 configuration could be stabilised with an adsorption energy of $-1.306\,\mathrm{eV}$ due to the increase of the transition barrier towards the B1–O1 site. This is not caused by direct interaction with the monomer in the next unit cell but by the subtle distortion of the surface geometry where the unoccupied RuO_6 octahedron with its apical oxygen O2 is slightly less tilted compared to the pristine case (9.5°). Adsorption at the B3–O1 site yields the same adsorption energy as for the low coverage case. Finally, the only site where a molecular adsorbate could be stabilised was B4–O1 with an adsorption energy almost identical to the B3–O1 case for both high and low coverage (see table 6.13). Compared to the binary CaO the adsorption energy is $\approx 700\,\mathrm{meV}$ higher, see Hu et al. [185] and appendix A.2. As the Ca–Ca distance is $8.8\,\%$ increased compared to the binary oxide, similar to $Sr_3Ru_2O_7$, the reason for this large increase in reactivity is attributed to the additional tilting of the octahedra.

On the (1×1) surface the adsorption energy at the B1–O1 site was also calculated with the PBE functional and the benchmark RPA method. The PBE functional gives an adsorption energy of $-1.365\,\mathrm{eV}$. The resulting difference to the van-der-Waals corrected calculations ($E_{Ads} = -1.574\,\mathrm{eV}$) suggests a van-der-Waals contribution of $\approx 210\,\mathrm{meV}$, slightly more than for the binary oxide ($160\,\mathrm{meV}$, see appendix A.2). For the RPA calculations, some modifications to the computational parameters had to be applied. To reduce the computational effort the vacuum in the unit cell was decreased to around $10\,\mathrm{Å}$ and the $\vec{k}$-point grid was reduced to a Γ-centred $4 \times 4 \times 1$ mesh. The adsorption energy calculated in the RPA of $-1.434\,\mathrm{eV}$ shows that the optB86b functional slightly overestimates the van-der-Waals contributions to the adsorption energy compared to the many-electron benchmark calculation. For the binary oxide the RPA predicts an adsorption energy of $-0.816\,\mathrm{eV}$ (see appendix A.2).

The STM simulations show the water monomer as a bright spot positioned on top of the wide channels of the pristine substrate for both positive and negative bias voltages (see figs. 6.23 and 6.25). In the occupied states the contrast between adsorbate and substrate is slightly higher. The bright spots are slightly shifted from the centre of the bright surface lines due to the slight shift of the $(OH)_{ads}$ from the Ca–Ca bridge. Additionally, the bright spot is slightly elongated towards the surface hydroxyl. At high coverage the bright spots of the $(OH)_{ads}$ cover the bright lines of the substrate almost completely, only at positive bias voltage remnants of these are visible. The simulations agree very well with the experiment (see fig. 6.20a).

Table 6.12.: Adsorption energies in eV of a H_2O monomer on both the (1×1) and (3×3) model cell, i.e. ½ and 1/18 ML coverage calculated using the optB86b functional. The adsorbate is not stable at the B4 position.

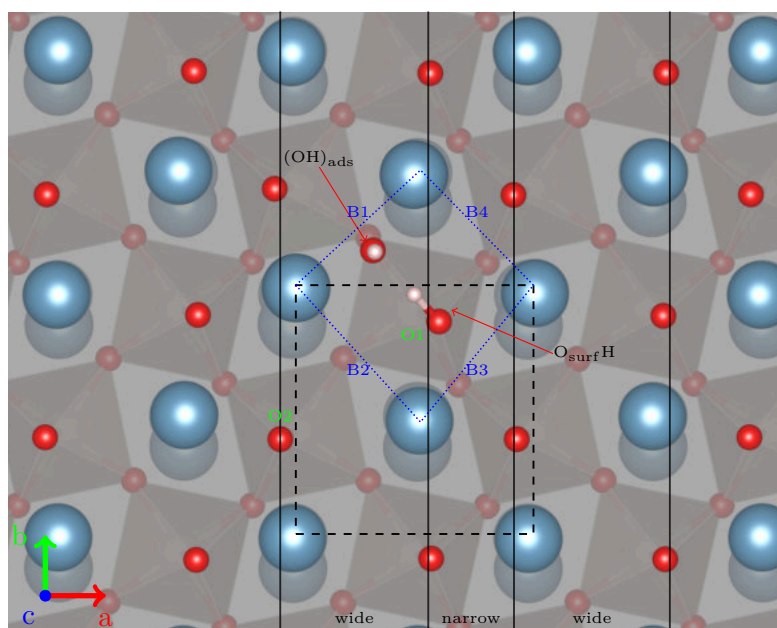| E_{Ads} [eV]	(1×1)	(3×3)
B1–O1	-1.574	-1.642
B2–O1	-1.301	-1.443
B3–O1	-0.779	-0.784

Figure 6.21.: Dissociated H_2O adsorbed at the most stable B1 bridge position. Black dashed line: (1×1) surface unit cell. Blue dotted lines indicate the four possible Ca–Ca bridge sites available to the $(OH)_{ads}$.

6.4.2. (2×1) Structure

As discussed in the previous chapter, increasing the water coverage leads to repulsive interaction between the adsorbates. This prevents the formation of a fully covered surface (i.e. $1 \, ML \, H_2O$), as has been shown in experiments which hint at a zig-zag (2×1) structure [5]. Several models were investigated in a (2×2) surface unit cell with four adsorbed H_2O molecules. A parallel configuration (fig. 6.24b) was compared to a zig-zag structure (fig. 6.24a) where one row of H_2O molecules was shifted parallel to the direction of the wide channels of the pristine surface by half a unit cell, i.e. one monomer adsorbed at a B1–O1 site and one at a B2–O2 site. Additionally, a second, "defective" zig-zag structure was investigated where in one row one adsorbate was shifted by half a unit cell, giving a mixed parallel-zig-zag structure.

The calculated adsorption energies per H_2O molecule show slight repulsive interaction between the water molecules even in the zig-zag configuration ($\Delta \, E_{Ads} = 20 \, meV$ compared to $1/9 \, ML$ coverage). The parallel configuration is virtually identical to the (1×1) model mentioned before, reflected in the identical adsorption energy. Shifting one row of adsorbed H_2O by half a unit cell (see fig. 6.24c) gives an adsorption energy difference of only $\approx 10 \, meV$. This arrangement would reflect a criss-cross pattern of rows of H_2O in a direction intersecting rows of H_2O in b direction. The zig-zag structure is $53 \, meV$ per H_2O molecule more stable, so one would expect to find this configuration at a much

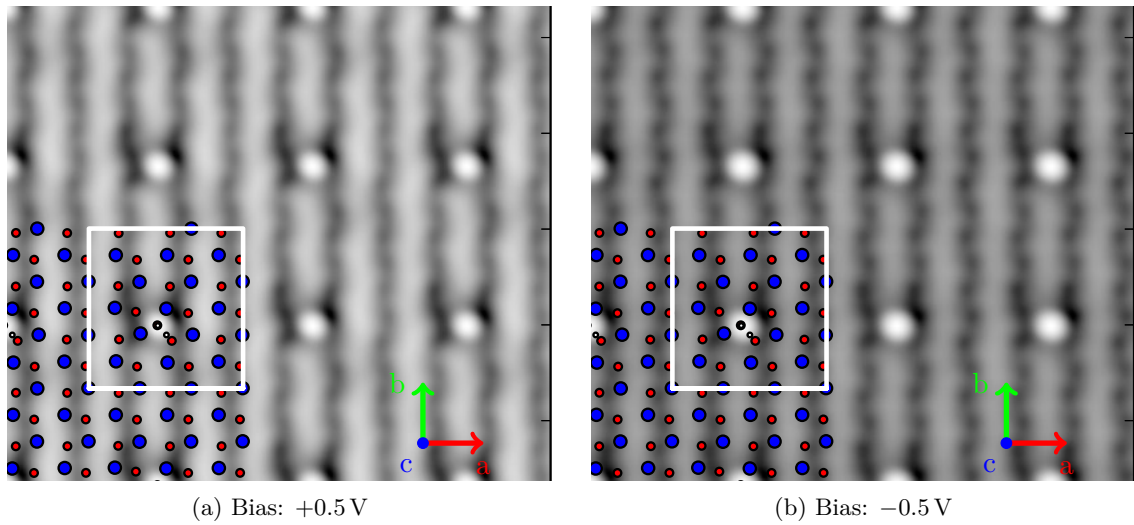(a) Bias: $+0.5\,\mathrm{V}$ (b) Bias: $-0.5\,\mathrm{V}$

Figure 6.22.: STM simulation of the H_2O monomer on a (3×3) $Ca_3Ru_2O_7$ surface unit cell. The $(OH)_{ads}$ is visible as a bright spot at both positive and negative bias voltages. The spot is slightly shifted off the centre of the familiar bright lines of the pristine surface since the $(OH)_{ads}$ does not sit directly on the Ca–Ca bridge.
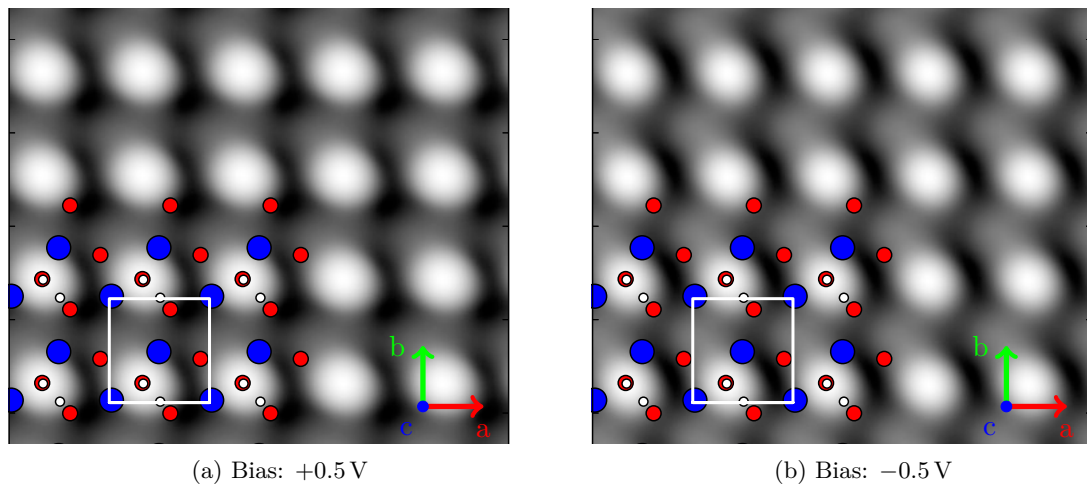

(a) Bias: $+0.5\,\mathrm{V}$ (b) Bias: $-0.5\,\mathrm{V}$

Figure 6.23.: STM simulation of the H_2O monomer on a (1×1) $Ca_3Ru_2O_7$ surface unit cell. The $(OH)_{ads}$ is visible as a bright spot at both positive and negative bias voltages. Due to the high coverage the bright substrate lines are almost not visible anymore.

higher probability in the experiment.

Comparing the Tersoff-Hamann STM simulations with the experimental STM images shown in fig. 6.20b very good agreement is found. Due to the slight shift of the $(OH)_{ads}$ from the centre of the Ca–Ca bridge, the zig-zag structure shows double rows of bright spots located on the wide channels of the substrate, one shifted by half a unit cell in the b direction of the unit cell. Narrow dark gaps separate the individual rows with slightly wider dark rows between the double rows.

Table 6.13.: Adsorption energies in eV per H_2O of four dissociated H_2O molecules on a (2×2) surface unit cell. The zig-zag structure is more preferred than the parallel configuration since here the distance between the adsorbates is maximised.

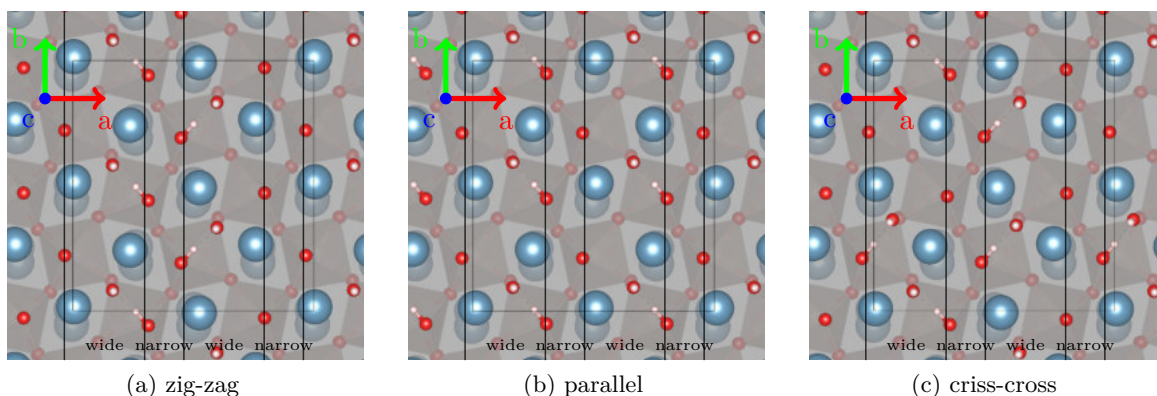| E_{Ads} [eV]	(2×2)
zig-zag	-1.622
parallel	-1.570
criss-cross	-1.575

(a) zig-zag   (b) parallel   (c) criss-cross

Figure 6.24.: 4 H_2O adsorbed on a (2×2) unit cell. The zig-zag configuration is most stable, a parallel or criss-cross pattern would incur an energy penalty of $50\,meV$.

6.4.3. (1×3) Structure

Further increases of the water coverage in the experiment results in (1×3) domains covering at first small parts and then almost all of the surface. The STM pictures now show prominent areas of the substrate covered by rows of bright double spots, separated by areas of different bright-dark double spots at lower brightness. Interestingly, the
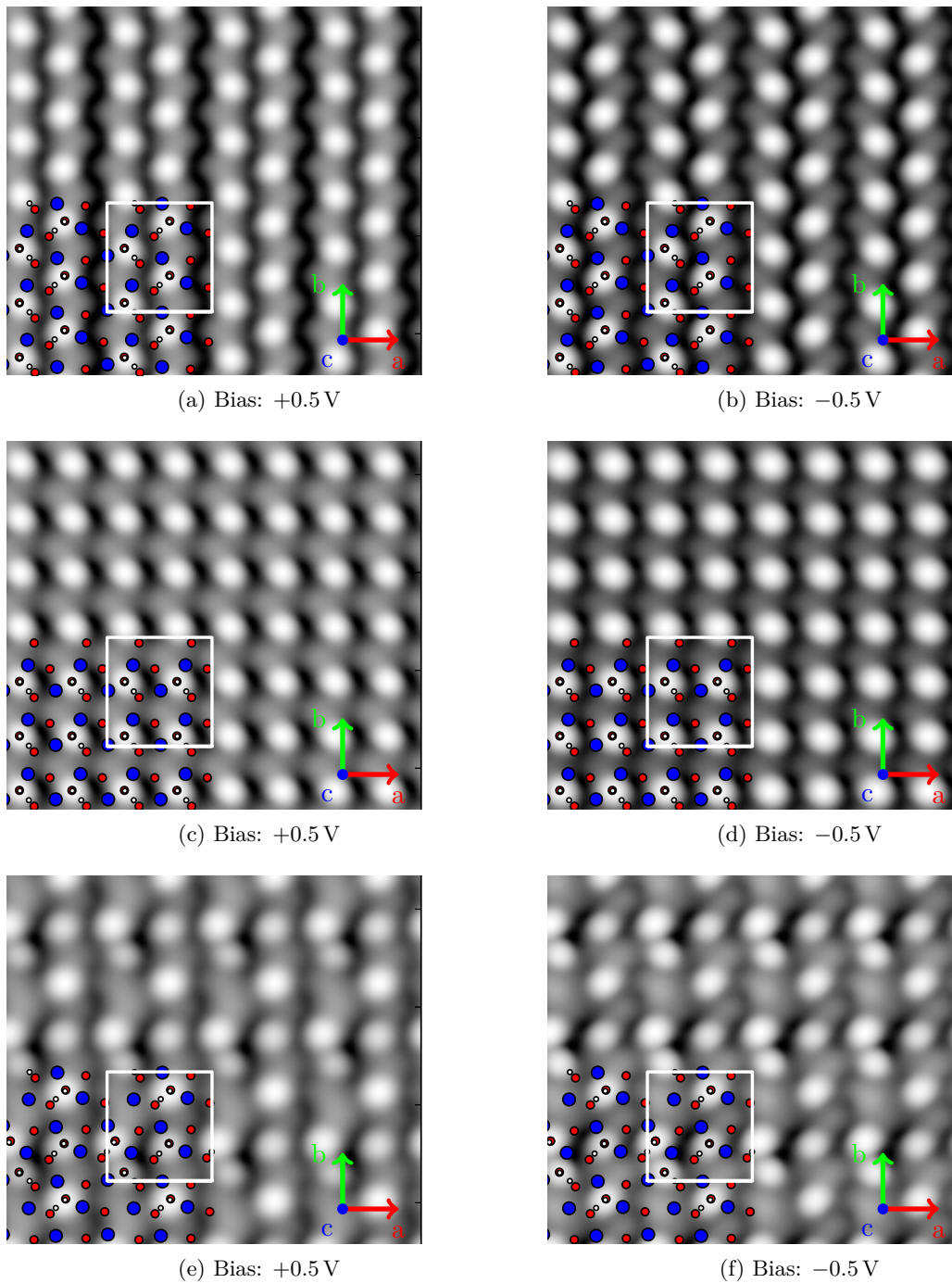
(a) Bias: $+0.5\,\mathrm{V}$

(b) Bias: $-0.5\,\mathrm{V}$

(c) Bias: $+0.5\,\mathrm{V}$

(d) Bias: $-0.5\,\mathrm{V}$

(e) Bias: $+0.5\,\mathrm{V}$

(f) Bias: $-0.5\,\mathrm{V}$

Figure 6.25.: STM simulation of four H_2O adsorbed on a (2×2) $Ca_3Ru_2O_7$ surface unit cell. In all cases the $(OH)_{ads}$ is visible as a bright spot at both positive and negative bias voltages. At this coverage the bright/dark pattern of the pristine surface is not visible anymore.

bright areas do not show a zig-zag structure like in the (2×1) configuration. The spots are always visible on top of the bright substrate rows.

To model this structure a (1×3) unit cell was created and, just like before, water molecules were placed at various B1–O1 sites. In this model cell the adsorption energy of a water monomer is 11 meV lower than in the (3×3) due to the slight repulsion of the H_2O in the next unit cell. Increasing the number of adsorbates in this model lowers the adsorption energy further by 22 meV for two H_2O in two separate (1×1) surface unit cells and by 19 meV for two H_2O next to each other, suggesting slight preference towards the formation of dimers. A third water molecule added to this chain yielding, a trimer formation, reduces the adsorption energy per H_2O even further by 33 meV with respect to the dimer. Finally, the comparison of a 4-molecule structure forming a trimer and a monomer to a double dimer structure again show the preference of the water molecules to form dimers. All adsorption energies are shown in table 6.14.

Tersoff-Hamann STM simulations of the dimer and double dimer structures are in very good agreement with the experiment, showing the dimers as bright double spots, see fig. 6.26.

The experiments published by Halwidl, Mayr-Schmölzer, et al. [5] reveal that the adsorbed water molecules show a particular pattern at ⅓ ML coverage consisting of dimer-like features. These bean-shaped features show both an equally bright variant and one where one part is much brighter than the other. To study these features several proposed modifications to the water overlayer were tested. First, in a single dimer model on the (1×3) surface the surface hydroxyl was moved to another apical oxygen. For the first iteration of these calculations the proton was just moved into the next unit cell, creating a dimer consisting of one H_2O adsorbed at a B1–O1 site and one at a B2–O1 site, see fig. 6.27a for an illustration. This configuration is 116 meV less stable than a single dimer and shows that, due to the preference to form a dimer, less stable sites can also be stabilised (for a monomer this site is 200 meV less stable). Nevertheless, the STM simulation depicted in figs. 6.28b and 6.28c does not show the same difference in brightness found in the STM measurements. For another test model the proton was moved to the apical oxygen in the next unit cell, effectively breaking its hydrogen bond to the adsorbed $(OH)_{ads}$, as depicted in fig. 6.27d. The resulting structure is 412 meV less stable than a single dimer, indicating that such a structure would be very unstable. The $(OH)_{ads}$ separated from its surface hydroxyl is tilted by 55.6° from the axis normal to the surface while the direction of the $(OH)_{ads}$ of the intact monomer is normal to the surface. The STM simulation of this model show a bright-dark dimer structure at negative bias voltages and a very bright spot indicating the separated hydroxyl at positive bias voltages. The brighter spot in the dimer feature is created by the tilted $(OH)_{ads}$ separated from the surface hydroxyl and the darker spot by the intact monomer. The bright spot is shifted from the surface hydroxyl towards the Ca–Ca bridge. Again, the simulations agree very well with the experiment (see fig. 6.20c).

(a) two dimers   (b) Bias: $+0.5\,\mathrm{V}$ (c) Bias: $-0.5\,\mathrm{V}$

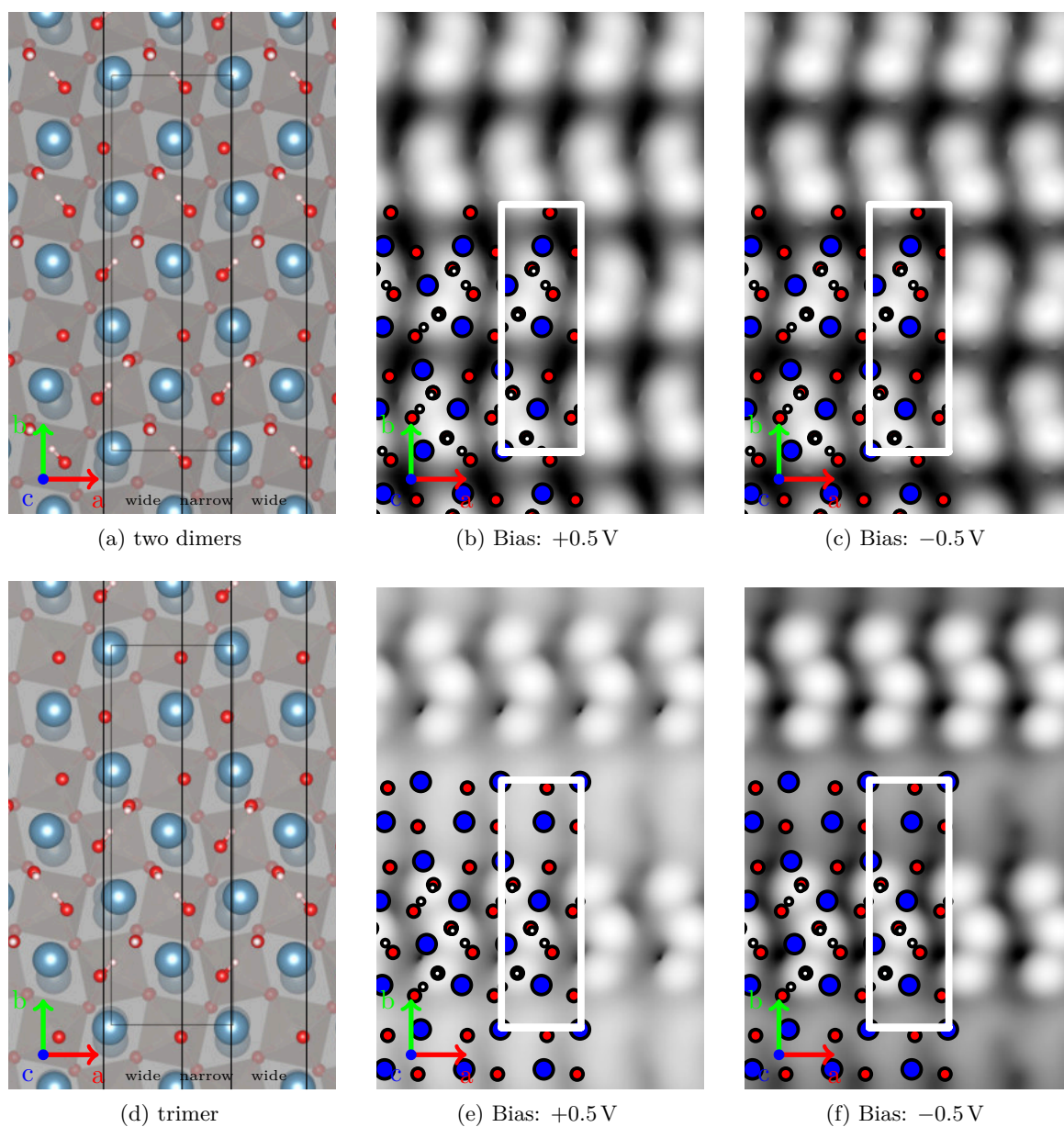(d) trimer   (e) Bias: $+0.5\,\mathrm{V}$ (f) Bias: $-0.5\,\mathrm{V}$

Figure 6.26.: Top view of the (1×3) model cell with (a)-(c) two dimers and (d)-(f) one trimer. The dimers form a bean-shaped, undulating pattern where the bright spots are generated by the $(OH)_{ads}$ adsorbed on top of the wide surface channels.
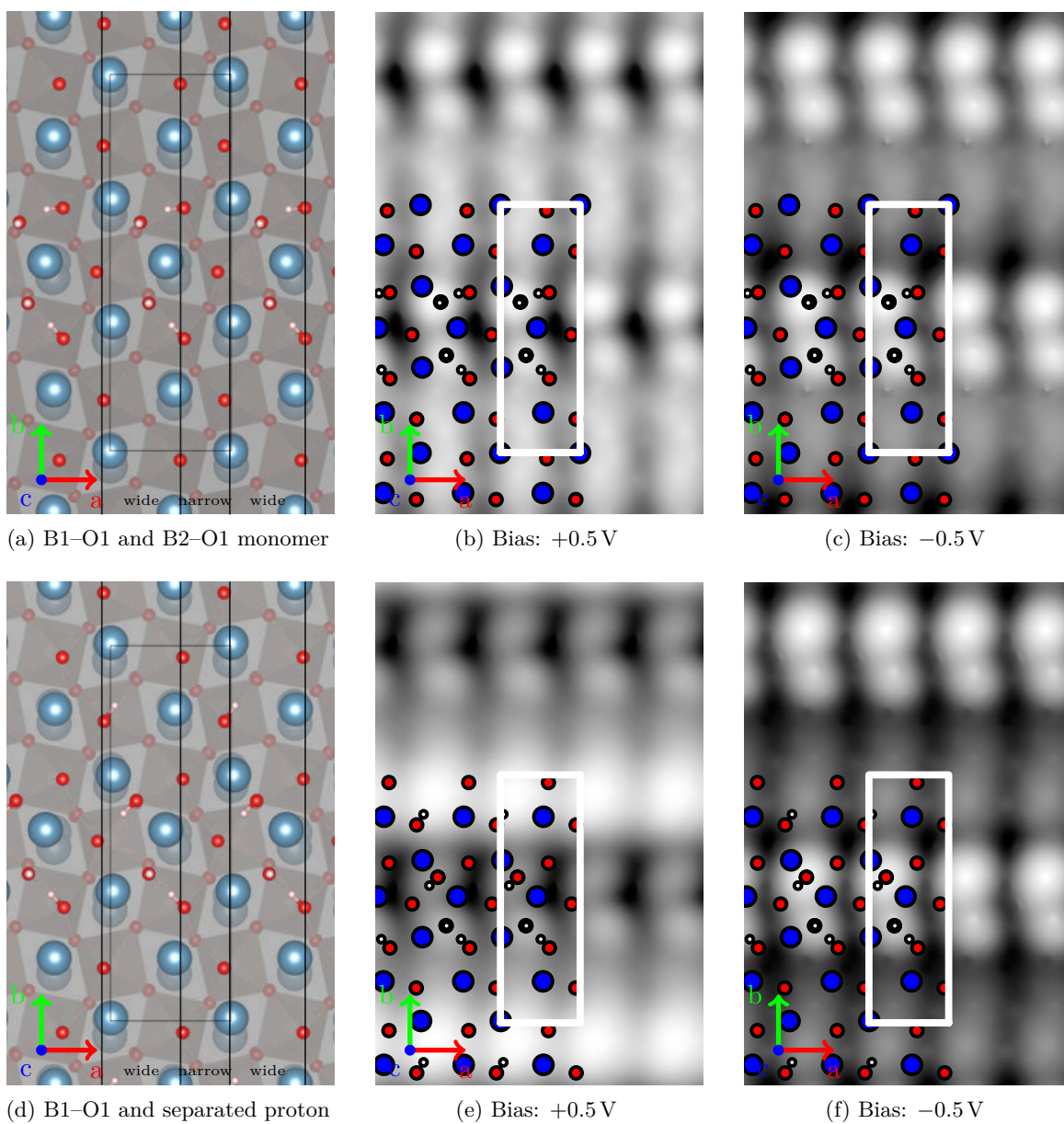
(a) B1–O1 and B2–O1 monomer   (b) Bias: $+0.5\,\mathrm{V}$ (c) Bias: $-0.5\,\mathrm{V}$

(d) B1–O1 and separated proton   (e) Bias: $+0.5\,\mathrm{V}$ (f) Bias: $-0.5\,\mathrm{V}$

Figure 6.27.: Top view of the (1×3) model cell with ((a)) one B1–O1 and one B2–O1 monomer, ((d)) one B1–O1 monomer and one $(OH)_{ads}$ separated from the surface hydroxyl. (b) - (c), (e) - (f): STM simulation of the aforementioned structures.

225

Table 6.14.: Adsorption energies in eV of dissociated H_2O molecules per H_2O on a (1×3) surface unit cell.

# H_2O	E_{Ads} [eV]]
1	-1.631
2	-1.609
2, dimer	-1.612
3, trimer	-1.579
4, 1 trimer	-1.562
4, 2 dimer	-1.585
2, 1H shifted, v1	-1.493
2, 1H shifted, v2	-1.197

6.4.4. (1×1) Structure: Full Coverage

To simulate the experimental saturation water coverage on the $Ca_3Ru_2O_7$ substrate, all Ca–Ca bridge sites of the (1×1) were occupied by water molecules. The adsorption energy per H_2O in the fully relaxed structure is reduced by $159\,meV$ to $-1.483\,eV$ due to repulsive interaction between the adsorbed water molecules. In contrast to $Sr_3Ru_2O_7$ at full coverage (see section 6.1.4) no recombination to molecular water can be observed. At full coverage the surface hydroxyl is slightly longer at $1.046\,Å$ compared to the monomer, but the hydrogen bond formed between the surface H_s and the adsorbed $(OH)_{ads}$ is shorter at $1.500\,Å$. The STM simulations show bright undulating lines on top of the bright lines formed by the pristine surface (see figs. 6.28b and 6.28c) which are formed by the usual bright spots indicating the $(OH)_{ads}$.

Table 6.15.: Mean adsorption energy in eV of 2 dissociated H_2O molecules per H_2O on a (1×1) surface unit cell, representing full coverage.

	E_{Ads} [eV]
Full coverage	-1.483

6.4.5. Core Level Shifts

The core level shifts for the $Ca_3Ru_2O_7$ structures were calculated using the same procedure as for the $Sr_3Ru_2O_7$ and Sr_2RuO_4, described in section 6.3. Again the main goal was the identification of the oxygen sites in both bulk and slab structures and the assignment of the H_2O species in measured XPS spectra, therefore only the binding energies of the O $1s$ states were calculated in both the initial state (IS) and the final state (FS)
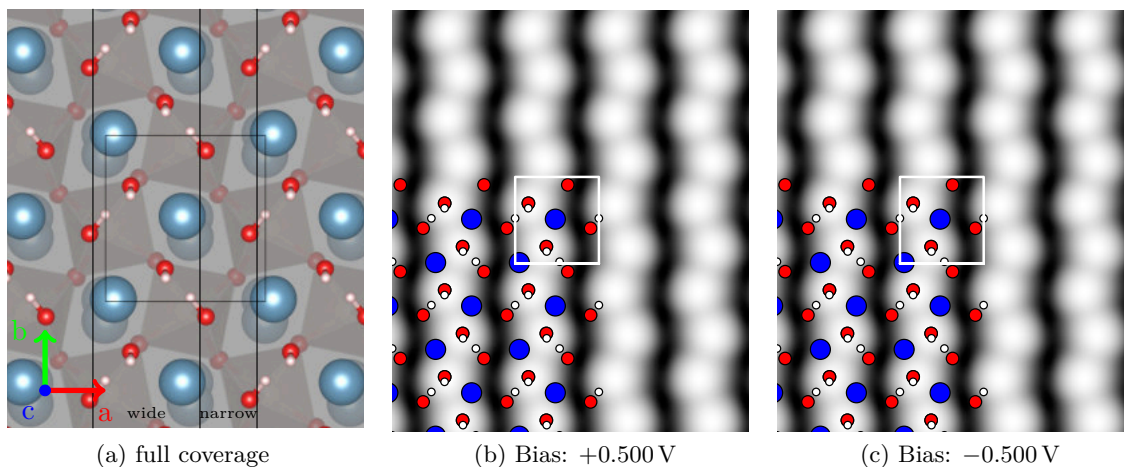
| (a) full coverage | (b) Bias: $+0.500\,\text{V}$ | (c) Bias: $-0.500\,\text{V}$ |

Figure 6.28.: STM simulation of the H_2O monomer at full coverage on a (1×1) model cell. The $(OH)_{ads}$ form bright, undulating lines on top of the bright line structure of the pristine surface.

approximation. All calculations were performed using the optB86b functional on the fully optimised structures at the corresponding computational settings. Again, shifts in the binding energy are given with respect to the most weakly bound state, and positive differences indicate stronger binding energies.

$Ca_3Ru_2O_7$ Bulk

The O $1s$ binding energies were calculated for a larger bulk unit cell where the cell was doubled in both a and b direction to shield the excited site from interactions with sites in the next unit cell due to the periodic boundary conditions. In both the initial state and final state approximations four distinct O $1s$ core level binding energies can be observed, one more than for the two strontium ruthenates. Two originate from the planar $O_{RuO_2,1}$ and $O_{RuO_2,2}$ sites in the RuO_2 plane as due to the tilt of the RuO_6 octahedra two oxygen atoms are tilted towards the rock-salt interface ($O_{RuO_2,1}$) and the other two tilt towards the central CaO plane ($O_{RuO_2,2}$). Similar to $Sr_3Ru_2O_7$ two apical sites exist, one at the rock-salt interface ($O_{rocksalt}$) and one in the CaO plane (O_{CaO}) at the centre of the $CaRuO_3$ double layer.

Both approaches show the O $1s$ states with the lowest binding energy at the apical $O_{rocksalt}$ site, as shown in table 6.16. In the initial state approximation the $O_{RuO_2,1}$, $O_{RuO_2,2}$, and O_{CaO} sites exhibit a shift of $0.75\,\text{eV}$, $0.76\,\text{eV}$, and $0.83\,\text{eV}$ to higher ending energies. The final state approximation shows the different ordering with shifts of $0.54\,\text{eV}$, $0.60\,\text{eV}$, and $0.73\,\text{eV}$ for the $O_{RuO_2,1}$, O_{CaO}, and $O_{RuO_2,2}$ sites respectively. Again the size of the unit cell is important to shield the excited site from its mirror site, as for the primitive unit cell the calculated binding energy difference between e.g.

227

$O_{rocksalt}$ and $O_{RuO_2,2}$ is just $0.55\,eV$ in the final state approximation. Since the core level shifts in the $Ca_3Ru_2O_7$ bulk are very small ($<1\,eV$), it is difficult to obtain good experimental data of the O $1s$ states, especially with standard laboratory equipment. As seen in the XPS data in fig. 6.29, which was measured using a non-monochromatised Mg $K\alpha$ X-ray source, the bulk material is only visible as a broad peak at $529.2\,eV$ [5].

Table 6.16.: Core level shifts in eV of the O $1s$ states of bulk $Ca_3Ru_2O_7$ in the initial and final state approximation with respect to the most weakly bound state. The $Ca_3Ru_2O_7$ unit cell was doubled in a and b direction.

Core level shifts [eV]	Initial State	Final State
	$Ca_3Ru_2O_7$ bulk	
$O_{rocksalt}$	0	0
O_{CaO}	0.82	0.60
$O_{RuO_2,1}$	0.75	0.54
$O_{RuO_2,2}$	0.76	0.73
	$Ca_3Ru_2O_7$ slab	
$O_{surface}$	0.01	−0.21
$O_{rocksalt}$	−0.03	0
O_{CaO}	0.78	0.49
$O_{RuO_2,1}$	0.78	0.58
$O_{RuO_2,2}$	0.77	0.66

$Ca_3Ru_2O_7$ Slabs

To calculate the O $1s$ binding energies of the $Ca_3Ru_2O_7$ slab structures, a thick slab consisting of two double layers of $CaRuO_3$ including one rock salt interface was used. The unit cell was again doubled in a and b direction and the O $1s$ states of the first double layer were calculated. The core levels at the rock salt interface $O_{rocksalt}$ show almost no shift with respect to the bulk values. The O $1s$ levels of the O_{RuO_2} in the RuO_2 plane and the O_{CaO} in the CaO plane are slightly lower than for the $Ca_3Ru_2O_7$ bulk, as shown in table 6.16. At the surface, the initial state calculation shows almost no shift, while in the final state approximation the O $1s$ level is shifted by $0.21\,eV$ to lower binding energies, similar to the O $1s$ surface state on the $Sr_3Ru_2O_7(001)$ surface ($0.19\,eV$). A test calculation on a unit cell tripled in both a and b direction showed no difference in the O $1s$ shifts in the final state approximation.

H_2O on $Ca_3Ru_2O_7$ Slabs

The core level shifts of the H_2O adsorbate calculated for several structures provided a good tool to help interpret the experimental XPS data provided by Halwidl, Mayr-Schmölzer, et al. [5]. As can be seen in fig. 6.29 the $Ca_3Ru_2O_7$ bulk shows a broad peak

at $\approx$529.2 eV. After dosing some water, a shoulder towards higher binding energies starts to form, indicating first the (1×3), then the $c(2\times6)$ and finally the line structure, shifted by approximately 1.8 eV to 1.4 eV. The separated peak shifted by $\approx$3.9 eV higher binding energies only appears after dosing a large amount of water, indicating an overlayer of molecular water.

Taking the bulk $O_{rocksalt}$ level as a reference, like in the case of H_2O adsorbed on $Sr_3Ru_2O_7$, the calculated O 1s core levels of the dissociated monomer on the (3×3) model cell shows a shift of 0.30 eV in the initial (IS) and of 2.23 eV in the final (FS) state approximation, referenced to the bulk $O_{rocksalt}$ level. The O 1s level of the oxygen site right below the $(OH)_{ads}$ which forms the surface hydroxyl shifts by 0.66 eV and 1.64 eV, respectively. Increasing the H_2O coverage on the model cell leads to a small variation of this shift: for a dissociated H_2O on the (1×1) the core level shift is 0.34 eV (IS) and 2.30 eV (FS). The O 1s states of the H_2O adsorbate on the (2×1) zig-zag structure exhibit a shift of 0.28 eV and 2.25 eV, while for the (2×1) parallel structure the core levels are shifted by 0.35 eV and 2.32 eV for the initial and final state calculations, respectively. The first model where the core level shifts differ significantly is the (1×3) cell. Here the four water molecules that form the double dimer structure show O 1s level shifts of 0.02 eV to 0.23 eV (IS) and 2.06 eV to 2.27 eV in the final state approximation. At full coverage, the initial state calculation shows a shift of -0.20 eV towards lower binding energies, while in the final state approximation this level shifts by 1.85 eV towards higher binding energies. Finally, the molecular H_2O stabilised on the (1×1) unit cell shows a shift of 1.85 eV (IS) and 4.25 eV (FS) to higher binding energies. Compared to the case of water adsorbed on the $Sr_3Ru_2O_7(001)$ surface the absolute positions of the O 1s states of the adsorbed molecules do not significantly differ.

To map the calculated core level shifts to the experimental curves these shifts were also calculated with respect to the averaged binding energy over the upper half of the first double layer including the surface oxygen $O_{surface}$ level. As shown in fig. 6.29, in the final state approximation the resulting shifts show good agreement with the experimental XPS curves. For the initial state configuration this results in a negative shift of the O 1s levels of the adsorbate, see table 6.17. This is caused by both the general underestimation of the core level shift in this method and the 0.11 eV to 0.20 eV larger shift between rock-salt and RuO_2 O 1s levels.

Generally, the DFT calculations show that while the final state approximation still underestimates the O 1s binding energy shifts, it has proven to be a reliable tool to aid in the explanation of XPS spectra of water adsorbates.
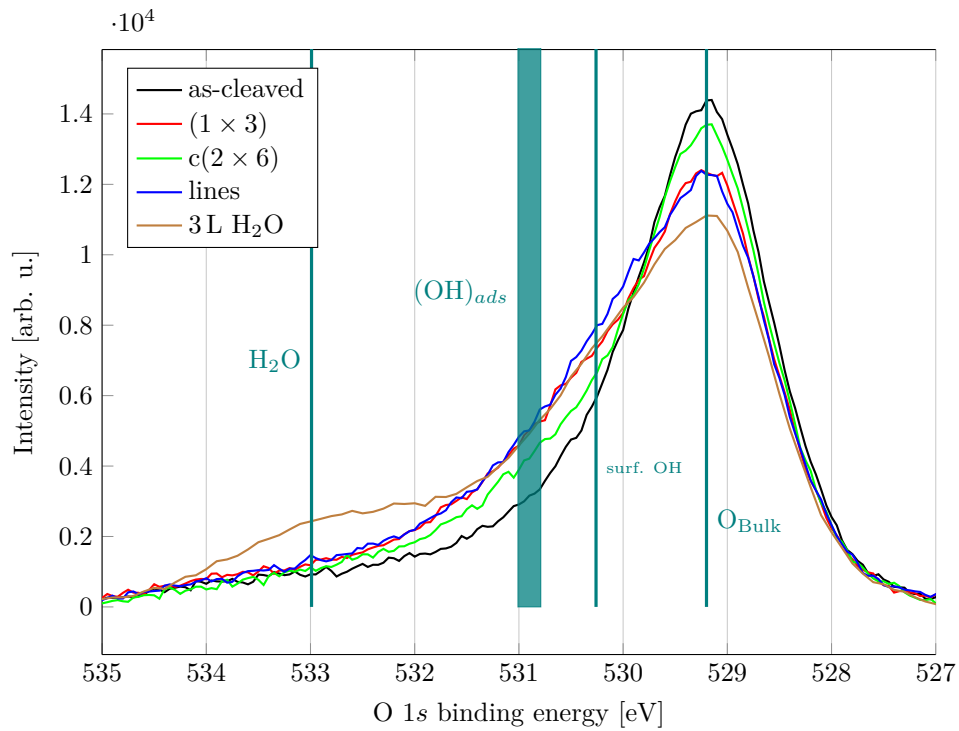
Figure 6.29.: XPS spectra of H_2O adsorbed on the $Ca_3Ru_2O_7(001)$ surface at different coverages, as published in Halwidl, Mayr-Schmölzer, et al. [5]. The shoulder between $530.0\,eV$ and $531.0\,eV$ corresponds to the $c(2 \times 6)$, (1×3) and (1×1) structures. Exposing the full monolayer to water at $105\,K$ leads to the peak at $533.1\,eV$, assigned to molecular water. The vertical lines represent the calculated core level shifts referenced to the experimental surface peak, nicely indicating the smaller and larger O $1s$ shift for dissociated and molecular adsorbed H_2O.

Table 6.17.: O 1s core level shifts in eV of the adsorbed H$_2$O calculated in the final state approximation, referenced to the O 1s binding energies at both the RuO$_2$ layer and at the rock salt interface of the Ca$_3$Ru$_2$O$_7$ slab.

Core level shifts [eV]	O$_{\text{RuO}_2}$		O$_{\text{rocksalt}}$	
	Initial State	Final State	Initial State	Final State
Monomer, dissoc., (3×3)	−0.48	1.61	0.30	2.23
Monomer, dissoc., (1×1)	−0.43	1.68	0.34	2.30
Monomer, mol., (1×1)	1.07	3.63	1.85	4.25
(2×1), zig-zag	−0.50	1.63	0.28	2.25
(2×1), parallel	−0.42	1.70	0.35	2.32
(2×1), dimer	−0.76 to −0.54	1.44 to 1.65	0.23 to 0.02	2.27 to 2.06
Full coverage, (1×1)	−0.97	1.23	−0.20	1.85

6.5. Summary

The DFT studies of water adsorption of the ruthenates show that some trends derived from other rock-salt-type binary oxides also hold for certain ternary oxides. Nevertheless, the exact structure of the AO-terminated rock-salt surface of the strontium and calcium based ruthenates plays a decisive role for the order of the adsorbed phases. Both ruthenates are, like the related binary oxides, quite reactive leading to dissociative adsorption of water monomers with adsorption energies of −1.260 eV for Sr$_3$Ru$_2$O$_7$ and −1.640 eV for Ca$_3$Ru$_2$O$_7$. The binding energy is increased compared to the related binary oxides to −1.082 eV and −0.816 eV for the SrO(001) and CaO(001) surfaces, respectively. For both Sr$_3$Ru$_2$O$_7$ and Ca$_3$Ru$_2$O$_7$, the resulting (OH)$_{\text{ads}}$ and H fragments stay connected through a hydrogen bond. For Sr$_3$Ru$_2$O$_7$ the dissociated water monomer is mobile, rotating around the split-off surface hydroxyl with a predicted activation energy of 169 meV, similar to the theoretically predicted behaviour for BaO [186]. On Ca$_3$Ru$_2$O$_7$ on the other hand, the tilting of the octahedra changes the surface structure decisively with respect to the related CaO, leading to immobile, very strongly bound dissociated water monomers. The subsurface structure also plays an influential role for the strontium ruthenate. While the formation of dimers is predicted on both Sr$_3$Ru$_2$O$_7$(001) and Ca$_3$Ru$_2$O$_7$(001), the stability of the these dimers depends on the rotations of the octahedra. On Sr$_3$Ru$_2$O$_7$ the hydroxyls agglomerate next to each other where the tilt and rotation of the RuO$_6$ octahedra is most accommodating, while on Ca$_3$Ru$_2$O$_7$ dimer formation is only seen at higher coverages and only along one crystallographic direction, following the "wide''-"narrow" periodicity of the surface structure. Further increase of the H$_2$O coverage on the strontium ruthenate leads to one-dimensional chain structures. Such 1D structures have only been observed on a CaO(001) surface [193] where they

were formed by aggregates of dissociated and molecular water. Sites adjacent to the 1D structures on $Sr_3Ru_2O_7$ are passivated and are only occupied at higher coverage by more weakly bound molecular H_2O, trapped in cages formed by the dissociated H_2O. The calcium ruthenate on the other hand exclusively adsorbs dissociated water until full coverage. The comparison of these two materials highlights the decisive differences in the surface reactivity and structure of the adsorbed water over-layer driven by the different rotation and tilting of the octahedra. The combination of Tersoff-Hamann STM simulations, core level shift and adsorption energy calculations have shown very good agreement to experiments, and thus confirm that the present DFT simulations allow the identification of the driving mechanism for the formation of the different adsorption structures. Two combined experimental and theoretical papers detailing the adsorption studies on $Sr_3Ru_2O_7$ and $Ca_3Ru_2O_7$ were published by Halwidl, Stöger, Mayr-Schmölzer, et al. [2] and Halwidl, Mayr-Schmölzer, et al. [5], respectively, in highly rated academic journals.

7. Adsorption of O_2 on (001) Ruthenate Surfaces and its Charge State

As discussed in the previous chapters, the ternary transition metal oxides $Sr_3Ru_2O_7$ and $Ca_3Ru_2O_7$ discussed in this work exhibit interesting properties with regard to the reaction kinetics of water. Much research has been done regarding the oxygen transport properties and oxygen reduction reactions for other perovskite materials [194–197], while the adsorption of molecular oxygen is less well understood. Recently, Staykov et al. [198] have done theoretical and experimental oxygen activation and dissociation studies on strontium titanate $SrTiO_3$, concluding that dissociation of O_2 on its SrO terminated surface is disfavoured, but oxygen vacancies can increase the activity of this surface. Additionally, charge transfer into the O_2 adsorbate is predicted only in the presence of oxygen vacancies, in this case leading to the adsorption of O_2 as a superoxo (O_2^-) species. A similar mechanism has recently been studied for La_2NiO_4, another Ruddelsden-Popper series perovskite, where Akbay et al. [199] describe oxygen adsorption and dissociation at the defect free LaO-terminated $La_2NiO_4(001)$ surface. Here, a superoxo species is also predicted already for the stoichiometric surface, as charge is transferred from the surface La atoms to the adsorbed oxygen.

This chapter will cover the adsorption studies of O_2 molecules on pure and Ca-doped $Sr_3Ru_2O_7$, and $Ca_3Ru_2O_7$. The calculations were performed at both low and high coverages. The adsorption geometries and energies on the different substrates are described, including a discussion of the charge state of the adsorbed O_2 molecule. A theoretical paper describing presented study of adsorption of oxygen molecule on pure and Ca-doped $Sr_3Ru_2O_7(001)$ surfaces was recently submitted [8], and a combined experimental and theoretical academic paper detailing the O_2 adsorption studies on $Ca_3Ru_2O_7(001)$ was published by Halwidl, Mayr-Schmölzer, et al. [6].

7.1. Strontium Ruthenate

The adsorption studies of O_2 on the $Sr_3Ru_2O_7$ strontium ruthenate were done in a similar manner as the calculations for H_2O adsorption. Oxygen molecules were placed on the two model cells c(2 × 2) and c(4 × 4), enabling the investigation of molecular O_2 adsorption at various coverages. The computational settings were the same as used for the H_2O adsorption calculations: $3 \times 3 \times 1$ and $6 \times 6 \times 1$ Γ-centred $\vec{k}$-point grids for the c(4 × 4) and c(2 × 2) model cells respectively and an energy cutoff of 400 eV. The calculations were performed primarily using the optB86b functional. For the smaller c(2×2) model cell the adsorption energies of selected optB86b-optimised structures were

also evaluated using the hybrid HSE06 functional and the many-electron ACFDT-RPA approach.

7.1.1. Low Coverage: c(4×4) Model Cell

To study the adsorption behaviour of molecular O_2, the oxygen molecule was relaxed from three different starting configurations on the c(4×4) model cell. In the first model the O_2 was positioned at the centre of a Sr–Sr bridge position, for the two other models the adsorbate was tilted slightly and moved in the direction of one Sr atom. The difference between the two latter starting configurations is only the rotation of the octahedra in the first sublayer, see fig. 7.1. Considering that disregarding the rotational symmetry there are 12 Sr–Sr bridge positions this model yields an O_2 coverage of $\frac{1}{16}$ monolayer (ML), referenced to the number of available Sr–Sr bridge sites in the model cell.

The calculations predict the same relaxed equilibrium position for all three starting positions. In the first relaxed position the O_2 molecule moves into the direction of one of the neighbouring strontium atoms (Sr$_I$) and tilts by 28.8°, but the final placement is still at the bridge between Sr$_I$ and Sr$_{II}$ (see fig. 7.1). The oxygen molecule is expanded to 1.354 Å compared to 1.236 Å for molecular O_2 calculated with the optB86b functional. The distances d(O$_I$–Sr$_I$) and d(O$_{II}$–Sr$_{II}$) to the closest Sr atom are 2.511 Å and 2.506 Å respectively. Both strontium atoms close to the O_2 adsorbate get slightly pulled out of the surface by 29 pm and 17 pm for Sr$_I$ and Sr$_{II}$ respectively. The octahedra at each side of the adsorbed molecule are tilted 3.0° away from the adsorbate position. In the second final configuration the O_2 molecule is positioned similarly next to the opposite strontium (Sr$_{II}$). The tilting angle in this case is 28.6° and the adsorbate-strontium distances d(O$_I$–Sr$_{II}$) and d(O$_{II}$–Sr$_I$) are 2.518 Å and 2.506 Å respectively, virtually identical to the first tilted configuration. The adsorption energies for both configurations is almost identical, indicating a small preference of the latter configuration, see table 7.1.

The same model cell was also used to test two different high coverage structures. In both cases 8 O_2 molecules were placed on the 12 available bridge sites, only considering a parallel arrangement of the oxygen molecules, yielding $\frac{1}{2}$ ML coverage. In the first model the adsorbate molecules were arranged behind each other along the orientation of the O_2 in two straight vertical columns, separated by one empty row of Sr–Sr bridges (see figs. 7.3a and 7.3b). For the second model the O_2 molecules were stacked in two horizontal lines, while keeping the orientation of the individual molecules intact. An illustration of the initial positions of this "stack" configuration is given in figs. 7.3c and 7.3d.

Increasing the coverage generally causes repulsive interaction between the adsorbate molecules of about 0.35 eV at a distance of 5.230 Å, as indicated by the change in adsorption energy per O_2 in table 7.1 of the fully relaxed structures. In the first structure, comprised of the straight vertical lines, the O_2 are adsorbed in similar local configurations as for the monomer, but due to the close packing the tilting angle of the O_2 is increased to 33.7°. Additionally, the distance to the nearest Sr atoms is increased:

d(O_I–Sr_I) to 2.604 Å and d(O_{II}–Sr_{II}) to 2.552 Å. The strontium atoms experience similar displacement out of the crystal to the monomer case at 33 pm.

The more stable "stack" formation on the other hand shows different behaviour: here the oxygen adsorbates are adsorbed in an alternating flat and tilted configuration. The tilted adsorbates show a slightly smaller angle of 26.9°, while the seemingly flat molecules exhibit only a very small tilting angle of 2.6°. Both tilted and flat O_2 are displaced from the centre line between the Sr atoms along their orientation. While the tilted adsorbate shows similar distances to the nearest Sr (2.531 Å and 2.523 Å for d(O_I–Sr_I) and d(O_{II}–Sr_{II}) respectively) for the flat molecule, the distances to the respective strontium atoms are much larger: 2.655 Å and 2.670 Å.

Table 7.1.: Adsorption energy in eV per O_2 molecule on the c(4×4) model cell at $^1/_{16}$ ML coverage. The two tilted configurations differ only in the rotation of the octahedra below the Sr atom the adsorbate moves towards.

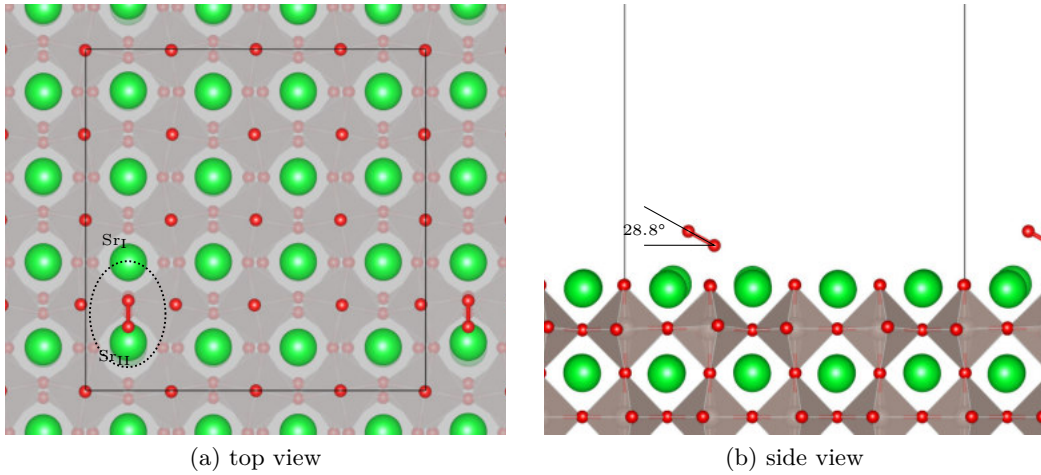| c(4×4)	E_{Ads} [eV]
Tilted near Sr_I	-1.418
Tilted near Sr_{II}	-1.412
2 Lines	-0.992
2 Stacks	-1.075

(a) top view   (b) side view

Figure 7.1.: Relaxed structure of one O_2 molecule adsorbed on the c(4×4) model cell at a Sr–Sr bridge position, indicated by the dotted circle. Here, the adsorbate is tilted towards Sr_{II}.
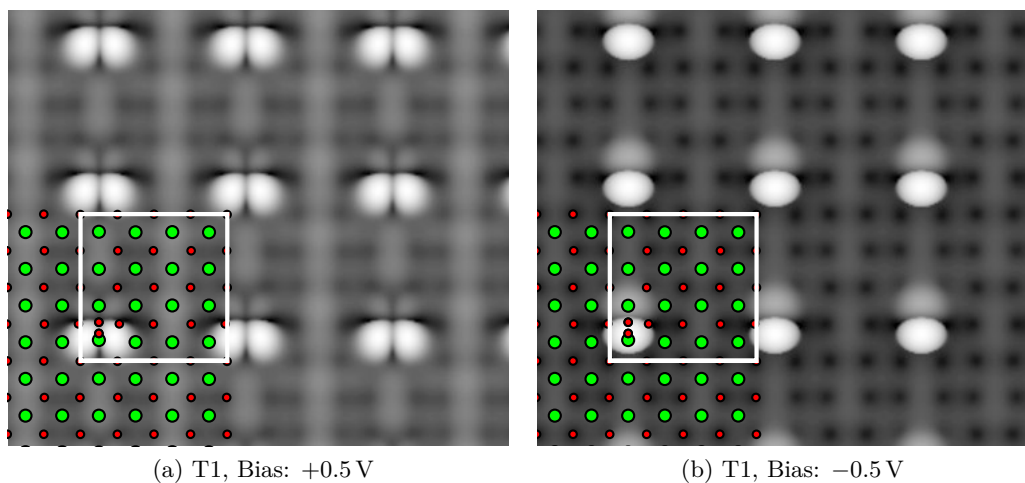
235

(a) T1, Bias: $+0.5\,\text{V}$ (b) T1, Bias: $-0.5\,\text{V}$

Figure 7.2.: STM simulation of one O_2 adsorbed on the c(4 × 4) $Sr_3Ru_2O_7$ model cell at $\pm0.5\,\text{V}$ bias voltage. At positive bias voltage the adsorbate shows a bright and a dark double lobe where the bright part corresponds to the upper oxygen atom. At negative bias voltage the O_2 molecule only shows a singular bright spot at the upwards tilted part of the adsorbed O_2.

7.1.2. High Coverage: c(2 × 2) Model Cell

The small c(2 × 2) model cell was used to study the adsorption of O_2 molecules at higher coverages. Additionally, different adsorption configurations were tested where the adsorbate was rotated or vertically adsorbed. As mentioned before, all structures were optimised using the optB86b functional.

¼ ML Coverage

At ¼ ML coverage multiple starting configurations were tested. First the O_2 molecule was positioned at a Sr–Sr bridge, starting from both a symmetric flat position and from a configuration where the O_2 was moved towards a Sr atom and tilted upwards. The two tilted configurations can be distinguished by the rotation of the octahedra in the subsurface layer and the resulting mobility of the Sr ion: for the first model (T1) the octahedra are rotated away from the Sr where the O_2 is adsorbed along the direction of the O_2 molecule (fig. 7.4a), in the second (T2) model the octahedra are rotated towards the Sr, impeding its movement along the direction of the O_2 molecule.

The fully relaxed structures were similar to the low coverage case described in section 7.1.1 where the flat configuration was not stable. In all cases the two tilted configurations turned out to be favoured (see table 7.2) with the T1 position being slightly more stable (16 meV, see table 7.2). Due to the repulsive interaction of the O_2 and the apical surface oxygen atoms the octahedra at each side of the Sr–Sr bridge tilt 4.7°
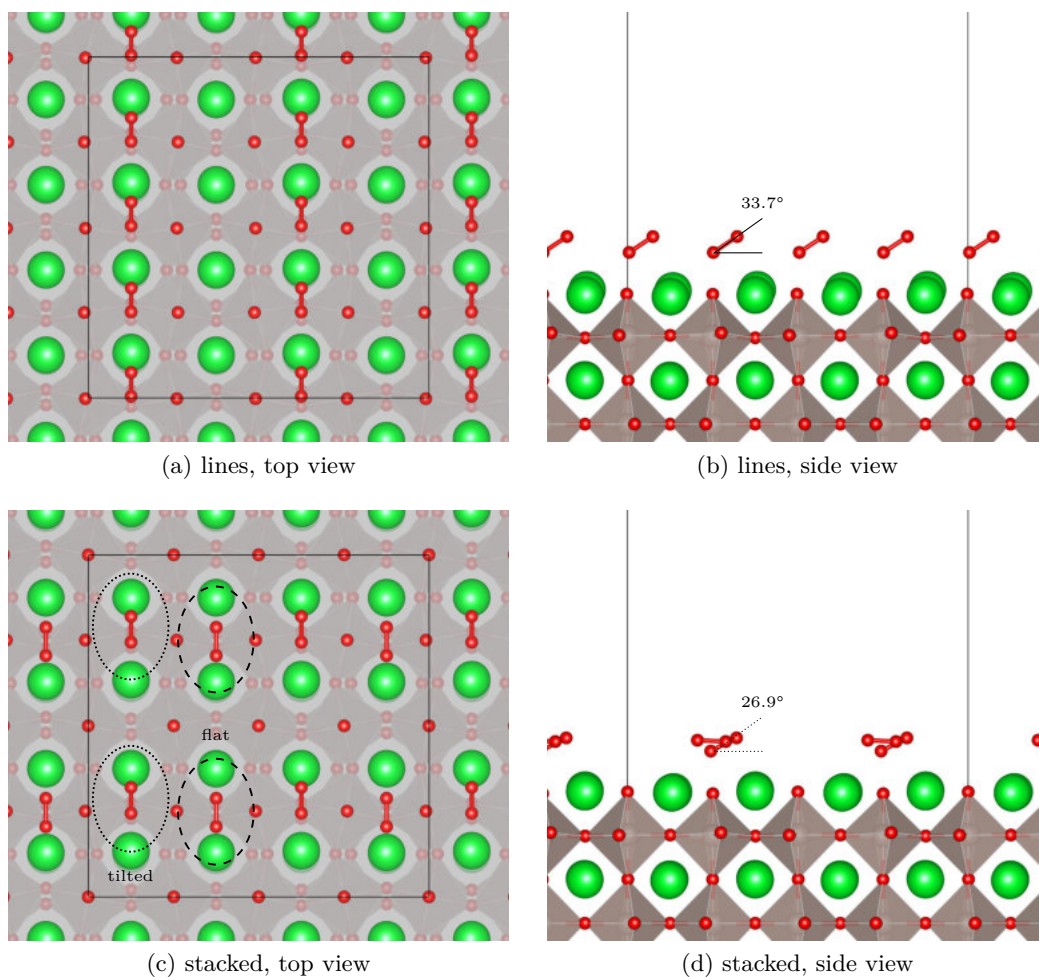
(a) lines, top view

(b) lines, side view

(c) stacked, top view

(d) stacked, side view

Figure 7.3.: Eight O_2 molecules adsorbed on the large $c(4 \times 4)$ model cell. In (a) and (b) the adsorbate molecules are arranged in two vertical lines, occupying every Sr–Sr bridge along the orientation of the O_2 molecule. Here all adsorbates tilt in the same direction. In the stacked structure where the adsorbate covers every Sr–Sr bridge in the horizontal direction ((c), (d)) every second adsorbate is tilted by 26.9° and every other O_2 is nearly flat.

237

away from the adsorbate. The distances of the oxygen atoms of the adsorbate to the nearest strontium atoms are $2.494\,\text{Å}$ for $d(O_I\text{–}Sr_I)$ and $2.517\,\text{Å}$ for $d(O_{II}\text{–}Sr_{II})$ in the T1 model. In the T2 configuration the distances are slightly more symmetric at $2.510\,\text{Å}$ and $2.503\,\text{Å}$ for $d(O_I\text{–}Sr_I)$ and $d(O_{II}\text{–}Sr_{II})$ respectively. In both tilted configurations the oxygen molecule is elongated to $1.347\,\text{Å}$. The tilting angle is $30.8°$ and $28.9°$ for the T1 and T2 structure respectively.

Another adsorption configuration studied using the same $c(2 \times 2)$ model cell was a vertical arrangement of the O_2 molecule, see fig. 7.4c. Here the O_2 was placed vertically on top of a Sr atom. While the final relaxed configuration is stable, the comparison of the adsorption energies shows that a vertical O_2 molecule binds much more weakly to the substrate than in the tilted arrangement. The distance of the lower oxygen atom of the adsorbate to the strontium atom below at $2.483\,\text{Å}$ is shorter than for the tilted configurations, but due to the reduced interaction with the substrate the length of the O_2 is a little shorter at $1.290\,\text{Å}$.

Dissociation of the O_2 molecule is energetically quite unfavourable, as is shown in a fourth model illustrated in fig. 7.4d. Here two oxygen atoms were placed directly above two strontium atoms in the $c(2 \times 2)$ unit cell. The relaxed structure shows that this positioning is not stable as the oxygen atoms move close to the apical oxygen of the RuO_6 octahedra, finally resting in a zig-zag formation forming surface oxyls. The calculated adsorption energy of $-0.666\,\text{eV}$ referenced to the O_2 molecule of this structure is much lower than for the structures where the O_2 molecule is still intact, indicating that $>0.73\,\text{eV}$ would be needed to dissociate the oxygen molecule. The distance of the oxyl and the nearest Sr atom is $2.480\,\text{Å}$ and the bond formed with the apical oxygen is $1.497\,\text{Å}$ long.

STM simulations show that the O_2 molecule exhibits a distinct pattern, shown in fig. 7.5. In the most stable tilted T1 structure the adsorbate is visible as a bright spot which is slightly distorted towards the closer Sr atom in the occupied states, while in the unoccupied states it exhibits a 2-fold symmetric lobe-like pattern that is brighter in the direction of the upper oxygen of the tilted molecule. The T2 structure shows the same pattern but mirrored along the horizontal axis. The vertically adsorbed O_2 molecule shows a very large bright spot at both positive and negative bias voltages. Lastly, the dissociated configuration displays a zig-zag pattern of bright dots which originate from the separated O_2 fragments and the apical oxygen atoms they bind to. For positive bias voltage the same pattern is more pronounced.

½ ML Coverage

Upon further increase of the coverage more complex adsorption configurations start to form since the two O_2 molecules can be arranged in multiple ways on the $c(2 \times 2)$ model cell. It can either be in a line structure with the O_2 occupying every Sr–Sr bridge along their bond axis (fig. 7.6a) or a parallel configuration where two molecules are positioned side by side (fig. 7.6b). The O_2 can also be arranged in a zig-zag configuration where every second Sr–Sr bridge is occupied, while the next row is shifted by half a unit cell (fig. 7.6c). Finally, a configuration was tested where the two molecules are located at
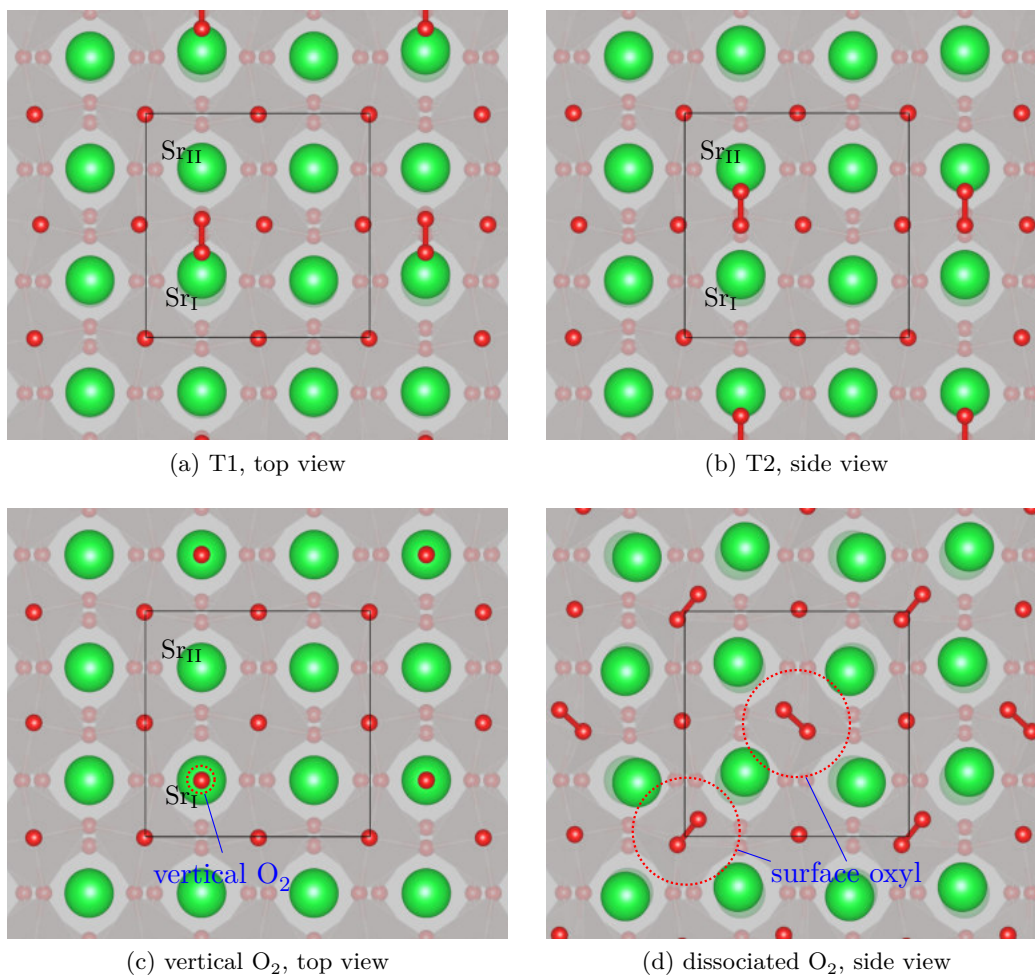
(a) T1, top view

(b) T2, side view

(c) vertical O_2, top view

(d) dissociated O_2, side view

Figure 7.4.: Fully relaxed model cell with one O_2 adsorbed on the $c(2 \times 2)$ model cell (¼ ML coverage). (a): one tilted O_2 displaced towards Sr_I. (b): one tilted O_2 displaced towards Sr_{II}. (c): one vertical O_2 adsorbed on top of the Sr_I. (d): dissociated O_2. The initial structure had the O atoms directly above two Sr atoms at maximum distance. In the relaxed structure the oxygen atom form a bond with two apical oxygen atoms.

(a) T1, Bias: +0.5 V

(b) T1, Bias: −0.5 V

(c) T2, Bias: +0.5 V

(d) T2, Bias: −0.5 V

(e) vertical, Bias: +0.5 V

(f) vertical, Bias: −0.5 V

(g) dissociated, Bias: +0.5 V

(h) dissociated, Bias: −0.5 V
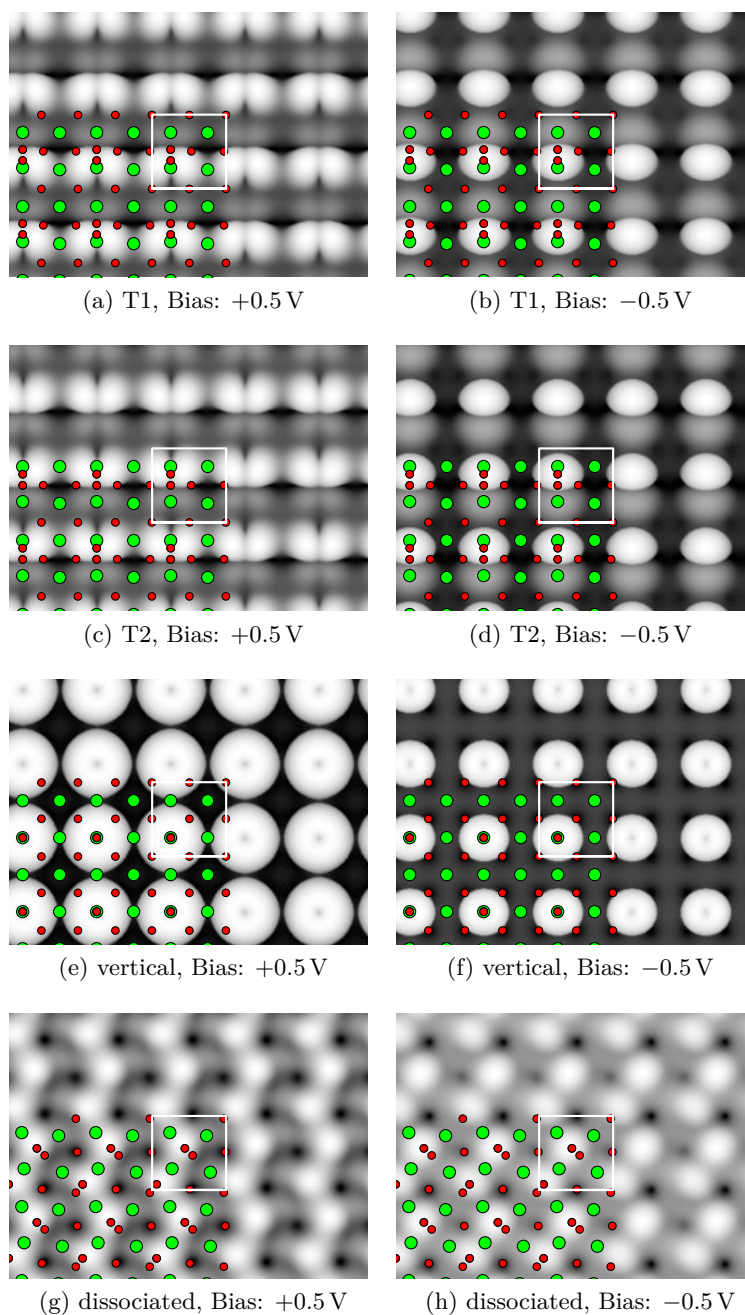
Figure 7.5.: STM Simulations of one O_2 adsorbed on the c(2 × 2) model cell at ±0.5 V bias voltage. (a), (d), (c): tilted T1 and T2 model. At positive bias voltage the O_2 shows a bright double lobe structure, at negative bias voltage a bright spot. (f): vertically adsorbed O_2, the molecule shows a very large bright spot. (g): dissociated O_2. Both apical and adsorbed oxygen display as bright spots in a zig-zag structure. At negative bias voltage the O spots are less smeared out compared to positive bias voltage.

two bridge sites and rotated by 90° (fig. 7.6d).

The relaxed structures show that the O_2 molecules start to experience repulsive interaction, see table 7.2. Since both the line and parallel arrangement show quite low adsorption energies (see table 7.2) it follows that the adsorbate prefers to maximise the distance between O_2 molecules when the molecules are arranged in a parallel structure. From the rotated initial configuration on the other hand both O_2 molecules are displaced towards the strontium atom that is shared by their bridge positions and rotate to an angle of 14.1° between each other. Both adsorbate molecules exhibit a tilting angle of 27.5° and 27.4°. In both the parallel and the zig-zag configuration the adsorbate molecules are almost flat with a tilting angle of ≈1°. This is not the case for the line configuration, here the tilting angle of 8.4° is larger than for ¼ ML coverage. Again, like for ¼ ML coverage, two different line configurations exist where one is T1-like and the other T2-like. Here the energy difference between the T1 and T2 configuration is more pronounced at 28 meV.

Full Coverage

At full coverage (1 ML) four oxygen molecules are adsorbed in one surface unit cell, i.e. one O_2 per RuO_6 octahedron. DFT predicts multiple stable configurations of the adsorbates, ranging from various vertical to flat configurations.

The most stable structure is one where the O_2 molecules adsorb in a clustered configuration around an apical oxygen of a nearby RuO_6 octahedron with an adsorption energy of -0.952 eV per O_2 molecule, see fig. 7.7a. Here, two O_2 are adsorbed at Sr–O bridge sites, sharing the same apical oxygen atom. The two pairs of O_2 show a mixture of weakly and strongly tilted arranged. One of the oxygen atoms of the O_2 molecule is located at the Sr–Sr bridge, and the molecules are tilted by 16° to 30°. The octahedra around which the O_2 molecules cluster are tilted by 4° and 8°. The two pairs of O_2 show a mirror symmetry along the $[1\bar{1}0]$ plane, therefore the molecules form a wavy double line along the $[\bar{1}10]$ direction. The O–O bond length is slightly reduced to 1.230 Å. Another configuration where the two pairs of O_2 are clustered around surface Sr and are rotated by 90° towards each other (see fig. 7.7b) is 20 meV less stable. Here the O_2 molecules are tilted by 21° to 23°. A third vertical configuration, shown in fig. 7.7c, where the adsorbates are positioned in the middle of the Sr–Sr bridge, maximising the distance between the adsorbed O_2, is 257 meV less stable than the most stable grouped structure. Finally, a parallel arrangement where all Sr–Sr bridges are occupied is predicted to be 130 meV less stable than the most stable clustered configuration (see fig. 7.7d).

The stability of a line structure, where each Sr–Sr bridge is occupied by an O_2 molecule, is less than the first two vertical configurations with an adsorption energy of -0.822 eV. In this case the adsorbate molecules are almost completely flat, in contrast to the line structure at ½ ML coverage. Also, the O_2 molecules sit at the centre of the bridges. For the final adsorption configuration that was tested the O_2 molecules were placed on each Sr–Sr bridge surrounding the same apical oxygen atom, forming a square. These positions are not stable, the molecules move on top of the strontium atoms and rotate in random directions. This configuration is also much less stable than the double line
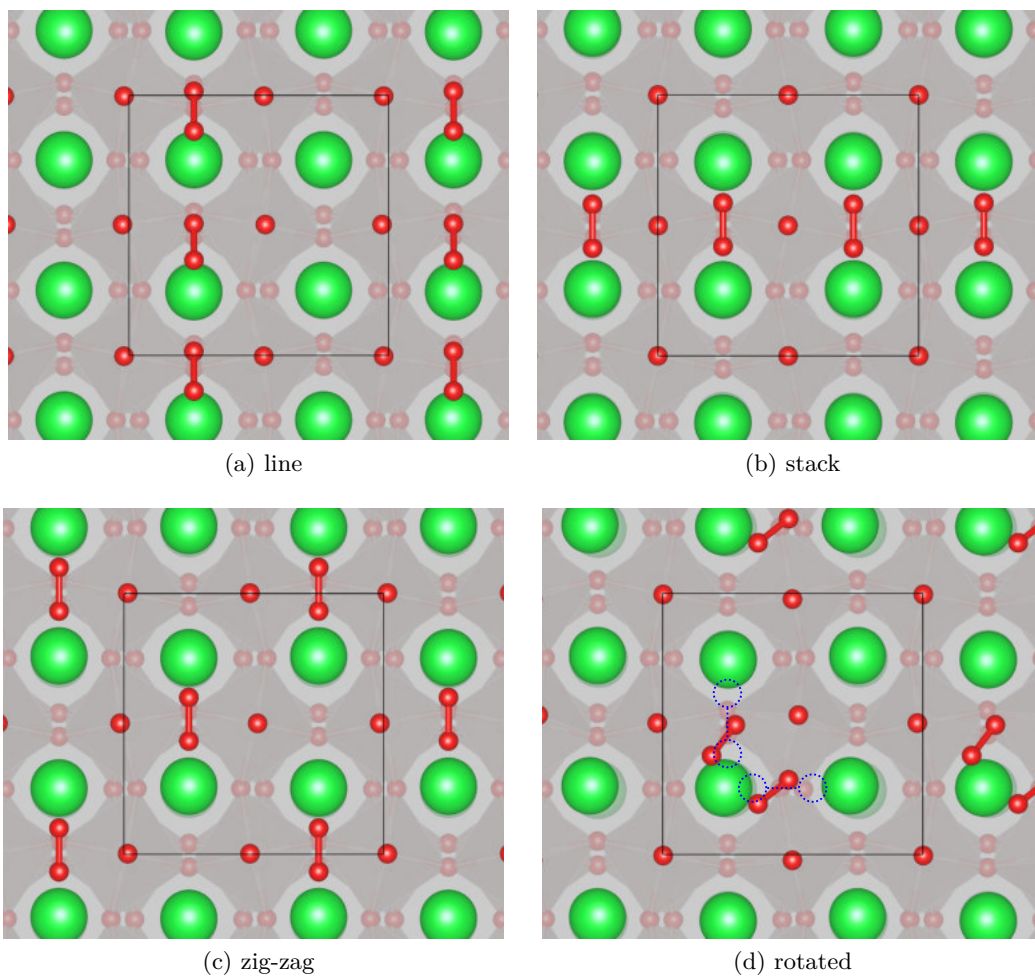
(a) line

(b) stack

(c) zig-zag

(d) rotated

Figure 7.6.: Top views of the fully relaxed models at ½ ML coverage. (a): adsorbate molecules arranged in a vertical line separated by an empty column. (b): O_2 molecules stacked next to each other along the horizontal axis. Both adsorbed molecules are almost flat. (c): two O_2 arranged at diagonal Sr–Sr bridges at maximum distance. (d): dotted lines indicated the initial placement of the two O_2 molecules on two Sr–Sr bridges at 90°. After the relaxation both adsorbates rest close to the Sr at the shared corner.

structure ($E_{Ads} = -0.718\,eV$).

(a) vertical O_2 around Sr

(b) vertical O_2 around O

(c) vertical O_2 at Sr–Sr bridges

(d) double lines
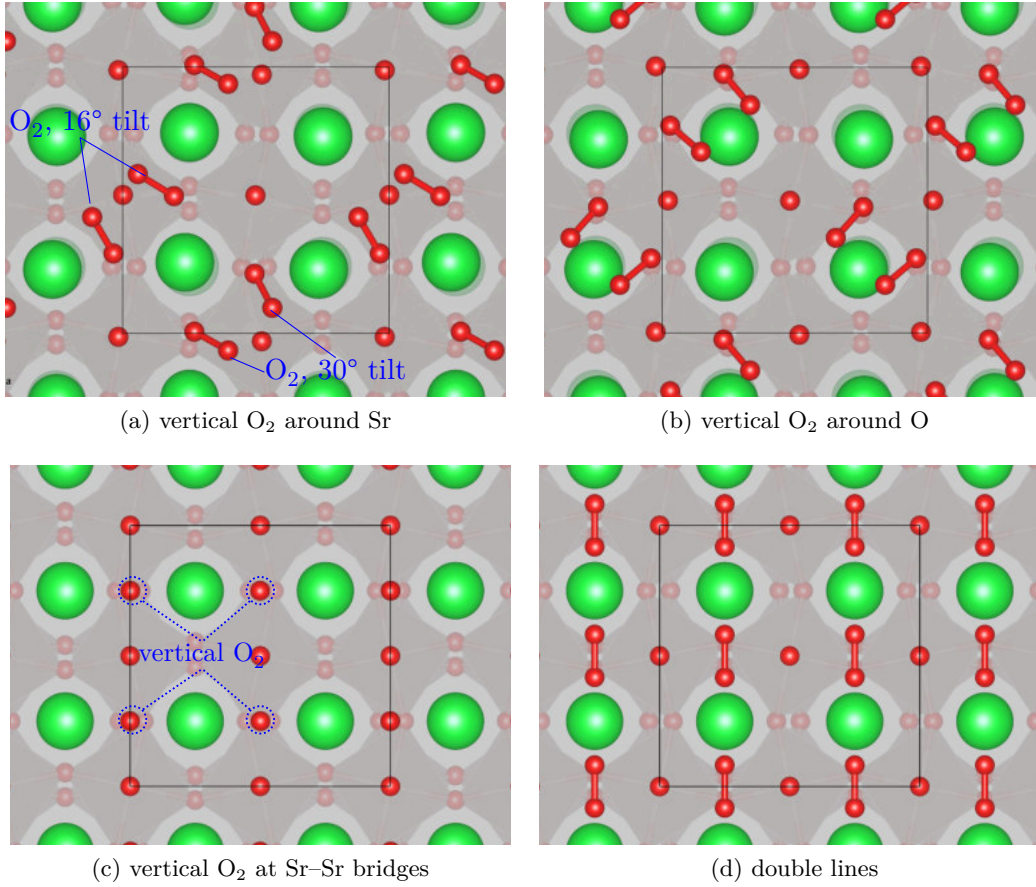
Figure 7.7.: Top view of the fully relaxed small model cell with 4 adsorbed O_2 molecules (full coverage). (a): O_2 molecules form two pairs of clusters around an apical O of a RuO_6 octahedron. (b): clustered arrangement of the O_2 around surface cations. The two pairs are rotated by 90°. (c): vertical arrangement at Sr–Sr bridge sites at maximum distance. (d): flat O_2 covering every Sr–Sr bridge site in a double line structure.

HSE06 and RPA adsorption energies

To evaluate the potential error bars of several effects, including the electron affinity of the adsorbate and the polarisation effects, both hybrid and many-electron total energy calculations were performed on select model cells using the HSE06 functional and the ACFDT-RPA methods. To reduce the computational effort the a $4 \times 4 \times 1$ and $3 \times 3 \times 1$ Γ-centred $\vec{k}$-point grid was used for the HSE06 and RPA calculations, respectively. In

the latter case, the energy cutoff was increased to $450\,\text{eV}$ and another set of potentials was used (see table F.3). All results are shown in table 7.2. As will be explained in more detail in section 7.1.3, the overestimation of the electron affinity at the DFT level leads to an artificial increase of the adsorption energies of O_2 adsorbed on the $Sr_3Ru_2O_7(001)$ surface. This effect is already apparent for the low-coverage case of ¼ ML coverage where the adsorption energy is reduced by $\approx 0.4\,\text{eV}$ (see table 7.2), almost identical to the value found on $Ca_3Ru_2O_7$ (see section 7.3.6 and [6, 8]). The HSE06 functional yields an even larger decrease of the adsorption energy of $\approx 0.5\,\text{eV}$, probably due to the worse description of polarisation effects. At higher coverage, both HSE06 and RPA values show that at the DFT level the repulsion between the adsorbed O_2 molecules is underestimated. While the parallel and zig-zag arrangements only show a reduction of the adsorption energy by about $0.2\,\text{eV}$ to $0.3\,\text{eV}$ at the RPA level, the most favoured DFT configuration where the O_2 cluster at a surface cation is now much less stable (E_{Ads} $= -0.519\,\text{eV}$). Again, the HSE06 results show a similar effect. The enhanced repulsion at the HSE06 and RPA level can tentatively be assigned to a different hybridisation of the clustered O_2 molecules with the surface. The additional tilting of the clustered configuration results in a rehybridisation where the O_2 $2p$-$\pi^*_\perp$ orbital (see section 7.1.3) is partially emptied, while for the line-wise adsorption the additional electron is transferred only into the originally unoccupied O_2 $2p$-$\pi^*_\parallel$ orbital.

At full coverage the trend continues, again the clustered adsorption configurations show a much larger reduction of their adsorption energies, while the double line structure is now the most stable structure ($E_{Ads} = -0.488\,\text{eV}$).

To visualise the large differences between the DFT (optB86b) and RPA adsorption energies a phase diagram of O_2 adsorption was calculated, see fig. 7.8. While DFT predicts that a full monolayer can be adsorbed at typical ultra-high vacuum conditions, the phase diagram based on the RPA values shows that a full monolayer is unlikely and that evenly spaced adsorption configurations are clearly favoured.

7.1.3. O_2 Charge State

For oxygen adsorbed on the $Sr_3Ru_2O_7(001)$ surface, the density of states shows that charge is transferred into the adsorbate, creating a charged O_2^- superoxo species at both high and low coverage. The additional charge at the O_2^- originates from the Ru layer of the substrate where the charge is transferred from nearby RuO_6 octahedra. The strontium atoms do not contribute at all as analysis of the Bader charges shows that their formal charge of $+2$ is unchanged. As shown in fig. 7.9a, plotting the charge difference indicates that the Sr^{2+} are just slightly polarised but that ruthenium atoms in the RuO_6 plane are slightly depleted. The charge is transferred into a half-filled π^* state of the oxygen molecule. This π^* orbital lies in the yz plane and points towards the surface alkaline ions. The plot of the magnetisation density, fig. 7.9b, only shows the other π^* orbital which is still only half filled since it solely contributes the magnetic moment of the adsorbed O_2^-. Another indication of the charge state of the O_2^- is the shift of the vibrational stretching frequency from $1580\,\text{cm}^{-1}$ for the free molecule to $1132\,\text{cm}^{-1}$ and $1153\,\text{cm}^{-1}$ for the T1 and T2 configuration at ¼ ML coverage, respectively. This is

Table 7.2.: Adsorption energy in eV per O_2 molecule on the $c(2 \times 2)$ model cell. The different configurations are illustrated in figs. 7.5 to 7.7.

	E_{Ads} [eV]		
$c(2 \times 2)$	optB86b	HSE06	RPA
1 O_2, ¼ ML coverage			
Tilted, T1	-1.397		-0.956
Tilted, T2	-1.381	-0.911	-1.004
Vertical	-0.894		
Dissociated	-0.666	-0.093	-0.021
2 O_2, ½ ML coverage			
Line, T1	-0.996	-0.523	-0.539
Line, T2	-0.968		-0.537
Parallel	-0.980	-0.676	-0.896
Zig-zag	-1.114	-0.753	-0.890
Clustered	-1.138	-0.287	-0.519
4 O_2, full coverage			
Sr–Sr bridge, line	-0.822	-0.431	-0.488
Clustered, parallel	-0.952	-0.065	-0.327
Clustered, rotated	-0.932	-0.012	-0.351
Vertical, at Sr–Sr bridges	-0.695	-0.267	
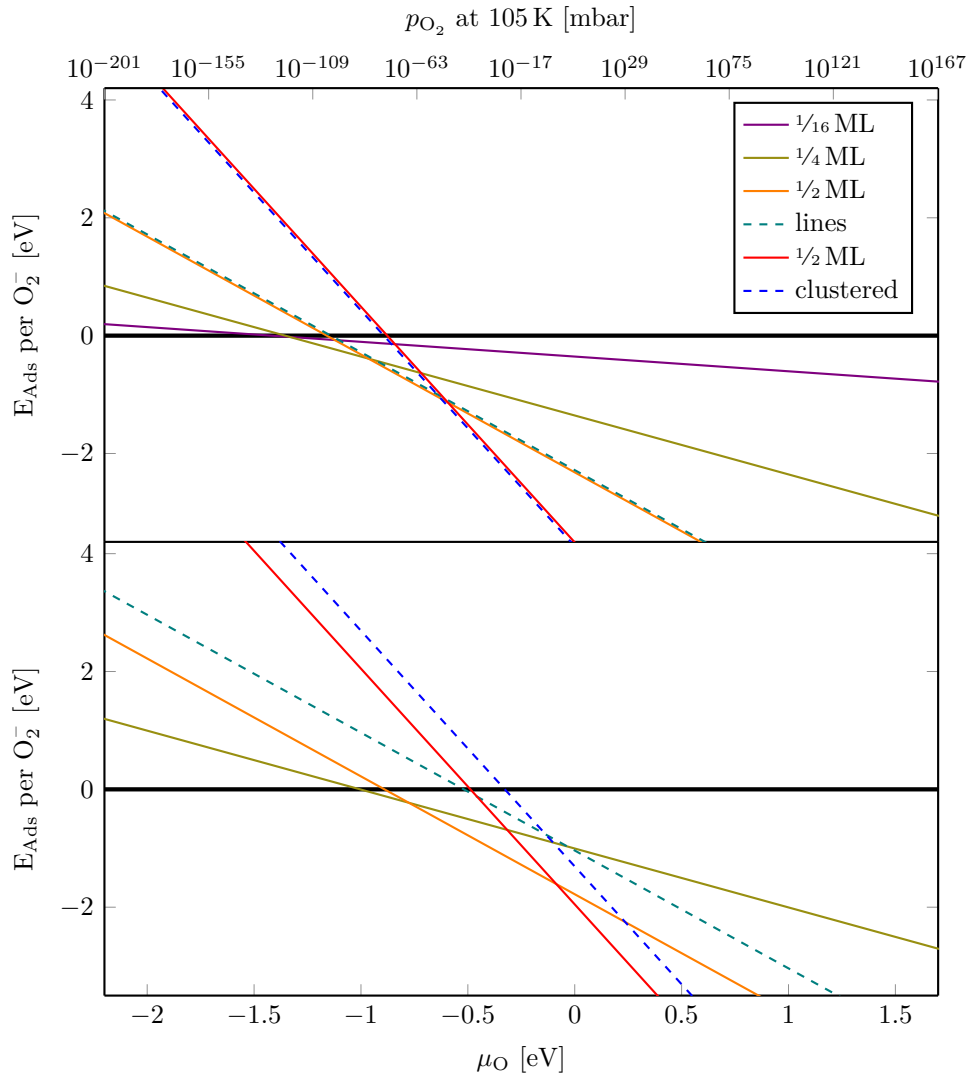
Figure 7.8.: Phase diagram of adsorption, calculated with the optB86b vdW-DFT functional and the many-electron RPA method as a function of the chemical potential μ_O of oxygen.

comparable to the charged gas phase O_2^- molecule which shows a stretching frequency of $1182\,\mathrm{cm}^{-1}$ (see appendix E.2). The HOMO-LUMO gap of the adsorbate is quite small, just $<0.5\,\mathrm{eV}$, resulting in an overestimation of the electron affinity of the O_2^- molecule. Since the transfer of charge is therefore artificially made easier, the adsorption energy is overestimated as well. Employing a hybrid functional like HSE06 does lead to a better description of the electron affinity, but yields a half-metallic electronic ground state for the substrate (see fig. 7.11). The adsorption energy adsorption energy predicted by the hybrid functional is reduced to $-0.590\,\mathrm{eV}$. In an advanced many-electron approach the adsorption energy can be calculated in the random phase approximation (RPA) which for the small $c(2 \times 2)$ model cell yields an adsorption energy of $-0.956\,\mathrm{eV}$ and $-1.004\,\mathrm{eV}$ for the tilted T1 and T2 configurations, respectively. This is $0.441\,\mathrm{eV}$ less than the van-der-Waals corrected optB86b results ($E_{\mathrm{Ads}} = -1.397\,\mathrm{eV}$, see table 7.2), showing that standard (van-der-Waals corrected) DFT greatly overestimates O_2^- adsorption energies on $Sr_3Ru_2O_7(001)$. The corresponding DOS calculated with the many-electron G_0W_0 method shows an opening of the HOMO-LUMO gap of the O_2^- to about $3.4\,\mathrm{eV}$, similar to the HSE06 results (see fig. 7.11).

(a) charge density difference   (b) magnetisation density
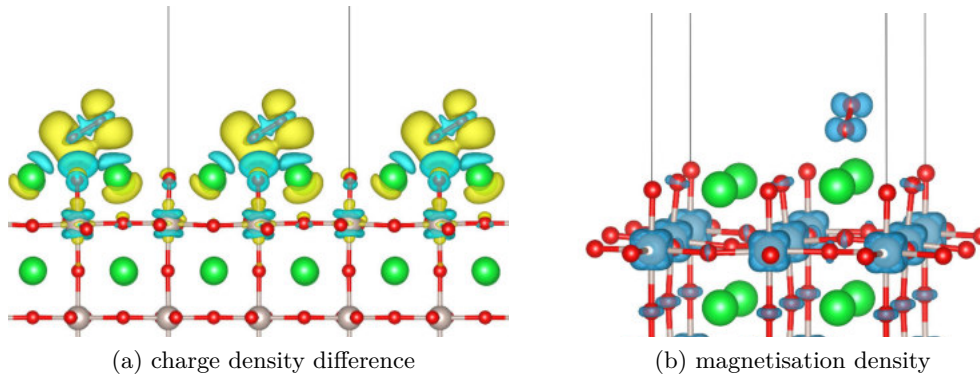
Figure 7.9.: Plot of the (a) charge density difference and (b) magnetisation density plot of one O_2^- adsorbed on the $c(2 \times 2)$ $Sr_3Ru_2O_7$ model cell. Yellow and cyan areas indicate positive and negative charge differences, respectively. Dark blue: positive spin density. The Sr atoms close to the adsorbate are slightly polarised.

7.1.4. Core Level Shifts

The O $1s$ binding energies of the adsorbed O_2^- molecule on pure $Sr_3Ru_2O_7$ were calculated in both the initial state (IS) and for a few selected structures in the final state (FS) approximation. From the experiment it is known that molecular O_2 usually shows a shift of $3\,\mathrm{eV}$ [200, 201].

Here the O $1s$ states of the oxygen atoms at the rocksalt layer of the $Sr_3Ru_2O_7$ bulk system were selected as reference binding energies since only this substrate was used in

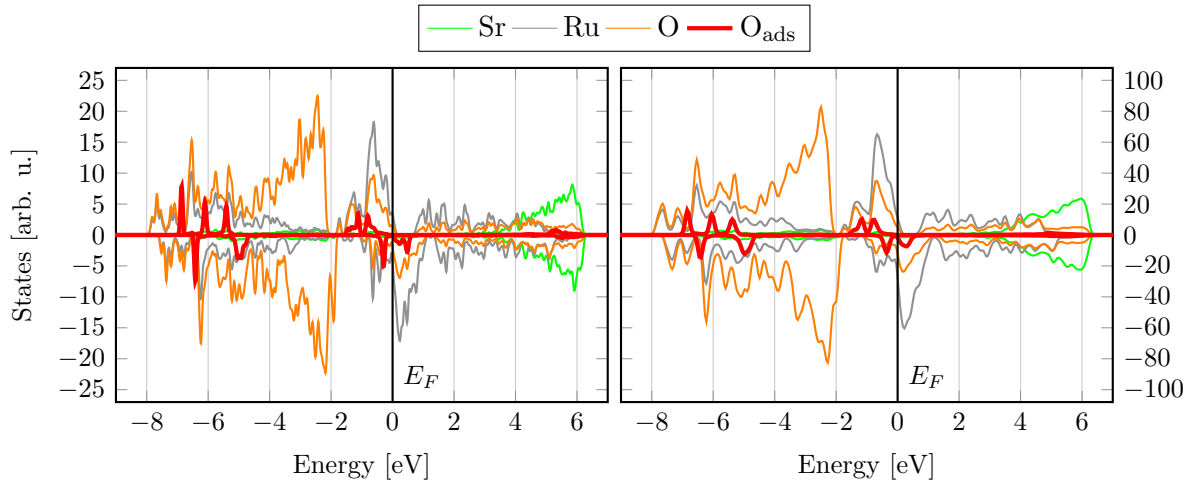Figure 7.10.: DOS calculated with the optB86b functional of one O_2^- adsorbed on $Sr_3Ru_2O_7$. Left: c(2 × 2), right: c(4 × 4) model cells. The O_2^- states in the right plot are magnified by a factor of 4.
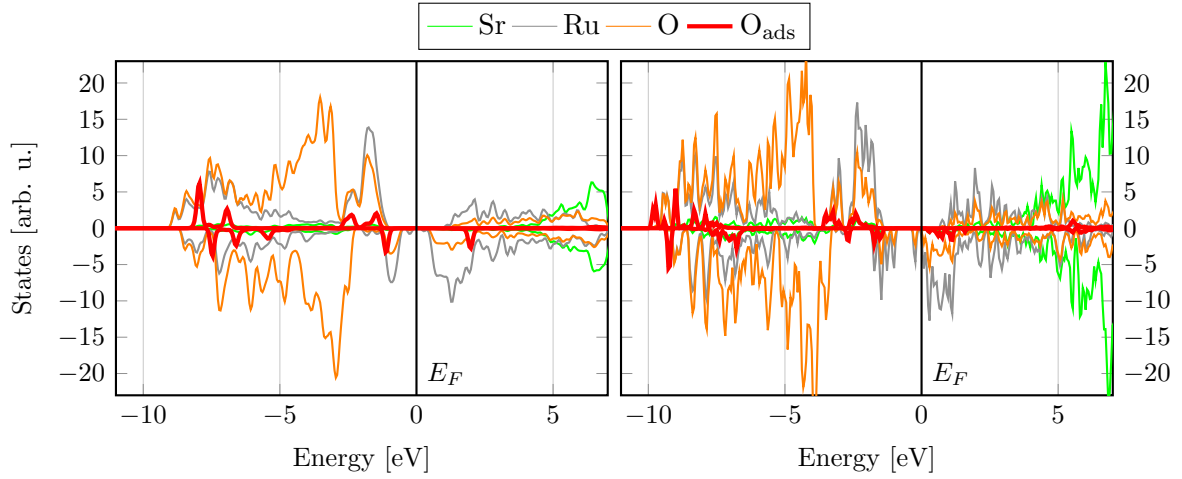

Figure 7.11.: DOS calculated with the HSE06 functional (left) and the G_0W_0 method (right, PBE initial wave function) of one O_2^- adsorbed on $Sr_3Ru_2O_7$. The HOMO-LUMO gap of the O_2^- is increased to $3.13\,\mathrm{eV}$ and about $3.4\,\mathrm{eV}$ for HSE06 and G_0W_0, respectively.

the calculations. For the Sr_2RuO_4 substrate one would simply have to add $454\,meV$ to the core level shifts.

On the small model cell the adsorbed O_2^- molecule in the tilted T1 (see fig. 7.4a) configuration shows a core level shift in the initial state approximation of $1.8\,eV$ and $1.9\,eV$ to higher binding energies. The O $1s$ states of the adsorbate in the second tilted T2 configuration shift slightly less at $1.88\,eV$ and $1.78\,eV$. The difference of $0.1\,eV$ reflects the different local environment of the two oxygen atoms of the adsorbate. In the final state approximation the T1 structure shows a core level shift of $0.55\,eV$ and $0.49\,eV$ to higher binding energies, much less than in the initial state calculations. The reason for this underestimation of the O $1s$ binding energies lies in the underestimation of the HOMO-LUMO gap of the adsorbate: since in the final state approximation the electron is in fact transferred to the conduction band, it is immediately trapped in the unoccupied p-state of the adsorbate close to the fermi level. This effect will be discussed in more detail in section 7.3.7.

Table 7.3.: O $1s$ core level shifts in eV towards higher binding energies of O_2^- adsorbed on $Sr_3Ru_2O_7$, referenced to the $Sr_3Ru_2O_7$ bulk.

Core Level Shifts [eV]	Initial State	Final State
Tilted, T1, O_I	1.90	0.55
Tilted, T1, O_{II}	1.80	0.49
Tilted, T2, O_I	1.88	
Tilted, T2, O_{II}	1.78	
Vertical, O_I	2.77	1.38
Vertical, O_{II}	2.76	0.78

7.2. Calcium Doped Strontium Ruthenate

7.2.1. High Coverage: c(2×2) Model Cell

The adsorption behaviour of oxygen molecules was also studied on the heavily doped c(2×2) model cell. The same as with the studies of water adsorption, due to the introduction of the Ca vacancy, two additional adsorption sites (Ca–Sr bridge sites) are available.

The adsorption energies show that similar to the case of water adsorption the introduction of the calcium dopant increases the reactivity of the substrate, even when the adsorbate is not located at an adsorption site close to the Ca dopant. Compared to the pure $Sr_3Ru_2O_7$ substrate at ¼ ML coverage the adsorption at the most favoured site is $51\,meV$ stronger, see table 7.2. In this configuration the O_2 molecule adsorbs at a Sr–Sr bridge site like on the undoped substrate as shown in fig. 7.12a. The distances of the oxygen atoms of the adsorbate to the nearest metal atoms are $2.499\,\text{Å}$ and its tilting

angle 28.9°. The second most favoured adsorption site is found at a Ca–Sr bridge with the O_2 molecule tilted towards the Ca dopant and an adsorption energy of -1.426 eV. In this case both the Ca and the Sr atom forming the bridge are displaced from their equilibrium positions, both move in the same direction along the orientation of the adsorbate (fig. 7.12b). The O_2 molecule is situated closer to the Ca dopant at a distance of 2.323 Å while the distance to the Sr atom is 2.533 Å. In this configuration the tilting angle of the adsorbate is lowest at 25.9°. The rotations of the octahedra in the first subsurface layer again influence the strength of the displacement: the Ca atom, where the octahedra are rotated towards it moves by 25 pm while the Sr atom is shifted by 45 pm since the octahedra are rotated away from its direction of movement. This effect is also visible in the second adsorption site at a Ca–Sr bridge where the O_2 molecule is rotated by 90°, shown in fig. 7.12c. In this case the adsorbate binds 139 meV more weakly to the substrate at a tilting angle of 40.5°. The Ca dopant is displaced farther than before due to both its smaller size and the rotation towards the direction of its movement, shifting by 42 pm while the Sr atom moves only 33 pm.

In addition to the tilted configurations, the stability of a vertically adsorbed oxygen molecule was assessed as well. In the case of the calcium doped $Sr_3Ru_2O_7$ surface the binding energy of such an adsorbate is very similar to the pure surface with a 60 meV preference to adsorption on top of the Ca dopant. Nevertheless, stability of these structures could only be achieved by restraining the molecule in the vertical configuration. Letting it relax in all directions leads to a tilted adsorption configuration.

At higher (½ ML) coverage both O_2 molecules adsorb in a parallel pattern, but in contrast to the pure $Sr_3Ru_2O_7$ case both molecules are almost flat with an adsorption energy of -1.062 eV per O_2. The adsorbate at the Ca–Sr bridge tilts only 7.9° while the one at the Sr–Sr bridge by 3.3°. The adsorbates cause displacements of the surface metal atoms, again the Ca atom shifts the most by 17 pm while one Sr atom moves 12 pm. The other two Sr atoms in the small model are displaced by $\approx$7 pm.

Table 7.4.: Adsorption energy in eV per O_2 molecule on the c(2 × 2) $Sr_3Ru_2O_7$ model cell, doped with one Ca atom.

c(2 × 2) + 1Ca	E_{Ads} [eV]
1 O_2, ¼ ML coverage	
Ca–Sr, tilted to Sr	-1.287
Ca–Sr, tilted to Ca	-1.426
Sr–Sr, T2	-1.401
Sr–Sr, T1	-1.448
Vertical on Ca	-0.893
Vertical on Sr	-0.833
2 O_2, ½ ML coverage	
Parallel	-1.062

(a) Ca–Sr, T1

(b) Ca–Sr, T2

(c) Sr–Sr, T1

(d) Sr–Sr, T2

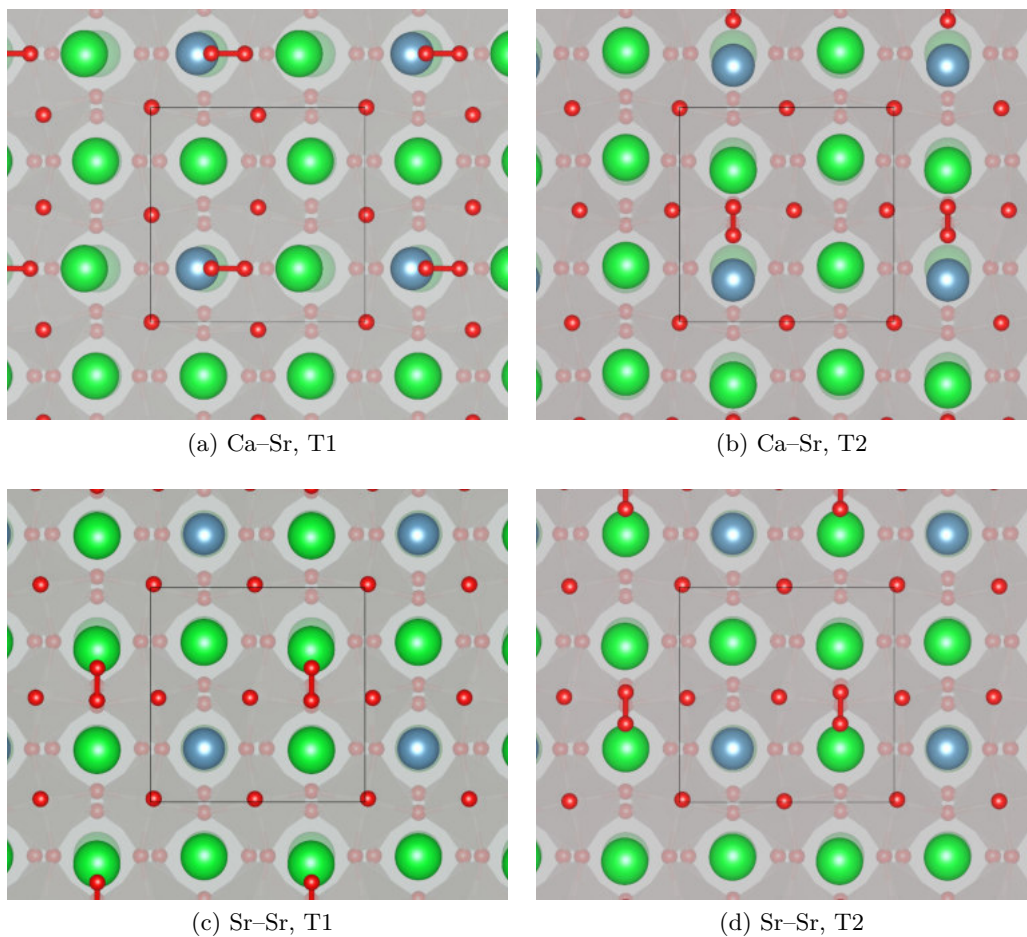Figure 7.12.: One O_2 molecule adsorbed on the small c(2×2) Ca-doped $Sr_3Ru_2O_7$ model cell. (a), (b): adsorption at Ca–Sr bridge sites. (c), (d): adsorption at Sr–Sr bridge sites both close and far from the dopant site.

251

7.2.2. Low Coverage: c(4×4) Model Cell

On the large c(4×4) model cell only the adsorption of a single O_2 monomer per unit cell was studied, yielding $\frac{1}{16}$ ML coverage. The oxygen molecule was placed both in the vicinity and far away from the Ca dopant to investigate its influence on the adsorption behaviour. In all cases the molecule was placed in the middle of either a Sr–Sr (see figs. 7.13a and 7.13b) or a Ca–Sr bridge (see figs. 7.13c and 7.13d). It should be noted that in contrast to the case of water adsorption the reactivity of the surface is not increased at the dopant site as the adsorption energy of the O_2 molecule is less on a Ca–Sr bridge than on a Sr–Sr bridge. Interestingly, the highest adsorption energy is found at a Sr–Sr bridge close to the Ca dopant, probably due to the greater flexibility of the substrate compared to the undoped case. The configuration is almost identical to the pure $Sr_3Ru_2O_7$ surface as the tilting angle of the O_2 molecule is 28.6° and it expands to 1.351 Å. At the Sr–Sr bridge far from the Ca dopant the O_2 molecule is almost flat at a tilting angle of 6.3° and it is also less expanded with a length of 1.339 Å. Finally, both Ca–Sr configurations show a displacement and a tilting of the adsorbed molecule in the direction of the Ca dopant. In both cases the adsorbate is fairly flat at 4.7° and 7.9° for the "Ca–Sr flipped" and the "Ca–Sr" case respectively.

The STM simulations (fig. 7.14) show a similar pattern: the O_2 molecule is always the brightest feature with the substrate spots visible in the area in-between. At positive bias voltages a two-fold lobe feature separated a the centre of the O–O bond can be observed while at negative bias voltages the adsorbate exhibits a 4-fold symmetric lobe structure. The tilting angle influences the brightness of the spot where the upper part of the molecule is brighter than the part closer to the substrate, as can be seen in the simulations of the various structures.

Table 7.5.: Adsorption energy in eV per O_2 molecule on the c(4×4) $Sr_3Ru_2O_7$ model cell, doped with one Ca atom at $\frac{1}{16}$ ML coverage.

c(4×4) + 1Ca	E_{Ads} [eV]
Sr–Sr, near Ca	−1.494
Sr–Sr, far from Ca	−1.442
Ca–Sr flipped	−1.427
Ca–Sr	−1.411

7.2.3. O$_2$ Charge State

While the introduction of a calcium dopant does have an effect on the adsorption behaviour as described in section 7.2, slightly increasing the adsorption energy of an adsorbed O_2 molecule, there is no change in the charge state of the adsorbate compared to the pure $Sr_3Ru_2O_7$ surface. As can be seen in fig. 7.15, the oxygen molecule again adsorbs as a superoxo species, regardless of the adsorption position. The projected DOS
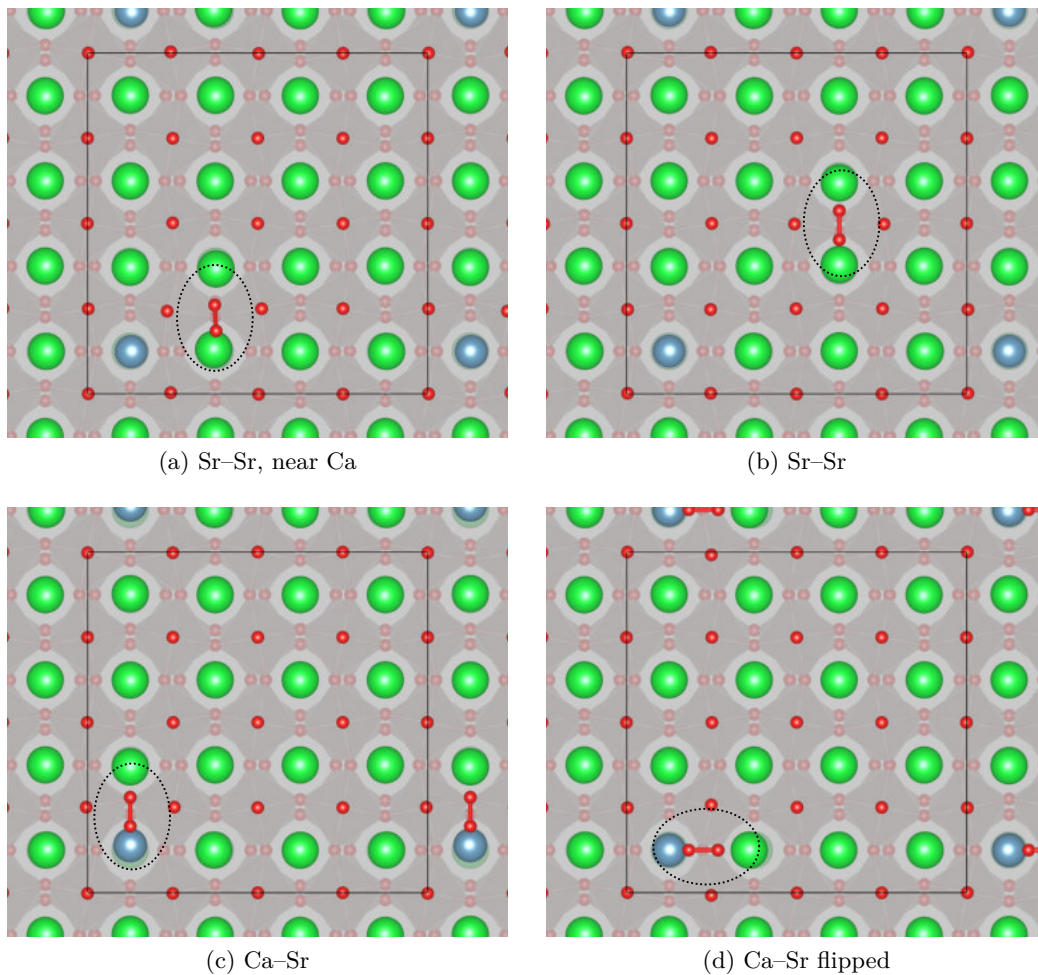
(a) Sr–Sr, near Ca

(b) Sr–Sr

(c) Ca–Sr

(d) Ca–Sr flipped

Figure 7.13.: One O_2 molecule adsorbed on the large c(4×4) Ca-doped $Sr_3Ru_2O_7$ model cell. (a), (b): adsorption at Sr–Sr bridge sites both close and far from the dopant site, (c), (d): adsorption at Ca–Sr bridge sites.

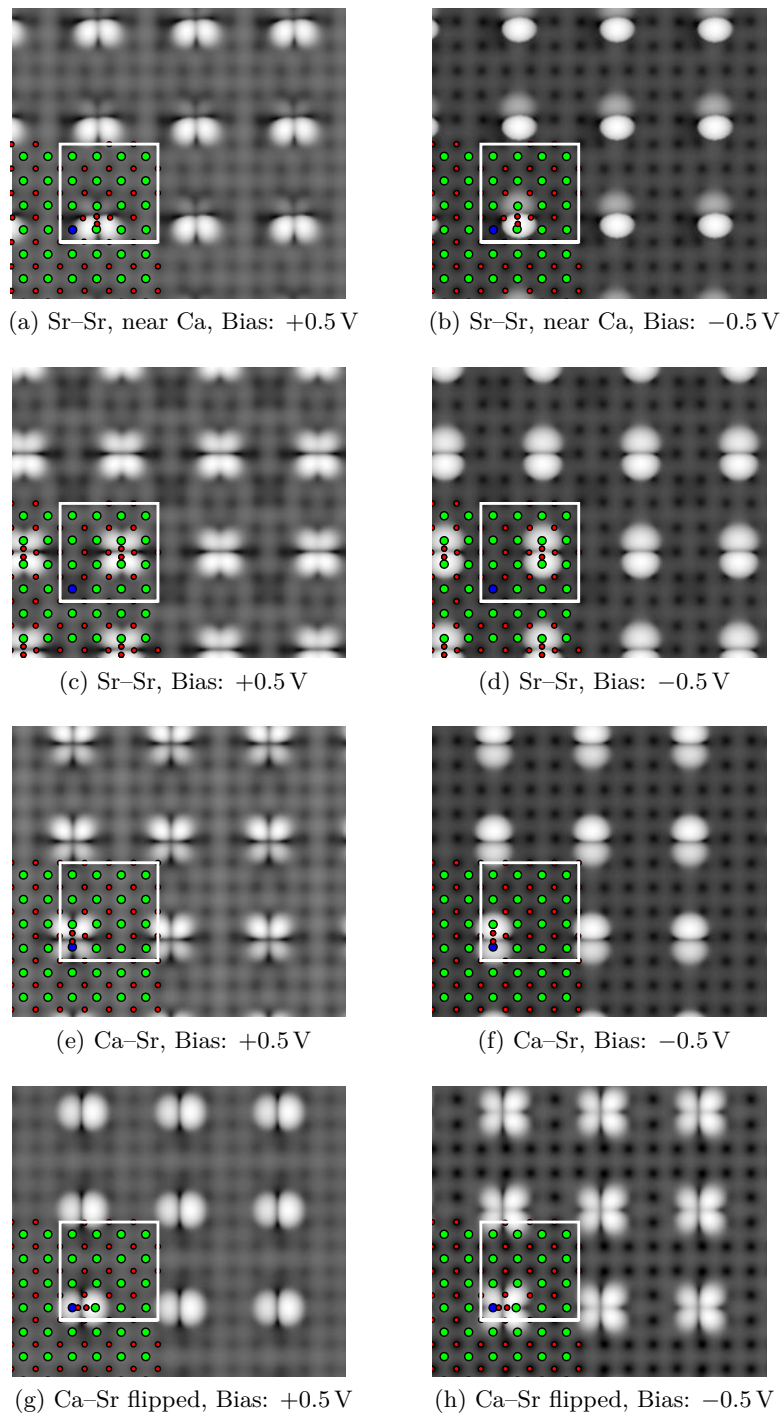(a) Sr–Sr, near Ca, Bias: $+0.5\,V$

(b) Sr–Sr, near Ca, Bias: $-0.5\,V$

(c) Sr–Sr, Bias: $+0.5\,V$

(d) Sr–Sr, Bias: $-0.5\,V$

(e) Ca–Sr, Bias: $+0.5\,V$

(f) Ca–Sr, Bias: $-0.5\,V$

(g) Ca–Sr flipped, Bias: $+0.5\,V$

(h) Ca–Sr flipped, Bias: $-0.5\,V$

Figure 7.14.: STM simulations of one O_2 molecule adsorbed on the large c(4 × 4) Ca-doped $Sr_3Ru_2O_7$ model cell at $\pm0.5\,eV$ bias voltage. The O_2 shows as a bright double feature at negative bias voltages and a 4-fold symmetric lobe feature at positive bias voltages. The tilted adsorption causes the brightness of these features to differ as the part of the O_2 close to the surface is much darker ((a), (b)).

254

of the Ca dopant shows no hybridisation with the p states of the adsorbed O_2^-, indicating that the dopant does not play a role in the charging of the adsorbate. Regardless of the adsorption site, at a Ca–Sr or a Sr–Sr bridge a Bader charge analysis shows that the surface cations do not change from their formal ionic charges (Ca^{2+}, Sr^{2+}).
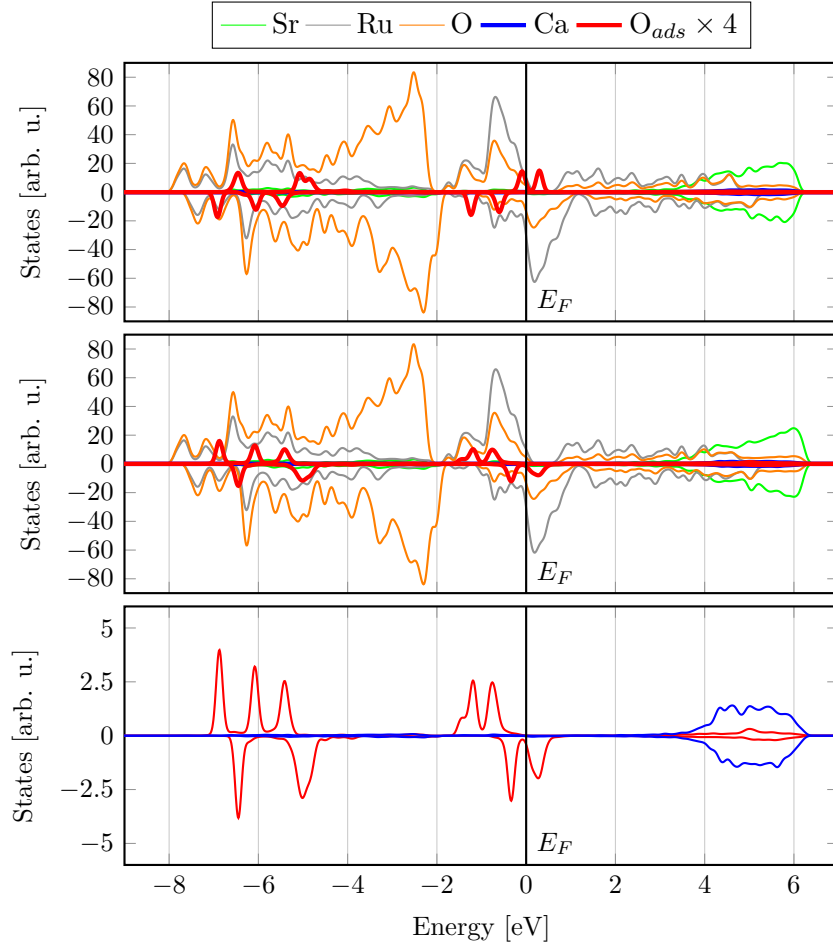
Figure 7.15.: O_2^- adsorbed on Ca-doped $Sr_3Ru_2O_7$ at ¹⁄₁₆ ML coverage. Top: O_2^- adsorbed at Ca–Sr bridge. Middle: O_2^- adsorbed at Sr–Sr bridge. The DOS shows antiferromagnetic coupling of the O_2^- to the substrate. Bottom: Magnification of O_2^- and Ca dopant states. In the top plot the O_2^- states are flipped compared to the adsorption on the pure $Sr_3Ru_2O_7(001)$ because the O_2^- couples antiferromagnetic to the substrate. Except for the magnified plot (bottom), the O_2^- states are multiplied by 4.

7.3. Calcium Ruthenate

In recent experiments published by Halwidl, Mayr-Schmölzer, et al. [6] a low dose of molecular oxygen was deposited at low temperature on the pure $Ca_3Ru_2O_7(001)$ surface. Atomic force microscopy (AFM) measurements at $0\,V$ sample bias voltage show the individual O_2 molecules as dark spots. STM measurements show the adsorbate as bright spots. At higher coverage a (2×1) overlayer appears (see fig. 7.16), forming bright rows along the [010] direction on a dark background located on top of the bright rows which already arise on the pristine surface (see section 5.5.4). These bright lines are separated by alternating wide and narrow gaps leading to a double row structure. Every second row is shifted by half a unit cell along its direction yielding a zig-zag pattern. The O_2 layer desorbs completely above a temperature of $200\,K$. This corresponds to an activation energy of $0.546\,eV$[1] according to Redhead [202].

(a) STM: (2×1) O_2^- overlayer (b) (2×1) O_2^-, defect site (c) AFM: (3×1) O_2^- overlayer

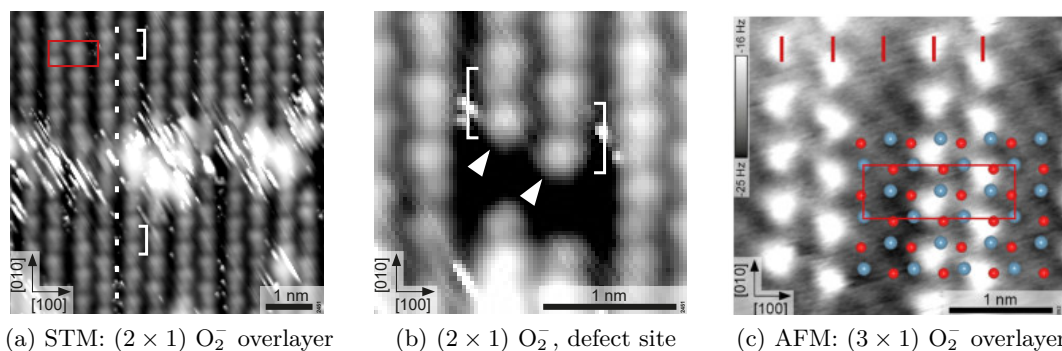Figure 7.16.: (a) Image of the (2×1) O_2^- overlayer with the adsorbate forming bright elongated spots with a dark node at the centre. The bright rows show some undulation. (b) Detailed image close to a surface defect. (c) AFM image of a partially covered sample, showing a (3×1) structure. O_2^- and surface oxygen atoms are imaged as intense and faint bright spots, respectively. STM parameters: $I_t = 0.05\,nA$, $T = 78\,K$, and $U_s = +1.0\,V$. AFM parameters: $A = 500\,pm$, $V_s = 0\,V$, $T_s = 4.8\,K$, courtesy of Halwidl, Mayr-Schmölzer, et al. [6].

The adsorption of O_2 molecules on the $Ca_3Ru_2O_7(001)$ surface was studied at both low and high coverages. To cover the low coverage case a single O_2 was placed on a (3×3) $Ca_3Ru_2O_7$ surface cell. This reflects a ¹⁄₁₈ ML coverage with respect to the available Ca–Ca bridge sites available in the surface unit cell, considering that O_2 adsorbs at alkaline atom bridge sites on both the related binary oxide CaO and on $Sr_3Ru_2O_7(001)$. At higher coverage (½ ML) two different structures were studied, a zig-zag arrangement in a (2×1) unit cell and a parallel structure on the (1×1) surface unit cell.

---

[1] Heat rate: $\approx 0.020\,K/s$

257

As has been discussed in sections 5.3.3 and 5.5.4, depending on temperature, $Ca_3Ru_2O_7$ can exhibit either a metallic or an insulating state. To properly capture the properties of both phases, the calculations were done using computational approaches able to capture the respective state. Initially, all calculations were performed with the optB86b functional which yields a metallic solution. To simulate the insulating phase, calculations were performed using the DFT+U approach, both neglecting and including van-der-Waals contributions, and—where applicable—with the HSE06 functional. The results for the metallic phase were confirmed with the so-called Grimme-D3 [32] method described in section 2.6, which allows a better distinction between local and non-local contributions. This approach results in similar adsorption energies and local configurations as the optB86b functional. For the (3×3) unit cell the DFT+U approach was used exclusively. Finally, the adsorption energies were also calculated in the benchmark random phase approximation (RPA) for the (2×1) unit cell since the previously mentioned DFT approaches yield too high adsorption energies compared to the experiment.

The computational parameters were akin to the settings used for the water adsorption calculations. Generally, an energy cutoff of $400\,eV$ was used for all initial calculations. Since for the RPA and G_0W_0 calculations a different, harder set of potentials was used (see table F.3), the energy cutoff was increased to $450\,eV$ at a later stage. These potentials introduced by Klimeš et al. [203] are approximately norm-conserving and improve the scattering behaviour and therefore the G_0W_0 quasiparticle energies. For the small (1×1) model cell a $6 \times 6 \times 1$ $\vec{k}$-point grid was sufficient to reach electronic convergence of $<1\,meV$ per atom. The $\vec{k}$-point meshes for the larger unit cells were determined by dividing the $\vec{k}$-point grid according to the multiplier of the new unit cell, yielding e.g. a $2 \times 2 \times 1$ $\vec{k}$-point grid for the large (3×3) model cell.

7.3.1. Metallic $Ca_3Ru_2O_7$

Low Coverage: (3×3) Model Cell

As has been described in section 5.5.4, the broken symmetry of the $Ca_3Ru_2O_7(001)$ surface due to the orthorhombic distortion leads to a distinct pattern of wide and narrow channels, resulting in alternating bright and dark rows in the STM images. This is caused by the tilting of the octahedra away from the centre line parallel to the b direction of the crystal in the wide channels. The width of the Ca–Ca bridge sites changes as well as the wide channel shows a width of $3.989\,\text{Å}$ and the narrow channel of $3.743\,\text{Å}$. The O_2 molecule was then placed at both Ca–Ca bridge sites in the same fashion as for the $Sr_3Ru_2O_7$ substrate and the model cell was relaxed using the optB86b functional, modelling the metallic state of the substrate. As mentioned before, a $2 \times 2 \times 1$ $\vec{k}$-point grid was used.

The calculations show that the most stable adsorption site is on top of a "wide" instead of a "narrow" row with an adsorption energy of $-1.400\,eV$. Adsorption on a "narrow" row incurs an energy penalty of $390\,meV$. To estimate the contribution of dispersion effects to the adsorption energy the relaxation of these structures were repeated using the PBE functional, yielding a van-der-Waals contribution of about $280\,meV$.

Figure 7.17a shows the O_2 molecule adsorbed on a "wide" substrate row in a rotated and tilted configuration. As mentioned before, the "wide" rows are indicated by the tilting of the octahedra away from the centre line. At the equilibrium adsorption position the adsorbate is not located directly on the Ca–Ca bridge like in the case of $Sr_3Ru_2O_7$ but shifted towards the octahedron that is tilted at an angle of 90° away from the bridge and rotated by 11.9°. This corresponds to a rotation of 33.4° with respect to the b axis of the unit cell. As the octahedron half a unit cell above is tilted parallel to the direction of the Ca–Ca bridge, its apical oxygen atom is closer to the bridge and pushes the O_2 adsorbate into the other direction, causing a shift of the O_2 molecule from the centre line of the Ca–Ca bridge. This causes a tilting of the O_2 by 29.1°, slightly larger than on the $Sr_3Ru_2O_7(001)$ surface (26.9°). The distances to the nearest metal atoms are 2.348 Å and 2.371 Å, reflecting a further shift of the adsorbate from the middle of the bridge towards one of the metal surface atoms. Again the adsorbed O_2 molecule is elongated to 1.346 Å like on the $Sr_3Ru_2O_7$ substrate (1.354 Å). The adsorbate causes slight distortion of the substrate in that RuO_6 octahedra in its vicinity contract slightly by about 0.160 Å^3 (1.5 %) and 0.060 Å^3 (0.6 %) with respect to the octahedron volume of 10.690 Å on the pure surface.

An adsorption configuration of the O_2 molecule on a "narrow" row is disfavoured by 0.440 eV (optB86b) compared to the "wide" rows. The rotation of the adsorbate with respect to the b crystallographic axis is much more pronounced at 51.1°, but just 9.7° with respect to the Ca–Ca bridge. The tilting of the O_2 is less than on the "wide" row at 6.2°, and the molecule is slightly shorter at 1.322 Å. Since the Ca–Ca bridge crossing the "narrow" rows is shorter than for the "wide" rows (3.583 Å vs 3.987 Å) and the distances between the atoms of the O_2 molecule and the metal substrate atoms ($d(O_I–Ca_I) = 2.859$ Å and $d(O_{II}–Ca_I) = 2.863$ Å) are similar to the most favourable position the O_2 is pushed outwards from the surface, resting at a distance of 2.264 Å from the substrate. Again contraction of the two octahedra close to the adsorbate can be observed: 0.209 Å^3 (2.0 %) for the nearest and 0.105 Å^3 (1.0 %) for the one opposite of the Ca–Ca bridge.

The STM simulations of the adsorbed O_2 molecule (see fig. 7.18) show the molecule as a "wide" feature positioned almost directly on top of the "wide" substrate rows. At positive bias voltage the O_2 molecules exhibits a 4-fold symmetric feature with its brighter parts near at the upwards tilted oxygen atom while at negative bias voltage a double lobe feature can be seen. Again the brighter lobe is positioned on the upwards tilted oxygen atom. The STM simulation of the O_2 adsorbed on the "narrow" row shows the familiar double feature at negative bias voltage and a 4-fold lobe-like structure at positive bias voltages, similar to the O_2 adsorbed on the $Sr_3Ru_2O_7$ and Ca–doped $Sr_3Ru_2O_7$ surface (see figs. 7.2 and 7.14). Here the brightness of the double feature is very even due to the similar relative positions of the surface Ca atoms forming the bridge site with respect to the O_2 atoms.

Table 7.6.: Adsorption energy in eV per O_2 molecule on $Ca_3Ru_2O_7$ at ⅟₁₈ ML coverage, located both on a wide and narrow row sites.

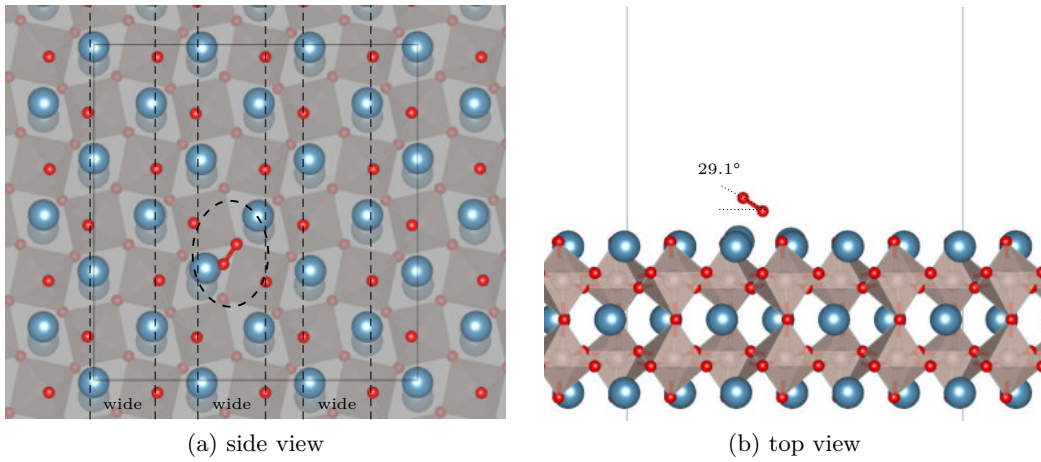| (3×3) unit cell	E_{Ads} [eV]
wide	
optB86b	-1.400
PBE	-1.124
narrow	
optB86b	-0.953
PBE	-0.823

(a) side view

(b) top view

Figure 7.17.: One O_2 adsorbed on a bright line on the (3×3) $Ca_3Ru_2O_7(001)$ model cell. The O_2 is tilted by 29.1° and rotated by 33.4° with respect to the crystallographic b axis.

(a) wide row, bias $+0.5\,\mathrm{eV}$ (b) wide, bias $-0.5\,\mathrm{eV}$
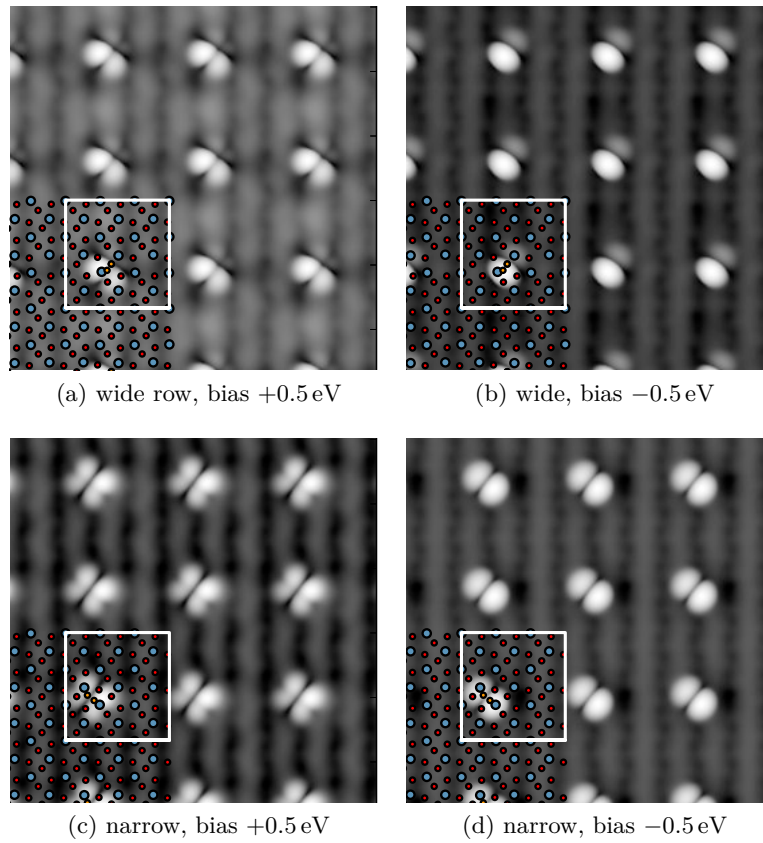
(c) narrow, bias $+0.5\,\mathrm{eV}$ (d) narrow, bias $-0.5\,\mathrm{eV}$

Figure 7.18.: STM Simulations of one O_2 adsorbed on the (3×3) $Ca_3Ru_2O_7$ surface unit cell at $\pm 0.5\,\mathrm{eV}$ bias voltage. The adsorbed O_2 molecule is indicated by a bright feature, which forms a double lobe at negative bias voltage ((b) and (d)) where the dark line separating the two lobes marks the centre of the O–O bond. At positive bias voltage the bright feature is split again, forming a 4-fold symmetric spot.

7.3.2. High Coverage

The high coverage case was modelled using a (2×1) model cell which allows both a parallel and zig-zag placement of the O_2 molecules. The adsorbate was again placed at Ca–Ca bridge sites in accordance with the low coverage case. In a first step only the metallic phase of the substrate was modelled employing the optB86b functional. To sample the Brillouin zone a $3 \times 6 \times 1$ Γ-centred $\vec{k}$-point grid was chosen and the energy cutoff was set to $400 \, eV$.

The complete relaxation of these four structures reveals a clear preference of the O_2 molecules to adsorb on top the wide lines in the zig-zag arrangement. The adsorbate molecules are, similar to the "flat" case on the (3×3) unit cell, positioned between one surface Ca atom and an apical oxygen atom of a RuO_6 octahedron (see fig. 7.19a). Both O_2 in the surface unit cell are almost flat, showing tilting by only $0.7°$ and $1.5°$ with respect to the surface plane. The O_2 molecules rotate by $3.3°$ and $8.3°$ counter clockwise with respect to the b axis of the unit cell, leading to an asymmetric arrangement. This might be induced by the tilting of the RuO_6 octahedra as those close to the adsorbate molecules tilt by $20.5°$ and $21.9°$, in contrast to the $13.1°$ tilting angle in the clean surface. Additionally, the volume of three out of four RuO_6 octahedra changes. The volume of the two octahedra closest to the adsorbates are reduced by $0.465 \, Å^3$ and $0.294 \, Å^3$ from the $10.690 \, Å^3$ in the clean surface while the remaining octahedron contracts by $0.089 \, Å^3$. The stronger tilting of the octahedra also causes a slight shift in the Ca lattice, displacing two consecutive rows of surface calcium atoms by $\approx 47 \, pm$ towards the centre line of the wide row. The slight differences of the two adsorbate molecules in their local geometry is also evident in the atomic distances. The first O_2 molecule $(O_{2,1})$ which is only slightly rotated is more closely positioned to the closest Ca atoms at distances of $2.294 \, Å$ and $2.343 \, Å$ the second one $(O_{2,2})$ is positioned closer $(2.361 \, Å$ and $2.347 \, Å)$. The O–O distance of $(O_{2,1})$ is slightly longer than of $(O_{2,2})$ at $1.395 \, Å$ compared to $1.356 \, Å$. The distortion of the RuO_6 octahedra is also noticeable in their volume. The two octahedra close to the adsorbate molecules contract by $0.465 \, Å^3$ (4.4%) and $0.294 \, Å^3$ (2.8%) compared to the octahedron volume in the pure surface. The other two octahedra in the top layer that are more distant to the adsorbates contract much less ($0.089 \, Å^3$ or 0.8%) or not at all.

A parallel arrangement of the oxygen molecules on the wide lines as shown in fig. 7.19c is $164 \, meV$ per O_2 less favourable. Here both O_2 molecules adsorb at identical positions given by the symmetry of the unit cell. The adsorbates lie quite flat at an angle of $4.2°$ on the surface and almost parallel to the b axis. As can be seen in fig. 7.19c the adsorbate molecules are again positioned between a surface Ca atom and the apical oxygen of a RuO_6 octahedron. In contrast to the zig-zag configuration all octahedra show only slight contraction of $0.220 \, Å^3$ and a larger tilting angle of $17.1°$. Again the surface Ca atoms shift slightly by $28 \, pm$ towards the centre line of the wide row. In this arrangement of the adsorbate the contraction is evenly distributed over all RuO_6 octahedra at $\approx 0.22 \, Å^3$ or $\approx 2\%$.

Similar to the low coverage case described in section 7.3.1 the narrow rows on the

$Ca_3Ru_2O_7$ surface are disfavoured adsorption sites. Both a zig-zag and a parallel arrangement of the O_2 molecules show an energy penalty of 448 meV and 649 meV for the two configurations, respectively. In both cases the O_2 molecules are slightly shifted from the Ca–Ca bridge sites, at a respective angle of 14.2° for the parallel and 10.7° (11.7°) for the $O_{2,1}$ ($O_{2,2}$) for the zig-zag arrangement. On the narrow rows the adsorbate is contracted to 1.318 Å (1.300 Å) for the parallel (zig-zag) configuration. The tilting angle of the O_2 is 8.1° (6.2° and 7.1°) for the parallel (zig-zag) case. Adsorption on the narrow rows does not distort the surface as much as on the wide rows, the contraction of the RuO_6 octahedra is just 0.220 Å^3 for the parallel and 0.221 Å^3 for the zig-zag configuration. This translates into a contraction of about 2 % for both the zig-zag and the parallel case.

The Tersoff-Hamann STM simulations in fig. 7.20 show the O_2 adsorbate mostly indicated as a bright, wide spot. Due to the high coverage the surface structure is hidden below the adsorbate. When adsorbed on the wide rows, the large bright features indicating the O_2 molecules are not detected exactly on top of the molecule, but rather in-between two O_2. The narrow dark feature between the bright blobs actually marks the middle of the O–O bond. This pattern holds true for both positive and negative bias voltages and agrees very well with the experiment shown in fig. 7.16a. The parallel configuration on the wide lines shows a very regular pattern, which is for positive bias only slightly changed due to the slight tilting of the molecules. For the zig-zag configuration depicted in figs. 7.20a and 7.20b the STM simulations show double rows of wide lobes, which are separated by a narrow valley, positioned on top of the narrow substrate rows. The position of the valley switches at alternating bias voltage. When adsorbed on the narrow rows (figs. 7.20c, 7.20d, 7.20g and 7.20h), the O_2 molecules generate a very uneven pattern, both in zig-zag and parallel configuration.

Table 7.7.: Adsorption energies in eV per O_2 molecule on the (2×1) $Ca_3Ru_2O_7$ at high coverage, calculated with the optB86b functional.

(2×1) unit cell	E_{Ads} [eV]
zig-zag, bright	−1.164
zig-zag, dark	−0.716
parallel, bright	−1.000
parallel, dark	−0.351

Van-der-Waals Contributions

The van-der-Waals contributions can be estimated from a forcefield-based approach such as the Grimme DFT-D3 method introduced by Grimme et al. [32]. As described in section 2.6, in this method the dispersion term is added to the conventional Kohn-Sham DFT energy in the method, taking the local geometry of the ions into account when

(a) zig-zag, bright   (b) zig-zag, dark

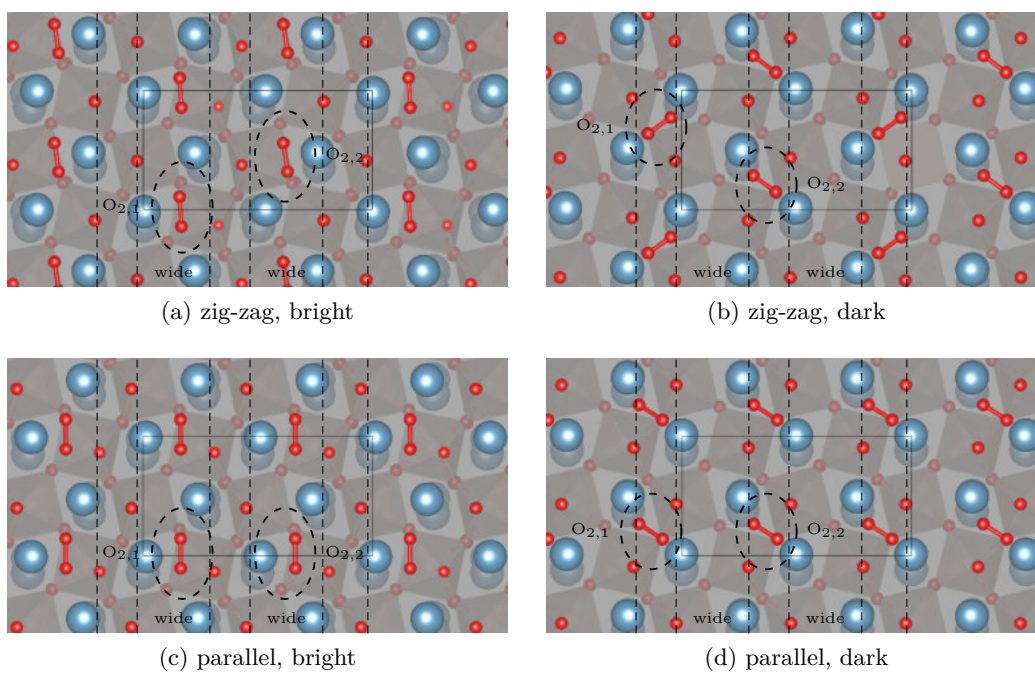(c) parallel, bright   (d) parallel, dark

Figure 7.19.: Two O_2 adsorbed on the (2×1) $Ca_3Ru_2O_7(001)$ model cell. (a) and (b) depict the zig-zag structure adsorbed on wide and narrow rows, respectively. (c) and (d) in parallel arrangement on wide and narrow rows, respectively.
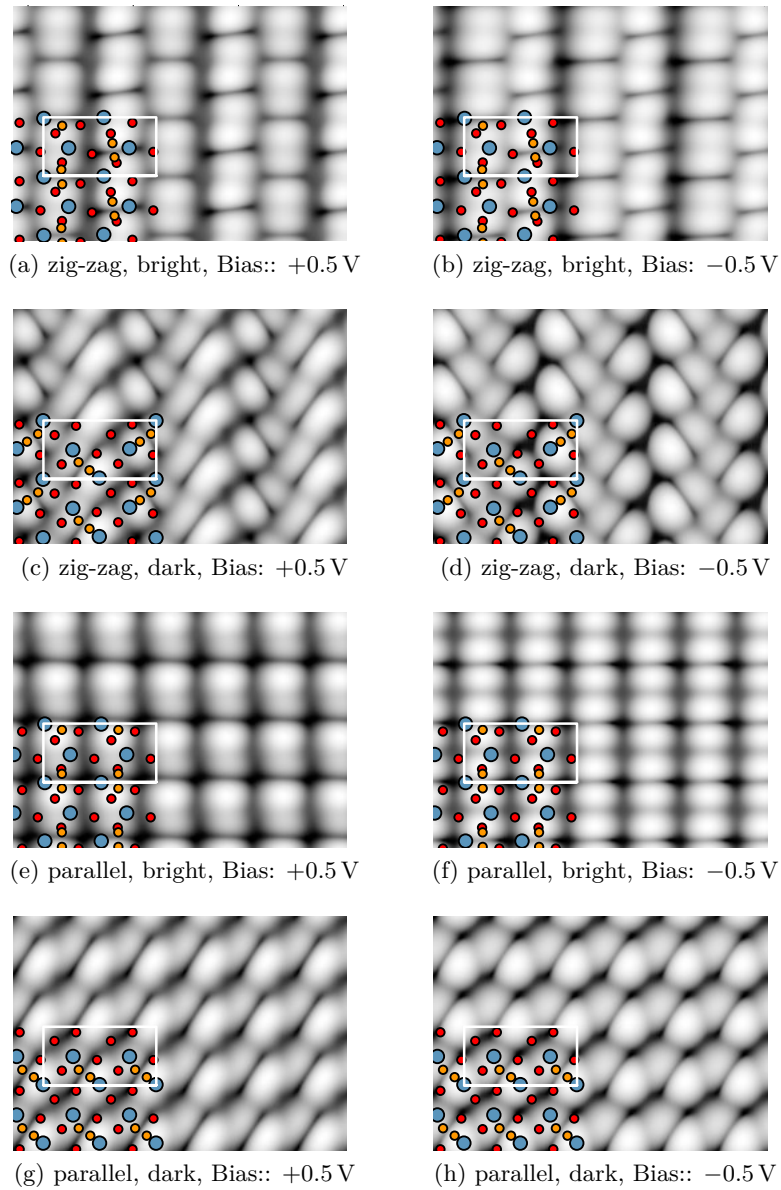
(a) zig-zag, bright, Bias:: $+0.5\,\mathrm{V}$

(b) zig-zag, bright, Bias: $-0.5\,\mathrm{V}$

(c) zig-zag, dark, Bias: $+0.5\,\mathrm{V}$

(d) zig-zag, dark, Bias: $-0.5\,\mathrm{V}$

(e) parallel, bright, Bias: $+0.5\,\mathrm{V}$

(f) parallel, bright, Bias: $-0.5\,\mathrm{V}$

(g) parallel, dark, Bias:: $+0.5\,\mathrm{V}$

(h) parallel, dark, Bias:: $-0.5\,\mathrm{V}$

Figure 7.20.: STM simulation of two O_2 adsorbed on a (2×1) $Ca_3Ru_2O_7(001)$ unit cell. Ca atoms blue, oxygen of the substrate red, adsorbed O_2 orange. On the wide lines the O_2 are visible as wide features; the narrow line separating these wide spots marks the centre of the O–O bond.

calculating the dispersion coefficients C_{6ij}. Since the additional computational effort for this method is very small compared to a standard DFT calculation it can also be used for very large systems. Additionally, the results obtained by the DFT-D3 approach were cross-checked with the optB86b functional.

Since these calculations serve as a basis for the advanced many-body techniques G_0W_0 and RPA (see section 2.7) a few parameters were changed from the previous studies. Since it is advisable to use PAW potentials which offer a better description of the scattering properties at high energies for G_0W_0 calculations, the "_GW" set of potentials[2] were used. Additionally, the energy cutoff was increased to 450 eV. For the $\vec{k}$-point grid the same Γ-centred $4 \times 6 \times 1$ $\vec{k}$-point mesh was used. Again, all structures were fully relaxed until the residual forces were <0.010 eV/Å. To reduce the computational effort only the (2×1) model in the flat zig-zag configuration, where the O_2 was adsorbed on the bright lines, was studied. The initial atomic positions were taken from the previous calculations with the optB86b functional. Since the current implementation of the RPA does not allow for the calculation of atomic forces for metallic system, the model cells were pre-relaxed with various DFT methods.

To further study the adsorption energy landscape, the optB86b model cell was relaxed with the PBE functional. The O_2 molecules move slightly from their initial positions until they are positioned in almost straight lines. The O_2 are rotated at just $\approx 3°$, one row clockwise and the other row counterclockwise. The tilting angle of the adsorbate molecules to the surface is larger at $13.9°$, much larger than seen initially with the optB86b functional. The RuO_6 octahedra in the surface layer contract, the two close to the adsorbates by 1.7% and the other two in the model cell by 0.4%. Similar to the optB86b structure the octahedra next to the adsorbate also tilt by $19.3°$, compared to $13.2°$ in the pure surface. The adsorption energy per O_2 molecule is significantly lower at -0.933 eV.

Interestingly, another stable adsorption configuration was found that is just 6 meV more stable than the more or less flat structure. This small difference suggests that the adsorption energy landscape is very shallow. Here the O_2 molecules are positioned much closer to the Ca–Ca bridge (see fig. 7.21b), similar to the tilted configuration found on the low coverage (3×3) model. The tilting angle of both O_2 is $29.9°$ and they rotate by $31.8°$ with respect to the direction of the bright substrate rows. The oxygen atom that is positioned closer to the Ca atom is shifted perpendicular to the surface, causing the increased tilting of the molecules. The RuO_6 octahedra are in this case all expanded. The two close to the molecule expand only by 0.8% while the other two expand by 1.7%. All octahedra tilt more than in the pure surface, the two close ones by $14.3°$ and the other two by $17.3°$. Nevertheless, the flat configuration is more favourable than the tilted one by ≈ 40 meV, as indicated by table 7.8.

Now both flat and tilted structures were recalculated with the DFT-D3 method. Again the flat configuration is 70 meV more stable than the tilted one. In the relaxed flat model cell the O_2 are rotated more than in the flat PBE structure $(5.6°)$ and the tilting angle with respect to the $Ca_3Ru_2O_7$ surface is much larger at $10°$. This structure shows

---

[2] _GW Potentials of the v.52 set, see table F.3

266

the largest expansion of the RuO_6 octahedra close to the O_2 at 2.7% and they tilt by $19.5°$. Compared to the previously optB86b equilibrium structure the O_2 adsorb in a more symmetric manner with the DFT-D3 method. The relaxed tilted structure is almost unchanged to the tilted PBE structure. Here the O_2 tilt by $29.9°$ with respect to the surface and rotate by $28.6°$. The distortion of the octahedra is almost identical at a contraction of 0.8% and 1.5%, as is their tilting at $14.9°$. The comparison of the adsorption energies obtained with the DFT-D3 method to PBE calculations show a van-der-Waals contribution of $154\,meV$ to $174\,meV$.

In a final step both the tilted and flat structures relaxed with the DFT-D3 method were recalculated using the optB86b functional to double-check the previous results. The flat structures could also be stabilized with a slight energy penalty of $52\,meV$ compared to the asymmetric optB86b structure. The rotation of the O_2 molecules at $8.8°$ is larger than for the DFT-D3 structure while the tilting angle is just $4.6°$. The RuO_6 octahedra are like with the previous cases contracted (here by 1.8% from $10.690\,Å^3$) when they are positioned next to the adsorbates.

To summarise, the energy landscape is very shallow when neglecting van-der-Waals contributions. Both the van-der-Waals corrected DFT-D3 and optB86b functionals show a preference of the flat structure where the O_2 molecules are arranged in almost straight lines.

Table 7.8.: Comparison of the adsorption energies in eV of two O_2 molecules on the (2×1) $Ca_3Ru_2O_7$ model cell, calculated with the PBE and the van-der-Waals corrected optB86b and Grimme-D3 functionals.

(2×1) unit cell	E_{Ads} [eV]
flat	
optB86b	-1.199
DFT-D3	-1.110
PBE	-0.933
tilted	
optB86b	-1.108
DFT-D3	-1.049
PBE	-0.889

7.3.3. Insulating $Ca_3Ru_2O_7$

Pristine $Ca_3Ru_2O_7$ surface

As described before, the optB86b functional can not be used in conjunction with the DFT+U method which is able to describe the insulating state of the substrate at the DFT level. Therefore Grimme's DFT-D3 method was combined with the DFT+U approach
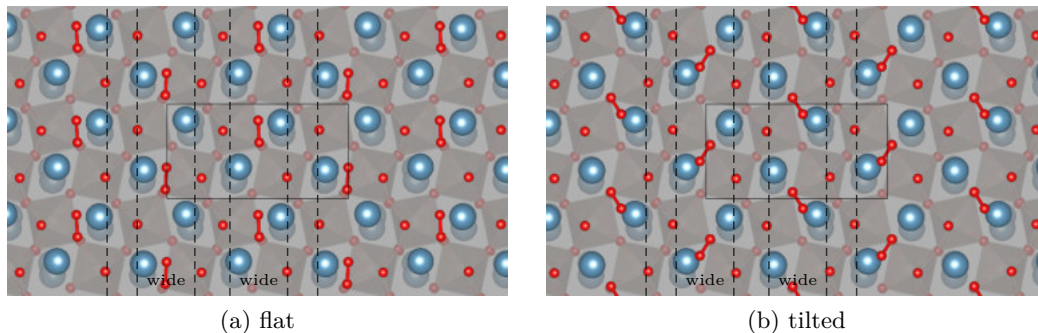
(a) flat	(b) tilted

Figure 7.21.: (a) depicts the flat, (b) the tilted zig-zag configuration of O_2 adsorbed on the (2×1) model, relaxed with the PBE functional. The two van-der-Waals corrected functionals yield similar equilibrium structures.

introduced in section 2.4 to account for both the electronic state and the van-der-Waals contributions. The second method able to describe the insulating phase involves so-called hybrid functionals (see section 2.5). The computational effort for this method is at least two orders of magnitude larger than for standard DFT calculations, therefore it can only be sensibly used with small systems. The particular flavour used here to account for the exact exchange is implemented in the HSE06 functional [28]. All calculations using the DFT+U were done using the same computational settings as in the previous section. To reduce the computational effort to a sensible value for the HSE06 calculations the $\vec{k}$-point grid was reduced to a Γ-centred $2 \times 4 \times 1$ grid, resulting in 6 irreducible $\vec{k}$-points.

To determine a value of $U - J$ which corresponds to the insulating phase test calculations on the bare substrate unit cell at increasing values of $U - J$ were performed. As can be seen in table 7.9, the bare $Ca_3Ru_2O_7$ slab stays metallic until a value of $U - J = 3\,\text{eV}$ where a band gap is opened up of $1.153\,\text{eV}$ and $0.662\,\text{eV}$ for the spin up and the spin down channel. Further increasing the on-site interaction term to up to $6\,\text{eV}$ as expected leads to larger values of the band gap, see table 7.9. This behaviour can also be seen when comparing the plotted densities of states at various values of $U - J$ in fig. 7.22: at the fermi level the DOS is dominated by the ruthenium states in both spin channels where the ruthenium d states hybridise with the oxygen p states. Due to the increased on-site repulsion term this large feature is split into two, opening the band gap at values of $U - J = \geq 3\,\text{eV}$. These split off features start to merge with the rest of the DOS as the on-site interaction is increased.

The calculation employing the hybrid HSE06 functional shows similar splitting of the ruthenium states and the introduction of a band gap of $1.827\,\text{eV}$ in the spin up and of $1.218\,\text{eV}$ in the spin down channel. In contrast to the DFT+U calculations the split off ruthenium feature in the occupied states is still separated from the bulk of the electronic structure.

The pristine $Ca_3Ru_2O_7$ slabs do not exhibit significant structural changes at the in-

troduction of the Hubbard U. The HSE06 calculations on the other hand lead to a structure where all octahedra contract compared to the DFT-D3 structures. Interestingly two neighbouring octahedra contract by $3.4\,\%$ while the other two contract by $3\,\%$, resulting in double rows of equally compressed octahedra along the b axis.

Table 7.9.: Calculated global band gaps in eV of the pristine 2-layer (2×1) $Ca_3Ru_2O_7$ slab for different values of $U - J$, performed with the DFT-D3 method.

$U - J$ [eV]	spin up	spin down
0	metallic	metallic
1	metallic	metallic
2	metallic	metallic
3	1.153	0.662
4	1.599	1.126
5	2.042	1.618
6	2.392	2.115
HSE06	1.827	1.318

Adsorption of O_2 on Insulating $Ca_3Ru_2O_7$: Low Coverage

The low coverage unit cell was relaxed using the DFT+D3 approach at a value of $U - J = 0\,\text{eV}$ and $U - J = 4\,\text{eV}$ to determine whether the phase transition would induce any structural changes. Compared to the structural parameters presented before in section 7.3.1 using the optB86b functional to the relaxed structure calculated using Grimme's DFT-D3 approach with $U - J = 0\,\text{eV}$ leads to very similar results. The adsorbed O_2 molecule is slightly more rotated with respect to the b-axis of the substrate ($34.3°$) and by $10.8°$ with respect to the Ca–Ca bridge. The distances between its components to the closest calcium atom of the substrate is slightly larger ($2.356\,\text{Å}$, $2.376\,\text{Å}$). The main structural difference lies in the volumes of the octahedra: as already seen for the clean surface the DFT-D3 approach yields slightly larger ($1.1\,\%$) volumina. The adsorption of an O_2 molecule again causes slight contraction of the octahedra where ones volume is reduced by $2.0\,\%$ and the octahedron closest to the adsorbate by $0.8\,\%$, denoted as Oct_A and Oct_B in fig. 7.23a. The remaining octahedra in the unit cell have to accommodate for the structural stress. For example, an octahedron far away from the adsorption site expands by $0.2\,\%$ (Oct_C). Using this functional the adsorption energy is lower than for the optB86b functional at $-1.294\,\text{eV}$.

The calculation for the insulating phase was performed using the same DFT-D3 approach but choosing a value of $U - J = 4\,\text{eV}$. This results in a global band gap of $2.063\,\text{eV}$ in the spin up channel and of $0.552\,\text{eV}$ in the spin down channel[3]. The adsorption energy is only slightly reduced to $-1.287\,\text{eV}$ compared to the metallic phase. The adsorbate
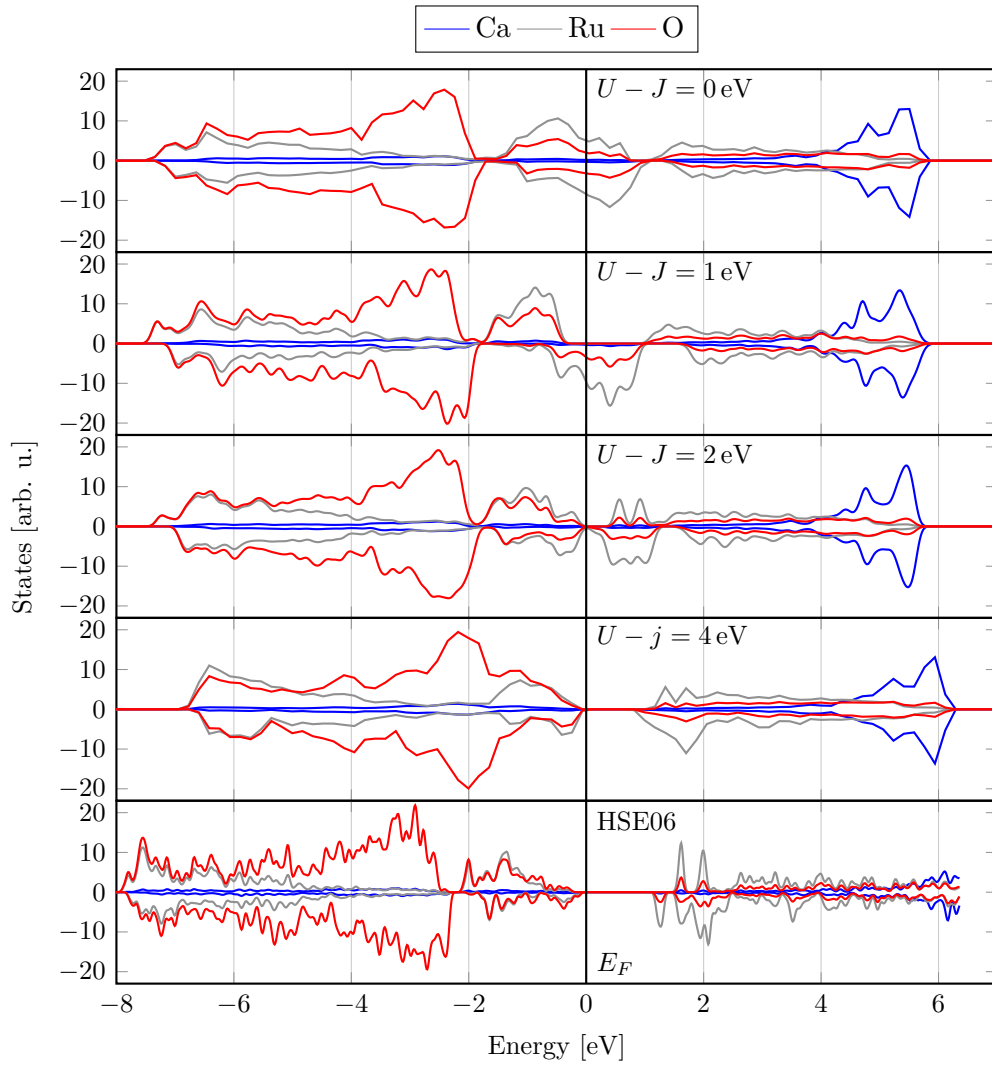
---

[3]Calculated using ISMEAR=-5

Figure 7.22.: Calcium, ruthenium and oxygen densities of states of the 2-layered $Ca_3Ru_2O_7$ slab at increasing values of U, calculated using the DFT-D3 and HSE06 methods.

is rotated by 31.2° with respect to the *b*-axis and by 14.1° with respect to the Ca–Ca bridge. Compared to the metallic calculation the distances between O_2 and the nearest Ca atoms is slightly larger (2.366 Å and 2.398 Å). The reason for these differences lies in an enhanced octahedral distortion close to the adsorbate: the aforementioned Oct_A is contracted by 6.6 % while Oct_B is slightly expanded by 0.3 %. This is caused by strongly localised charge transfer which will be described in detail in section 7.3.4.

(a) metallic
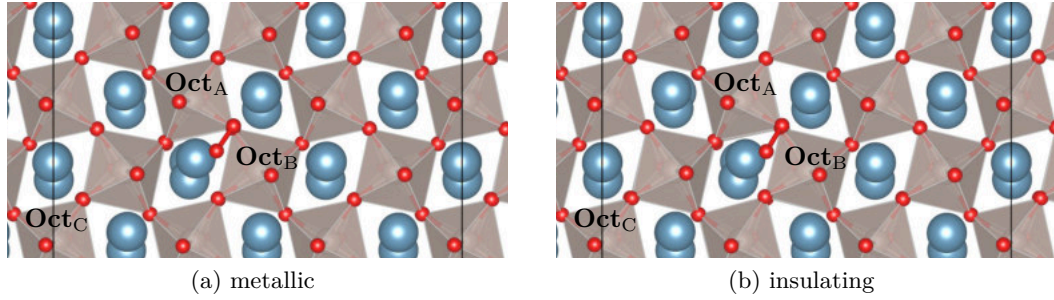
(b) insulating

Figure 7.23.: Magnified top view of one O_2 adsorbed on the (3×3) $Ca_3Ru_2O_7$ model cell (⅑ ML coverage). (a) depicts the metallic, (b) the insulating case. The calculations were performed in the DFT-D3+U regime at $U - J = 0\,\text{eV}$ and $U - J = 4\,\text{eV}$ respectively. The two structures show only minuscule visual differences.

Adsorption of O_2 on Insulating $Ca_3Ru_2O_7$: High Coverage

Using the optimised structures for the metallic $Ca_3Ru_2O_7$ substrate calculated with the DFT-D3 method as initial configurations, another set of calculations using the DFT-D3 method at increasing values of the Hubbard U complemented by HSE06 calculations were done to evaluate the adsorption energies and band gaps of the insulating $Ca_3Ru_2O_7$ phase. As is indicated in fig. 7.24 and table 7.10 the system stays metallic for the DFT-D3 method up to the maximum chosen value of $U - J = 6\,\text{eV}$, at which the pristine surface exhibits a gap of 2.120 eV in the spin down channel. Only for the tilted configuration the spin up channel shows a band gap at $U - J \geq 3\,\text{eV}$. This can be explained by studying the density of states: the on-site interaction term that is introduced in the DFT+U method is only added to the Ru *d*-states, opening the gap in the pristine surface structure. The degeneration of the π-states of the O_2 molecule is lifted due to charge transfer, resulting in double peaks in the DOS. This will be explained in more detail in section 7.3.4. For now it is important to note that the interaction of the O_2^- with the substrate causes a splitting of the π-states in the spin down channel around the fermi level. The antibonding π^*-state above E_F then hybridises with subsurface Ru *d*-states, negating the repulsive effect of the DFT+U method, leading to hybrid states in the gap at the surface of the $Ca_3Ru_2O_7$ slab. In essence, the electronic state of the slab does not change and it is not really metallic, since the mid-gap states only exist at the surface

where the O_2^- is adsorbed, i.e. the adsorbate induces surface metallisation. Adding an additional artificial on-site interaction term ($U - J = 4.5\,\mathrm{eV}$, $(U - J)_{O_{ads}} = 6\,\mathrm{eV}$) to the oxygen π states of the adsorbate pushes the unoccupied π^*-states in the minority channel of the adsorbate to higher energies and the hybrid states in the gap vanish, yielding a gap of $0.987\,\mathrm{eV}$ and $1.433\,\mathrm{eV}$ in the majority and minority channels, respectively. As noted in table 7.10, the tilted configuration exhibits less interaction with the surface compared to the flat one, therefore inducing less surface states in the gap. The comparison with the HSE06 calculation confirms this behaviour: here the unoccupied spin down π^*-states of the charged O_2^- molecule are located at a much higher energy and the substrate is now fully insulating.

Table 7.10.: Calculated global band gaps of the pristine 2-layer (2×1) $Ca_3Ru_2O_7$ slab for different values of $U - J$, performed with the DFT-D3 method. At lower values of $U - J$, the adsorbed O_2^- induces mid-gap states at the surface of the slab, leading to surface metallisation.

$U - J$ [eV]	flat O_2^-, [eV]		tilted O_2^-, [eV]	
	spin up	spin down	spin up	spin down
0	metallic	metallic	metallic	metallic
1	metallic	metallic	metallic	metallic
2	metallic	metallic	metallic	metallic
3	surf. met.	surf. met.	1.426	surf. met.
4	surf. met.	surf. met.	1.564	surf. met.
5	surf. met.	surf. met.	1.507	surf. met.
6	2.021	surf. met.	1.268	surf. met.
4.5, $(U - J)_{O_{ads}} = 6\,\mathrm{eV}$	0.987	1.433		
HSE06	1.369	1.369	0.525	0.525

The choice of calculation method also has implications on the fully relaxed structure parameters and the adsorption energies. As can be seen in table 7.11 the adsorption energies are more or less constant up to the transition to the insulating phase. At a value of $U - J = 4\,\mathrm{eV}$ the adsorption energy per O_2 molecule is reduced by $218\,\mathrm{meV}$ compared to the value for $U - J = 2\,\mathrm{eV}$. Additionally the tilted structure becomes slightly more favoured compared to the flat structure. Further increasing the on-site interaction term lowers the adsorption energy even more. The preference of the O_2 to adsorb on the wide channels still holds for the insulating phase as the adsorption energy of an O_2 molecule adsorbed on the dark rows is $-0.626\,\mathrm{eV}$ at $U - J = 4\,\mathrm{eV}$, just slightly lower than for the metallic substrate. The HSE06 calculations lead to adsorption energies of $-0.582\,\mathrm{eV}$ and $-0.618\,\mathrm{eV}$ for the flat and the tilted structure, respectively, much lower than for the DFT-D3+U calculations ($\approx 170\,\mathrm{meV}$, see section 7.3.2).

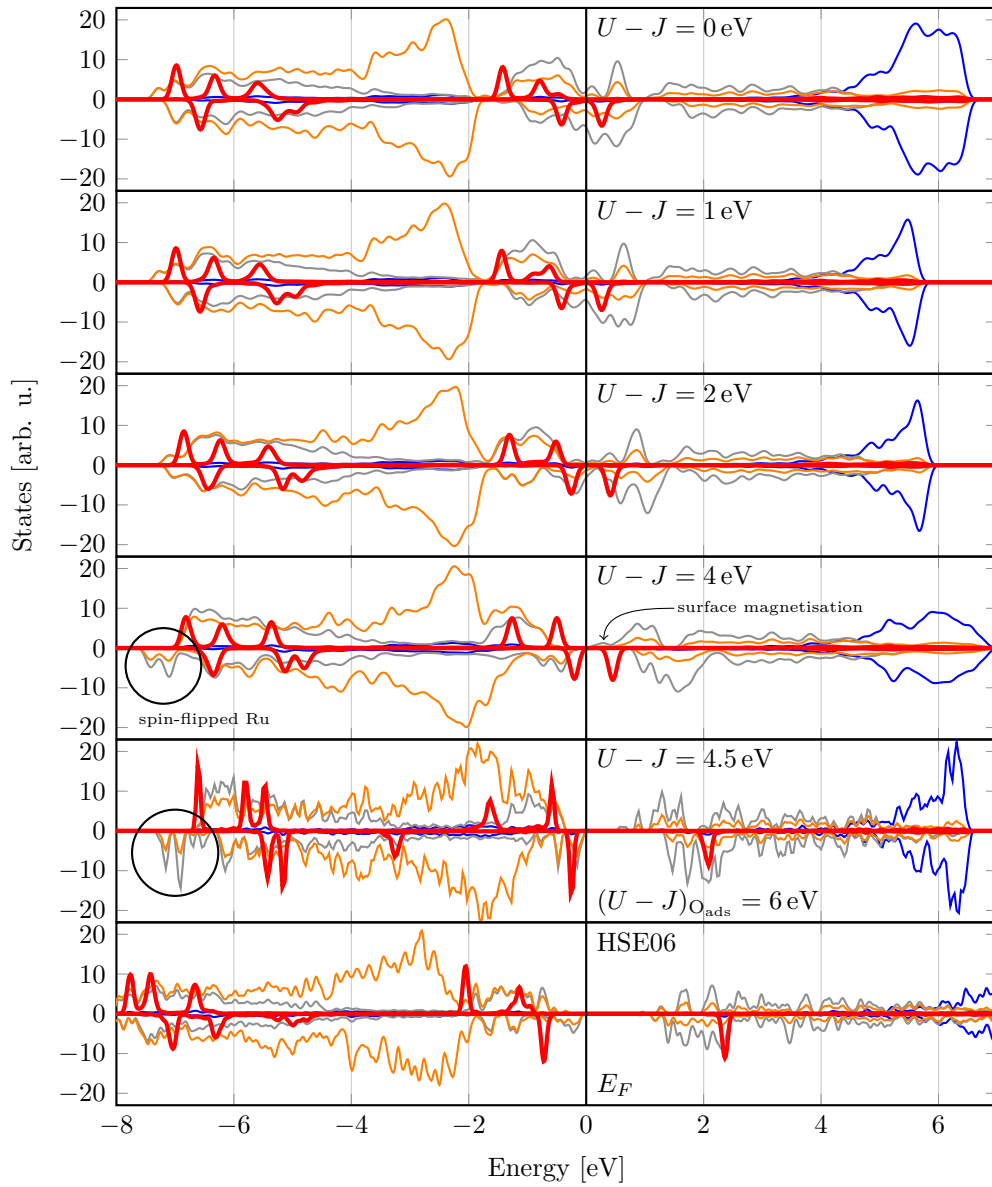In contrast to the pristine surface the O_2 adsorbate causes structural changes in the

Figure 7.24.: Calcium, ruthenium, substrate and adsorbed oxygen densities of states of the 2-layered $Ca_3Ru_2O_7$ slab at increasing values of $U - J$, with two O_2^- adsorbed in the flat configuration, calculated using the DFT-D3 and HSE06 methods. As discussed in section 7.3.5, the transition to the insulating state induces a flip of the surface Ru spins located below the O_2^-, indicated by the solid circles.

$Ca_3Ru_2O_7$ slab, similar to the metallic phase (see section 7.3.2), noticeable in particular by the change in volume and tilting of the surface octahedra marked in fig. 7.25. The structural distortions are compared to the surface slabs relaxed with the respective computational method. In the flat configuration, while the octahedra next to the adsorbed O_2 molecules ($Oct_{A,B}$ in fig. 7.25a) contract by 2.7 % in the metallic phase (the other two surface octahedra ($Oct_{C,D}$) in the surface unit cell are almost unchanged), this distortion is more pronounced in the insulating phase. As an example, the relaxation using Grimme's DFT-D3 approach with an $U - J = 4\,\text{eV}$ yield a contraction of the same two octahedra by 5 %, while the remaining two expand by 2.8 %. Similar behaviour is found using the hybrid functional where the octahedra $Oct_{A,B}$ contract by 5.2 % and expanded by 3 % respectively (see fig. 7.25b). The tilting of the octahedra is not significantly affected by these distortions. The rotation of the adsorbed molecules is slightly changed, it is increased to 6° for the DFT-D3+U approach but reduced to 4.5° in the HSE06 calculations. The tilting of the adsorbate with respect to the surface also changes accordingly, to 9.4° and 11.8° respectively. The length of the O_2 molecule is 1.340 Å and 1.350 Å for the two approaches, respectively. The structural difference of the surface between metallic and insulating phase leads to minimal changes of the distances between O_2 molecule and the Ca atoms. The DFT-D3+U method yields oxygen-calcium distances of 2.367 Å and 2.353 Å for the O_I–Ca_I and a O_{II}–Ca_I case, while the HSE06 functional yields 2.352 Å and 2.346 Å, respectively.

The tilted adsorption configurations exhibit similar distortions of the surface octahedra. Interestingly, the pattern created by the distorted octahedra is reversed compared to the flat configurations. In the metallic phase the octahedra $Oct_{A,B}$ contract only slightly by 0.8 % but $Oct_{C,D}$ by 1.5 %. In the insulating phase the volume changes are more pronounced as $Oct_{A,B}$ expand by 2.3 % (2.7 %) for the DFT-D3 with $U - J = 4\,\text{eV}$ (HSE06) calculation while $Oct_{C,D}$ contract by 4.7 % (5.0 %) respectively.

These structural changes can be explained by the charge transfer mechanism which is covered in detail in the following section 7.3.4.

7.3.4. O_2 Charge State

As mentioned before, the O_2 adsorbs as a charged superoxo (O_2^-) species on the insulating $Ca_3Ru_2O_7$ substrate. For the metallic substrate one would expect similar behaviour to stoichiometric and Ca-doped $Sr_3Ru_2O_7(001)$, described in sections 7.1.3 and 7.2.3. The metallic-insulating transition might also change the charging behaviour, and this will be elucidated in the following section for both low and high oxygen coverage. The source of the transferred charge will also be explained in more detail.

Low Coverage

Figure 7.26b shows the projected density of states of the O_2 molecule and of particular ruthenium states indicated in fig. 7.26a around the Fermi level for both the metallic and the insulating substrate. Two of the selected ruthenium atoms (Ru_X, Ru_Y) are located close to the O_2^- adsorption site while the third ruthenium (Ru_Z) is located far away.

(a) Grimme-D3, flat

(b) HSE06, flat

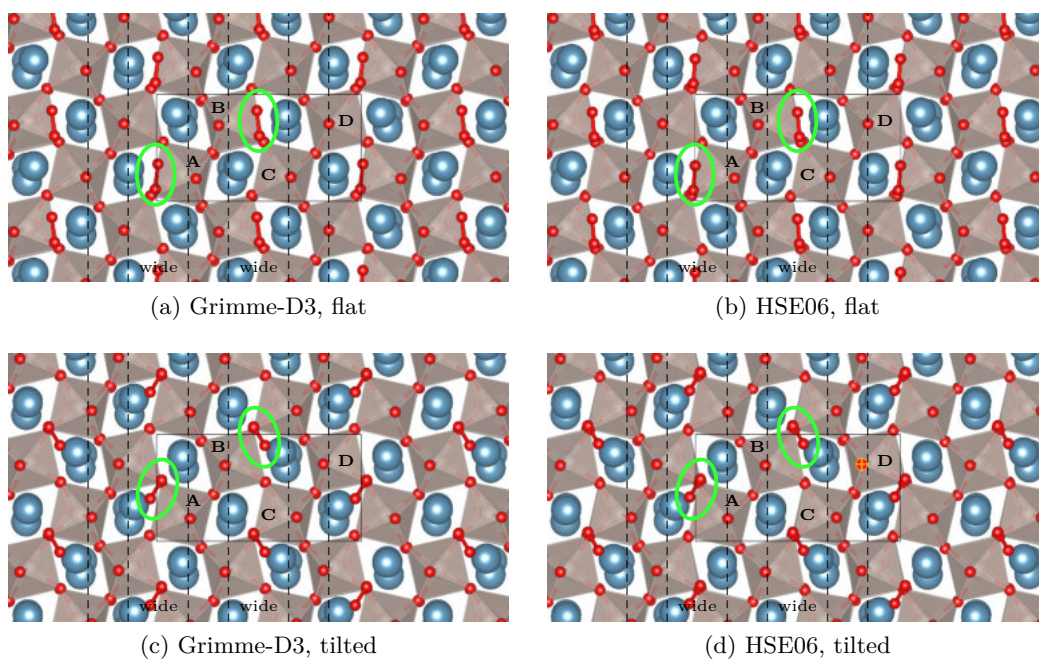(c) Grimme-D3, tilted

(d) HSE06, tilted

Figure 7.25.: Two O_2 molecules adsorbed on the (2×1) $Ca_3Ru_2O_7$ surface. Depicted are both the flat and tilted configurations calculated for the metallic (DFT-D3: (a), (c)) and for the insulating phase (HSE06: (b), (d)). The four distinct surface octahedra are labeled A-D.

275

Table 7.11.: Adsorption energy in eV per O_2 molecule on $Ca_3Ru_2O_7$ performed with the PBE functional, the DFT+D3 approach including van-der-Waals corrections, and the HSE06 functional.

$U - J$ [eV]	E_{Ads} [eV]	
PBE+U	flat	tilted
0	-0.933	-0.889
1	-0.947	-0.931
2	-0.938	-0.965
3	-0.906	-0.941
4	-0.677	-0.690
DFT-D3+U	flat	tilted
0	-1.111	-1.041
1	-1.122	-1.079
2	-1.112	-1.124
3	-1.004	-1.022
4	-0.902	-0.915
5	-0.795	-0.803
HSE06	-0.582	-0.618

In the metallic state the ruthenium d-states at these sites are very similar. In the spin up channel the occupied states are mostly located between $\approx -1.8\,\text{eV}$ and E_{Fermi}. In the spin down channel the ruthenium states are located in an energy range between $-0.8\,\text{eV}$ to $1\,\text{eV}$. Due to the interaction with the substrate, the oxygen π states are split and the additional electron is transferred into a π^*-state in the spin down channel, with lobes pointing towards the substrate, similar to the case of O_2^- adsorption on the $Sr_3Ru_2O_7(001)$ surface. In the insulating state, calculated using Grimme's DFT-D3 approach and an $U - J = 4\,\text{eV}$, the ruthenium states are split in the spin down channel, opening up the band gap, while the positions of the O_2^- π states are unchanged compared to the metallic state. One of the ruthenium atoms now shows a significantly different DOS compared to the other two: the spin up Ru_X states close to the Fermi level are shifted downwards by about $0.8\,\text{eV}$ and the filled states at the Fermi level in the spin down channel are now unoccupied. Again the electron is transferred into the lower energy part of the split O_2 adsorbate π^*-states. This indicates that in the metallic case the electron transferred into the adsorbate originates from the valence band, while in the insulating case the electron is transferred from a ruthenium atom close by. This can also be visualised by plotting the difference of the charge densities by subtracting the charge density of the pristine $Ca_3Ru_2O_7$ slab from the charge difference of the fully relaxed structure including the O_2 adsorbate, see fig. 7.27. A positive charge difference is coloured yellow while the cyan areas denote the volume lacking charge after the O_2

adsorption. The comparison of the metallic to the insulating phase shows that in both cases the O_2 molecule gains charge from the substrate, but in the metallic case the electron originates from the Fermi level. In the insulating case the negative charge difference is mostly localised at d-like states of the Ru_X atom. A small amount of charge is also transferred from other ruthenium atoms close to the adsorption site.

High Coverage

At high coverage the charging of the adsorbed O_2 molecules is also apparent in both the metallic and the insulating case. In all cases, the negatively charged O_2^- shows the familiar split of the π states in both spin channels, see fig. 7.29. A Bader charge analysis shows that the formal charge of the nearby Ca atoms is not changed from the formal $+2$ charge. The charge state of the adsorbed O_2 is also indicated in the vibrational stretching frequency $1123\,\mathrm{cm^{-1}}$ ($139\,\mathrm{meV}$) and $1100\,\mathrm{cm^{-1}}$ ($136\,\mathrm{meV}$) for the metallic and insulating case, respectively. The comparison of the ruthenium states of the pristine surface to the structure including the adsorbate shows large differences with respect to the computational approach. In all graphs the selected individual ruthenium atoms are indicated by the letters A, B and C according to fig. 7.28: Ru_A and Ru_B denote ruthenium atoms at the upper surface of the $Ca_3Ru_2O_7$ slab. The former denote Ru close to the O_2^- adsorption site and the latter Ru which are located farther from the adsorption position. The Ru_C indicate ruthenium atoms at the lower surface of the slab where no O_2 is adsorbed. While no charge is transferred from the A-site cations, those Ca close to the adsorbate are slightly polarised, as can be seen in fig. 7.30. Considering the gas phase O_2 molecule in the triplet state, the two perpendicular π^* molecular orbitals (MO) are occupied by just one electron each which results in a magnetic moment of $2\,\mathrm{\mu B}$. In the adsorbed superoxo case, the electron is transferred into the minority channel of one π^*, therefore reducing the magnetic moment of the molecule. As can be seen in fig. 7.31, the fully occupied π^* is oriented towards the surface cation while the magnetic moment of $1\,\mathrm{\mu B}$ is caused by the perpendicular half-filled π^* state.

In the case of the insulating substrate, calculated using the DFT-D3+U approach, including van-der-Waals corrections and an $U-J = 4\,\mathrm{eV}$, the DOS of the pristine surface (see fig. 7.29) shows no variance in the electronic structure of the individual ruthenium atoms. The HSE06 functional yields a similar DOS for the pristine slab. In the metallic case, the addition of the charged O_2^- shows some differences in the individual Ru states which can be attributed to the slight structural changes of the surface layer that happen after adsorption (see section 7.3.2). A slight depletion of the states of both Ru_A and Ru_B compared to the Ru_C (located at the bottom of the $Ca_3Ru_2O_7(001)$ slab) is visible due to the charge transfer to the adsorbate. In the insulating case the calculations performed with both the DFT+U approach and the hybrid functional show that the source of the charge transfer is much more localised. As is shown in fig. 7.29, after adsorption and charging of the O_2 molecule the DOS calculated with both methods show a depletion of Ru_A states in the spin down channel and a shift to lower energies in the spin up channel, suggesting that this site is the main source of the charge transferred to the O_2^-. The Ru_B states also show a slight downward shift in the spin down channel compared to the
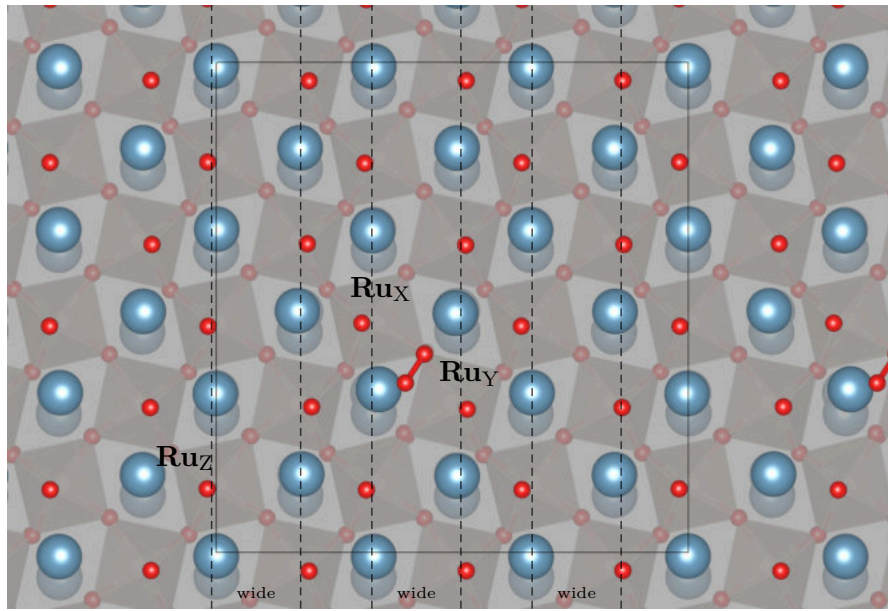
(a) O_2^- adsorbed on a (3×3) $Ca_3Ru_2O_7$ model cell
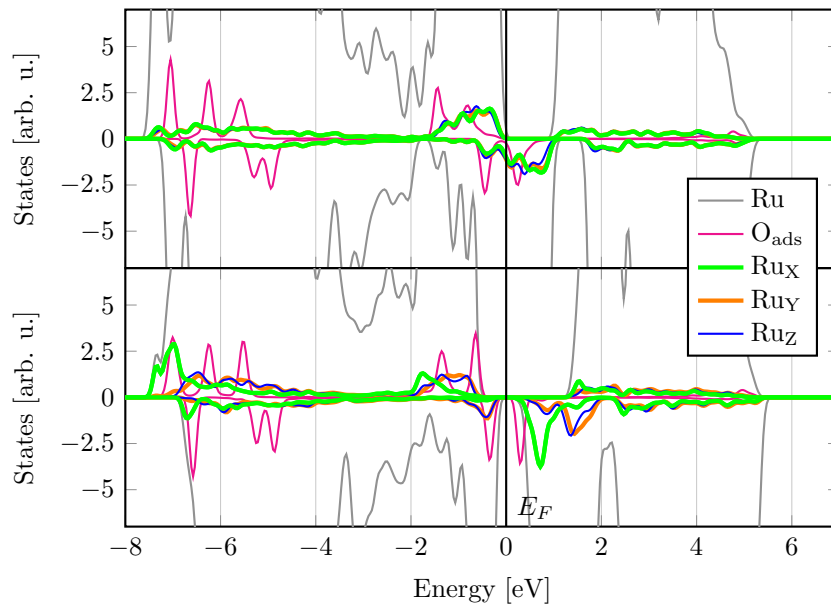
(b) Top: metallic DOS, bottom: insulating DOS

Figure 7.26.: DOS of one O_2^- adsorbed on the (3×3) $Ca_3Ru_2O_7$ model cell. Top DOS: metallic, bottom DOS: insulating substrate. The calculations were performed in the DFT-D3+U regime at $U - J = 0\,\text{eV}$ and $U - J = 4\,\text{eV}$, respectively. Compared to the Ru_Y and Ru_Z, the Ru_X show a depletion of the d-states at the Fermi level in the minority channel.

(a) metallic
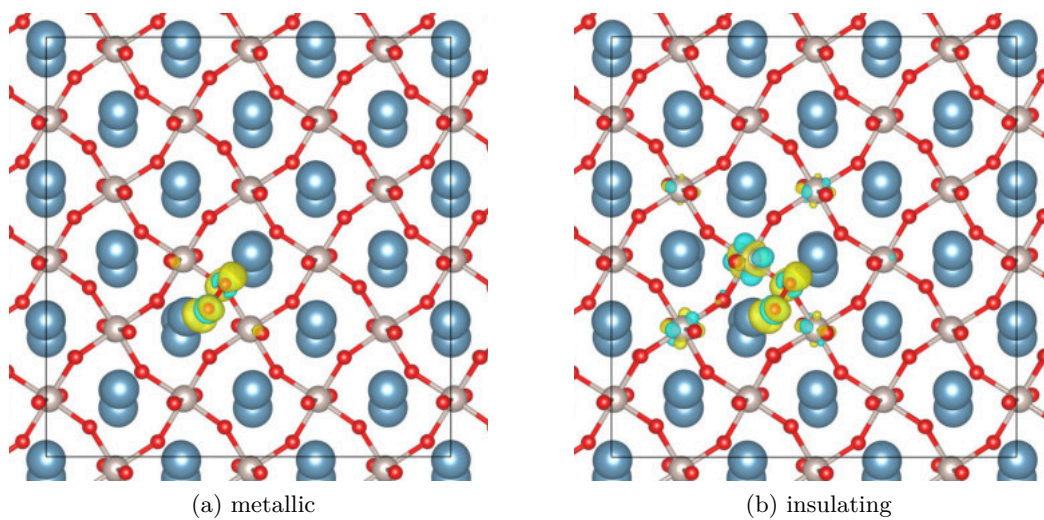
(b) insulating

Figure 7.27.: Charge difference plot of one O_2 adsorbed on the (3×3) $Ca_3Ru_2O_7$ model cell. (a) depicts the metallic, (b) the insulating case. The calculations were performed in the DFT-D3+U regime at $U - J = 0\,\mathrm{eV}$ and $U - J = 4\,\mathrm{eV}$ respectively. Yellow areas indicate additional charge transferred to the O_2. In the insulating case the more localised source of the charge is indicated by the cyan areas.

Ru$_C$ states caused by the structural distortion at the surface but next to no difference in the area below the peak.
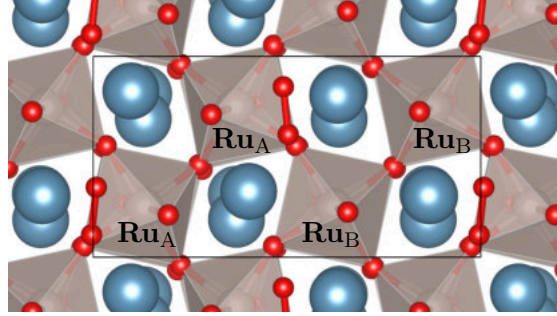
(a) 2 O$_2^-$ on the (2×1) Ca$_3$Ru$_2$O$_7$ model cell

Figure 7.28.: Sketch of the zig-zag configuration on the (2×1) model cell, indicating the different ruthenium atoms plotted in fig. 7.29. Ru$_A$ sites are located close to the adsorbed O$_2^-$ molecules, Ru$_B$ in between. Ru$_C$ are located at the bottom of the slab.

G_0W_0 **Densities of States**

The densities of states were also calculated in the advanced many-body GW approximation since this approach should give an improved description of the quasi-particle energies. As a first benchmark, the DOS of the Ca$_3$Ru$_2$O$_7$ bulk was evaluated using a single-shot G_0W_0 approach. Depending on whether the G_0W_0 calculation is started from the metallic or insulating state, the resulting DOS of the slab is also metallic or insulating, respectively, as shown in fig. 7.32. To calculate a proper insulating wave-function a PBE+U ($U - J = 4.5$ eV) calculation was done initially since lower values of U lead to a half-metallic system in the single-shot G_0W_0. Starting from these pre-calculated orbitals the many-electron G_0W_0 calculation yields an insulating system with a band gap of 1.21 eV. As a comparison, the hybrid HSE06 functional yields a band gap of 1.275 eV for the Ca$_3$Ru$_2$O$_7$ bulk.

For the pristine slab the many-body G_0W_0 calculation yields similar results for the band gap compared to the bulk calculations, where it was shown that the choice of initial wave function is essential to reach the desired metallic or insulating phase. Here, to generate the insulating wave function, an $U - J$ value of 4.5 eV for the initial PBE+U calculation was sufficient, yielding a band gap of almost 2 eV, much larger than for the bulk (see fig. 7.33). For an initial wave function generated with an $U - J = 4$ eV the pristine Ca$_3$Ru$_2$O$_7$ slab still shows metallic behaviour as there are still some partially filled Ru d states at the Fermi edge.

In the G_0W_0 DOS of the (2×1) model cell including the O$_2^-$ adsorbate (fig. 7.34) shows the decisive difference to the DOS calculated both with standard DFT-D3 and the hybrid HSE06 functional. Starting from an initial metallic wave function, the projected states
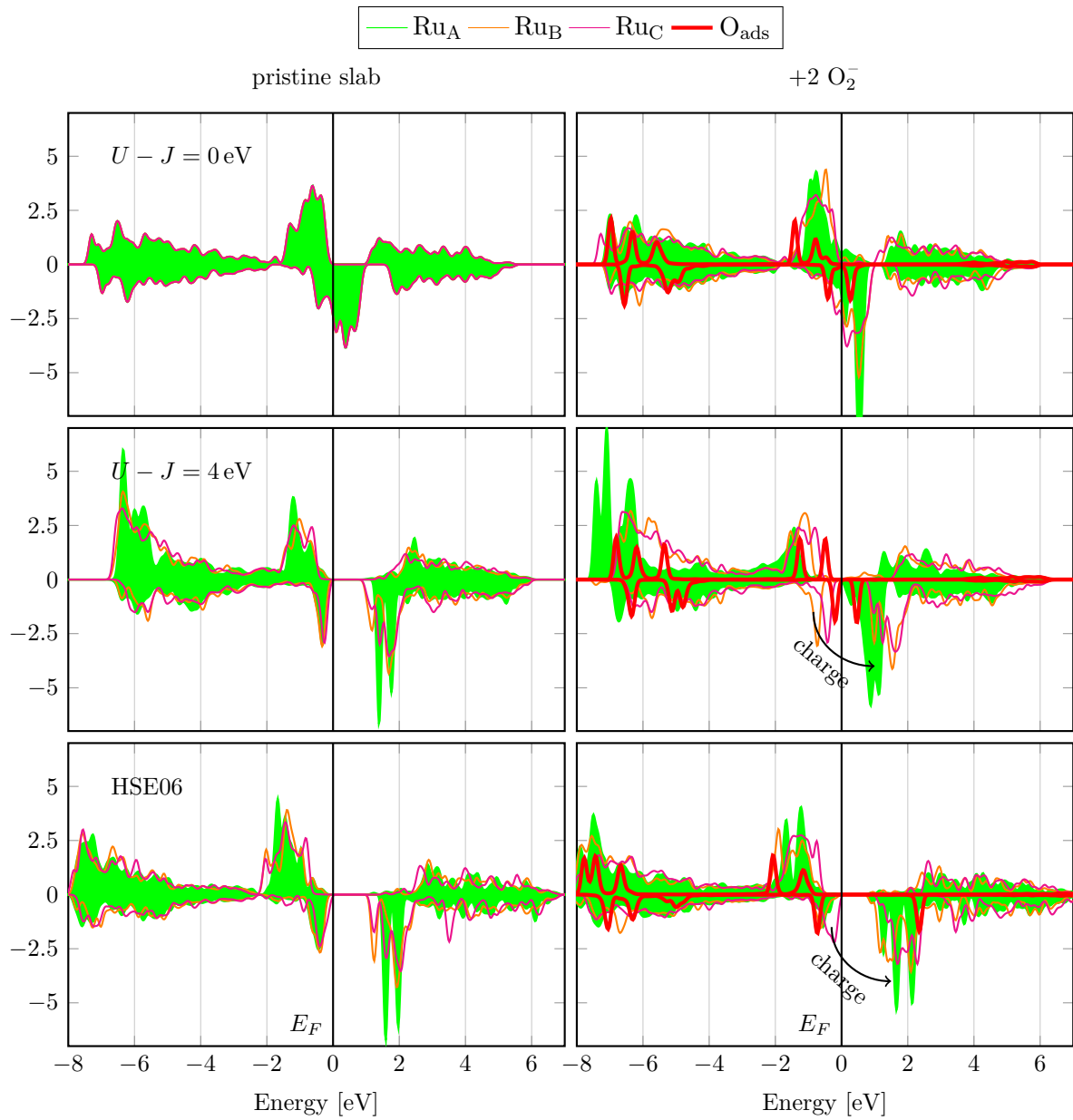
Figure 7.29.: Left: DOS of the pristine (2×1) slab, Right: DOS of the (2×1) $Ca_3Ru_2O_7$ model cell with two O_2^- adsorbed. Ru_A which are the source of most of the charge in green, remaining surface Ru_B states are coloured orange. Ru_C denote the Ru at the clean bottom side of the slab, see fig. 7.28 for the labelling convention. The calculations were performed in the DFT-D3+U regime at $U - J = 0\,eV$ and $U - J = 4\,eV$ respectively and with the HSE06 functional.
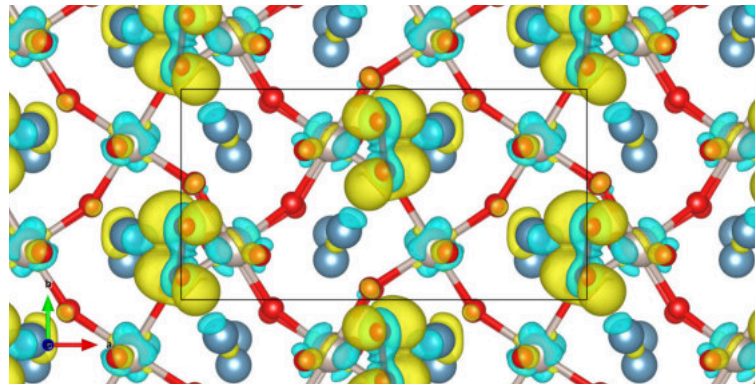
(a) metallic
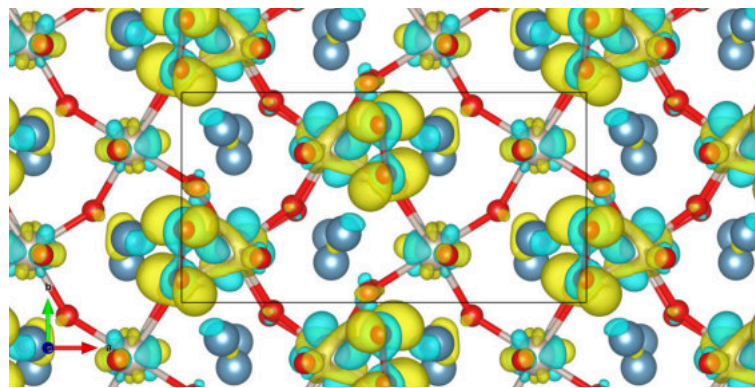
(b) insulating, DFT+U, $U - J = 4\,\text{eV}$
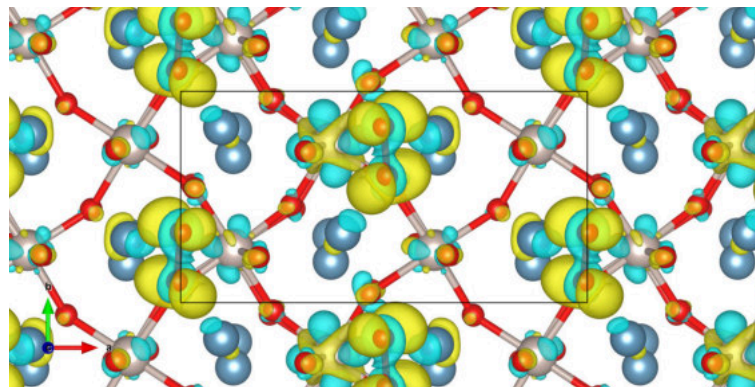
(c) insulating, HSE06
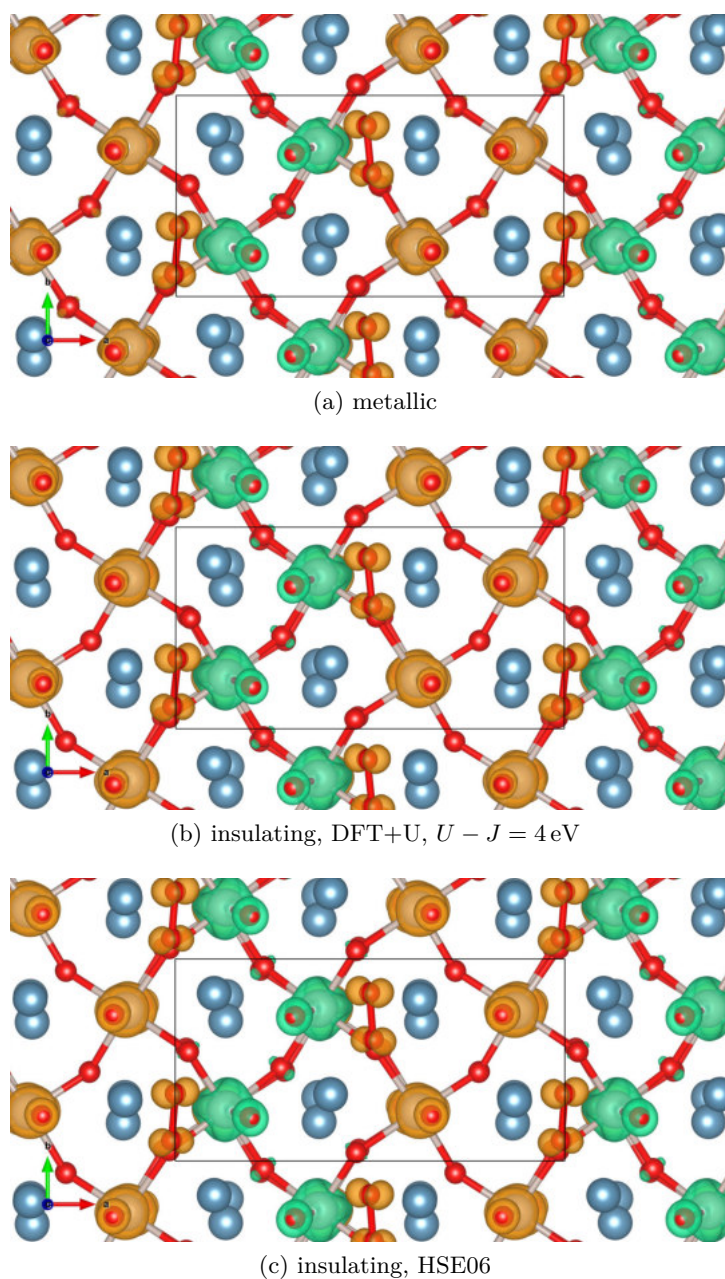
Figure 7.30.: Charge difference plot of one O_2^- adsorbed on the (2×1) $\text{Ca}_3\text{Ru}_2\text{O}_7$ model cell. (a) depicts the metallic, (b) and (c) the insulating case. The calculations were performed in the DFT-D3+U regime at $U - J = 0\,\text{eV}$ and $U - J = 4\,\text{eV}$ respectively and with the HSE06 functional. Charge is transferred from the cyan Ru d states of the substrate to π-like states of the O_2^-, indicated in yellow.

282

(a) metallic

(b) insulating, DFT+U, $U - J = 4\,\mathrm{eV}$

(c) insulating, HSE06

Figure 7.31.: Magnetisation density plot of one O_2^- adsorbed on the (2×1) $Ca_3Ru_2O_7$ model cell. (a) depicts the metallic, (b) and (c) the insulating case. The calculations were performed in the DFT-D3+U regime at $U - J = 0\,\mathrm{eV}$ and $U - J = 4\,\mathrm{eV}$ respectively and with the HSE06 functional. The charged O_2^- state is well visible in the positive magnetisation density at the O atoms, indicated by a π-orbital-shaped volume coloured in orange. The electron transferred from the substrate occupies the second perpendicular π state where the magnetic moment vanishes. The green volume around the Ru atoms indicates negative spin density (see section 7.3.5).
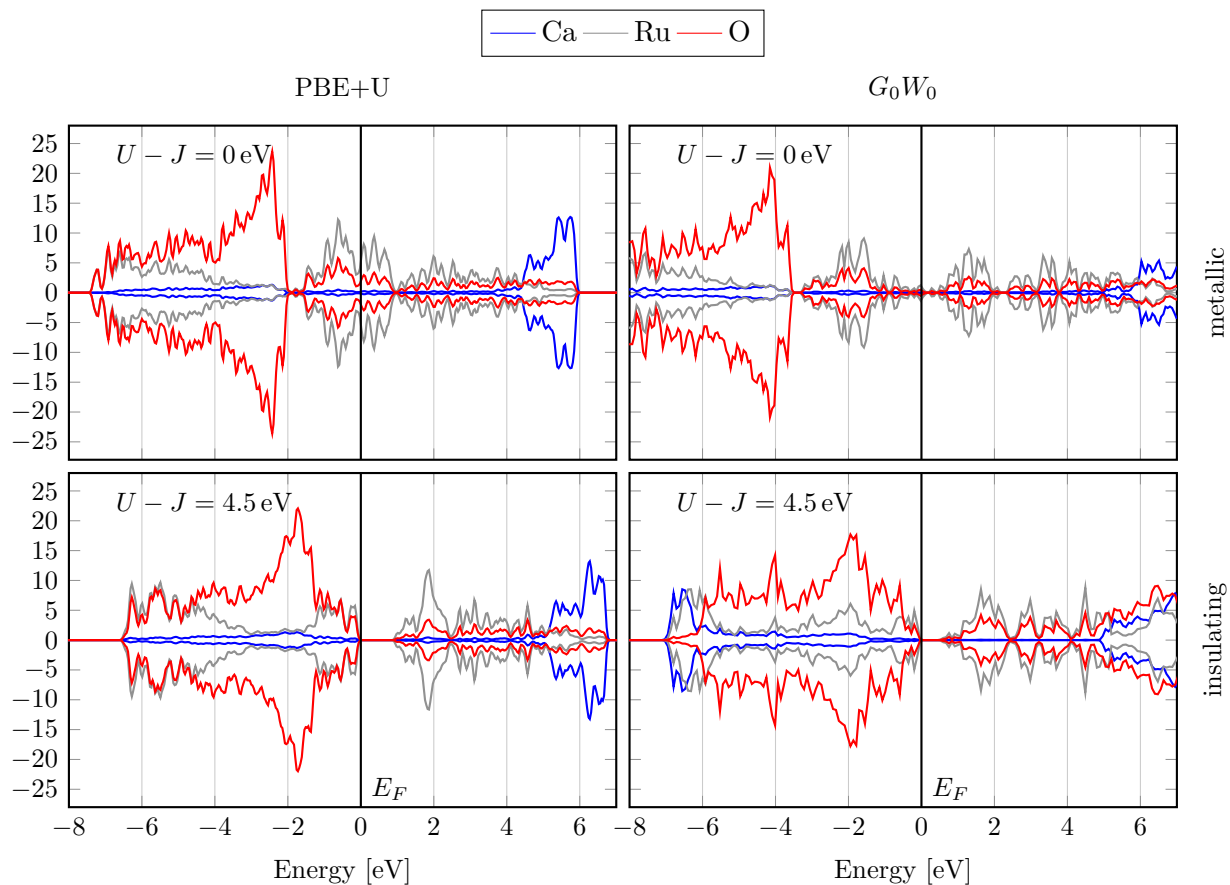
283

Figure 7.32.: DOS of bulk $Ca_3Ru_2O_7$, calculated with the PBE+U (left column) and the G_0W_0 (right column) approaches. To yield the metallic or insulating ground state for the G_0W_0 calculations the initial wave function was generated using the PBE functional at $U - J = 0\,\mathrm{eV}$ and $U - J = 4.5\,\mathrm{eV}$, respectively.
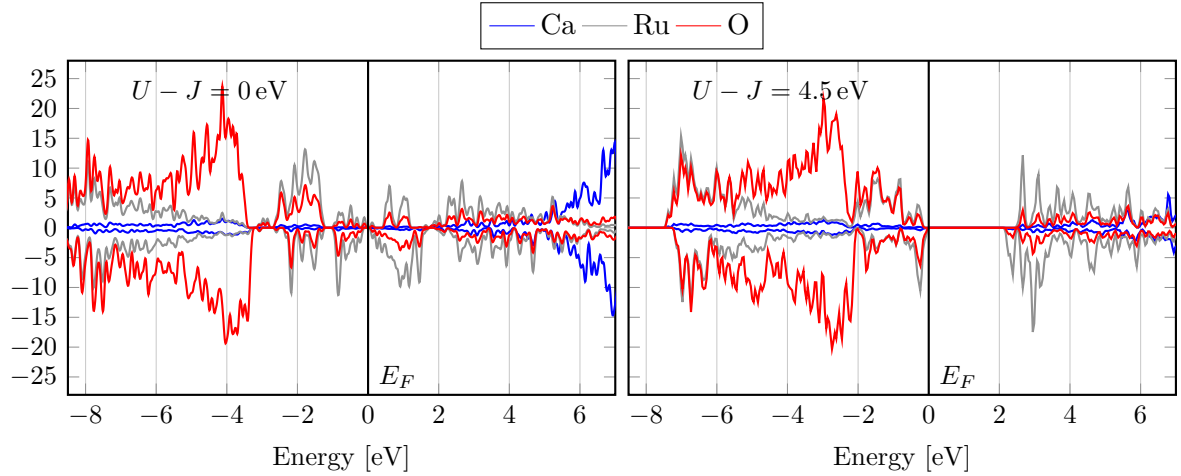
Figure 7.33.: DOS of the (2×1) $Ca_3Ru_2O_7$ substrate model, calculated in the G_0W_0 approach. The initial wave function was generated using the PBE functional at $U - J = 0\,eV$ for the metallic state and $U - J = 4.5\,eV$ for the insulating state.

of the substrate are not much different from the pristine substrate case. However, the unoccupied antibonding π^* states of the O_2^- adsorbate are shifted to higher energies compared to the DFT calculation, increasing its HOMO-LUMO gap to about $1.7\,eV$ from the PBE value of $0.7\,eV$. The DOS obtained from a single-shot G_0W_0 calculation starting from an initial wave function obtained from a DFT+U calculation with $U - J = 4\,eV$ does not show a completely insulating state of the substrate. Here there are still a few Ru d states at the Fermi level. Increasing $U - J$ to $4.5\,eV$ finally lead to an insulating solution with a band gap for the substrate of about $1\,eV$. The π states of the adsorbate are now more localised and show a much larger shift than for the metallic case, increasing the HOMO-LUMO gap of the O_2^- further to about $3.4\,eV$. To determine the validity of the obtained HOMO-LUMO gap another single-shot G_0W_0 calculation was done with a $(U - J)_{Ru} = 4.5\,eV$ applied to the ruthenium d states and an additional $(U - J)_{O_{ads}} = 6\,eV$ applied to the π states of the adsorbed oxygen. As is shown in the lower right panel of fig. 7.34, the substrate again shows a few Ru d states at the Fermi level. The bonding π states of the O_2^- are broadened compared to the previous calculations, but the HOMO-LUMO gap of the adsorbate is just slightly increased.

7.3.5. Magnetic Order

In sections 5.3.3 and 5.5.4 the magnetic order of the $Ca_3Ru_2O_7$ bulk and surface was described. While the energy differences between the various magnetic configurations are small, they can play a role in the calculation of the adsorption energy, especially in the insulating case. The adsorption energy was therefore calculated for the (2×1) model cell in a two double-layer configuration with two O_2 molecules in the zig-zag con-
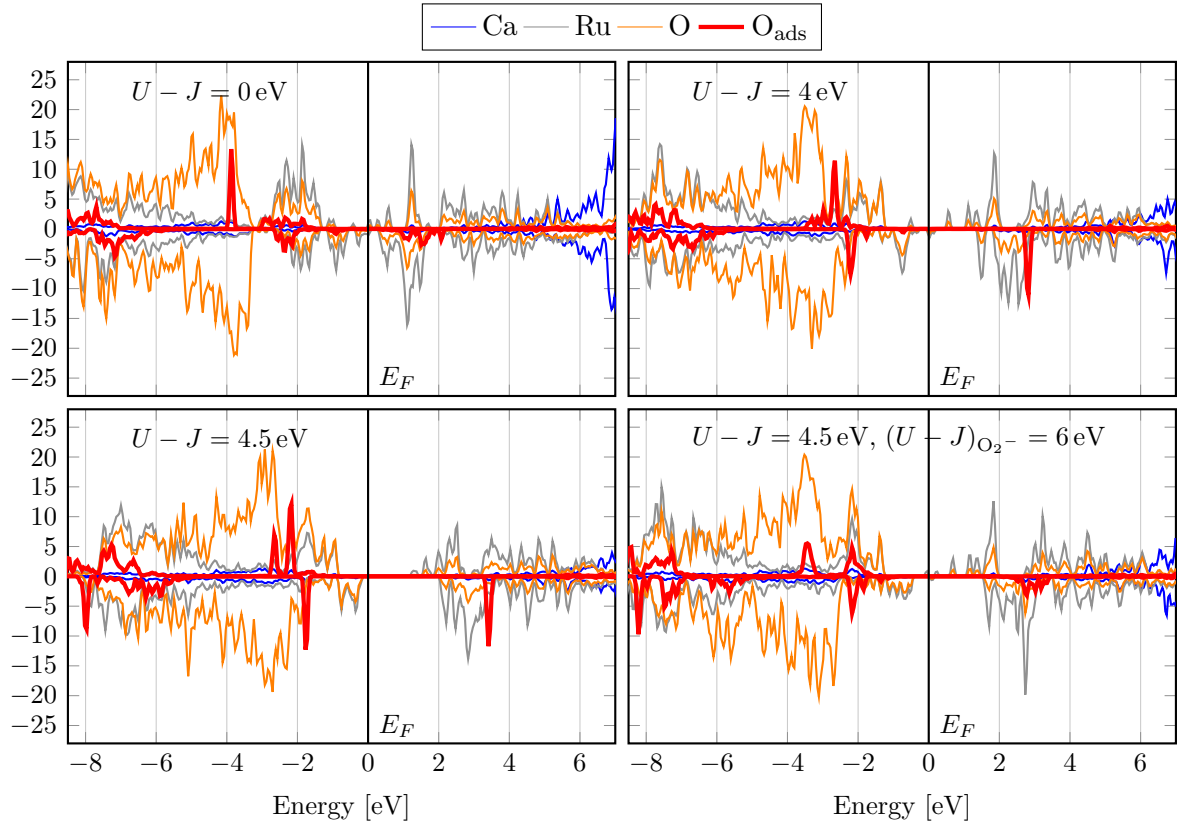
Figure 7.34.: G_0W_0 DOS of the (2×1) $Ca_3Ru_2O_7$ model with two adsorbed O_2^-. The initial wave function was generated using the PBE functional at $U - J = 0\,eV$ for the metallic state (top left), $U - J = 4\,eV$ (top right) and $U - J = 4.5\,eV$ for the insulating state. For the bottom right plot an additional $U - J = 6\,eV$ was added to the π-states of the adsorbed O_2^-.

286

figuration which was completely relaxed using the van-der-Waals corrected GrimmeD3 functional. Like for the slab calculations discussed in section 5.5.4 the magnetic moments in the "lower" layer were set to ferromagnetic coupling in the layer plane and the "upper" $Ca_3Ru_2O_7$ layer was coupled antiferromagnetically. Then either one or two selected spins located at the Ru atoms of the surface layer were flipped with respect to the direction of the moments of the surface layer, yielding two additional surface configurations, shown in fig. 7.35: "1flip" and "2flip". The "2flip" state corresponds to the ground state configuration described in section 5.5.4. As the adsorbed O_2 molecules also show a remaining magnetic moment of $1\,\mu B$ they can, too, couple ferro- or antiferromagnetically to the substrate, giving rise to two more magnetic states. For ferromagnetic coupling $(O_{2,FM})$ the magnetic moments of the molecule and the surface double layer are all aligned in the same direction, for the $O_{2,AFM}$ configuration the spins of the adsorbates are flipped with respect to this surface double layer.

Table 7.12 shows the difference of the total energies of the various magnetic configurations with respect to the ground state. For the metallic substrate, the DFT calculations predict ferromagnetic coupling both between the O_2 adsorbate and the substrate and of the ruthenium atoms within the $Ca_3Ru_2O_7$ double layer. For the insulating substrate, calculated by adding a Hubbard U parameter to the ruthenium d states of $4\,eV$, still ferromagnetic coupling between adsorbate and substrate is predicted. Additionally, in the ground state the ruthenium spins next to the adsorbates flip, showing antiferromagnetic coupling to the other surface ruthenium atoms. Antiferromagnetic coupling of the O_2 molecule to the "2flip" configuration is $26\,meV$ less favourable. Figure 7.35 shows an illustration of the different magnetic configurations.

Table 7.12.: Total energy differences in meV between different magnetic configurations of the two O_2^- adsorbed on the (2×1) $Ca_3Ru_2O_7(001)$ model cell. The AFM-coupled "1flip" configuration could not be stabilised.

ΔE [meV]	DFT-D3	DFT-D3, $U - J = 4\,eV$
$O_{2,AFM}$	358	85
$O_{2,FM}$	0	92
1flip, $O_{2,AFM}$		87
1flip, $O_{2,FM}$	210	98
2flip, $O_{2,AFM}$	349	26
2flip, $O_{2,FM}$	500	0

7.3.6. RPA Calculations

As described in the previous sections, the adsorption energies can differ greatly between different computational approaches. While the DFT+U calculations are computationally efficient and properly describe the metallic phase of $Ca_3Ru_2O_7$, the correct choice

(a) O_2^- FM

(b) O_2^- AFM

(c) O_2^- FM, 1 RuO$_6$ flipped

(d) O_2^- AFM, 1 RuO$_6$ flipped

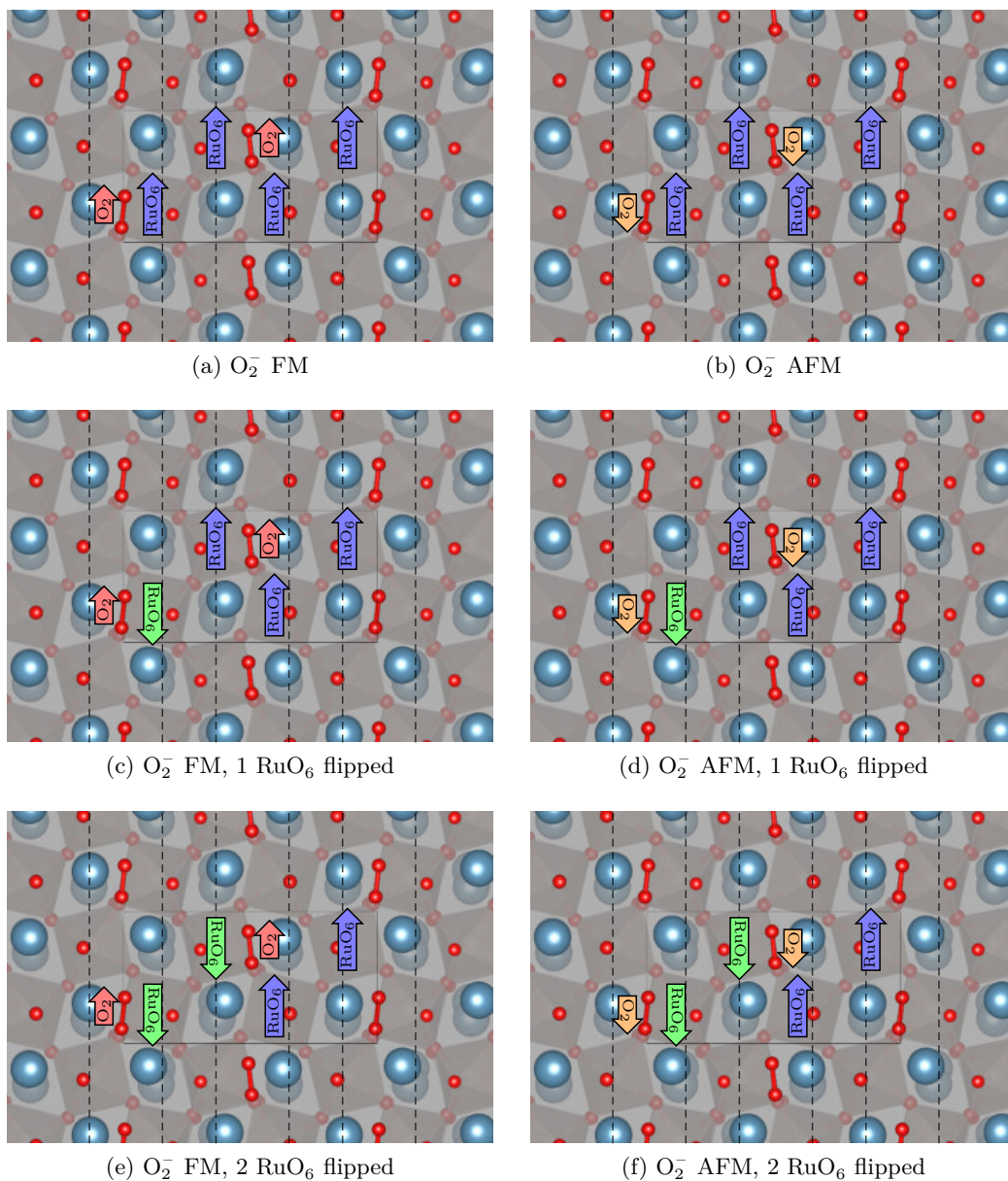(e) O_2^- FM, 2 RuO$_6$ flipped

(f) O_2^- AFM, 2 RuO$_6$ flipped

Figure 7.35.: Left column: ferromagnetic (FM) coupling between O_2^- and substrate, right column: antiferromagnetic (AFM) coupling. The magnetic moment of none, one, or two Ru atoms close to the adsorbate can be flipped with respect to the rest of the slabs Ru moments, as shown in the top, middle, and bottom rows, respectively.

of the Hubbard U parameter heavily influences the calculated band gaps and adsorption energies for the insulating phase. Likewise, the position of the antibonding oxygen π^* state is too close to the fermi level, resulting in the overestimation of the adsorption energy. The HSE06 hybrid functional on the other hand captures the insulating state properly even though the band gap is much larger as experimentally found. The adsorption energy on the other hand is much closer to the experimental value.

To overcome the deficiencies of the previously mentioned methods, the random phase approximation (RPA) and the G_0W_0 approach were used as benchmarks to calculate adsorption energies and the densities of states. Since the computational effort is more than two orders of magnitude greater than for the hybrid calculations, the RPA adsorption energies were only calculated for pre-relaxed (2×1) structures. As for the technical details, the GW energy cutoff[4] was set to $200\,\text{eV}$ and the number of ω points[5] which are used to evaluate the integration over ω was set to 20, ensuring convergence of the correlation energy. All calculations were based upon PBE wave functions and therefore the metallic phase of $Ca_3Ru_2O_7$.

Since the calculation of forces in the RPA is computationally too expensive considering the size of the model cell the RPA total energy was calculated for structures that were pre-relaxed using the standard DFT and hybrid functionals, resulting from the calculations described in sections 7.3.2 and 7.3.3. This was done for both the substrate reference and the $(2 \times 1)+2O_2$ model cell and the adsorption energy was then referenced to the most favoured substrate structure.

The advanced many-electron calculations do not change the electronic state of the substrate: starting from a metallic wave-function the many-body result is still metallic while an insulating initial wave-function also results in an insulating state. This insulating result can be achieved by starting from DFT+U or HSE06 initial wave-functions. Here, the initial insulating wave-functions were created by tuning the band gap by adding the on-site term to both the ruthenium d-states and the π-states of the adsorbed O_2. Otherwise the hybridised states of the O_2^- and ruthenium in the spin down channel would stay right above the fermi edge, resulting in a half-metallic solution.

$Ca_3Ru_2O_7$ Substrate

The comparison of the RPA total energies of the pristine surface structure shows that the various DFT and hybrid approaches lead to quite high total energy differences. Table 7.13 shows that the most favoured surface structure is the one relaxed using the PBE functional. Changing the magnetic order in the surface (see section 7.3.5) without further relaxation incurs an energy penalty of $280\,\text{meV}$ (PBE) and $358\,\text{meV}$ (RPA). Relaxation of the substrate structure using the optB86b functional results in a similar structure, but the magnetic order is switched so that the so-called "2flip" order is more favourable. Interestingly the structures calculated in the insulating phase are much less favoured in the RPA, especially the one relaxed with the hybrid HSE06 functional which

---

[4]VASP setting: ENCUTGW.
[5]VASP setting: NOMEGA.

is almost $1\,\mathrm{eV}$ disfavoured.

Table 7.13.: RPA energy differences in eV of the (2×1) $\mathrm{Ca_3Ru_2O_7}$ substrate reference slab pre-relaxed using the indicated DFT and hybrid approaches. The most favoured configuration was found for the ferromagnetic solution relaxed with the PBE functional.

Configuration	$E_{\mathrm{Ads,PBE}}$	$E_{\mathrm{Ads,RPA}}$
HSE06		
FM	0.898	0.956
2flip	0.912	1.112
DFT-D3+U, $U - J = 4\,\mathrm{eV}$		
FM	0.278	0.336
2flip	0.435	0.604
optB86b		
FM	0.290	0.403
2flip	0.051	0.039
PBE		
FM	0.000	0.000
2flip	0.280	0.358

RPA Adsorption Energies

To find the ground state structure in the RPA the same procedure was performed for the (2×1) model structures with the adsorbed $\mathrm{O_2^-}$, pre-relaxed using the aforementioned DFT and hybrid approaches. Due to the aforementioned computational effort the RPA total energy was calculated for only a selection of these structures. As can be seen in table 7.14 the adsorption energies calculated in the RPA are generally much lower than the DFT results shown in tables 7.8 and 7.11 for both the metallic and the insulating phase. One important contribution lies in the incorrect description of the unoccupied states of the $\mathrm{O_2}$ molecule in standard DFT, resulting in easier charging thereof. The HOMO-LUMO gap of the adsorbate is just $0.70\,\mathrm{eV}$ in standard DFT calculations, employing the HSE06 hybrid functional increases that to $3.10\,\mathrm{eV}$. The densities of states calculated with the G_0W_0 approach show that these advanced many-body methods alleviate this problem and increase the HOMO-LUMO gap of the $\mathrm{O_2}$ to about $1.70\,\mathrm{eV}$. The RPA confirms the standard DFT results that the $\mathrm{O_2}$ molecule adsorbs much more favourably on the bright lines of the $\mathrm{Ca_3Ru_2O_7}$ substrate, reflected in the very low adsorption energy of $149\,\mathrm{meV}$ at the dark lines. Also, in both the metallic and the insulating phase, the flat configuration is more favoured than the tilted configuration which was found to be more stable in the insulating phase using van-der-Waals corrected DFT. The RPA results also

predict a preference for the same magnetic order as the optB86b calculations: ferromagnetic coupling of all ruthenium spins in the slab is less favoured by 73 meV compared to the flipping of two spins below the O_2 molecules. The flat adsorption configuration on the bright substrate lines is the most favoured adsorption configuration where the model cell relaxed using the optB86b functional exhibits an RPA adsorption energy of 723 meV. The same arrangement of the O_2^- relaxed with the DFT-D3 approach yields a slightly lower RPA adsorption energy of 650 meV. As expected, the structures exhibiting distortions of the substrate due to the transition to the insulating phase yield a lower RPA adsorption energy of 480 meV and 359 meV for the DFT-D3+U, $U - J = 4$ eV, and the HSE06 approaches, respectively. This pattern persists for the tilted adsorption configuration which are even more disfavoured. Additionally, the RPA results suggest that the strong distortion of the octahedra yielded by the HSE06 functional are an artefact of this functional.

Comparing the adsorption energies calculated using the hybrid HSE06 functional (0.58 eV) to the DFT values (1.19 eV) would suggest that structural changes or the metallic-insulating phase transition would be the cause. Nevertheless, the structural differences between these structures are very small. As mentioned before, the size of the HOMO-LUMO gap of the adsorbate change by a large amount depending on the computational method used. Due to the charge transfer into the O_2^-, the electron affinity, which describes the cost to add an additional electron into the molecule, changes. Rienstra-Kiracofe et al. [204] have shown that standard DFT strongly overestimates the electron affinity of molecular O_2 compared to hybrid approaches which artificially increases the DFT adsorption energies. Although, while HSE06 now better describes the electron affinity, the polarisability of the O_2 adsorbate and the size of the substrate band gap are not well described. The RPA approach alleviates these problem by properly accounting for both the band gaps (see section 7.3.4) and the van-der-Waals contributions to the adsorption energies.

7.3.7. Core level Shifts

The core level shifts of the O_2^- adsorbate were calculated in both the initial and final state approximation, as explained in earlier chapters. To cover both the metallic and the insulating (or bad-metallic state) of the substrate Grimme's DFT-D3+U approach combined with a $U - J = 4$ eV was used. XPS measurements have shown that at saturation coverage O $1s$ peak of the O_2^- has a binding energy of 532.6 eV and the O $1s$ peak of the substrate at 529.2 eV binding energy, resulting in a shift of 3.4 eV. Neutral O_2 shows O $1s$ binding energies between 536 eV and 538 eV [200, 201], therefore the adsorbed species was determined to be a charged superoxo species.

The calculations show that in the initial state approximation the charged O_2^- species shows a chemical shift of 1.3 eV (1.6 eV) for the metallic (insulating) phase towards higher binding energies, a much smaller shift than in the experiment [6]. Again this can be attributed to the large underestimation of binding energies in the initial state approximation. The final state approximation unfortunately does not yield a better results (0.4 eV), since the excited electron is transferred into antibonding π^*-state the

Table 7.14.: Adsorption energies per O_2^- molecule of the (2×1) high coverage model structure calculated in the RPA, starting from a metallic PBE wave function. The structures were pre-relaxed with functionals indicated in the first column. In all cases the magnetic ground state indicated by the DFT calculations was chosen as starting configuration for the RPA. For the flat, optB86b-relaxed structure, ferromagnetic coupling yields lower stability in the RPA as well.

Configuration	E_{Ads} [eV]
Dark, optB86b	-0.149
Tilted, Grimme-D3, $U - J = 0\,\text{eV}$	-0.621
Tilted, Grimme-D3, $U - J = 4\,\text{eV}$	-0.419
Tilted, HSE06	-0.110
Flat, Grimme-D3, $U - J = 0\,\text{eV}$	-0.687
Flat, Grimme-D3, $U - J = 4\,\text{eV}$	-0.480
Flat, HSE06	-0.359
Flat, optB86b, FM	-0.650
Flat, optB86b, AFM	-0.723

adsorbate, creating an O_2^{2-}. This additional charging effect, well visible in the projected DOS of the adsorbate (see fig. 7.36), leads to an over screening and therefore a too high total energy of the excited system, resulting in a large underestimation of the O $1s$ binding energies of the adsorbate. The bulk O $1s$ states are captured well and are comparable to the H_2O adsorption case discussed in section 6.4.5.
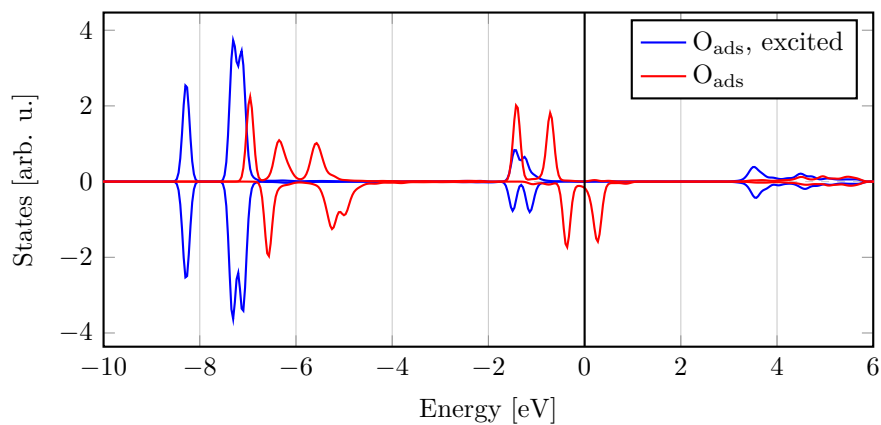
(a) $O_2/Ca_3Ru_2O_7$, metallic substrate
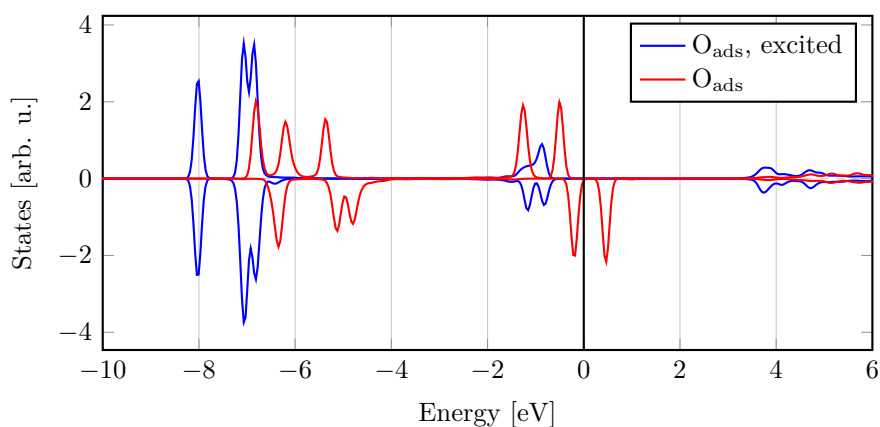
(b) $O_2/Ca_3Ru_2O_7$, insulating substrate

Figure 7.36.: DOS of the (a) metallic and (b) insulating high coverage structure. The O $1s$ electron of one oxygen atom (blue) of the O_2^- is excited and transferred into the valence band, creating an O_2^{2-}.

7.4. Summary

The simulations again have proven that DFT is a very good tool to study adsorption behaviour on complex surfaces. Nevertheless, some effects are not properly captured, requiring the use of more advanced methods like hybrid functionals or many-body approaches. In the present case, it could be shown that oxygen adsorbs molecularly as a superoxo on both $Sr_3Ru_2O_7(001)$ and $Ca_3Ru_2O_7(001)$ surfaces. In the low coverage case, DFT predicts adsorption at Cation-Cation bridges for both the $Sr_3Ru_2O_7(001)$ and $Ca_3Ru_2O_7(001)$ surfaces. The shorter lattice constant of $Ca_3Ru_2O_7$ leads to a displacement from the idealised Ca–Ca bridge position and the O_2^- molecule is located between surface cation and an apical oxygen of a RuO_6 octahedron. The calculated van-der-Waals corrected adsorption energies are quite high at around $-1.4\,eV$ for both oxides. Doping the $Sr_3Ru_2O_7$ surface with calcium atom further increases its reactivity, yielding an adsorption energy of about $-1.5\,eV$. At high coverage, the adsorption energy decreases to $-1.00\,eV$ and $-1.16\,eV$ for $Sr_3Ru_2O_7$ and $Ca_3Ru_2O_7$, respectively. The experimentally found zig-zag structure of the adsorbed O_2 molecules on $Ca_3Ru_2O_7$ was well reproduced in STM simulations. Since $Ca_3Ru_2O_7$ shows a metallic-insulating transition at $48\,K$, the influence of this transition on O_2 adsorption behaviour was studied. At the DFT+U level, the dependence of the adsorption energy on the gap is small at values of U that yield a band gap close to the experimental value. At higher value of U and therefore much larger band gaps the adsorption energy is greatly reduced. The HSE06 calculation also yields a much lower adsorption energy of $-0.58\,eV$ but a way too large band gap. The metallic-insulating transition introduces distortions of the surface octahedra: the larger the gap, the larger is the contraction of the octahedra right next to the adsorbate, up to $5\,\%$ for the HSE06 calculations. The origin of the charge transfer is localised at the Ru of the same contracted octahedra, well visible in the charge difference plots. On the other hand, for the metallic substrate phase the electron transferred to the O_2^- originates from the valence band of the metallic substrate.

The charge transfer is mainly driven by the electronic state of the substrate, as the comparison with the earlier mentioned adsorption studies on La_2NiO_4 [199] and $SrTiO_3$ [198] shows. The surface of both the strontium titanate and strontium ruthenate are SrO terminated at virtually identical lattice constants. The DFT results presented in the current study predict superoxo adsorption only on the ruthenate surface, while Staykov et al. [198] report adsorption of a neutral O_2 molecule on the pristine $SrTiO_3$ surface. A charged O_2^- is only predicted for defective $SrTiO_3$ surfaces. Additionally, the comparison of the studied $Ca_3Ru_2O_7$ case with the La_2NiO_4 [199] shows that the structural flexibility of the substrate does not drive the charge transfer, since for the nickelate the charge is transferred from the lanthanum ions, leading to the adsorption of O_2 as a superoxo or a peroxo species, dependent on the adsorption site. For both ruthenates, a Bader charge analysis shows that the surface cations do not gain or lose charge and just some polarisation due to the nearby adsorbate is found. Therefore, in contrast to the nickelate where the charge is transferred from the A-site cation, for both ruthenates the energetic levels of the B-site ion govern the charging mechanism.

Additionally, the presented adsorption studies indicate shortcomings of standard DFT with respect to the description of certain properties of these complex materials. While the charge transfer mechanism is captured by standard DFT, an accurate representation of structural and electronic properties is only given at a higher level of theory. This is especially apparent in the calculated adsorption energy of the charged O_2^- since several contributions have to be taken into account. Comparing the PBE and PBE+U ($U - J = 4\,\text{eV}$) results (see table 7.11), modelling the electronic phase transition to the insulating substrate, the common overestimation of the polarisability of the surface contributes about $0.2\,\text{eV}$ to the adsorption energy. Including van-der-Waals corrections to the calculations contribute a similar amount (see table 7.8). Finally, the HOMO-LUMO gap of the adsorbed O_2^- is underestimated in both standard and van-der-Waals corrected DFT, causing an underestimation of the adsorption energy. The electron affinity, defined as the cost of adding an additional electron to the structure, of the gas phase O_2 differs depending on the level of theory. Comparing advanced quantum chemical CCSD(T) [205] calculations to the PBE and HSE06 results reported in this work show a difference of about $0.15\,\text{eV}$, close to the difference of the calculated adsorption energies yielded by the PBE and HSE06 functionals. Additionally, the predicted value heavily depends on the correct choice of the basis set. For the O_2^- adsorbed on $Ca_3Ru_2O_7(001)$ and $Sr_3Ru_2O_7(001)$ surfaces this was confirmed by high level hybrid calculations with the HSE06 functional and the use of the many-electron RPA approach which yields a more accurate description of all previously mentioned factors. Here, the HOMO-LUMO gap of the adsorbate is properly described in the G_0W_0 framework and the calculations predict adsorption energies of $-1.00\,\text{eV}$ for $Sr_3Ru_2O_7$ at ¼ and $-0.69\,\text{eV}$ for $Ca_3Ru_2O_7$ at ½ ML coverage, respectively. For $Ca_3Ru_2O_7$, this agrees much better to the experiment. The O_2^- charge state also influences the evaluation of the core level shifts. While the initial state calculation correctly shows a core level shift of the O 1s states of the adsorbate to higher binding energies, this is not the case for the final state approximation. Here an electron is excited but directly transferred to the unoccupied π^* orbital, creating a peroxo adsorbate and the resulting over screening leads to large artefacts in the predicted O 1s binding energies. A combined experimental and theoretical academic paper detailing the discussed O_2^- adsorption studies on $Ca_3Ru_2O_7(001)$ was published by Halwidl, Mayr-Schmölzer, et al. [6]. Recently, a theoretical paper regarding O_2^- adsorption on pure and Ca-doped $Sr_3Ru_2O_7(001)$ surfaces was submitted by Mayr-Schmölzer et al. [8].

8. Adsorption of CO on (001) Ca$_3$Ru$_2$O$_7$

8.1. Introduction

The studies presented in the previous chapters showed that both H$_2$O and O$_2$ adsorb at O–O bridge sites on the (001) surface. This is not the case for CO: Stöger et al. [179] have shown that on Sr$_3$Ru$_2$O$_7$(001), CO first adsorbs weakly in a precursor state above an apical surface oxygen at 78 K with a calculated (PBE) adsorption energy of -0.66 eV. Heating the sample to 100 K activate the CO molecule and transforms it into a strongly (PBE: -2.17 eV) bound metal carboxylate by breaking the Ru–O bond and forming a Ru–C bond. The Ru–OCO carboxylate is bent with an O–C–O angle of 118.7° and the two oxygen atoms point towards Sr–Sr bridge sites. This surface carboxylate is able to rotate by 90° around its C atom due to the high symmetry of the Sr$_3$Ru$_2$O$_7$(001) surface. DFT calculations show a rotational transition barrier of just 0.44 eV, which can be overcome by scanning with the STM tip at $+2.4$ eV sample bias voltage. In STM, the physisorbed and chemisorbed states can be distinguished since the former appears as a bright spot centred above a surface oxygen, while the carboxylate forms dark crosses, each with one thick and one thinner arm.

In this chapter, a DFT study of CO adsorbed on the Ca$_3$Ru$_2$O$_7$(001) is presented. Recent experiments by Mayr-Schmölzer, Halwidl, et al. [9] show that on the related Ca$_3$Ru$_2$O$_7$(001) surface, adsorbed CO shows similar behaviour since again both a physisorbed and a chemisorbed adsorption mode are present. The different surface symmetry highlighted in section 5.5.2 and **??** on the other hand does lead to significant differences between Ca$_3$Ru$_2$O$_7$ and Sr$_3$Ru$_2$O$_7$. In STM (see fig. 8.1a), the precursor mode appears as large dark spots elongated along the [010] direction with and additional bright dot at the adsorption site, which is displaced from the centre of the bright channel in either [100] or [$\bar{1}$00] direction. Overlaying the lattice unit cells reveals that the CO precursor occupies two distinct adsorption sites in the unit cell. As shown in fig. 8.1b, those with the bright dot oriented towards the [100] or [$\bar{1}$00] direction are separated by a full or half integer number of lattice constants along [010], respectively.

In the experiment, the chemisorbed state can be activated either by annealing or by scanning the sample with an increased positive sample bias voltage of $+1.40$ eV. After one STM scan with these parameters, at the sites previously identified as precursor adsorption sites the bright spots transform into uneven, dark crosses with almost circular bright halos (see fig. 8.1c). A scan taken at high resolution (see fig. 8.1d) reveals that these dark crosses consist of two short lines at 90° angle. Again, two different orientations of these crosses can be identified where those with identical orientation show full integer shifts along [010]. As is detailed in this chapter, DFT predicts similar behaviour to

(a) Precursor

(b) Lattice overlay

(c) Mixed precursor and carboxylate
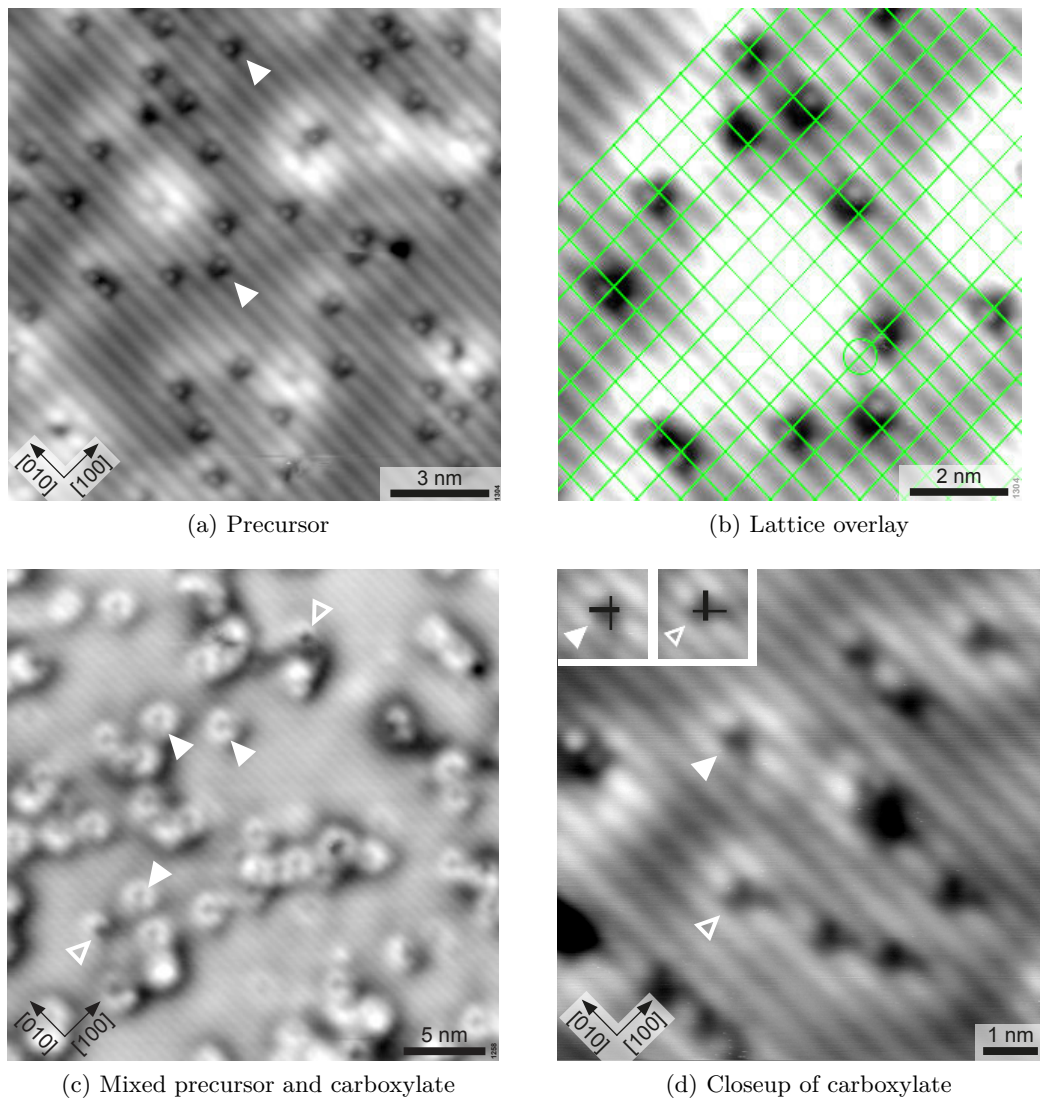

(d) Closeup of carboxylate

Figure 8.1.: (a) STM image after dosing 0.002 Langmuir CO. Molecules appear as dark spots on the bright surface channels with an additional shifted bright dot. (b) Overlay of the lattice unit cells showing the registry of the adsorption sites. STM parameters: $I_t = 0.1\,\text{nA}$, $T = 78\,\text{K}$, and $U_s = +0.4\,\text{V}$. (c) Transformation of the CO precursor (open triangles) into carboxylate species (full triangles). STM parameters: $I_t = 0.1\,\text{nA}$, $T = 78\,\text{K}$, and $U_s = +0.3\,\text{V}$. (d) Chemisorbed species. Inset shows a sketch of the two orientations of the cross-like shapes. STM parameters: $I_t = 0.1\,\text{nA}$, $T = 78\,\text{K}$, and $U_s = +0.5\,\text{V}$. Images courtesy of Mayr-Schmölzer, Halwidl, et al. [9].

297

CO adsorbed on the $Sr_3Ru_2O_7$(001) surface, in good agreement with the mentioned experiments. The results of this study were submitted in a combined experimental and theoretical paper [9].

8.2. Results

To simulate the adsorption of CO molecules on the $Ca_3Ru_2O_7$(001) surface at varying coverages a (1×1) and a (2×2) model cell, reflecting ½ and ⅛ ML coverage defined by the number of octahedra in the surface unit cell, were chosen. All calculations were performed with the optB86b functional, using the lattice parameters determined in section 5.3.3. The Γ-centred $\vec{k}$-point grid was adjusted according the number of surface unit cells, resulting in a $6 \times 6 \times 1$ and a $3 \times 3 \times 1$ grid for the (1×1) and the (2×2) model cells, respectively. The energy cutoff was set to $400\,eV$, as described in section 6.4. Additionally, PBE calculations were performed on some model cells to facilitate a comparison with earlier calculations on $Sr_3Ru_2O_7$ [179]. While this approach does neglect the effect of the lattice constant of the substrate on adsorption energies, the comparison with PBE calculations performed by Josef Redinger on a (3×3) model cell at the PBE optimised lattice parameters only showed a small deviation [9].

8.2.1. Physisorption

½ ML coverage

As a first step, a CO molecule was placed on the (1×1) $Ca_3Ru_2O_7$ model cell to study its preferred adsorption site and orientation. For two initial configurations, the CO molecule was rotated such that the oxygen pointed towards the $Ca_3Ru_2O_7$(001) surface, while for a third the molecule was rotated by 180° so that the carbon atom of the CO molecule pointed downwards. In the latter configuration the molecule was placed on top of a surface Ca atom in a vertical arrangement, while for the two former the CO was placed on top of a surface oxygen and a surface calcium atom. After relaxation, for all three cases the CO molecule is not positioned perfectly upright anymore. The most favourable adsorption site was reached by starting from a placement of the CO on top of an oxygen atom with the C pointing downward at an adsorption energy of $-0.474\,eV$. The CO is then displaced from the O_{top} position towards a surface Ca atom so that it is positioned at a Ca–O bridge site. It tilts by 37.9° away from the surface Ca and the tilting with respect to the vertical axis is lowest at 8.7°. The second most favoured adsorption site was found on top of a surface Ca with the carbon pointing downwards. Flipping the CO molecule around so that its oxygen component points towards the surface Ca reduces the adsorption energy at this site further to $-0.209\,eV$. Here, the tilting is just slightly larger at 13.9°. These three adsorption configurations are shown in fig. 8.2.

To study different arrangements of the adsorbed CO at the same coverage, two CO molecules were then placed on a (2×1) $Ca_3Ru_2O_7$(001) model cell. The CO molecules were first arranged in a parallel structure at similar adsorption sites found for the (1×1) model cell. The adsorption energy per CO for this configuration is $-0.493\,eV$, not much
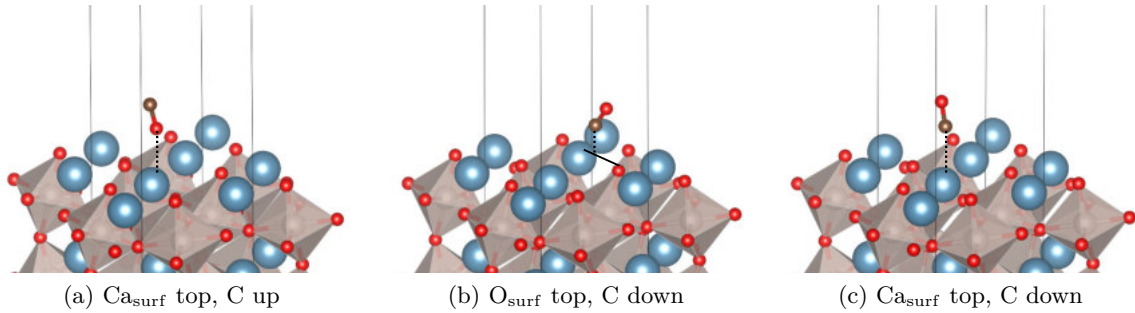
(a) Ca$_{surf}$ top, C up   (b) O$_{surf}$ top, C down   (c) Ca$_{surf}$ top, C down

Figure 8.2.: Adsorption of one CO molecule on the (1×1) Ca$_3$Ru$_2$O$_7$(001) model. Ca, Ru, O, and C atoms coloured blue, grey, red, and brown.

different for the smaller model cell. For the zig-zag configurations the CO were placed in two rows along the b axis, but shifted by half a unit cell. The two rows can either be separated by a bright or a dark surface row. Since these bright and dark features are caused by the tilting of the surface octahedra away from and towards each other, respectively, this means that in the "dark" zig-zag configuration the CO are slightly closer together. After relaxation of these zig-zag structures it can be seen that one CO forms a bond with a surface oxygen atom. The other CO adsorbs at a Ca–O bridge site close by. Both zig-zag structures show stronger binding of the CO molecules to the surface than the parallel configuration, indicating repulsive interaction between the adsorbed CO.

⅛ ML coverage

Further reducing the coverage to ⅛ ML, i.e. one CO adsorbed on a (2×2) model cell, increases the adsorption energy to $-0.849\,\text{eV}$. Similar to the precursor adsorption mode described by Stöger et al. [179] on the Sr$_3$Ru$_2$O$_7$(001) surface, the CO adsorbs on top of an apical O$_{surf}$ atom of a RuO$_6$ octahedron with a C–O$_{surf}$ distance of $1.420\,\text{Å}$, right at the edge of a bright channel. As shown in 8.4a, the precursor molecule is tilted by $37.5°$ towards the [110] direction, opposite to the tilt of the RuO$_6$ octahedron below. Also, the O of the CO is tilted by $28.7°$ degree in the [010] direction. Compared to the gas phase molecule, the C–O bond length is increased from $1.139\,\text{Å}$ to $1.252\,\text{Å}$. Additionally, the apical oxygen of the RuO$_6$ octahedron is pulled upwards by the adsorbed CO precursor, leading to an increase of the Ru–O$_{surf}$ bond length by $9\,\%$ to $2.139\,\text{Å}$. The STM simulation of this low coverage structure shows the CO molecule indicated by a moon shaped bright feature with an additional bright spot in the occupied states (see 8.4c). In the unoccupied states the oxygen atom of the CO is indicated by a large dark and bright spot, both shifted from the bright channel line. To compare the adsorption energy of the precursor with the PBE results obtained by Stöger et al. [179] the optB86b-relaxed structures was further investigated using the PBE functional. These calculations pre-

dict no significant change in the adsorption configuration and an adsorption energy of $-0.605\,\text{eV}$.

8.2.2. Chemisorption

⅛ ML coverage

The chemisorbed adsorption mode was simulated by replacing the apical oxygen of one RuO_6 octahedron by a carbon atom and placing the two remaining oxygen atoms close to Ca–Ca bridge sites, similar to the configuration found on $Sr_3Ru_2O_7(001)$ [179]. After relaxation, the resulting carboxylate is located almost at the centre of the surrounding Ca atoms with an O–C–O angle of 120.3°. The two oxygen atoms are aligned with the [110] direction and point towards nearby Ca–Ca bridge sites. The resulting O–Ca distances range from $2.396\,\text{Å}$ to $2.547\,\text{Å}$. The apical oxygen atom of the octahedron below the carboxylate is replaced by a carbon atom with an Ru–C bond length of $2.044\,\text{Å}$. Compared to the pristine RuO_6 octahedron, the central Ru atom is lifted by $0.110\,\text{Å}$ in [001] direction towards the surface. A top view of the surface carboxylate is shown in 8.4d. Performing a rotation of the carboxylate by 90° as shown in 8.4g reduces the stability by 69 meV. This can be understood by analysing the distances between the apical oxygen of the octahedra surrounding the adsorption site and the oxygen of the carboxylate. These O–O distances are maximised for the most favoured configuration shown in 8.4d since the octahedra are tilted perpendicular to the Ca–Ca bridges next to the O of the carboxylate. For the 69 meV less stable configuration the respective octahedra would be tilted directly towards and away from the adsorption site. The O–O repulsion distorts the Ru–O_{surf} bond of the former octahedron, leading to the lowered stability of this configuration. To calculate the barrier of rotation the carboxylate was rotated by 45° and relaxed only in the y and z direction, blocking any rotation. The calculations predict a barrier of rotation of $0.570\,\text{eV}$. The STM simulations agree well with the experiment, see 8.4e. In both occupied and unoccupied states, the carboxylate is shown as an uneven, large dark spot, slightly shifted from the bright channel line. Again, the carboxylate was also evaluated using the PBE functional, yielding an adsorption energy of $-1.853\,\text{eV}$ and $-1.781\,\text{eV}$ for the unrotated and rotated adsorption configurations shown in fig. 8.4d and fig. 8.4g, respectively.

8.3. Discussion

Compared to earlier reports of CO adsorbed on the $Sr_3Ru_2O_7(001)$ surface, both experiment and DFT calculations show similar adsorption behaviour on $Ca_3Ru_2O_7(001)$. While the predicted binding energy of the precursor of $-0.849\,\text{eV}$ is much higher than on $Sr_3Ru_2O_7(001)$ ($E_{Ads} = -0.66\,\text{eV}$ [179]), this can mainly be attributed to the optB86b functional used in the current calculations which includes van-der-Waals corrections. Indeed, evaluating the binding energy with the PBE functional at the optB86b lattice parameters yields $-0.605\,\text{eV}$. In both cases, bond lengths and O_{surf}–C–O angles of the precursor are very similar. Nevertheless, due to the tilting of the octahedron, the

Table 8.1.: Calculated adsorption energies of molecular CO on the $Ca_3Ru_2O_7(001)$ surface. The PBE adsorption energies were obtained at the optB86b-optimised lattice constant for the substrate.

Configuration	E_{Ads} [eV]
$1\,CO@(1 \times 1)$	
Ca_{surf} top, C up	-0.209
O_{surf} top, C down	-0.474
Ca_{surf} top, C down	-0.334
$2\,CO@(2 \times 1)$	
parallel	-0.493
zig-zag, bright	-0.585
zig-zag, dark	-0.605
$1\,CO@(2 \times 2)$, precursor	
PBE	-0.605
optB86b	-0.849
$1\,CO@(2 \times 2)$, carboxylate	
PBE	-1.853
optB86b	-2.044
$1\,CO@(2 \times 2)$, rotated carboxylate	
PBE	-1.781
optB86b	-1.976

(a) (2×1), parallel   (b) (2×1), zig-zag, bright   (c) (2×1), zig-zag, dark
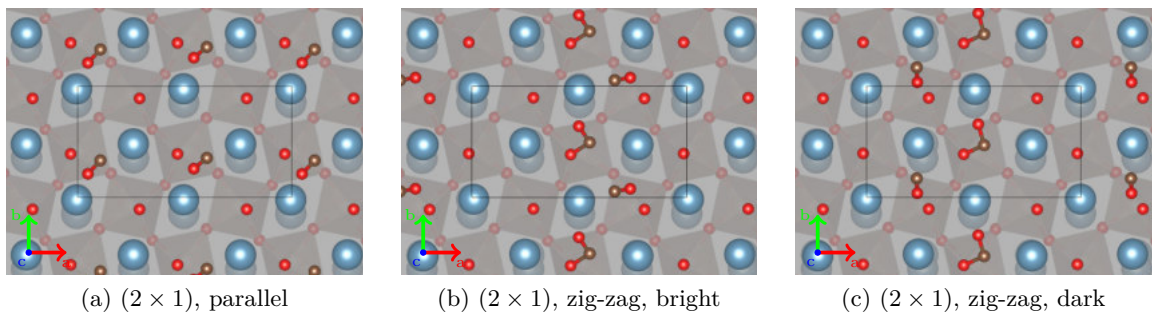
Figure 8.3.: Adsorption of two CO molecule on the (2×1) $Ca_3Ru_2O_7(001)$ model. Ca, Ru, O, and C atoms coloured blue, grey, red, and brown.

(a) ⅛ ML, precursor

(b) STM, bias: $+0.4\,\mathrm{eV}$

(c) STM, bias: $-0.4\,\mathrm{eV}$

(d) ⅛ ML, carboxylate

(e) STM, bias: $+0.5\,\mathrm{eV}$

(f) STM, bias: $-0.5\,\mathrm{eV}$

(g) ⅛ ML, rotated carboxylate

(h) STM, bias: $+0.5\,\mathrm{eV}$

(i) STM, bias: $-0.5\,\mathrm{eV}$
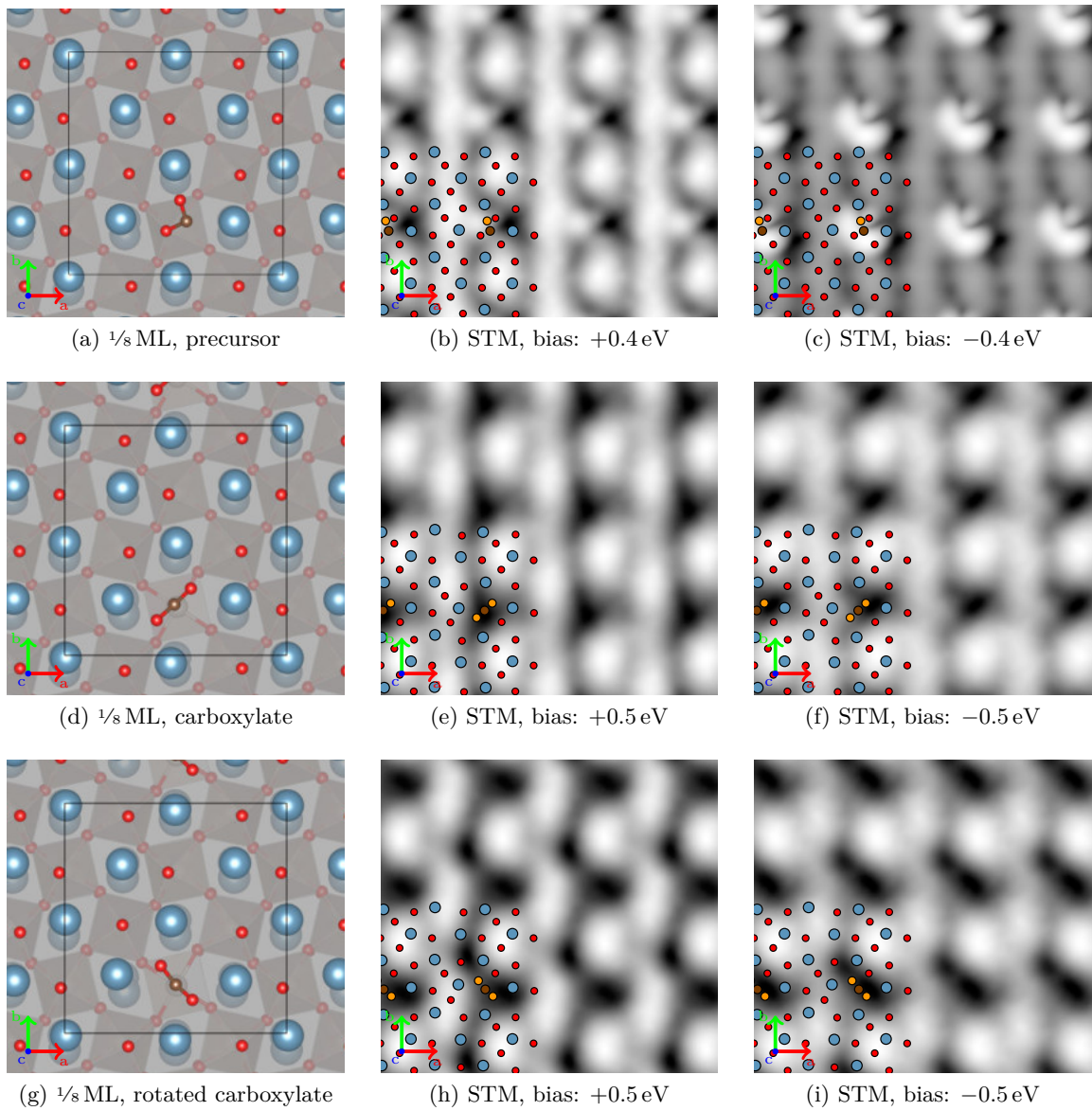
Figure 8.4.: Top row: (a): adsorption of the CO precursor on the (2×2) $Ca_3Ru_2O_7(001)$ model. (b) - (c): STM simulation. Middle row: (d): chemisorbed carboxylate, centred between the surrounding Ca atoms. (e) - (f): STM simulation. Middle row: (g): chemisorbed carboxylate, centred between the surrounding Ca atoms, rotated by 90°. (h) - (i): STM simulation. Ca, Ru, O, and C atoms coloured blue, grey, red, and brown.

Ru–O_{surf}–C angle is significantly smaller on $Ca_3Ru_2O_7$ at 111.4° than on $Sr_3Ru_2O_7$, where it is 143°. Stöger et al. [179] suggested that tip-induced removal of the precursor at a sample bias voltage of +0.4 eV was caused by the excitation of a molecule-surface vibrational mode at ≈120 meV. However, on $Ca_3Ru_2O_7$ a significantly higher sample bias voltage (+1.0 eV) is needed to remove the precursor, although the energy of the corresponding vibrational mode is just 183 meV [9].

For the chemisorbed mode the different surface symmetry caused by the tilting of the octahedra of $Ca_3Ru_2O_7$(001) compared to $Sr_3Ru_2O_7$(001) causes a reduced activity. This is indicated by the lower binding energy predicted for $Ca_3Ru_2O_7$(001) of −2.044 eV (optB86b) compared to that on $Sr_3Ru_2O_7$(001) of 2.17 eV (PBE). Clearly, the van-der-Waals correction plays a larger role for the precursor mode, while the carboxylate is more influenced by the distinct surface geometries. Indeed, PBE calculations performed on the (2×2) model yield an even lower binding energy of −1.853 eV. It should also be noted that on $Ca_3Ru_2O_7$(001) not the whole $RuCO_5$ octahedron is tilted, but that just the Ru–C bond is tilted by 8.2° with respect to the Ru–O_{apical} bond below. This kink of the O–Ru–C axis does not exist on $Sr_3Ru_2O_7$(001) since the octahedra of the clean surface are not tilted in the first place and the carboxylate adsorbs above a surface O or on top of a Ru, respectively. On $Sr_3Ru_2O_7$(001), the tip-induced desorption of the chemisorbed mode at a sample bias voltage of +2.7 eV was explained by electron capture into the lowest antibonding O–CO orbital at +2.4 eV. On $Ca_3Ru_2O_7$(001), DFT predicts the same O–CO orbital slightly higher at +2.7 eV, in agreement with the higher sample bias voltage of +3.0 eV needed to remove the carboxylate species. Due to the lower symmetry of the $Ca_3Ru_2O_7$ unit cell no tip-induced rotation of the COO carboxylate was observed.

A. Binary Alkaline Oxides

For the comparison with the SrO and CaO like ruthenate (001) surfaces this chapter deals with the bulk and (001) surface structure of the binary alkaline oxides SrO, CaO, and MgO. Additionally, some results of H_2O and O_2 adsorption calculations using different functionals are presented. Due to the lower complexity of these compounds and smaller unit cell size they were used as test systems for the advanced many-body approaches (RPA).

All three binary oxides crystallise in the NaCl rock salt structure (space group: $Fm\bar{3}m$). Although the primitive unit cell would only consist of one atom of each species a unit cell with 4 formula unit was used in the calculations, mainly to facilitate the modelling of the (001) surface. The calculations of the bulk properties were done using the PBE, PBEsol, optB86b, and the HSE06 functional at well converged computational parameters.

A.1. Bulk Properties

As a first step to determine the bulk properties of the three alkaline oxides, convergence tests with respect to the $\vec{k}$-point grid and the energy cutoff were performed. For all three compounds convergence could be reached with a $8 \times 8 \times 8$ Γ-centred $\vec{k}$-point grid (35 irreducible $\vec{k}$-points). Since the volume of the unit cell was optimised along with the shape and the internal ionic positions[1], the energy cutoff was set to $750\,eV$ for SrO and CaO and to $950\,eV$ for MgO to minimise the Pulay stress.

All four tested functional result in a good description of the lattice constant of all three binary alkaline oxides. Nevertheless, the deviation is smallest for the HSE06 functional at $<0.1\,\%$ for all compounds. Considering the optB86b functional here the description of the lattice constant is exceptional for SrO, while for CaO and MgO the deviation is small at $-0.3\,\%$ and $0.4\,\%$ respectively. Surprisingly the lattice constants obtained from the PBEsol functional show a higher error ($-0.5\,\%$, $-0.7\,\%$, and $0.2\,\%$ for SrO, CaO, and MgO) than for the optB86b case, considering that the PBEsol functional was tuned to give a better description of the crystal structure. For the PBE functional the obtained lattice parameter was generally too large by up to $1.1\,\%$ for MgO.

A.2. Water Adsorption

The calculations of water adsorption on all binary alkaline oxides were performed on a 6 layer thick slab and just one surface unit cell of the oxide. This yields a coverage

---

[1]VASP Setting: ISIF = 3

Table A.1.: Lattice constants in Å of SrO, CaO, and MgO. Experimental data was taken from Villars and Cenzual [206] and Smith and Leider [207], respectively.

a [Å] Functional	SrO	CaO	MgO
optB86b	5.159	4.796	4.230
PBE	5.204	4.838	4.257
PBEsol	5.134	4.777	4.219
HSE06	5.162	4.808	4.208
Exp.	5.159	4.811	4.212

of ½ H_2O when considering the number of distinct Ca–Ca bridge sites. Due to time constraints the adsorption behaviour was only investigated for a selection of functionals, see table A.3. For the optB86b, PBE and HSE06 calculations the lattice constants determined by the respective functional were used. Since the RPA calculations are many orders of magnitude more expensive than standard DFT calculations, the relaxed configurations determined by the optB86b functional served as starting points.

The cutoff energies for the optB86b and PBE calculations were identical to the bulk calculations. For the HSE06 functional the cutoff energy was reduced to $400\,\mathrm{eV}$ to be able to relax the system in a sensible amount of time. A $6 \times 6 \times 1$ Γ-centred $\vec{k}$-point grid was determined to be able to guarantee accurate results.

The initial adsorption configurations were modelled according to the results by Hu et al. [185] and to the knowledge gained by the water adsorption studies done on $Sr_3Ru_2O_7$ and $Ca_3Ru_2O_7$. The final states found after relaxing the structures show that both the SrO and the CaO surface are quite reactive, preferring dissociated adsorption of H_2O molecules. On MgO the water molecules adsorb intact. The adsorption energies given by the optB86b functional are ≈160 meV larger than for the PBE functional, indicating that the van-der-Waals interactions play a non-negligible role in the molecular adsorption energies. For the HSE06 functional the adsorption energies were only calculated for the dissociated configurations. Here the values were only slightly higher than for the PBE functional, except for SrO, indicating that a more accurate description of the exchange part of the functional does not play a large role.

As shown in fig. A.1 the trend described by Hu et al. [185] could be confirmed for all functionals: for both SrO and CaO the dissociated molecule adsorbs at a metal atom bridge with the split off proton binding to a surface oxygen forming a surface hydroxyl. For MgO the intact H_2O molecule forms a hydrogen bond with a surface oxygen, as can be seen in fig. A.1c. Some subtle differences in the bond lengths exist considering the different functionals: e.g. in the case of SrO the length of the hydrogen bond between surface hydroxyl and $(OH)_{ads}$ is 1.489 Å, 1.477 Å, and 1.485 Å for HSE06, optB86b, and PBE, respectively.

Table A.2.: Adsorption energy in eV per H_2O molecule on a $(1 \times 1 \times 3)$ unit cell of SrO, CaO, and MgO. Molecular and dissociated adsorption are indicated by "m" and "d", respectively.

| E_{Ads} [eV] | SrO | | CaO | | MgO |
Functional	m	d	m	d	m
optB86b	−0.217	−1.225	−0.215	−0.888	−0.519
PBE	−0.090	−1.076	−0.077	−0.727	−0.342
HSE06		−1.128		−0.757	−0.325
RPA	−0.126	−1.082	−0.257	−0.816	

Table A.3.: Bond lengths in Å of one adsorbed H_2O molecule on a $(1 \times 1 \times 3)$ unit cell of SrO, CaO, and MgO. On SrO and CaO the molecule dissociates, on MgO the H_2O stays intact.

| | Bond Lengths [Å] | | |
Functional	H_s-$(OH)_{ads}$	$(O–H)_{ads}$	$(O–H)_{surf}$
	SrO		
optB86b	1.477	0.970	1.043
PBE	1.485	0.968	1.041
HSE06	1.489	0.958	1.019
	CaO		
optB86b	1.365	0.971	1.094
PBE	1.375	0.969	1.087
HSE06	1.383	0.958	1.058
	MgO		
optB86b	1.712	0.972	1.004
PBE	1.671	0.974	1.009
HSE06	1.690	0.962	0.992

(a) SrO	(b) CaO	(c) MgO
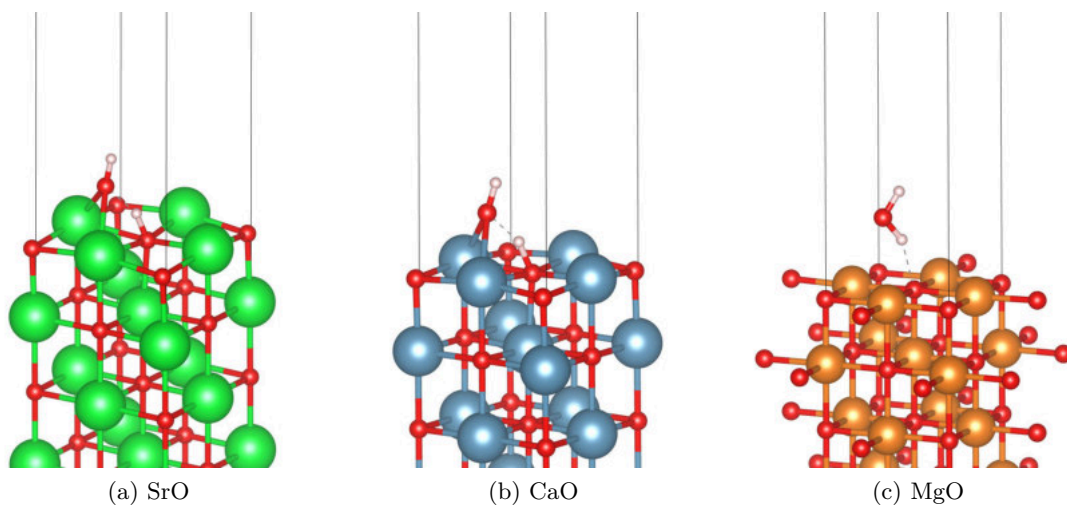
Figure A.1.: One O_2 adsorbed on the SrO, CaO, and MgO (001) surfaces. Water prefers dissociative adsorption on the former two oxide surfaces, and molecular adsorption on MgO.

A.3. Oxygen Adsorption

The binary alkaline oxides SrO and MgO were also used as a test system for the adsorption of oxygen molecules. The $(1 \times 1 \times 3)$ model cell ($\frac{1}{4}$ coverage) for these calculations were taken over from the water adsorption calculations and the same computational setting were used. Additionally a lower coverage ($\frac{1}{16}$) system on a $(2 \times 2 \times 3)$ model cell was tested. To reduce the computational effort the energy cutoff was reduced to $400\,\mathrm{eV}$ and a $3 \times 3 \times 1$ Γ-centred $\vec{k}$-point grid was used.

For the CaO(001) surface the equilibrium position of the O_2 molecule is at a highly symmetric Ca–Ca bridge position. The optB86b functional predicts atomic distances between the oxygen atoms of the adsorbate and the alkaline metal atoms of $2.850\,\text{Å}$, and the length of the O_2 is $1.250\,\text{Å}$. For the PBE functional the Ca–O distances are increased to $2.985\,\text{Å}$, while the O_2 bond length is the same. The HSE06 functional yields a positive adsorption energy, i.e. no adsorption.

At lower coverage the optB86b functional predicts two structures at almost similar stability. In the first predicted structure the O_2 adsorbate is positioned in an asymmetric Ca–Ca bridge configuration, shifted close to one alkaline atom. The Ca–O distances change to $2.642\,\text{Å}$ and $2.771\,\text{Å}$ while the O_2 is slightly elongated to $1.272\,\text{Å}$. This causes the O_2 to tilt by $4.5°$. The PBE functional yields a similar configuration, but here the placement of the O_2 molecule is even more asymmetric since the first Ca–O distance is now $2.746\,\text{Å}$ and the second Ca–O distance $2.988\,\text{Å}$. The adsorbate is elongated to $1.264\,\text{Å}$ and the tilting with respect to the surface is just $2.3°$. In the second stable configuration predicted by the optB86b functional the O_2 is rotated by $35.3°$ from the

Ca–Ca bridge, leading to a position almost parallel to the *b* axis. Compared to the tilted configuration this rotated structure is just 21 meV less favourable. The PBE functional does yield a local minimum in this adsorption configuration, but a positive adsorption energy. For the optB86b calculation, the Ca–O distances are slightly asymmetric at 2.693 Å and 2.774 Å. The O–O distance is 1.271 Å, similar to the tilted configuration. In all cases the O_2 molecule is not charged, as shown in the plotted density of states in fig. A.3.

On the SrO(001) surface the situation is pretty similar to the CaO case. At low coverage the optB86b functional again predicts a tilted and a flat adsorption configuration. For the former case, which is the global equilibrium structure, the O_2 is slightly displaced from the central Sr–Sr site towards one of the alkaline atoms. The latter case incurs an energy penalty of 57 meV, here the O_2 is positioned in the middle of the bridge. The predicted Sr–O distances are 2.820 Å for the tilted and 2.896 Å for the flat case. The O_2 bond is elongated to 1.272 Å and 1.262 Å with respect to the free molecule (1.236 Å).

At lower coverage both functionals predict the tilted and the rotated adsorption configuration. In contrast to the CaO substrate, for SrO the order of stability is reversed, i.e. the rotated configuration is the most stable one. The energy differences are 28 meV and 107 meV for the optB86b and the PBE functional, respectively. The optB86b and PBE functionals predict a rotation of 6° and 0.9° with respect to the *b* axis. The Sr–O distances are 2.797 Å and 2.767 Å for the optB86b functional and 2.840 Å for the PBE functional. The O_2 bond length predicted by both functionals is 1.280 Å. In the case of tilted adsorption which is 28 meV less stable the optB86b functional yields Sr–O distances of 2.741 Å and 2.833 Å. For the PBE functional the final adsorption configuration (107 meV less stable) is in the middle of the Sr–Sr bridge, leading to Sr–O distances of 2.900 Å.

Table A.4.: Adsorption energies in eV per adsorbed O_2 molecule on a $(1 \times 1 \times 3)$ unit cell of SrO and CaO. On CaO the HSE06 functional yields a positive adsorption energy.

E_{Ads} [eV]	SrO		CaO		
Functional	$(1 \times 1 \times 3)$	$(2 \times 2 \times 3)$	$(1 \times 1 \times 3)$	$(2 \times 2 \times 3)$	
				tilted	rotated
optB86b	−0.458	−0.513	−0.298	−0.368	−0.347
PBE	−0.174	−0.316	−0.090	−0.160	0.111
HSE06	−0.167		0.027		

(a) (1×1) SrO, flat

(b) (1×1) SrO, tilted

(c) (1×1) CaO, flat

(d) (1×1) CaO, tilted

(e) (2×2) SrO, flat

(f) (2×2) SrO, tilted

(g) (2×2) CaO, flat

(h) (2×2) CaO, tilted
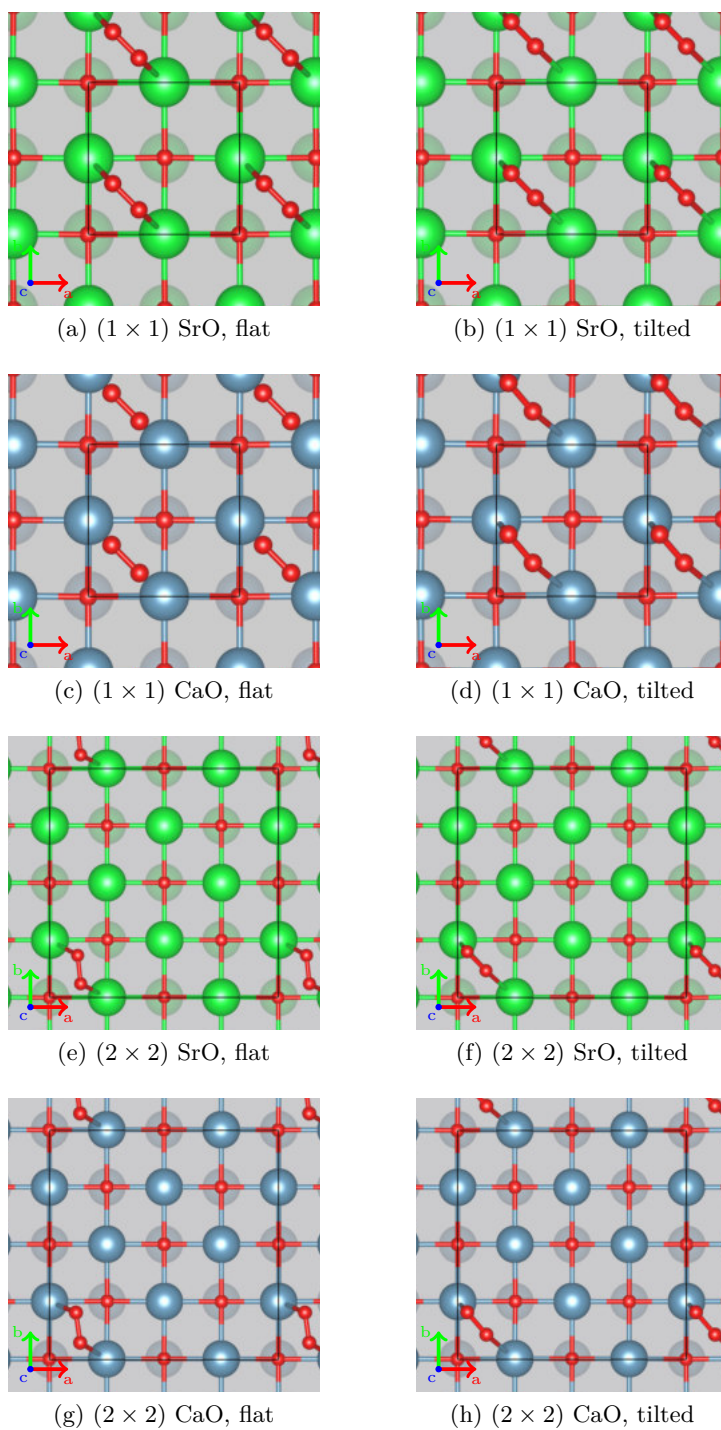
Figure A.2.: Top view of the final adsorption configurations of O_2 on the (1×1) and (2×2) surface unit cells of SrO(001) and CaO(001).
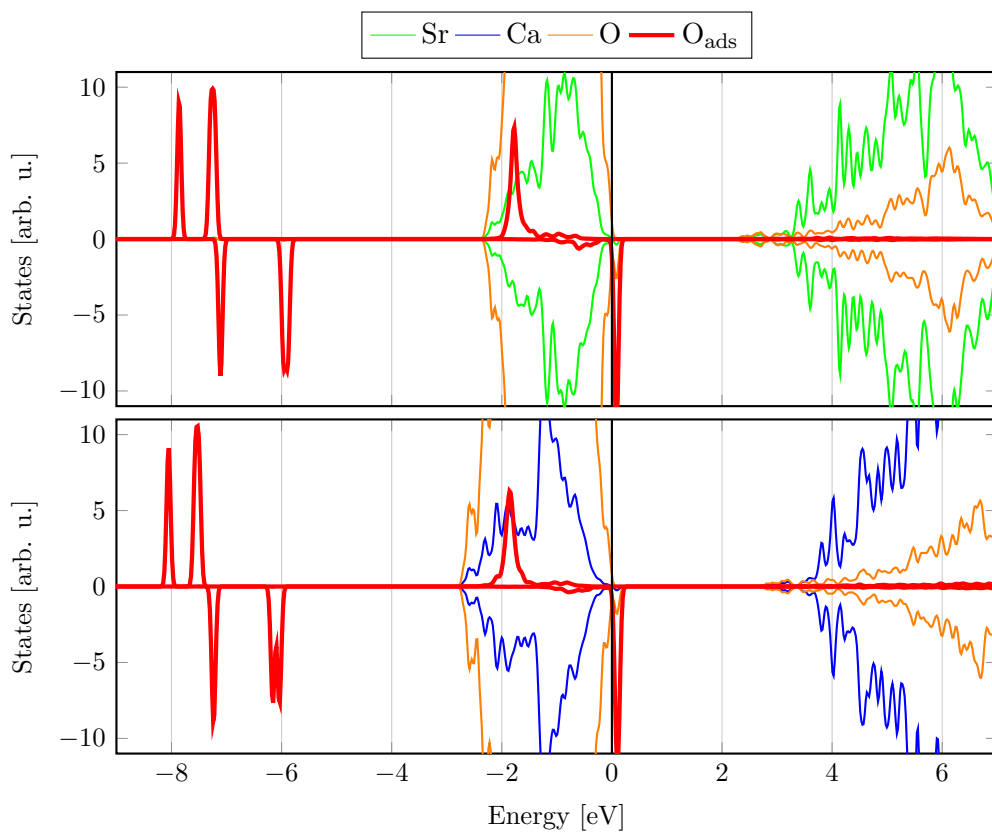
Figure A.3.: DOS of one O_2 at adsorbed on a (2×2) (top) SrO(001) and (bottom) CaO(001) model cell calculated with the optB86b functional. The oxygen π^* states are degenerate, indicating adsorption as a neutral O_2.

B. Zirconia Surfaces

B.1. Surface Energy

The surface energy of various cutting planes of ZrO_2 phases were calculated according to earlier research done by Christensen and Carter [115]. For these calculations slabs were cut out of the respective bulk phases at their equilibrium lattice constants. For the cubic and tetragonal phase 3-layered slabs and for the monoclinic phase 4-layered slabs were used. All calculations were performed only with the PBE functional and at an energy cutoff of $540\,eV$. The $\vec{k}$-point grid used for each phase are listed in table B.1. As shown in B.2, DFT predicts the highest stability for the cubic(111), the tetragonal(111), and the monoclinic($\bar{1}11$) surfaces, respectively.

Table B.1.: K-point grids used for the calculations on the ZrO_2 slabs.

	$\vec{k}$-point grid
cubic	$6 \times 6 \times 1$
tetragonal	$6 \times 6 \times 1$
monoclinic	$5 \times 5 \times 1$

B.2. Oxygen Vacancies

The oxygen vacancy formation energies V_O were calculated for the most stable cubic and monoclinic surfaces as determined in appendix B.1. To obtain these values one oxygen atom was removed from the respective slab structure and the resulting unit cell was relaxed. The V_O was then calculated according to

$$V_O = E_{\mathrm{Slab}} - E_{\mathrm{Slab+Vacancy}} - E_{O_2}/2 \tag{B.1}$$

as the difference of the total energy of the unmodified slab, and the sum of the total energy of the modified slab and half the O_2 reference. All calculations were performed using the optB86b functional at the respective bulk lattice constant. In the case of the c(111), a slab structure consisting of six trilayers was used to properly model bulk behaviour in the ZrO_2 layers below the oxygen vacancy. For the monoclinic slab, the slab contained four ZrO_2 trilayers. $4 \times 4 \times 1$ and a $5 \times 5 \times 1$ Γ-centred $\vec{k}$-point grids were chosen for the cubic and the monoclinic slab, respectively. The energy cutoff was set to $400\,eV$.

The calculated vacancy formation energy shows values of around $6.966\,eV$ for the formation of a defect at the c(111) surface, and for the monoclinic m($\bar{1}11$) this value is even slightly higher ($7.175\,eV$). Due to the symmetry of the unit cell all upper oxygen

Table B.2.: PBE surface energies of selected surface terminations of cubic, tetragonal and monoclinic ZrO_2.

Surface Plane	Surface Energy [eV/Å^2]	Surface Energy [mJ/m^2]
cubic		
110	0.0746	1195.6
111	0.0486	779.4
tetragonal		
101	0.0875	1402.6
110	0.0663	1063.0
001	0.0643	1030.5
111	0.0632	1013.2
monoclinic		
010	0.2156	3454.1
−101	0.1060	1697.6
011	0.0951	1523.1
100	0.0880	1409.4
101	0.0850	1361.9
001	0.0787	1260.5
110	0.0731	1170.9
111	0.0670	1072.8
−111	0.0556	891.4

sites are equal in the c(111), but for the monoclinic unit cell there are five possible defect sites, one of which is a 2-fold coordinated oxygen atom. All other surface O are 3-fold coordinated and sit at different heights. The comparison of the vacancy formation energies shows the lowest value for the 2-fold coordinated surface oxygen, with differences to the other sites of up to 286 meV, see table B.3.

Table B.3.: Vacancy formation energies for the c(111) and m($\bar{1}$11) surfaces in eV, calculated with the optB86b functional. The various oxygen defect sites for the m($\bar{1}$11) are indicated in fig. B.1a.

Defect Site	V_O [eV]
c(111)	
$O_{surface}$	6.966
m($\bar{1}$11)	
O1	7.263
O2	7.175
O3	7.460
O4	7.282
O5	7.260

(a) m($\bar{1}$11), top view

(b) c(111), top view
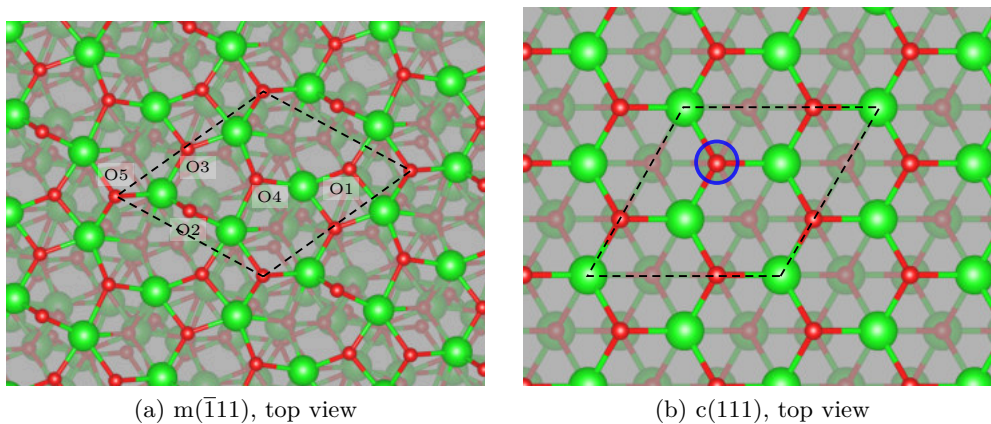
Figure B.1.: Studied defect sites on the (a) monoclinic m($\bar{1}$11) and (b) cubic c(111) surfaces. In the former case the oxygen sites are identified by numbers, in the latter by the blue circle.

B.3. H$_2$O Adsorption on ZrO$_2$ Surfaces

The adsorption energies of water adsorbed on the bulk m($\bar{1}$11) surface were evaluated using different DFT functionals and methods. For all calculations the optB86b optimised lattice constant was chosen for the ZrO$_2$ bulk. The PBE and optB86b values were obtained from the fully relaxed respective structures, while for the HSE06 and RPA values only static calculations of the optB86b optimised structures were done. Additionally, to further reduce the computational effort the model cells were simplified by removing the lower two ZrO$_2$ layers, resulting in a two-layer slab. The PBE and optB86b calculations on the m($\bar{1}$11) surface were done using an energy cutoff of 540 eV while for the HSE06 and RPA calculations it was set to 550 eV. Additionally, for the latter the *GW* energy cutoff was set to 250 eV. Furthermore, the PBE, optB86b, HSE06 and RPA adsorption energies were evaluated for the hydroxylate m($\bar{1}$11) surface described in section 4.2.1 in the same manner as described before, see table B.5.

The comparison of the full coverage structure with one dissociated H$_2$O and the one with the H$_2$O at P4 removed (E$_{H_2O,\#4}$, see section 4.2.1 and fig. 4.11) on the pristine surface shows that all methods yield a binding energy of this H$_2$O molecule of at least 0.743 eV, much larger than the expected value for a single hydrogen bond (see appendix C). For both the PBE and optB86b functional the hydroxylation of the surface leads to a significant reduction of the binding energy of the water molecules to the surface of up to 175 meV to 191 meV at ¼ ML coverage and of 260 meV at full coverage. The RPA adsorption energies on the other hand only show a reduction of 148 meV at low coverage and of 40 meV at full coverage.

C. Bulk Water

The total energy of hexagonal (1h) bulk water was determine to estimate the strength of hydrogen bonds in water films. The unit cell of 1H bulk water consists of four formula units of H$_2$O, each of which form two hydrogen bonds to neighbouring H$_2$O molecules (see fig. C.1). The DFT values were obtained with an energy cutoff of 600 eV and a $4 \times 4 \times 4$ Γ-centred $\vec{k}$-point grid. For the RPA calculations the energy cutoff was reduced to 550 eV, the *GW* cutoff was set to 350 eV, and the same $\vec{k}$-point grid was used. The equilibrium volumina were obtained using a fit to the Birch-Murnaghan equation of state (see section 2.9).

The obtained DFT values agree very well with previously published results by Gillan et al. [208], Santra et al. [209], and Fang et al. [210], each who provide a comprehensive account of the performance of different DFT approaches to the description of water. In general, most DFT methods yield an overestimation of the binding energy in bulk water, up to about 100 meV for the van-der-Waals corrected functionals. Additionally, the equilibrium volume is underestimated compared to the experiment, especially for

Table B.4.: Comparison of the adsorption energies per water molecule in eV calculated with different methods of water adsorbed on the monoclinic $m(\bar{1}11)$ surface. The letters "m" and "d" indicate molecular and dissociated adsorption, respectively. $E_{H_2O,\#4}$ denotes the binding energy of a fourth water molecule. The exact adsorption configurations are discussed in section 4.2.1.

# of H$_2$O	Functional			
	optB86b	PBE	HSE06	RPA
	$m(\bar{1}11)$			
1 H$_2$O, P1, m	−0.910	−0.696	−0.856	−0.863
1 H$_2$O, P2, m	−0.868	−0.587	−0.635	−0.715
1 H$_2$O, P3, m	−1.098	−0.794	−0.948	−1.048
1 H$_2$O, P1, d	−1.274	−1.024	−1.244	−1.157
1 H$_2$O, P2, d	−1.327	−0.972	−0.894	−0.967
1 H$_2$O, P3, d	−1.241	−0.962	−1.137	−1.148
4 H$_2$O, 4m	−0.965	−0.691	−0.705	−0.750
4 H$_2$O, 3m, 1d	−1.197	−0.924	−0.945	−0.979
3 H$_2$O, 2m, 1d	−1.282	−0.976	−1.010	−1.057
$E_{H_2O,\#4}$	−0.943	−0.771	−0.749	−0.743

Table B.5.: Comparison of the adsorption energies per water molecule in eV calculated with different methods. The molecules are adsorbed undissociated on the hydroxylated $m(\bar{1}11)$ surface. $E_{H_2O,\#4}$ denotes the binding energy of a fourth water molecule. The exact adsorption configurations are discussed in section 4.2.1.

# of H$_2$O	Functional			
	optB86b	PBE	HSE06	RPA
	$m(\bar{1}11)$			
1 H$_2$O, P1, m	−0.771	−0.505	−0.765	−0.737
1 H$_2$O, P2, m	−0.833	−0.554	−0.577	−0.575
1 H$_2$O, P3, m	−0.923	−0.620	−0.759	−0.900
4 H$_2$O, 4m	−0.931	−0.659	−0.687	−0.710
3 H$_2$O, 3m	−0.889	−0.664	−0.698	−0.727
2 H$_2$O, 2m	−0.772	−0.458	−0.417	−0.491
$E_{H_2O,\#4}$	−1.057	−0.645	−0.656	−0.657

the van-der-Waals corrected functionals. Many-body approaches like quantum Monte Carlo (DMC) [211] yield much better agreement of the calculated heat of formation with the experimental value of 610 meV [212]. The present calculations show that the HSE06 functional greatly improves the binding energies, while still underestimating the H–O bond lengths and therefore the equilibrium volume. The RPA functional, after full relaxation of the RPA forces, greatly improves on the description of the bond lengths while yielding worse binding energies at just 500 meV. The DFT and RPA binding energies reported in this work are lower compared to previous calculations by Macher et al. [213], but for both methods a shift of about 30 meV is found. Additionally, Macher et al. [213] report an about 2 % larger equilibrium volume predicted by the RPA. The present calculations yield a deviation from the experimental volume of below 0.200 %.

Table C.1.: Heat of formation, equilibrium volume, and hydrogen bond length of hexagonal (1h) water calculated with various computational methods.

Functional	Heat of formation [meV]	Equilibrium volume [$\mathring{A}^3$]
PBE	639	30.63
optB86b	710	29.70
optB88	699	30.12
HSE06	605	30.93
RPA	500	32.09
Exp. [212]	610	32.05
DMC [211]	605	31.69

D. Adsorption on Ca$_3$Ru$_2$O$_7$(001)

This section will give a short overview of some additional adsorption studies performed on the Ca$_3$Ru$_2$O$_7$(001) surface, mostly for testing purposes.

D.1. Atomic O

To test the stability of a dissociated oxygen molecule two O atoms were placed at separate positions on top of the (2×1) Ca$_3$Ru$_2$O$_7$(001) model cell. These calculations were all performed with the optB86b functional, yielding the metallic phase of Ca$_3$Ru$_2$O$_7$. The $\vec{k}$-point grid and the energy cutoff of 450 eV were identical to the calculations described in section 7.3.2. The adsorption energies were calculated with the total energy of the O$_2$ molecules as the reference.
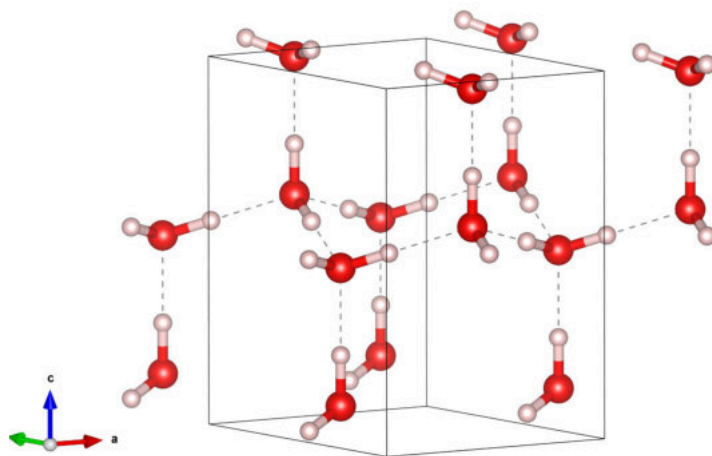
Figure C.1.: Unit cell of 1h hexagonal water, formed by four H$_2$O molecules. Additional molecules from the next unit cells are shown to better illustrate the pattern formed by the H$_2$O.

The relaxations were started from various initial positions. First, the fully relaxed configurations of two O_2 adsorbed in the zig-zag formation, both in the flat and tilted variant, were chosen as starting points and one O atom of each adsorbed O_2 was deleted from the unit cell. After full relaxation, it was determined that the oxygen atom prefers to move towards the apical O of a RuO_6 octahedron close by, forming a surface oxyl with bond lengths of $1.470\,\text{Å}$ to $1.490\,\text{Å}$. The adsorption energy per O atom of the most favoured configuration was $-0.360\,\text{eV}$, much less than for the intact O_2 molecule ($-1.199\,\text{eV}$). Depending on the initial position of the adsorbed O atom, the rotation of this surface oxyl with respect to the tilting of the octahedron has a small influence on the stability of the system, as the adsorbed O prefers to rotate towards one of the Ca–Ca bridge sites close by (see fig. D.1). In the most favourable configuration both adsorbed O would form such a bond to an apical oxygen atom. Two other, less stable final adsorption configurations yielded only one surface oxyl while the other adsorbed O was located at the centre of a Ca–Ca bridge. These configurations are $92\,\text{meV}$ and $124\,\text{meV}$ less stable. A configuration where both O were manually placed at Ca–Ca bridge sites was $286\,\text{meV}$ less stable.

Finally, to test the influence of the coverage on the adsorption energy a single O atom was positioned close to one apical oxygen atom, but the calculated adsorption energy of $-0.324\,\text{eV}$ is not much different. The difference might be caused by subtle differences of the structural changes of the substrate. Rotating the surface oxyl to the Ca–Ca bridge opposite of the tilting direction incurs an energy penalty of $19\,\text{meV}$.

Table D.1.: Calculated adsorption energies of atomic O on the (2×1) $Ca_3Ru_2O_7(001)$ surface.

Configuration	# O	E_{Ads} [eV]
2 Oxyls	2	-0.358
1 Oxyl, 1 Bridge, #1	2	-0.266
1 Oxyl, 1 Bridge, #2	2	-0.234
2 Bridge	2	-0.071
1 Oxyl	1	-0.324
1 Oxyl, rotated	1	-0.305

D.2. Atomic H

The adsorption of atomic hydrogen was tested at different coverages. First on the (1×1) model one and two hydrogen atoms were added to the unit cell, followed by adsorption of two H atoms on the (2×1) model. Finally, one and two H were placed on the (3×3) $Ca_3Ru_2O_7(001)$ model. In all cases, the hydrogen atom was placed next to an exposed apical oxygen atom, resulting in a surface hydroxyl with a bond length of $0.977\,\text{Å}$. All calculations were performed with the optB86b functional using the same settings defined

(a) 2 Oxyls

(b) 2 O at Ca–Ca bridges

(c) 1 Oxyl, 1 Bridge, #2

(d) 1 Oxyl, 1 Bridge, #1

(e) 1 Oxyl

(f) 1 Oxyl, rotated
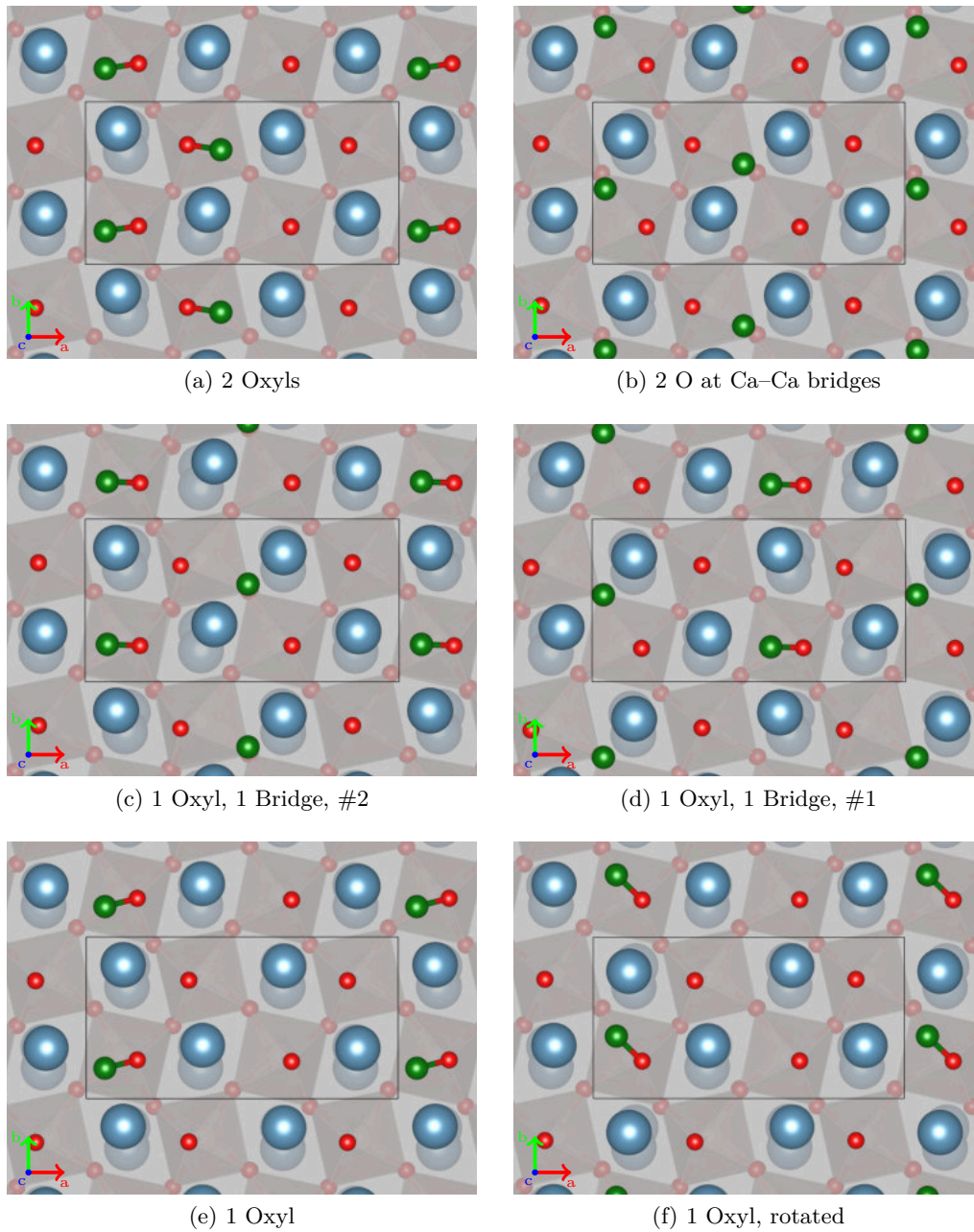
Figure D.1.: Adsorption configurations of atomic oxygen adsorption on the (2×1) Ca$_3$Ru$_2$O$_7$(001) model cell. Ca, Ru, O, and H atoms are coloured blue, grey, red, and white, while the adsorbed O is coloured green.

for the respective surface model cell defined in section 6.4.

At full coverage, the adsorption energy is $-0.222\,\text{eV}$, increasing to $-0.534\,\text{eV}$ at $\frac{1}{18}$ coverage. On the (2×1) model cell adsorption on both the bright and dark surface structures was tested, resulting in a preference for adsorption on the bright lines. Comparing the adsorption energy on this model to the equally covered (1×1) model shows that the surface hydroxyls prefer to cluster, forming lines in b direction. Figure D.2 shows the fully relaxed configurations.

Table D.2.: Calculated adsorption energies of atomic H on the (2×1) $Ca_3Ru_2O_7(001)$ surface.

Coverage	E_{Ads} [eV]
1	-0.222
$\frac{1}{2}$	-0.287
$\frac{1}{2}$, zig-zag, bright	-0.410
$\frac{1}{2}$, zig-zag, dark	-0.345
$\frac{1}{9}$	-0.491
$\frac{1}{18}$	-0.534

D.3. Work Function

In surface science, the work function W is defined as the the minimum energy that has to be supplied to a bulk system to move an electron from the solid to a point in vacuum. It is given by the formula

$$W = -e\phi - E_F$$

where $-e$ refers to the charge of an electron, ϕ to the electrostatic potential and E_F to the Fermi level. The term $-e\phi$ can easily be calculated using VASP by the analysis of the total electrostatic potential[1]. After setting the tag LVHAR in the INCAR file to .TRUE. the file LOCPOT contains the electrostatic contributions to the local potential, the ionic and the Hartree potential. This can then be averaged over the surface plane and evaluated at the minimum in the vacuum between the two sides of the slab. To get useful results the studied slab has to be symmetric, otherwise the work function of the two sides of the slab would not be identical and dipole correction would need to be activated.

The work function was calculated for both the pristine $Ca_3Ru_2O_7(001)$ surface and for adsorbed oxygen. To converge the results with respect to the slab thickness the $Ca_3Ru_2O_7$ slabs used for the adsorption calculations were mirrored in c direction, yielding a two double-layer thick $Ca_3Ru_2O_7$ structure, as shown in fig. D.3a. The same

---

[1] VASP setting: LVHAR=.T.

(a) (1×1), full coverage

(b) (1×1), ½ coverage

(c) (2×1), ½ coverage, bright

(d) (2×1), ½ coverage, dark

(e) (3×1), ⅑ coverage

(f) (3×1), ¹⁄₁₈ coverage
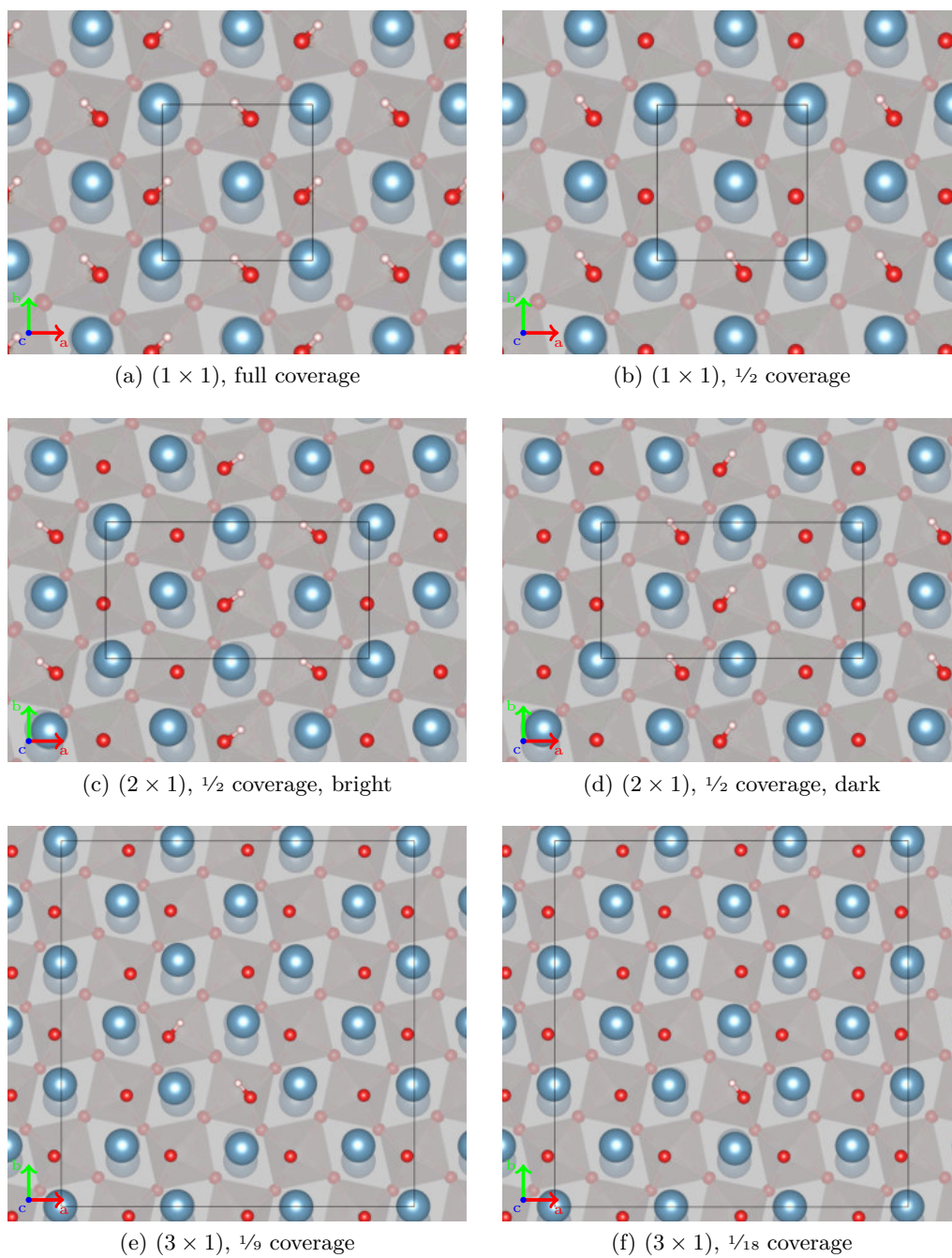
Figure D.2.: Adsorption of atomic hydrogen as a surface hydroxyl on the $Ca_3Ru_2O_7(001)$ surface. Ca, Ru, O, and H atoms coloured blue, grey, red, and white.

321

procedure was performed for the (2×1) model with two O_2^- adsorbed in the zig-zag configuration. Additionally, the vacuum separating the two surfaces in the unit cell was increased. All cells were fully relaxed using the optB86b functional.

Figure D.4 shows a plot of the total local potential along the c axis normal to the surface plane. The maximum of the averaged total local potential in the middle of the vacuum was used to calculate $e\phi$. For the pristine slab and the O_2^- covered model cells, the DFT predicts a work function of $3.07\,\text{eV}$ and $5.44\,\text{eV}$, respectively. Compared to experimental values published by Halwidl, Mayr-Schmölzer, et al. [5] using Kelvin probe force microscopy, the DFT values are very good for the pristine slab but too high for the O_2^- covered surface. The general increase after adsorption of O_2^- is due to the additional surface dipole moment created by the negatively charged adsorbate, which also contributes to the discrepancy to the experimental value.

Table D.3.: Calculated and experimental work function in eV of the pristine and O_2^--covered $Ca_3Ru_2O_7(001)$.

	pristine	O_2^--covered
$-e\phi$	3.52	5.00
E_F	0.449	-0.438
W	3.07	5.44
W_{Exp}	3.00	4.60

E. The O_2 Gas Phase Molecule

E.1. Bond Lengths

To obtain the correct reference structure for the adsorption calculations on $Ca_3Ru_2O_7$ and $Sr_3Ru_2O_7$ the total energy of the O_2 gas phase molecule was obtained from a fully relaxed single molecule calculations. The unit cell used to perform these calculations was chosen to be slightly asymmetric and a sufficient amount of vacuum. The two oxygen atoms were then placed at the origin and at the experimental distance along the z axis. To get the correct triplet state of the O_2 molecule, the calculation has to be started with an initial magnetic moment on both oxygen atoms[1]. For the charged O_2^-, the number of electrons in the system was set to 13[2]. Additionally, the size of the unit cell had to

---

[1] VASP setting: MAGMOM = 1.0 1.0.

[2] VASP setting: NELECT = 13

(a) clean (1×1) double layer slab

(b) $(2 \times 1) + 2\,O_2$, symmetric double layer slab
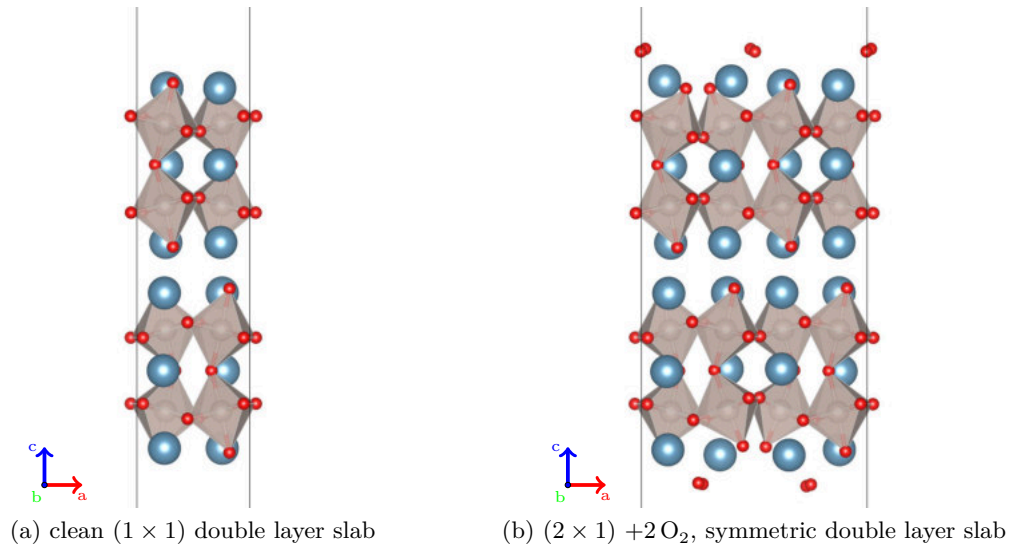
Figure D.3.: Model cells used for the calculation of the local potential. Both consist of two double layers separated by a rock-salt interface. Ca, Ru, O coloured in blue, grey, and red.
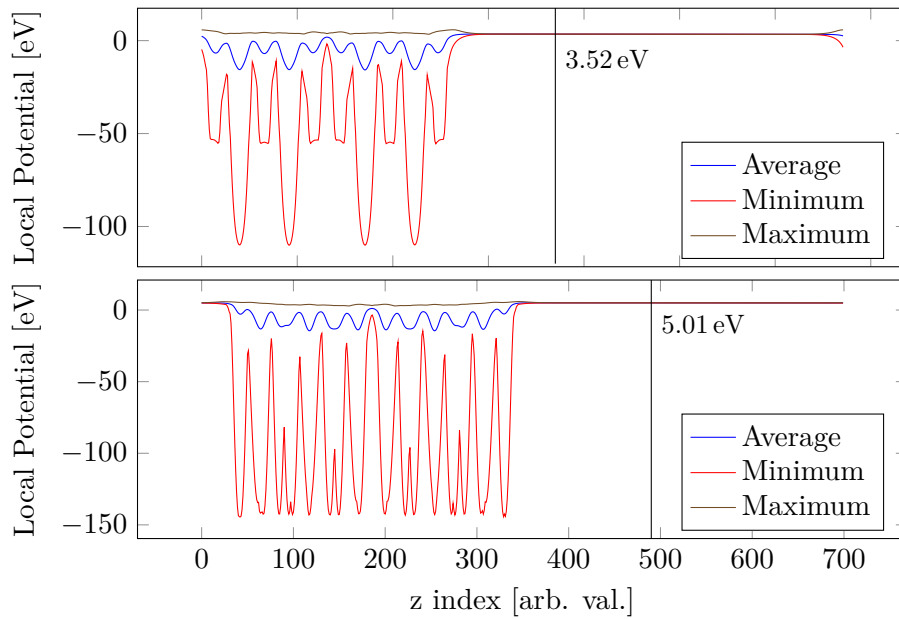
Figure D.4.: Averaged, maximum and minimum of the total local potential parallel to the surface plane. For the pristine slab, the four perovskite layers are easily visible.

be reduced ($a = 7\,\text{Å}$) since due to limitations of the VASP code the proper occupancies could not be achieved, leading to unphysical "ghost states". To compensate for this additional charge, an additional background charge was added to the model cell using the built in dipole correction feature[3]. The cutoff energy was increased to $450\,\text{eV}$ and just one $\vec{k}$-point at the Γ point was used for the calculations.

All functionals yield O–O bond lengths which are about $1.6\,\%$ larger than the experimental values for the O_2 molecule, while the calculations for the charged O_2^- result in O–O distances of about $1.36\,\text{Å}$.

Table E.1.: Bond lengths calculated for the O_2 and O_2^- molecules with various functionals.

[Å]	neutral O_2	superoxide O_2^-
Exp.	1.207 [214]	1.350 [215]
PBE	1.227	1.360
optB86b	1.228	1.356
DFT-D3	1.227	1.360

E.2. Vibrational Frequencies

The vibrational frequencies of the O_2 and O_2^- gas phase molecules were calculated in the same asymmetric model cell at the fully relaxed O–O bond length. The cutoff energy was increased to $450\,\text{eV}$ and just one $\vec{k}$-point at the Γ point was used for the calculations. The vibrational frequencies were calculated using a simple finite differences approach implemented in VASP[4] which yields all phonon frequencies at the Γ point. To properly compare the frequencies to those of the adsorbed molecule the calculations were performed with the PBE, the optB86b, and Grimmes DFT-D3 approach. Compared to the experimental values published by Long and Ewing [214] for the neutral O_2, both PBE and DFT-D3 yield very good agreement, while the optB86b functional predicts a slightly lower number of lines per cm. For the charged molecule the measured vibrational stretching mode is reduced to $1150\,\text{cm}^{-1}$. The DFT results are deviate by a larger amount compared to the neutral O_2, yielding frequencies between $1182\,\text{cm}^{-1}$ and $1194\,\text{cm}^{-1}$, see table E.2.

---

[3]VASP setting: IDIPOL = 4
[4]VASP setting: IBRION = 5

Table E.2.: Vibrational stretching frequencies calculated for the O_2 and O_2^- molecules with various functionals. The measured values were taken from Long and Ewing [214] and Krupenie [216] for O_2 and O_2^-, respectively.

	neutral O_2	superoxide O_2^-
Exp.	1580[214]	1150[216]
PBE	1580	1194
optB86b	1572	1182
DFT-D3	1580	1190

F. PAW Potentials

	Zr	Pt	Pd	O	H
Name	Zr_sv	Pt	Pd	O	H
Date	Jan 04 2005	Jan 05 2001	Jan 04 2001	Apr 08 2002	Jun 15 2001
Default energy cutoff	229.898	230.283	250.925	400.000	250.00
Valence configuration	4s4p5s4d	s1d9	s1d9	s2p4	
Augmentation Energy [eV]	461.257	358.966	416.230	605.392	400.000
Core Radius [a_0]	2.500	2.500	2.600	1.520	1.100

Metal Adatoms (see section 4.1)			

	Au	Ag	Pd	Ni
Name	Au	Ag	Pd	Ni
Date	Oct 04 2007	Apr 02 2005	Jan 04 2005	Aug 02 2007
Default energy cutoff	229.943	249.844	250.925	269.532
Valence configuration	s1d10	s1d10	s2p4	s2p4
Augmentation Energy [eV]	356.670	412.496	416.230	544.565
Core Radius [a_0]	2.500	2.500	2.600	2.300

Table F.1.: PAW potentials bundled with VASP used for all calculations done involving Zirconia presented in chapters 3 and 4 and appendix B.

	Sr	Ca	Ru	O	C	H
Name	Sr_sv	Ca_sv	Ru_sv	O	C	H
Date	Sep 07 2000	Sep 06 2000	Jan 28 2008	Apr 08 2002	Apr 08 2002	Jun 15 2001
Default energy cutoff	229.353	266.622	318.855	400.000	400.000	250.000
Valence configuration	4s4p5s	3s3p4s	4p5s4d	s2p4	s2p2	
Augmentation Energy [eV]	366.804	420.852	556.476	605.392	644.873	400.00
Core Radius [a_0]	2.500	2.300	2.150	1.520	1.500	1.100

Table F.2.: PAW potentials bundled with VASP used for all calculations performed on the ruthenates presented in chapter 5 and appendix D and the binary alkaline oxides described in appendix A.

	Sr	Ca	Ru	O	H
Name	Sr_sv_GW	Ca_sv_GW	Ru_sv_GW	O_GW	H_GW
Date	Mar 23 2010	Mar 31 2010	Mar 23 2010	Mar 19 2012	Apr 21 2008
Default energy cutoff [eV]	224.817	281.430	321.200	434.431	300.000
Valence configuration	4d2 5s0	2sp6s2s0.01	4s4p5s4d	s2p4	
Augmentation Energy [eV]	540.414	478.321	721.356	1139.609	500.000
Core Radius [a_0]	2.800	2.500	2.300	1.600	1.100

Table F.3.: PAW potentials bundled with VASP used for the G_0W_0 and RPA calculations described in chapter 7, introduced by Klimeš et al. [203].

Bibliography

[1] J I J Choi, W Mayr-Schmölzer, et al. "The growth of ultra-thin zirconia films on $Pd_3Zr(0001)$". en. In: *J. Phys. Condens. Matter* 26.22 (June 2014), p. 225003. DOI: 10.1088/0953-8984/26/22/225003.

[2] Daniel Halwidl, Bernhard Stöger, Wernfried Mayr-Schmölzer, et al. "Adsorption of water at the SrO surface of ruthenates". In: *Nat. Mater.* 15.4 (Dec. 2015), pp. 450–455. DOI: 10.1038/nmat4512.

[3] Hao Li, Joong-Il Jake Choi, Wernfried Mayr-Schmölzer, et al. "Growth of an Ultrathin Zirconia Film on Pt_3Zr Examined by High-Resolution X-ray Photoelectron Spectroscopy, Temperature-Programmed Desorption, Scanning Tunneling Microscopy, and Density Functional Theory". In: *J. Phys. Chem. C* (Jan. 2015), pp. 2462–2470. DOI: 10.1021/jp5100846.

[4] Joong Il Jake Choi, Wernfried Mayr-Schmölzer, et al. "Metal Adatoms and Clusters on Ultrathin Zirconia Films". In: *J. Phys. Chem. C* 120.18 (May 2016), pp. 9920–9932. DOI: 10.1021/acs.jpcc.6b03061.

[5] Daniel Halwidl, Wernfried Mayr-Schmölzer, et al. "Ordered hydroxyls on $Ca_3Ru_2O_7(001)$". In: *Nat. Commun.* 8.1 (Dec. 2017), p. 23. DOI: 10.1038/s41467-017-00066-w.

[6] Daniel Halwidl, Wernfried Mayr-Schmölzer, et al. "A Full Monolayer of Superoxide: Oxygen Activation on the Unmodified $Ca_3Ru_2O_7(001)$ Surface". In: *Journal of Materials Chemistry A* (2018). DOI: 10.1039/C8TA00265G.

[7] Peter Lackner, Jan Hulva, Joong-Il Jake Choi, Eva Maria Köck, Wernfried Mayr-Schmölzer, et al. "Water adsorption at zirconia: from the $ZrO_2(111)/Pt_3Zr(0001)$ model system to powder samples". In: *Journal of Materials Chemistry A* (2018). DOI: 10.1039/C8TA04137G.

[8] Wernfried Mayr-Schmölzer, Florian Mittendorfer, and Josef Redinger. "Adsorption of superoxo O_2^- species on the pure and Ca-doped $Sr_3Ru_2O_7(001)$ surface". In: *Surface Science, accepted* (2018).

[9]   Wernfried Mayr-Schmölzer, Daniel Halwidl, et al. "Adsorption of CO on the $Ca_3Ru_2O_7(001)$ surface". In: *Surface Science, accepted* (2018).

[10]   Brian C. H. Steele and Angelika Heinzel. "Materials for fuel-cell technologies". In: *Nature* 414.6861 (Nov. 2001), pp. 345–352. DOI: 10.1038/35104620.

[11]   Eberhard Engel and Reiner M. Dreizler. *Density Functional Theory*. Theoretical and Mathematical Physics. Berlin, Heidelberg: Springer Berlin Heidelberg, 2011. DOI: 10.1007/978-3-642-14090-7.

[12]   M. Born and R. Oppenheimer. "Zur Quantentheorie der Molekeln". In: *Ann. Phys.* 389.20 (1927), pp. 457–484. DOI: 10.1002/andp.19273892002.

[13]   P. Hohenberg and W. Kohn. "Inhomogeneous Electron Gas". In: *Phys. Rev.* 136.3B (Nov. 1964), B864–B871. DOI: 10.1103/PhysRev.136.B864.

[14]   W. Kohn and L. J. Sham. "Self-Consistent Equations Including Exchange and Correlation Effects". In: *Phys. Rev.* 140.4A (Nov. 1965), A1133–A1138. DOI: 10.1103/PhysRev.140.A1133.

[15]   D. M. Ceperley and B. J. Alder. "Ground state of the electron gas by a stochastic method". In: *Phys. Rev. Lett.* 45.7 (1980), pp. 566–569. DOI: 10.1103/PhysRevLett.45.566.

[16]   John P. Perdew, Kieron Burke, and Matthias Ernzerhof. "Generalized Gradient Approximation Made Simple". In: *Phys. Rev. Lett.* 77.18 (Oct. 1996), pp. 3865–3868. DOI: 10.1103/PhysRevLett.77.3865.

[17]   A. D. Becke. "Density-functional exchange-energy approximation with correct asymptotic behavior". In: *Phys. Rev. A* 38.6 (Sept. 1988), pp. 3098–3100. DOI: 10.1103/PhysRevA.38.3098.

[18]   Kieron Burke, John P. Perdew, and Yue Wang. "Derivation of a Generalized Gradient Approximation: The PW91 Density Functional". In: *Electron. Density Funct. Theory*. Boston, MA: Springer US, 1998, pp. 81–111. DOI: 10.1007/978-1-4899-0316-7_7.

[19]   T. C. Leung, C. T. Chan, and B. N. Harmon. "Ground-state properties of Fe, Co, Ni, and their monoxides: Results of the generalized gradient approximation". In: *Phys. Rev. B* 44.7 (1991), p. 2923. DOI: 10.1103/PhysRevB.44.2923.

[20]   K. Terakura et al. "Band theory of insulating transition-metal monoxides: Band-structure calculations". In: *Phys. Rev. B* 30.8 (1984), pp. 4734–4747. DOI: 10.1103/PhysRevB.30.4734.

[21]   S. L. Dudarev et al. "Electron-energy-loss spectra and the structural stability of nickel oxide: An LSDA+U study". In: *Phys. Rev. B* 57.3 (1998), pp. 1505–1509. DOI: 10.1103/PhysRevB.57.1505.

[22]   Takao Kotani. "Ab initio random-phase-approximation calculation of the frequency-dependent effective interaction between 3d electrons: Ni, Fe, and MnO". In: *J. Phys. Condens. Matter* 12.11 (2000), pp. 2413–2422. DOI: 10.1088/0953-8984/12/11/307.

[23] M. Springer and F. Aryasetiawan. "Frequency-dependent screened interaction in Ni within the random-phase approximation". In: *Phys. Rev. B* 57.8 (1998), pp. 4364–4368. DOI: 10.1103/PhysRevB.57.4364.

[24] John P Perdew, Matthias Ernzerhof, and Kieron Burke. "Rationale for mixing exact exchange with density functional approximations Rationale for mixing exact exchange with density functional approximations". In: *J. Chem. Phys.* 105.1996 (1996), pp. 9982–9985. DOI: 10.1063/1.472933.

[25] Jochen Heyd and Gustavo E Scuseria. "Efficient hybrid density functional calculations in solids: assessment of the Heyd-Scuseria-Ernzerhof screened Coulomb hybrid functional." In: *J. Chem. Phys.* 121.3 (July 2004), pp. 1187–92. DOI: 10.1063/1.1760074.

[26] Jochen Heyd, Gustavo E. Scuseria, and Matthias Ernzerhof. "Erratum: "Hybrid functionals based on a screened Coulomb potential" [J. Chem. Phys. 118, 8207 (2003)]". In: *J. Chem. Phys.* 124.21 (2006), p. 219906. DOI: 10.1063/1.2204597.

[27] Jochen Heyd, Gustavo E. Scuseria, and Matthias Ernzerhof. "Hybrid functionals based on a screened Coulomb potential". In: *J. Chem. Phys.* 118.18 (2003), p. 8207. DOI: 10.1063/1.1564060.

[28] Aliaksandr V. Krukau et al. "Influence of the exchange screening parameter on the performance of screened hybrid functionals". In: *J. Chem. Phys.* 125.22 (2006). DOI: 10.1063/1.2404663.

[29] M. Dion et al. "Van der Waals Density Functional for General Geometries". In: *Phys. Rev. Lett.* 92.24 (June 2004), pp. 22–25. DOI: 10.1103/PhysRevLett.92.246401.

[30] Jiří Klimeš, David R Bowler, and Angelos Michaelides. "Chemical accuracy for the van der Waals density functional." In: *J. Phys. Condens. Matter* 22.2 (Jan. 2010), p. 022201. DOI: 10.1088/0953-8984/22/2/022201.

[31] Jiří Klimeš, David Bowler, and Angelos Michaelides. "Van der Waals density functionals applied to solids". In: *Phys. Rev. B* 83.19 (May 2011), pp. 1–13. DOI: 10.1103/PhysRevB.83.195131.

[32] Stefan Grimme et al. "A consistent and accurate ab initio parametrization of density functional dispersion correction (DFT-D) for the 94 elements H-Pu." In: *J. Chem. Phys.* 132.15 (Apr. 2010), p. 154104. DOI: 10.1063/1.3382344.

[33] V M Galitskii. "The energy spectrum of a non-ideal Fermi gas". In: *Sov. Phys. JETP-USSR* 7.1 (1958), pp. 104–112.

[34] V. M. Galitskii and A. B. Migdal. "Application of Quantum Field Theory Methods to the Many Body Problem". In: *Sov. Phys. JETP* 34.1 (1958), p. 96.

[35] F Aryasetiawan and O Gunnarsson. "The GW method". In: *Reports Prog. Phys.* 61.3 (Mar. 1998), pp. 237–312. DOI: 10.1088/0034-4885/61/3/002.

[36] Lars Hedin. "New Method for Calculating the One-Particle Green's Function with Application to the Electron-Gas Problem". In: *Phys. Rev.* 139.3A (Aug. 1965), A796–A823. DOI: 10.1103/PhysRev.139.A796.

[37] M. Shishkin and G. Kresse. "Implementation and performance of the frequency-dependent GW method within the PAW framework". In: *Phys. Rev. B* 74.3 (2006), pp. 1–13. DOI: 10.1103/PhysRevB.74.035101.

[38] Joachim Paier, Martijn Marsman, and Georg Kresse. "Dielectric properties and excitons for extended systems from hybrid functionals". In: *Phys. Rev. B - Condens. Matter Mater. Phys.* 78.12 (2008), pp. 1–4. DOI: 10.1103/PhysRevB.78.121201.

[39] F. Fuchs et al. "Quasiparticle band structure based on a generalized Kohn-Sham scheme". In: *Phys. Rev. B* 76.11 (2007), pp. 1–8. DOI: 10.1103/PhysRevB.76.115109.

[40] Fabien Bruneval and Miguel A L Marques. "Benchmarking the starting points of the GW approximation for molecules". In: *J. Chem. Theory Comput.* 9.1 (2013), pp. 324–329. DOI: 10.1021/ct300835h.

[41] D. C. Langreth and J. P. Perdew. "The exchange-correlation energy of a metallic surface". In: *Solid State Commun.* 17.11 (1975), pp. 1425–1429. DOI: 10.1016/0038-1098(75)90618-3.

[42] O. Gunnarsson and B. I. Lundqvist. "Exchange and correlation in atoms, molecules, and solids by the spin-density-functional formalism". In: *Phys. Rev. B* 13.10 (May 1976), pp. 4274–4298. DOI: 10.1103/PhysRevB.13.4274.

[43] David C Langreth and John P Perdew. "Exchange-correlation energy of a metallic surface: Wave-vector analysis". In: *Phys. Rev. B* 15.6 (Mar. 1977), pp. 2884–2901. DOI: 10.1103/PhysRevB.15.2884.

[44] E. K U Gross and Walter Kohn. "Local density-functional theory of frequency-dependent linear response". In: *Phys. Rev. Lett.* 55.26 (1985), pp. 2850–2852. DOI: 10.1103/PhysRevLett.55.2850.

[45] Erich Runge and E. K U Gross. "Density-functional theory for time-dependent systems". In: *Phys. Rev. Lett.* 52.12 (1984), pp. 997–1000. DOI: 10.1103/PhysRevLett.52.997.

[46] G. Kresse and J. Furthmüller. "Efficient iterative schemes for ab initio total-energy calculations using a plane-wave basis set". In: *Phys. Rev. B* 54.16 (Oct. 1996), pp. 11169–11186. DOI: 10.1103/PhysRevB.54.11169.

[47] G. Kresse and J. Furthmüller. "Efficiency of ab-initio total energy calculations for metals and semiconductors using a plane-wave basis set". In: *Comput. Mater. Sci.* 6.1 (July 1996), pp. 15–50. DOI: 10.1016/0927-0256(96)00008-0.

[48] Peter E. Blöchl, O. Jepsen, and O. K. Andersen. "Improved tetrahedron method for Brillouin-zone integrations". In: *Phys. Rev. B* 49.23 (June 1994), pp. 16223–16233. DOI: 10.1103/PhysRevB.49.16223.

[49] G Kresse and D. Joubert. "From ultrasoft pseudopotentials to the projector augmented-wave method". In: *Phys. Rev. B* 59.3 (Jan. 1999), pp. 1758–1775. DOI: 10.1103/PhysRevB.59.1758.

[50] M. Shishkin and G. Kresse. "Self-consistent GW calculations for semiconductors and insulators". In: *Phys. Rev. B* 75.23 (2007), pp. 1–9. DOI: 10.1103/PhysRevB.75.235102.

[51] M. Shishkin, M. Marsman, and G. Kresse. "Accurate quasiparticle spectra from self-consistent GW calculations with vertex corrections". In: *Phys. Rev. Lett.* 99.24 (2007), pp. 14–17. DOI: 10.1103/PhysRevLett.99.246403.

[52] Judith Harl and Georg Kresse. "Accurate Bulk Properties from Approximate Many-Body Techniques". In: *Phys. Rev. Lett.* 103.5 (July 2009), p. 056401. DOI: 10.1103/PhysRevLett.103.056401.

[53] Judith Harl and Georg Kresse. "Cohesive energy curves for noble gas solids calculated by adiabatic connection fluctuation-dissipation theory". In: *Phys. Rev. B - Condens. Matter Mater. Phys.* 77.4 (2008), pp. 1–8. DOI: 10.1103/PhysRevB.77.045136.

[54] Judith Harl, Laurids Schimka, and Georg Kresse. "Assessing the quality of the random phase approximation for lattice constants and atomization energies of solids". In: *Phys. Rev. B - Condens. Matter Mater. Phys.* 81.11 (2010). DOI: 10.1103/PhysRevB.81.115126.

[55] Merzuk Kaltak, Jiří Klimeš, and Georg Kresse. "Low scaling algorithms for the random phase approximation: Imaginary time and laplace transformations". In: *J. Chem. Theory Comput.* 10.6 (2014), pp. 2498–2507. DOI: 10.1021/ct5001268.

[56] Merzuk Kaltak, Jiří Klimeš, and Georg Kresse. "Cubic scaling algorithm for the random phase approximation: Self-interstitials and vacancies in Si". In: *Phys. Rev. B* 90.5 (Aug. 2014), p. 054115. DOI: 10.1103/PhysRevB.90.054115.

[57] F. D. Murnaghan. "Finite Deformations of an Elastic Solid". In: *Am. J. Math.* 59.2 (Apr. 1937), p. 235. DOI: 10.2307/2371405.

[58] Francis Birch. "Finite Elastic Strain of Cubic Crystals". In: *Phys. Rev.* 71.11 (June 1947), pp. 809–824. DOI: 10.1103/PhysRev.71.809.

[59] Karsten Reuter and Matthias Scheffler. "Composition, structure, and stability of $RuO_2(110)$ as a function of oxygen pressure". In: *Phys. Rev. B* 65.3 (Dec. 2001), p. 035406. DOI: 10.1103/PhysRevB.65.035406.

[60] Aysegul Aygun et al. "Novel thermal barrier coatings that are resistant to high-temperature attack by glassy deposits". In: *Acta Mater.* 55.20 (Dec. 2007), pp. 6734–6745. DOI: 10.1016/j.actamat.2007.08.028.

[61] Isabelle Denry and J. Robert Kelly. "State of the art of zirconia for dental applications". In: *Dent. Mater.* 24.3 (2008), pp. 299–307. DOI: 10.1016/j.dental.2007.05.007.

[62] Stephen A. Steiner et al. "Nanoscale zirconia as a nonmetallic catalyst for graphitization of carbon and growth of single- and multiwall carbon nanotubes". In: *J. Am. Chem. Soc.* 131.34 (2009), pp. 12144–12154. DOI: 10.1021/ja902913r.

[63] David G Barton et al. "Structure and Electronic Properties of Solid Acids Based on Tungsten Oxide Nanostructures". In: *J. Phys. Chem. B* 103.4 (Jan. 1999), pp. 630–640. DOI: 10.1021/jp983555d.

[64] K. Tanabe and T. Yamaguchi. "Acid-base bifunctional catalysis by ZrO_2 and its mixed oxides". In: *Catal. Today* 20.2 (1994), pp. 185–197. DOI: 10.1016/0920-5861(94)80002-2.

[65] Jane P. Chang, You-Sheng Lin, and Karen Chu. "Rapid thermal chemical vapor deposition of zirconium oxide for metal-oxide-semiconductor field effect transistor application". In: *J. Vac. Sci. Technol. B Microelectron. Nanom. Struct.* 19.5 (2001), p. 1782. DOI: 10.1116/1.1396639.

[66] Balázs Králik, Eric Chang, and Steven Louie. "Structural properties and quasiparticle band structure of zirconia". In: *Phys. Rev. B* 57.12 (Mar. 1998), pp. 7027–7036. DOI: 10.1103/PhysRevB.57.7027.

[67] Akihiro Kushima and Bilge Yildiz. "Oxygen ion diffusivity in strained yttria stabilized zirconia: where is the fastest strain?" In: *J. Mater. Chem.* 20.23 (2010), p. 4809. DOI: 10.1039/c000259c.

[68] Xin Xia, Richard Oldman, and Richard Catlow. "Computational Modeling Study of Bulk and Surface of Yttria-Stabilized Cubic Zirconia". In: *Chem. Mater.* 21.15 (Aug. 2009), pp. 3576–3585. DOI: 10.1021/cm900417g.

[69] G. Stapper et al. "Ab initio study of structural and electronic properties of yttria-stabilized cubic zirconia". In: *Phys. Rev. B* 59.2 (Jan. 1999), pp. 797–810. DOI: 10.1103/PhysRevB.59.797.

[70] R. Krishnamurthy et al. "Oxygen Diffusion in Yttria-Stabilized Zirconia: A New Simulation Model". In: *J. Am. Ceram. Soc.* 87.10 (Jan. 2005), pp. 1821–1830. DOI: 10.1111/j.1151-2916.2004.tb06325.x.

[71] W Göpel, G Reinhardt, and M Rösch. "Trends in the development of solid state amperometric and potentiometric high temperature sensors". In: *Solid State Ionics* 136-137.1-2 (Nov. 2000), pp. 519–531. DOI: 10.1016/S0167-2738(00)00410-0.

[72] Yongtie Yan et al. "Solid-state sensor for sulfur oxides based on stabilized zirconia and metal sulphate". In: *Chem. Lett.* 21.4 (Apr. 1992), pp. 635–638. DOI: 10.1246/cl.1992.635.

[73] M. Mori et al. "Cubic-stabilized zirconia and alumina composites as electrolytes in planar type solid oxide fuel cells". In: *Solid State Ionics* 74.3-4 (1994), pp. 157–164. DOI: 10.1016/0167-2738(94)90206-2.

[74] C. J. Howard, R. J. Hill, and B. E. Reichert. "Structures of ZrO_2 polymorphs at room temperature by high-resolution neutron powder diffraction". In: *Acta Crystallogr. Sect. B Struct. Sci.* 44.2 (Apr. 1988), pp. 116–120. DOI: 10.1107/S0108768187010279.

[75] Klaus Meinel et al. "STM, LEED, and DFT characterization of epitaxial ZrO_2 films on Pt(111)". In: *Surf. Sci.* 562.1-3 (Aug. 2004), pp. 204–218. DOI: 10.1016/j.susc.2004.06.035.

[76] Peter Lackner et al. "Construction and evaluation of an ultrahigh-vacuum-compatible sputter deposition source". In: October (2017), pp. 1–6. URL: http://arxiv.org/abs/1710.06377.

[77] Moritz Antlanger, Wernfried Mayr-Schmölzer, et al. "$Pt_3Zr(0001)$: A substrate for growing well-ordered ultrathin zirconia films by oxidation". In: *Phys. Rev. B* 86.3 (July 2012), p. 035451. DOI: 10.1103/PhysRevB.86.035451.

[78] Wernfried Mayr-Schmölzer. "First-Principle Studies of Zirconia and its Interface to Platinum-Zirconium Alloys". Technical University Vienna, 2012. URL: http://permalink.obvsg.at/AC07813958.

[79] F. Mittendorfer et al. "Graphene on Ni(111): Strong interaction and weak adsorption". In: *Phys. Rev. B - Condens. Matter Mater. Phys.* 84.20 (2011), pp. 2–5. DOI: 10.1103/PhysRevB.84.201401.

[80] J Tersoff and Dr Hamann. "Theory and application for the scanning tunneling microscope". In: *Phys. Rev. Lett.* 50.25 (1983), p. 1998. DOI: http://dx.doi.org/10.1103/PhysRevLett.50.1998.

[81] K. Meinel et al. "Surface and interface structures of epitaxial ZrO2 films on Pt(111): Experiment and density-functional theory calculations". In: *Phys. Rev. B* 74.23 (Dec. 2006), p. 235444. DOI: 10.1103/PhysRevB.74.235444.

[82] Jakub Planer. *Ab initio calculations of ultra thin zirconia films and zirconia-rhodium(111) interfaces.* Project report. TU Vienna, 2016.

[83] Joong-Il Jake Choi. "Studies of Zirconia Surfaces On the Atomic Scale". PhD thesis. TU Vienna, 2016. URL: http://katalog.ub.tuwien.ac.at/AC13110516.

[84] L Brewer. "A most striking confirmation of the Engel metallic correlation". In: *Acta Metall.* 15.3 (1967), pp. 553–556. DOI: 10.1016/0001-6160(67)90088-0.

[85] W Hume-Rothery. "The Engel-Brewer theories of metals and alloys". In: *Prog. Mater. Sci.* 13.0 (1968), pp. 229–265. DOI: http://dx.doi.org/10.1016/0079-6425(68)90022-4.

[86] J. K. Stalick and R. M. Waterstrat. "The zirconium-platinum phase diagram". In: *J. Alloys Compd.* 430.1-2 (2007), pp. 123–131. DOI: 10.1016/j.jallcom.2006.04.055.

[87] R.M Waterstrat, A Shapiro, and A Jeremie. "The palladium–zirconium phase diagram". In: *J. Alloys Compd.* 290.1-2 (Aug. 1999), pp. 63–70. DOI: 10.1016/S0925-8388(99)00127-9.

[88] A Raman and K Schubert. "Structural Investigations in some T 4-T 9 Homology and Quasihomology Alloy Systems". In: *Z. Met.* 55.11 (1964), pp. 704–710.

[89] A E Dwight and P E Beck. "Close-packed Ordered Structures in Binary AB$_3$ Alloys of Transition Elements". In: *Trans. Met. Soc. AIME* 215 (1959).

[90] Sam De Waele et al. "Error estimates for density-functional theory predictions of surface energy and work function". In: *Phys. Rev. B* 235418.23 (2016), pp. 1–13. DOI: 10.1103/PhysRevB.94.235418.

[91] Jian Wang and Shao Qing Wang. "Surface energy and work function of fcc and bcc crystals: Density functional study". In: *Surf. Sci.* 630 (2014), pp. 216–224. DOI: 10.1016/j.susc.2014.08.017.

[92] Nicholas E. Singh-Miller and Nicola Marzari. "Surface energies, work functions, and surface relaxations of low-index metallic surfaces from first principles". In: *Phys. Rev. B - Condens. Matter Mater. Phys.* 80.23 (2009), pp. 1–9. DOI: 10.1103/PhysRevB.80.235407.

[93] Abhirup Patra et al. "Properties of real metallic surfaces: Effects of density functional semilocality and van der Waals nonlocality". In: *Proc. Natl. Acad. Sci.* (Oct. 2017), p. 201713320. DOI: 10.1073/pnas.1713320114.

[94] W T Moore, D C Frost, and K A R Mitchell. "The Zanazzi-Jona and Pendry reliability indices compared in LEED crystallographic analyses for five surfaces". In: *J. Phys. C Solid State Phys.* 15.3 (1982), p. L5. DOI: 10.1088/0022-3719/15/3/001.

[95] Antonio Ruiz Puigdollers and Gianfranco Pacchioni. "Reducibility of ZrO_2/Pt_3Zr and ZrO_2/Pt 2D films compared to bulk zirconia: a DFT+U study of oxygen removal and H_2 adsorption". In: *Nanoscale* (2017). DOI: 10.1039/C7NR01904A.

[96] Daniele Stradi et al. "Method for determining optimal supercell representation of interfaces". In: *J. Phys. Condens. Matter* 29.18 (May 2017), p. 185901. DOI: 10.1088/1361-648X/aa66f3.

[97] Javier Carrasco, Andrew Hodgson, and Angelos Michaelides. "A molecular perspective of water at metal interfaces". In: *Nat. Mater.* 11.8 (July 2012), pp. 667–674. DOI: 10.1038/nmat3354.

[98] Javier Carrasco, Jiří Klimeš, and Angelos Michaelides. "The role of van der Waals forces in water adsorption on metals". In: *J. Chem. Phys.* 138.2 (Jan. 2013), p. 024708. DOI: 10.1063/1.4773901.

[99] John W. Arblaster. "Crystallographic Properties of Ruthenium". In: *Platin. Met. Rev.* 57.2 (Apr. 2013), pp. 127–136. DOI: 10.1595/147106713X665030.

[100] Michael Bott et al. "Pt(111) reconstruction induced by enhanced Pt gas-phase chemical potential". In: *Phys. Rev. Lett.* 70.10 (Mar. 1993), pp. 1489–1492. DOI: 10.1103/PhysRevLett.70.1489.

[101] Andreas Stierle. *private communication, unpublished.* 2016.

[102] Shuichi Nosé. "A unified formulation of the constant temperature molecular dynamics methods". In: *J. Chem. Phys.* 81.1 (1984), pp. 511–519. DOI: 10.1063/1.447334.

[103] William G. Hoover. "Canonical dynamics: Equilibrium phase-space distributions". In: *Phys. Rev. A* 31.3 (1985), pp. 1695–1697. DOI: 10.1103/PhysRevA.31.1695.

[104] Martin Setvin et al. "Direct view at excess electrons in TiO_2 rutile and anatase". In: *Phys. Rev. Lett.* 113.8 (2014), pp. 1–5. DOI: 10.1103/PhysRevLett.113.086402.

[105] R. Schaub et al. "Oxygen Vacancies as Active Sites for Water Dissociation on Rutile $TiO_2(110)$". In: *Phys. Rev. Lett.* 87.26 (2001), p. 266104. DOI: 10.1103/PhysRevLett.87.266104.

[106] M. W. Chase. "NIST-JANAF Thermochemical Tables for Oxygen Fluorides". In: *J. Phys. Chem. Ref. Data* 25.2 (1996), pp. 551–603. DOI: 10.1063/1.555992.

[107] Cristina O. De González and Eduardo A. García. "An X-ray photoelectron spectroscopy study of the surface oxidation of zirconium". In: *Surf. Sci.* 193.3 (Jan. 1988), pp. 305–320. DOI: 10.1016/0039-6028(88)90438-4.

[108] Yatsuhisa Nagano. "Standard enthalpy of formation of platinum hydrous oxide". In: *J. Therm. Anal. Calorim.* 69.3 (2002), pp. 831–839. DOI: 10.1023/A:1020651805170.

[109] F J Mompean, J Perrone, and M Illemassène. *Chemical Thermodynamics of Zirconium*. Chemical Thermodynamics. Elsevier Science, 2005. URL: https://books.google.at/books?id=E-2CAg6Mhc4C.

[110] Jan-Dierk Grunwaldt et al. "Comparative Study of Au/TiO_2 and Au/ZrO_2 Catalysts for Low-Temperature CO Oxidation". In: *J. Catal.* 186.2 (1999), pp. 458–469. DOI: 10.1006/jcat.1999.2564.

[111] Xin Zhang, Hai Wang, and Bo Qing Xu. "Remarkable nanosize effect of zirconia in Au/ZrO_2 catalyst for CO oxidation". In: *J. Phys. Chem. B* 109.19 (2005), pp. 9678–9683. DOI: 10.1021/jp050645r.

[112] Juan Li et al. "Influence of zirconia crystal phase on the catalytic performance of Au/ZrO_2 catalysts for low-temperature water gas shift reaction". In: *Appl. Catal. A Gen.* 334.1-2 (2008), pp. 321–329. DOI: 10.1016/j.apcata.2007.10.020.

[113] J.H. Bitter, K. Seshan, and J.A. Lercher. "The State of Zirconia Supported Platinum Catalysts for CO_2/CH_4 Reforming". In: *J. Catal.* 171.1 (1997), pp. 279–286. DOI: 10.1006/jcat.1997.1792.

[114] J. D. McCullough and K. N. Trueblood. "The crystal structure of baddeleyite (monoclinic ZrO_2)". In: *Acta Crystallogr.* 12.7 (July 1959), pp. 507–511. DOI: 10.1107/S0365110X59001530.

[115] A Christensen and Emily Carter. "First-principles study of the surfaces of zirconia". In: *Phys. Rev. B* 58.12 (Sept. 1998), pp. 8050–8064. DOI: 10.1103/PhysRevB.58.8050.

[116] Ricardo Grau-Crespo et al. "Theoretical investigation of the deposition of Cu, Ag, and Au atoms on the $ZrO_2(111)$ surface". In: *J. Phys. Chem. C* 111.111 (2007), pp. 10448–10454. DOI: 10.1021/jp0704057.

[117] Min Yu and Dallas R. Trinkle. "Accurate and efficient algorithm for Bader charge integration". In: *J. Chem. Phys.* 134.6 (2011), pp. 1–8. DOI: 10.1063/1.3553716.

[118] W Tang, E Sanville, and G Henkelman. "A grid-based Bader analysis algorithm without lattice bias." In: *J. Phys. Condens. Matter* 21.8 (2009), p. 084204. DOI: 10.1088/0953-8984/21/8/084204.

[119] Edward Sanville et al. "Improved grid-based algorithm for Bader charge allocation". In: *J. Comput. Chem.* 28.5 (Apr. 2007), pp. 899–908. DOI: 10.1002/jcc.20575.

[120] Graeme Henkelman, Andri Arnaldsson, and Hannes Jónsson. "A fast and robust algorithm for Bader decomposition of charge density". In: *Comput. Mater. Sci.* 36.3 (2006), pp. 354–360. DOI: 10.1016/j.commatsci.2005.04.010.

[121] Richard F.W. Bader. "A Quantum Theory of Molecular Structure and Its Applications". In: *Chem. Rev.* 91.5 (1991), pp. 893–928. DOI: 10.1021/cr00005a013.

[122] R. F. W. Bader. "Atoms in molecules". In: *Acc. Chem. Res.* 18.1 (1985), pp. 9–15. DOI: 10.1021/ar00109a003.

[123] Richard F.W. Bader. "Molecular Fragments or Chemical Bonds?" In: *Acc. Chem. Res.* 8.1 (1975), pp. 34–40. DOI: 10.1021/ar50085a005.

[124] Joachim Paier, Christopher Penschke, and Joachim Sauer. "Oxygen defects and surface chemistry of ceria: Quantum chemical studies compared to experiment". In: *Chem. Rev.* 113.6 (2013), pp. 3949–3985. DOI: 10.1021/cr3004949.

[125] María Marta Branda et al. "On the difficulties of present theoretical models to predict the oxidation state of atomic Au adsorbed on regular sites of $CeO_2(111)$". In: *J. Chem. Phys.* 131.9 (2009). DOI: 10.1063/1.3216102.

[126] Patricia A. Thiel and Theodore E. Madey. "The interaction of water with solid surfaces: Fundamental aspects". In: *Surf. Sci. Rep.* 7.6-8 (1987), pp. 211–385. DOI: 10.1016/0167-5729(87)90001-X.

[127] M Henderson. "The interaction of water with solid surfaces: fundamental aspects revisited". In: *Surf. Sci. Rep.* 46.1-8 (May 2002), pp. 1–308. DOI: 10.1016/S0167-5729(01)00020-6.

[128] G. S. Herman et al. "Experimental Investigation of the Interaction of Water and Methanol with Anatase-$TiO_2(101)$". In: *J. Phys. Chem. B* 107.12 (2003), pp. 2788–2795. DOI: 10.1021/jp0275544.

[129] M. J. Stirniman et al. "The adsorption and desorption of water on single crystal MgO(100): The role of surface defects". In: *J. Chem. Phys.* 105.3 (1996), pp. 1295–1298. DOI: 10.1063/1.471993.

[130] Z. Zhang et al. "Imaging water dissociation on $TiO_2(110)$: Evidence for inequivalent geminate OH groups". In: *J. Phys. Chem. B* 110.43 (2006), pp. 21840–21845. DOI: 10.1021/jp063619h.

[131] Michael A. Henderson and Scott A. Chambers. "HREELS, TPD and XPS study of the interaction of water with the α-$Cr_2O_3(001)$ surface". In: *Surf. Sci.* 449.1-3 (Mar. 2000), pp. 135–150. DOI: 10.1016/S0039-6028(99)01246-7.

[132] Michael A Henderson, Stephen A Joyce, and James R Rustad. "Interaction of water with the (1×1) and (2×1) surfaces of α-$Fe_2O_3(012)$". In: *Surf. Sci.* 417.1 (1998), pp. 66–81. DOI: 10.1016/S0039-6028(98)00662-1.

[133] Sergey V. Ushakov and Alexandra Navrotsky. "Direct measurements of water adsorption enthalpy on hafnia and zirconia". In: *Appl. Phys. Lett.* 87.16 (2005), pp. 1–3. DOI: 10.1063/1.2108113.

[134] Michaela Kogler et al. "Hydrogen surface reactions and adsorption studied on Y_2O_3, YSZ, and ZrO_2". In: *J. Phys. Chem. C* 118.16 (2014), pp. 8435–8444. DOI: 10.1021/jp5008472.

[135] Thomas M. Orlando, Alex B. Aleksandrov, and Janine Herring. "Electron-Stimulated Desorption of H^+, H^{2+}, OH^+, and $H^+(H_2O)_n$ from Water-Covered Zirconia Surfaces". In: *J. Phys. Chem. B* 107.35 (2003), pp. 9370–9376. DOI: 10.1021/jp030117k.

[136] Witold Piskorz et al. "Periodic DFT and Atomistic Thermodynamic Modeling of the Surface Hydration Equilibria and Morphology of Monoclinic ZrO_2 Nanocrystals". In: *The Journal of Physical Chemistry C* 115.49 (Dec. 2011), pp. 24274–24286. DOI: 10.1021/jp2086335.

[137] Satu T. Korhonen, Monica Calatayud, and A. Outi I. Krause. "Stability of Hydroxylated $(\bar{1}11)$ and $(\bar{1}01)$ Surfaces of Monoclinic Zirconia: A Combined Study by DFT and Infrared Spectroscopy". In: *The Journal of Physical Chemistry C* 112.16 (Apr. 2008), pp. 6469–6476. DOI: 10.1021/jp8008546.

[138] A. Von Hippel. "Ferroelectricity, domain structure, and phase transitions of barium titanate". In: *Rev. Mod. Phys.* 22.3 (1950), pp. 221–237. DOI: 10.1103/RevModPhys.22.221.

[139] J. B. Goodenough. "Jahn-Teller Phenomena in Solids". In: *Annu. Rev. Mater. Sci.* 28.1 (Aug. 1998), pp. 1–27. DOI: 10.1146/annurev.matsci.28.1.1.

[140] S. N. Ruddlesden and P. Popper. "New compounds of the K_2NiF_4 type". In: *Acta Crystallogr.* 10.8 (Aug. 1957), pp. 538–539. DOI: 10.1107/S0365110X57001929.

[141] Andrew Peter Mackenzie and Yoshiteru Maeno. "The superconductivity of Sr_2RuO_4 and the physics of spin-triplet pairing". In: *Rev. Mod. Phys.* 75.2 (2003), pp. 657–712. DOI: 10.1103/RevModPhys.75.657.

[142] Y. Maeno et al. "Superconductivity in a layered perovskite without copper". In: *Nature* 372.6506 (Dec. 1994), pp. 532–534. DOI: 10.1038/372532a0.

[143] Yoshiteru Maeno, T. Maurice Rice, and Manfred Sigrist. "The intriguing super-conductivity of strontium ruthenate". In: *Phys. Today* 54.1 (2001), pp. 42–47. DOI: 10.1063/1.1349611.

[144] A. Tamai et al. "Fermi Surface and van Hove Singularities in the Itinerant Meta-magnet $Sr_3Ru_2O_7$". In: *Phys. Rev. Lett.* 101.2 (2008), pp. 9–12. DOI: 10.1103/PhysRevLett.101.026407.

[145] Shin-Ichi Ikeda et al. "Ground state in $Sr_3Ru_2O_7$: Fermi liquid close to a fer-romagnetic instability". In: *Phys. Rev. B* 62.10 (2000), R6089–R6092. DOI: 10.1103/PhysRevB.62.R6089.

[146] R a Borzi et al. "Formation of a nematic fluid at high fields in $Sr_3Ru_2O_7$." In: *Science (80-.).* 315.5809 (2007), pp. 214–217. DOI: 10.1126/science.1134796.

[147] S. A. Grigera. "Magnetic Field-Tuned Quantum Criticality in the Metallic Ruthen-ate $Sr_3Ru_2O_7$". In: *Science (80-.).* 294.5541 (Oct. 2001), pp. 329–332. DOI: 10.1126/science.1063539.

[148] P. B. Allen et al. "Transport properties, thermodynamic properties, and electronic structure of $SrRuO_3$." In: *Phys. Rev. B* 53.8 (1996), pp. 4393–4398. DOI: 10.1103/PhysRevB.53.4393.

[149] L. Klein et al. "Anomalous Spin Scattering Effects in the Badly Metallic Itinerant Ferromagnet $SrRuO_3$". In: *Phys. Rev. Lett.* 77.13 (1996), pp. 2774–2777. DOI: 10.1103/PhysRevLett.77.2774.

[150] Satoru Nakatsuji, Shin Ichi Ikeda, and Yoshiteru Maeno. "Ca_2RuO_4: New Mott Insulators of Layered Ruthenate". In: *J. Phys. Soc. Japan* 66.7 (1997), pp. 1868–1871. DOI: 10.1143/JPSJ.66.1868.

[151] M. Braden et al. "Crystal and magnetic structure of Ca_2RuO_4; Magnetoelas-tic coupling and the metal-insulator transition". In: *Phys. Rev. B* 58.2 (1998), pp. 847–861. DOI: 10.1103/PhysRevB.58.847.

[152] Yoshiyuki Yoshida et al. "Crystal and magnetic structure of $Ca_3Ru_2O_7$". In: *Phys. Rev. B* 72.5 (Aug. 2005), p. 054412. DOI: 10.1103/PhysRevB.72.054412.

[153] L. Walz and F. Lichtenberg. "Refinement of the structure of Sr_2RuO_4 with 100 and 295 K X-ray data". In: *Acta Crystallogr. Sect. C Cryst. Struct. Commun.* 49.7 (July 1993), pp. 1268–1270. DOI: 10.1107/S0108270192013143.

[154] Q. Huang et al. "Neutron Powder Diffraction Study of the Crystal Structures of Sr_2RuO_4 and Sr_2IrO_4 at Room Temperature and at 10 K". In: *J. Solid State Chem.* 112.2 (Oct. 1994), pp. 355–361. DOI: 10.1006/jssc.1994.1316.

[155] J.S. Gardner, G. Balakrishnan, and D.McK. Paul. "Neutron powder diffraction studies of Sr_2RuO_4 and $SrRuO_3$". In: *Phys. C Supercond.* 252.3-4 (Oct. 1995), pp. 303–307. DOI: 10.1016/0921-4534(95)00495-5.

[156] T. Vogt and D. J. Buttrey. "Low-temperature structural behavior of Sr_2RuO_4". In: *Phys. Rev. B* 52.14 (Oct. 1995), R9843–R9846. DOI: 10.1103/PhysRevB.52.R9843.

338

[157] J. J. Neumeier et al. "Magnetic, thermal, transport, and structural properties of $Sr_2RuO_{4+\delta}$: Enhanced charge-carrier mass in a nearly metallic oxide". In: *Phys. Rev. B* 50.24 (Dec. 1994), pp. 17910–17916. DOI: 10.1103/PhysRevB.50.17910.

[158] Hk. Müller-Buschbaum and J. Wilkens. "Ein Beitrag über Sr_2RuO_4 und $Sr_3Ru_2O_7$ Zur Oktaederstreckung von M4+ in K_2NiF_4- und $Sr_3Ti_2O_7$-Typ-Verbindungen". In: *Zeitschrift für Anorg. und Allg. Chemie* 591.1 (Dec. 1990), pp. 161–166. DOI: 10.1002/zaac.19905910118.

[159] Q. Huang et al. "Oxygen displacements and search for magnetic order in $Sr_3Ru_2O_7$". In: *Phys. Rev. B* 58.13 (1998), pp. 8515–8521. DOI: 10.1103/PhysRevB.58.8515.

[160] H. Shaked et al. "Neutron Diffraction Study of the Structural Distortions in $Sr_3Ru_2O_7$". In: *J. Solid State Chem.* 154.2 (2000), pp. 361–367. DOI: 10.1006/jssc.2000.8796.

[161] G Cao, S McCall, and J.E. Crow. "Observation of itinerant ferromagnetism in layered $Sr_3Ru_2O_7$ single crystals". In: *Physical Review B* 55.2 (1997), pp. 672–675. DOI: 10.1103/PhysRevB.55.R672.

[162] Pablo Rivero, Vincent Meunier, and William Shelton. "Half-metallic ferromagnetism in $Sr_3Ru_2O_7$". In: *Phys. Rev. B* 95.19 (May 2017), p. 195106. DOI: 10.1103/PhysRevB.95.195106.

[163] G. Cao et al. "Observation of a Metallic Antiferromagnetic Phase and Metal to Nonmetal Transition in $Ca_3Ru_2O_7$". In: *Phys. Rev. Lett.* 78.9 (1997), pp. 1751–1754. DOI: 10.1103/PhysRevLett.78.1751.

[164] H. Liu et al. "Raman-scattering study of the charge and spin dynamics of the layered ruthenium oxide $Ca_3Ru_2O_7$". In: *Phys. Rev. B* 60.10 (1999), R6980–R6983. DOI: 10.1103/PhysRevB.60.R6980.

[165] C. S. Snow et al. "Pressure-Tuned Collapse of the Mott-Like State in $Ca_{n+1}Ru_nO_{3n+1}$ ($n = 1, 2$): Raman Spectroscopic Studies". In: *Phys. Rev. Lett.* 89.22 (2002), p. 226401. DOI: 10.1103/PhysRevLett.89.226401.

[166] D. J. Singh and S. Auluck. "Electronic Structure and Bulk Spin-Valve Behavior in $Ca_3Ru_2O_7$". In: *Phys. Rev. Lett.* 96.9 (Mar. 2006), p. 097203. DOI: 10.1103/PhysRevLett.96.097203.

[167] Guo-Qiang Liu. "Mott transition and magnetic anisotropy in $Ca_3Ru_2O_7$". In: *Phys. Rev. B* 84.23 (2011), p. 235137. DOI: 10.1103/PhysRevB.84.235137.

[168] Bernhard Stöger et al. "Point defects at cleaved $Sr_{n+1}Ru_nO_{3n+1}$ surfaces". In: *Phys. Rev. B* 90.16 (Oct. 2014), p. 165438. DOI: 10.1103/PhysRevB.90.165438.

[169] I. A. Firmo et al. "Evidence from tunneling spectroscopy for a quasi-one-dimensional origin of superconductivity in Sr_2RuO_4". In: *Phys. Rev. B - Condens. Matter Mater. Phys.* 88.13 (2013), pp. 1–10. DOI: 10.1103/PhysRevB.88.134521.

[170] B. I. Barker et al. "STM studies of individual Ti impurity atoms in Sr_2RuO 4". In: *Phys. B Condens. Matter* 329-333.II (2003), pp. 1334–1335. DOI: 10.1016/S0921-4526(02)02158-0.

[171] Y. Pennec et al. "Cleaving-temperature dependence of layered-oxide surfaces". In: *Phys. Rev. Lett.* 101.21 (2008), pp. 1–4. DOI: 10.1103/PhysRevLett.101.216103.

[172] R. Matzdorf. "Ferromagnetism Stabilized by Lattice Distortion at the Surface of the p-Wave Superconductor Sr_2RuO_4". In: *Science (80-.).* 289.5480 (Aug. 2000), pp. 746–748. DOI: 10.1126/science.289.5480.746.

[173] H. Kambara et al. "Scanning Tunneling Microscopy and Spectroscopy of Sr_2RuO_4". In: *AIP Conf. Proc.* Vol. 850. AIP, 2006, pp. 539–540. DOI: 10.1063/1.2354823.

[174] Guorong Li et al. "Atomic-Scale Fingerprint of Mn Dopant at the Surface of $Sr_3(Ru_{1-x}Mn_x)_2O_7$". In: *Scientific Reports* 3.1 (Dec. 2013), p. 2882. DOI: 10.1038/srep02882.

[175] Jinho Lee et al. "Heavy d-electron quasiparticle interference and real-space electronic structure of $Sr_3Ru_2O_7$". In: *Nat. Phys.* 5.11 (2009), pp. 800–804. DOI: 10.1038/nphys1397.

[176] T Hanaguri. "Development of high-field STM and its application to the study on magnetically-tuned criticality in $Sr_3Ru_2O_7$". In: *J. Phys. Conf. Ser.* 51.1 (Nov. 2006), pp. 514–521. DOI: 10.1088/1742-6596/51/1/117.

[177] R. Matzdorf et al. "Surface structural analysis of the layered perovskite Sr_2RuO_4 by LEED $I(V)$". In: *Phys. Rev. B* 65.8 (2002), p. 085404. DOI: 10.1103/PhysRevB.65.085404.

[178] Bernhard Stöger. "Surface Defects and Adsorption on Strontium Ruthenates". PhD thesis. Technical University Vienna, 2014. URL: http://www.ub.tuwien.ac.at/diss/AC12148236.pdf.

[179] Bernhard Stöger et al. "High Chemical Activity of a Perovskite Surface: Reaction of CO with $Sr_3Ru_2O_7$". In: *Phys. Rev. Lett.* 113.11 (Sept. 2014), p. 116101. DOI: 10.1103/PhysRevLett.113.116101.

[180] Zhe Qu et al. "Complex electronic states in double-layered ruthenates $(Sr_{1-x}Ca_x)_3Ru_2O_7$". In: *Phys. Rev. B - Condens. Matter Mater. Phys.* 80.11 (2009), pp. 1–7. DOI: 10.1103/PhysRevB.80.115130.

[181] Zhe Qu et al. "Effect of disorder on quantum phase transition in the double layered ruthenates $(Sr_{1-x}Ca_x)_3Ru_2O_7$". In: *Phys. Rev. B - Condens. Matter Mater. Phys.* 86.1 (2012), pp. 1–6. DOI: 10.1103/PhysRevB.86.014434.

[182] Jin Peng et al. "Interplay between the lattice and spin degrees of freedom in $(Sr_{1-x}Ca_x)_3Ru_2O_7$". In: *Phys. Rev. B - Condens. Matter Mater. Phys.* 82.2 (2010), pp. 1–8. DOI: 10.1103/PhysRevB.82.024417.

[183] M. A. Peña and J. L.G. Fierro. "Chemical structures and performance of perovskite oxides". In: *Chem. Rev.* 101.7 (2001), pp. 1981–2017. DOI: 10.1021/cr980129f.

[184] Radosław Włodarczyk et al. "Structures of the Ordered Water Monolayer on MgO(001)". In: *J. Phys. Chem. C* 115.14 (Apr. 2011), pp. 6764–6774. DOI: 10.1021/jp200112c.

[185] Xiao Liang Hu et al. "Trends in water monomer adsorption and dissociation on flat insulating surfaces". In: *Phys. Chem. Chem. Phys.* 13.27 (2011), p. 12447. DOI: 10.1039/c1cp20846b.

[186] Henrik Grönbeck and Itai Panas. "*Ab-initio* molecular dynamics calculations of H_2O on BaO(001)". In: *Phys. Rev. B* 77.24 (2008), p. 245419. DOI: 10.1103/PhysRevB.77.245419.

[187] Graeme Henkelman and Hannes Jónsson. "A dimer method for finding saddle points on high dimensional potential surfaces using only first derivatives". In: *J. Chem. Phys.* 111.15 (1999), pp. 7010–7022. DOI: 10.1063/1.480097.

[188] John D. Wrigley, Mark E. Twigg, and Gert Ehrlich. "Lattice walks by long jumps". In: *J. Chem. Phys.* 93.4 (1990), p. 2885. DOI: 10.1063/1.459694.

[189] R. D. Shannon. "Revised effective ionic radii and systematic studies of interatomic distances in halides and chalcogenides". In: *Acta Crystallogr. Sect. A* 32.5 (1976), pp. 751–767. DOI: 10.1107/S0567739476001551.

[190] Lukas Köhler. "Ab-initio Berechnung von Core-Level Shifts mit der PAW Methode". PhD thesis. University of Vienna, 2003, p. 68. URL: http://ubdata.univie.ac.at/AC03767808.

[191] Lukas Köhler and Georg Kresse. "Density functional study of CO on Rh(111)". In: *Phys. Rev. B* 70.16 (Oct. 2004), pp. 1–9. DOI: 10.1103/PhysRevB.70.165405.

[192] M. Malvestuto et al. "Electronic structure trends in the $Sr_{n+1}Ru_nO_{3n+1}$ family ($n = 1, 2, 3$)". In: *Phys. Rev. B* 83.16 (2011), p. 165121. DOI: 10.1103/PhysRevB.83.165121.

[193] Xunhua Zhao et al. "Formation of water chains on CaO(001): What drives the 1D growth?" In: *J. Phys. Chem. Lett.* 6.7 (2015), pp. 1204–1208. DOI: 10.1021/acs.jpclett.5b00223.

[194] S. Royer, D. Duprez, and S. Kaliaguine. "Oxygen mobility in $LaCoO_3$ perovskites". In: *Catal. Today* 112.1-4 (2006), pp. 99–102. DOI: 10.1016/j.cattod.2005.11.020.

[195] Jin Suntivich et al. "Design principles for oxygen-reduction activity on perovskite oxide catalysts for fuel cells and metal–air batteries". In: *Nat. Chem.* 3.8 (2011), pp. 647–647. DOI: 10.1038/nchem.1093.

[196] Kevin J. May et al. "Influence of oxygen evolution during water oxidation on the surface of perovskite oxide catalysts". In: *J. Phys. Chem. Lett.* 3.22 (2012), pp. 3264–3270. DOI: 10.1021/jz301414z.

[197] Rosalba a. Rincón et al. "Activation of oxygen evolving perovskites for oxygen reduction by functionalization with Fe–N_x/C groups". In: *Chem. Commun.* 50.94 (2014), pp. 14760–14762. DOI: 10.1039/C4CC06446A.

[198] Aleksandar Staykov et al. "Oxygen Activation and Dissociation on Transition Metal Free Perovskite Surfaces". In: *Chem. Mater.* 27.24 (Dec. 2015), pp. 8273–8281. DOI: 10.1021/acs.chemmater.5b03263.

[199] Taner Akbay et al. "The interaction of molecular oxygen on LaO terminated surfaces of La_2NiO_4". In: *J. Mater. Chem. A* 4.34 (2016), pp. 13113–13124. DOI: 10.1039/C6TA02715F.

[200] Martin Setvin et al. "Electron transfer between anatase TiO_2 and an O_2 molecule directly observed by atomic force microscopy". In: *Proc. Natl. Acad. Sci.* (2017), p. 201618723. DOI: 10.1073/pnas.1618723114.

[201] C. Puglia et al. "Physisorbed, chemisorbed and dissociated O_2 on Pt(111) studied by different core level spectroscopy methods". In: *Surf. Sci.* 342.1-3 (1995), pp. 119–133. DOI: 10.1016/0039-6028(95)00798-9.

[202] P.A. Redhead. "Thermal desorption of gases". In: *Vacuum* 12.4 (July 1962), pp. 203–211. DOI: 10.1016/0042-207X(62)90978-8.

[203] Jiří Klimeš, Merzuk Kaltak, and Georg Kresse. "Predictive *GW* calculations using plane waves and pseudopotentials". In: *Phys. Rev. B* 90.7 (Aug. 2014), p. 075125. DOI: 10.1103/PhysRevB.90.075125.

[204] Jonathan C. Rienstra-Kiracofe et al. "Atomic and molecular electron affinities: Photoelectron experiments and theoretical computations". In: *Chem. Rev.* 102.1 (2002), pp. 231–282. DOI: 10.1021/cr990044u.

[205] Russell D. III Johnson. *NIST Computational Chemistry Comparison and Benchmark Database*. 2016. URL: http://cccbdb.nist.gov/.

[206] Pierre Villars and Karin Cenzual, eds. *SrO Crystal Structure: Datasheet from "PAULING FILE Multinaries Edition – 2012" in SpringerMaterials*. URL: http://materials.springer.com/isp/crystallographic/docs/sd_0378532.

[207] D. K. Smith and H. R. Leider. "Low-temperature thermal expansion of LiH, MgO and CaO". In: *J. Appl. Crystallogr.* 1.4 (1968), pp. 246–249. DOI: 10.1107/S0021889868005418.

[208] Michael J. Gillan, Dario Alfè, and Angelos Michaelides. "Perspective: How good is DFT for water?" In: *J. Chem. Phys.* 144.13 (Apr. 2016), p. 130901. DOI: 10.1063/1.4944633.

[209] Biswajit Santra et al. "On the accuracy of van der Waals inclusive density-functional theory exchange-correlation functionals for ice at ambient and high pressures". In: *The Journal of Chemical Physics* 139.15 (Oct. 2013), p. 154702. DOI: 10.1063/1.4824481.

[210] Yuan Fang et al. "Ice phases under ambient and high pressure: Insights from density functional theory". In: *Physical Review B* 87.21 (June 2013), p. 214101. DOI: 10.1103/PhysRevB.87.214101.

[211] Biswajit Santra et al. "Hydrogen Bonds and van der Waals Forces in Ice at Ambient and High Pressures". In: *Phys. Rev. Lett.* 107.18 (Oct. 2011), p. 185701. DOI: 10.1103/PhysRevLett.107.185701.

[212] Edward Whalley. "Energies of the phases of ice at zero temperature and pressure". In: *J. Chem. Phys.* 81.9 (Nov. 1984), pp. 4087–4092. DOI: 10.1063/1.448153.

[213] M. Macher et al. "The random phase approximation applied to ice". In: *The Journal of Chemical Physics* 140.8 (Feb. 2014), p. 084502. DOI: 10.1063/1.4865748.

[214] Charles A. Long and George E. Ewing. "Spectroscopic investigation of van der Waals molecules. I. The infrared and visible spectra of $(O_2)_2$*". In: *J. Chem. Phys.* 58.11 (June 1973), pp. 4824–4834. DOI: 10.1063/1.1679066.

[215] Kent M. Ervin et al. "The Only Stable State of O_2^- Is the X $^2\Pi_g$ Ground State and It (Still!) Has an Adiabatic Electron Detachment Energy of 0.45 eV". In: *J. Phys. Chem. A* 107.41 (Oct. 2003), pp. 8521–8529. DOI: 10.1021/jp0357323.

[216] Paul H Krupenie. "The Spectrum of Molecular Oxygen". In: *J. Phys. Chem. Ref. Data* 1.2 (Apr. 1972), pp. 423–534. DOI: 10.1063/1.3253101.

Wernfried Mayr-Schmölzer

Dipl.-Ing.

Personal Information

Date of birth	June 7th, 1983
Nationality	Austria

Education

1989–1993	**Primary School**, *Volksschule der Erzdiözäse Wien*, Vienna, grades 1–4.
1993–2001	**Secondary School**, *Akademisches Gymnasium Wien*, Vienna, grades 5–12.
2001–2012	**Diploma Studies**, *TU Wien*, Vienna, Master Thesis: First-Principles Studies of Zirconia and its Interface to Platinum-Zirconium Alloys. Supervised by Prof. Josef Redinger
2012–2018	**Ph.D. Studies**, *TU Wien*, Vienna, Ph.D. Thesis: Adsorption of Small Molecules and Metal Adatoms on Complex Oxide Surfaces: a Density Functional Theory Study. Supervised by Prof. Josef Redinger

Work

2002–2003	**Civil Service**, *Johanniter Unfall Hilfe*, Vienna.
2003–2005	**Voluntary Community Service**, *Johanniter Unfall Hilfe*, Vienna.

Teaching

2007–2011	**Tutor**, *Institute of Applied Physics*, TU Wien. Tutor for the *Laborübungen I–III* and *Datenverarbeitung I–II* courses.

Publications

[1] W. Mayr-Schmölzer, D. Halwidl, F. Mittendorfer, M. Schmid, U. Diebold, and J. Redinger, "Adsorption of CO on the $Ca_3Ru_2O_7(001)$ surface," *Surface Science, accepted*, Sep. 2018.

[2] W. Mayr-Schmölzer, F. Mittendorfer, and J. Redinger, "Adsorption of superoxo O_2^- species on the pure and Ca-doped $Sr_3Ru_2O_7(001)$ surface," *Surface Science, accepted*, Sep. 2018.

[3] P. Lackner, J. Hulva, J.-I. J. Choi, E. M. Köck, W. Mayr-Schmölzer, J. Pavelec, U. Diebold, F. Mittendorfer, J. Redinger, B. Klötzer, G. S. Parkinson, and M. Schmid, "Water adsorption at zirconia: from the $ZrO_2(111)/Pt_3Zr(0001)$ model system to powder samples," *Journal of Materials Chemistry A*, Aug. 2018. DOI: 10.1039/C8TA04137G.

[4] D. Halwidl, W. Mayr-Schmölzer, M. Setvin, D. Fobes, J. Peng, Z. Mao, M. Schmid, F. Mittendorfer, J. Redinger, and U. Diebold, "A Full Monolayer of Superoxide: Oxygen Activation on the Unmodified $Ca_3Ru_2O_7(001)$ Surface," *Journal of Materials Chemistry A*, Apr. 2018. DOI: 10.1039/C8TA00265G.

[5] D. Halwidl, W. Mayr-Schmölzer, D. Fobes, J. Peng, Z. Mao, M. Schmid, F. Mittendorfer, J. Redinger, and U. Diebold, "Ordered hydroxyls on $Ca_3Ru_2O_7(001)$," *Nat. Commun.*, vol. 8, no. 1, p. 23, Dec. 2017. DOI: 10.1038/s41467-017-00066-w.

[6] J. I. J. Choi, W. Mayr-Schmölzer, I. Valenti, P. Luches, F. Mittendorfer, J. Redinger, U. Diebold, and M. Schmid, "Metal Adatoms and Clusters on Ultrathin Zirconia Films," *J. Phys. Chem. C*, vol. 120, no. 18, pp. 9920–9932, May 2016. DOI: 10.1021/acs.jpcc.6b03061.

[7] D. Halwidl, B. Stöger, W. Mayr-Schmölzer, J. Pavelec, D. Fobes, J. Peng, Z. Mao, G. S. Parkinson, M. Schmid, F. Mittendorfer, J. Redinger, and U. Diebold, "Adsorption of water at the SrO surface of ruthenates," *Nat. Mater.*, vol. 15, no. 4, pp. 450–455, Dec. 2015. DOI: 10.1038/nmat4512.

[8] H. Li, J.-I. J. Choi, W. Mayr-Schmölzer, C. Weilach, C. Rameshan, F. Mittendorfer, J. Redinger, M. Schmid, and G. Rupprechter, "Growth of an Ultrathin Zirconia Film on Pt_3Zr Examined by High-Resolution X-ray Photoelectron Spectroscopy, Temperature-Programmed Desorption, Scanning Tunneling Microscopy, and Density Functional Theory," *J. Phys. Chem. C*, p. 150 127 093 244 008, Jan. 2015. DOI: 10.1021/jp5100846.

[9] J. I. J. Choi, W. Mayr-Schmölzer, F. Mittendorfer, J. Redinger, U. Diebold, and M. Schmid, "The growth of ultra-thin zirconia films on $Pd_3Zr(0001)$," en, *J. Phys. Condens. Matter*, vol. 26, no. 22, p. 225 003, Jun. 2014. DOI: 10.1088/0953-8984/26/22/225003.